LEABHARLANN CHOLÁISTE NA TRÍONÓIDE, BAILE ÁTHA CLIATH | TRINITY COLLEGE LIBRARY DUBLIN
Ollscoil Átha Cliath | The University of Dublin

Terms and Conditions of Use of Digitised Theses from Trinity College Library Dublin

Copyright statement

All material supplied by Trinity College Library is protected by copyright (under the Copyright and Related Rights Act, 2000 as amended) and other relevant Intellectual Property Rights. By accessing and using a Digitised Thesis from Trinity College Library you acknowledge that all Intellectual Property Rights in any Works supplied are the sole and exclusive property of the copyright and/or other IPR holder. Specific copyright holders may not be explicitly identified. Use of materials from other sources within a thesis should not be construed as a claim over them.

A non-exclusive, non-transferable licence is hereby granted to those using or reproducing, in whole or in part, the material for valid purposes, providing the copyright owners are acknowledged using the normal conventions. Where specific permission to use material is required, this is identified and such permission must be sought from the copyright holder or agency cited.

Liability statement

By using a Digitised Thesis, I accept that Trinity College Dublin bears no legal responsibility for the accuracy, legality or comprehensiveness of materials contained within the thesis, and that Trinity College Dublin accepts no liability for indirect, consequential, or incidental, damages or losses arising from use of the thesis for whatever reason. Information located in a thesis may be subject to specific use constraints, details of which may not be explicitly described. It is the responsibility of potential and actual users to be aware of such constraints and to abide by them. By making use of material from a digitised thesis, you accept these copyright and disclaimer provisions. Where it is brought to the attention of Trinity College Library that there may be a breach of copyright or other restraint, it is the policy to withdraw or take down access to a thesis while the issue is being resolved.

Access Agreement

By using a Digitised Thesis from Trinity College Library you are bound by the following Terms & Conditions. Please read them carefully.

I have read and I understand the following statement: All material supplied via a Digitised Thesis from Trinity College Library is protected by copyright and other intellectual property rights, and duplication or sale of all or part of any of a thesis is not permitted, except that material may be duplicated by you for your research use or for educational purposes in electronic or print form providing the copyright owners are acknowledged using the normal conventions. You must obtain permission for any other use. Electronic or print copies may not be offered, whether for sale or otherwise to anyone. This copy has been supplied on the understanding that it is copyright material and that no quotation from the thesis may be published without proper acknowledgement.

Chiral Lanthanide-Directed Self-Assembly: Ligand Substitution as a Path to Functionally Diverse Supramolecular Complexes

David F. Caffrey, B.A. (Mod.)

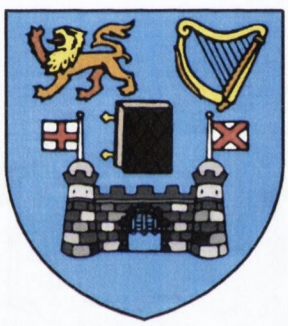

University of Dublin
Trinity College

Based on research carried out under the direction of
Prof. Thorfinnur Gunnlaugsson

A thesis submitted to the School of Chemistry, University of Dublin, Trinity College for the degree of Doctor of Philosophy

TRINITY COLLEGE
5 JAN 2015
LIBRARY DUBLIN

Thesis 10808

Declaration

This thesis is submitted for the degree of Doctor of Philosophy to the University of Dublin, Trinity College and has not been submitted before for any degree or examination to this or any other university. Other than where acknowledged, all work described herein is original and carried out by the author alone. Permission is granted so that the Library may lend or copy this thesis upon request. This permission covers only single copies made for study purposes, subject to normal conditions of acknowledgment.

David F. Caffrey

Acknowledgements

First and foremost, I would like to extend great thanks to my supervisor Prof. Thorri Gunnlaugsson for his constant enthusiasm, guidance and encouragement throughout my Trinity years.

I wish to thank all the members of staff in the School of Chemistry, with special mention given to Dr. John O'Brien, Dr. Manuel Ruether, Dr. Martin Feeney, and Dr. Gary Hessman for their assistance with characterisation.

I would like to take this time to offer my deepest thanks to the TG group. Firstly, thanks to the past group members (would need another 300 pages to list you all!) who I've waved out the door in my time here. Can't believe you all left me behind! To drop a few names, big thanks to Rob and Brian. I think the group misses the craic you guys brought to the place, especially on nights out. For fear of my life, I dare not forget Ms. Truman and Ms. Boyle! To Elaine, I honestly don't think I could survive without the constant updates you provide on the lives of the latest Z-list celebrities *du jour*, so thanks for keeping me up to speed and for being a good friend. To Laura, all I can say is thank you for your personal recommendation! All jokes aside, thanks for being a great friend from undergrad, right to now. I can always count on you for a bit of unintentional comedy (always at your expense). Suppose the biggest complement/insult I can give is that you've never changed. To Stefano, thanks for introducing me to the wonders of Rocco.

Massive thank you to all the post-docs; Steve, Oxana, Miguel, Emma, Komala, and Salvador. Steve and Oxana, I'll never be able to thank you guys enough for the help you've given me these past years. I'll be forever indebted to you two. More importantly, though, you've been great friends this whole time, and I've really enjoyed meeting up outside the confines of work. The same goes for Miguel, the calming influence of the group. Thank you for all your help with the X-ray analysis, I really appreciate it. P.S. I know you enjoy being a post-doc and all, but I promise to do my best to get you that private investigator job you've always dreamed of.

Huge thanks to the PhD crew; Dawn, Joe, Esther, Fergus, Sachi, and Sam. To Dawn, you've been a friend right from the start. I'd like to say we've come a long way together, but we've been stuck in Trinity since forever so I suppose I can nix that idea. Thanks Joe for reminding me, even in the murky depths of thesis writing, that my #futurematters. Fergus, look after yourself, and try and survive the PhD experience (meant literally, broken glass is extremely dangerous!). To Sachi, you've been a good friend and a great addition to the group, make sure to go home at some stage though eh. Sam, I leave in your capable hands a project on the cusp of greatness.

Going beyond the walls of Trinity College, a big thanks to the LNO gang for shaving a few years off my life! Thinking back to Erasmus and Regensburg, I have to mention both Brian and Jeff. To Brian, cheers for the lunchtime shoots over in McTurcaills. Delighted we're now both "owning it" in the corporate world. Jeff, thanks must be given for bringing a bit of class, decency, and a voice of reason to an otherwise depraved mob.

To my family, thanks for all the support throughout my never-ending student years. No more, I promise! That said, I fully expect you to read every last page of this thesis. No more excuses for not knowing what I've been doing these last four years. On a more serious note though, thanks for standing by me in difficult times these past few years and, more importantly, for always inspiring me to work hard and educate myself.

Lastly, the biggest thanks must go to Esther. I couldn't have got through this whole ordeal without your support and, most of all, endless patience. You've helped pick me up these past few months when the going got a bit tough and, for that, I'll never be able to thank you enough. Happy times to come now. I can finally get them big money jobs and spoil you rotten....within reason though!!!

"Life is a series of experiences, each one of which makes us bigger, even though sometimes it is hard to realise this. For the world was built to develop character, and we must learn that the setbacks and grieves which we endure help us in our marching onward."

Henry Ford

Abstract

Entitled "Chiral Lanthanide-Directed Self-Assembly: Ligand Substitution as a Path to Functionally Diverse Supramolecular Complexes", this thesis is divided into seven chapters.

Chapter 1, the introduction, aims to address topics pertinent to the research described in the following chapters. This chapter begins with an overview of the lanthanide metal ions, detailing the advantages offered by their unique photophysical and magnetic properties. An account of the various strategies employed for their inclusion into supramolecular complex designs is then given, focusing primarily on the macrocyclic and self-assembly approaches. Upon review of some recent lanthanide macrocyclic systems, the remainder of the chapter serves to introduce lanthanide-directed self-assembly. A comprehensive literature review of relevant examples of monometallic, multimetallic, and chiral lanthanide self-assemblies is first provided, before later describing related systems developed previously within the Gunnlaugsson group, the designs of which inspired this PhD project.

Chapter 2 presents the synthesis and photophysical evaluation of a series of chiral luminescent Eu(III) self-assembly complexes, distinguished from one another by their ligand pyridyl *para*-substituent. The analysis of these systems, which include propyl-, propargyl-, and polyethoxy-substituted analogues, is communicated as a comparative study, exploring the impact of the ligand substituent on a range of complex properties. Complex formation and stability in solution were probed through photophysical titrations, with the polyethoxy derivatives permitting study in a partially aqueous solvent medium. Their luminescence efficiencies were further established through quantum yield measurements. Ultimately, the effects of the substituent, in terms of both stability and quantum yield, were proven to be mostly negligible, confirming this modification strategy to be an effective one.

Chapter 3 investigates the ability of chiral Eu(III) self-assemblies, analogous to those described in Chapter 2, but with terminal dibenzo[24]crown-8 macrocycles, to form tris[2]-pseudorotaxanes with a novel histaminyl(ferrocenylmethyl)ammonium thread. On account of the electron donating character of the ferrocenyl group, threading was predicted to induce concomitant Eu(III)-centred emission quenching. Accordingly, photophysical titrations were relied upon to evaluate the occurrence of the threading event. A sensible series of control titrations were also performed to help strengthen the argument for formation of the desired higher-order structures.

Chapter 4 discusses the *Click Chemistry*-mediated delivery of an acetyl-protected β-D-galacto-pyranoside unit to the pyridyl 4-position of the same ligand framework used in Chapters 2 and 3 for tris-chelate formation. Spectrophotometric titrations in CH_3CN verified that the terminally appended monosaccharide moiety did not impede the self-assembly of

tris-chelates with Eu(III). Analogous measurements in competitive protic methanol yielded inconsistent, unexplainable results, with further experiments supporting the existence of a kinetic effect in this case. In reference to potential bio-application, these glycosylated self-assemblies have been developed as model systems to aid in the future design of comparable systems capable of interacting with lectin proteins. Interactions of this nature will allow for cell binding specificity, facilitating the application of complexes of this kind as bio-imaging agents.

Chapter 5 describes the design and synthesis of chiral multimetallic Eu(III) edifices, using self-assembly methods, from ditopic chiral ligands which possess the same binding motif as those reported in Chapters 2 – 4. Extensive analysis, with particular emphasis on photophysical studies, affirmed the construction of polynuclear complexes with 2:3 (M:L) stoichiometries, both *in situ* and synthetically. For these systems, a tetrahedral structure is proposed, consisting of four Eu(III) ions and six ligand molecules, where the metal ions are positioned at the four vertices of a tetrahedron.

Chapter 6 chronicles the development of a series of luminescent multimeric ternary lanthanide-cyclen self-assemblies, and is split into two main parts. The first part of this chapter is devoted to photophysically evaluating the production of dimeric ternary Eu(III)- and Tb(III)-cyclen complexes from a bridging ditopic dpa-based linker and triacetamide-substituted cyclen complexes. Conclusive proof of formation of the dimeric species was attained by non-linear regression analysis fitting of the luminescence titration data. The ability of the ternary Tb(III) analogue to function as a responsive anion sensor was later demonstrated in luminescent displacement assays where, to varying extents, anions were shown to trigger a *switching off* of the metal-centred emission upon Tb(III) binding. The second part of this chapter is concerned with the formation of trimeric ternary Eu(III)- and Tb(III)-cyclen complexes from a tritopic carboxylate ligand in aqueous solution, with this design validated by photophysical means.

Finally, Chapter 7 outlines the experimental procedures, and presents the synthesis and characterisation of the compounds discussed within this thesis. Following this, literature references and Appendices are provided, the latter containing supplementary experimental data to support the work described in the main text.

Abbreviations

$1/T_1$	spin-lattice relaxation rate
$1/T_2$	spin-spin relaxation rate
A	proportionality constant
A	absorption
Å	angstrom (1×10^{-10} M)
A^-	anion
A:C	anion to complex ratio
A_L	absorption of left-handed polarised light
$A_{MD,0}$	spontaneous emission probability of the $J = 0$ transition *in vacuo*
Ar	antenna ground state
A_R	absorption of right-handed polarised light
ar	aryl
^{1}Ar	antenna singlet excited state
^{3}Ar	antenna triplet excited state
AuNP	gold nanoparticle
B	brightness
bipy	bipyridines
$\beta_{M:L}$	overall stability constant
br	broad
BSA	bovine serum albumin
^{t}Bu	tert-butyl
C:T	complex to thread ratio
carbo	carbohydrate
CD	circular dichroism
CHO	Chinese hamster ovarian cells
cm	centimetre
CN	coordination number
COSY	correlation spectroscopy
Cp	cyclopentadiene
CPL	circularly polarised luminescence
CuAAC	Cu(I)-catalysed azide-alkyne cycloaddition
cyclen	1,4,7,10-tetraazacyclododecane
δ	chemical shift

D	doublet
Dd	doublet of doublets
Dm	decimetre
DMAP	4-(dimethylamino)pyridine
DMF	dimethylformamide
DNA	deoxyribonucleic acid
DO3A	1,4,7,10-tetraazacyclododecane-1,4,7-triacetic acid
DOTA	1,4,7,10-tetraazacyclododecane-1,4,7,10-tetraacetic acid
DOTAla	1,4,7,10-tetraazacyclododecane-1,4,7-triacetic acid-10-alanine
Dpa	dipicolinic acid
DTPA	diethylene triamine pentaacetic acid
ε	molar absorption coefficient
E	energy
E	integrated emission
EDCI.HCl	*N*-(3-dimethylaminopropyl)-*N'*-ethylcarbodiimide
eq.	equivalent
ES	electrospray ionisation
ET	energy transfer
EtOAc	ethyl acetate
EtOH	ethanol
FRET	fourier resonance energy transfer
G	gram
g_{lum}	luminescence dissymmetry factor
GLUT	glucose transporter
H	hour
Hex	hexane
HRMS	high resolution mass spectrometry
HMBC	heteronuclear multi-bond correlation spectroscopy
HOBt	1-hydroxybenzotriazole hydrate
HOMO	highest occupied molecular orbital
HPLC	high performance liquid chromatography
HSQC	heteronuclear single-quantum correlation spectroscopy
Hz	hertz
H*v*	energy
I	emission intensity

I_0	emission intensity in absence of substrate
I_L	emission intensity of left-handed polarised light
Im	imidazole
I_R	emission intensity of left-handed polarised light
IR	infrared
ISC	intersystem crossing
I_{tot}/I_{MD}	total integrated emission to integrated emission ratio for $J = 0$ transition
J	coupling constant
K	kelvin
kHz	kilohertz
$K_{M:L}$	stepwise stability constant
$k_{O\text{-}D}$	rate constant in deuterated solvent
$k_{O\text{-}H}$	rate constant in non-deuterated solvent
L	ligand
L:C	ligand to complex ratio
λ_{exc}	excitation wavelength
LMCT	ligand-to-metal charge transfer
Ln	lanthanide
*Ln	lanthanide excited state
LUMO	lowest unoccupied molecular orbital
M	molar or molecular ion (as relevant)
M	multiplet
m.p.	melting point
m/z	mass to charge ratio
M:L	metal to ligand ratio
MALDI	matrix-assisted laser absorption ionisation
MeOD	deuterated methanol
MeOH	methanol
Mg	milligram
MHz	megahertz
Min	minute
mL	millilitre
mM	millimolar
MM2	molecular mechanics
Mmol	millimole

MOF	metal-organic framework
Mol	mole
MRI	magnetic resonance imaging
Ms	millisecond
N	solvent refractive index
Naph	naphthalene
NIH-3t3	mouse skin fibroblasts
NIR	near-infrared
Nm	nanometre
NMR	nuclear magnetic resonance
Ns	nanosecond
η_{sens}	efficiency of ligand-to-metal energy transfer
OLED	organic light emitting diode
PC-3	human prostate cancer cells
PET	photo-induced electron transfer
pH	$-\log [H_3O^+]$
Phta	phthalimide
pK_a	$-\log K_a$ where K_a is the acidity constant
Ppm	parts per million
Py	pyridine
Pybox	pyridine-bis(oxazoline)
Q	quencher
Q	quartet
Q	number of metal-bound water molecules
Q_L^{Ln}	luminescence quantum yield
Q_{Ln}^{Ln}	intrinsic quantum yield
R	donor-acceptor distance
RBF	round bottomed flask
RT	room temperature
S	electron spin
S	singlet or second (as relevant)
S_0	singlet ground state
S_1	first singlet excited state
T	luminescent lifetime
T	triplet

T_1	first triplet excited state
T_{1e}	electron relaxation time
TAME	1,1,1-tris(aminomethyl)ethane
TBA	tetrabutylammonium
TEA	triethylamine
THF	tetrahydrofuran
τ_{obs}	observed lifetime
TOCSY	total correlation spectroscopy
$\tau_{O\text{-}D}$	lifetime in deuterated solvent
$\tau_{O\text{-}H}$	lifetime in non-deuterated solvent
τ_{rad}	radiative lifetime
Ts	tosyl
TsCl	4-toluenesulfonyl chloride
UV-vis	ultraviolet-visible
μM	micromolar
ms	microsecond
V	volt
v/*v*	volume to volume ratio
w/*v*	weight to volume ratio
x	number of metal-bound N-H oscillators

Table of Contents

Chapter 1 – Introduction

1 Introduction 1

1.1 Lanthanide metal ions 2

1.1.1 Properties and advantages 2

1.1.2 Photophysical properties of the lanthanides 3

1.1.3 Lanthanide luminescent quenching 9

1.2 Principles of efficient ligand design for lanthanides 10

1.3 Lanthanide macrocyclic complexes 12

1.3.1 Various applications of lanthanide-based aza macrocycles 13

1.4 Lanthanide self-assembly 17

1.4.1 Monometallic lanthanide self-assemblies 18

1.4.2 Multimetallic lanthanide self-assemblies 24

1.5 Chirality and the lanthanides 29

1.5.1 Chiroptical spectroscopic techniques: circular dichroism and circularly polarised luminescence 30

1.5.2 Conferring chirality to luminescent lanthanide complexes 32

1.5.3 Chiral self-assembly 32

1.6 Advances in the Gunnlaugsson research group 35

1.6.1 Modifying the Trinity Sliotar 37

1.7 Work described within this thesis 40

Chapter 2 – Synthesis and Photophysical Evaluation of Chiral Luminescent Lanthanide Sliotar Complexes

2 Introduction 43

2.1 Design of the enantiomeric ligand pairs 41 – 43 44

2.2 Synthesis and characterisation of the enantiomeric ligand pairs 41 – 43 45

2.3 Solid state X-ray crystallographic analysis of ligand 43R 48

2.4 Synthesis and characterisation of Eu(III) complexes of 41 – 43 49

2.5 Solid state X-ray crystallographic analysis of Eu(III) complexes 52

2.6 Photophysical properties of Eu.(41 – 43)$_3$ 55

2.7 Circular dichroism studies of ligands 41 – 43 and their Eu(III) complexes 56

2.8 Circularly polarised luminescence studies of Eu.(41 – 43)$_3$ 58

2.9 Determination of metal-bound water molecules for Eu.(41 – 43)$_3$ 60

2.10 UV-vis and luminescence titration studies 61

2.10.1 Titration experimental details 62

2.10.2 UV-vis and luminescence titrations of **43R** with Eu(CF_3SO_3)$_3$ in CH_3CN 63

2.10.3 UV-vis and luminescence titrations of **43R** with Eu(CF_3SO_3)$_3$ in MeOH 64

2.10.4 UV-vis and luminescence titrations of **43R** with Eu(CF_3SO_3)$_3$ in H_2O/MeOH 66

2.10.5 Determination of complex binding constants 67

2.10.6 Fitting of the titration data 68

2.11 Quantum yield and sensitisation efficiency determination 72

2.12 Conclusion 75

Chapter 3 – Photophysical Investigation of Tris[2]pseudorotaxane Self-Assembly with Crown Ether-Sliotar Conjugates

3 Introduction 77

3.1 Design of the enantiomeric ligand pair 51S and 51R and the histaminyl-(ferrocenylmethyl)ammonium thread 56 80

3.2 Synthesis and characterisation of the enantiomeric ligand pair 51S and 51R and the histaminyl(ferrocenylmethyl)ammonium thread 56 80

3.3 Synthesis and characterisation of Eu(III) complexes of 51S and 51R 85

3.4 Photophysical properties of Eu.51S$_3$ and Eu.51R$_3$ 87

3.5 Circular dichroism studies of ligands 51S and 51R and their Eu(III) complexes 88

3.6 Circularly polarised luminescence studies of Eu.51S$_3$ and Eu.51R$_3$ 89

3.7 Determination of metal-bound water molecules for Eu.51S$_3$ and Eu.51R$_3$ 90

3.8 UV-vis and luminescence titration studies of 51S and 51R 91

3.8.1 Titration experimental and data fitting details 92

3.8.2 UV-vis and luminescence titrations of **51R** with Eu(CF_3SO_3)$_3$ in $CHCl_3$/CH_3CN 92

3.9 Photophysical investigation of tris[2]pseudorotaxane formation 95

3.9.1 Titration experimental and data fitting details 95

3.9.2 UV-vis and luminescence titrations of **Eu.51S$_3$** with thread **56** in $CHCl_3$/CH_3CN 96

3.9.3 Control spectrophotometric titrations of **Eu.41S$_3$** and **Eu.43S$_3$** with thread **56** in $CHCl_3/CH_3CN$ **100**

3.9.4 Control spectrophotometric titrations of **Eu.41S$_3$**, **Eu.43S$_3$**, and **Eu.51S$_3$** with thread **53** in $CHCl_3/CH_3CN$ **105**

3.9.5 UV-vis spectroscopic investigation into the interaction of threads **53** and **56** with the dibenzo[24]crown-8 compound **63** **108**

3.10 Conclusion **111**

Chapter 4 – Synthesis and Photophysical Analysis of Glycosylated Sliotar Derivatives

4 Introduction **115**

4.1 Design of the enantiomeric ligand pair 69S and 69R **117**

4.2 Synthesis and characterisation of the enantiomeric ligand pair 69S and 69R **118**

4.3 Synthesis and characterisation of Eu(III) complexes of 69S and 69R **121**

4.4 Photophysical properties of Eu.69S$_3$ and Eu.69R$_3$ **123**

4.5 Circular dichroism studies of ligands 69S and 69R and their Eu(III) complexes **124**

4.6 Circularly polarised luminescence studies of Eu.69S$_3$ and Eu.69R$_3$ **125**

4.7 Determination of metal-bound water molecules for Eu.69S$_3$ and Eu.69R$_3$ **126**

4.8 UV-vis and luminescence titration studies of 69S and 69R **127**

4.8.1 Titration experimental and data fitting details **127**

4.8.2 UV-vis and luminescence titrations of **69S** with $Eu(CF_3SO_3)_3$ in CH_3CN **128**

4.9 Kinetic studies with Eu.69S$_3$ in CH_3CN and MeOH **131**

4.10 Conclusion **133**

Chapter 5 – Design and Photophysical Evaluation of Chiral Multimetallic Lanthanide Self-Assemblies

5 Introduction **137**

5.1 Design of the enantiomeric ligand pair 72S and 72R **138**

5.2 Synthesis and characterisation of the enantiomeric ligand pair 72S and 72R **138**

5.3 UV-vis and luminescence titration studies of 72S and 72R **141**

5.3.1 Titration experimental and data fitting details **141**

5.3.2 UV-vis and luminescence titrations of **72R** with $Eu(CF_3SO_3)_3$ in $CHCl_3/CH_3CN$ 142

5.4 Synthesis and characterisation of Eu(III) complexes of 72S and 72R 146

5.5 Determination of metal-bound water molecules for Eu.72S and Eu.72R (M:L = 2:3) 148

5.6 Circular dichroism studies of ligands 72S and 72R and their Eu(III) complexes 149

5.7 Circularly polarised luminescence studies of Eu.72S and Eu.72R (M:L = 2:3) 150

5.8 Conclusion 152

Chapter 6 – Development of Multimeric Ternary Lanthanide-Cyclen Systems for Application in Anion Sensing

6 Introduction 155

6.1 Design of the dimeric ternary cyclen complex 86-$(Ln.75)_2$ 161

6.2 Synthesis and characterisation of ligand 86 and complex Ln.75 162

6.3 UV-vis and luminescence titration studies of 86 and Ln.75 165

6.3.1 Titration experimental and data fitting details 165

6.3.2 UV-vis and luminescence titrations of **86** with **Eu.75** in MeOH 166

6.3.3 UV-vis and luminescence titrations of **86** with **Tb.75** in MeOH 169

6.4 Luminescent displacement assays for the detection of anions by 86-$(Tb.75)_2$ 171

6.4.1 Experimental and data fitting details for luminescent displacement assays 172

6.4.2 Results of luminescent displacement assays 172

6.5 Design of the trimeric ternary cyclen complex 87-$(Ln.75)_3$ 176

6.6 UV-vis and luminescence titration studies of 87 and Ln.75: titration experimental and data fitting details 178

6.6.1 UV-vis and luminescence titrations of **87** and **Eu.75** in 0.1 M Tris buffer (pH 7.4) 178

6.6.2 UV-vis and luminescence titrations of **87** and **Tb.75** in 0.1 M Tris buffer (pH 7.4) 181

6.7 Conclusion 184

Chapter 7 – Experimental

7 General experimental details 187

7.1 UV-vis absorption and luminescence spectroscopy 188

7.2 Luminescence lifetime measurements 189

7.3 Circular dichroism and circularly polarised luminescence measurements 189

7.4 X-ray crystallographic characterisation 190

7.5 General experimental procedures 191

7.6 Experimental details for Chapter 2 191

7.7 Experimental details for Chapter 3 200

7.8 Experimental details for Chapter 4 206

7.9 Experimental details for Chapter 5 209

7.10 Experimental details for Chapter 6 212

References

References 217

Appendices

Appendices – Method Theory 229

Appendix 2 232

Appendix 3 271

Appendix 4 290

Appendix 5 297

Appendix 6 304

Chapter 1

Introduction

1 Introduction

The field of supramolecular chemistry represents an area of scientific research that is constantly expanding and evolving, with its foundations firmly rooted in three fundamental concepts; fixation, coordination, and recognition. Principally based upon the formation of highly complex molecular systems by the association of two or more chemical species, this multidisciplinary field has, through its application, helped to bridge the gap between the chemical, biological, and physical sciences.[1,2] The construction of such supramolecular systems is primarily achieved by exploitation of a whole host of non-covalent intermolecular interactions including hydrogen bonding, metal-coordination, π-π stacking, electrostatic binding, and van der Waals forces, and has led to the discovery of a vast array of complex structures with extensive functionalities in disciplines as varied as materials chemistry,[3,4] catalysis,[5,6] and biological and cellular imaging.[7,8]

This relatively new area of research received the ultimate endorsement in 1987 when Charles J. Pedersen, Donald J. Cram, and Jean-Marie Lehn were awarded the Nobel Prize in Chemistry for their studies dedicated to the development and investigation of crown ethers,[9] cavitands,[10] and cryptands,[11,12] respectively. Such an achievement served to profoundly inspire chemists endeavouring to gain a greater understanding of the nature of the non-covalent host-guest and molecular recognition processes that underpin the creation of these supramolecular species, and has influenced the synthesis of a range of suitable acyclic and macrocyclic ligands such as polyaminocarboxylates,[13] podands,[14] porphyrins,[15] and calixarenes.[16] Self-assembly embodies a comparably more contemporary approach geared towards the design of advanced complex entities, and takes advantage of both the metal electric field and weak intermolecular interactions to self-assemble small molecular building blocks around a metal ion.[12,17]

In recent years, Gunnlaugsson and co-workers, in addition to the groups of Bünzli, Piguet, Raymond *etc.* have devoted significant research efforts towards marrying the desired electronic properties of the lanthanide metal ions with the underlying principles of the self-assembly strategy of engineering elaborate luminescent mono and multimetallic edifices and devices. The work described in this thesis, therefore, signifies an opportunity to expand on this acquired knowledge base, with the main objective being the design, synthesis, and analysis of novel chiral luminescent lanthanide supramolecular self-assembled complexes. In order to grant a full understanding and appreciation of the research detailed within this thesis, this introduction chapter will aim to cover the relevant topics, beginning with an explanation of the special characteristics of the lanthanide metal ions, namely their distinctive

photophysical and magnetic properties, before introducing some salient examples of their use in supramolecular chemistry.

1.1 Lanthanide metal ions

The unique magnetic and photophysical properties of the lanthanide series have received great attention in recent times, most notably within the domain of supramolecular chemistry.[18,19] Vitally, the past few years have witnessed immense efforts made in the construction of novel structurally defined lanthanide-based supramolecular systems.[20] Built with a view to exploiting the highly distinctive features of the metal, these systems provide applicability in a wide variety of diverse areas, examples being the development of superior organic light-emitting diodes (OLEDs),[3,21] pH sensors,[22-24] and luminescent bioprobes.[25,26] As a result of the characteristic coordination chemistry of the lanthanide metal ions, there presently exists a strong demand for the controlled metal-directed formation of functional supramolecular lanthanide architectures from modest building blocks. However, the employment of lanthanide ions to template the synthesis of luminescent supramolecular structures is comparatively less explored to that achieved with transition metal ions.[27,28] Consequently, the work discussed in this thesis intends to address this deficit.

1.1.1 Properties and advantages

The lanthanides (Ln) reside within the *f*-block of the periodic table of elements, consisting of the fifteen elements from lanthanum (^{57}La) to lutetium (^{71}Lu). Contrary to the fact that the name translates as *rare earth*, the Ln metals are in fact quite prevalent in nature, each more common in the earth's crust than gold, silver, or platinum. They are quite unique among the elements, with the exception of the actinides, in resembling each other so markedly in their chemical properties, particularly oxidation states.[28,29] Known to exist in their most stable trivalent state, the Ln(III) ions have been shown to possess [Xe]$4f^n$ (n = 0 – 14) electronic configurations characterised by a gradual filling of the 4*f* orbitals, which are effectively shielded from the external environment by filled outer core 5*s* and 5*p* subshells.[28,30] Each member also displays a close chemical and coordination behavioural homogeneity owing to the small, regular decrease in ionic radius across the *f*-block series; this phenomenon being termed the *lanthanide contraction*.[31] Furthermore, the Ln(III) metal ions have the ability to form strong coordinating bonds of a non-directional electrostatic nature with an assortment of ligands due to their associated high charge densities and ionisation potentials.[31] They can therefore be described as being hard Lewis acids, demonstrating a specific binding preference for ligands containing atoms of a hard Lewis

basic character, for example, oxygen, nitrogen, or fluorine. Additionally, in light of the large and variable coordination numbers of these metal ions, ranging from eight to nine in solution, optimisation of this strategy for the formation of high stability lanthanide complexes necessitates the incorporation of several hard donor atoms into the ligand structure. In an effort to capitalise on this, complexation of Ln(III) ions commonly involves the use of combinations of amines and carboxylic groups as ligands.[32]

However, it is the unique magnetic and photophysical properties they exhibit that famously attract the chemical community, appealing especially to those operating within the realm of supramolecular chemistry, for which unlimited possibilities from an application standpoint can be envisaged.[33,34] The distinctive photophysical properties of the Ln(III) and the advantages they present will be detailed in the next section.

1.1.2 Photophysical properties of the lanthanides

Most applications of Ln(III) supramolecular devices are derived from the fine-tuning of the metal optical features and coordination requirements.[28] The unique spectroscopic properties affiliated with the Ln(III) are essentially a product of the shielding of the 4*f* electrons from the ligand field by the $5s^2$ and $5p^6$ orbitals. It is these 4*f* electrons that are capable of undergoing intraconfigurational *f-f* electronic transitions, giving rise to spectra presenting characteristic narrow line-like emission bands that can span both the ultraviolet-visible (UV-vis) and near-infrared (NIR) regions.[35,36] Excluding both La(III) and Lu(III), the majority of the Ln(III) ions are luminescent; luminescence being a term used for a whole range of phenomena caused by radiative decay, *via* photon emission, from an electronically excited state.[30,31] While some bear fluorescent character [Pr(III), Nd(III), Ho(III), Er(III), and Yb(III)], others have phosphorescent character [orange Sm(III), red Eu(III), Gd(III) which emits in the UV, green Tb(III), yellow Dy(III), and blue Tm(III)] or display both.[19] Fluorescence is, by definition, a spin-allowed $S_1 \rightarrow S_0$ emission process that occurs without spin conversion and within a time frame of $10^{-12} - 10^{-6}$ s, this being in direct contrast with phosphorescence, which is a slower process that involves a change in spin multiplicity ($T_1 \rightarrow S_0$), taking from 10^{-6} s to as much as several seconds.[19,28,37] Population of the Ln(III) excited state can be typically attained by direct excitation of an electron into a higher energy 4*f* orbital, as well as through energy transfer from the surroundings of the metal ion. As a consequence, the intensity of the subsequent emission has been found to be directly linked to how efficiently this excited state(s) can be populated and so, as a result, some Ln(III) are more emissive than others.[18,31]

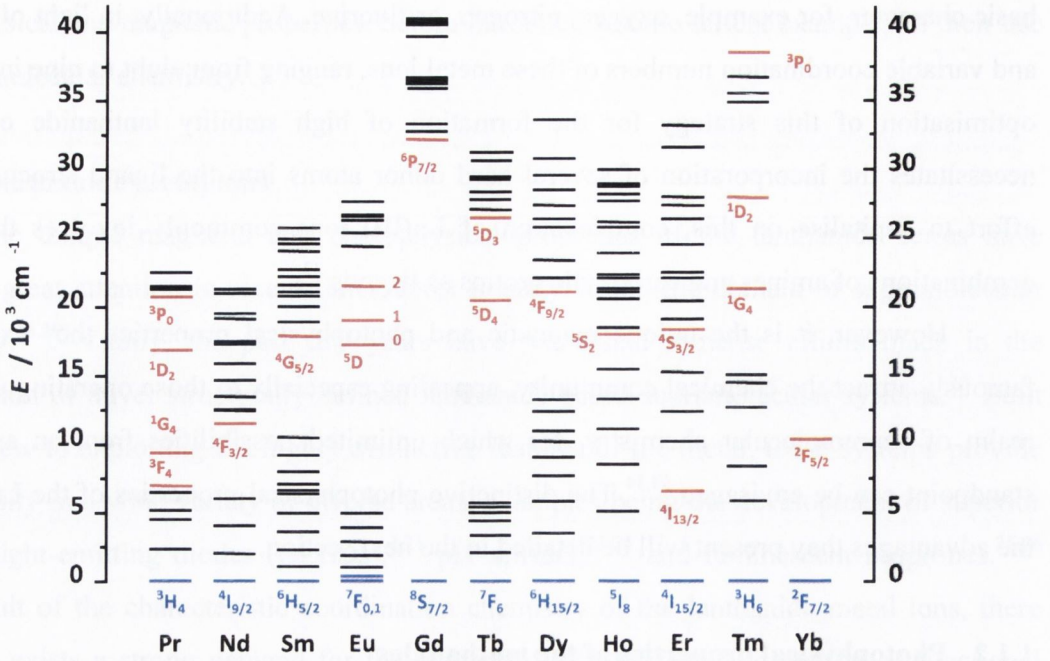

Figure 1.1: *Partial energies diagram for the Ln(III) aquo ions. The main luminescent levels are drawn in red, while the ground state level is indicated in blue.*[28]

Considering the vast array of electronic levels generated by the Ln(III) ions, it can also be seen how the intrinsic quantum yields (Q_{Ln}^{Ln}) and, hence, emission properties of the metals differ significantly depending on the size of the energy gap between the lowest excited state and the highest vibronic level of the ground state (Figure 1.1).[28] Deactivation of the excited state by light emission is permanently in competition with quenching by non-radiative processes, usually in the form of energy transfer to alternative vibrational modes that approximately match the energy gap, such as high frequency O-H and N-H oscillators present in various solvent molecules and often incorporated into the ligand design.[38,39] Accordingly, the smaller the gap existing between the highest occupied (HOMO) and lowest unoccupied (LUMO) molecular orbitals of the Ln(III), the more facile deactivation by means of non-radiative pathways becomes, ultimately delivering a reduced emission efficiency. Eu(III) and Tb(III), which both emit in the visible region, demonstrate the highest relative luminescence efficacy of the series on account of their large energy gaps, $\Delta E_{Eu}(^5D_0 \rightarrow {}^7F_6) = 12300\ cm^{-1}$ and $\Delta E_{Tb}(^5D_4 \rightarrow {}^7F_0) = 14800\ cm^{-1}$, as depicted in Figure 1.1, facilitating their use as practical luminescent devices.[40,41]

Ln(III) luminescence is known to be long-lived as deactivation of the excited state depends on Laporte forbidden *f-f* transitions. These transitions entail a parity disallowed redistribution of electrons within the 4*f* subshell, affording lifetimes of emission falling in the range of microseconds [Yb(III) and Nd(III)] to milliseconds [Eu(III) and Tb(III)].[42] This

delay in excited state luminescence decay, coupled with the observed long wavelength emissions that exhibit narrow line-like bands, makes the Ln(III) ions extremely attractive candidates for employment into time-gated luminescent probes and sensors for application *in vivo*.[43,44] High contrast *in vivo* optical imaging has traditionally suffered from several intrinsic effects caused by the interaction of light with biological tissues, namely scattering and the autoflourescence of different endogenous molecules upon UV-vis irradiation. However, the possibility of time-resolved detection methods that operate by virtue of a delay in excitation of the probe and measurement of the luminescence has helped pave the way for the use of Ln(III) in biological imaging.[45,46] Such a delay permits the short-lived autoflourescence (ns timescale) and light scattering of the biological background to decay to negligible levels (Figure 1.2), providing a vastly enhanced signal-to-noise ratio.[42,47,48]

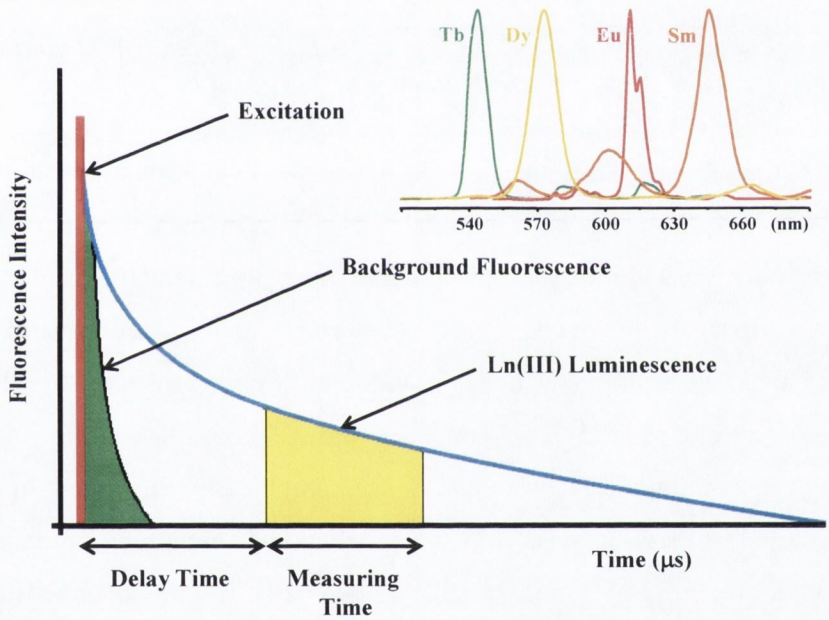

Figure 1.2: *Illustration of the time delay between excitation and recording of the emission, to avoid short-lived autoflourescence. (Inset) Emission spectra of luminescent β-diketonate complexes of Tb(III), Dy(III), Eu(III), and Sm(III).*[47]

Despite the previously described appeal of the Ln(III), there exists a number of drawbacks associated with their use that demand studied attention. One of the major disadvantages that must be recognised and overcome in order to maximise their capability as luminescent probes is that excitation of the metal ion is dependent on these aforementioned spin-forbidden *f-f* electronic transitions. Interactions with the outside chemical environment are limited by shielding of the 4*f* orbitals, resulting in remarkably faint and narrow transitions, characterised by very low molar absorption coefficients (ε) (often less than 4 M^{-1}

cm^{-1}),[49,50] and making direct excitation very inefficient.[48,51] An intense laser beam can be in fact used to circumvent this problem to yield the characteristic Ln(III) emission.[52]

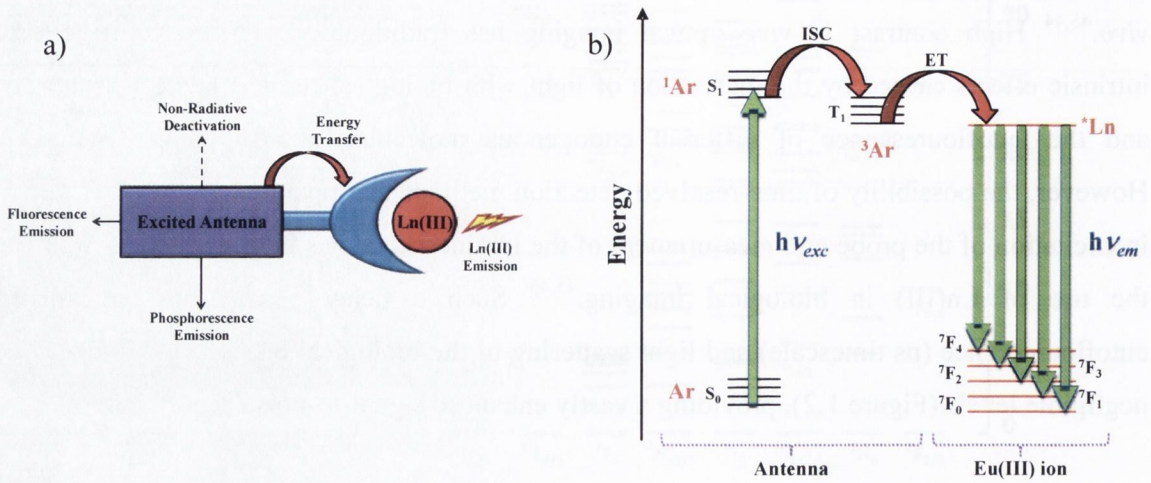

Figure 1.3: *a) Schematic representation of the antenna effect. b) Simplified Jablonski diagram showing the most probable sensitisation pathway for a Eu(III) ion.*[53]

However, the most proficient and versatile way of solving this dilemma is through the so-called *antenna effect*, whereby high molar absorptivity sensitising chromophores function as antennae with the ability to transfer the energy absorbed to the Ln(III) excited state, shown schematically in Figure 1.3a. Aromatic and polyaromatic groups are typically selected to fulfil this sensitisation function, which is rendered more effective by the measured incorporation of these π-rich moieties into appropriate coordinating ligands.[42,51,54] This indirect form of generating Ln(III) luminescence, graphically illustrated in a simplified Jablonski diagram (that does not take into account ligand-to-metal charge transfer (LMCT) and intermolecular processes) (Figure 1.3b),[53,55] generally occurs in three steps: (i) light harvesting by the aromatic antennae of the ligand, (ii) energy transfer to the metal ion, and (iii) metal-centred emission.

The sensitisation pathway is initiated by the absorption of a photon of light ($h\nu$), the wavelength of which corresponds to the excitation energy required by the antenna ground state (Ar) to generate a singlet excited state (^{1}Ar). This energy is subsequently transferred to the antenna triplet state (^{3}Ar) *via* intersystem crossing (ISC), a spin-forbidden phenomenon. Nevertheless, the probability of singlet-triplet transitions occurring is emphatically increased by the presence of the coordinated heavy metal atom, which promotes improved spin-orbit coupling, thus aiding ISC.[56] Population of the Ln(III) excited state (*Ln), $^5D_0$ in the case of Eu(III), is realised through an intramolecular energy transfer process (ET) from the triplet state of the sensitising unit. From this point, radiative deactivation from this populated state

to the electronic levels of the ground state, ^7F_J for Eu(III) ($J = 0 - 6$), gives rise to the representative Ln(III) emission spectrum.

Careful consideration must be paid to numerous factors shown to play an integral role in the competency of the energy transfer from ligand to Ln(III). Selection of a suitable antenna requires the chromophore triplet excited state energy to lie at least 1700 cm^{-1} above that of the accepting Ln(III) level.[42] Thermally activated back energy transfer adept at repopulating the triplet state comes into effect if this energy gap is less than 1500 cm^{-1}, raising the lifetime of ^3Ar and, in turn, the likelihood of quenching by non-radiative modes. The two most extensively studied visible-emitting Ln(III) ions, Eu(III) and Tb(III), have their excited states ($^5D_0$ and $^5D_4$) positioned at 17200 cm^{-1} and 20500 cm^{-1}, respectively. For this reason, chromophores such as bipyridines,[57] terpyridines,[58] substituted phenyls,[59] and naphthyl groups[60] have become popular choices.

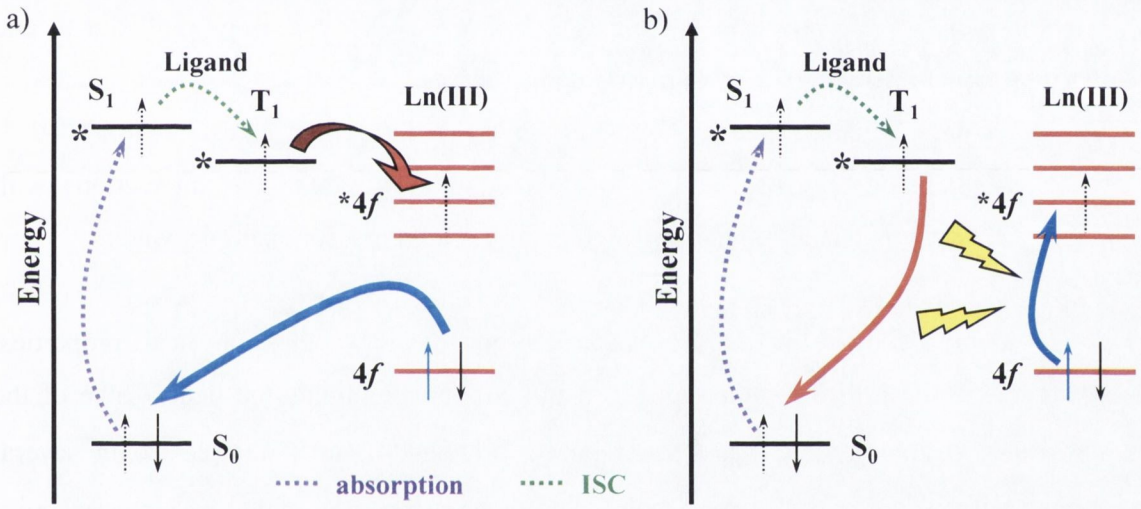

Figure 1.4: *a) Schematic representation of the Dexter (exchange), and b) Förster (dipole-dipole) mechanisms for energy transfer.*[61]

There are two postulated mechanisms used to describe the energy transfer process that sensitises the Ln(III) excited state; the Dexter (exchange) mechanism (Figure 1.4a) and the Förster (dipole-dipole) mechanism (Figure 1.4b), both of which display a strict distance dependence.[62,63] The former is a through-bond, short range interaction that involves a double electron transfer and, as such, needs a favourable overlap between the donor ligand and acceptor metal orbitals. The relationship that governs this dependence on the distance between the antenna and Ln(III) is defined as e^{-r} dependency, where r represents the donor-acceptor distance.[62] With regards to the latter, the Förster mechanism is proposed to operate by means of the coupling between the respective dipole moments of the antenna triplet state

and that of the 4*f* orbitals of the Ln(III). Contrastingly, this is a through-space interaction that holds a dependency factor of r^{-6}.[63] Indeed, there is frequent debate amongst those in the scientific community as to which of the two hypotheses holds true. Regardless, the strength of both pathways can be boosted by reducing the distance between the metal ion and excited chromophore, leading to enhanced photophysical properties.

Consistently in competition with both the sensitisation of the metal and its subsequent emission are a variety of non-radiative and radiative deactivations modes not depicted in Figure 1.3b.[30,42,50] In an effort to secure exceptionally emissive Ln(III)-based systems, it is imperative that these pathways are minimised. They include:

- Spin-allowed radiative decay from the ^{1}Ar singlet excited state to the Ar ground state manifesting as ligand-centred fluorescence.
- Spin-forbidden radiative decay from the ^{3}Ar triplet excited state to the Ar ground state manifesting as ligand-centred phosphorescence.
- Non-radiative deactivation of the ^{1}Ar singlet excited state by collisional and vibrational interactions with surrounding molecules.
- Molecular oxygen assisted quenching of the ^{3}Ar triplet excited state.
- Non-radiative decay of the Ln(III) excited state by vibrational interactions with surrounding molecules containing high energy oscillators, for example, water.

In summary, the Ln(III) ions benefit from desirable photophysical properties. Examination of the information presented in this section highlights the dependence of the luminescence quantum yields (Q_L^{Ln}) of ligand-coordinated Ln(III) complexes on several important factors.[64] Efficient ^{1}Ar $\rightarrow$ ^{3}Ar intersystem crossing is promoted by increased spin-orbit coupling attributed to the presence of the heavy metal, while meticulous ligand design that aims to bridge the distance between the antenna and the Ln(III) metal centre can ensure effective energy transfer. By taking the above measures, the lifetimes of both the ^{1}Ar and ^{3}Ar excited states can be successfully shortened, consequently helping to minimise these effects. Of all these detrimental factors, however, it is the combination of non-radiative quenching processes that ultimately proves to be most crucial in determining the final luminescence efficacy. The long lifetime of the Ln(III) excited state, and its susceptibility to non-radiative vibrational deactivation by a collection of high frequency oscillators (O-H, N-H, and to a lesser extent C-H) is of particular relevance,[38,39] and will be elaborated on in the following section.

1.1.3 Lanthanide luminescent quenching

As discussed earlier, vibrational energy transfer from the Ln(III) excited state to coordinated or diffusing high frequency oscillators, most notably water molecules, results in quenching of the luminescence. This represents one of the major competitive deactivation pathways and transpires *via* energy transfer from the Ln(III) excited state to energy-matched O-H stretching vibrations. Accordingly, lower Ln(III) excited state energies provide for more proficient energy dissipation by this mechanism,[65] with experimental studies demonstrating the number of metal-bound water molecules (q) to be directly proportional to the rate of quenching. This relationship has been mathematically quantified by Horrocks and co-workers for empirical calculation of the number of O-H oscillators directly bound to the metal ion centre in Eu(III) complexes,[66,67] with refinement delivered by Parker *et al.* to account for the effect of N-H vibrations.[38] The method is derived from the assumption that, in deuterated solvents, the relatively low energy O-D oscillators have a minimal contribution to the deactivation process.[47] Through measurement of the difference in luminescent lifetimes in both H_2O ($\tau_{O\text{-}H}$) and D_2O ($\tau_{O\text{-}D}$), the hydration state (q value) can be calculated from **Equation 1.1**, used exclusively for Eu(III) complexes.

$$q^{Eu(III)} = A[(1/\tau_{O\text{-}H} - 1/\tau_{O\text{-}D}) - 0.25 - 0.075x] \pm 0.5 \qquad \textbf{Equation 1.1}$$

A is termed the proportionality constant and is specific for a given Ln(III) ion, 1.2 ms in the case of Eu(III) in water. The correction terms of − 0.25 and − 0.075 correspond to the quenching by second sphere water molecules and N-H oscillators, respectively, where x is the number of these N-H oscillators bound to the metal.

The undeniable effect of vibration-induced deactivation processes on luminescent Ln(III) species cannot be understated. For that very reason, numerous considerations must be made when synthesising appropriate ligands for complexation. A strong desire currently exists among supramolecular chemists to create emissive Ln(III) materials possessing rigid metal environments free of high energy vibrations and capable of obstructing solvent-coordination, underlining the need for polydentate ligands incorporating light-harvesting chromophores into their structures.[42,68,69] The fundamental principles behind the intelligent design of ligands for the effective coordination and sensitisation of Ln(III) will be discussed in the next section.

1.2 Principles of efficient ligand design for lanthanides

Supramolecular chemistry has long been concerned with the rationalisation of innovative ligand design to facilitate the construction of complex molecular edifices. In addition to the previously explained features with respect to energy transfer processes and the minimisation of non-radiative deactivation, synthetic chemists are constantly challenged in the development of robust complexation strategies that recognise and successfully negate many of the obstacles inherent to the use of the Ln(III).[28] The chemical lability and large coordination requirements of these rare earth ions symbolise two such difficulties that must be navigated, the former serving as a major hindrance to potential *in vivo* application.[19] In view of this, endeavouring to improve both the thermodynamic and kinetic stabilities of the resulting complex becomes of paramount importance when tailoring ligands for facile Ln(III)-coordination.

The metal complexation process is known to be primarily driven by entropic factors, with dehydration of both cation and ligand(s) acting as the main driving force in aqueous solution by way of the associated positive entropy contribution to the overall Gibbs free energy. This conclusion can be made from the fact that the dehydration step is endothermic and thermodynamically unfavourable.[19,28] Utilising polydentate ligands that require minimal reorganisation and are equipped to saturate the inner metal coordination sphere has been comprehensively proven to be the best synthetic approach for accessing luminescent Ln(III) supramolecular architectures of high stability. Through the presence of multiple hard donor atoms, ligands of this variety permit stronger metal-binding interactions on account of the accompanied chelate effect.[19]

The properties of Ln(III) complexes are evidenced to be intrinsically linked to the geometry around the metal centre, this being typically trigonal prismatic or square antiprismatic.[30] Figure 1.5 illustrates the three main methodologies developed over the past decades for constructing functional mono and multimetallic Ln(III) edifices of different geometries. The first approach is centred around the use of macrocyclic ligands, desired for their ability to fully enclose the Ln(III) ion and fulfil the high coordination demands of the metal (Figure 1.5a).[70] An alternative strategy that provides the chemist with an excellent handle to control complex stoichiometry while simultaneously achieving advantageous thermodynamic stabilities is built upon the employment of acyclic polydentate ligands or podands (Figure 1.5b).[71-74] Lastly, self-assembly serves to empower the chemist with the necessary means to access sophisticated multicomponent edifices through the action of the metal actively directing smaller complementary ligands around its centre (Figure 1.5c).[75]

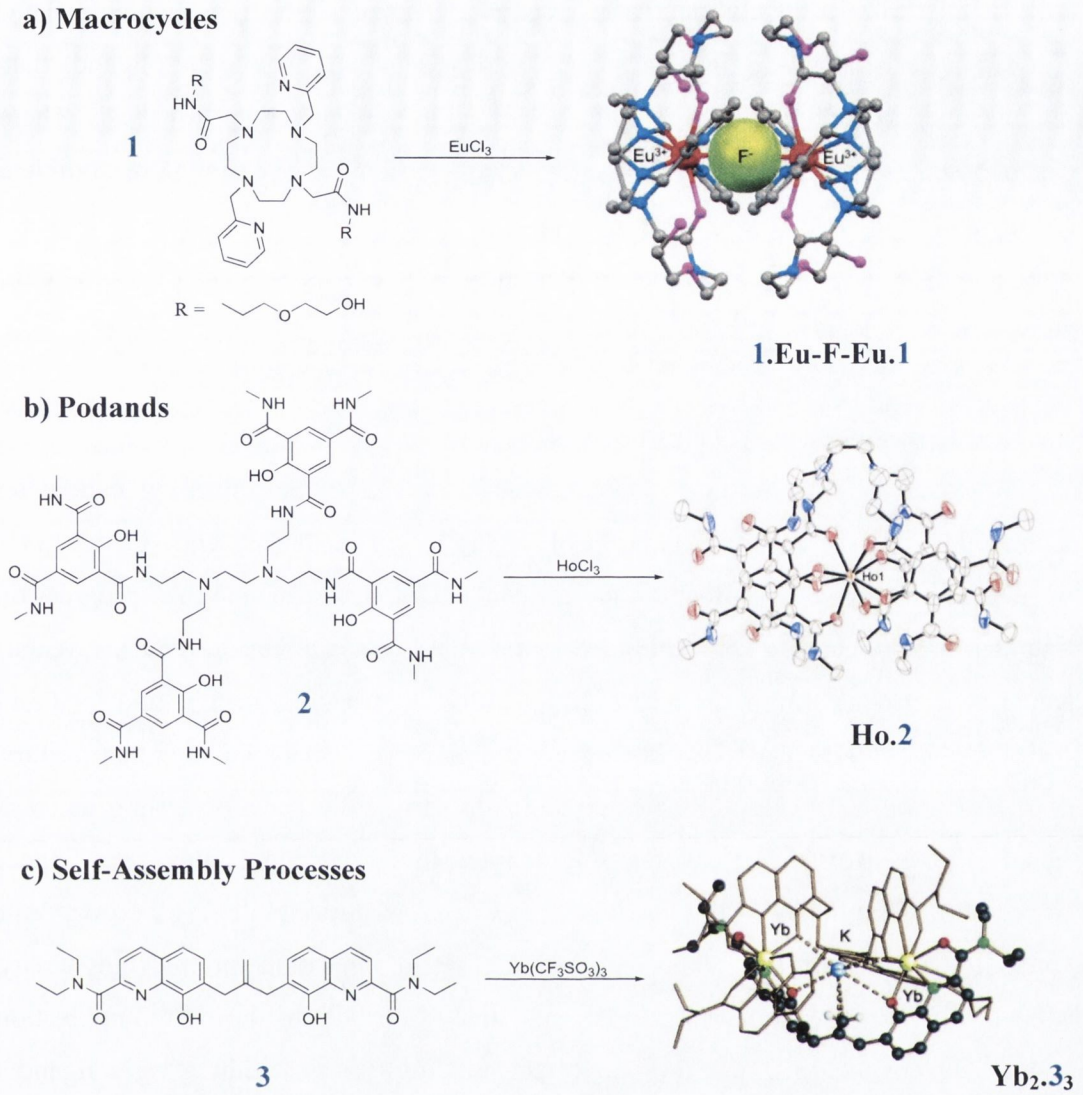

Figure 1.5: *Synthetic strategies for inserting Ln(III) ions into supramolecular systems: a) Derivatised macrocyclic ligand for Eu(III) complexation based on the 1,4,7,10-tetraaza-cyclododecane framework.*[70] *b) Podand approach enlisting a combination of four 2-hydroxyisophthalamide arms for binding of Ho(III).*[71] *c) Self-assembly methods for forming complex supramolecular architectures e.g. binuclear Yb(III) helicate systems.*[75]

To summarise, advanced Ln(III)-coordinating ligands should meet a number of defined criteria:

- A chromophore either integrated in the ligand structure or independently coordinated to the metal ion. This must absorb light efficiently (high ε value) and allow competent population of the Ln(III) excited state.
- Shielding of the complex from the quenching effects of high energy X-H vibrations (X = O, N, C), which cause non-radiative deactivation.
- High thermodynamic stability and kinetic inertness attained by following a range of strategies that avail of polydentate ligands.

Of the three central complexation strategies, it is exclusively those which make use of self-assembly processes and, to a comparatively lesser extent, macrocyclic ligands that bear most relevance to the bulk of the research described in the chapters of this thesis. Therefore, the subsequent sections of this introductory chapter intend to give a more complete and studied explanation of the principles that underscore these two methodologies, with accompanying examples from the recent literature. The next section will focus on lanthanide macrocyclic complexes.

1.3 Lanthanide macrocyclic complexes

Macrocyclic ligands have time and again proven to be appealing candidates for implementation in the supramolecular field, owing to the innate tendency of the Ln(III) to favour large coordination numbers in aqueous media. Constant demand for progression and refinement has triggered a fascinating evolution in this class of ligand over the years, with novel structures conferring rich and varied functions. The original idea behind the first class of macrocyclic Ln(III) receptors entailed the use of pre-organised cavities that perform the dual role of housing several donor heteroatoms to satisfy the hard, polarising metal centre situated in rings with diameters precisely adapted to correspond to the size of the guest cation, thus, essentially operating by a *lock and key* principle *e.g.* crown ethers,[76] coronands,[77] and cryptands.[78] This combination of pre-organisation and matching cavity size guarantees a minimal reorganizational enthalpy contribution during complexation.[19,28] Another key advantage is the fixation of the binding atoms within a rigid ligand core, ensuring a reduced entropic effect relative to that witnessed for analogous acyclic polydentate ligands carrying an equal amount of donor atoms. The resultant improvement in thermodynamic stability observed in comparison to linear analogues having an equal number of chelate rings is referred to as the *macrocyclic effect*.[79]

Based on an ambition to address the limitations of pre-organised ligands while still retaining the aforementioned benefits, this method was soon subtly modified to usher in a new generation of chelating macrocycles. Ligands of this type are classified as *pre-disposed* and find their foundations closely rooted in the *induced fit* concept,[19,28] whereby more flexible scaffolds are functionalised with pendant arms capable of wrapping around and engulfing the metal to form an enclosed cavity *e.g.* cyclen,[80,81] calixarenes,[82] and cyclodextrin derivatives.[83] The strength of the metal-ligand interaction and its associated enthalpy reduction helps compensate for the adverse entropic contributions required by the increased levels of reorganisation in respect to *pre-organised* systems.

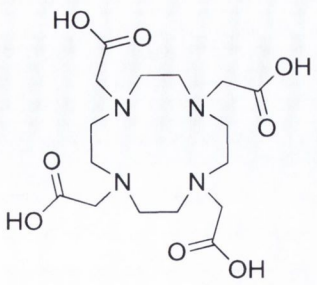

4

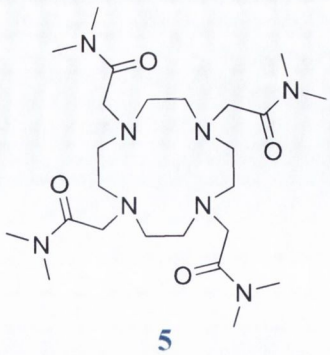

5

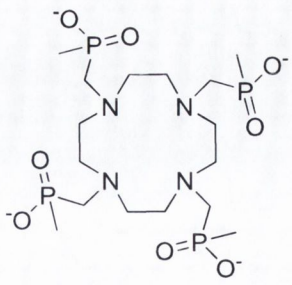

6

Substituted aza-macrocycles profiting from the *pre-disposed* tactic, such as those derived from the 1,4,7,10-tetraazacyclododecane (cyclen) framework, have been explored thoroughly for their skill in forming kinetically inert and thermodynamically stable metal complexes.[65,84] Offering four macrocyclic donor atoms, with additional donor atoms on the pendant arms, these ligands adequately fulfil the high coordination demands of the Ln(III), thus, explaining the great attraction of these systems. The above examples demonstrate the rich diversity of groups than can be used for functionalisation of the macrocyclic ring; such functionality commonly including carboxylates (**4**), amides (**5**), and phosphinates (**6**). Opportunely, functionalisation also allows the tethering of pendant arms possessing aromatic chromophores, which can then operate as Ln(III) sensitisers. A description of some of the current advances being made with regards to aza-macrocycles and their application will be delivered in the following section.

1.3.1 Various applications of lanthanide-based aza-macrocycles

The relative ease with which a wide collection of antenna moieties can be introduced to the donor amino groups of aza-macrocycles has opened the door to boundless applications for this family of luminescent Ln(III) complex.[50] Only through acute understanding of the photophysics characteristic to specific sensitising units can one begin to tune the overall properties of the macrocycle to confer precise function.

Emissive Ln(III) species constitute an emerging class of metal-based emissive probes that are being rigorously examined for use *in cellulo* for imaging purposes.[26,85,86] Parker and co-workers have made enormous strides in this area through the design and evaluation of an extensive library of visible-emitting Eu(III) and Tb(III) cellular imaging agents, produced on aza-macrocyclic platforms and selected because of their resilience to non-radiative quenching.[26] An ample range of chromophores have been meticulously investigated encompassing acridones,[87] tetraazatriphenylenes,[88] and azaxanthones,[89] with the antenna nature, form of linkage, and overall charge being the crucial determinants of cellular uptake

rate and localisation. An applicable example from the Parker research group centred around the selective staining of nuclear DNA by treatment with two constitutionally isomeric Tb(III)-cyclen complexes, **Tb.7** and **Tb.8**, possessing *trans*-related azaxanthone sensitisers.[90]

Tb.7

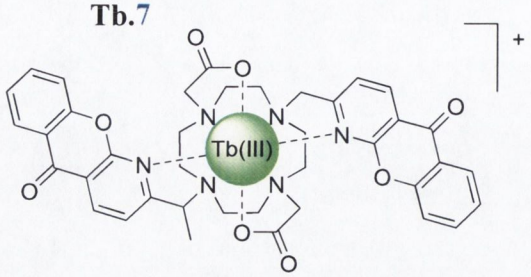

Tb.8

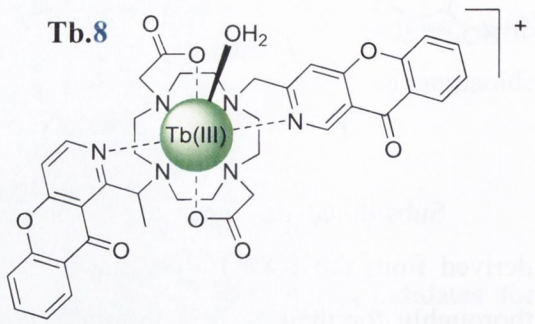

Administering the two complexes at low concentrations (< 1 μM) to HeLa cell lines revealed, by means of luminescence microscopy, chromosomal DNA staining in less than 10% of the total cell population upon excitation at 340 nm. Such an excitation wavelength (λ_{exc}) aids in the prevention of cellular damage normally caused by high energy UV-irradiation. The observed discriminatory pattern was consistent with preferential labelling of those cells undergoing replication, a vital biological process called mitosis, whereby the selectivity seen can be accredited to the diminished membrane integrity experienced throughout the pathway. Cells at each stage of the mitotic cycle were visualised and discerned by real-time monitoring of these Tb(III)-based optical probes, arising from the noted affinity for exposed nuclear DNA. Absorption and excitation spectroscopic titrations performed by sequential additions of calf thymus DNA to both **Tb.7** and **Tb.8** showed neither a spectral shift nor any hypochroism in the azaxanthone chromophore, indicative of a binding interaction that is not primarily intercalative.

More recently, Parker *et al.* have reported on the development of a set of intensely emissive Eu(III) complexes that utilised nonadentate carboxylate- and phosphinate-substituted triazacyclononane ligands for the selective time-gated imaging of cellular mitochondria.[91] Each structure contained three *para*-aryl-alkynyl chromophores absorbing strongly within a biologically beneficial spectral window of 310 – 340 nm, enabling efficient Eu(III)-sensitisation. The detected red emission displayed brightness values (B, where $B = \varepsilon \times Q_L^{Ln}$) in the range of 15000 – 30000 M^{-1} cm^{-1}, an order of magnitude greater than that previously recorded for analogous systems in the literature, auguring well for future roles in FRET bioassays and as 2-photon probes.[92] Incubation of **Eu.9** (10mM) in growth media of mouse skin fibroblasts (NIH-3T3), Chinese hamster ovarian (CHO), and human prostate

cancer (PC-3) cells highlighted selective mitochondrial staining, optically confirmed by confocal fluorescence microscopy in conjunction with co-localisation studies.

Eu.9

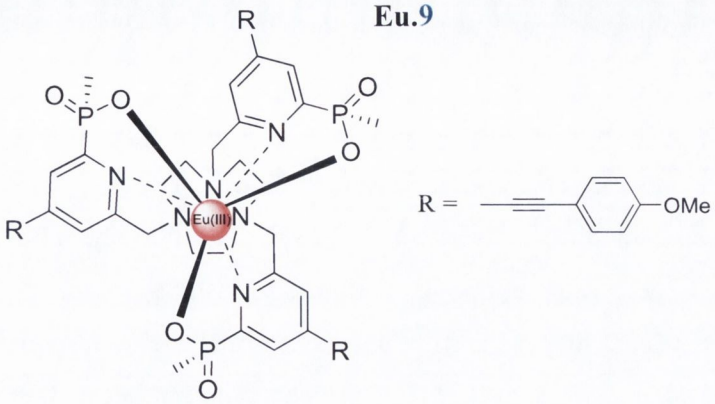

The past decade or so has witnessed a sizeable shift in favour of Ln(III) from which emission in the NIR region of the electromagnetic spectrum is feasible. Indeed, bioprobes comprised of NIR-emitting Ln(III) ions have lately been subject to heightened interest in view of their potential to act as biomedical reporters, especially for *in vivo* optical tumour detection.[93-96] This growing fascination is inherently founded on the basis that these probes permit better tissue penetration than visible light, which coincidentally results in greater detection sensitivity and lower scattering due to low biological autofluorescence in the NIR energy domain.[96,97] Penetration can range from a few millimetres to several centimetres and is linked to the fact that the principle absorbers of visible (haemoglobin) and infrared light (water, lipids) have inferior absorption coefficients in the NIR region.[98] In an effort to exploit these features, aza-macrocycles have long been relied upon to produce robust thermodynamically stable chelates of NIR-active Nd(III), Er(III), and Yb(III), harnessing the emissive properties of the ions for multiple functions.

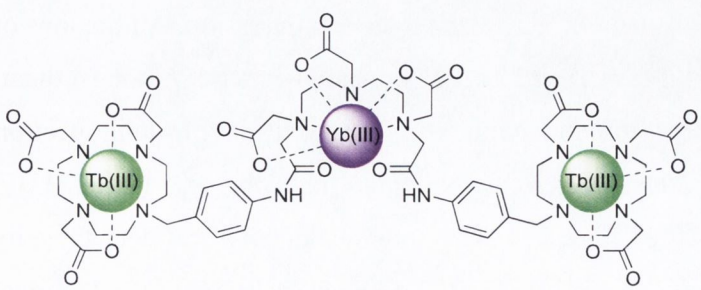

Yb.Tb$_2$.10

Yb.11a/b

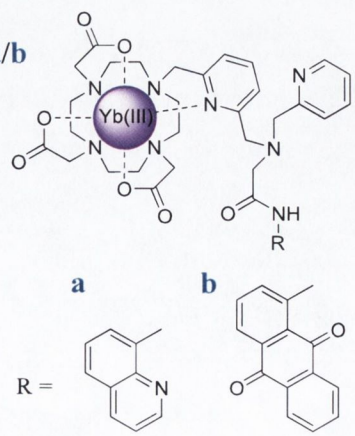

Developed in collaboration between Faulkner and Pope, the hetero-trimetallic complex **Yb.Tb$_2$.10** represents the first and only reported case of Ln(III)-centred NIR emission sensitised by a Ln(III) ion.[99] Evidence of the successful Tb(III) → Yb(III) energy transfer was provided upon direct excitation of the Tb(III) absorption band at 488 nm, which gave rise to characteristic Yb(III) emission at 980 nm. Also noteworthy was the complexation strategy used, which in effect served as a fitting example of an effective marriage of the podand and macrocyclic design, with the derivatised DTPA binding site and two tetra-substituted cyclen moieties selectively coordinating to one Yb(III) and two Tb(III) ions, respectively. Pope *et al.* later applied a more diagnostic approach to their Yb(III)-based systems **Yb.11a** and **Yb.11b**, which were designed to behave as responsive NIR probes in the presence of selected *d*-block cations.[100] Through excitation of the 8-aminoquinoline or 1-amino-9,10-anthroquinone substituent (**Yb.11a** and **Yb.11b**, respectively), modulation of the emission intensity was carefully monitored following addition of up to 10 eq. of Hg(II), with a dramatic four-fold enhancement observed for **Yb.11a**. The noted increase in NIR emission was proposed to originate from a significant reduction in non-radiative quenching, with this believed to be a consequence of Hg(II)-binding inducing increased structural rigidity and shielding of the central Yb(III) ion.

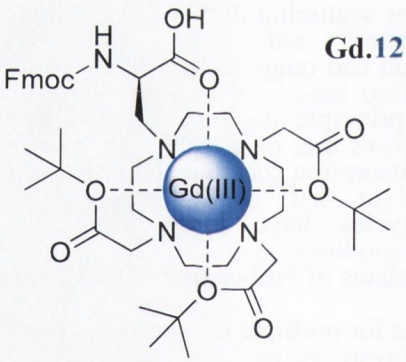

Gd.12

Aza-macrocyclic systems that avail of the unique magnetic properties of the Ln(III) have enjoyed enduring popularity, thus, benefitting from constant progression. All the ions of the *f*-block series, with the exception of La(III) and Lu(III), are paramagnetic. Amongst them, Gd(III) bears a high electron spin (S = 7/2) and symmetric S-state, leading to long electron relaxation times (T_{1e}). This has the added bonus of augmenting both the spin-lattice ($1/T_1$) and spin-spin ($1/T_2$) relaxation rates of proximate water proton nuclei, an effect detectable by magnetic resonance imaging (MRI).[101] As a result, Gd(III) complexes are presently the most prevalent MRI contrast agents in clinical practice,[84] with signal enhancement in regions of

the body with high localisation.[101] A prime example is the latest investigations by Caravan *et al.*, which were centred around the analine-substituted derivative of Gd(DOTA), Gd(DOTAla) (**Gd.12**), being a favourable tool for high field, high relaxivity MRI compared to the clinically approved contrast agent [Gd(DO3A)(H_2O)].[102] Solid phase peptide synthesis was also facilitated through Fmoc protection of the DOTAla cyclen ligand, while Gd(III)-coordination to both the amino acid side chain and amide carbonyl groups ensured rigid attachment.

Spanning the applications of biological imaging, NIR emission and MRI contrast agents, this section has aimed to communicate pertinent examples of current research trends, not just exclusive to Ln(III) macrocyclic chemistry, but to Ln(III) supramolecular chemistry as a whole. More fundamental to the work described within this thesis, however, is an alternate strategy that contrastingly deploys multiple acyclic ligands to satisfy the large metal coordination demands, opening up an avenue to complex development through which control of precise geometry and final function can be realised.[103] This method, called self-assembly, will be discussed in depth in the following sections.

1.4 Lanthanide self-assembly

The study of self-assembly processes influences almost all aspects of modern inorganic chemistry as it encompasses elements from across the periodic table and traverses all spatial domains.[104] Founded on principles of molecular recognition and self-organisation, self-assembly, by definition, entails the spontaneous and reversible association of molecules or ions to form larger, more complex molecular entities according to basic information contained in the molecules themselves.[104-106] In this manner, molecular information stored within complementary chemical building blocks is expressed through key recognition events that provide the necessary means for directing these smaller components in the formation of organised, well-defined supramolecular architectures.[106] Such recognition effectively manifests in the form of the weak intermolecular interactions that help hold the structures together, and include metal-coordination, hydrogen bonding, π-π stacking, *etc.*

Recent years have seen an increased surge in interest in the metal-directed construction of self-assembled molecular systems.[107] Through production of a myriad of novel supramolecular species such as organometallic clusters,[108] triangular complexes,[109] and linear and circular helicates,[110,111] the use of templating techniques to introduce greater complexity and function have so far proven to be extremely rewarding. In many cases, the metal ion is simply a structural motif to impart the correct connectivity and geometry required of the assembly. Nonetheless, the distinctive properties of the metal employed can

be intelligently channelled to transfer desirable functionality to the final structure.[107] In light of this, the Ln(III) ions, with their high electric fields and large coordination requirements, have lately been sought for their ability to direct the formation of complex mono and multimetallic self-assemblies of controlled geometry, which in-turn incorporate the unique photophysical and magnetic properties of the metals.[28] Only through the inclusion of sensitising chromophores within the chosen ligand can this be achieved by the *antenna effect* previously explained in Section 1.1.2. Having developed in years gone by a more universal and reasoned understanding of the parameters that govern this method, which is under strict thermodynamic control,[17,112] the rational and premeditated design of luminescent Ln(III) systems using small ligand sub-units, such as bipyridines (bipy) and dipicolinic acid (dpa) derivatives, is now more accessible than ever.[112]

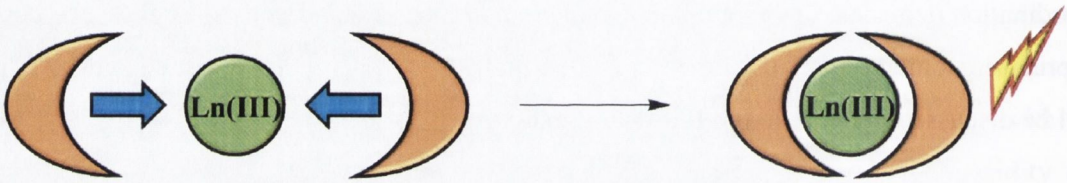

Figure 1.6: *Simplified cartoon depiction of the construction of a luminescent Ln(III) self-assembled system.*

The use of Ln(III)-directed synthesis to template the creation of higher order assemblies has been explored by many researchers to date, with pioneering contributions from the groups of Bünzli, Piguet, and Gunnlaugsson amongst others.[103,113] Consequently, it has emerged as a privileged strategy for the engineering of mono and multimetallic edifices. To help emphasise this point, some relevant literature examples of contemporary advances in the field of Ln(III) self-assembly will be presented and summarised to establish a better context and appreciation of the work undertaken for the purpose of this thesis.

1.4.1 Monometallic lanthanide self-assemblies

Among the different strategies devised for the synthesis of luminescent Ln(III) complexes, the self-assembly of modest tridentate ligands around a single Ln(III) centre has been demonstrated time and again to be a convenient route to beautiful and functional monometallic systems.[47,114,115] With impressive stability towards complex dissociation, ligands derived from the tridentate dpa framework have, for the past few decades, been successfully implemented to carry out this role. In terms of luminescence efficacy, dpa is

renowned for efficient sensitisation of the visible-emitting Eu(III) and Tb(III) ions,[116,117] affording satisfactory quantum yields in both solution and the solid state, and to a lesser extent, in the NIR regions for Nd(III) and Yb(III).[118,119] These properties, combined with facile synthesis, have led to Ln(III)-dpa complexes being used as reference standards for luminescence quantum yield determination,[116] along with further application in areas as diverse as protein crystallography,[120] two-photon scanning microscopy,[121] and NMR method development.[122]

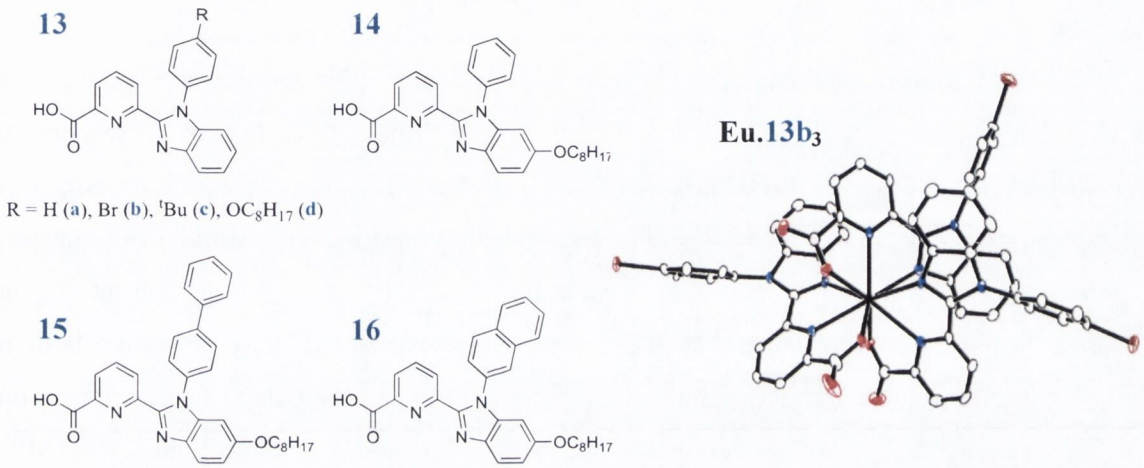

Bünzli *et al.* have dedicated tremendous efforts to the design and synthesis of metal-directed Ln(III) self-assemblies, typically accomplished by derivation of the dpa ligand core. One recent contribution from Bünzli and co-workers reported on the assembly of a set of *N*-aryl-benzimidazole pyridine-2-carboxylic acid ligands (**13** – **16**) with Eu(III) to give discrete mononuclear complexes of 1:3 (M:L) stoichiometry.[123] *N*-Aryl compounds of this type had in the past found limited use in coordination chemistry because of anticipated steric hindrance to metal-binding.[124,125] Nevertheless, X-ray crystallographic studies showed the structures of these Eu(III) complexes to be acutely similar to those of *N*-alkyl analogues published previously, despite the increased steric bulk.[126] The global objective of this work, however, was to ultimately ascertain the influence of ligand structure on the luminescence quantum yield (Q_L^{Ln}). *Para*-substition of the *N*-phenyl ring in **13a** – **d** was proven to have no effect on Q_L^{Ln}, even though perturbation of the ligand triplet states had occurred. In contrast, a marked reduction in Q_L^{Ln} was observed upon grafting an octyl chain at the C-6 atom of the benzimidazole antenna (**14** – **16**), suggesting future modification would be best situated at the *N*-aryl group considering the negligible effect on the Eu(III) luminescence.

17

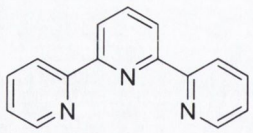

18

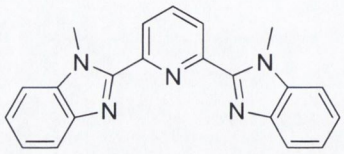

Eu.18$_3$

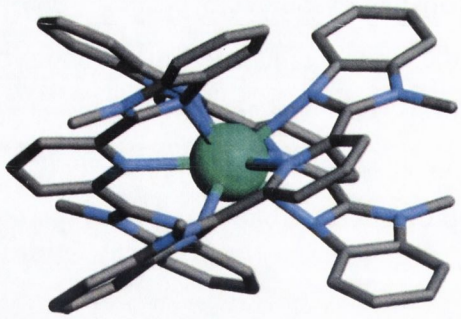

Piguet and co-workers have long been concerned with probing the plethora of thermodynamic and steric parameters that dictate the final structure and corresponding stability of metal-driven self-assemblies. In 2009, studies were extended to the investigation of tridentate terpyridine (**17**) and 2,6-bis(1-methylbenzimidazol-2-yl)pyridine (**18**) chelating ligands, whose formation of triple-helical complexes was, by way of repulsive interligand interactions that serve to destabilise the complex, deemed to be anti-cooperative both in solution and in the solid state.[127] Their findings brought them to conclude that complexation of **17** and **18**, each adapted for producing planar 1:1 and helical 1:2 and 1:3 (M:L) stoichiometric complexes with trivalent Ln(III) ions, was especially sensitive to solvation effects and the nature of the counter-anion. Moreover, the larger coordination cavity offered by **18** compared to **17** generated 1:3 (M:L) species of improved stability and kinetic inertness.

Eu.19$_3$

19

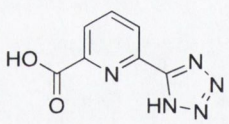

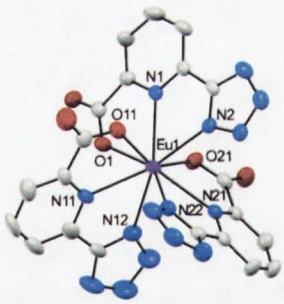

Eu.20$_3$

20

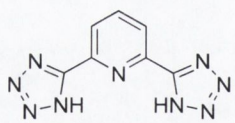

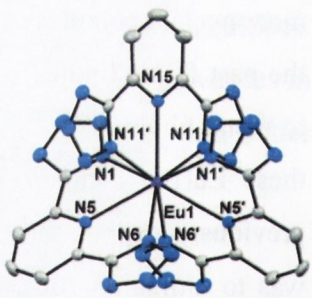

Developed by Mazzanti *et al.*, the simple ligand structural units **19** and **20** signify another profitable alteration of the original dpa skeleton for the assembly of strongly luminescent, water soluble tris-chelate Ln(III) complexes.[128] In the case of **20**, replacement of the two carboxylic acid groups with light-harvesting tetrazole chromophores bathochromically shifted the complex absorption window, relative to that of dpa, towards the visible region (*ca.* 330 nm), a promising feature with respect to prospective application in

biomedical analysis. Furthermore, NMR and X-ray studies confirmed a pseudo-D_3, triple-helical complex structure for **19** and **20** in both solution and the solid state. Measurement of the solid state luminescence quantum yields for the Eu(III) and Tb(III) complexes of **20** gave Q_L^{Ln} values of 61% and 65%, respectively, which are among some of the highest reported in the literature, including those of the corresponding dpa complexes. The superior values obtained could possibly be attributed to a comparatively more efficient energy transfer to the Ln(III) centre from **20**, a hypothesis supported by an experimentally calculated reduction in the triplet excited state energy of the ligand.

21

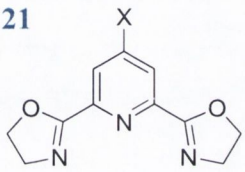

X = H (**a**), OMe (**b**), Br (**c**)

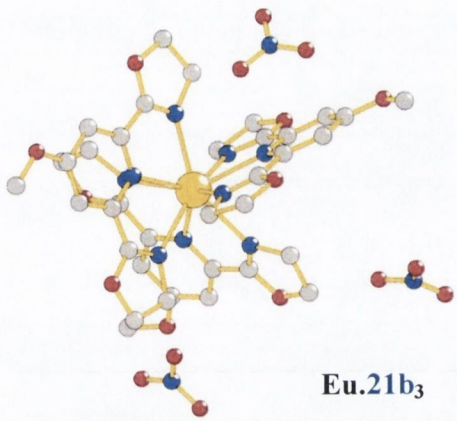

Eu.21b$_3$

The synthetic attachment of pyridine-bis(oxazoline) (Pybox) sensitising antennae to the dpa ligand scaffold has been a tactic effectively utilised by de Bettencourt-Dias *et al.* for the construction of homoleptic, monometallic Ln(III) systems.[129,130] Through introduction of *para*-functionality to the central pyridine ring in the form of electron-donating methoxy and electron-withdrawing bromo groups (**21b** and **21c**, respectively), studies pertaining to this ligand set were undertaken in an attempt to explore the potential effects of ligand derivatisation on the overall properties of the resultant complexes.[129] Specific care and attention were given to the identification and explanation of changes in stoichiometric M:L ratios, complex stabilities, and luminescence quantum yields. X-ray analysis of crystals grown following complexation of each ligand with varying equivalents of Eu(III) or Tb(III) salts revealed a wide array of Ln(III) self-assemblies exhibiting incredibly rich structural diversity. Examination of the crystal structures of the thermodynamically favoured 1:3 (M:L) Eu(III) species showed a nine-coordinate complex system completely absent of π-π stacking, with the vertices of the metal-ligand bonds adopting the geometry of a distorted trigonal prism. UV-vis and luminescence titrations accounted for the successive formation of 1:1, 1:2, and 1:3 (M:L) stoichiometries in solution, for which it was discovered that bromo-substituted

21c formed the most stable complexes of the ligand series; log $\beta_{1:3}$ = 15.5 and 15.4 for Eu(III) and Tb(III), respectively. With a Q_L^{Ln} value of 36% in acetonitrile, the Eu(III) complex of **21c** was also found to display the highest quantum yield of the ligand family, most probably explained by the fact that it holds the lowest triplet state energy of the three ligands.

Until recently, the biggest obstacle faced by Ln(III)-Pybox complexes was a lack of solubility in aqueous media, therefore, severely restricting any potential biological value. From an application standpoint, water solubility is a physical criterion that is undeniably attractive to the chemist when designing novel devices, opening doors for utilisation in far ranging fields such as biological imaging and anion sensing.[131,132] Additionally, the modern day demand for greener manufacturing processes, for instance in catalysis, has prompted an ever-increasing drive for more environmentally benign processes, which use water as a non-toxic solvent alternative.[133,134]

22

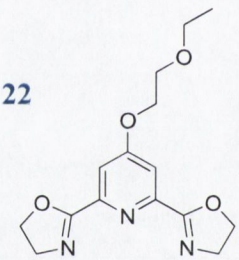

22.H_2O

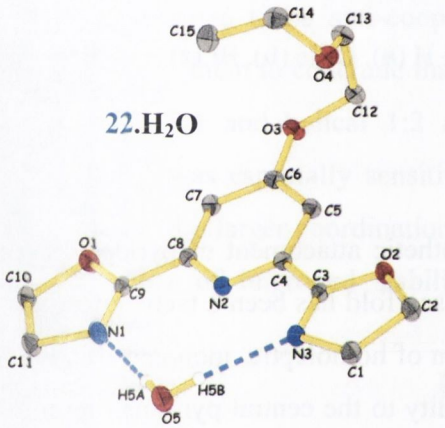

de Bettencourt-Dias and co-workers managed to overcome this inherent drawback of the Pybox systems by substitution of a hydrophilic ethylene glycol ethyl ether chain at the ligand pyridyl 4-position (**22**). This subtle structural revision gave rise to the metal-templated production of stable, water soluble complexes with a variety of Ln(III) ions.[135] Shown to possess solubility in both water and common organic solvents, the luminescence quantum yields of the Eu(III) and Tb(III) mononuclear species demonstrated an appreciably high degree of solvent independence, with Q_L^{Ln} values in water reaching 30% and 26%, respectively. The lack of influence held by the solvent over Q_L^{Ln} reflected a fully saturated coordination sphere capable of shielding the metal centre, a theory reinforced by the long luminescence lifetimes. Fitting of luminescence titration data confirmed complexation of **22** to adhere to the same speciation profile as that of **21a – c**. The log $\beta_{1:3}$ values of 13.8 and

12.7 determined for Eu(III) and Tb(III), respectively, were indeed greater than those obtained for **21a** and **21b**, but less than that of the bromo-derivative **21c**.

23

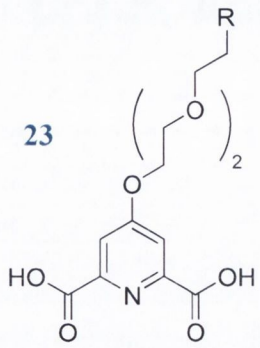

Phta =

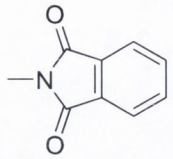

R = OMe (**a**), OH (**b**), Phta (**c**), NH_2 (**d**)

Water-solubilising polyethoxyethylene chains were equally integral to a recent collaboration between Chauvin and Bünzli, devoted to the study of four *para*-substituted dpa ligands bearing various terminal groups (**23a – d**).[136] Contrary to the other examples given in this section, no additional aromatic chromophores were introduced to the dpa carboxylic acid sites. The ability of these coordinating ligands to form stable monometallic **Ln.23$_3$** complexes in solution was probed by UV-vis spectrophotometric titrations. Calculated binding constants for the Eu(III) tris-chelates in the range of log $\beta_{1:3} \approx 19 - 20$ pointed to terminal *para*-chain functionality having minimal effect on final complex stability. This finding was in clear contrast to the luminescence quantum yields, which were found to differ from 12% (**23a**) to as much as 29% (**23d**). Further rigorous analysis of the quantum yield data showed the non-radiative deactivation pathways in play to be unaffected by the nature of the terminal substituent, with variations arising from differences in the Ln(III)-sensitisation efficiencies. These results unequivocally highlight the remarkable fine-tuning of the complex photophysical properties through alteration of the terminal ligand functionality, and are potentially indicative of how the luminescence might be modulated upon coupling at this location with different biological substrates, boding well for possible bioprobe application.

The innate capacity of the Ln(III) to direct the assembly of monometallic supramolecular devices is a theme that runs at the very heart of this project. Accordingly, the research described within this section has been meticulously chosen so as to give an adequate insight into advances and developments which have, to varying extents, both inspired and influenced the systems described in the later chapters of this thesis. Attention will now be

turned to the exploitation of self-assembly methods for the design of a diverse range of multimetallic Ln(III) architectures.

1.4.2 Multimetallic lanthanide self-assemblies

Representing a steep progression from comparatively more simple monometallic species, the strategic inclusion of Ln(III) ions into structurally intricate polymetallic edifices poses a fascinating challenge to the chemist.[137] By incorporation of multiple coordinating units into ligand design, self-assembly presents as an indispensable tool for the preparation of novel multinuclear systems, for which there is currently such heightened demand.[103,137] For many researchers, the attraction held is primarily motivated by a desire to further control and manipulate the unique Ln(III) photophysical and magnetic properties for beneficial function.[103] Others are conversely inspired to simply build beautiful complex architectures, previously envisaged but thought to be beyond reach. Regardless of motive, a passion has been ignited that has fuelled the development of a whole host of elegant and eye-catching structures, the likes of which can only be achieved by self-assembly methods, for example, helicates,[138,139] cage compounds,[140,141] and metal-organic frameworks.[142,143]

Helical metal-coordination compounds, or helicates, have been fundamental topological targets for chemical synthesis for the past two decades.[144,145] The term helicate was introduced for the first time in 1987 by Jean-Marie Lehn to describe a polynuclear complex composed of several intertwining ligand strands coordinated to a series of metal ions defining the helical axis.[139,144] Ever since the development by Lehn *et al.* of the first trimetallic double-stranded Cu(I) helicate, and its subsequent definition as such, a huge number of polymetallic structures fulfilling this criteria have been reported.[144,146] The use of Ln(III) ions to induce helicate self-assembly, though less explored than that accomplished with the *d*-block metals,[147] constitutes a fantastically thriving area of modern supramolecular chemistry.

Unquestionably, no discussion of Ln(III)-based helicates is complete without referencing the ground-breaking work conducted by the Piguet research group. Taking a profoundly in-depth approach to system analysis, with particular emphasis placed on thermodynamics and photophysics, their findings have immeasurably contributed to a more rational comprehension of the factors that regulate helicate formation and emission.[148,149] Shifting focus more recently to heterometallic 3*d*-4*f* helicate systems, Piguet *et al.* reported in 2012 on the design and intriguing NIR-emitting properties of a novel trinuclear **CrYbCr.24$_3$** triple-stranded helicate.[150] Building on earlier studies of an analogous bimetallic Cr(III)-Yb(III) system,[151-153] optimisation of long-lived NIR Yb(III)-centred emission was made

viable by the sensitising capabilities of the two Cr(III) chromophores present. To this end, rate-limiting Cr(III) → Yb(III) energy transfer processes were found to extend NIR lifetimes from a sub-microsecond to millisecond range, in essence, mirroring the millisecond decay of the trivalent Cr(III) donors. The authors suggest that delayed NIR emission, made feasible by intermetallic communication in systems such as **CrYbCr.24$_3$**, may find practice in the time-gated detection and quantification of trace targets in biological media.

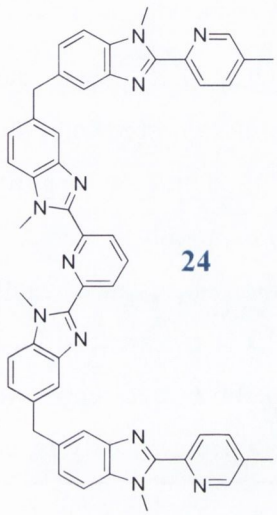

24

CrYbCr.24$_3$

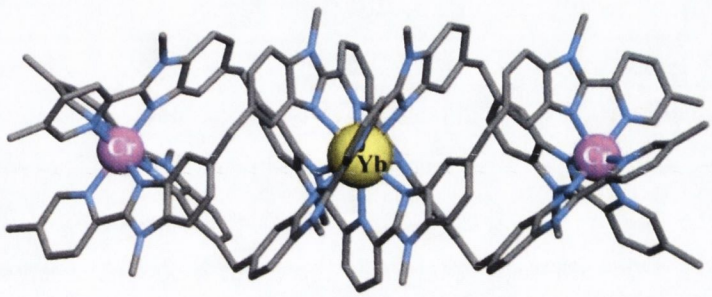

Additional to the directing effects imparted by the Ln(III) ions, the role of the metal counter-anion in templating self-assembly formation can be equally crucial. Subject of a 2013 publication, Liu and co-workers have visually demonstrated, by means of comprehensive crystallography, the susceptibility of a newly developed La(III) helicate to dramatic topological change based on the counter-anion employed, and its intrinsic ability to template assemblies.[154]

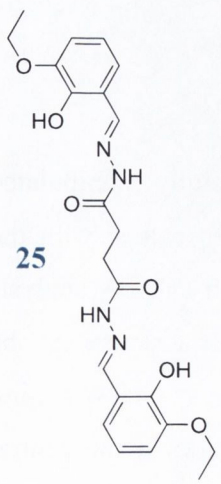

25

[La$_6$.25$_6$](ClO$_4$)$_3$

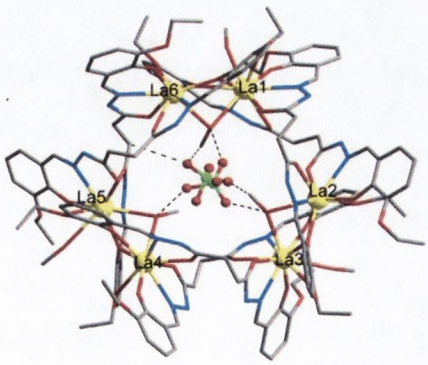

[La$_4$.25$_4$(NO$_3$)](NO$_3$)$_3$

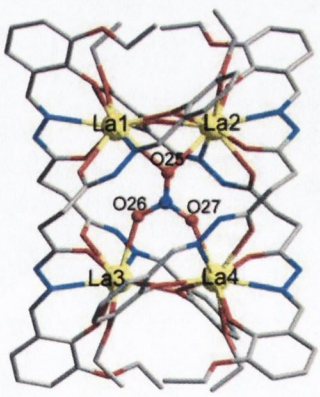

In the presence of tetrahedral ClO_4^-, the construction of a hexanuclear circular helicate **[La$_6$.25$_6$](ClO$_4$)$_3$** was induced. Contrastingly, trigonal planar NO_3^- stimulated the assembly of a compact tetranuclear linear helicate **[La$_4$.25$_4$(NO$_3$)](NO$_3$)$_3$**. Both La(III) structures were claimed to be the first examples of their respective kind, with the former system proving especially novel due to these circular high nuclearity variants being relatively rare.[155,156] Furthermore, the dynamic transformation of the circular helicate into its linear analogue was observed upon the addition of nitrate salts, suggesting the NO_3^- anion to be the more potent structural regulator of the two.

Three-dimensional multimetallic edifices possessing appropriately sized cavities present as exceptional candidates for the selective binding of distinct guest species such as cations and anions.[157] Supramolecular host-guest assemblies, therefore, signify an advancement of a field that has typically been the domain of purely organic, often macrocyclic receptor molecules.[105] In particular, polynuclear cages have gathered considerable momentum in light of the resolute efforts of several key researchers; Fujita,[158] Nitschke,[159] and Raymond,[160] to name but a few. Consequently, host-guest cage systems have proven to be extremely profitable, notably in the development of new catalysts, energy conversion devices, and chemical separation techniques.[161]

26

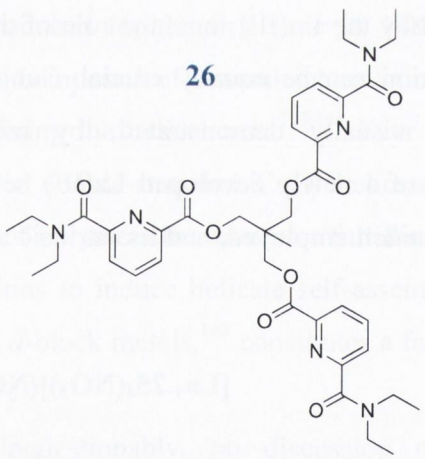

[Eu$_4$.26$_4$](OH)(ClO$_4$)$_{11}$

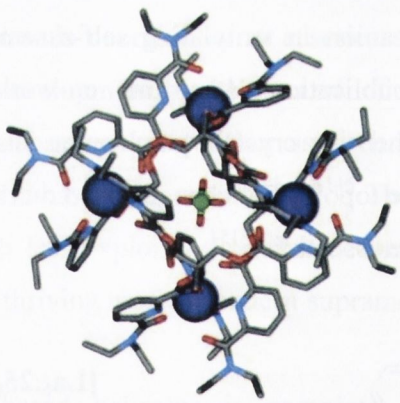

Using dpa-derivatised tripodal ligands, Hamacek *et al.* have tactfully manipulated self-assembly strategies for the formation of tetranuclear Ln(III) cage structures, with the desired aim of using the enclosed cavities for potential host-guest chemistry. X-ray analysis of the Eu(III) complexation product of the triester **26** revealed the structure to be **[Eu$_4$.26$_4$](OH)(ClO$_4$)$_{11}$**, confirming a tetrahedral metal ion arrangement and helical wrapping of the ligand strands.[161] The molecular structure also evidenced occupation of the central cavity by a single ClO_4^- anion. This finding was in stark contrast to that seen for a near

identical Tb(III) assembly in which no encapsulation was detected, and could be attributed to a subtle difference in ligand structure.[162] In the case of **26**, the *exo*-CH_3 of the ligand was oriented away from the cavity, whereas in the previously reported example, for which secondary amides substitute the ester functionalities of **26**, the same group had an *endo*-CH_3 conformation and was positioned detrimentally within the cavity. Taking advantage of **[Eu$_4$.26$_4$](OH)(ClO$_4$)$_{11}$** to investigate host-guest interactions, detailed NMR studies showed the ability of this system to exchange the embedded ClO_4^- for a range of different ions, for example, BF_4^-, Im^-, and Br^-.

27

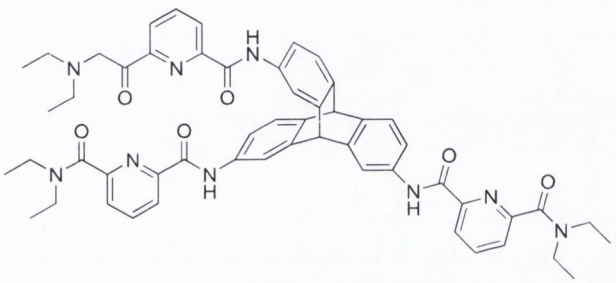

[Eu$_4$.27$_4$](ClO$_4$)$_{12}$

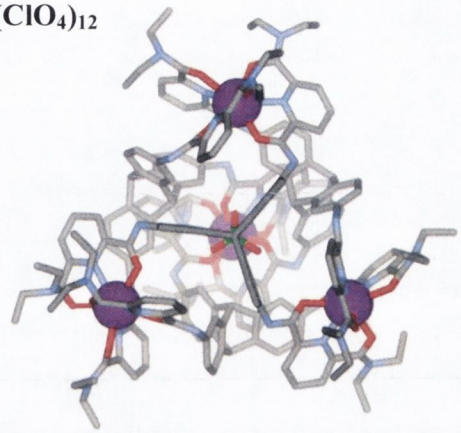

With a view to expanding the inner cavity of these supramolecular cages, Hamacek and co-workers have since modified the ligand structure of **26** by replacement of the 1,1,1-tris(aminomethyl)ethane (TAME) linker with an aromatic triptycene unit.[163] Unambiguous proof of an increase in cavity size was supplied upon inspection of the crystallographic data, which exposed an extension of the intermetallic distance in **[Eu$_4$.27$_4$](ClO$_4$)$_{12}$**, a tetranuclear tetrahedral cage system reminiscent of the Eu(III) analogue of **26**. Consistent also with the previous cage structure was the presence of an enclosed ClO_4^- anion, for which preliminary NMR experiments demonstrated an exchange mechanism for BF_4^-. As a result of the enlarged cavity, future work by the Hamacek group will concentrate on the capacity of **[Eu$_4$.27$_4$](ClO$_4$)$_{12}$** to accommodate larger anionic guests.

Greatly indebted to the efforts of esteemed researchers such as Omar Yaghi,[164,165] the emergence of metal-organic frameworks (MOFs) in recent times represents a quantum leap in the progression and evolution of functional multimetallic self-assemblies.[166] Constructed by the assembly of metal ions with suitable organic linkers, MOFs comprise a family of crystalline materials famed for ultra high porosity and huge internal surface areas.[142,166] The ability to tune pore size and incorporate differing function into the framework makes these

structures enormously flexible towards diverse application in molecular storage,[167] drug delivery,[168] and catalysis.[169] Receiving ever-growing attention, however, are those MOF systems which are shown to exhibit advantageous photophysical characteristics.[170] For this reason, MOFs derived from trivalent Ln(III) ions have been identified as a promising class of materials to address the increasing demand for new luminescent devices.[171]

28

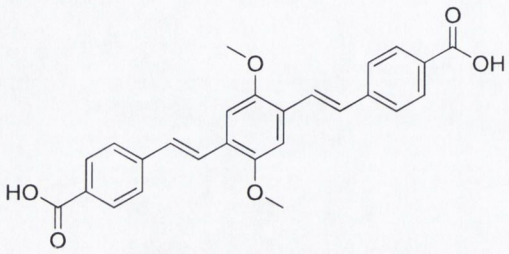

Yb–28 MOF

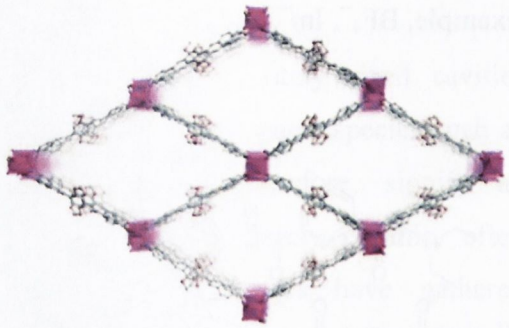

A tremendously innovative approach was taken by Petoud *et al.*, who proposed an original barcoding system based on polymetallic Ln(III) MOFs.[172] Containing multiple NIR-emitting Ln(III) ions, the described **Er_xYb_{1-x}–28 MOFs** were shown to simultaneously emit several independent NIR signals following excitation at a single wavelength. By control of the relative metal stoichiometry, the composition of the resultant framework could be confidently predicted, thus, affording the opportunity to tune the individual emission intensities and obtain unique NIR barcode fingerprints. By virtue of the linear correlation between the Er(III) and Yb(III) emission band intensities to their respective percentage composition in the MOF, the number of barcodes available may be increased by simply changing the metal ratio.

Zheng and co-workers have productively utilised a microporous, red-emitting Eu(III) MOF for the sensing of Fe(III) and Zn(II) metal cations.[170] The crystal structure of **Eu–29 MOF** showed the central triazinyl motif of the bridging tricarboxylate ligands to direct into the channels of the framework. As a consequence, the Lewis basic donor nitrogen atoms of **29** were thought to be optimally positioned and readily accessible for interaction with Lewis acidic analytes. Such interaction was expected to alter the ligand electronic structure and, hence, modulate the luminescent output in some form. This hypothesis was validated by titrations conducted with a series of metal cations, for which Fe(III) and Zn(II) provided the most intriguing results. In contrasting fashion, Fe(III) was found to cause complete quenching of the luminescence, as opposed to Zn(II), which stimulated a dramatic *ca.* 3.5

fold enhancement. In the presence of Fe(III), the luminescence lifetime of **Eu–29 MOF** was measured on a nanosecond scale, alluding to the fact that population of the Eu(III) excited state was essentially blocked. A substantial lengthening of lifetime was conversely seen upon Zn(II) addition, which had the supplementary effect of increasing the luminescence quantum yield of the system from 16% to 49%.

29

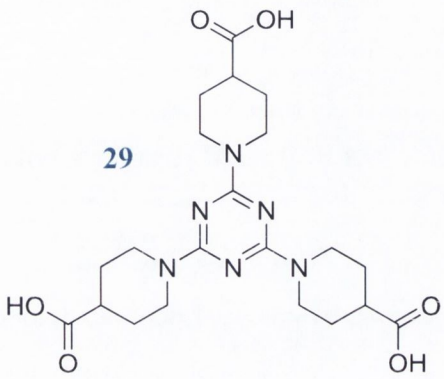

Eu–29 MOF

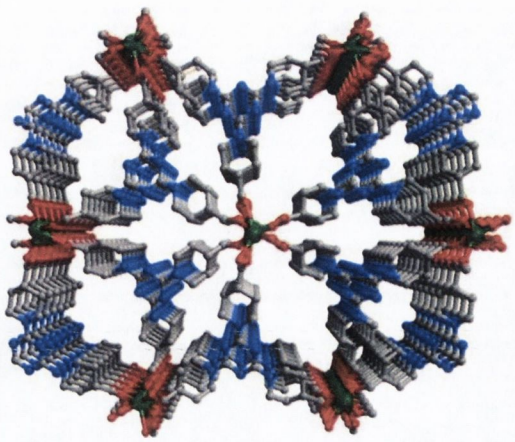

The research examples illustrated within this section have been carefully selected to accentuate both the practicality and adaptability of self-assembly methodologies for the design of both aesthetically pleasing and functional multimetallic Ln(III) systems. In the context of this project, the self-assembly strategies applied have been further refined for an added level of sophistication, namely the use of chiral ligands for the formation of chiroptically pure Ln(III) complexes. With an eye to supramolecular Ln(III) chemistry, a detailed discussion of the nature, detection, and application of chirality will be provided in the coming sections.

1.5 Chirality and the lanthanides

Chirality, the property whereby a molecule devoid of a symmetry axis exists as two non-superimposable mirror images called enantiomers, is expressed not only at the molecular level, but also at the supramolecular level.[173,174] Although the differences between chiral species may appear trivial, the subtle change in three-dimensional structure has the potential to radically transform any interaction of the system with the surrounding environment.[175,176] Owing to the significance of host-guest chemistry, recent decades have experienced an appreciable surge in enthusiasm for the development of artificial chiral host species (or probes) capable of recognising chiral guest molecules or biomolecules,[177,178] for instance, DNA and proteins.[179,180] In terms of application, the mode of action of these probes is

normally dependent on one of the enantiomers displaying greater selectivity or binding affinity for a given chiral analyte.[181] Indeed, such discriminatory behaviour can be invaluable with regards to understanding the very nature of chiral interactions.

The flourishing popularity of chiral probes is chiefly born out of the fact that chiral recognition is fundamental to a large variety of chemical and biological phenomena.[181] Consequently, the demand for new chiral systems with the possibility to report on such key events is bigger than ever. A description of the two most important spectroscopic tools for the detection of chirality will be delivered in the next section.

1.5.1 Chiroptical spectroscopic techniques: circular dichroism and circularly polarised luminescence

Circular dichroism (CD) is a form of spectroscopy that works by measuring the difference (ΔA) in the absorption of left-handed polarised light (A_L) compared to right-handed polarised light (A_R), with differences arising as a result of structural asymmetry. The intensity of the resultant signal is described by **Equation 1.2**.[182]

$$\Delta A = A_L - A_R \qquad \textbf{Equation 1.2}$$

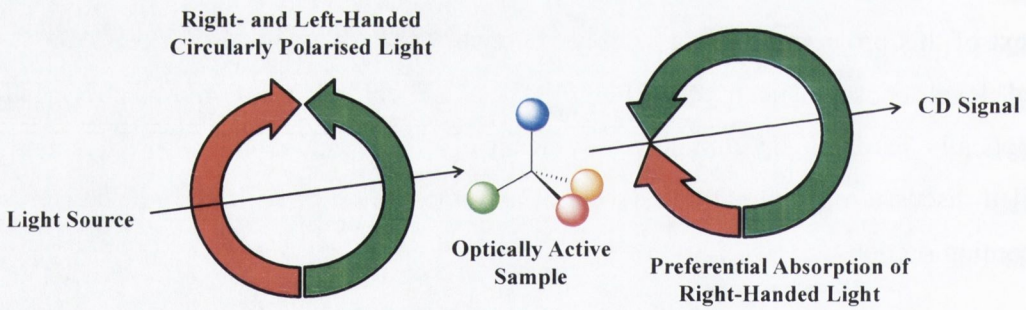

Figure 1.7: *Simplified graphic of the differential absorption of right- and left-handed polarised light by a chiral molecule to produce a measurable CD signal.*

Generated by a CD spectrometer, the electric field vector of a circularly polarised light beam propagates in a helical manner, thus, mimicking the helical pattern by which electrons flow. Considering electronic transitions entail distributions of different handedness, the interaction of this light with a chiral molecule, for which the electrons have no symmetry plane, differs for both left- and right-handed photons (see Figure 1.7). For this reason, chiral molecules absorb the two polarised light forms to varying extents, giving rise to distinct positive and negative CD signals dependent on the chirality. In comparison, achiral species,

where a plane of symmetry exists, absorb left- and right-handed light equally to yield little or no signal.

Serving as an attractive complementary tool, circularly polarised luminescence (CPL) spectroscopy specifically measures the differential spontaneous emission of left- and right-handed circularly polarised light by a chiral luminescent system.[183] The intensity of the CPL signal is defined by **Equation 1.3**, in which I_L and I_R are the emission intensities of the left- and right-handed components, respectively, with ΔI being the difference.[184]

$$\Delta I = I_L - I_R \qquad \textbf{Equation 1.3}$$

At a particular wavelength, the degree of CPL is reported in terms of the luminescence dissymmetry factor, g_{lum} (**Equation 1.4**).[184]

$$g_{lum} = \frac{2(I_L - I_R)}{(I_L + I_R)} \qquad \textbf{Equation 1.4}$$

With CD and CPL both reliant on the same general aspects of molecular structure, electronic CPL spectroscopy may be regarded as the emission analogue of CD spectroscopy.[184] The main difference between the two, however, is that CD reflects the structural properties of the ground electronic state of a system, whereas CPL reflects those properties of the luminescent excited states.[185] Though CPL has been detected for chiral organic molecules and transition metal complexes,[186,187] it is best exemplified by chiral Ln(III) systems.[181,184] Large g_{lum} values, as high as 1.38 (the theoretical maximum of g_{lum} being 2),[188] can be obtained for selected transitions of the latter, compared to chiral organic systems where the extent of circular polarisation is almost always less than 0.01.[189] The undoubted suitability of Ln(III) complexes for CPL spectroscopy has naturally inspired the development of CPL responsive Ln(III) probes with the faculty to inform on local chirality by changes to the circular polarisation of the emission.[184] Distinguished researchers including Parker and Muller have led to the growth of such systems,[188,190-192] which combine the sensitivity of luminescence measurements with the high specificity of the CPL signal for the chiral environment.[174]

Contrary to organic chemistry, where accepted methods for accessing enantiopure compounds are commonplace, the formation of optically pure coordination complexes with controlled stereochemistry is comparably more challenging. General strategies towards chiral Ln(III) systems will be described in the next section.

1.5.2 Conferring chirality to luminescent lanthanide complexes

In order for a luminescent Ln(III) complex to possess chiral character and exploit the powerful CPL potential of these ions, the metal must reside within a chiral environment.[181] To achieve this effect, there exists two principle, but contrasting strategies. The first method for the introduction of chirality to supramolecular systems involves the use of achiral ligands with the ability to assemble around the metal centre in a chiral spatial arrangement, as evidenced from the generation of double and triple helices, or from the helical twist of a macrocyclic ligand.[112,174,193] In most cases, this strategy gives a racemic mixture of the two enantiomeric forms,[194] which may be separated into an enantiomerically pure state by spontaneous resolution or HPLC over chiral stationary phases, for example.[195,196] Nonetheless, purification can be exceedingly difficult because of the lability of the Ln(III) ions.

A far more convenient approach for the synthesis of enantiopure Ln(III) edifices employs non-racemic chiral ligands, whose defined stereochemistry is transferred to the metal in a controlled manner.[174,181,190] This phenomenon is known as *pre-determined chirality*,[197,198] and is most commonly realised through the inclusion of at least one asymmetric carbon in the ligand structure (provided racemisation does not occur).[181] Regrettably, definitive stereochemical predictability has so far proven elusive, underscored by a susceptibility of the metal stereochemistry to change following the most subtle of ligand structural modifications.[174] Despite the aforementioned drawback, this strategy for transmitting chirality remains the more popular of the two, and was preferred for the chiral systems constructed for the purpose of this thesis. Appropriately, some recent literature highlights of chiral Ln(III) self-assembly, with attention to CPL studies, will be discussed in the following section.

1.5.3 Chiral self-assembly

Self-assembly plays a pivotal role in the formation of chiral structures in both the chemical and biological sciences. With application of these systems in chiral molecular recognition and bioanalyte sensing,[174,199] a control of chirality in self-assembled supramolecular architectures is paramount for the development of enantiopure chiroptical probes and sensors.[26,174,181] In particular, chiral Ln(III)-based assemblies are presently favoured for their capacity to lend their unique photophysical properties adequately to CPL, an analytical technique increasingly prevalent in chiral biological probing.[26,200,201]

The creation of monometallic Ln(III) complexes of *pre-determined chirality* from enantiopure ligands is well-established.[202,203] Complementing the work done thus far, Muller

et al. have enlisted the diphenyl-substituted enantiomeric ligand pair, **30S** (*S*,*S*) and **30R** (*R*,*R*), for the assembly of tris-chelate mononuclear chiral complexes from a range of visible- and NIR-emitting Ln(III) ions [Eu(III), Tb(III), and Yb(III)].[204] NMR and luminescence titrations revealed the predominance of the 1:3 (M:L) stoichiometry in acetonitrile, emphasised by the large associated binding constant for the Eu(III) system; log $\beta_{1:3}$ = 23.8. Moreover, an independence of the strongly active CPL signal of **Eu.30$_3$** (g_{lum} = 0.19) from the polarisation of the light source was discerned, consistent with the presence of only one diastereomeric species in solution for both enantiomers. In the solid state, the diastereomeric nature of the complexes was conclusively confirmed by X-ray crystallography, which showed the Δ or Λ metal stereochemistry to be induced by the chiral character of the coordinating ligands (**30S** and **30R**, respectively).

30S (*S*,*S*)

30R (*R*,*R*)

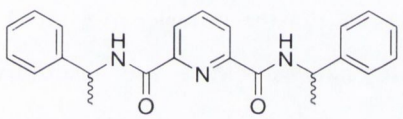

Λ-Eu.30R$_3$

Δ-Eu.30S$_3$

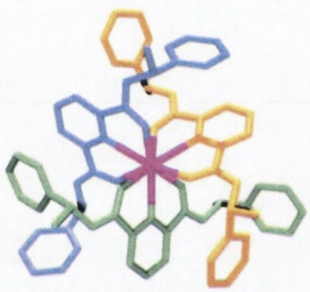

Relative to monometallic chiral systems, reported examples of enantiopure polynuclear Ln(III) assemblies are limited. Recent progress in the guise of a self-assembled Eu(III) triangle was made by Mazzanti and co-workers using only the (*S*) enantiomer of a chiral bipyoxazoline ligand (**31S**).[205] Intriguingly, NMR analysis uncovered the assembly process and affiliated chirality transfer to be highly concentration dependent. At concentrations less than 7 mM, the diastereomeric mononuclear complexes **Δ-Eu.31S$_2$** and **Λ-Eu.31S$_2$** formed with a mild preference for the latter (Λ/Δ ≈ 1.8). However, the appearance of an additional set of signals in the ^{1}H-NMR spectrum at concentrations in excess of 14 mM was accredited to the evolution of a trimetallic homochiral complex **ΔΔΔ-[Eu.31S$_2$]$_3$**. Confirmation of the stereochemical assignment of this triangular Eu(III) system was attained from the X-ray crystal structure, in which co-crystallisation with **Λ-Eu.31S$_2$** was discovered. The exclusive observation of the ΔΔΔ trimetallic species ultimately showcased the inability of the assembly to occur for **Λ-Eu.31S$_2$**, pointing to a mechanism under

stringent diastereoselective control and representing a rare example of homochiral recognition.

31S (*S*,*S*)

31R (*R*,*R*)

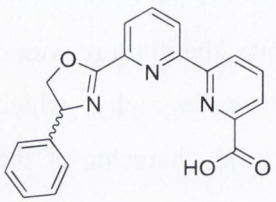

ΔΔΔ-[Eu.31S$_2$]$_3$

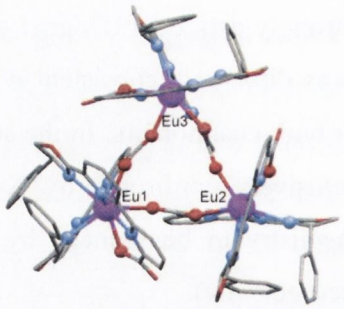

Eu.[(Λ-Eu.31R$_2$).(Δ-Eu.31R$_2$)]$_3$

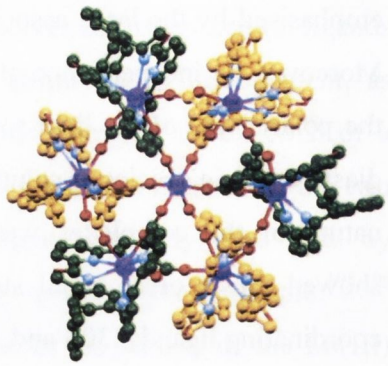

In 2012, the Mazzanti group communicated an extensive update to this work, detailing the separate formation of enantiomeric heptanuclear Eu(III) wheels from the same ligand pair **31S** (*S*,*S*) and **31R** (*R*,*R*).[206] Claimed by the authors to be the largest chiral Eu(III) complexes produced to date, the construction of these multimetallic cyclic structures was accomplished through the controlled addition of an excess of Eu(III) to a diastereomeric mix of **Δ-Eu.31S/R$_2$** and **Λ-Eu.31S/R$_2$**. NMR titrations were conducted to elucidate the assembly pathway, which was found to proceed through intermediates corresponding to the previously reported triangular systems (ΔΔΔ for **31S** and ΛΛΛ for **31R**).[205] Inspection of the crystallographic data showed the final assemblies to be composed of alternating Δ and Λ mononuclear subunits to give **Eu.[(Λ-Eu.31S/R$_2$).(Δ-Eu.31S/R$_2$)]$_3$** heptametallic wheels, hence, signifying a form of diastereoselectivity originating from heterochiral recognition. Additionally, in-depth monitoring of the CPL activity throughout the synthetic procedure further verified the established pathway, with the trimeric intermediate displaying one of the highest g_{lum} values (g_{lum} = 0.45) in the literature for Eu(III).

The concept of chirality, and its foundation in innumerable recognition events, is inherently complex. Nevertheless, an improved comprehension of the many facets of this spatial isomerism, and the role it plays, can be acquired through the synthetic development and subsequent analysis of novel chiral systems. For this purpose, the use of chiral ligands for the metal-directed self-assembly of enantiopure complexes has been routinely validated. Within the Gunnlaugsson research group, the formation of highly innovative chiral luminescent Ln(III) self-assembled complexes and helicates has been focal to research endeavours for many years now. This work, from which a great deal of expertise has been amassed, will be subject to discussion in the next section.

1.6 Advances in the Gunnlaugsson research group

The research of the Gunnlaugsson group encompasses an expansive range of diverse disciplines, with interests spanning the development of cation and anion sensors,[207-210] Ru(II)-coordination complexes,[211-213] naphthalamide DNA binders,[214-217] responsive Ln(III)-AuNP conjugates,[218-220] and supramolecular gels.[221] Chief amongst this variety, and of direct relevance to this research project, is Ln(III) self-assembly. As demonstrated in Section 1.4, self-assembly provides both an effective and flexible route for the synthesis of robustly stable luminescent supramolecular architectures. Geared towards elevating the work to another level, the Gunnlaugsson group has focused intensely on the incorporation of chiral sensitising antennae into acyclic ligand subunits for the formation of chiral luminescent Ln(III) assemblies. Such systems have been the recipient of considerable attention in recent years, with particular enthusiasm shown for the design of efficient chiral probes for *in vivo* application.[222]

Applying self-assembly principles, Gunnlaugsson and co-workers have designed a series of chiral mononuclear Ln(III) complexes from a variety of ligands, all consisting of an amide-substituted central pyridine coordinating unit. This binding motif serves as a successful revision of the dpa ligand framework, and has been continuously elected for use in view of the presence of a tridentate cavity optimal for the assembly of homoleptic Ln(III) tris-chelates (see Section 1.4.1). In 2007, Gunnlaugsson *et al.* published the synthesis, crystallographic characterisation, and chiroptical spectroscopic behaviour of a collection of chiral supramolecular complexes, formed through separate complexation of the enantiomeric ligand pair **32S** (*S*,*S*) and **32R** (*R*,*R*) with a range of $Ln(CF_3SO_3)_3$ salts [Sm(III), Eu(III), Tb(III), Nd(III), and Yb(III)].[223]

32S (*S*,*S*)
32R (*R*,*R*)

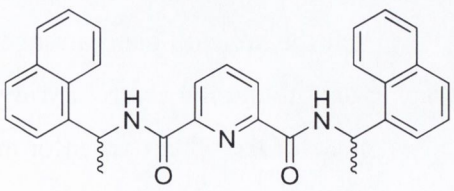

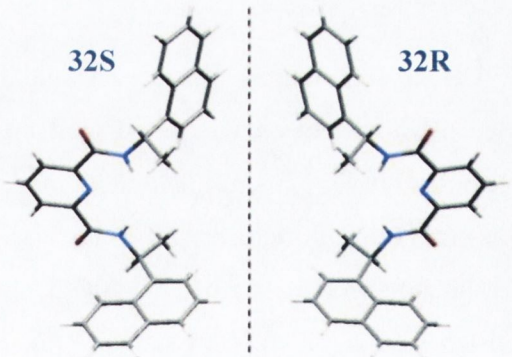

The ligands were synthesised in a single amide-coupling step, whereby the chirality was introduced in the form of two flanking chiral naphthalene moieties, endowed with the

ability to readily sensitise the Ln(III)-centred luminescence. Slow evaporation of the two ligands from CH_2Cl_2 afforded suitable crystals for X-ray diffraction studies, which clearly showed the C_2 ligand symmetry while simultaneously highlighting the enantiomeric relationship between the compounds, a fact reinforced by CD spectroscopy.

Concerning the Ln(III) complexes, NMR and ESI mass spectrometry confirmed the expected 1:3 (M:L) stoichiometry for all systems. Hydration state (q) values were determined to be approximately zero for the Eu(III) analogue, indicative of coordinative saturation in aqueous media and consistent with the generation of a nine-coordinate Ln(III) species from the self-assembly of three ligands about a single metal centre. The progression of the complexation process in solution was monitored by UV-vis and luminescence titrations, which again accentuated the predominance of the **Ln.32S/R$_3$** system. From these measurements, binding constants in the range of $\log \beta_{1:3} = 20 - 22$ were calculated for the Eu(III) complexes of **32S** and **32R** in acetonitrile.[224]

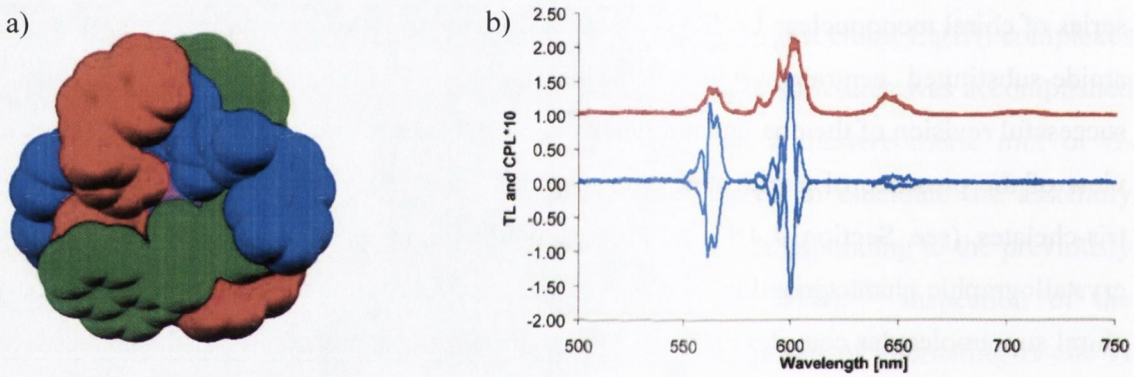

Figure 1.8: *a) X-ray crystal structure of the* ***Tb.32R$_3$*** *complex showing the helical ligand arrangement. b) The luminescence emission spectrum of the* ***Sm.32S$_3$*** *complex (red) and the circularly polarised emission spectra of the two Sm(III) complex enantiomers (blue).*

Valuable structural insight was gained through X-ray analysis of the solid state complexes, which not only exposed their highly symmetrical, bundle-type appearance, but also demonstrated the overall complex chirality arising from the helical ligand arrangement. With regards to stability, a review of the crystallographic data found the central pyridyl ring of each ligand to intercalate between the naphthalene antennae of the other two, informing of the existence of stabilising π-π stacking interactions throughout the structures (Figure 1.8a). From a chiral perspective, these results showed **32S** and **32R** to give rise to enantiopure Ln(III) complexes of opposite helicity, proof that the assembly process was in fact diastereoselective and hinged on the choice of ligand enantiomer. Upon assignment, this relationship was simplified to **32S** and **32R** conferring Δ and Λ metal stereochemistry,

respectively. Indisputable spectroscopic evidence of the chirality transfer was provided using CPL techniques. With the metals now residing within a chiral pocket, the enantiomeric Ln(III) complexes predictably yielded CPL spectra consisting of emission signals of equal magnitude but opposite sign (Figure 1.8b). Furthermore, the reasonably large g_{lum} dissymmetry factors established the assemblies to be homochiral in solution.

In light of the high thermodynamic stabilities and strong chiral emissions, these enantiomeric monometallic complexes stood to represent a significant landmark in the advancement of Ln(III) self-assembly within the Gunnlaugsson group. Owing to their shape and structure, which bore an uncanny resemblance to the ball used in the Gaelic sport of hurling, they were named *The Trinity Sliotars*. Indeed, these original chiral sliotars have been heavily influential to the assemblies produced in the group since, where the goal has always been to modify the parent structure in new and exciting ways. An up-to-date account of recent successes in this area will be delivered in the next section.

1.6.1 Modifying the Trinity Sliotar

Implemented to great effect, and distinguishing the ligand set **33** – **35**, was a modification strategy founded on variation of the chiral antennae of **32**. Replacing the naphthalene units for chiral tryptophan antennae, ligands **33S** (*S*,*S*) and **33R** (*R*,*R*) presented as a more radical departure from the original structure.[225] Unexpectedly, the trends and subsequent fitting of UV-vis and luminescence titrations confirmed the dominant formation of a 1:2 (M:L) complex for both Eu(III) and Tb(III). The complete absence of the anticipated 1:3 (M:L) stoichiometry, also apparent from mass spectrometry, was accredited to the relative increase in steric hindrance around the metal ion.

33S (*S*,*S*)
33R (*R*,*R*)

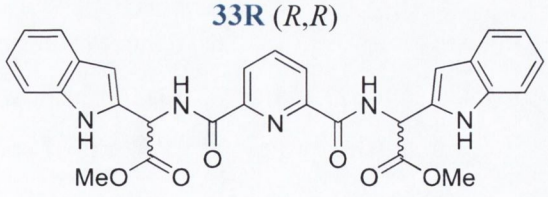

34S (*S*,*S*)
34R (*R*,*R*)

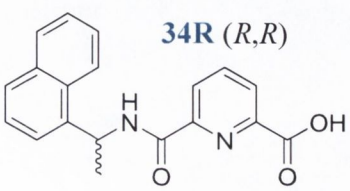

35S (*S*,*S*)
35R (*R*,*R*)

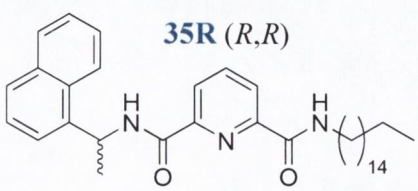

Carrying only a single naphthalene chromophore, the ligand pair **34** was developed as an asymmetrical analogue of **32**.[226] Utilising many of the same characterisation techniques, **34S** (*S*,*S*) and **34R** (*R*,*R*) were similarly shown to form 1:3 (M:L) complexes with several Ln(III) ions. Observation of phosphorescence spectral changes in the Eu(III) titrations of both ligands helped to identify luminescence intensity maxima upon the addition of 0.33 eq. of metal, evidential of the favoured formation of **Eu.34S/R$_3$** in solution. MM2 molecular modelling calculations were suggestive of a *half helicate* complex topology being most plausible, for which the three ligand antennae were positioned on the same side. This model exhibited a more open structure to that seen for **32**, perhaps explaining the slight reduction in the binding constants. As before, the ability of the respective ligands to dictate complex chirality was demonstrated by CPL spectroscopy.

The synthetic attachment of a long hydrophobic hexadecyl chain to the carboxylic acid terminus of **34** was later performed to give **35S** (*S*,*S*) and **35R** (*R*,*R*), ligands perfectly equipped for the genesis of chiral amphiphilic Ln(III) self-assemblies.[227] Not only studied in solution, the enantiomeric **Eu.35S/R$_3$** systems were applied in the construction of stable self-assembled monolayers at the air-water interface. Employing Langmuir-Blodgett techniques, these chiral monolayers were then transferred to quartz slides to form luminescent Eu(III) films, from which the chiral emission was probed using CPL. The described systems, which acted as the first examples in their class, were designed with the view to satisfy the rising demand for supramolecular assemblies that can be further organised into functional devices. This movement into the realm of materials chemistry, therefore, reflects an enormous degree of versatility on behalf of chiral Ln(III) sliotar derivatives.

Through coupling of suitable spacer groups, the structure of **32** has since been adapted to include an additional binding pocket for the assembly of chiral bimetallic triple-stranded Ln(III) helicates, the first examples of which were developed from **36S** (*S*,*S*) and **36R** (*R*,*R*).[228] For this pair, the formation of **Eu$_2$.36S/R$_3$** helical species was ably demonstrated through rigorous analytical investigation. Significantly, the evolution of the metal-centred phosphorescence was monitored by Eu(III) titrations in acetonitrile, where the emission was observed to be most intense following the addition of 0.7 eq. of metal. This observation, allied with the NMR titration trends, emphasised the dominance of the desired 2:3 (M:L) stoichiometry in solution. In addition, excitation of the naphthalene antennae was found to sensitise Eu(III)-centred CPL emission of opposite sign, proving **Eu$_2$.36S$_3$** and **Eu$_2$.36R$_3$** to exist as enantiomers.

36S (*S*,*S*)

36R (*R*,*R*)

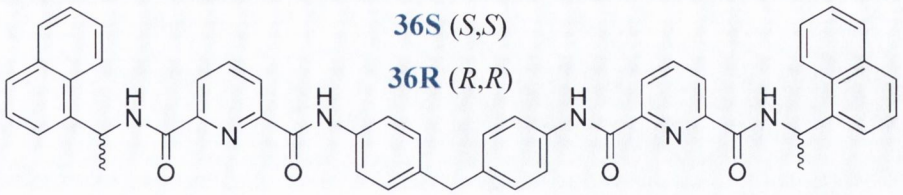

37S (*S*,*S*)

37R (*R*,*R*)

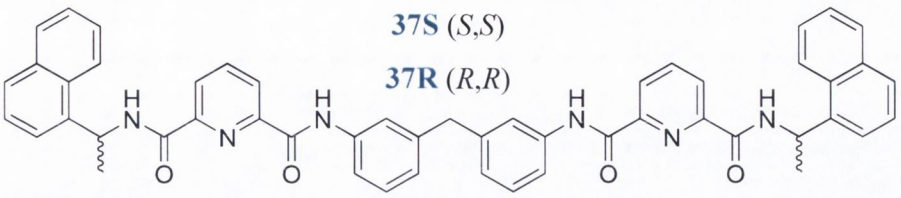

38S (*S*,*S*)

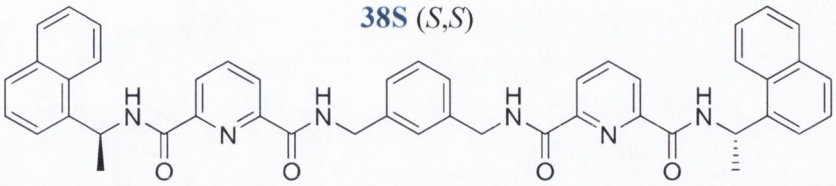

By incorporation of a *meta*-methylenediphenyl spacer that contrasted to the *para*-arrangement of **36**, ligands **37S** (*S*,*S*) and **37R** (*R*,*R*) were designed with the intent of studying the effects of ligand structural isomerism on helicate formation.[229] Interestingly, fitting of the UV-vis and luminescence titrations ascertained both ligands to form 2:3 (M:L) Eu(III) helicates of enhanced stability compared to those built before. An explanation for this improved binding was sought from MM2 models, which indicated the presence of a comparatively more *squeezed* complex cavity for **37**. This reduction in cavity size was foreseen to permit tighter coordination of the two Eu(III) ions in $\mathbf{Eu_2.37S/R_3}$, with a concurrent increase in stabilising π-π forces. Switching to a xylene spacer, ligand **38S** (*S*,*S*) was also shown to form 2:3 (M:L) helicates of comparable stability with a series of Ln(III).[230]

Briefly described with accompanying examples in Section 1.4.1,[135,136] the introduction of *para*-functionality to the dpa pyridine ring represents a synthetic modification whose application to Ln(III) sliotar systems, though in its relative infancy, offers massive promise. Possessing the exact same core as **32** and differing only through substitution of the pyridyl 4-position, the enantiomeric ligand pairs **39** and **40** have been previously synthesised to pursue this strategy (X = OH and Cl for **39** and **40**, respectively), with work pertaining to these compounds reported in the PhD thesis of Dr N. S. Murray.[231] Analysis of the Ln(III) complexation products of these chiral compounds in both solution and the solid state established the prevailing formation of 1:3 (M:L) complexes analogous to the original sliotar systems of **32**, with CD and CPL spectroscopy shedding light on the chirality transfer from

ligand to later supramolecular system. Supplementary to this, the calculated log $\beta_{1:3}$ binding constants, being of the same approximate magnitude as those measured for **Ln.32S/R$_3$**, showed both substituents to have negligible effects on complex stability. Consequently, these *para*-positioned groups can be proposed as excellent reactive handles for the attachment of new and varied functionality anticipated to extend away from the metal ion centre, whilst having minimal effect on the overall stability of the luminescent self-assembly.

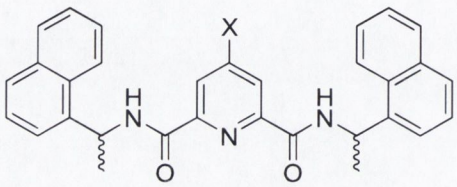

39S (*S*,*S*); **39R** (*R*,*R*): X = OH

40S (*S*,*S*); **40R** (*R*,*R*): X = Cl

Eu.40S$_3$

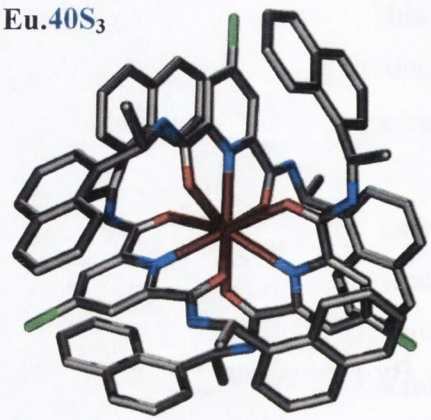

With an ample choice of different moieties for grafting to this point, unlimited opportunities for the conferral of new properties and function to these chiral sliotar complexes can be envisaged. Capitalising on the relatively unexplored potential of this modification tactic, the global objective of this research project has been the development of chiral luminescent Ln(III) sliotar analogues with novel *para*-functionality.

1.7 Work described within this thesis

The fundamental objective of the research reported in this thesis was to enrich the contribution of the Gunnlaugsson group to the field of supramolecular Ln(III)-directed self-assembly. Building on work previously conducted within the group, an expansive library of chiral luminescent Ln(III) self-assembled complexes were developed and analysed, with particular importance attached to comprehensive photophysical studies. The majority of the systems to be described were based on the dpa-derivatised chiral sliotar framework, with multiple variations of this complex motif achieved by the introduction of a broad range of functionality to the ligand pyridyl 4-position.

In Chapter 2, the design, synthesis, and photophysical evaluation of a collection of chiral Eu(III) sliotar analogues, each differentiated by their terminal ligand substituent, will be described. Encompassing propyl-, propargyl-, and polyethoxy-appended derivatives, the

analysis of these systems is structured in the form of a comparative study, one contrived to explore the effects of ligand *para*-modification on complex properties such as stability and luminescence quantum yield. Emphasis will be predominantly placed on the polyethoxy systems, which facilitated *in situ* spectrophotometric measurements in a mixed aqueous solvent system. Importantly, this chapter serves as an invaluable source of reference for the work detailed throughout the remainder of this thesis.

In Chapter 3, investigation into the amenability of the chiral sliotar design for the creation of higher-order structures will be discussed. Specifically, discussion will focus on the facility of Eu(III) sliotar derivatives with terminal dibenzo[24]crown-8 macrocycles to spontaneously generate tris[2]pseudorotaxanes with a novel histaminyl(ferrocenylmethyl)-ammonium thread. For this design, threading was anticipated to occur with concomitant quenching of the Eu(III)-centred luminescence *via* electron donation from the ferrocenyl group. Operating under this hypothesis, it was envisaged that formation of the predicted assemblies could be photophysically tracked. Accordingly, the main bulk of this chapter is dedicated to photophysical examination.

In Chapter 4, the *Click Chemistry*-mediated delivery of a protected β-D-galacto-pyranoside unit to the pyridyl 4-position of the sliotar ligand scaffold will be explored. Ultimately, this chapter is devoted to establishing whether the appended monosaccharide interferes with the self-assembly of analogous Eu(III) tris-chelate sliotars, with a view to potential future employment as bio-imaging agents, which tactfully exploit carbohydrate-lectin interactions for binding specificity.

In Chapter 5, the application of self-assembly methodology for the construction of chiral multimetallic Eu(III) edifices from ditopic sliotar-related ligands will be chronicled. By incorporation of two Ln(III)-binding termini, these ligands were structurally equipped to promote the formation of polynuclear complexes.

In Chapter 6, the development of a series of luminescent multimeric ternary Ln(III)-cyclen self-assemblies will be accounted. Discussion will be primarily concerned with the photophysical evaluation of dimeric ternary Ln(III) complexes (where Ln = Eu or Tb), in which two triacetamide-substituted cyclen molecules are bridged by a ditopic dpa-based linker. The potential utility of the Tb(III) analogue as an anion sensor, probed by means of luminescent displacement assays, will then be detailed. Thereafter, attention will shift to studying the self-assembly of trimeric ternary Ln(III) complexes (where Ln = Eu or Tb), a design that conversely avails of a planar tritopic benzoate ligand.

Lastly, in Chapter 7, general experimental procedures and relevant characterisation data are provided for all compounds synthesised.

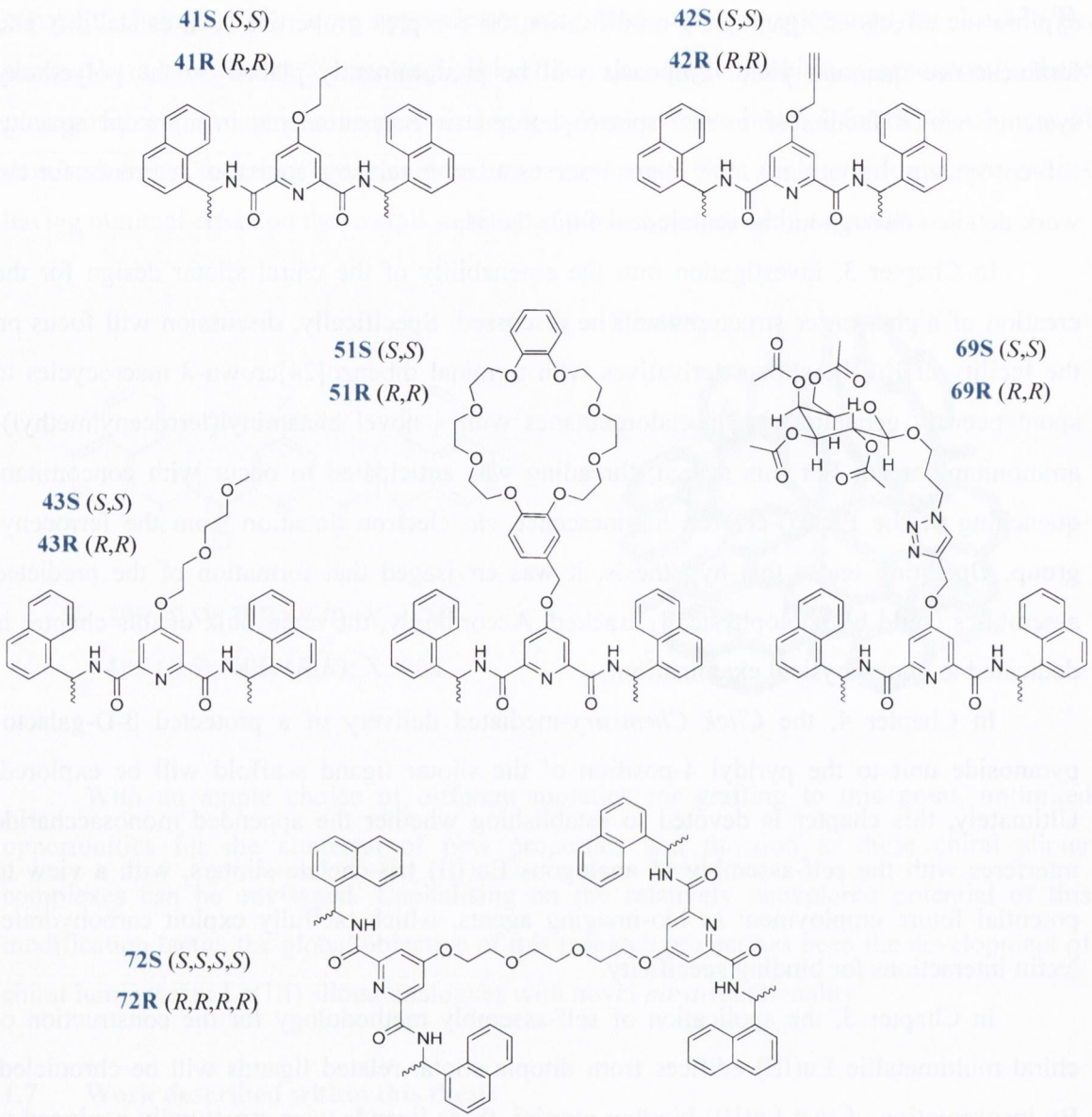

Figure 1.9 *Chemical structures of the chiral sliotar ligand analogues synthesised for this PhD project (the compound numbering corresponds to their order in the later chapters).*

Chapter 2

Synthesis and Photophysical Evaluation of Chiral Luminescent Lanthanide Sliotar Complexes

2 Introduction

As previously discussed in Chapter 1, the incorporation of Ln(III) ions into complex supramolecular architectures can allow for the distinctive photophysical properties of the metals to be precisely modulated and fine-tuned for novel application. As a result, Ln(III) supramolecular chemistry has recently emerged as a thriving research specialty within the broader discipline.[18,19] With a view to designing functional mono and multimetallic Ln(III) systems, the use of self-assembly methods, whereby the metal actively directs complex formation from smaller complementary subunits, has repeatedly proven invaluable.[28,107] In recent years, Gunnlaugsson and co-workers have availed of an intelligent refinement of this strategy, by employing chiral ligands for the diastereoselective synthesis of enantiopure luminescent Ln(III) assemblies. The first breakthrough in this regard came in the form of the chiral coordination complexes called *Trinity Sliotars*, assembled from the enantiomeric pair of chiral pyridyl ligands **32S** (*S,S*) and **32R** (*R,R*) (see Section 1.6).[223] Shown to possess high stabilities and enviable CPL emissions, these systems have consequently helped to inspire the design of a whole variety of self-assemblies produced in the group since.[225-230] Of significant relevance to the work described in this thesis, however, was a modification tactic centred on the introduction of *para*-functionality to the structure of **32**, with early success achieved in the form of the ligand pairs **39** and **40** (X = OH and Cl, respectively).[231]

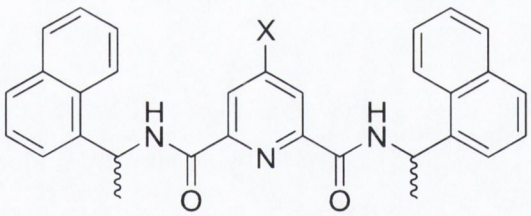

32S (*S,S*); **32R** (*R,R*): X = H

39S (*S,S*); **39R** (*R,R*): X = OH

40S (*S,S*); **40R** (*R,R*): X = Cl

Eager to build on this preliminary foundation, the principle aim of this research project was the development of an extensive, varied collection of *para*-substituted sliotar analogues, all formed by chemical attachment to the nucleophilic 4-hydroxy group of **39**. Through intensive analysis of these chiral Ln(III) species, the potential of this structural adaptation for unlocking superior complex properties and function could be explored, with the substituent not predicted to hinder complex formation on account of its strategic positioning. For the purpose of this chapter, ligands **41** – **43** were designed.

2.1 Design of the enantiomeric ligand pairs 41 – 43

All three ligand pairs were derived from 4-hydroxypyridine-2,6-dicarboxylic acid (chelidamic acid), a commercially available dpa variant. As explained in Section 1.4, this binding motif has been commonly integrated into the design of many Ln(III)-coordinating ligands. Ligands based on this framework are capable of fulfilling the large coordination demands of the Ln(III) to yield saturated tris-chelates through coordinate bond formation with the pyridyl nitrogen and two carbonyl oxygen atoms.[112,116,117,128]

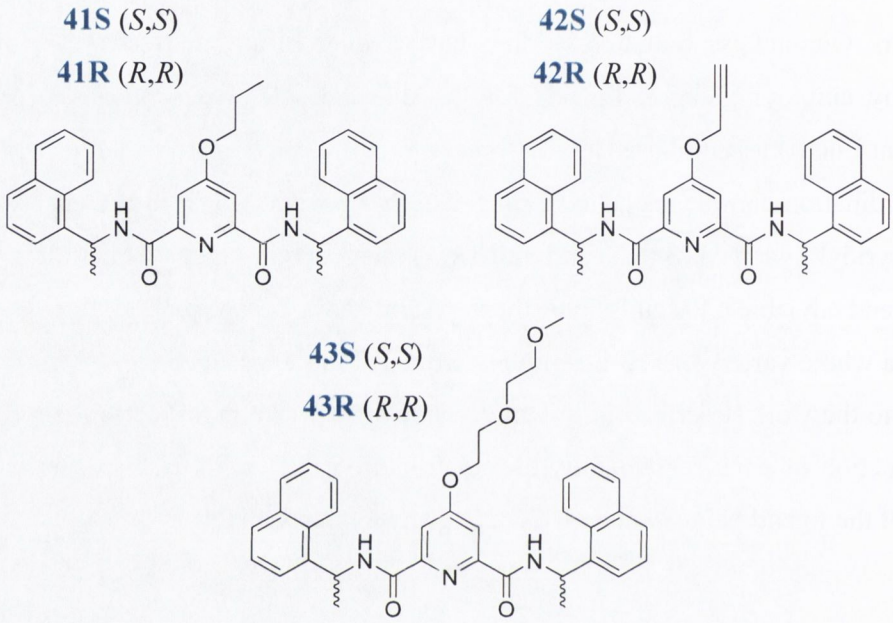

Visible-emitting Eu(III) was selected as the Ln(III) of choice in view of its relatively high luminescence efficacy and resistance to quenching by molecular oxygen.[24] However, direct excitation of Eu(III) is inherently troublesome due to the low metal ion extinction coefficients and large energy gaps between ground and emissive states.[48,51] This particular problem can, nevertheless, be overcome through use of an appropriate sensitising antenna to indirectly populate the Eu(III) excited state. With strong near-UV absorption and a low-lying triplet state, naphthalene and its many derivatives have been shown to be well equipped to promote Eu(III) excitation by the *antenna effect*.[232,233] For this reason, chiral 1-(1-naphthyl)-ethylamine chromophores were preferred to perform the Ln(III)-sensitisation function for these systems. Owing to the presence of an asymmetric carbon, these naphthyl groups are further endowed with the unique capacity to transfer chirality to the resultant complex, and were stationed at both the 2- and 6-pyridyl positions of the chelidamic acid scaffold. Moreover, the *para*-hydroxy group of this framework offers a suitable reactive site for the grafting of functionality by nucleophilic substitution chemistry.

Developed first was the ligand pair **41S** (*S*,*S*) and **41R** (*R*,*R*), each substituted at the hydroxy terminus with a propyl chain. By removal of the proximate second-sphere O-H quenching vibrations of the hydroxy group, substitution at this position was expected to increase the luminescence efficiency relative to **Ln.39$_3$** *via* a reduction in non-radiative quenching. Ligands **42S** (*S*,*S*) and **42R** (*R*,*R*), on the other hand, were terminated with a propargyl moiety. This terminal alkyne group imparts the structure with rich potential for further synthetic elaboration by Cu(I)-catalysed azide-alkyne cycloadditions, reactions that fall under the scope of the field known trivially as *Click Chemistry* (further discussion in Chapter 4).[234] Of particular importance, and serving as the primary focus of this chapter, are the enantiomeric pair **43S** (*S*,*S*) and **43R** (*R*,*R*). Up to this point, the greatest limitation of sliotar systems previously studied has been a lack of aqueous solubility, restricting their analysis to organic media. In an effort to address this, the structure of **43** includes a long polyethoxy chain, a function with demonstrated ability for conferring water solubility in supramolecular Ln(III) complexes.[135,136,235] This alteration could present opportunities for the future development of chiral luminescent probes for application *in vivo*.

The work described in this chapter ultimately forms the basis of a comparative study, similar in nature to those conducted by Bünzli and Bettencourt-Dias *et al.*,[129,136] details of which can be found in Section 1.4.1. Not only exclusive to **41** – **43**, but extended to earlier ligand analogues too, this study was constructed to provide a comprehensive photophysical investigation into the effects of *para*-substitution on complex stability, luminescence quantum yield, and metal-sensitisation efficiency.

2.2 Synthesis and characterisation of the enantiomeric ligand pairs 41 – 43

The first step in the design of ligands **41** – **43** concerned the coupling of two chiral naphthalene antennae **45** to the carboxylic groups of chelidamic acid **44**.[231] As shown in Scheme 2.1, this coupling reaction involved initial stirring of the appropriate enantiomer (either *S* or *R*) of commercially available 1-(1-naphthyl)-ethylamine **45** with 1-hydroxy-benzotriazole hydrate (HOBt) and chelidamic acid **44** in anhydrous THF at 0 °C for 30 min. After this, the coupling reagent *N*-(3-dimethylaminopropyl)-*N'*-ethylcarbodi-imide (EDCI.HCl) was added along with triethylamine, and the mixture stirred under argon for an additional 30 min at 0 °C and a further 48 h at room temperature. Upon completion, the insoluble residue present was filtered off and the solvent removed under reduced pressure. The resulting crude product was then dissolved in CH_2Cl_2 and washed with 0.1 M HCl, saturated aqueous $NaHCO_3$, and H_2O. Purification was achieved using flash silica column chromatography (gradient elution 100:0 → 95:5; CH_2Cl_2/MeOH), followed by precipitation

from H_2O to afford a cream coloured solid obtained in 63% and 56% yield for **39S** and **39R**, respectively. The amide NH signal at 8.55 ppm and aromatic CH resonances from 8.25 – 7.54 ppm observed in the ^1H NMR (400 MHz, CD_3CN) spectra of both enantiomers were indicative of successful coupling of the naphthalene moieties.

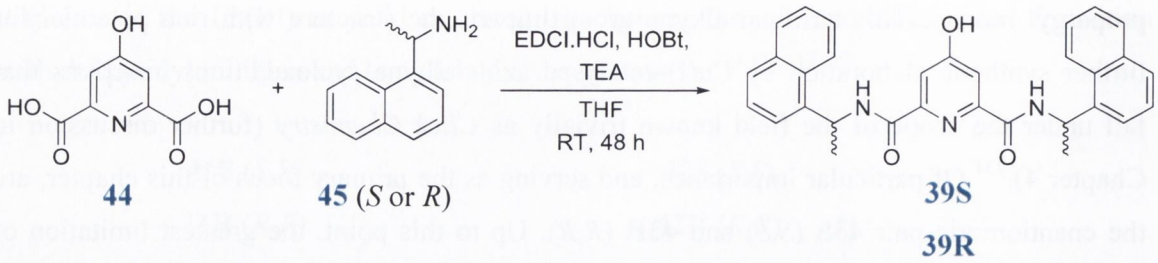

44 **45** (*S* or *R*) **39S** **39R**

Scheme 2.1: *Synthetic pathway for* ***39****.*

The final step in ligand development required synthetic attachment of the relevant functionality to the 4-hydroxy group of **39**. In the case of **43**, the synthesis of a sufficiently reactive polyethoxy chain derivative, 1-iodo-2-(2-methoxy-ethoxy)ethane **48**, which would later facilitate tethering to this position, was undertaken (see Scheme 2.2).[236]

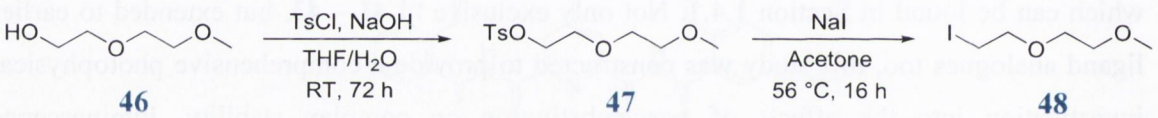

46 **47** **48**

Scheme 2.2: *Synthetic pathway for* ***48****.*

To tosylate the free alcohol moiety, diethylene glycol monomethyl ether **46** and 4-toluenesulfonyl chloride were reacted in the presence of NaOH for 72 h in a THF/H_2O solvent mixture. The reaction solution was extracted with $CHCl_3$, and the solvent evaporated to yield **47** as a colourless oil in 60% yield. The formation of the tosylated chain was evidenced in the ^1H NMR (400 MHz, $CDCl_3$) spectrum, where the appearance of a singlet at 2.44 ppm and two aromatic doublets at 7.79 ppm and 7.33 ppm, corresponding to the tosyl group, could be identified. In the next step, NaI and **47** were refluxed in acetone for 16 h to exchange the tosyl for the iodine functionality. The white precipitate formed was separated by suction filtration before removing the solvent and dissolving in $CHCl_3$. The organic phase was washed with H_2O and brine and the solvent evaporated to give **48** as a brown oil in a highly pure form with 74% yield. Confirmation of the expulsion of the tosyl group was provided by the ^1H NMR (400 MHz, $CDCl_3$) spectrum, from which the previously discussed tosyl signals were no longer visible.

Introduction of the *para*-substituents was accomplished by adhering to the protocol shown in Scheme 2.3.[237] These reactions were initiated by stirring either **39S** or **39R** with anhydrous K_2CO_3 in anhydrous DMF for 30 min at 25 °C. The pertinent alkylating agent; 1-bromopropane **49**, propargyl bromide **50**, or the iodo reagent **48** (producing **41**, **42**, or **43**, respectively) was subsequently added, and the mixture was heated for 72 h at 80 °C. After cooling to room temperature, the solvent was removed and the residue dissolved in CH_2Cl_2. Washing with both 1% acetic acid (aqueous) and H_2O, before recrystallisation from EtOH, gave the desired products **41** – **43** as white solids in yields ranging from 32 – 67% (full details in Chapter 7).

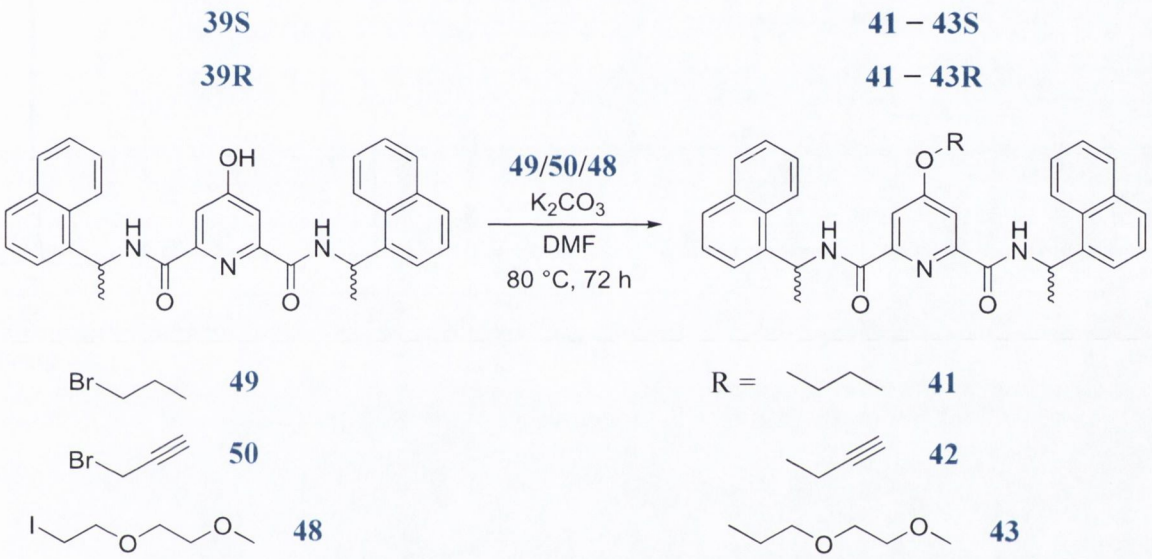

Scheme 2.3: *General synthetic pathway for **41**, **42**, and **43**.*

^{1}H NMR techniques were helpful in elucidating key structural information, with full assignment of the peaks made possible through a range of H-H COSY, HSQC, and HMBC experiments. The downfield aromatic region of each spectrum contained signals correlating to the protons of the central pyridyl ring and two flanking naphthalene groups. Examination further upfield verified appendage of each chain. For **41** (Figure A2.2), the three resonances at 4.04 ppm, 1.83 ppm, and 1.02 ppm, with a combined integral of 7, can be attributed to the propyl chain. In the spectrum of **42** (Figure A2.3), the alkynyl CH appeared as a triplet at 2.58 ppm integrating to 1. Supporting synthesis of the polyethoxy analogue **43** was the ^{1}H NMR (600 MHz, $CDCl_3$) spectrum (Figure 2.1), from which the characteristic signals of the chain at 4.27 – 3.57 ppm (CH_2) and 3.38 ppm (CH_3) were clearly visible, thus, proof of its existence within the final structure. In addition to NMR techniques, other methods such as

infrared (IR) spectroscopy and high resolution mass spectrometry (HRMS) were employed for complete characterisation of these final compounds (see Chapter 7).

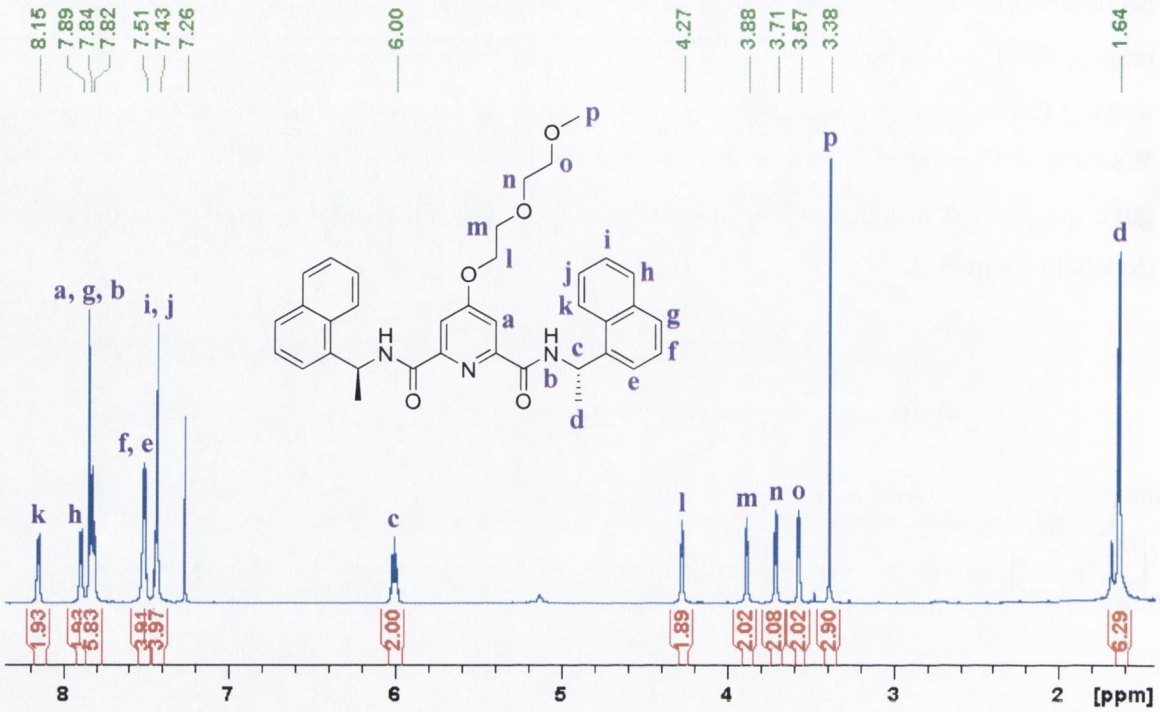

Figure 2.1: *^{1}H NMR (600 MHz, $CDCl_3$) spectrum of ligand **43S**.*

2.3 Solid state X-ray crystallographic analysis of ligand 43R

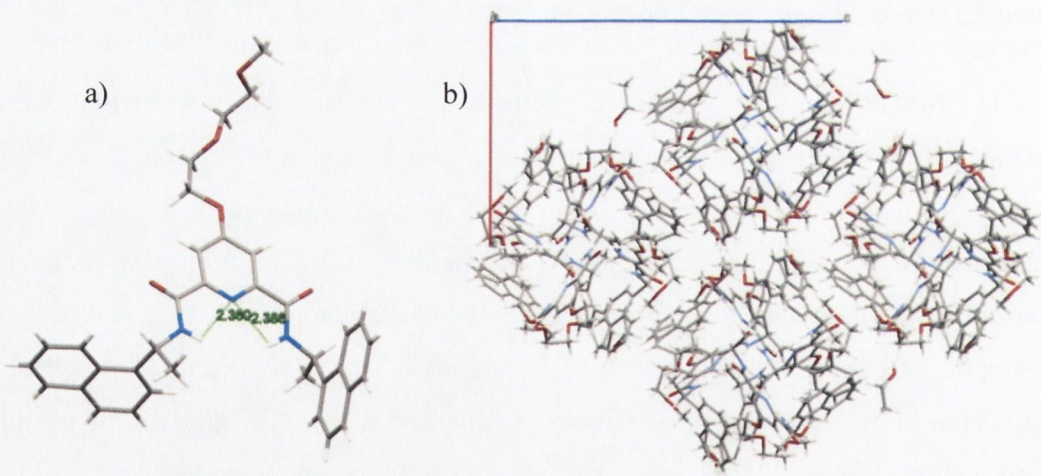

Figure 2.2: *a) X-ray crystal structure (capped stick) of ligand **43R** highlighting the hydrogen bonding between the amide NH protons and pyridyl nitrogen atom (second ligand molecule and solvent molecules omitted for clarity). b) X-ray packing diagram of **43R** viewed down the b-axis.*

Clear plate-shaped single crystals of the polyethoxy-substituted ligand **43R** were grown by EtOH recrystallisation, permitting collection of the X-ray crystal structure, with structural determination conducted by Dr. M. Martinez-Calvo of the Gunnlaugsson group. The ligand was found to crystallise in the chiral orthorhombic $P2_12_12_1$ space group, and contained two ligand molecules, along with two interstitial EtOH solvent molecules in the asymmetric unit (see Figure 2.2a – only one ligand molecule shown and solvent molecules omitted for clarity). In terms of ligand arrangement, the amide NH protons were orientated towards the central pyridyl ring, allowing the formation of hydrogen bonds with the pyridyl nitrogen atom. Additionally, these amido protons were capable of hydrogen bonding to the carbonyl oxygen atom of the neighbouring molecule, with this intermolecular interaction repeated throughout the structure to give a hydrogen bonded chain of molecules.

2.4 Synthesis and characterisation of Eu(III) complexes of 41 – 43

The synthesis of the Eu(III) complexes of **41** – **43** was achieved by refluxing, under microwave irradiation, the relevant ligand with 0.33 eq. of $Eu(CF_3SO_3)_3$ for 20 min in HPLC grade MeOH solution (Scheme 2.4). Selection of the 1:3 (M:L) molar ratio was made with the objective of constructing coordinatively saturated Eu(III) tris-chelates analogous to the original sliotar systems **Eu.32S/R$_3$** (CN = 9).[223] Vapour diffusion of diethyl ether into the reaction solutions was done to precipitate the complexes, which were isolated by filtration as white crystalline solids in yields from *ca.* 68 – 82%. In each case, verification of successful metal complexation was provided by ^{1}H NMR, HRMS, elemental analysis, and IR.

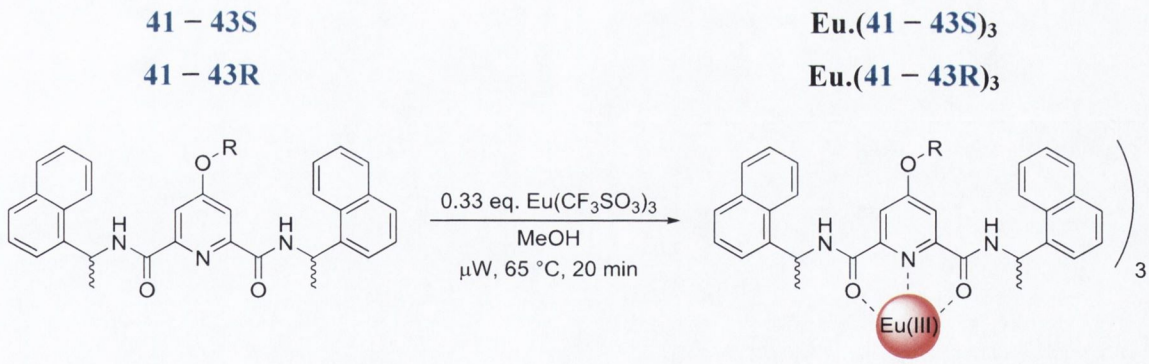

Scheme 2.4: *General synthetic pathway for* ***Eu.(41 – 43S)$_3$*** *and* ***Eu.(41 – 43R)$_3$*** *by complexation of* ***41 – 43*** *with* $Eu(CF_3SO_3)_3$.

The paramagnetic nature of the Ln(III) ions bears a heavy influence on their complex ^{1}H NMR spectra. Indeed, protons in close proximity to the paramagnetic centre are known to be greatly impacted by the unpaired *f* electrons of the metal, which enable a more efficient

relaxation of their nuclear spins. This ultimately has the effect of broadening their proton resonances, with an accompanied chemical shift of the signal frequency relative to the free ligand.[238] With regards to **Eu.(41 – 43)$_3$**, the ^{1}H NMR (400 MHz, CD_3OD-d_4) spectra of all six complexes displayed a characteristic broadening and shifting of their signals, an effect pointing to successful metal ion-ligand complexation (Figure 2.3, Figure A2.4 – A2.8). As with their corresponding ligands, the complex spectra were found to be identical for both enantiomers in a pair, and showed each to exhibit a high degree of symmetry in solution.

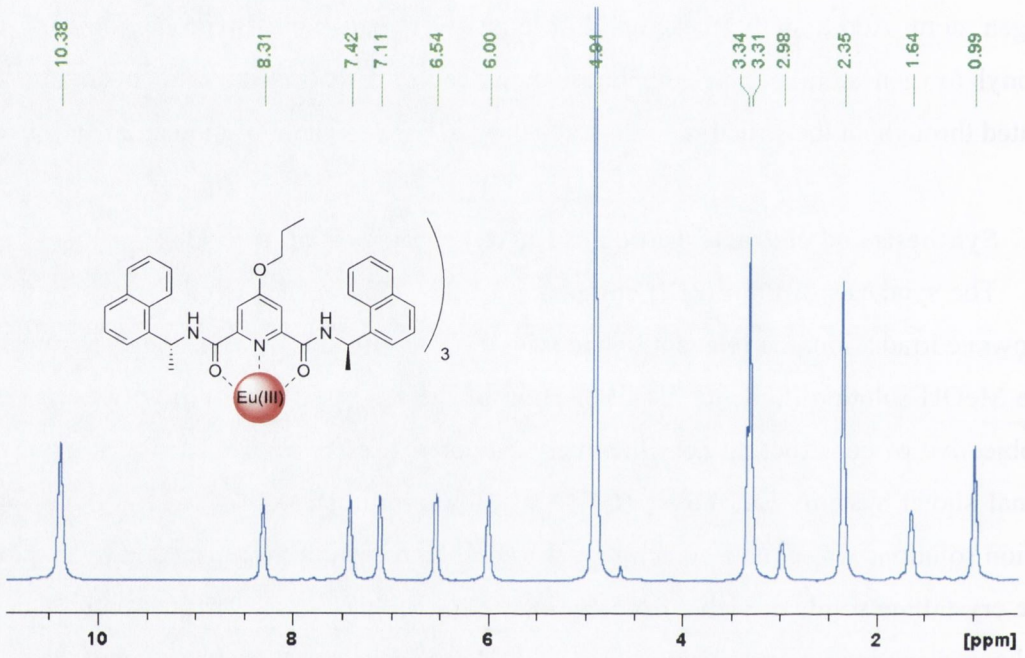

Figure 2.3: *^{1}H NMR (400 MHz, CD_3OD-d_4) spectrum of complex* ***Eu.41R$_3$****.*

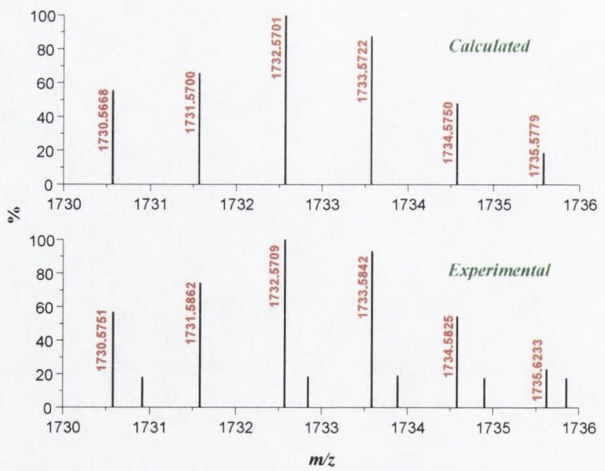

Figure 2.4: *The calculated and experimental isotopic distribution patterns (MALDI$^+$) for complex* ***Eu.42R$_3$*** *showing the 1:3 (M:L) stoichiometric pattern for a molecular species of formula [M – 3CF$_3$SO$_3$ – 2H]$^+$ (spectra are normalised – dominant peak set to 100%).*

These Eu(III) complexes were further characterised by HRMS analysis ($MALDI^+$), which established the desired 1:3 (M:L) composition. Figure 2.4 shows the calculated and experimental isotopic distribution patterns for complex **Eu.42R$_3$** (see Figure A2.9 – A2.13 for the patterns of the other complexes). For all systems, the shape and distribution of the experimentally detected pattern was found to closely match that calculated for a molecular species of formula $[M - 3CF_3SO_3 - 2H]^+$, where M = **[Eu.L$_3$](CF$_3$SO$_3$)$_3$**. These findings were, therefore, indicative of a parent structure possessing the predicted 1:3 (M:L) complex stoichiometry, a fact reinforced by the elemental analysis.

Table 2.1: *Summary of the experimentally found m/z peaks for* ***Eu.(41 – 43)$_3$****, and their corresponding values calculated for a molecular species of formula* $[M - 3CF_3SO_3 - 2H]^+$.

Complex	*m/z* (experimental)	*m/z* (calculated)
Eu.41S$_3$	1744.6824	1744.6640
Eu.41R$_3$	1744.6713	1744.6640
Eu.42S$_3$	1732.5735	1732.5701
Eu.42R$_3$	1732.5709	1732.5701
Eu.43S$_3$	1924.7225	1924.7277
Eu.43R$_3$	1924.7211	1924.7277

Additional to NMR and mass spectrometry techniques, IR spectroscopy is another valuable tool in probing the occurrence of metal complexation, relying on the susceptibility of the vibrational bands associated with the bound ligand groups to undergo a frequency change upon coordination.[193]

Table 2.2: *Summary of the IR stretching frequencies (cm^{-1}) of the amide carbonyl groups of the free ligands* ***41 – 43*** *and their corresponding complexes* ***Eu.(41 – 43)$_3$****.*

Compound	Free Ligand C=O Stretch (cm^{-1})	Complex C=O Stretch (cm^{-1})
41S	1659	1618
41R	1658	1618
42R	1643	1618
42R	1645	1619
43S	1655	1619
43R	1655	1619

The simplest band to follow in the spectra of **41 – 43** (free and complex) was that of the amide carbonyl groups thought to be directly coordinated to the Eu(III) ion. Indeed, there was an observed shift of the carbonyl IR stretching frequency to a lower wavenumber upon complexation, therefore, endorsing the participation of the carbonyl bonds in coordination. A summary of these frequency changes for the three enantiomeric pairs is shown in Table 2.2. All the data presented in this section combined to prove formation of the complexes using synthetic means.

2.5 Solid state X-ray crystallographic analysis of Eu(III) complexes

Consistent with the self-assembly of nine-coordinate Eu(III) ion complexes, HRMS and elemental analysis supplied the first evidence of the 1:3 (M:L) stoichiometry in the complex set **Eu.(41 – 43)$_3$**. Visual evidence corroborating this 1:3 (M:L) stoichiometry was subsequently acquired by X-ray crystallographic analysis of the complexes, with structural determination managed in the case of **Eu.41S$_3$** and **Eu.43S$_3$**. Crystallographic elucidation was also achieved for the previously developed hydroxy-substituted analogue **Eu.39R$_3$**, which served as an example of a *para*-derivatised sliotar comprised of ligands with (*R*,*R*) stereochemistry. It requires stating in advance that the R factor indices for **Eu.39R$_3$** (8.32) and **Eu.41S$_3$** (8.20) were outside acceptable limits, such that complete structural resolution was not achievable. Nevertheless, for the purpose of this study, these crystal structures will be described. The crystal structure of **Eu.43S$_3$**, however, was fully resolved with R factor = 5.36 (all relevant crystallographic parameters are listed in Tables A2.2 – A2.4).

Clear, colourless plate-shaped crystals of **[Eu.39R$_3$](ClO$_4$)$_3$**, **[Eu.41S$_3$](ClO$_4$)$_3$**, and **[Eu.43S$_3$](CF$_3$SO$_3$)$_3$** were all grown by the slow evaporation of methanolic solutions, with X-ray crystal structure analysis carried out by both Dr. M. Martinez-Calvo and Dr. J. A. Kitchen of the Gunnlaugsson group. Identical to the original sliotar systems **Ln.32S/R$_3$**,[223] both **Eu.39S$_3$** and **Eu.41S$_3$** crystallised with hexagonal symmetry in the chiral monoclinic *P6$_3$22* space group, whereas **Eu.43S$_3$** crystallised in the related *P6$_3$* space group (see Figure 2.5). The bundle-type topologies of the structures were fully apparent upon inspection, the structures proving to be isomorphous and isostructural both to each other and the original designs. Specifically, the pyridine ring of each ligand molecule was found to be intercalated between the naphthyl groups of the other two, enabling triple π-π stacking interactions that contributed to the overall stability of the complexes. Furthermore, the pyridyl *para*-moieties extended outwards, away from the metallic cores, effectively underlining the suitability of this position for functionalisation without negatively altering the sliotar architecture.

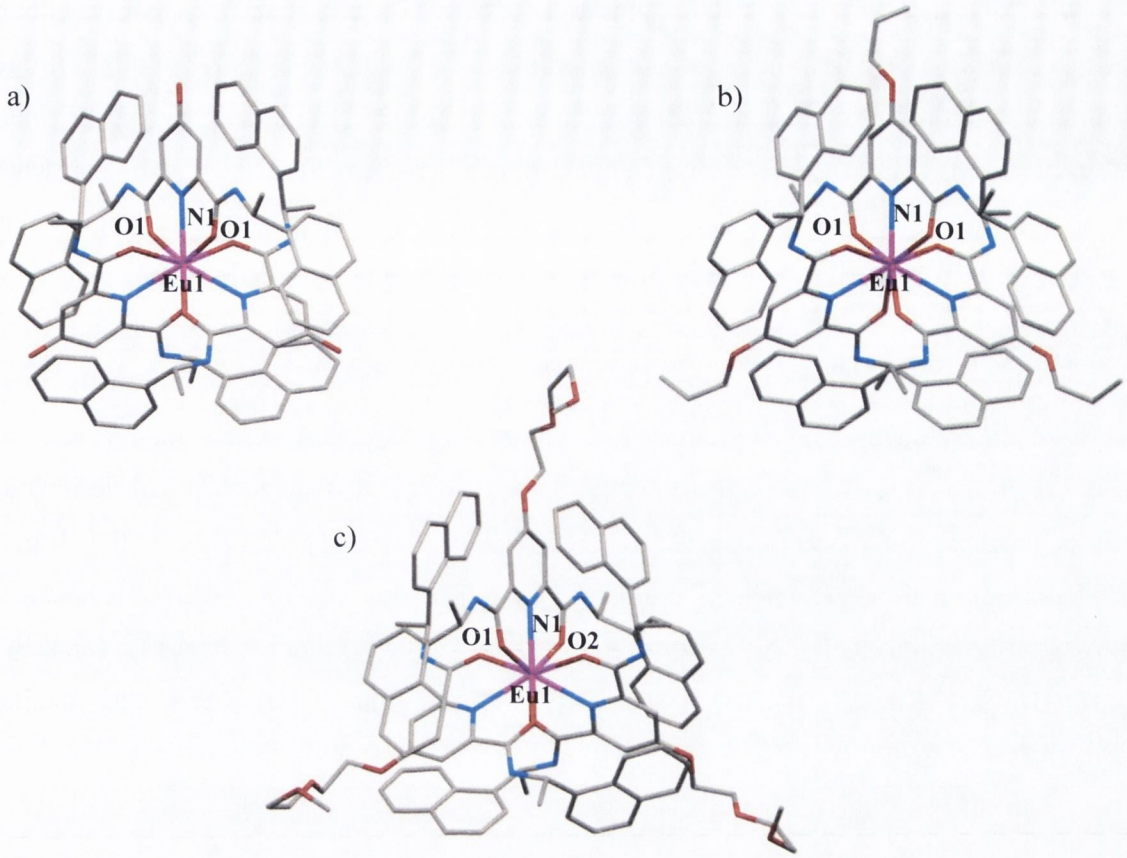

Figure 2.5: *X-ray crystal structures (capped stick) of the complexes a)* ***Eu.39R$_3$****, b)* ***Eu.41S$_3$****, and c)* ***Eu.43S$_3$*** *showing the helical arrangement of ligands around the central Eu(III) ion (counter-anions and solvent molecules omitted for clarity).*

Table 2.3 *Summary of the Eu-O and Eu-N bond lengths procured from the X-ray crystal structures of* ***Eu.39R$_3$****,* ***Eu.41S$_3$****, and* ***Eu.43S$_3$****.*

Bond	Bond Length (Å)		
	Eu.39R$_3$	Eu.41S$_3$	Eu.43S$_3$
Eu-O	2.407 (4)	2.415 (4)	2.417 (4) (O1)
Eu-O	2.407 (4)	2.415 (4)	2.417 (4) (O1)
Eu-O	2.407 (4)	2.415 (4)	2.417 (4) (O1)
Eu-O	2.407 (4)	2.415 (4)	2.421 (4) (O2)
Eu-O	2.407 (4)	2.415 (4)	2.421 (4) (O2)
Eu-O	2.407 (4)	2.415 (4)	2.421 (4) (O2)
Eu-N	2.528 (7)	2.529 (7)	2.548 (4)
Eu-N	2.529 (7)	2.529 (7)	2.548 (4)
Eu-N	2.529 (7)	2.529 (7)	2.548 (4)

In reference to the metal ion connectivity, the Eu(III) ion in each system was bound by three ligand molecules, independently coordinating through their central pyridyl nitrogen atom and carbonyl oxygen atoms to afford a nine-coordinate tri-capped trigonal prismatic N_3O_6 geometry. Table 2.3 summarises the coordinate bond lengths to the Eu(III) ion, where it could be seen that, the N-Eu bond lengths were longer than the O-Eu bond lengths, thus, demonstrative of a weaker binding in the former case. Further correlating with the original complexes was the helical manner in which the ligands wrapped around the metal ion, which resulted in the creation of chiral complexes. Indeed, from the crystal structures, the metal stereochemistry of the (*S*) enantiomers **Eu.41S$_3$** and **Eu.43S$_3$**, and (*R*) enantiomer **Eu.39R$_3$** could be assigned as Δ and Λ, respectively. As anticipated, this stereochemical designation corresponded to that found for **Ln.32S/R$_3$**. The flack parameters, which indicate the absolute configuration of the molecules, were obtained by refinement with the OLEX 2 program. In all cases, the complexes gave rise to a flack value of ≈ 0; **Eu.39R$_3$** = 0.04 (4), **Eu.41S$_3$** = 0.012 (10), and **Eu.43S$_3$** = 0.00 (0), therefore, confirming that these species were obtained with enantiomeric purity.

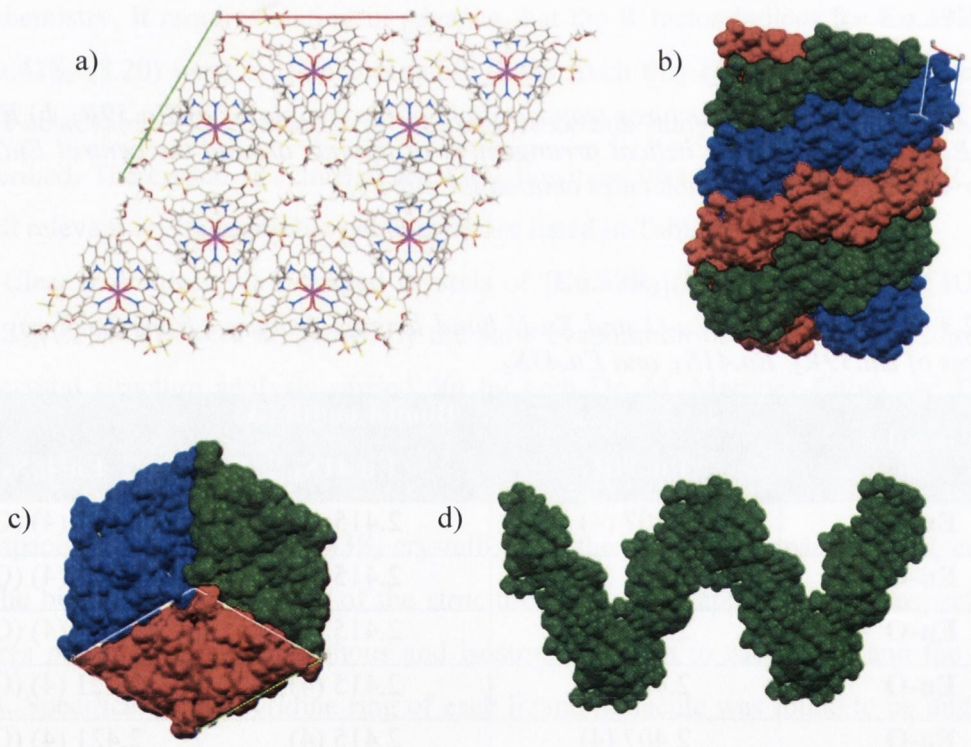

Figure 2.6: *a) X-ray packing diagram (capped stick) of* ***Eu.43S$_3$*** *viewed down the c-axis showing both the presence of channels and the orientation of the ligand polyethoxy chains into these cavities. b) X-ray packing diagram (space-filled) of* ***Eu.43S$_3$*** *propagated down the c-axis showing the helical packing arrangement of complex molecules with c) viewed down the c-axis and d) focusing on a single complex strand only.*

Figure 2.6a presents the packing diagram for complex **Eu.43S$_3$**, viewed down the crystallographic *c*-axis. The striking packing arrangement was a product of the formation of intermolecular hydrogen bonds between the amide NH protons and the oxygen atoms of the $CF_3SO_3^-$ counter-anions. Similar to the original complexes, packing in this fashion gave rise to the formation of channels running down the *c*-axis. In the example of **Eu.43S$_3$**, however, the polyethoxy chains of the constituent ligands were noticed to be orientated into these cavities. Additional to the helical wrapping of ligands within the complex molecules, the molecules themselves were found to pack in a helical arrangement, as shown in Figure 2.6b.

Having successfully synthesised and characterised the complex set **Eu.(41 – 43)$_3$**, the next step was to evaluate their unique photophysical properties by means of both UV-vis and luminescence spectroscopy.

2.6 Photophysical properties of Eu.(41 – 43)$_3$

UV-vis absorption, phosphorescence excitation and emission spectra were recorded for all complexes of the set **Eu.(41 – 43)$_3$** in MeOH. Owing to the near identical spectral morphology seen across the full complex series, the spectra of complex **Eu.43S$_3$**, shown in Figure 2.7, may be used as suitably representative examples. The UV-vis spectra of all the complexes were comprised of two main bands; a high energy one at 220 nm and a longer wavelength band centred at 281 nm, the latter arising from the π-π^* transitions of the naphthalene units (see Figure A2.14a, A2.15a, A2.16a, A2.17a, and A2.18a for **Eu.41S$_3$**, **Eu.41R$_3$**, **Eu.42S$_3$**, **Eu.42R$_3$**, and **Eu.43R$_3$**, respectively).

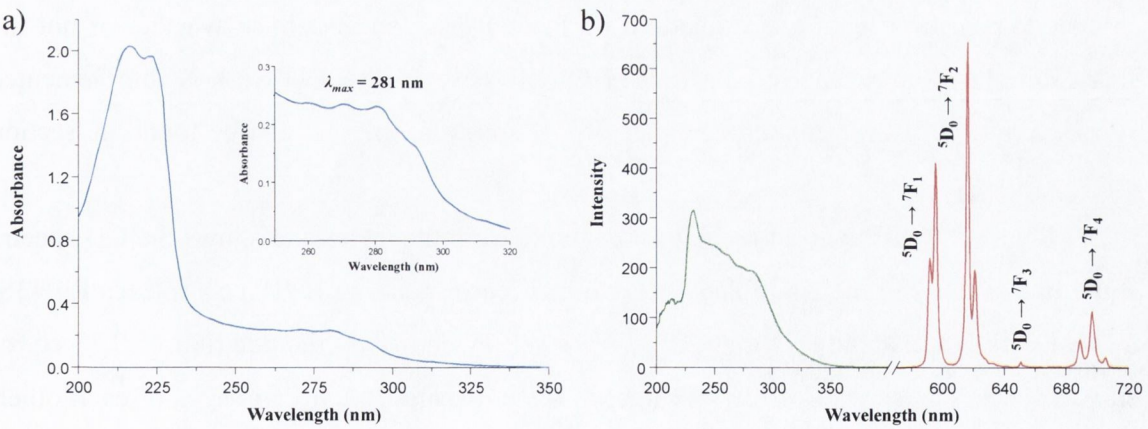

Figure 2.7: *a) UV-vis absorption and b) phosphorescence excitation (green) and emission (red) spectra (λ_{exc} = 281 nm) of* ***Eu.43S$_3$*** *(ca. 8.3 × 10^{-6} M) recorded in MeOH at 298 K.*

Permitting indirect sensitisation of the Eu(III) ion excited state, these chromophoric naphthalene groups represent a critical design feature of the complexes. The incorporation of

two such antennae into the structures of **41** – **43** was implemented to aid population of the $^5D_0$ level of the Eu(III) ion at 17250 cm^{-1} *via* energy transfer from the optimally positioned naphthyl triplet state at *ca.* 20000 cm^{-1}.[232,233] Upon excitation into the naphthalene band at 281 nm (λ_{exc}), Eu(III)-centred phosphorescence spectra were recorded for all complexes, thus, confirming energy transfer to the metal. As evidenced from Figure 2.7b (see Figure A2.14b, A2.15b, A2.16b, A2.17b, and A2.18b for **Eu.41S$_3$**, **Eu.41R$_3$**, **Eu.42S$_3$**, **Eu.42R$_3$**, and **Eu.43R$_3$**, respectively), the spectra displayed the characteristic line-like emission bands that are synonymous with the Ln(III) ions, with emissions falling in the red-visible region of the electromagnetic spectrum specific to Eu(III). These distinctive, highly resolved bands can be assigned to the transitions from the electronically excited $^5D_0$ state of the Eu(III) ion to the ground ^7F_J state; where $J = 1$ (split; 591 and 595 nm), 2 (split; 616 and 620 nm), 3 (650 nm), and 4 (split; 688, 696, and 705 nm). Notable by its absence in the spectra was the electronic-dipole $J = 0$ transition, this telling of the highly symmetrical nature of the complexes in solution.[239]

Spectroscopic techniques offer a highly practical means of analysing supramolecular Ln(III) complexes, and have been exploited at length to gather information pertinent to the systems described within this chapter. Central to these endeavours was the use of chiroptical spectroscopy to investigate the diastereoselectivity of the self-assembly process, a topic to be addressed in the next sections.

2.7 Circular dichroism studies of ligands 41 – 43 and their Eu(III) complexes

CD spectra of the ligands **41** – **43** and their complexes were recorded in CH_3CN in order to verify the enantiomeric relationship in each pair, and establish whether or not the ligand chirality was transferred to the later Ln(III) system. This CD work is complemented by a description of the general principles of CD spectroscopy that can be found in Section 1.5.1.

Figure 2.8 serves as an archetypal example from the series and shows the CD spectra of the ligand stereoisomers **43S** and **43R** and their corresponding Eu(III) complexes **Eu.43S$_3$** and **Eu.43R$_3$**, the latter two formed by *in situ* self-assembly by the addition of 0.33 eq. of $Eu(CF_3SO_3)_3$. The spectra of the free ligands were essentially mirror images of each other, thus, underlining the enantiomeric nature of the pair. Ligand **43S** exhibited a large negative band centred at 217 nm, and a less intense positive band at 227 nm with a shoulder at 246 nm. The spectrum of ligand **43R** was the exact opposite in both the shape and sign of the dichroism bands. Thereafter, the CD spectra of the two Eu(III) complexes were recorded. As shown in Figure 2.8, both a large negative and positive band with maxima at 214 nm and 227

nm, respectively, were observed for **Eu.43S$_3$**. The spectrum of **Eu.43R$_3$** was found to be a mirror image, consisting of both a large positive band at 214 nm and a large negative band at 227 nm. Comparison of the free ligand spectra to those of their complexes highlighted substantial differences with regards to the intensity of the CD signal. The original ligand bands at 217 nm and 227 nm were noted to be greatly enhanced upon complexation, with the former also experiencing a minor blue shift to 214 nm. Such changes in the optical activity can be accredited to the induction of further topological chirality during the self-assembly process, originating from the helical ligand arrangement in these mononuclear complexes.

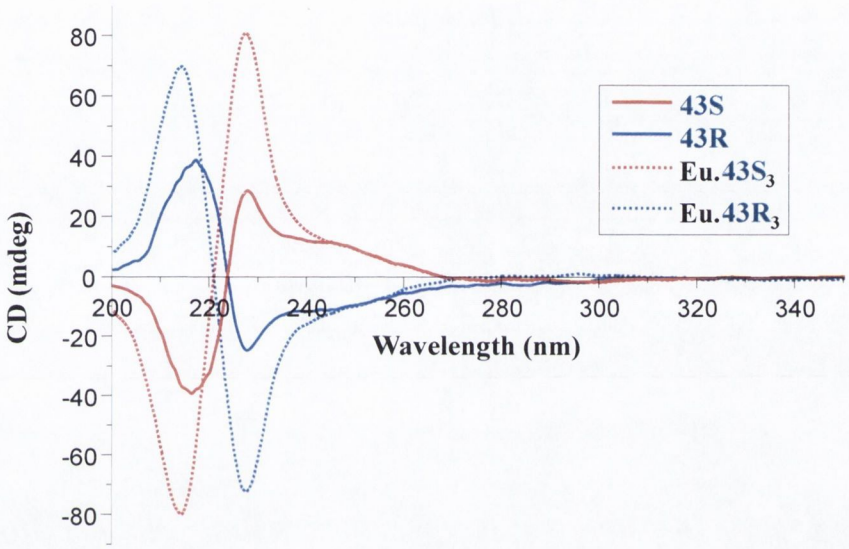

Figure 2.8: *CD spectra of ligand solutions (1.7 × 10^{-5} M) of **43S** and **43R** recorded in CH_3CN at 298 K before (solid lines) and after (dashed lines) the addition of 0.33 eq. of $Eu(CF_3SO_3)_3$ to give the complexes "**Eu.43S$_3$**" and "**Eu.43R$_3$**", respectively.*

For the CD spectra of ligands **41** and **42** (Figure A2.19 and A2.20, respectively), the sign of the dichroism bands was shown to match **43** for both enantiomers of free ligand and complex *i.e.* for the whole range, all (*S*) species were parallel in signal sign, with the same true of (*R*). Interestingly, the sign of the bands was found to conform to that of the original sliotar systems **Eu.32S$_3$** and **Eu.32R$_3$** developed by Gunnlaugsson *et al.*,[223] thus, proving the *para*-substituent of **41** – **43** to have minimal effect on complex chirality. Similar also to **43** was the increase in signal intensity for the two main bands triggered by complexation.

To summarise, the complexes of ligands **41** – **43** gave CD spectra revealing exciton signals of opposite sign and approximately equal magnitude for a given pair. Based on this data, it was wholly plausible to assume that the chirality of the ligand was both retained and conferred to the Eu(III) complex, thus, signifying the formation of an enantiomeric pair of complexes *via* a self-assembly mechanism under strict diastereoselective control.

2.8 Circularly polarised luminescence studies of Eu.(41 – 43)$_3$

One of the lesser studied features of Ln(III) luminescence is the feasibility of CPL spectroscopy, a technique that operates as the emission analogue of CD to offer highly specific information regarding the chiral environment of the emitting metal ion complex.[240] Employed to considerable effect for the work reported in this thesis, a more comprehensive discussion of the theory underpinning this chiroptical tool can be found earlier in Section 1.5.1.

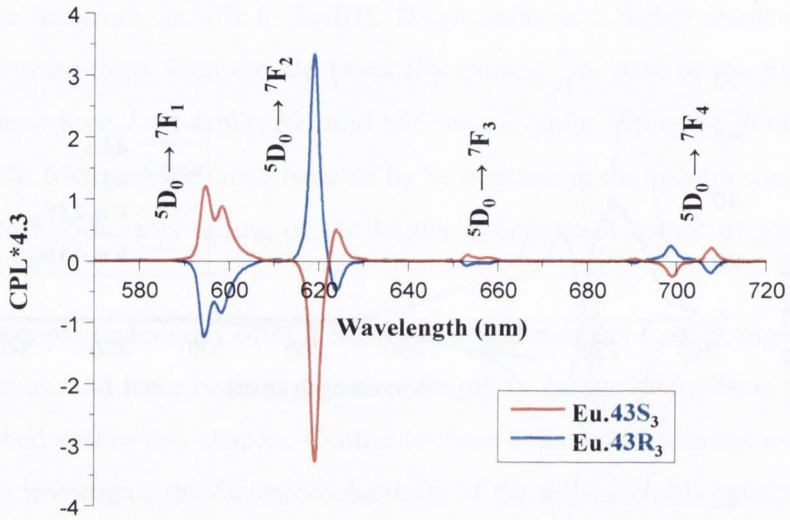

Figure 2.9: *CPL emission spectra of* ***Eu.43S$_3$*** *and* ***Eu.43R$_3$*** *recorded in CH_3CN at 298 K (λ_{exc} = 281 nm).*

CPL analysis of the complex set **Eu.(41 – 43)$_3$** was performed in collaboration with Dr. R. D. Peacock at the University of Glasgow, with all spectra recorded in CH_3CN at 298 K (λ_{exc} = 281 nm). The resulting spectra of **Eu.41S/R$_3$**, **Eu.42S/R$_3$**, and **Eu.43S/R$_3$** are shown in Figure A2.21, Figure A2.21, and Figure 2.9, respectively. Evident from the spectra for each complex pair were CPL signals of opposite sign for all transitions, reaffirming the existence of optically active supramolecular species of opposing chirality, a fact previously concluded from the CD studies. Furthermore, comparison between either of the (*S*) or (*R*) spectra for the full complex series highlighted large spectral uniformity across the entire range for both stereochemical assignments. Indeed, all (*S*) enantiomers were identical in the shape and sign of their spectra, an observation also valid for the (*R*) enantiomers.

The CPL spectra of the (*S*) enantiomeric complexes all contained a positive band for the J = 1 transition, split at 595 nm and 598 nm, and a large negative band corresponding to the hypersensitive J = 2 transition centred at 619 nm, and with a positive split at 624 nm. Conversely, the (*R*) enantiomeric species exhibited a negative signal for the J = 1 transition at

595 nm, and a positive band at 619 nm with a negative split at 624 nm arising from the $J = 2$ transition. The profiles of these CPL spectra also clearly matched those of the original sliotar complexes **Eu.32S/R$_3$** and their hydroxy derivatives **Eu.39S/R$_3$**.[223,231]

To express the magnitude of the CPL effect, values for the luminescence dissymmetry factor (g_{lum}) were then calculated for the $J = 1$ and 2 transitions, utilising **Equation 1.4** from Section 1.5.1 (values listed in Table 2.4). For all complexes, the determined values were in excellent agreement. Reviewing literature data helped to emphasise the strong CPL activity of these systems, whose g_{lum} values were shown to be appreciably larger than those reported for an analogous chiral Eu(III) system developed by Muller and co-workers ($g_{lum} = \pm 0.19$ for the $J = 1$ transition of **Eu.30S/R$_3$**; see Section 1.5.3 for additional details).[204] Such large g_{lum} values can be rationalised as a combination of two main factors, namely the chirality of the ligand and the topological chirality from the helical ligand arrangement, with both contributing to the total CPL activity. The obtained values were also comparable to those measured for the original sliotar systems *i.e.* + 0.22 / − 0.24 for the $J = 1$ transition and – 0.26 / + 0.25 for the $J = 2$ transition of complex **Eu.32S/R$_3$**.[241]

Table 2.4: *Summary of the g_{lum} dissymmetry factor values calculated from the CPL spectra of* ***Eu.(41 – 43)$_3$*** *for the $J = 1$ and 2 transitions at 595 nm and 619 nm, respectively.*

Complex	g_{lum} value 595 nm ($J = 1$)	g_{lum} value 619 nm ($J = 2$)
Eu.41S$_3$	+ 0.31	− 0.26
Eu.41R$_3$	− 0.29	+ 0.22
Eu.42S$_3$	+ 0.27	− 0.23
Eu.42R$_3$	− 0.27	+ 0.21
Eu.43S$_3$	+ 0.31	− 0.26
Eu.43R$_3$	− 0.32	+ 0.27

Reconciling the spectral and g_{lum} similarities seen among **Eu.32$_3$**, **Eu.39$_3$**, and **Eu.(41 – 43)$_3$** with the unique dependence of CPL sign and magnitude on the chiral surroundings of the metal, it is clear that the substituent holds no bearing on complex chirality in this case. Considering the aforementioned equivalence of these spectra to those of **Eu.32$_3$**, assignment of the metal stereochemistry was permissible based on previous X-ray determination of the original system helicity; Δ for **Eu.32S$_3$** and Λ for **Eu.32R$_3$** (see Section 1.6). Taking these results as a reference, the complexes **Eu.(41 – 43S)$_3$** and **Eu.(41 – 43R)$_3$** were assigned as Δ and Λ, respectively. This assignment was further confirmed by the X-ray crystallographic

analysis specific to these systems, where **Eu.41S$_3$** and **Eu.43S$_3$** were found to possess Δ chirality also (see Section 2.5).

The results herein effectively demonstrate the chirality of the complexes to be driven by asymmetric induction, a mechanism whereby the metal stereochemistry (either Δ or Λ) is selectively controlled by the absolute configuration of the chiral naphthyl antennae. The next step was to then study the formation, stability, and stoichiometry of these complexes in solution. Thus, the following sections will centre on how photophysical spectroscopy was used to elucidate such information.

2.9 Determination of metal-bound water molecules for Eu.(41 – 43)$_3$

Trivalent Ln(III) ions are known to possess large coordination requirements, generally nine for Eu(III) ions. If this prerequisite cannot be met by suitable coordinating ligands, the remaining metal sites will be occupied by solvent molecules, such as water. As previously discussed, ligands derived from the dpa chemical unit have been shown to coordinate *via* the nitrogen of the central pyridyl ring, as well as two carbonyl oxygen atoms, to give 1:3 (M:L) stoichiometric complexes. Accordingly, the Eu(III) ion will be coordinatively saturated with no bound solvent, a result anticipated for **Eu.(41 – 43)$_3$**.

The excited state lifetimes of the synthesised complexes **Eu.(41 – 43)$_3$** were examined to allow determination of their respective hydration states (q) and, therefore, the number of solvent molecules within the Eu(III) centre first coordination sphere. These measurements involved measuring the lifetimes of each complex in H_2O ($\tau_{O\text{-}H}$) and D_2O ($\tau_{O\text{-}D}$) by indirect excitation of Eu(III) at 281 nm. The q values were subsequently determined by applying the recorded lifetimes to the refined Horrocks equation developed by Parker *et al.*, **Equation 1.1** (see Section 1.1.3).[38,66,67] As a precautionary note, q value calculations should be taken with a degree of care due to the associated high error (± 0.5). By recording the exponential decay of the Eu(III)-centred luminescence with respect to time, the lifetimes of the complexes were ascertained. In all instances, the data was best fit to a mono-exponential decay, which gave the lifetime measurements shown in Table 2.5, with q values ≈ 0 calculated for each species. For further affirmation, the lifetimes of the various complexes were also measured in both non-deuterated ($\tau_{O\text{-}H}$) and deuterated ($\tau_{O\text{-}D}$) methanol. As to be expected, these lifetimes were markedly longer than those observed in water, explicable by the presence of one less O-H and O-D oscillator in MeOH and MeOD, respectively. Using **Equation 1.1**, but this time taking a proportionality constant (A) equal to 2 ms for Eu(III) in methanol, q values ≈ 0 were again obtained (Table 2.5). The determined q values were evidential of zero bound solvent molecules in the six complexes, thus, supporting the obstruction of solvent from the metal

ion, and the retention and predominance of the nine-coordinate 1:3 (M:L) stoichiometry in solution. Moreover, there existed sufficient correlation with both the elemental and X-ray analysis, which identified the same complex composition in the solid state. Fundamentally, these results bode extremely well for the ability of these supramolecular systems to function as proficient luminescent devices free of first-sphere solvent quenching.

Table 2.5: *Lifetime measurements of* ***Eu.(41 – 43)$_3$*** *in water (H_2O and D_2O) and methanol (MeOH and MeOD) with their corresponding rate constants (k) and calculated q values. Each lifetime is an average of six measurements with different gate times.*

Complex	Solvent	$\tau_{O\text{-}H}$ (ms)	$\tau_{O\text{-}D}$ (ms)	$k_{O\text{-}H}$ (ms^{-1})	$k_{O\text{-}D}$ (ms^{-1})	q (± 0.5)
Eu.41S$_3$	Water	1.34 ± 0.02	1.61 ± 0.02	0.75	0.62	− 0.15
	Methanol	1.68 ± 0.01	4.48 ± 0.01	0.60	0.22	+ 0.24
Eu.41R$_3$	Water	1.43 ± 0.01	1.58 ± 0.02	0.70	0.63	− 0.22
	Methanol	1.67 ± 0.02	4.47 ± 0.01	0.60	0.22	+ 0.25
Eu.42S$_3$	Water	1.54 ± 0.01	2.33 ± 0.02	0.65	0.43	− 0.04
	Methanol	1.63 ± 0.03	4.20 ± 0.04	0.61	0.24	+ 0.25
Eu.42R$_3$	Water	1.52 ± 0.01	3.20 ± 0.04	0.66	0.31	+ 0.11
	Methanol	1.63 ± 0.02	4.01 ± 0.01	0.61	0.25	+ 0.23
Eu.43S$_3$	Water	1.51 ± 0.03	3.00 ± 0.09	0.66	0.33	+ 0.09
	Methanol	1.68 ± 0.01	4.47 ± 0.03	0.60	0.22	+ 0.24
Eu.43R$_3$	Water	1.57 ± 0.02	2.88 ± 0.10	0.64	0.35	+ 0.05
	Methanol	1.67 ± 0.01	4.37 ± 0.02	0.60	0.23	+ 0.24

The experimental data up to this point implies that the *para*-functionality of ligands **41** – **43** does not restrict or hinder their capacity to form 1:3 (M:L) complexes analogous to the original sliotar complexes **Eu.32S$_3$** and **Eu.32R$_3$**.[223] However, to gain a truly sensible understanding of the role played by the substituent in complex formation and its effect on overall stability, the stepwise self-assembly process must be explored in real time. To allow this, UV-vis absorption and luminescence spectrophotometric titrations were performed.

2.10 UV-vis and luminescence titration studies

With a view to quantifying the complexation process in solution, a series of UV-vis absorption and luminescence titrations were carried out so as to investigate the coordinational behaviour of ligands **41** – **43** towards Eu(III) ion, and assess the stoichiometric M:L species

present. All titrations were performed by adhering to the principles of the so-called dilution method, where aliquots of a metal ion stock solution were added to a known concentration solution of the ligand, with measurements taken at controlled intervals until no further spectral changes occurred. As was done for the original sliotars developed from **32**, the spectroscopic measurements for the full ligand range **41** – **43** were initially performed in CH_3CN to facilitate direct comparison. Titrations of the 4-hydroxy ligand **39** in CH_3CN, first done by Dr. N. S. Murray of the Gunnlaugsson group, were also repeated to include the same number of points as those of the newly synthesised derivatives. Selection of this aprotic organic solvent was primarily governed by solubility reasons, but was also made so as to analyse the assembly in a low competition solvent medium.

Of all the *para*-substituted derivatives studied, the most extensive photophysical analysis was conducted for the polyethoxy analogue **43**. Through inclusion of a water-solubilising polyethoxy chain, this design was envisaged to permit examination of the self-assembly mechanism and associated species evolution in more competitive polar solvents, with the primary goal of moving into aqueous media. As a result, titrations of **43** were also completed in MeOH, before finally progressing to a mixed aqueous system, H_2O/MeOH (1:1; *v*/*v*). These studies were undertaken to evaluate the effects of solvent polarity changes on complex formation, and to probe the potential existence of a hydrophobic effect driving the process. In addition, the aqueous titrations could be used to provide insight as to the promise of analogous future systems to potentially function as bio-applicable luminescent probes.

2.10.1 Titration experimental details

All studies were performed in CH_3CN, with further analysis of ligands **43S** and **43R** in MeOH and H_2O/MeOH (1:1; *v*/*v*) to examine the nature of the binding process in solvent media of varying polarity and hydrogen bonding character. In each case, stock solutions (3 mL, 1×10^{-5} M) of the relevant ligand were prepared and titrated against known volumes of a standard solution of $Eu(CF_3SO_3)_3$. UV-vis absorption and phosphorescence spectra were subsequently recorded following metal addition, after an equilibration time of 5 min. All titrations were repeated in triplicate to ensure reproducibility. It should be stated in advance that the titrations of **39**, **41**, **42** and **43** showed the two enantiomers, in each pair, to exhibit near identical behaviour, albeit within experimental error. For this specific reason, discussion in the next three sections will deal exclusively with the photophysical titrations of **43R** (data for all other titrations can be found in Appendix 2). Selection of ligand **43R** for elaboration was made in light of the extended nature of its analysis, notably the different solvent studies.

2.10.2 UV-vis and luminescence titrations of **43R** with $Eu(CF_3SO)_3$ in CH_3CN

Firstly, the self-assembly process between Eu(III) and **43R** was studied through UV-vis and luminescence titrations in CH_3CN, the aprotic solvent in which the original sliotar ligands **32S** and **32R** had been analysed. Figure 2.10 presents the UV-vis absorption spectra and derived binding isotherms for the titration with $Eu(CF_3SO_3)_3$. With regards to the longer wavelength region, the spectra were characteristic of substituted naphthyl derivatives,[242,243] and consisted of a band centred at 281 nm (ε = 15589 M^{-1} cm^{-1} for free ligand) with two shoulders at 271 nm and 292 nm (Figure 2.10a). Addition of Eu(III) caused this band to undergo a hypochromic shift, while stimulating the appearance of a new band at *ca.* 310 nm. Such spectral changes led to the formation of isosbestic points at 267 nm and 297 nm. This was all accompanied by the continual broadening of the naphthyl absorption band with each addition. Figure 2.10b shows the binding isotherms for the complexation process. The profile at 310 nm follows the formation of a new band, and is in accordance with the evolution of a new species in solution. Absorbance at 281 nm and 292 nm was also found to decrease with increasing amounts of Eu(III), which is to be expected as these wavelengths correspond to the free ligand absorbance. These effects continued up until the formation of a plateau at *ca.* 0.3 eq. of Eu(III), results indicative of the dominant self-assembly of the 1:3 (M:L) complex.

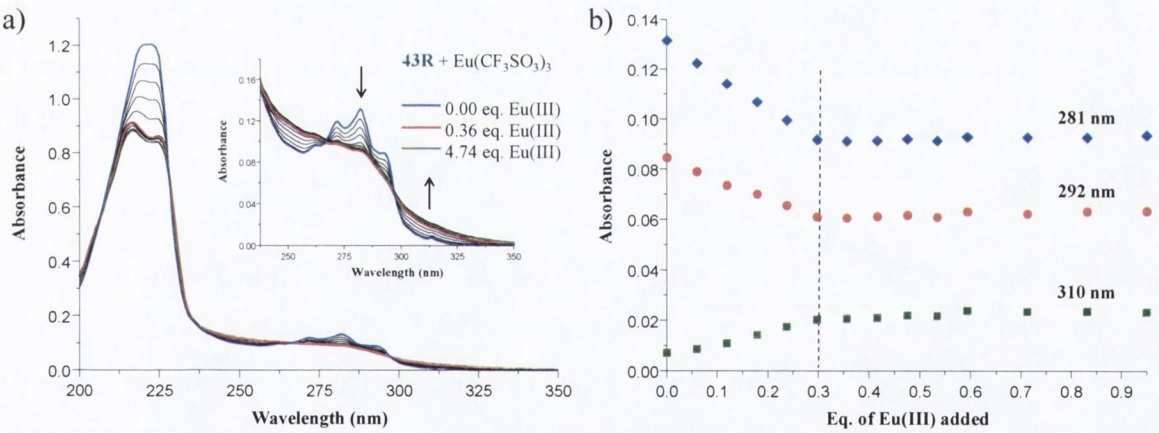

Figure 2.10: *a) Changes in the absorption spectra of **43R** (1×10^{-5} M) upon titrating with $Eu(CF_3SO_3)_3$ (0.00 → 4.74 eq.) in CH_3CN at 298 K. b) Binding isotherms for the titration measured at 281 nm, 292 nm, and 310 nm.*

Phosphorescence spectra were also recorded by exciting the same solutions used in the UV-vis titration at 281 nm. The overlaid spectra and titration profiles are shown in Figure 2.11. All spectra exhibited the characteristic Eu(III) emission structure, with bands positioned at 595 nm, 616 nm, 650 nm, and 696 nm representing the J = 1 – 4 transitions, respectively (Figure 2.11a), thus, matching the spectrum of the pre-synthesised complex (Figure 2.7b).

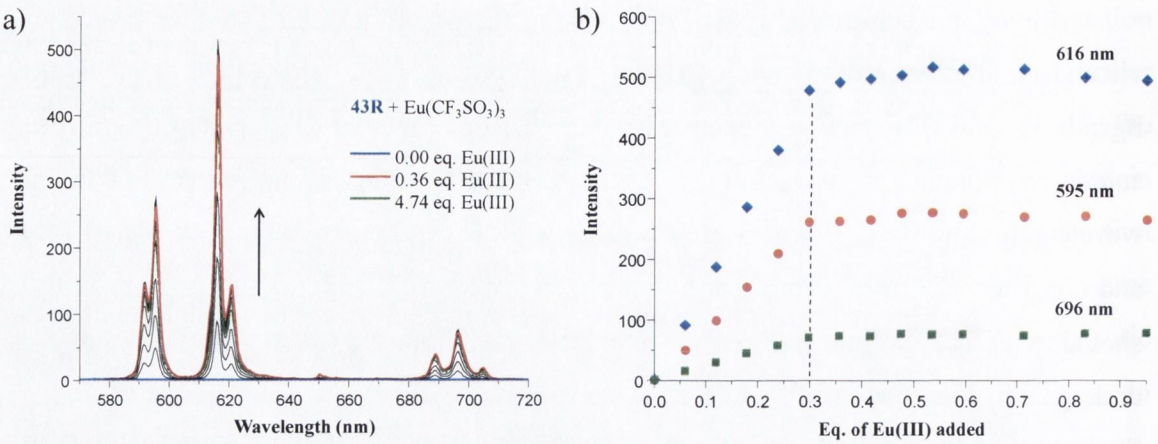

Figure 2.11: *a) Evolution of the phosphorescence emission in the titration of* ***43R*** *(1×10^{-5} M) with $Eu(CF_3SO_3)_3$ (0.00 → 4.74 eq.) in CH_3CN at 298 K (λ_{exc} = 281 nm). b) Binding isotherms for the titration measured at 595 nm, 616 nm, and 696 nm.*

Upon stoichiometric additions of the metal, the structural integrity of the bands did not undergo any noteworthy changes, for example, in their splitting pattern. However, all bands experienced an increase in intensity with successive additions of Eu(III), underlining the *switching on* of the metal-centred luminescence. This phosphorescent enhancement at 595 nm, 616 nm, and 696 nm is clearly visible from the binding isotherms (Figure 2.11b), and serves as a proof of principle for the energy transfer from the naphthyl groups to the Eu(III) ion following coordination. As was the case in the UV-vis titration data, a plateau at *ca.* 0.3 eq. of Eu(III) ion existed in the titration binding profiles, therefore, reinforcing the predominance of the 1:3 (M:L) stoichiometric species in solution.

2.10.3 UV-vis and luminescence titrations of 43R with $Eu(CF_3SO)_3$ in MeOH

With the objective of analysing the self-assembly mechanism in a more competitive protic medium, UV-vis and luminescence titrations were subsequently undertaken in MeOH. The UV-vis titration showed the behaviour and morphology of the absorption spectra to be analogous to that seen in CH_3CN upon Eu(III) addition; a decrease in the absorption band at 281 nm (ε = 15607 M^{-1} cm^{-1} for free ligand) was observed, accompanied by the concurrent formation of a new band at *ca.* 310 nm (see Figure 2.12a). This gave rise to a concomitant isosbestic point at 297 nm, evidential of the self-assembly of a new complex species in solution. These trends are shown in the binding isotherms displayed in Figure 2.12b. From these profiles, a plateau at *ca.* 0.35 eq. of Eu(III) is observable for the bands at 281 nm, 292 nm, and 310 nm.

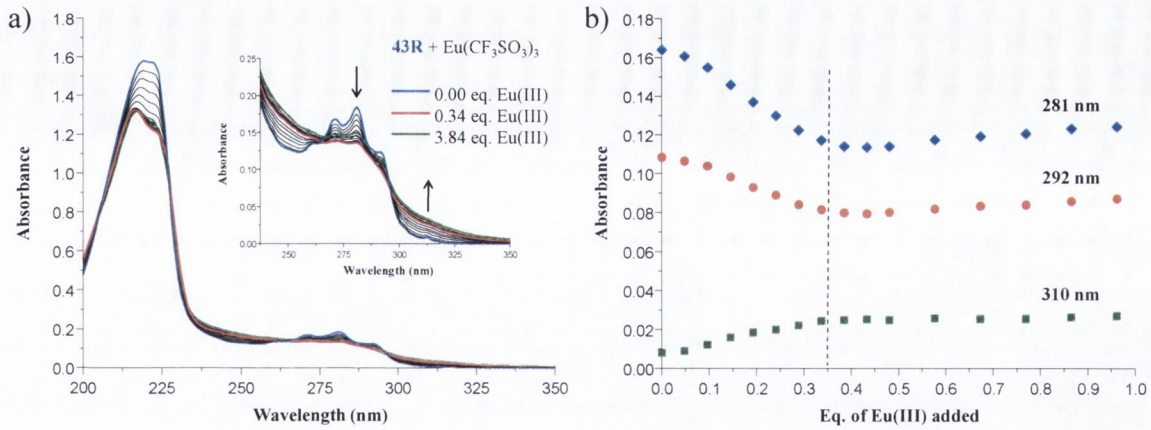

Figure 2.12: *a) Changes in the absorption spectra of* ***43R*** *(1×10^{-5} M) upon titrating with $Eu(CF_3SO_3)_3$ (0.00 → 3.84 eq.) in MeOH at 298 K. b) Binding isotherms for the titration measured at 281 nm, 292 nm, and 310 nm.*

Following additions, the solutions were excited at 281 nm to yield phosphorescence spectra (Figure 2.13a). As previously witnessed for the phosphorescence titrations in CH_3CN, characteristic Eu(III) ion emission spectra were obtained through addition of the metal ion, evidence of energy transfer to the Eu(III) centre. Indeed, the four emission bands, $J = 1 - 4$, were shown to increase in intensity after each addition, with no change in the overall spectral structure.

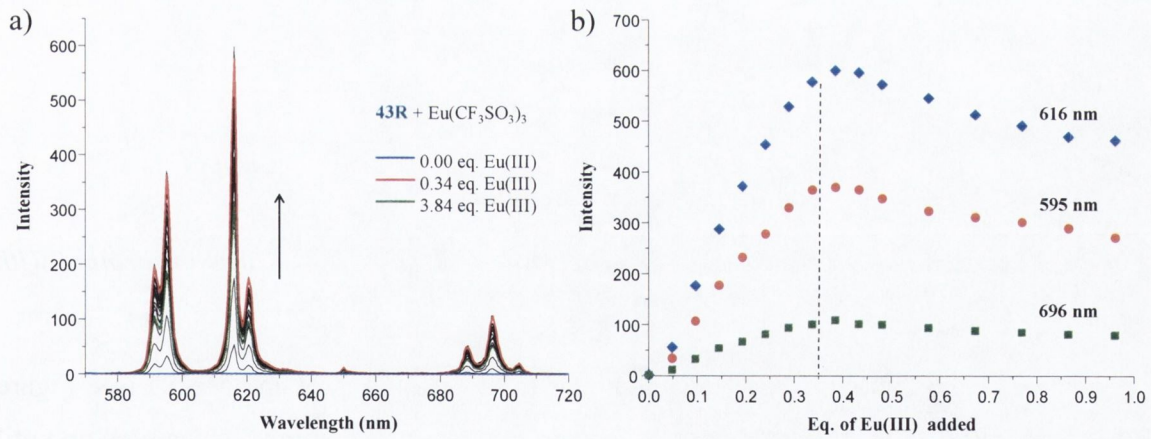

Figure 2.13: *a) Evolution of the phosphorescence emission in the titration of* ***43R*** *(1×10^{-5} M) with $Eu(CF_3SO_3)_3$ (0.00 → 3.84 eq.) in MeOH at 298 K (λ_{exc} = 281 nm). b) Binding isotherms for the titration measured at 595 nm, 616 nm, and 696 nm.*

Examination of the binding isotherms revealed an intensity maximum at *ca.* 0.35 eq. of Eu(III), agreeing with the UV-vis titration and hinting at the prevalence of the 1:3 (M:L) stoichiometry. Beyond this point, a sizeable decrease in emission intensity was observed with

the addition of further Eu(III) aliquots, an effect attributed to the formation of a less emissive minor species in solution with reduced ligand-coordination. Relative to the CH_3CN titrations, this emission reduction at metal ion excess was more pronounced on account of the superior capacity of MeOH to non-radiatively quench the excited state of the exposed Eu(III) ion.

2.10.4 UV-vis and luminescence titrations of 43R with $Eu(CF_3SO)_3$ in H_2O/MeOH

One of the major design elements of ligands **43S** and **43R** was the polyethoxy chain tethered to the pyridyl 4-position. As previously stated, incorporation of this functionality was planned to confer a degree of complex water solubility so as to facilitate photophysical evaluation in aqueous media, with a potential view to future bioapplication. With this in mind, a series of photophysical titrations were conducted in H_2O/MeOH (1:1; *v/v*) mix to elucidate information pertaining to the complexation process in this strongly competitive, polar aqueous solvent system.

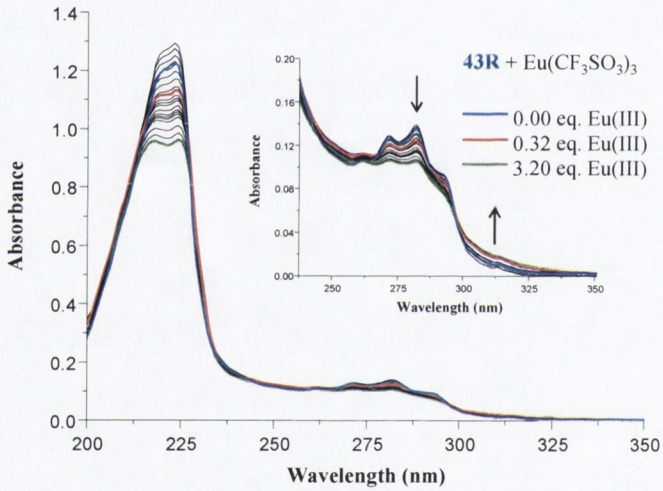

Figure 2.14: *Changes in the absorption spectra of **43R** (1×10^{-5} M) upon titrating with $Eu(CF_3SO_3)_3$ (0.00 → 3.20 eq.) in H_2O/MeOH (1:1; v/v) at 298 K.*

The UV-vis titrations were again similar to those in CH_3CN and MeOH (see Figure 2.14). In contrast to these, absorbance at 281 nm was found to continually decrease up until completion of the titration (Figure A2.37). However, the evolution of the band at 310 nm, associated with the construction of a new species in solution, proceeded up to *ca.* 0.35 eq. of Eu(III) before levelling off.

The spectra and binding isotherms for the accompanying phosphorescence titration are shown in Figure 2.15. For this titration, the changes in emission were comparably more defined than those seen for the absorbance measurements and, consequently, gave a more

identifiable trend. The profiles at 595 nm, 616 nm, and 696 nm all displayed a sharp, steady increase in intensity until *ca.* 0.35 eq. of Eu(III), at which point the increase became far less severe and more gradual. The continued intensity enhancement was in stark contrast to the earlier titrations, where a decrease in emission at higher quantities of Eu(III) ion was noted. Nevertheless, the discernible change in slope for the isotherms at *ca.* 0.35 eq. provided the strongest indication so far that ligand **43** retained the ability to self-assemble 1:3 (M:L) tris-chelates in a partially aqueous solvent.

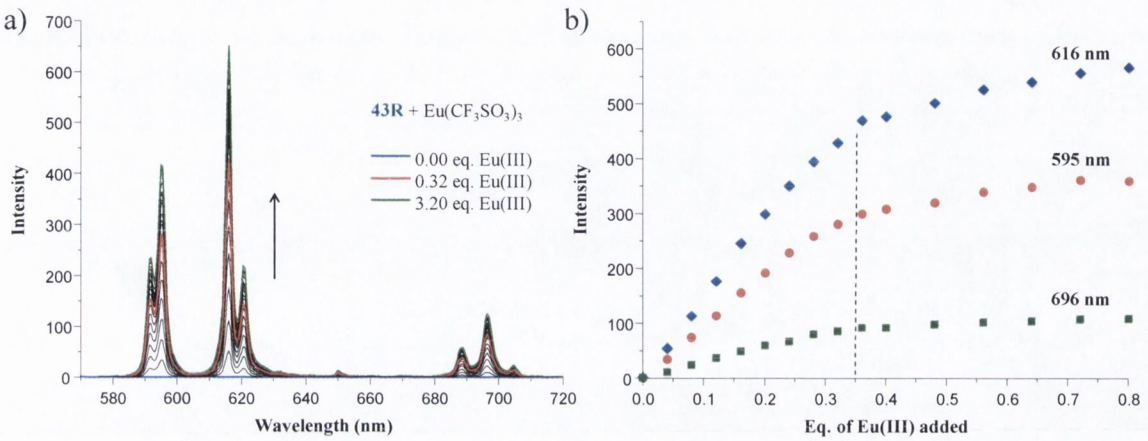

Figure 2.15: *a) Evolution of the phosphorescence emission in the titration of* ***43R*** *(1×10^{-5} M) with $Eu(CF_3SO_3)_3$ (0.00 → 3.20 eq.) in H_2O/MeOH (1:1; v/v) at 298 K (λ_{exc} = 281 nm). b) Binding isotherms for the titration measured at 595 nm, 616 nm, and 696 nm.*

For the full titration set (*i.e.* **39**, **41**, **42**, and **43**), a more definite determination of the complex species present, and their associated binding constants, could be obtained through mathematical fitting of the recorded data. Such constants act as a measure of overall complex stability and, thus, facilitate an understanding of the factors dictating metal complexation. A more global discussion of the fitting process, detailing the origin of these descriptive values, will be provided in the next section, before presenting the fitting results.

2.10.5 Determination of complex binding constants

Metal-ligand complexation involves the replacement of coordinated solvent molecules from the metal centre with ligand donor groups. For ligands **39**, **41**, **42**, and **43**, the tridentate pyridyl binding cavity affords three such donor atoms. As a consequence, three ligand molecules are required to generate coordinatively saturated **Eu.L$_3$** complexes, which satisfy the high coordination demands of the Eu(III) ion. The stepwise self-assembly route to these stoichiometric nine-coordinate species can be simply expressed in terms of the equilibria shown in **Equation 2.1 – 2.3**.

$$Eu^{3+} + L \xrightleftharpoons{K_{1:1}} [Eu.L]^{3+} \qquad \textbf{Equation 2.1}$$

$$[Eu.L]^{3+} + L \xrightleftharpoons{K_{1:2}} [Eu.L_2]^{3+} \qquad \textbf{Equation 2.2}$$

$$[Eu.L_2]^{3+} + L \xrightleftharpoons{K_{1:3}} [Eu.L_3]^{3+} \qquad \textbf{Equation 2.3}$$

The product of the individual formation constants ($K_{M:L}$) can then be calculated to give the overall complex stability constant ($\beta_{1:3}$), derived according to **Equation 2.4** and **Equation 2.5**.

$$Eu^{3+} + 3L \xrightleftharpoons{\beta_{1:3}} [Eu.L_3]^{3+} \qquad \textbf{Equation 2.4}$$

$$\beta_{1:3} = \frac{[Eu.L_3]^{3+}}{[Eu^{3+}][L]^3} = K_{1:1} \times K_{1:2} \times K_{1:3} \qquad \textbf{Equation 2.5}$$

These numerical values serve to quantify complex stability, and are influenced by the number of coordination sites, the metal ion and ligand solvation energies,[244] as well as the structure and flexibility of the ligands. For the work described in this thesis, determination of these values was made feasible through fitting of the changes in the UV-vis and/or phosphorescence spectra upon titration with Ln(III) salts. Data fitting was achieved in all instances using the non-linear least-squares regression program SPECFIT®.[245,246] A more detailed account of SPECFIT®, and how it operates can be found in the Appendix.

2.10.6 Fitting of the titration data

In each and every case, fitting of the UV-vis and phosphorescence titration data was attempted. UV-vis data fitting, though successful for the vast majority of titrations, was not possible in certain instances, such as for ligand **42S** in CH_3CN, and ligands **43S** and **43R** in both MeOH and H_2O/MeOH (1:1; *v/v*). In the latter case, the difficulty in fitting can perhaps be explained by the lack of any clear, prominent trends in the titration profiles (see Section 2.10.4). In contrast, excellent phosphorescence fits were obtained for the complete titration series. Accordingly, discussion in this section will solely reference phosphorescence fitting; the binding constants from which are concisely summarised in both Table 2.6 and Table 2.7 (all fits and their speciation graphs can be found in Appendix 2). Table 2.6 also includes the

UV-vis binding constants, which nicely complement the phosphorescence values, meaning the proposed binding models have been validated by two fitting strategies where possible.

Table 2.6: *Summary of the binding constants obtained through data fitting for the UV-vis and phosphorescence titrations of* **39**, **41**, **42**, *and* **43** *(1 × 10^{-5} M) with $Eu(CF_3SO_3)_3$ in CH_3CN, with percentage composition of the 1:3 (M:L) species at 0.33 eq. of Eu(III). *Value fixed.*

Ligand	Mode	log $\beta_{1:3}$	log $\beta_{1:2}$	log $\beta_{1:1}$	% of 1:3 (M:L) species at 0.33 eq. of Eu(III)
39S	**UV**	21.84 ± 0.87	–	7.76 ± 0.49	93
	Pho	21.48 ± 0.00*	–	6.89 ± 0.79	94
39R	**UV**	21.71 ± 0.65	–	7.49 ± 0.33	92
	Pho	21.48 ± 0.50	–	7.00 ± 0.31	93
41S	**UV**	23.25 ± 0.89	15.41 ± 0.77	8.04 ± 0.52	90
	Pho	22.95 ± 0.38	15.30 ± 0.00*	8.17 ± 0.22	90
41R	**UV**	22.12 ± 0.71	15.30 ± 0.61	7.41 ± 0.38	80
	Pho	22.12 ± 0.00*	14.85 ± 0.29	7.72 ± 0.18	86
42S	**UV**	–	–	–	–
	Pho	21.99 ± 0.61	13.75 ± 0.87	7.38 ± 0.35	93
42R	**UV**	21.51 ± 0.80	–	6.93 ± 0.44	94
	Pho	21.72 ± 0.00*	14.28 ± 0.35	7.23 ± 0.20	87
43S	**UV**	19.41 ± 0.36	–	6.35 ± 0.18	85
	Pho	19.86 ± 0.27	–	7.06 ± 0.18	83
43R	**UV**	20.60 ± 0.55	–	7.01 ± 0.27	89
	Pho	20.50 ± 0.31	–	7.03 ± 0.20	89

Table 2.6 presents the calculated binding constants for the species established from the fitting of the CH_3CN titrations (**39**, **41**, **42**, and **43**). Across the entire range, data fitting confirmed the presence of both the 1:1 and 1:3 (M:L) stoichiometries in solution, the latter proving formation of the desired complexes. For all titrations, examination of the relevant speciation graphs showed the 1:3 (M:L) species to be intensely favoured at reduced Eu(III) concentrations, with percentage formations ranging from 83% (**43S**) to as much as 94% (**39S**) upon addition of 0.33 eq. of metal ion. At excess Eu(III) ion concentrations, however, the equilibria were significantly displaced towards the generation of the less emissive 1:1

(M:L) complex, which accounts for the intensity decrease observed in the phosphorescence titrations. The fits of **41S**, **41R**, **42S**, and **42R** are distinguished from the others by virtue of detection of the 1:2 (M:L) stoichiometry. Observation of this species conforms to the set of equilibria equations described previously in Section 2.10.5 (**Equation 2.1 – 2.3**), and so one would anticipate its presence in all fits. In an attempt to rationalise the absence of the 1:2 (M:L) stoichiometry from the data fits of **39S**, **39R**, **43S**, and **43R**, a hypothesis has since been developed, informed by those fits in which the 1:2 (M:L) species has been recognised. Using the speciation graph of **41S** as an appropriate example (Figure 2.16b), the 1:2 (M:L) complex can be seen to be relatively minor at all stages of the titration. Resultantly, its formation may be disguised from the fitting program to prevent identification in some instances. The minor contribution of the 1:2 (M:L) species, coupled with the preference for the 1:1 (M:L) stoichiometry at Eu(III) ion excess, only helps to underline the stability of the 1:3 (M:L) self-assembly and explain the difficulties encountered in 1:2 (M:L) detection.

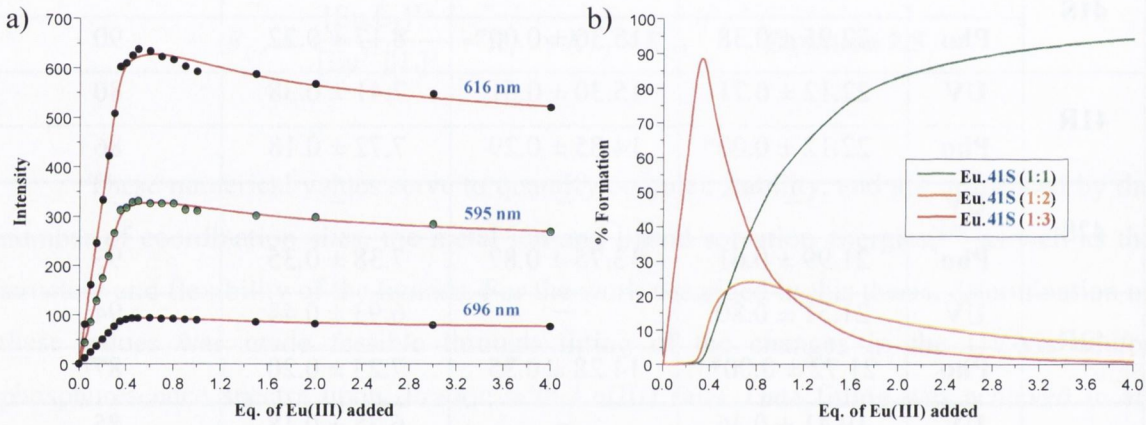

Figure 2.16: *a) Experimental binding isotherms for the phosphorescence titration of* **41S** *(1 × 10^{-5} M) with $Eu(CF_3SO_3)_3$ in CH_3CN at 298 K (λ_{exc} = 281 nm) and their corresponding fit by means of SPECFIT. b) Speciation-distribution diagram obtained from the fit.*

Upon closer inspection of the binding constants in Table 2.6, several conclusions can be drawn. Firstly, both the log $\beta_{1:1}$ and log $\beta_{1:3}$ values for **39**, **41**, and **42** were found to be of approximately equal magnitude for each ligand. Moreover, the individual stepwise stability constants were roughly additive, suggestive of a lack of obstruction with successive ligand coordination. Interestingly, despite sharing similar log $\beta_{1:1}$ values to the other ligands, the log $\beta_{1:3}$ values for the polyethoxy compounds **43S** and **43R** were determined to be *ca.* 1 order of magnitude smaller. Such findings suggest an increased degree of steric hindrance for **43** with each binding step, a restriction most likely originating from the larger *para*-functionality of the ligand. In spite of this, it should be stressed that these log $\beta_{1:3}$ values are still appreciably

large. Comparison of the constants in Table 2.6 to those of the non-derivatised sliotar ligands **32S** and **32R** proved highly informative. For ligand **32S**, values of log $\beta_{1:1}$ = 7.5 ± 0.2 and log $\beta_{1:3}$ = 21.5 ± 0.4 were obtained, with values of log $\beta_{1:1}$ = 7.7 ± 0.2 and log $\beta_{1:3}$ = 21.8 ± 0.3 obtained for ligand **32R** (reported in the PhD thesis of Dr. Christophe Lincheneau).[224] These quoted values match well with those listed in Table 2.6, especially for **39**, **41**, and **42**, and demonstrate the effects of pyridyl *para*-functionalisation to be mostly negligible. Based on these constants, one can conclude that the ligand modification strategy employed does not majorly impede the construction of highly stable 1:3 (M:L) complexes.

Table 2.7 summarises the binding constants derived from the titrations of **43** in the three different solvent media; CH_3CN, MeOH, H_2O/MeOH (1:1; *v/v*) (see Section 2.10.2 – 2.10.4). As before, values for the 1:1 and 1:3 (M:L) stoichiometries were ascertained in all solvent systems, with dominant production of the tris-species at 0.33 eq. of Eu(III) apparent from the distribution graphs (see Figure 2.17 as an example).

Table 2.7: *Summary of the binding constants obtained through data fitting for the phosphorescence titrations of* ***43*** *(1 × 10^{-5} M) with $Eu(CF_3SO_3)_3$ in CH_3CN, MeOH, H_2O/MeOH (1:1; v/v) with percentage composition of the 1:3 (M:L) species at 0.33 eq. of Eu(III).*

Solvent	Ligand	log $\beta_{1:3}$	log $\beta_{1:2}$	log $\beta_{1:1}$	% of 1:3 (M:L) species at 0.33 eq. of Eu(III)
CH_3CN	**43S**	19.86 ± 0.27	–	7.06 ± 0.18	83
	43R	20.50 ± 0.31	–	7.03 ± 0.20	89
MeOH	**43S**	20.06 ± 0.34	–	7.10 ± 0.16	87
	43R	20.71 ± 0.40	–	7.22 ± 0.18	91
H_2O/MeOH (1:1; *v/v*)	**43S**	19.61 ± 0.21	–	7.00 ± 0.00*	83
	43R	19.92 ± 0.28	–	7.00 ± 0.13	86

Perhaps the most intriguing aspect of the data communicated in Table 2.7 is the fact that the binding constants remain largely unchanged from one solvent to another. Generally, it would be foreseen that constants in the more competitive protic media of MeOH and H_2O/MeOH (1:1; *v/v*) would be reduced relative to CH_3CN. Considering the demonstrated solvent independence of **43**, it is therefore conceivable that a small hydrophobic effect is potentially in effect, driving complexation in the protic solvents. Most importantly, however, data fitting unambiguously confirmed **43** to self-assemble 1:3 (M:L) complexes in a partially aqueous

solvent mix, a fact suspected from the trends in the earlier titration isotherms (see Section 2.10.4).

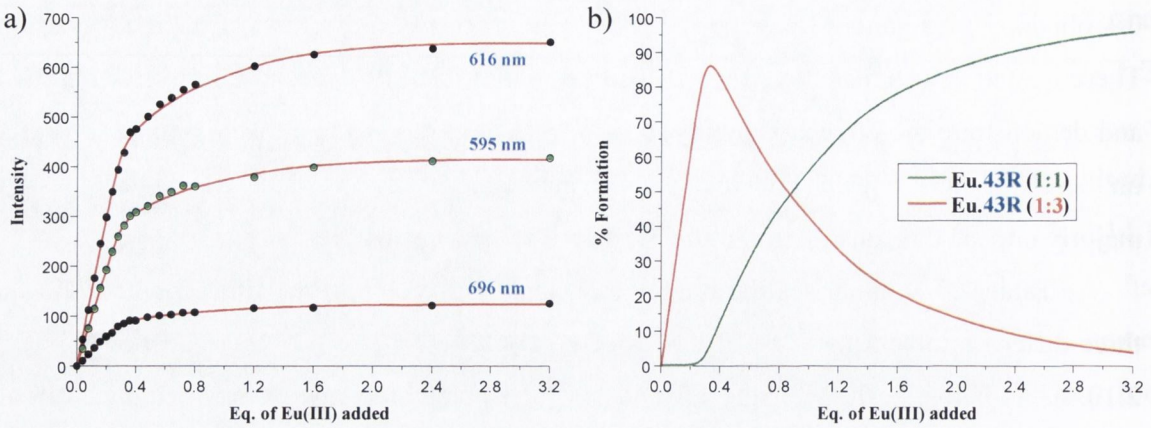

Figure 2.17: *a) Experimental binding isotherms for the phosphorescence titration of* **43R** *(1×10^{-5} M) with $Eu(CF_3SO_3)_3$ in H_2O/MeOH (1:1; v/v) at 298 K (λ_{exc} = 281 nm) and their corresponding fit by means of SPECFIT. b) Speciation-distribution diagram obtained from the fit.*

2.11 Quantum yield and sensitisation efficiency determination

A fundamental property of emissive species, the luminescence quantum yield (Q_L^{Ln}) characterises the ability of a luminescent entity to convert absorbed photons into emitted photons.[247] Consequently, an appreciation of its importance, and the factors regulating its magnitude, is imperative when designing efficient luminescent Ln(III) probes. For the work described in this chapter, the luminescence quantum yields (Q_L^{Ln}) were determined using a relative method with $Cs_3[Eu.(dpa)_3]\cdot 9H_2O$ complex in 0.1 M Tris buffer (pH = 7.45)(Q_L^{Ln} = 24.0 ± 0.25%) as the standard to which absorbance and emission intensity of the samples were compared according to **Equation A3**.[116,248] The estimated error for the quantum yield values is ± 10%. As part of these measurements, the luminescence lifetimes (τ_{obs}) were simultaneously recorded for the samples. Hence, τ_{rad} values could be calculated following determination of Q_L^{Ln} using **Equation A2**. This allowed calculation of the two parameters η_{sens} (sensitisation efficiency) and Q_{Ln}^{Ln} (intrinsic quantum yield) from **Equation A1**, these values being otherwise difficult to access. Indeed, knowledge of these two is beneficial for the optimisation of luminescent Ln(III) complex design, as they specify the efficiency of the individual steps that make emission possible.[249] **Equations A1 – A3** can be found in the Appendix, along with a more detailed explanation of the theory involved.

Measurements were firstly conducted for the complexes **Eu.39$_3$**, **Eu.41$_3$**, **Eu.42$_3$**, and **Eu.43$_3$** in CH_3CN, a solvent in which the systems had all been analysed in photophysical titrations. The data obtained from these measurements is shown in Table 2.8. It was evident upon analysing the collected data that, relative to each other, the various *para*-substituents have a mostly minimal effect on all parameters. However, there are a few subtle differences worth attention. Firstly, the Q_L^{Ln} values determined for the *para*-hydroxy derivatives **Eu.39S$_3$** and **Eu.39R$_3$** were slightly lower than those of the others. In view of the high frequency O-H oscillator present in the ligand structure, this reduction in Q_L^{Ln} can perhaps be explained by an increase in second-sphere quenching, a phenomenon reflected in the moderately lower τ_{obs} lifetimes. Notable also was the minor increase in Q_L^{Ln} for the alkynyl analogues **Eu.42S$_3$** and **Eu.42R$_3$**. Such an increase can be attributed to an improved sensitisation of the Eu(III) ion centre, as manifested by the larger η_{sens} values. As a whole, the Q_L^{Ln} values reported in Table 2.8 are marginally smaller than those measured for the original sliotar complexes **Eu.32S$_3$** and **Eu32R$_3$**; 7.6 ± 0.5% and 7.3 ± 0.4%, respectively. Again, the superior Q_L^{Ln} values of **Eu.32S$_3$** and **Eu32R$_3$** were essentially a product of a more facile sensitisation pathway, which was emphasised by η_{sens} values of 51.3% and 49.0% for the (*S*) and (*R*) enantiomer, respectively.[241]

Table 2.8: *Summary of the luminescence and intrinsic quantum yields, Eu(III) lifetimes and radiative lifetimes, and overall sensitisation efficiencies of* ***Eu.39$_3$***, ***Eu.41$_3$***, ***Eu.42$_3$***, *and* ***Eu.43$_3$*** *in CH_3CN at 298 K. All data obtained from measurements of the same solutions.*

Complex	Q_L^{Ln} (%)	τ_{obs} (ms)	τ_{rad} (ms)	Q_{Ln}^{Ln} (%)	η_{sens} (%)
Eu.39S$_3$	4.21 ± 0.15	1.72 ± 0.01	10.63	16.16	26.06
Eu.39R$_3$	4.17 ± 0.10	1.72 ± 0.01	10.57	16.22	25.71
Eu.41S$_3$	4.44 ± 0.09	1.79 ± 0.03	9.41	19.03	23.34
Eu.41R$_3$	4.87 ± 0.14	1.78 ± 0.05	9.64	18.51	26.32
Eu.42S$_3$	5.75 ± 0.21	1.76 ± 0.05	9.46	18.61	30.90
Eu.42R$_3$	5.82 ± 0.26	1.76 ± 0.01	9.53	18.49	31.47
Eu.43S$_3$	4.56 ± 0.14	1.77 ± 0.02	9.54	18.52	24.62
Eu.43R$_3$	4.84 ± 0.11	1.73 ± 0.03	9.60	18.06	26.80

Determination of Q_L^{Ln} values for **Eu.43S/R$_3$** in MeOH and H_2O/MeOH (1:1; *v/v*), as per the earlier titration studies, was completed as an additional form of analysis, with the results compiled in Table 2.9. The Q_L^{Ln} values in MeOH were only slightly lower than in CH_3CN, thus, proving the solvent effect to be relatively small, a fact confirmed by the

relative reduction in τ_{obs} lifetime. However, changing to the H_2O/MeOH (1:1; *v/v*) solvent medium yielded an unexpected increase of *ca.* 3% in Q_L^{Ln} compared to CH_3CN, despite the lifetime values remaining largely unchanged. With all other parameters strikingly similar to those in CH_3CN and MeOH, this enhancement can be ascribed to a dramatic increase of *ca.* 20% in η_{sens} values. Requiring further investigation, this result makes it abundantly clear that, for this particular system, the effect of the solvent on Q_L^{Ln} cannot be discounted. Based on the constant nature of the τ_{obs} values, one may conclude that the hydrophobic effect, as proposed in Section 2.10.6, does not increase the shielding of the Eu(III) ion. Nonetheless, it is sensible to hypothesise that, as a result of the associated hydrophobicity of the naphthyl groups, the improved sensitisation potentially stems from differences existing in the ligand desolvation process,[244] which may result in a tighter complex in the H_2O/MeOH (1:1; *v/v*) mix with a shorter metal-chromophore distance.[28]

Table 2.9: *Summary of the luminescence and intrinsic quantum yields, Eu(III) lifetimes and radiative lifetimes, and overall sensitisation efficiencies of* ***Eu.43S/R$_3$*** *in CH_3CN, MeOH, and H_2O/MeOH (1:1; v/v) at 298 K. All data obtained from measurements of the same solutions.*

Solvent	Complex	Q_L^{Ln} (%)	τ_{obs} (ms)	τ_{rad} (ms)	Q_{Ln}^{Ln} (%)	η_{sens} (%)
CH_3CN	**Eu.43S$_3$**	4.56 ± 0.14	1.77 ± 0.02	9.54	18.52	24.62
	Eu.43R$_3$	4.84 ± 0.11	1.73 ± 0.03	9.60	18.06	26.80
MeOH	**Eu.43S$_3$**	4.37 ± 0.15	1.67 ± 0.01	10.56	15.86	27.56
	Eu.43R$_3$	4.18 ± 0.19	1.66 ± 0.03	10.51	15.82	26.42
H_2O/MeOH (1:1; *v/v*)	**Eu.43S$_3$**	7.25 ± 0.25	1.67 ± 0.01	10.24	16.35	44.33
	Eu.43R$_3$	7.39 ± 0.27	1.64 ± 0.01	10.33	15.88	46.53

By and large, the variations seen amongst the different systems, the original sliotar complexes included, arise from changes in the luminescence sensitisation efficiency. From this, one can potentially speculate that the various substituents (and/or solvents) may impact the sensitisation process through modulation of the ligand triplet state energy, or by distortions of the Ln(III)-coordination environment. Notwithstanding the observed differences, the collated data serves to show that, without majorly limiting their ability to operate as effective luminescent probes, a wide range of *para*-functionality may be introduced to this complex family. Resultantly, the modification strategy employed within this chapter holds immense promise for extended elaboration, as will be demonstrated in subsequent chapters.

2.12 Conclusion

This chapter has concentrated on the design, synthesis, and photophysical evaluation of a variety of novel chiral luminescent Ln(III) complexes, formed *via* self-assembly from the enantiomeric ligand pairs **41**, **42**, and **43**. All ligands were based on the 4-hydroxy-pyridine-2,6-dicarboxylic acid framework, and equipped with two chiral naphthalene antenna suitable for sensitisation of the Ln(III) excited state. Differentiating the ligand pairs **41** – **43** was their terminal substituent, located at the pyridyl *para*-position and introduced by nucleophilic substitution of the 4-hydroxy group of the previously synthesised ligand **32**. Ligands **41S** (*S*,*S*) and **41R** (*R*,*R*) were functionalised at this location with a propyl chain, ligands **42S** (*S*,*S*) and **42R** (*R*,*R*) with an alkynyl propargyl chain, and ligands **43S** (*S*,*S*) and **43R** (*R*,*R*) with a polyethoxy chain. Through variation of the *para*-substituent, diverse extended analysis was subsequently used to provide the foundation for a comparative study probing the effects of this modification strategy.

The first section of this chapter focused on the synthesis and characterisation of the ligands and their Eu(III) complexes. Regarding the complexes, numerous techniques were employed to confirm successful formation. ^{1}H NMR spectroscopy verified complexation through an observed broadening and shifting of the proton signals, while simultaneously accentuating the symmetrical nature of each species in solution. HRMS and elemental analysis established the predicted 1:3 (M:L) stoichiometry for the synthesised complexes. Further substantiating this complex composition was the X-ray crystallographic analysis of **Eu.39R$_3$**, **Eu.41S$_3$**, and **Eu.43S$_3$**, which showed these structures to be isostructural to the original sliotars. Facilitated by the sensitising faculty of the naphthyl chromophores, the unique, highly distinctive photophysical properties of the complex series were effectively demonstrated upon indirect Eu(III) excitation at 281 nm, which gave rise to characteristic metal-centred phosphorescence.

The utilisation of chiral ligands was foreseen to give enantiopure self-assemblies by means of a diastereoselective chirality transfer. Evidence for this transfer was supplied by two chiroptical spectroscopic tools; CD and CPL. Addressing the former, CD spectra recorded for the complexes showed the retention of chirality following metal-binding. As with their respective ligands, the complexes developed from a given ligand pair yielded spectra of equal magnitude and opposite sign, proof of their opposing chirality. CPL spectroscopy effectively supplemented the CD studies, and confirmed residence of the Eu(III) ion within a chiral binding pocket. Moreover, the metal stereochemistry could be definitively assigned by correlating the sign of the spectra to crystallographic findings, with all (*S*) and (*R*) complexes shown to possess Δ and Λ helicity, respectively.

Photophysical measurements were later performed to aid identification of the stoichiometric species present in solution and ascertain their relative distribution. The hydration states (q) for all complexes were determined through luminescence lifetime measurements in both water (H_2O and D_2O) and methanol (MeOH and MeOD). Found to be ≈ 0 in each case, the calculated q values indicated the presence of zero bound solvent molecules, a result suggestive of the 1:3 (M:L) complex composition. Thereafter, UV-vis absorption and luminescence titrations of **41**, **42**, and **43** (and the hydroxy derivative **39**) with $Eu(CF_3SO_3)_3$ were conducted in CH_3CN. For all examples, fitting of the titration data by SPECFIT® unequivocally verified formation of the 1:3 (M:L) complex with high stability. Furthermore, comparison of the fitting results revealed only minor differences in the binding constants for the various ligands, thus, implying the effects of *para*-substitution to be mainly minimal. Additional titrations of **43** were carried out in MeOH and H_2O/MeOH (1:1; *v*/*v*) to assess the impact of the solvent on the self-assembly process, the latter titrations made possible by the terminal water-solubilising polyethoxy chain. Surveying the constants obtained, the formation and stability of the 1:3 (M:L) assembly was shown to be largely unaffected in the more competitive protic media relative to CH_3CN, potentially highlighting the existence of a hydrophobic effect.

Calculation of the Q_L^{Ln} values was undertaken to quantify the luminescence efficiencies of the complexes; **Eu.39$_3$**, **Eu.41$_3$**, **Eu.42$_3$**, and **Eu.43$_3$**. Differences in Q_L^{Ln} between the systems in CH_3CN were notably small, pointing to the influence of *para*-functionalisation being mostly negligible. Although reduced in comparison to the original sliotar **Eu.32$_3$**, the determined Q_L^{Ln} values remained sufficiently large to offer promise for future application as luminescent probes.

The results described throughout this chapter greatly complement the previous work of the Gunnlaugsson group relating to analogous Ln(III) self-assemblies. At the same time, this research symbolises a significant advancement, with the introduction of polyethoxy ligand functionality permitting spectroscopic analysis in a partially aqueous environment. Continuing with pyridyl *para*-substitution strategies, research is currently on-going within the group towards designing sliotar systems with full water solubility. One such approach being explored centres around the facile attachment of water-solubilising sulfonated alkyl chains, this approach having been successfully demonstrated recently by O'Shea *et al.*[250] To conclude, these findings strongly emphasise the attractiveness of Ln(III)-directed synthesis for the construction of novel self-assembly complexes.

Chapter 3

Photophysical Investigation of Tris[2]pseudorotaxane Self-Assembly with Crown Ether-Sliotar Conjugates

3 Introduction

Chapter 2 served as a comparative study, contrived to explore the effects of ligand pyridyl 4-substitution on chiral sliotar systems. Employing a range of *para*-functionalised derivatives, the impact of this substitution strategy on complex properties such as stability and luminescence quantum yield was rigorously investigated. Ultimately, extensive analysis confirmed the effects of *para*-modification to be mostly negligible, underlining both the feasibility and immense potential of this design. Building upon this foundation, the next challenge was geared towards the development of sliotar analogues incorporating more sophisticated terminal functionality, with considerable emphasis placed on channelling the properties of the appended group to confer novel complex function. To this end, the enantiomeric ligand pair **51S** (*S*,*S*) and **51R** (*R*,*R*) was designed, the structure of which included a terminal dibenzo[24]crown-8 substituent.

51S (*S*,*S*)
51R (*R*,*R*)

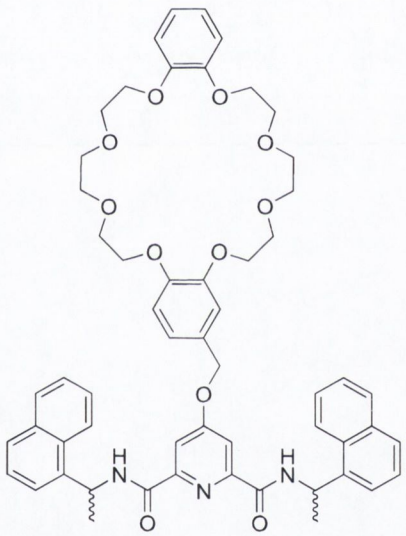

In reference to dibenzo[24]crown-8, Stoddart and co-workers were the first to recognise its aptitude for forming pseudorotaxanes in non-polar solvents with thread-like dialkylammonium salts (Scheme 3.1);[251,252] the term pseudorotaxane used to describe a non-stoppered supramolecular inclusion complex characterised by an acyclic molecule residing within the cavity of a macrocyclic one.[253] The complexes of dibenzo[24]crown-8, whose formation can be demonstrated by ^{1}H NMR spectroscopy in solution and by X-ray crystallography in the solid state, are known to be primarily stabilised by $^{+}$N-H…O and, to a lesser extent, C-H…O hydrogen bonds, with additional stability derived from π-π stacking interactions.[254] Indeed, since their inception, these systems have been expertly refined for the spontaneous creation of higher-order entities such as dendrimers,[255,256] and linear arrays.[257]

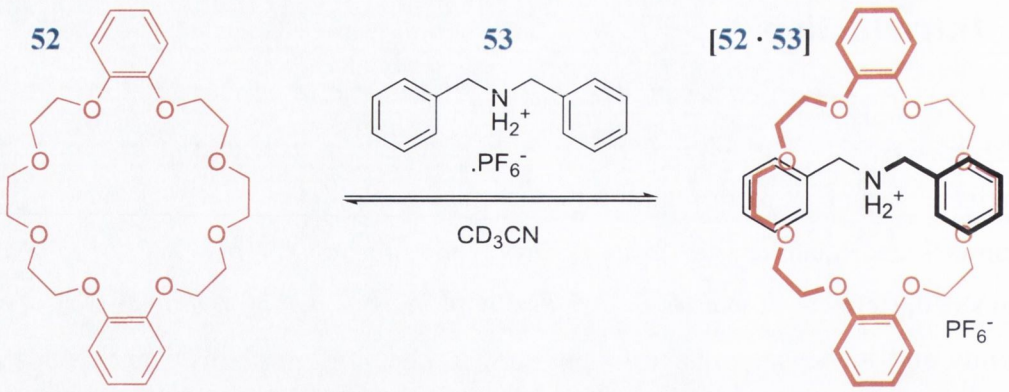

Scheme 3.1: *Schematic illustration of the interpenetration of dibenzo[24]crown-8 (**52**) by dibenzylammonium hexafluorophosphate (**53**) to give the pseudorotaxane **[52 · 53]**.*[251,252]

One recent advance in the field, profoundly relevant to this project, centred on the chemical attachment of a dibenzo[24]crown-8 functionality to the pyridyl 4-position of dpa to give a ditopic receptor.[258] Reported by Liu *et al.*, ligand **54** was then utilised to construct luminescent 1:3 (M:L) self-assemblies with Tb(III) ion. Intriguingly, successive additions of the benzyl(ferrocenylmethyl)ammonium thread **55** were shown to progressively quench the metal-centred emission of **Tb.54$_3$** (Scheme 3.2).

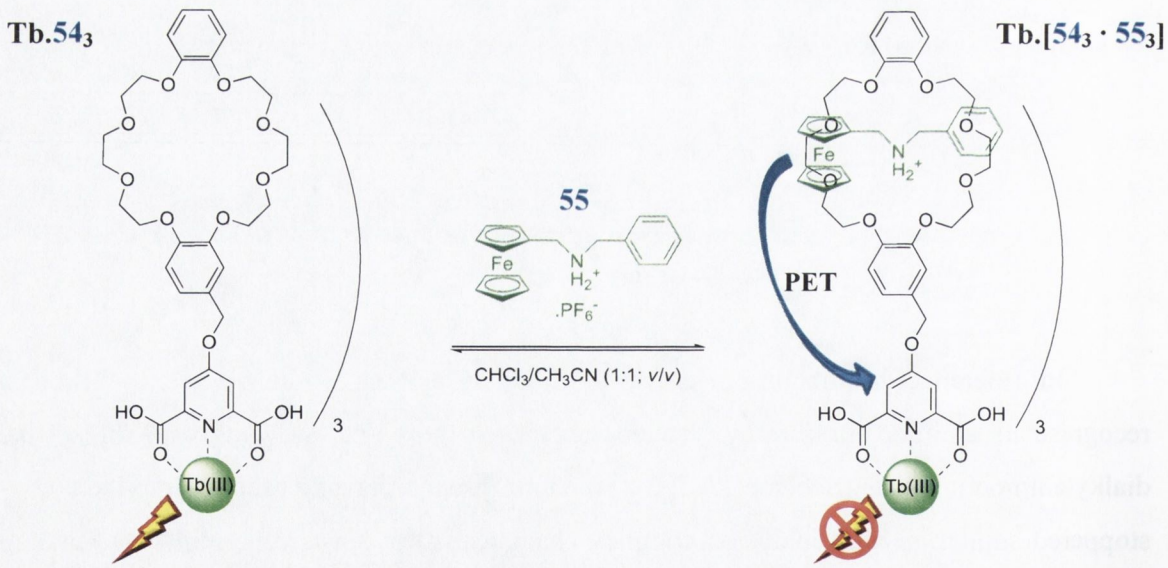

Scheme 3.2: *Schematic illustration of the formation of the tris[2]pseudorotaxane **Tb.[54$_3$ · 55$_3$]** from **Tb.54$_3$** and **55**, accompanied by PET quenching of the metal-centred emission.*[258]

This decrease in the luminescent output was accredited to an intramolecular photo-induced electron transfer (PET) process from the ferrocenyl moiety of **55** to the dpa unit of **54**, arising from the formation of a tris[2]pseudorotaxane **Tb.[54$_3$ · 55$_3$]**. The conclusion

offered was rationalised on two chemical grounds: (i) ferrocene is an exceptional electron donor, proven to act as an efficient triplet and Ln(III) excited state quencher,[259,260] and (ii) the synthesis of pseudorotaxanes from alkyl(ferrocenylmethyl)ammonium cations and dibenzo-[24]crown-8 is well-established.[261-263]

For the purpose of this chapter, the research undertaken set out to transfer the basic design principles implemented by Liu *et al.* to the chiral sliotar systems developed by Gunnlaugsson and co-workers, hence, the development of the chiral ligands **51S** and **51R**. Accordingly, the principle objective of this particular project was to first synthesise luminescent Eu(III) self-assemblies from **51S/R** (**Eu.51S/R$_3$**). Following successful complex synthesis, the dibenzo[24]crown-8 *para*-substituents of the three coordinated ligands were predicted to facilitate the assembly of tris[2]pseudorotaxanes from a novel alkyl(ferrocenyl-methyl)ammonium guest, with threading accompanied by concomitant emission quenching by a PET mechanism (see Scheme 3.3). Despite the apparent similarities, this design was distinguished by a number of factors, including the use of red-emitting Eu(III) and chiral chromophores, the latter making CPL emission viable. More importantly, however, was the thread employed (**56**), which consisted of a histamine group adjoined to the central ammonium cation. A more detailed description of the design strategy invoked will be provided in the next section.

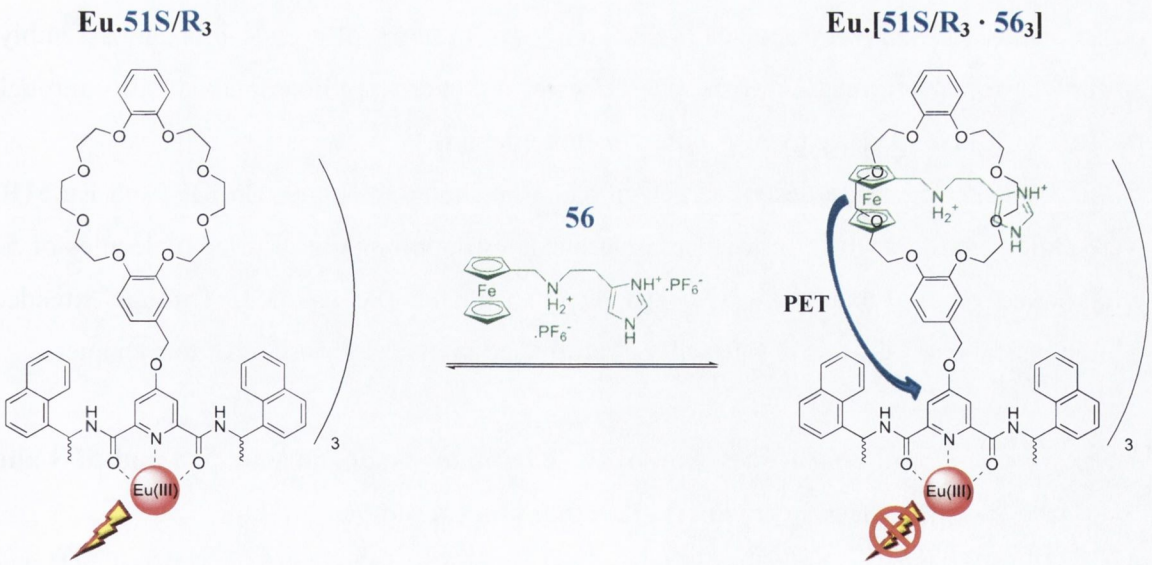

Scheme 3.3: *Schematic illustration of the proposed formation of the tris[2]pseudorotaxane* ***Eu.[51S/R$_3$ · 55$_3$]*** *from* ***Eu.51S/R$_3$*** *and* ***56****, accompanied by PET quenching of the metal-centred emission.*

3.1 Design of the enantiomeric ligand pair 51S and 51R and the histaminyl-(ferrocenylmethyl)ammonium thread 56

The enantiomeric pair **51S/R** was derived from 4-hydroxypyridine-2,6-dicarboxylic acid (chelidamic acid), as per the ligands reported in Chapter 2. In line with previous sliotar analogues, chiral 1-(1-naphthyl)-ethylamine groups were coupled to both the 2- and 6-pyridyl positions of the dpa framework. These chromophores were selected in view of their capacity to both sensitise Ln(III) emission and transfer chirality to the supramolecular self-assembly. Attachment of the dibenzo[24]crown-8 unit was achieved *via* nucleophilic substitution to the pyridine 4-hydroxy terminus. In spite of the large steric bulk associated with this crown ether function, the analysis detailed in Chapter 2 led one to rationalise that its presence would not severely restrict the self-assembly of 1:3 (M:L) stoichiometric Ln(III) complexes. Visible-emitting Eu(III) was again preferred for Ln(III) complexation, owing to the understanding gained through the studies in Chapter 2 for Eu(III) sliotar systems.

As already stated, the generation of pseudorotaxanes from dibenzo[24]crown-8 and dialkylammonium salts has been extensively reported.[251,252] With this in mind, the novel histaminyl(ferrocenylmethyl)ammonium thread **56** was designed. This thread was in fact a conjugate of histamine and ferrocene, linked *via* a central ammonium ion. The ferrocene moiety was integrated for its electron donor character, which was expected, upon threading of **56**, to result in quenching of the Ln(III)-centred emission, akin to the system of Liu.[258] Furthermore, **56** was synthesised as a hexafluorophosphate salt so as to provide solubility in organic solvents. This was done as organic solvents, in terms of pseudo-rotaxane assembly, are proven to drive threading of the guest species and aid overall complex stability through the absence of competitive hydrogen bonding interactions.[253,254]

By adhering to the described design plan, the sliotar analogues **Eu.51S$_3$** and **Eu.51R$_3$** were anticipated to each form tris[2]pseudorotaxanes upon binding of three molecules of **56** within the cavities of their terminal crown ether substituents (Scheme 3.3). Through extended photophysical analysis, this design will be scrutinised in the later sections of this chapter.

3.2 Synthesis and characterisation of the enantiomeric ligand pair 51S and 51R and the histaminyl(ferrocenylmethyl)ammonium thread 56

The first stage in the development of the enantiomeric ligand pair **51S** and **51R** was devoted to the synthesis of an electrophilic dibenzo[24]crown-8 chloro-derivative (**65**) (see Scheme 3.4), previously reported by Loeb *et al.*[264] The synthesis of **65**, which relied on a combination of literature procedures,[264-267] began with the mono-tosylation of triethylene glycol. In this step, triethylene glycol **57** and 4-toluenesulfonyl chloride were reacted in the

presence of NaOH for 3 h in a THF/H_2O mixture cooled to 5 °C. To ensure effective mono-substitution, a large molar excess of **57** (*i.e.* 10:1) was used. After completion, the reaction mixture was poured onto ice water, the organic layer was separated, and the aqueous phase was extracted with CH_2Cl_2. The combined organic layers were then washed with H_2O and evaporated to give **58** as a clear yellow oil in 52% yield. Verification of product formation was attained from the ^1H NMR (400 MHz, $CDCl_3$) spectrum, where appearance of a singlet at 2.44 ppm and two aromatic doublets at 7.79 ppm and 7.34 ppm, corresponding to the tosyl group, were identified (combined integral of 7 confirmed successful mono-tosylation).

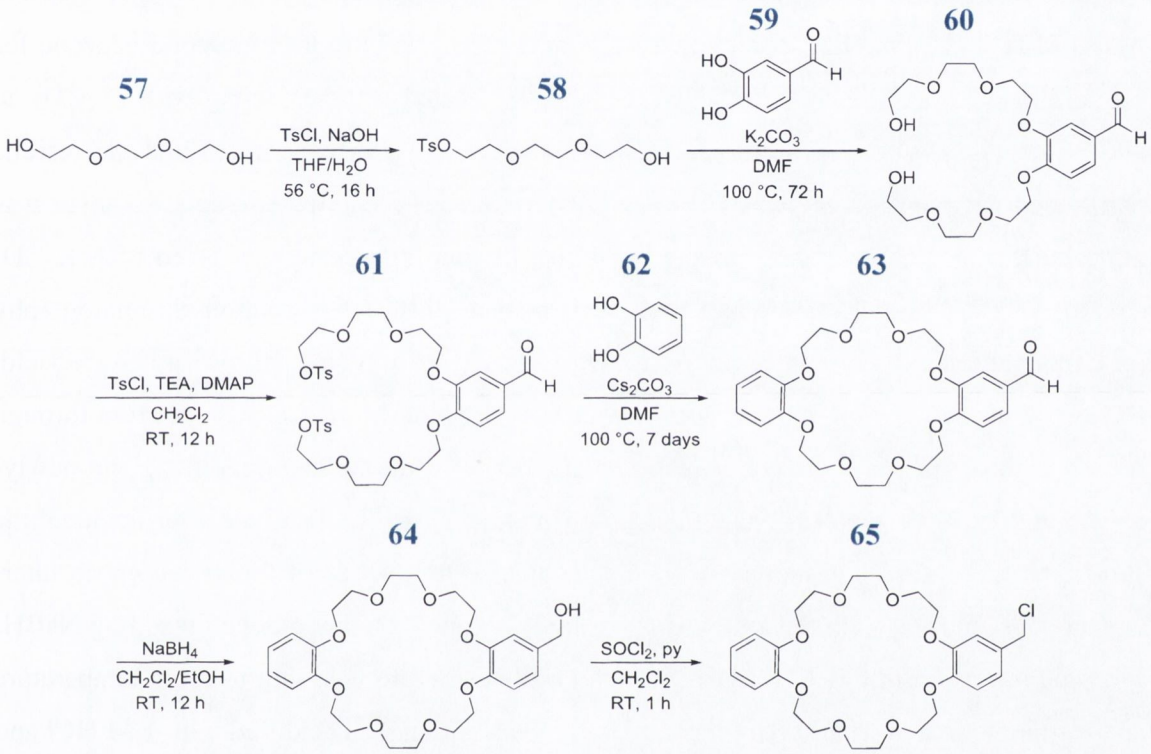

Scheme 3.4: *Synthetic pathway for* ***65****.*

In the following step, **58** was reacted with 3,4-dihydroxy-benzaldehyde **59** in a 2:1 ratio for di-substitution of the aromatic hydroxy groups. The reaction entailed initial stirring of **59** with anhydrous K_2CO_3 in anhydrous DMF for 30 min at room temperature, before the addition of **58** and heating to 100 °C for 72 h. Following heating, the mixture was filtered and the solvent was evaporated. The crude residue was partitioned between CH_2Cl_2 and an aqueous solution of K_2CO_3 (10% *w/v*) and then separated. Washing of the organic layer with K_2CO_3 solution and removal of solvent afforded **60** as a crude brown oil. Without further purification, 4-toluenesulfonyl chloride was slowly added to a solution of crude **60**, triethylamine, and 4-(dimethylamino)pyridine (catalytic amount) in dry CH_2Cl_2, maintaining

a temperature below 5 °C at all times. Upon full addition, the reaction mixture was allowed to reach room temperature and stirred overnight. Subsequently, the mixture was acidified with 5 M HCl and the organic layer separated. The organic phase was then washed with 2 M HCl and brine, with final purification achieved by flash silica column chromatography (gradient elution 80:20 → 20:80; Hex/EtOAc) to yield **61** as a pale yellow oil in 39% overall yield. In the ^{1}H NMR (400 MHz, $CDCl_3$) spectrum, the presence of a singlet at 9.82 ppm representing the aldehydic proton, and aromatic signals at both 7.45 – 7.39 ppm and 6.99 ppm established the benzaldehyde unit in the final structure. In addition, tosylation of the hydroxy substituents of the intermediate compound was evidenced, with the tosyl resonances observed at 7.77 ppm, 7.32 ppm, and 2.42 ppm. In order to introduce a second benzene for ring closure, **61** and 1,2-dihydroxybenzene **62** were heated together, along with Cs_2CO_3, at 100 °C for 7 days in anhydrous DMF. After, the solvent was evaporated and the residue partitioned between toluene and 10% *w/v* K_2CO_3 aqueous solution. The aqueous layer was extracted further with toluene and the combined organic phases were washed with K_2CO_3 solution. Finally, the crude product was purified using flash silica column chromatography (gradient elution 100:0 → 95:5; EtOAc/MeOH) to yield **63** as a pale yellow oil in 42% yield. Expulsion of the tosyl groups was seen in the ^{1}H NMR (400 MHz, $CDCl_3$) spectrum through the absence of the tosyl signals and the emergence of a multiplet representing the newly-constituted benzene ring at 6.90 – 6.82 ppm (integral of 4). To facilitate later nucleophilic substitution, the aldehyde moiety of **63** was subjected to a series of functional group inter-conversions, starting with reduction to the primary alcohol. This was done by adding $NaBH_4$ to a solution of **63** in CH_2Cl_2/EtOH (1:1; *v/v*) at 0 °C, before warming to room temperature and leaving to stir overnight. Upon completion, the solution was acidified with 1 M HCl and extracted with CH_2Cl_2. Washing the organic phase with 1 M $NaHCO_3$ and H_2O, followed by solvent removal gave **64** as a white solid in 96% yield. Transformation to the alcohol was confirmed by the disappearance of the aldehydic resonance from the ^{1}H NMR (400 MHz, $CDCl_3$) spectrum, combined with the appearance of a singlet at 4.56 ppm corresponding to the benzyl CH_2 group. The final step in the synthetic pathway for **65** set out to convert the alcohol to its related benzyl chloride. To achieve this, a solution of **64** in CH_2Cl_2 was added to a solution of both pyridine and thionyl chloride in CH_2Cl_2, and stirred for 1 h at room temperature. $CHCl_3$ was then added before pouring the solution onto ice water and extracting with CH_2Cl_2. The combined organic phases were washed with H_2O, 1 M $NaHCO_3$, and brine and the solvent removed. Precipitation of the product by addition of hexane to a concentrated CH_2Cl_2 solution yielded **65** as a pure white solid in 90% yield.

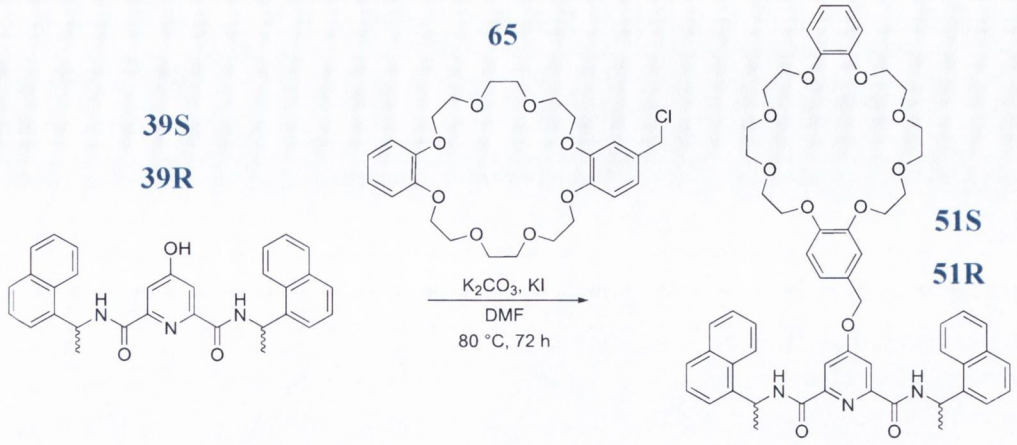

Scheme 3.5: *Synthetic pathway for* ***51S*** *and* ***51R****.*

Following the procedure shown in Scheme 3.5, the final step in ligand development was to introduce the crown ether to the pyridyl 4-hydroxy group of **39S** and **39R**, giving **51S** and **51R**, respectively (see Section 2.2 for the synthetic details of **39S/R**).[237] These reactions were initiated by first stirring **39** (either *S* or *R*) with anhydrous K_2CO_3 in anhydrous DMF for 30 min at 25 °C. Thereafter, the crown reagent **65** was added and the mixture heated was for 72 h at 80 °C. Upon cooling to room temperature, the solvent was removed under reduced pressure and the residue dissolved in CH_2Cl_2. Washing the organic phase with 1% acetic acid (aqueous) and H_2O, followed by trituration in EtOH afforded the desired products as yellow waxy solids in yields of 40% and 45% for **51S** and **51R**, respectively.

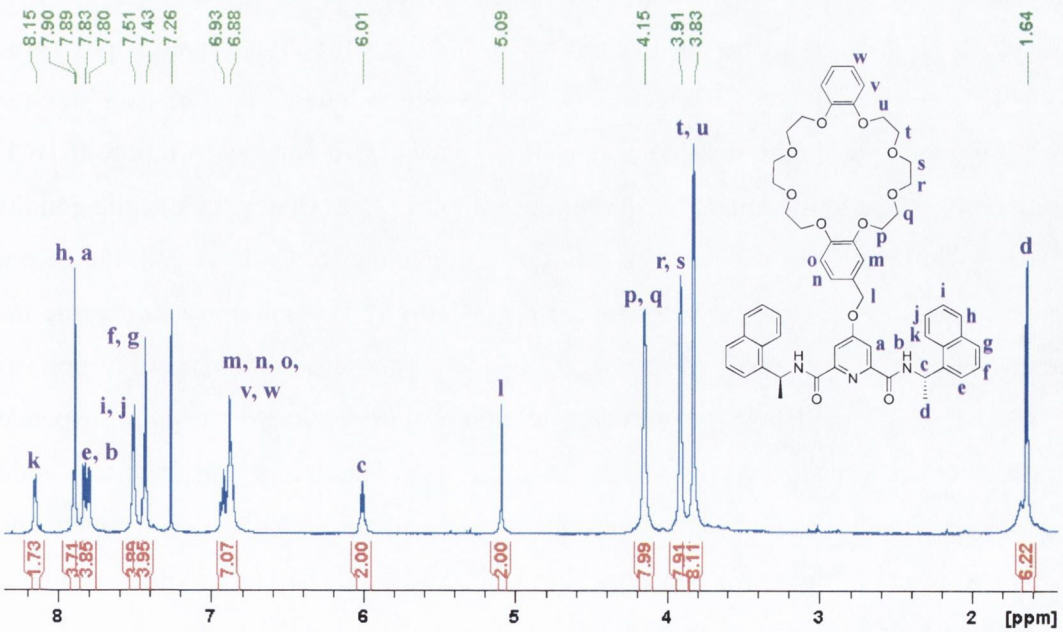

Figure 3.1: *^{1}H NMR (600 MHz, $CDCl_3$) spectrum of ligand* ***51S****.*

Full assignment of the product ^{1}H NMR (600 MHz, $CDCl_3$) spectra was completed using a range of 2D NMR experiments. In each spectrum (Figure 3.1 and Figure A3.2 for **51S** and **51R**, respectively), the downfield aromatic region consisted of signals correlating to the protons of the pyridyl and adjoined naphthyl rings. Further upfield, the presence of additional aromatic resonances (6.95 – 6.83 ppm) and four CH_2 signals (5.07 ppm, 4.15 ppm, 3.91 ppm, and 3.83 ppm), all assignable to the dibenzo[24]crown-8 function, confirmed its inclusion in the final structure.

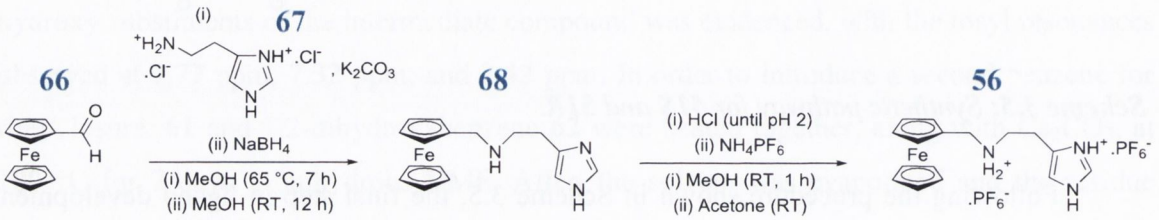

Scheme 3.6: *Synthetic pathway for* ***56****.*

Synthesis of the histaminyl(ferrocenylmethyl)ammonium thread **56** first involved a reductive amination reaction (Scheme 3.6), which required refluxing commercially available ferrocenecarboxaldehyde **66** and histamine dihydrochloride **67** together in the presence of anhydrous K_2CO_3 in dry MeOH for 7 h. Reduction of the resultant imine to its secondary amine was accomplished by cooling to 0 °C, before adding $NaBH_4$ and leaving the mixture to stir overnight at room temperature. The solution was then hydrolysed with ice water and the solvent was evaporated under reduced pressure. Dissolution of the crude product in CH_2Cl_2, followed by H_2O washing and purification by flash silica column chromatography (gradient elution 100:0 → 80:20; CH_2Cl_2/MeOH) yielded the amino intermediate **68** as a green solid. In order to make the ammonium chloride salt, a concentrated aqueous solution of HCl was subsequently added to a methanolic solution of **68** until pH 2. Under such acidic conditions, the thread would exist as a dication, a result of protonation occurring at both the secondary amine and at the imidazole ring (for which $pK_a \approx 5.8$).[268] For solubility in organic media, counter-anion exchange was implemented to convert from chloride to hexafluorophosphate salt. To execute the exchange, the solvent was first evaporated and the residue suspended in acetone. A concentrated aqueous solution of ammonium hexafluorophosphate was added to the suspension, which caused product dissolution. The organic solvent was removed, and the precipitated product filtered off, washed with H_2O, and air dried to give **56** as a dark green solid with an overall yield of < 5%.

Complete structural elucidation was made possible by NMR spectroscopy. In the ^{1}H NMR (400 MHz, CD_3CN-d_3) spectrum (see Figure A3.3), resonances attributable to the CH protons of the two aromatic termini were seen. Incorporation of the histaminyl imidazole group was confirmed by two singlets at 8.46 ppm and 7.24 ppm, with presence of ferrocene established by three singlets at 4.35 ppm, 4.25 ppm, and 4.18 ppm, corresponding to the cyclopentadienyl protons. Furthermore, verification of successful counter-anion exchange was given by the ^{19}F NMR (376 MHz, CD_3CN-d_3) spectrum (see Figure A3.4), from which a doublet at – 72.42 ppm was identified and assigned to the hexafluorophosphate anion. Other techniques such as IR spectroscopy and high resolution mass spectrometry were utilised to characterise the final compounds reported in this section. Full details of characterisation can be found in the experimental section of Chapter 7.

3.3 Synthesis and characterisation of Eu(III) complexes of 51S and 51R

Self-assembly formation of the Eu(III) complexes of **51S** and **51R** was achieved by refluxing the relevant ligand enantiomer with 0.33 eq. of $Eu(CF_3SO_3)_3$, under microwave irradiation, for 20 min in HPLC grade CH_3CN (Scheme 3.7). As per the earlier analogues (*i.e.* **41** – **43**), a 1:3 (M:L) molar ratio was used with the intent of synthesising homoleptic tris-chelates. After reflux, the complexes were precipitated by vapour diffusion of diethyl ether, and isolated by filtration as yellow solids in yields of 65% and 56% for **Eu.51S$_3$** and **Eu.51R$_3$**, respectively. The enantiomeric complexes were then characterised by ^{1}H NMR spectroscopy, elemental analysis, and IR.

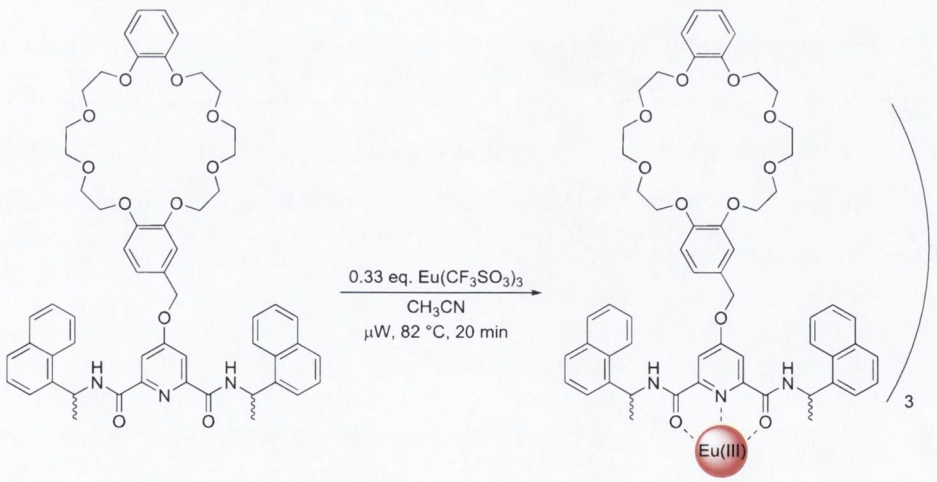

51S **Eu.51S$_3$**

51R **Eu.51R$_3$**

Scheme 3.7: *Synthetic pathway for* ***Eu.51S$_3$*** *and* ***Eu.51R$_3$*** *by complexation of* ***51S*** *and* ***51R*** *with* $Eu(CF_3SO_3)_3$.

Examination of the ^{1}H NMR (400 MHz, CD_3CN-d_3) spectra of **Eu.51S$_3$** and **Eu.51R$_3$** (Figure 3.2 and Figure A3.5, respectively) revealed a broadening and shifting of the proton resonances relative to the ligand, therefore, endorsing successful metal-ligand complexation. Moreover, both complex spectra were equivalent to one another, and showed each species to exist as a highly symmetrical entity in solution.

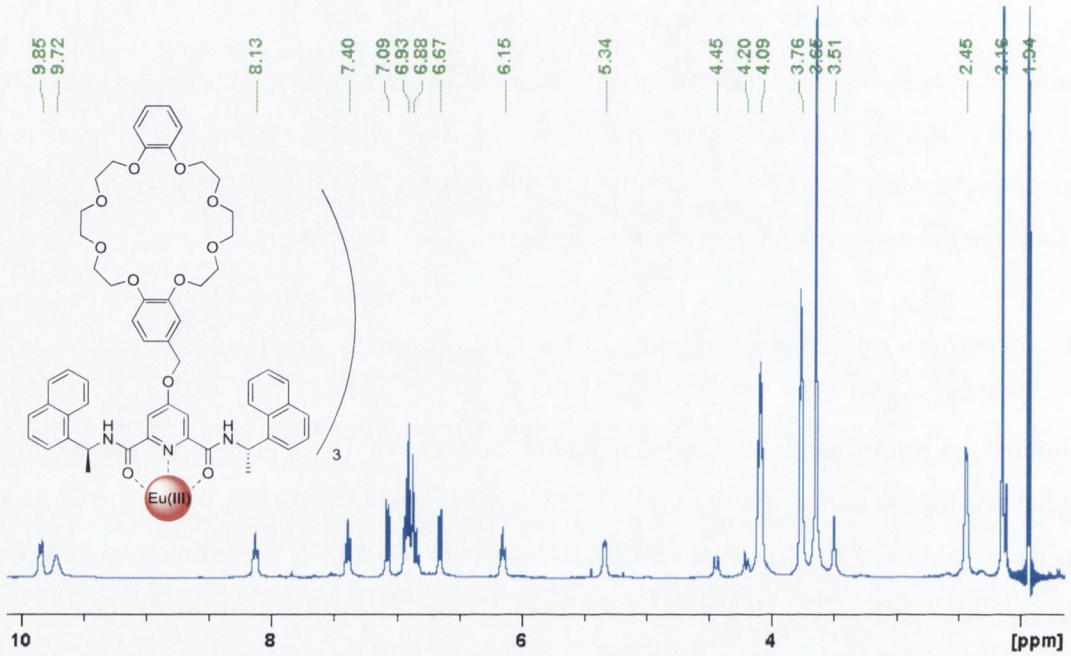

Figure 3.2: *^{1}H NMR (400 MHz, CD_3CN-d_3) spectrum of complex* ***Eu.51S$_3$****.*

The composition of the synthesised complexes was identified by elemental analysis, with both assemblies found to possess the predicted 1:3 (M:L) stoichiometry (full details in Chapter 7), therefore, proving 1:3 (M:L) complex formation. This data verified a molecular species with formula **[Eu.51S/R$_3$](CF$_3$SO$_3$)$_3$**, and provided the first hint that the formation of tris-chelates was not impeded by the terminal crown ether function. Unfortunately, HRMS analysis did not give hits for the 1:3 (M:L) species, despite the use of various carrier solvents and matrices, suggesting complex de-assembly prior to detection.

Table 3.1: *Summary of the IR stretching frequencies (cm^{-1}) of the amide carbonyl groups of the free ligands* ***51S*** *and* ***51R*** *and their corresponding complexes* ***Eu.51S$_3$*** *and* ***Eu.51R$_3$****.*

Compound	Free Ligand C=O Stretch (cm^{-1})	Complex C=O Stretch (cm^{-1})
51S	1657	1619
51R	1656	1619

Additional proof of complexation was derived from IR spectroscopy, with specific attention paid to the amide carbonyl stretches in both the free ligand and complex spectra. Such comparison for both **51S** and **51R** revealed a shift in the IR stretching frequency of these groups to a lower wavenumber upon complexation, thus, pointing to effective metal-binding. A summary of these changes is shown in Table 3.1.

Before evaluating the potential self-assembly of tris[2]pseudorotaxanes, the unique photophysical properties of **Eu.51S$_3$** and **Eu.51R$_3$** were extensively studied independent of **56**. Owing to strong similarities, the measurements described in the sections that precede pseudorotaxane discussion can be seen as complementary to those reported in Chapter 2.

3.4 Photophysical properties of Eu.51S$_3$ and Eu.51R$_3$

UV-vis absorption, phosphorescence excitation and emission spectra were recorded for the synthesised complexes of **Eu.51S$_3$** and **Eu.51R$_3$** in $CHCl_3/CH_3CN$ (1:1; *v/v*) *i.e.* the solvent mix in which all photophysical titrations described later were performed. In each case, the UV-vis spectrum consisted of two principle bands; a high energy band at 235 nm and a lower energy band centred at 281 nm, the latter of which was prescribed to the π-π^* transitions of the naphthalene antennae (see Figure 3.3a and Figure A3.6a for **Eu.51R$_3$** and **Eu.51S$_3$**, respectively).

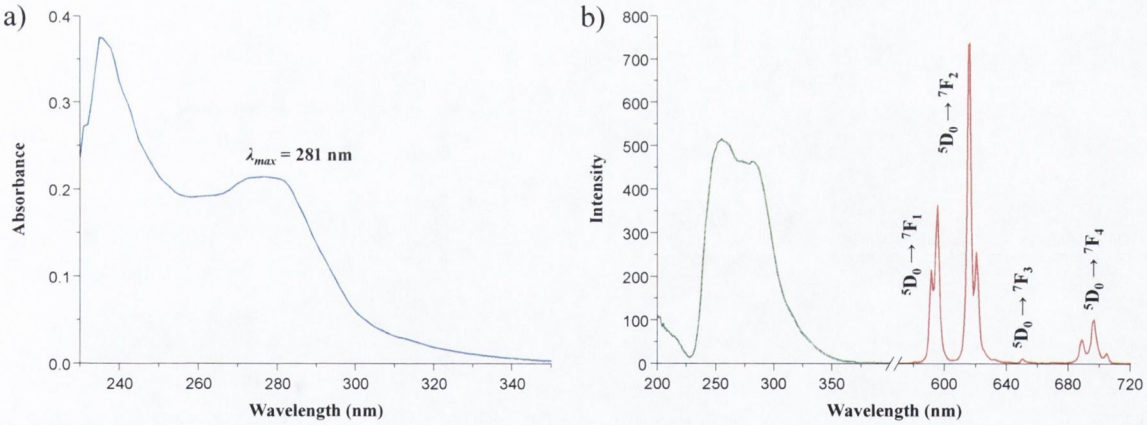

Figure 3.3: *a) UV-vis absorption and b) phosphorescence excitation (green) and emission (red) spectra (λ_{exc} = 281 nm) of* ***Eu.51R$_3$*** *(ca. 3.33 × 10^{-6} M) recorded in $CHCl_3/CH_3CN$ (1:1; v/v) at 298 K. of* ***Eu.51R$_3$****.*

The phosphorescence spectra displayed in Figure 3.3b (**Eu.51R$_3$**) and Figure A3.6b (**Eu.51S$_3$**) were acquired by excitation of the naphthyl chromophores at 281 nm (λ_{exc}), and helped unambiguously evidence energy transfer to the Eu(III) centre. Indeed, both spectra exhibited the characteristic emission band structure of the Eu(III) ion, with line-like bands

arising from radiative deactivation of the $^5D_0$ excited state to the ^7F_J ground state; where J = 1 – 4. Similar to the complex set **Eu.(41 – 43)$_3$** in Chapter 2 (Section 2.6), the electronic-dipole J = 0 transition was absent, thus, betraying the highly symmetrical nature of the complexes in solution, a fact reinforced by the complex ^{1}H NMR spectra.[239]

The ligands used were anticipated to exert diastereoselective control over the self-assembly process, leading to the construction of enantiomeric Eu(III) complexes. To probe the occurrence of chirality transfer, the chiroptical properties of both systems were explored.

3.5 Circular dichroism studies of ligands 51S and 51R and their Eu(III) complexes

The CD spectra of ligands **51S** and **51R** were recorded in $CHCl_3/CH_3CN$ (1:1; *v/v*) in search of spectroscopic evidence that verified the enantiomeric relationship between them. Following *in situ* self-assembly, achieved through the addition of 0.33 eq. of $Eu(CF_3SO_3)_3$, CD spectra of the resultant complexes **Eu.51S$_3$** and **Eu.51R$_3$** were then measured to assess whether chirality transfer had transpired. The overlaid CD spectra of both ligands and their complexes are shown in Figure 3.4.

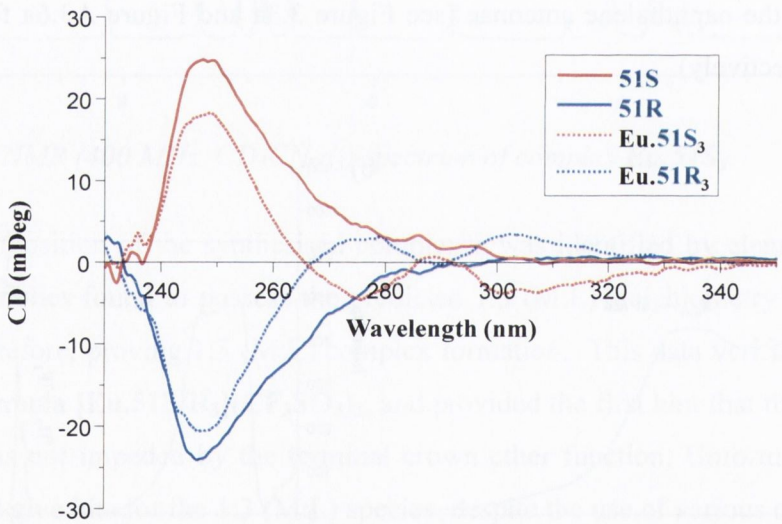

Figure 3.4: *CD spectra of ligand solutions (4.0 × 10^{-5} M) of **51S** and **51R** recorded in $CHCl_3/CH_3CN$ (1:1; v/v) at 298 K before (solid lines) and after (dashed lines) the addition of 0.33 eq. of $Eu(CF_3SO_3)_3$ to give the complexes "**Eu.51S$_3$**" and "**Eu.51R$_3$**", respectively.*

For the free ligands, the recorded spectra were essentially mirror images, therefore, accentuating their enantiomeric relationship. Ligand **51S** exhibited a widely spread positive band, extending from *ca.* 235 – 300 nm, with a maximum centred at 248 nm. Conversely, ligand **51R** showed the exact opposite spectrum, displaying a negative band from *ca.* 235 – 300 nm with a maximum at 248 nm. Upon *in situ* complex formation, the spectra underwent

significant morphological changes. In the complex spectrum of **Eu.51S$_3$**, the large positive band at 248 nm was found to decrease in intensity relative to the ligand. More interesting, however, was the evolution of two new negative bands, with one centred at 278 nm and the other at *ca.* 290 – 330 nm. As expected, the **Eu.51R$_3$** CD spectrum was a mirror image. Intriguingly, the emergence of the longer wavelength band in both complex spectra occurred in a region where no CD activity was detected for the free ligands. Consequently, one may assume this band to be a reflection of the topological chirality of the complexes, with this phenomenon stemming from a helical organisation of ligands around the metal ion.

In summary, the CD spectra of **Eu.51S/R$_3$** possessed exciton signals of opposite sign and approximately equal magnitude, thus, corroborating the diastereoselective formation of an enantiomeric complex pair. With the metal residing in a chiral pocket, CPL studies were next conducted to test the feasibility of metal-centred chiral emission.

3.6 Circularly polarised luminescence studies of Eu.51S$_3$ and Eu.51R$_3$

CPL spectra of the complexes **Eu.51S$_3$** and **Eu.51R$_3$** were recorded in $CHCl_3/CH_3CN$ (1:1; *v/v*) using an excitation wavelength of 281 nm. Performed in collaboration with Dr. R. D. Peacock, University of Glasgow, the resulting spectra acted as proof for the conferral of ligand chirality to the later supramolecular systems (see Figure 3.5).

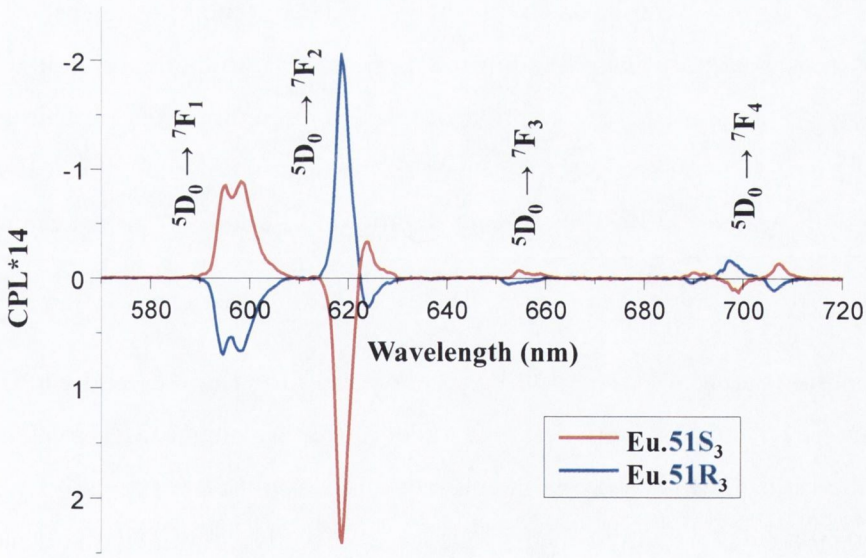

Figure 3.5: *CPL emission spectra of* ***Eu.51S$_3$*** *and* ***Eu.51R$_3$*** *recorded in $CHCl_3/CH_3CN$ (1:1; v/v) at 298 K (λ_{exc} = 281 nm).*

Indeed, the two Eu(III) complexes produced CPL signals of opposite sign for all the transitions, therefore, confirming their formation as chiroptically pure species of opposite

chirality. As predicted, both the shape and sign of the CPL spectra for both stereochemical assignments matched perfectly with that seen for the original sliotar systems (**Eu.32S/R$_3$**) and the analogues in Chapter 2 *i.e.* all (*S*) spectra were equivalent, with the same true of (*R*). Based on this correlation, the metal ion stereochemistry was assigned according to previous X-ray crystallographic elucidation of system helicity; Δ for **Eu.51S$_3$** and Λ for **Eu.51R$_3$** (see Section 2.8).

Table 3.2: *Summary of the g_{lum} dissymmetry factor values calculated from the CPL spectra of **Eu.51S$_3$** and **Eu.51R$_3$** for the J = 1 and 2 transitions at 595 nm and 619 nm, respectively.*

Complex	g_{lum} value 595 nm (J = 1)	g_{lum} value 619 nm (J = 2)
Eu.51S$_3$	+ 0.19	− 0.13
Eu.51R$_3$	− 0.17	+ 0.15

Applying **Equation 1.4** from Section 1.5.1, luminescence dissymmetry factors (g_{lum}) were calculated for the J = 1 and 2 transitions of the spectra, with the values obtained showing good agreement for the two complex enantiomers (see Table 3.2). While still high, an appreciable reduction in g_{lum} for the transitions was noted upon comparison to the values of **Eu.(41 – 43)$_3$** listed in Table 2.4. These relatively lower values seemingly suggest the influence of the ligand chirality on the metal ion to be lessened in the case of **Eu.51S/R$_3$**, potentially symptomatic of weaker binding and reduced conformational rigidity.[188]

Having demonstrated the formation of enantiopure complexes by chiral asymmetric induction, the next stage in analysis focused on the application of photophysical spectroscopy to ascertain both complex stoichiometry and stability in solution. Empirical calculation of the complex hydration states proved critical to these studies.

3.7 Determination of metal-bound water molecules for Eu.51S$_3$ and Eu.51R$_3$

Ligands **51S** and **51R** were designed to coordinate trivalent Ln(III) ions in a 1:3 (M:L) stoichiometric ratio. In this case, the bound metal ion would be coordinatively saturated by three ligand molecules, resulting in the absence of directly coordinated solvent molecules. The hydration states (q values) of the synthesised complexes **Eu.51S$_3$** and **Eu.51R$_3$** were, therefore, calculated to test this hypothesis through luminescence lifetime measurements.

Performed separately in water and methanol, the exponential decay of the Eu(III) ion excited state with respect to time was recorded for each complex in both the non-deuterated ($\tau_{O\text{-}H}$) and deuterated ($\tau_{O\text{-}D}$) solvent form, upon excitation of the naphthyl chromophores (λ_{exc}

= 281 nm). In all instances, lifetime values were obtained by fitting to a mono-exponential decay, with the values collected together in Table 3.3. Predictably, methanol lifetimes were longer than those recorded in water. Calculation of the *q* values was subsequently managed by treating the measured lifetimes with the modified Horrocks equation (**Equation 1.1** – see Section 1.1.3),[38,66,67] using a proportionality constant of A = 1.2 ms and 2.0 ms for water and methanol, respectively. For both complexes, *q* values ≈ 0 were obtained in the two solvent media (Table 3.3), clearly inferring a lack of solvent bound in the first-coordination sphere and implying a 1:3 (M:L) complex composition.

Table 3.3: *Lifetime measurements of* ***Eu.51S$_3$*** *and* ***Eu.51R$_3$*** *in water (H_2O and D_2O) and methanol (MeOH and MeOD) with their corresponding rate constants (k) and calculated q values. Each lifetime is an average of six measurements with different gate times.*

Complex	Solvent	$\tau_{O\text{-}H}$ (ms)	$\tau_{O\text{-}D}$ (ms)	$k_{O\text{-}H}$ (ms^{-1})	$k_{O\text{-}D}$ (ms^{-1})	q (± 0.5)
Eu.51S$_3$	Water	1.42 ± 0.01	1.53 ± 0.02	0.70	0.65	− 0.24
	Methanol	1.60 ± 0.02	3.46 ± 0.03	0.63	0.29	+ 0.17
Eu.51R$_3$	Water	1.33 ± 0.02	1.41 ± 0.01	0.75	0.71	− 0.25
	Methanol	1.58 ± 0.02	3.29 ± 0.03	0.63	0.30	+ 0.16

These *q* values support the elemental analysis in verifying the formation of nine-coordinate tris-complexes, albeit by synthetic methods. Photophysical titrations afforded an opportunity to monitor the self-assembly process under less forcing conditions. These were critical in understanding the effects of the crown substituent, and will be discussed next.

3.8 UV-vis and luminescence titration studies of 51S and 51R

Investigation of the stepwise self-assembly pathway for the complexation of Eu(III) by ligands **51S/R** was accomplished through UV-vis and luminescence titrations, with all studies conducted according to the so-called dilution method (see Section 2.10). In order to determine complex speciation and to quantify stability, the data was fit by non-linear least squares regression analysis upon completion. All measurements were performed in $CHCl_3$/ CH_3CN (1:1; *v/v*) mix, with this selection governed by a number of factors. Additional to solubility requirements, this solvent mix was chosen for consistency with the photophysical analysis performed later to probe tris[2]pseudo-rotaxane assembly. As stated in Section 3.1, aprotic organic solvents assist the threading of crown ethers by the removal of competitive hydrogen bonding.[253,254] This exact mix has been proven in the past to mediate the threading

process.[251,258] Also, on account of a reduced affinity for the metal ion, the macrocycle was not anticipated to interfere in binding at the derivatised dpa site (*e.g.* log $K_{1:1}$ = 3.14 for Eu(III) complex of dibenzo[18]-crown-6 in CH_3CN).[269]

3.8.1 Titration experimental and data fitting details

The titration studies in the next section were carried out in $CHCl_3/CH_3CN$ (1:1; *v/v*). In each case, a stock solution (3 mL; 1×10^{-5} M) of the relevant ligand (**51S** or **51R**) was prepared and titrated against a standard solution of $Eu(CF_3SO_3)_3$. With every addition, UV-vis absorption and phosphorescence spectra were recorded, allowing for 5 min equilibration each time. Titrations were repeated in triplicate to ensure reproducibility. Fits of the UV-vis and phosphorescence spectral changes were obtained for both ligands using the non-linear least squares regression program SPECFIT® for the equilibria set **Equation 2.1 – 2.5** (see Section 2.10.5), used to define the stepwise self-assembly process. Both enantiomers, within experimental error, displayed practically identical behaviour. Therefore, only photophysical titrations of **51R** will be discussed (spectra for the titrations of **51S** can be found in Appendix 3). However, discussion will reference both systems when addressing data fitting.

3.8.2 UV-vis and luminescence titrations of 51R with $Eu(CF_3SO_3)_3$ in $CHCl_3/CH_3CN$

The complexation process was analysed by probing the changes in the ligand UV-vis absorption spectrum upon titration with $Eu(CF_3SO_3)_3$. Prior to Eu(III) addition, the spectrum of **51R** resembled that of the ligands in Chapter 2, consisting of a characteristic naphthalene band centred at 281 nm (ε = 22511 M^{-1} cm^{-1}), with two small shoulders at 273 nm and 294 nm (Figure 3.6a).

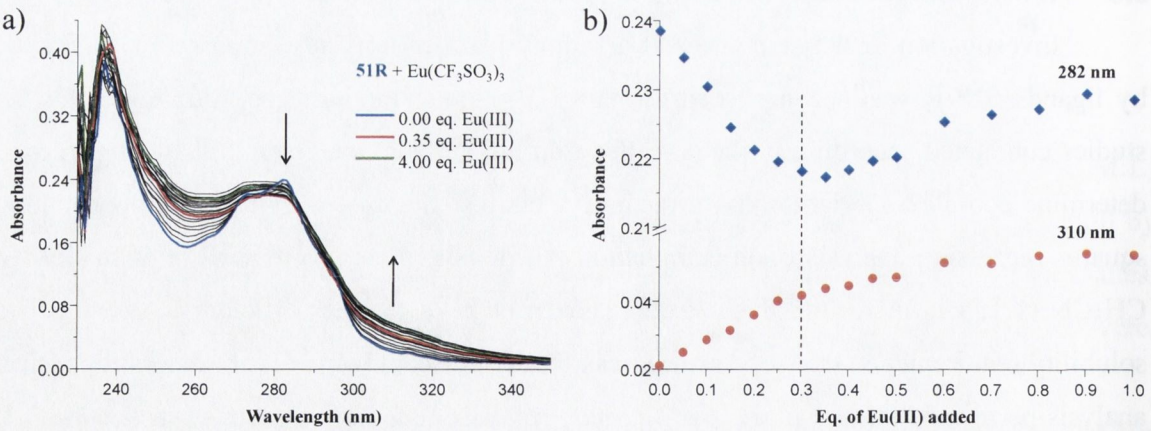

Figure 3.6: *a) Changes in the absorption spectra of **51R** (1×10^{-5} M) upon titrating with $Eu(CF_3SO_3)_3$ (0.00 → 4.00 eq.) in $CHCl_3/CH_3CN$ (1:1; v/v) at 298 K. b) Binding isotherms for the titration measured at 282 nm and 310 nm.*

With Eu(III) additions, this band experienced a hypochromic shift, accompanied by the development of a new band at *ca.* 310 nm. These effects were seen to continue, along with a loss of spectral definition, up until *ca.* 0.3 eq of Eu(III) ion. Thereafter, absorbance of the naphthyl band was found to slightly increase (*i.e.* hyperchromism). In the 282 nm binding isotherm, the described changes caused a pronounced negative to positive change in slope at *ca.* 0.3 eq. of Eu(III) (Figure 3.6b). Such a trend may be considered as an indicator for the 1:3 (M:L) complex stoichiometry and its predominance.

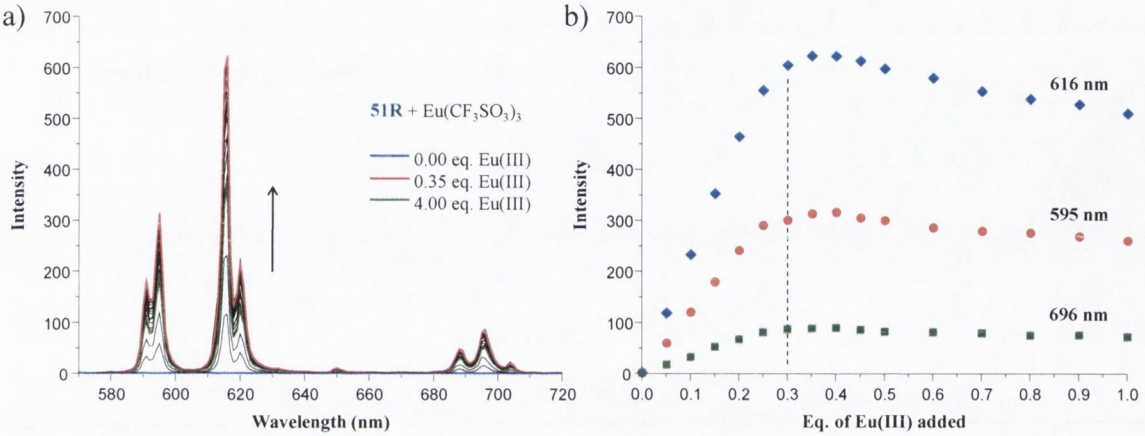

Figure 3.7: *a) Evolution of the phosphorescence emission in the titration of* ***51R*** *(1×10^{-5} M) with $Eu(CF_3SO_3)_3$ (0.00 → 4.00 eq.) in $CHCl_3/CH_3CN$ (1:1; v/v) at 298 K (λ_{exc} = 281 nm). b) Binding isotherms for the titration measured at 595 nm, 616 nm, and 696 nm.*

In the phosphorescence titration, a progressive *switching on* of the metal ion-centred emission was observed with indirect ligand excitation at 281 nm. Overlaid in Figure 3.7a, the spectra demonstrated the typical emission profile of trivalent Eu(III), with bands at 595 nm, 616 nm, 650 nm, and 696 nm for the $J = 1 - 4$ transitions, respectively. With no alteration of band structure (*i.e.* splitting pattern, *etc.*), emission intensity increased for all the transitions with additions of Eu(III) ion. This pattern was evident from the titration profiles (see Figure 3.7b), where the band intensity of the three wavelengths followed was seen to grow until *ca.* 0.3 eq. of Eu(III). At this point, however, the Eu(III)-centred emission began to decrease with further additions, thus, implying the formation of a less emissive species at Eu(III) excess. Therefore, with maximal intensity at *ca.* 0.3 eq. of the metal ion, one could again assume superior formation of the 1:3 (M:L) complex. Further evidence of Eu(III)-sensitisation was provided by the excitation spectra (Figure A3.8), which matched the absorption spectra.

For the two ligand enantiomers, the UV-vis and phosphorescence measurements gave trends implicating the dominance of the 1:3 (M:L) species. For a more conclusive account of the self-assembly, the spectral changes were fit for both titration modes with SPECFIT®. A

summary of the fitting results (*i.e.* species identified and their binding constants) is shown in Table 3.4. The UV-vis fits identified two stoichiometries in solution; the 1:1 and desired 1:3 (M:L) complex (Figure A3.9 and Figure A3.14 for **51R** and **51S**, respectively). In addition to these, the phosphorescence fits also recognised the 1:2 (M:L) complex (Figure 3.8 and Figure A3.15 for **51R** and **51S**, respectively). For all fits, the speciation graphs emphasised a great preference for the 1:3 (M:L) self-assembly at low Eu(III) ion concentrations, with maximal percentage formations at *ca.* 0.3 eq. of Eu(III). The contribution of the less coordinatively saturated complexes, however, was found to increase at Eu(III) excess. The formation of the less emissive 1:1 and 1:2 (M:L) species represent a sizable displacement of the equilibria, and help to explain the intensity decrease seen later in the phosphorescence titrations.

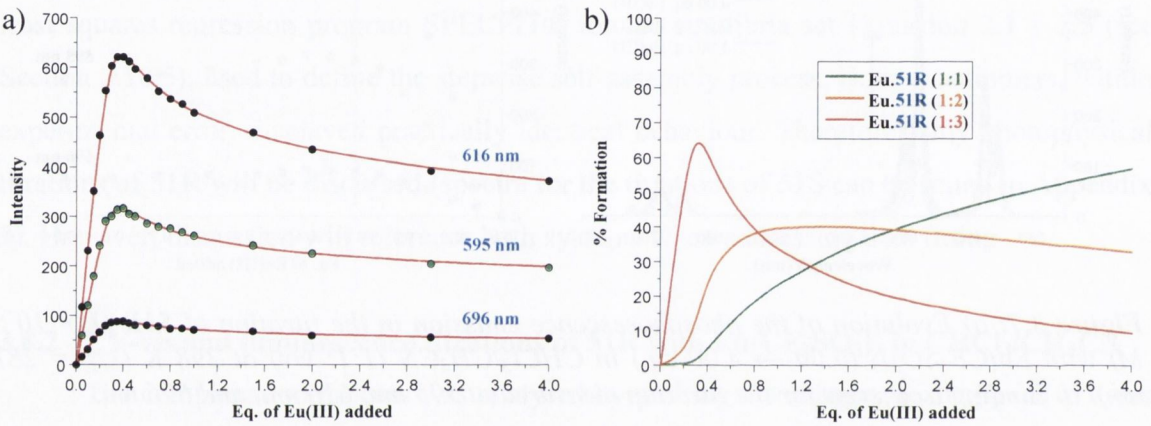

Figure 3.8: *a) Experimental binding isotherms for the phosphorescence titration of* ***51R*** *(1×10^{-5} M) with $Eu(CF_3SO_3)_3$ in $CHCl_3/CH_3CN$ (1:1; v/v) at 298 K (λ_{exc} = 281 nm) and their corresponding fit by means of SPECFIT. b) Speciation-distribution diagram obtained from the fit.*

In regards to the binding constants (see Table 3.4), there was acceptable agreement amongst the values for both enantiomers and fitting modes. The only minor exception was the log $\beta_{1:3}$ constant obtained from the **51S** phosphorescence fit, which was unusually large, yet close to related values. Indeed, the 1:3 (M:L) complexes were proven to form with good stability, despite the steric bulk of the pyridyl *para*-positioned crown. However, stability constant comparison with the values listed in Table 2.6 for the sliotar systems reported in Chapter 2 pointed to the crown function holding a partly detrimental effect on complex formation. Specifically, log $\beta_{1:3}$ constants measured for **51S** and **51R** were *ca.* 3 orders of magnitude smaller, thus, suggesting the large terminal group imparted a degree of steric restriction. The constraints placed on complex self-assembly were further reflected by the comparatively lower percentage formations determined for the 1:3 (M:L) species.

Table 3.4: *Summary of the binding constants obtained through data fitting for the UV-vis and phosphorescence titrations of* ***51S*** *and* ***51R*** *(1×10^{-5} M) with $Eu(CF_3SO_3)_3$ in $CHCl_3/CH_3CN$ (1:1; v/v), with percentage composition of the 1:3 (M:L) species at 0.33 eq. of Eu(III).*

Ligand	Mode	$\log \beta_{1:3}$	$\log \beta_{1:2}$	$\log \beta_{1:1}$	% of 1:3 (M:L) species at 0.33 eq. of Eu(III)
51S	**UV**	18.00 ± 0.35	–	5.77 ± 0.20	77
	Phos	20.02 ± 0.14	13.36 ± 0.18	7.07 ± 0.07	76
51R	**UV**	18.62 ± 0.46	–	6.77 ± 0.21	72
	Phos	18.65 ±0.11	12.48 ± 0.15	6.13 ± 0.10	64

With the exception of a decrease in relative stability, one must reiterate that ligands **51S** and **51R** spontaneously self-assembled **Eu.51S$_3$** and **Eu.51R$_3$**, respectively. Indeed, the design of these tris-chelates has been verified both synthetically and *in situ*. Having proven their formation, the next challenge was to assess the interactions between the histaminyl-(ferrocenylmethyl)ammonium thread **56** and the terminal macrocyclic ring of these sliotar systems. Interactions of these were predicted to facilitate the formation of tris[2]-pseudo-rotaxanes, leading to quenching of the Eu(III) luminescence by the electron donating action of the ferrocenyl moiety. In order to probe the self-assembly of such higher-order structures, photophysical investigation was undertaken.

3.9 Photophysical investigation of tris[2]pseudorotaxane formation

The potential influences of the ammonium thread **56** on the photophysical properties of **Eu.51S$_3$** and **Eu.51R$_3$** were evaluated in both UV-vis and luminescence titrations. These titrations were performed using the so-called dilution method (Section 2.10) in $CHCl_3$/ CH_3CN (1:1; *v/v*) solvent mix. With quenching anticipated, it was hoped that any spectral changes incurred would instruct on the nature of possible interactions. It should be stated prior that the titrations of thread **56** with **Eu.51S/R$_3$** produced partially inconclusive results, necessitating the performance of a series of control titrations. These control experiments employed complex sliotar derivatives (**Eu.41S$_3$** and **Eu.43S$_3$**) previously studied in Chapter 2, as well as an alternative dibenzylammonium thread (**53**) (to be discussed later).

3.9.1 Titration experimental and fitting details

All titration studies described hereafter were carried out in $CHCl_3/CH_3CN$ (1:1; *v/v*). Control titrations were conducted on one complex enantiomer only [*i.e.* (*S*)], operating under

the assumption that the results would be representative for a given enantiomeric pair. For each titration, a stock solution (3 mL; 3.33×10^{-6} M) of the relevant complex (**Eu.51S$_3$**, **Eu.51R$_3$**, **Eu.41S$_3$** or **Eu.43S$_3$**; all prepared using synthetic methods) was titrated against known volumes of a standard solution of the relevant thread (**56** or **53**). After additions, UV-vis absorption and phosphorescence spectra were recorded, giving 5 min to equilibrate. The titrations were repeated in triplicate to guarantee reproducibility.

$$\textbf{Eu.51S/R}_3 + \textbf{56} \overset{K_{1:1}}{\rightleftharpoons} \textbf{Eu.[51S/R}_3 \cdot \textbf{56]} \qquad \textbf{Equation 3.1}$$

$$\textbf{Eu.[51S/R}_3 \cdot \textbf{56]} + \textbf{56} \overset{K_{1:2}}{\rightleftharpoons} \textbf{Eu.[51S/R}_3 \cdot \textbf{56}_2\textbf{]} \qquad \textbf{Equation 3.2}$$

$$\textbf{Eu.[51S/R}_3 \cdot \textbf{56}_2\textbf{]} + \textbf{56} \overset{K_{1:3}}{\rightleftharpoons} \textbf{Eu.[51S/R}_3 \cdot \textbf{56}_3\textbf{]} \qquad \textbf{Equation 3.3}$$

$$\beta_{1:3} = K_{1:1} \times K_{1:2} \times K_{1:3} \qquad \textbf{Equation 3.4}$$

For the titrations between **Eu.51S/R$_3$** and **56**, fitting of the phosphorescence data was accomplished using the non-linear least squares regression program SPECFIT® (see Section 2.10.5) for the equilibria equation set **Equation 3.1 – 3.4**, which may potentially specify the step-by-step formation of a tris[2]pseudorotaxane.

3.9.2 UV-vis and luminescence titrations of Eu.51S$_3$ with thread 56 in CHCl$_3$/CH$_3$CN

Both complex enantiomers, **Eu.51S$_3$** and **Eu.51R$_3$**, were titrated with the histaminyl-(ferrocenylmethyl)ammonium thread **56**. Due to a close correlation between the two titration sets, this section will concentrate on the titrations of **Eu.51S$_3$**, with all spectra relevant to **Eu.51R$_3$** found in Appendix 3. The changes in the UV-vis absorption spectrum of complex **Eu.51S$_3$** were first analysed with additions of the thread **56**. Prior to treatment with **56**, the absorption spectrum corresponded to that described in Section 3.4 for the Eu(III) complex. The spectra underwent successive hyperchromic shifts with sequential additions of **56**, with the evolution of a new band centred at 360 nm also witnessed (Figure 3.9a). These effects continued up until titration completion. Informed by the absorption spectrum of **56** (Figure A3.16), which also absorbed at 360 nm, the appearance of this new band was prescribed to the thread compound. In fact, the titration profile at 360 nm showed absorbance to increase in a biphasic manner, with the greatest enhancement occurring up to *ca.* 3.5 eq. of **56** (Figure

3.9b), thus, implying a 1:3 (M:L) binding mode. The lack of linearity in these isotherms was mildly suggestive of some form of intermolecular interaction between **56** and **Eu.51R$_3$**.

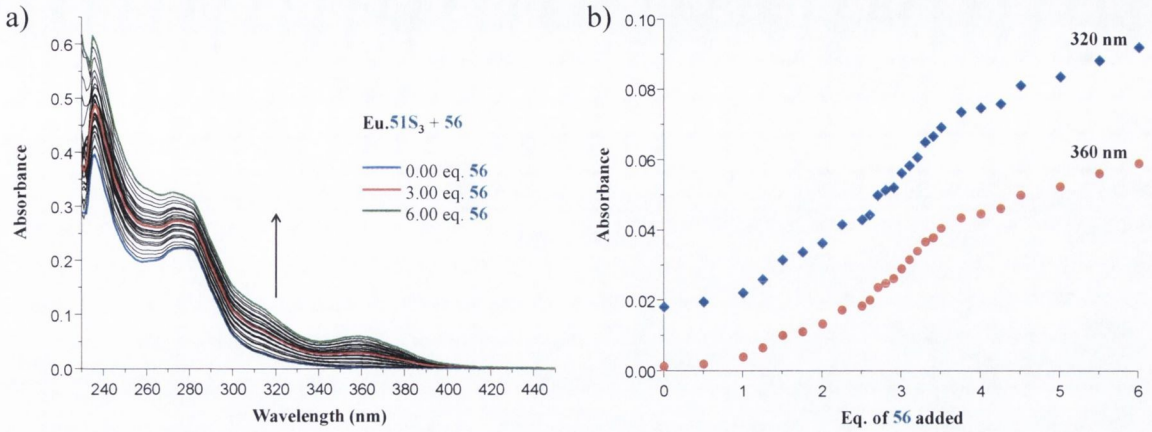

Figure 3.9: *a) Changes in the absorption spectra of* ***Eu.51S$_3$*** *(3.33 × 10^{-6} M) upon titrating with* **56** *(0.00 → 6.00 eq.) in $CHCl_3/CH_3CN$ (1:1; v/v) at 298 K. b) Binding isotherms for the titration measured at 320 nm and 360 nm.*

Phosphorescence spectra were recorded by exciting the same cell solutions used in the UV-vis titration (λ_{exc} = 281 nm), with quenching of the emission anticipated. As predicted, the addition of **56** induced quenching of the Eu(III)-centred luminescence (Figure 3.10a).

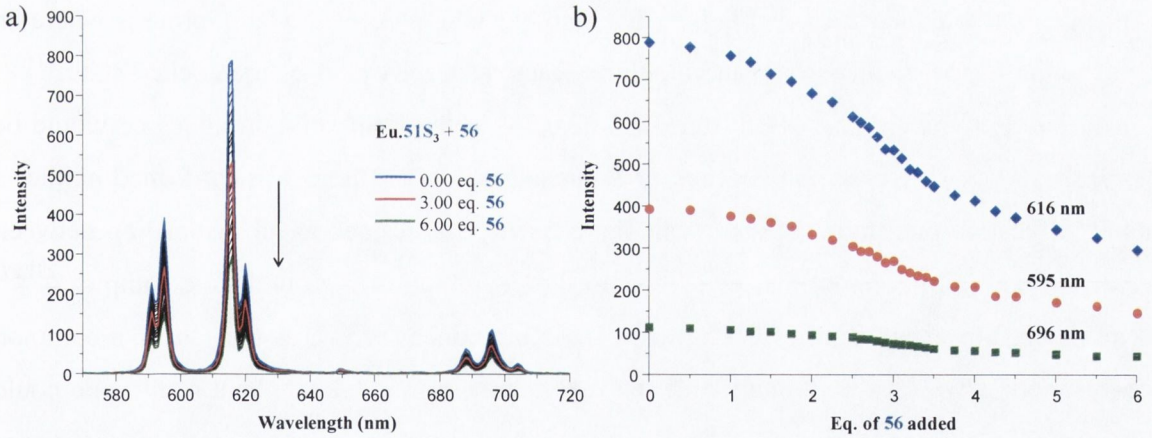

Figure 3.10: *a) Evolution of the phosphorescence emission in the titration of* ***Eu.51S$_3$*** *(3.33 × 10^{-6} M) upon titrating with* **56** *(0.00 → 6.00 eq.) in $CHCl_3/CH_3CN$ (1:1; v/v) at 298 K (λ_{exc} = 281 nm). b) Binding isotherms for the titration measured at 595 nm, 616 nm, and 696 nm.*

Rather unexpectedly, however, quenching persisted for the full titration – having been envisaged to significantly reduce after *ca.* 3 eq. of **56** – this being in line potentially with the continuing formation of a tris[2]pseudorotaxane where the ferrocenyl moiety of bound **56** is optimally positioned for electron transfer. Percentage quenching values for the hypersensitive

$J = 2$ band were measured to be 32% and 63% for 3 eq. and 6 eq. of **56**, respectively, proving the degree of quenching to be essentially uniform throughout.

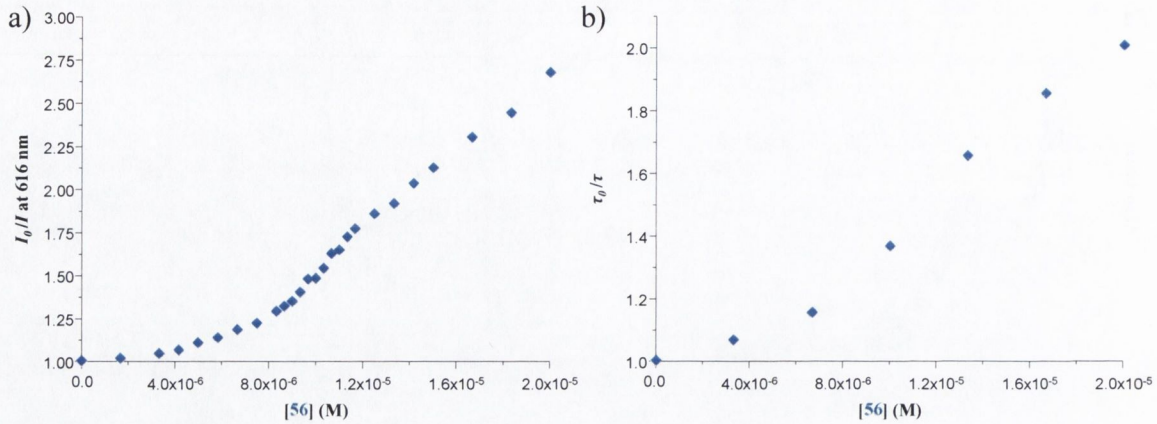

Figure 3.11: *Plots of a) I_0/I at 616 nm Vs. [**56**] (M) and b) τ_0/τ Vs. [**56**] for the titration of **Eu.51S$_3$** (3.33×10^{-6} M) with **56** (0.00 → 6.00 eq.) in $CHCl_3/CH_3CN$ (1:1; v/v) at 298 K (λ_{exc} = 281 nm).*

In an attempt to resolve the nature of the observed quenching, a Stern-Volmer plot of I_0/I for the $J = 2$ emission band (616 nm) against the molar concentration of **56** was plotted (Figure 3.11a). As discussed in Section 3.0, quenching was predicted to occur in this case by a photo-induced electron transfer from the ferrocenyl group of **56** to ligand **51S/R**. PET is a known form of dynamic quenching;[270] dynamic quenching defined as any process where an interaction of the quencher and luminophore leads to deactivation of the excited state.[271,272] For a purely dynamic process, a Stern-Volmer plot in the shape of a straight line would be expected.[271,272] However, the absence of a linear trend in Figure 3.11a confirmed neither a purely dynamic nor static process, with static quenching defined as an association between quencher and luminophore that gives way to the formation of a ground state complex.[271,272] The graph, however, displayed an upward curvature concave towards the *y*-axis, a common feature indicative of a combination of the two quenching models.[271] As a result, one could hypothesise a dynamic and static component to the quenching of **Eu.51S$_3$** by **56**; dynamic quenching in the form of electron transfer, and static quenching due to an association of the two species in solution. Verification of a dynamic contribution was gained by measuring the luminescent lifetime of **Eu.51S$_3$** throughout the titration (mono-exponential fitting). With a starting value of τ = 1.56 ms, the lifetime was found to incrementally reduce, reaching τ = 0.78 ms by completion, indicating deactivation of the Eu(III) excited state by **56** through dynamic quenching.[271,272] The lifetime results can be observed in the plot of τ_0/τ against [**56**] (M), where the increase in the value of τ_0/τ reflects the reduction in lifetime (Figure 3.11b).

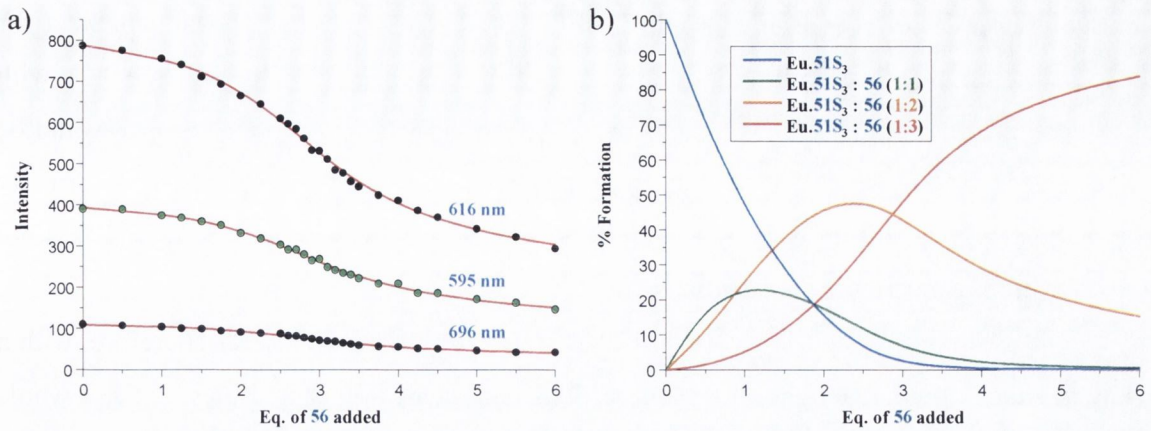

Figure 3.12: *a) Experimental binding isotherms for the phosphorescence titration of* ***Eu.51S$_3$*** *(3.33×10^{-6} M) with* **56** *in $CHCl_3/CH_3CN$ (1:1; v/v) at 298 K (λ_{exc} = 281 nm) and their corresponding fit by means of SPECFIT. b) Speciation-distribution diagram obtained from the fit.*

Attempts were made to fit the phosphorescence titration data to examine whether the quenching pattern relayed valuable information regarding the interaction between **56** and **Eu.51S/R$_3$**. The fits and corresponding speciation graphs for the titrations of **Eu.51S$_3$** and **Eu.51R$_3$**, obtained using SPECFIT®, are shown in Figure 3.12 and A3.21, respectively. Based on the evolving factor analysis which told of four emitting species, the fits for both complex enantiomers identified the self-assembly of three higher-order structures with C:T (where C:T is the complex to thread ratio) stoichiometric ratios of 1:1, 1:2, and 1:3, thus, implying a stepwise threading of **56**. As seen from Figure 3.12b, the 1:1 and 1:2 (C:T) assemblies were favoured at reduced concentrations of **56**. However, formation of the 1:3 (C:T) complex formed preferentially after *ca.* 3 eq. of **56**, with this ratio implicating the desired tris[2]pseudorotaxane **Eu.[51S/R$_3$ · 56$_3$]**.

Table 3.5: *Summary of the binding constants obtained through data fitting for the phosphorescence titrations of* ***Eu.51S$_3$*** *and* ***Eu.51R$_3$*** *(3.33×10^{-6} M) with* **56** *in $CHCl_3/CH_3CN$ (1:1; v/v), with percentage composition of the 1:3 (C:T) species at 6 eq. of* **56**. **Value fixed.*

Complex	log $\beta_{1:3}$	log $\beta_{1:2}$	log $\beta_{1:1}$	% of 1:3 (C:T) species at 6 eq. of Thread 56
Eu.51S$_3$	18.38 ± 0.10	12.63 ± 0.17	6.14 ± 0.00*	84
Eu.51R$_3$	18.51 ± 0.07	12.92 ± 0.11	6.17 ± 0.00*	79

It should be stressed that the fitting results be viewed with care, as underlined by the unusually large binding constants (Table 3.5). Liu et *al.* reported a log $K_{1:1}$ value of *ca.* 1 for the penetration of thread **55** through the crown-substituted ligand **54** (see Scheme 3.2), with this value determined by ^{1}H NMR methods.[258] Accordingly, comparable constants would be expected for the binding of **56** and **51S/R**. In this particular case, the cause of the abnormally large constants was most probably rooted in the fitting program used, as SPECFIT® is not ideal for probing such weak interactions.

To a certain extent, the results of these titrations were inconclusive. Therefore, with a view to shedding greater light on the interactions and quenching capabilities of **56**, a whole series of control titrations were conducted, with these discussed in the next two sections.

3.9.3 Control spectrophotometric titrations of Eu.41S$_3$ and Eu.43S$_3$ with thread 56 in CHCl$_3$/CH$_3$CN

The first set of control titration experiments were devoted to investigating the effects, if any, of thread **56** on complex sliotar analogues lacking the pyridyl crown ether function. For the purposes of this analysis, the complexes **Eu.41S$_3$** and **Eu.43S$_3$** (see Chapter 2) were selected for study in place of **Eu.51S/R$_3$** in equivalent titrations. Selection of **Eu.43S$_3$** was inspired by the ligand polyethoxy chains, in recognition of the presence of this motif in the dibenzo[24]crown-8 ring structure. These terminal chains were predicted to interact with **56** through the formation of hydrogen bonds, albeit to a lesser extent than with **Eu.51S/R$_3$**. In contrast, the choice of the propyl-substituted derivative **Eu.41S$_3$** was motivated by the need for a control that was not expected to associate with the thread in any manner.

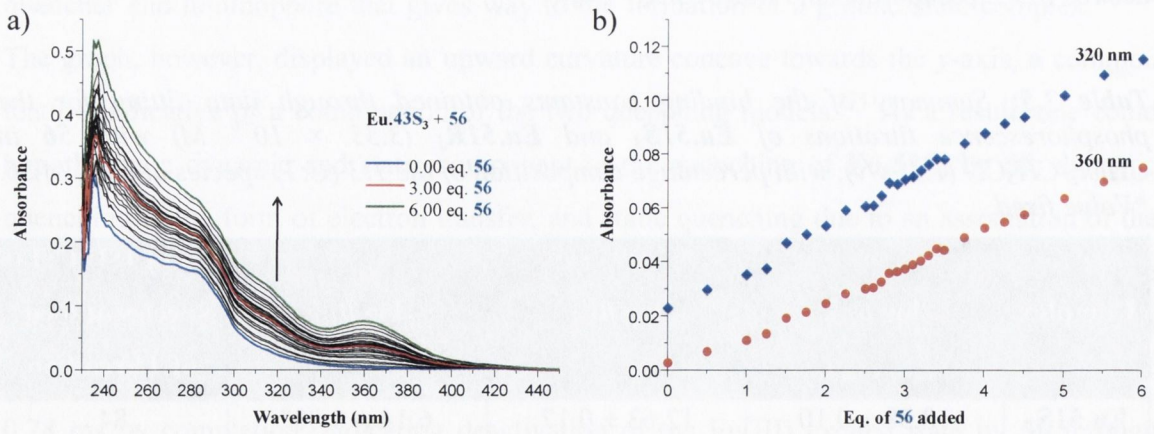

Figure 3.13: *a) Changes in the absorption spectra of* ***Eu.43S$_3$*** *(3.33 × 10^{-6} M) upon titrating with* **56** *(0.00 → 6.00 eq.) in CHCl$_3$/CH$_3$CN (1:1; v/v) at 298 K. b) Binding isotherms for the titration measured at 320 nm and 360 nm.*

Starting with the polyethoxy chain analogue **Eu.43S$_3$**, complex absorbance was found to hyperchromically increase with additions of the thread, accompanied by the emergence of a new band at 360 nm assignable to **56** *i.e* as was seen for **Eu.51S/R$_3$**. On this occasion, the binding isotherms followed a comparatively more linear trend (Figure 3.13).

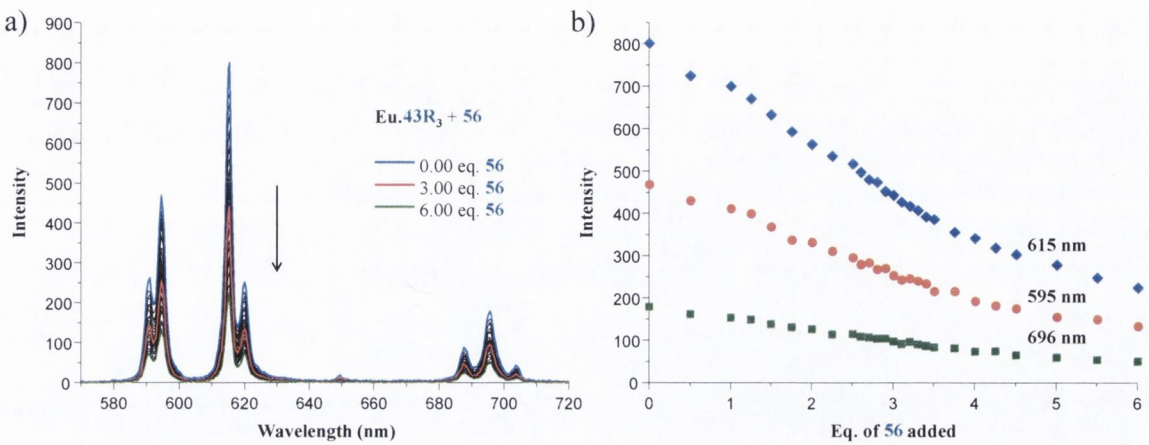

Figure 3.14: *a) Evolution of the phosphorescence emission in the titration of* ***Eu.43S$_3$*** *(3.33 × 10^{-6} M) upon titrating with* **56** *(0.00 → 6.00 eq.) in CHCl$_3$/CH$_3$CN (1:1; v/v) at 298 K (λ_{exc} = 281 nm). b) Binding isotherms for the titration measured at 595 nm, 615 nm, and 696 nm.*

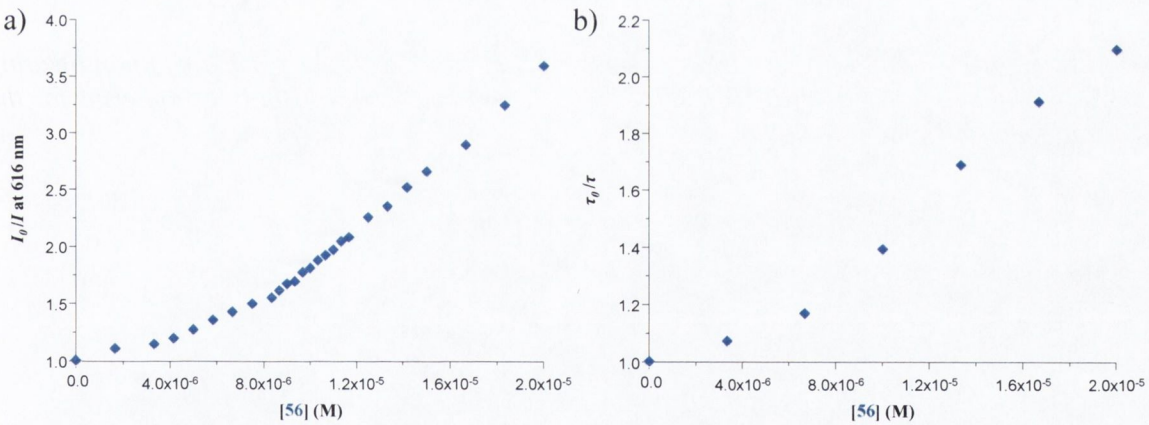

Figure 3.15: *Plots of a) I_0/I at 616 nm Vs. [56] (M) and b) τ_0/τ Vs. [56] for the titration of* ***Eu.43S$_3$*** *(3.33 × 10^{-6} M) with* **56** *(0.00 → 6.00 eq.) in CHCl$_3$/CH$_3$CN (1:1; v/v) at 298 K (λ_{exc} = 281 nm).*

Quenching of the metal ion-centred emission was seen again in the phosphorescence titration (Figure 3.14a). Incidentally, the percentage quenching values (45% and 72% for 3 eq. and 6 eq. of **56**, respectively) were determined to be appreciably larger than those found for **Eu.51S/R$_3$**, thus, pointing to a more facile Eu(III) excited state deactivation. Similar to **Eu.51S/R$_3$**, the Stern-Volmer plot of I_0/I at 616 nm against the molar concentration of **56**

exhibited an upward curvature towards the *y*-axis, this indicial of both dynamic and static quenching processes operating in concert (Figure 3.15a).[271] Moreover, the identification of the static component hinted at the aforementioned association of **56** and **Eu.43$_3$**, presumably through hydrogen bonding interactions at the polyethoxy chains. As seen before, the lifetime measurements established a dynamic quenching contribution, with this manifesting as a reduction in lifetime throughout the titration (see Figure 3.15b). Interestingly, the lifetime reduction was actually greater than that determined for **Eu.51S/R$_3$**, with τ = 1.66 ms and 0.70 ms at 0 eq. and 6 eq. of **56**, respectively, therefore, underscoring an improved efficiency of dynamic quenching over the crown analogue.

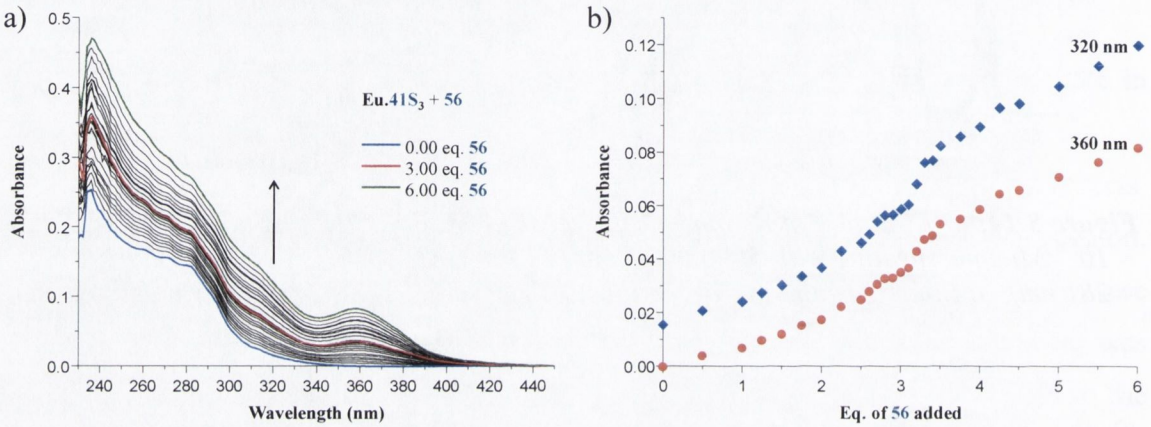

Figure 3.16: *a) Changes in the absorption spectra of* ***Eu.41S$_3$*** *(3.33 × 10^{-6} M) upon titrating with* **56** *(0.00 → 6.00 eq.) in CHCl$_3$/CH$_3$CN (1:1; v/v) at 298 K. b) Binding isotherms for the titration measured at 320 nm and 360 nm.*

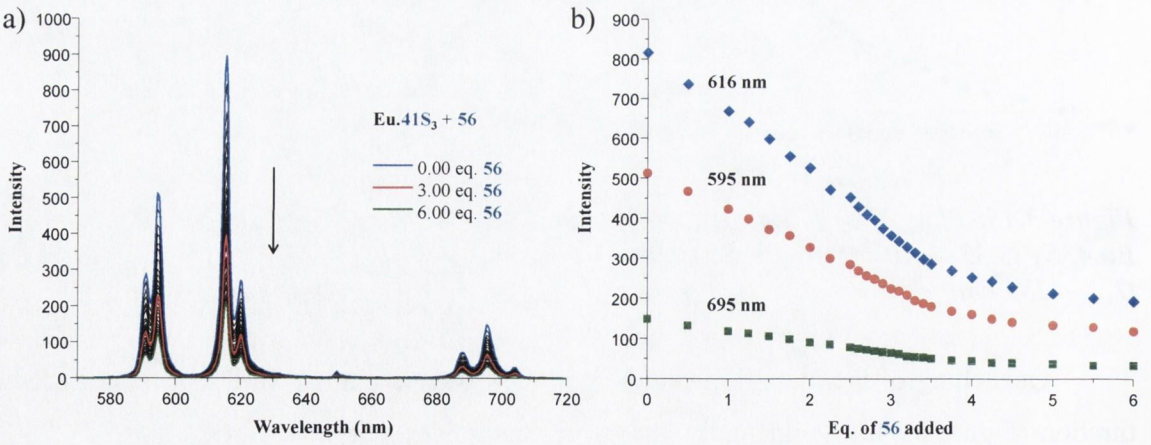

Figure 3.17: *a) Evolution of the phosphorescence emission in the titration of* ***Eu.41S$_3$*** *(3.33 × 10^{-6} M) upon titrating with* **56** *(0.00 → 6.00 eq.) in CHCl$_3$/CH$_3$CN (1:1; v/v) at 298 K (λ_{exc} = 281 nm). b) Binding isotherms for the titration measured at 595 nm, 615 nm, and 696 nm.*

With the propyl derivative **Eu.41S$_3$**, addition of **56** caused a hyperchromic increase across the spectrum, with the formation of a new absorption band at 360 nm (Figure 3.16). Such changes paralleled those identified from the titrations of **Eu.51S/R$_3$** and **Eu.43S$_3$**. Not only was quenching observed in the phosphorescence titration of **Eu.41S$_3$** (see Figure 3.17), but the quenching values were actually higher than those of both **Eu.51S/R$_3$** and **Eu.43S$_3$**. Calculated as 56% and 76% for 3 eq. and 6 eq. of **56**, respectively, these percentages were surprisingly large considering the foreseen lack of affinity between complex and guest.

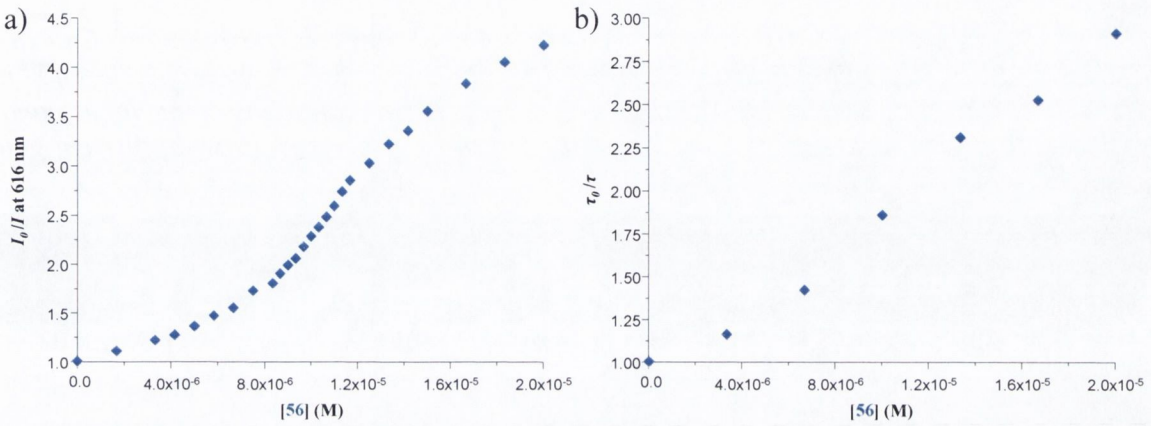

Figure 3.18: *Plots of a) I_0/I at 616 nm Vs. [56] (M) and b) τ_0/τ Vs. [56] for the titration of **Eu.41S$_3$** (3.33×10^{-6} M) with **56** (0.00 → 6.00 eq.) in $CHCl_3/CH_3CN$ (1:1; v/v) at 298 K (λ_{exc} = 281 nm).*

In the absence of static processes (as predicted for **Eu.41S$_3$**) one would anticipate a purely linear Stern-Volmer plot of I_0/I (616 nm) versus [**56**] (M). However, the plot for this phosphorescence titration displayed a clear deviation from linearity, the upward curvature potentially inferring participation of static quenching.[271] This result may be treated at this stage as being anomalous (to be revisited in Section 3.9.4). As would be expected given the relative efficiency of quenching in this system, the lifetime reduction discerned for **Eu.41S$_3$** was the largest of all systems; τ = 1.75 ms and 0.60 ms at 0 eq. and 6 eq. of **56**, respectively. Consequently, one can conclude that dynamic quenching is most effective in the case of the propyl complex.

All quenching and lifetime data for the titrations of **Eu.41S$_3$**, **Eu.43S$_3$**, **Eu.51S$_3$**, and **Eu.51R$_3$** with thread **56** are summarised in Table 3.6 and Table 3.7, respectively. In regards to percentage quenching of the J = 2 emission band, the values followed a general trend of **Eu.41S$_3$** > **Eu.43S$_3$** > **Eu.51S/R$_3$**. This trend of quenching efficiency was further reinforced by the luminescence lifetime measurements, where the overall percentage reduction in τ was again **Eu.41S$_3$** > **Eu.43S$_3$** > **Eu.51S/R$_3$**.

Table 3.6: *Summary of the percentage quenching values for the J = 2 emission band in the phosphorescence titrations of* ***Eu.41S$_3$****,* ***Eu.43S$_3$****,* ***Eu.51S$_3$****, and* ***Eu.51R$_3$*** *(3.33 × 10^{-6} M) with* **56** *(0.00 → 6.00 eq.) in $CHCl_3/CH_3CN$ (1:1; v/v) at 298 K (λ_{exc} = 281 nm).*

Eq. of 56	Eu.41S$_3$	Eu.43S$_3$	Eu.51S$_3$	Eu.51R$_3$
	% quenching (J = 2 band)			
3	56	45	32	34
6	76	72	63	64

Table 3.7: *Summary of lifetime measurements taken during the titrations of* ***Eu.41S$_3$****,* ***Eu.43S$_3$****,* ***Eu.51S$_3$****, and* ***Eu.51R$_3$*** *(3.33 × 10^{-6} M) with* **56** *(0.00 → 6.00 eq.) in $CHCl_3/CH_3CN$ (1:1; v/v) at 298 K (λ_{exc} = 281 nm). All obtained by fitting to a mono-exponential decay, with each lifetime an average of three measurements with different gate times.*

Eq. of 56	Eu.41S$_3$	Eu.43S$_3$	Eu.51S$_3$	Eu.51R$_3$
	τ (ms)			
0	1.75 ± 0.01	1.66 ± 0.03	1.56 ± 0.01	1.57 ± 0.03
1	1.51 ± 0.01	1.47 ± 0.01	1.47 ± 0.01	1.47 ± 0.02
2	1.24 ± 0.03	1.27 ± 0.02	1.35 ± 0.01	1.35 ± 0.03
3	0.94 ± 0.01	1.06 ± 0.02	1.14 ± 0.03	1.13 ± 0.01
4	0.76 ± 0.03	0.88 ± 0.02	0.94 ± 0.04	0.93 ± 0.01
5	0.70 ± 0.04	0.78 ± 0.01	0.84 ± 0.02	0.82 ± 0.02
6	0.60 ± 0.03	0.70 ± 0.04	0.78 ± 0.02	0.75 ± 0.01
Overall % reduction	66	58	50	52

Predicated on the observed trends, a number of conclusions could be drawn as to the interactions of **56**, and its emission quenching mechanism. Assuming the propyl derivative was not capable of associating with the thread, it was inherently logical to believe that the quenching seen in the example of **Eu.41S$_3$** was simply a product of collisional encounters facilitating electron transfer *i.e.* **56** did not require binding to fulfil its PET function. In fact, with varying degrees of association envisaged for both polyethoxy and crown analogues, the relatively higher quenching levels ascertained for **Eu.41S$_3$** were interpreted to suggest that quenching became more facile when **56** was allowed to collide, and not restricted from the complex core by intermolecular interactions with a terminal substituent. Such restrictions would be expected to be greatest in the case of **Eu.51S/R$_3$**, a situation in which threading of

56 through the crown moieties was imagined. Indeed, this was ultimately verified by the percentage quenching values, which were the lowest of the complex range. Fundamentally, this hypothesis satisfies the unique distance dependence known to limit PET processes,[271] with collisions enabling a bridging of the distance between donor and acceptor.

3.9.4 Control spectrophotometric titrations of Eu.41S$_3$, Eu.43S$_3$, and Eu.51S$_3$ with thread 53 in $CHCl_3/CH_3CN$

The control titrations discussed in the previous section were beneficial in answering some of the questions posed by the initial experiments with **Eu.51S/R$_3$** and **56**, particularly those in relation to the effects of dynamic quenching. The principle shortcoming, however, was the lack of information pertaining to static quenching. In an effort to address this, a new control set-up was devised, where the complexes **Eu.41S$_3$**, **Eu.43S$_3$**, and **Eu.51S$_3$** were each titrated against the dibenzylammonium hexafluorophosphate thread **53**. With known threading ability for dibenzo-[24]crown-8,[251,252] this simple salt was elected for use to explore the responsiveness of these complexes to a thread lacking the electron donor ferrocenyl moiety, thus, removing dynamic quenching forces.

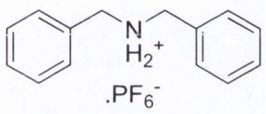

53

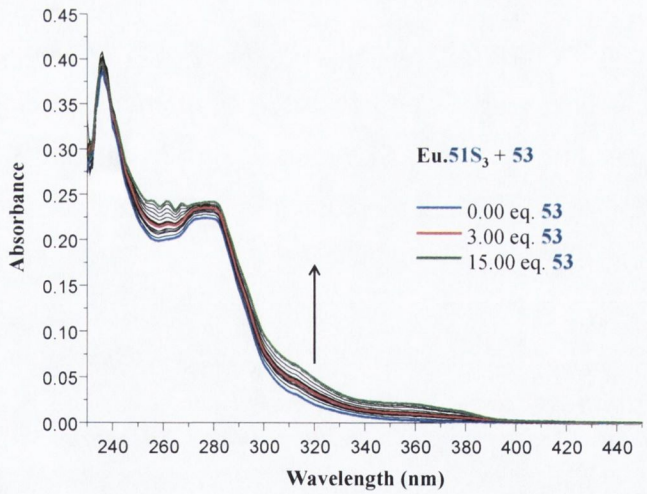

Figure 3.19: *Changes in the absorption spectra of* ***Eu.51S$_3$*** *(3.33 × 10^{-6} M) upon titrating with* **53** *(0.00 → 15.00 eq.) in $CHCl_3/CH_3CN$ (1:1; v/v) at 298 K.*

Comparison of the spectral changes in the UV-vis titrations of the three complexes proved especially informative. For the titration of the crown analogue **Eu.51S$_3$**, successive hyperchromic increases were witnessed in the range of *ca.* 230 – 275 nm, characterised by the emergence of three small peaks at 256 nm, 261 nm, and 267 nm (see Figure 3.19). This

increase was accredited to the absorbance of the thread, as seen in its absorption spectrum (Figure A3.25). More significantly, the changes in the longer wavelength region, notably the development of a band centred at 360 nm, occurred in a part of the spectrum in which **53** did not absorb. Tellingly, the evolution of this band was less pronounced in the UV-vis titrations of **Eu.43S$_3$** and **Eu.41S$_3$** (Figure A3.27 and Figure A3.31, respectively), possibly hinting at its origins in the threading of **53** through the ligand crown functionality.

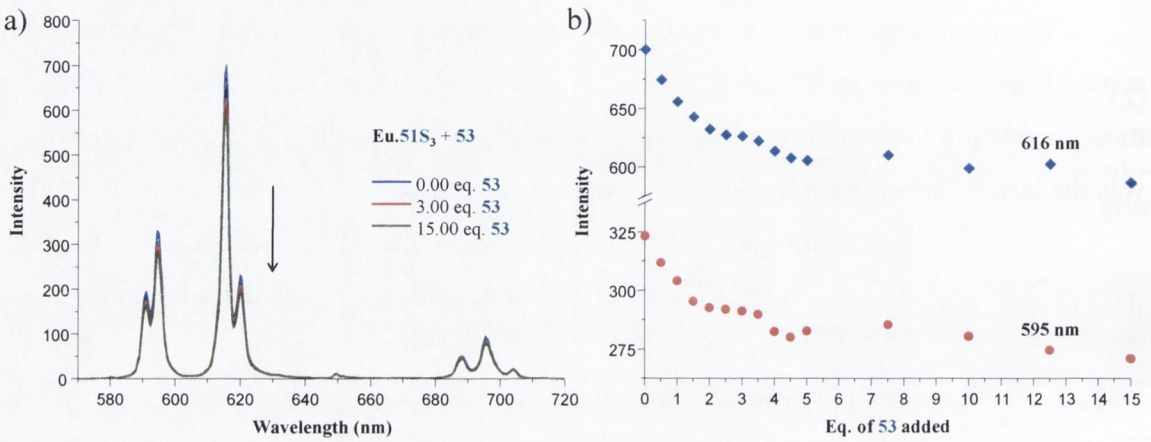

Figure 3.20: *a) Evolution of the phosphorescence emission in the titration of* ***Eu.51S$_3$*** *(3.33 × 10^{-6} M) upon titrating with* **53** *(0.00 → 15.00 eq.) in $CHCl_3/CH_3CN$ (1:1; v/v) at 298 K (λ_{exc} = 281 nm). b) Binding isotherms for the titration measured at 595 nm and 616 nm.*

The influence of the ferrocenyl-lacking thread **53** over the luminescence properties of the three complexes was evaluated in phosphorescence titrations, placing particular emphasis on the viability of quenching. For both **Eu.51S$_3$** and **Eu.43S$_3$** (Figure 3.20 and Figure A3.28, respectively) quenching was indeed observed, with the percentage quenching values of the *J* = 2 band listed in Table 3.8.

Table 3.8: *Summary of the percentage quenching values for the J = 2 emission band in the phosphorescence titrations of* ***Eu.41S$_3$****,* ***Eu.43S$_3$****, and* ***Eu.51S$_3$*** *(3.33 × 10^{-6} M) with* **53** *(0.00 → 15.00 eq.) in $CHCl_3/CH_3CN$ (1:1; v/v) at 298 K (λ_{exc} = 281 nm).*

Eq. of 53	Eu.41S$_3$	Eu.43S$_3$	Eu.51S$_3$
	% quenching (*J* = 2 band)		
3	–	3	11
15	–	10	16

As was anticipated with removal of the ferrocenyl group and its dynamic quenching faculty, these values were smaller than those measured in the related titrations with **56** (see Table 3.6). Intriguingly, no quenching was detected in the titration of **Eu.41S$_3$**, where the

addition of **53** was found to give rise to an initial minor luminescent enhancement (Figure A3.32). Under static considerations, the substantially larger quenching values measured for **Eu.51S$_3$** relative to **Eu.43S$_3$** were indicative of a stronger association between complex and thread, in agreement with pseudorotaxane formation. The concept of three molecules of **53** interpenetrating the individual crowns of complex **Eu.51S$_3$** was further advanced by the fact that 69% of the overall quenching seen occurred within the first 3 eq. of thread. Although comparatively smaller, the quenching of complex **Eu.43S$_3$** was interpreted as a sign of the capability of this complex to interact with such thread-like ammonium species. This was informed by the non-existence of quenching for **Eu.41S$_3$**, a result that dispelled any idea of static association between this complex and these threads, thus, accentuating the anomalous nature of the Stern-Volmer plot for the titration of **Eu.41S$_3$** and ferrocenyl **56** (Figure 3.18a).

Table 3.9: *Summary of lifetime measurements taken during the titrations of* ***Eu.41S$_3$****,* ***Eu.43S$_3$****, and* ***Eu.51S$_3$*** *(3.33 × 10^{-6} M) with* **53** *(0.00 → 15.00 eq.) in $CHCl_3/CH_3CN$ (1:1; v/v) at 298 K (λ_{exc} = 281 nm). All obtained by fitting to a mono-exponential decay, with each lifetime an average of three measurements with different gate times.*

Eq. of 53	Eu.41S$_3$	Eu.43S$_3$	Eu.51S$_3$
		τ (ms)	
0	1.69 ± 0.02	1.69 ± 0.01	1.51 ± 0.01
2	1.67 ± 0.02	1.68 ± 0.02	1.42 ± 0.03
3	1.65 ± 0.01	1.67 ± 0.04	1.42 ± 0.01
5	1.64 ± 0.02	1.66 ± 0.01	1.41 ± 0.01
10	1.64 ± 0.01	1.66 ± 0.03	1.42 ± 0.01
15	1.64 ± 0.01	1.67 ± 0.01	1.43 ± 0.02

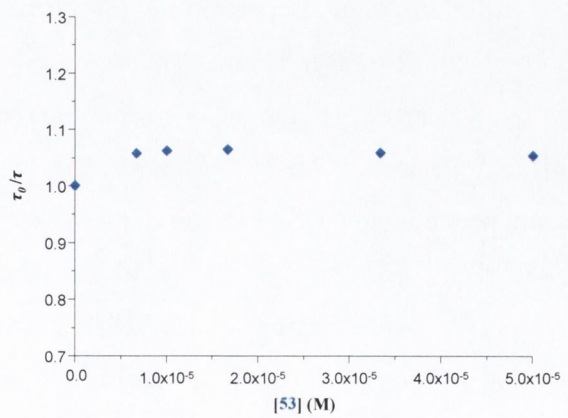

Figure 3.21: *Plots of τ_0/τ Vs. [53] for the titration of* ***Eu.51S$_3$*** *(3.33 × 10^{-6} M) with* **53** *(0.00 → 15.00 eq.) in $CHCl_3/CH_3CN$ (1:1; v/v) at 298 K (λ_{exc} = 281 nm).*

Confirmation of a purely static quenching model for thread **53** was obtained through luminescent lifetime measurements, with all three complexes displaying largely unchanged τ values upon additions of **53** (Table 3.9). Taking Figure 3.21 as a representative example, the resistance of the lifetimes to change was demonstrated in Stern-Volmer plots of τ_0/τ against [**53**] (M), where this resistance was exemplified by points following a straight line with slope ≈ 0. The constant nature of the lifetimes with increasing amounts of **53** confirmed also that de-assembly was not induced by the thread. Transferring this rationale to the titrations of **56**, it was highly improbable, on the experimental timescale, that the quenching arose due to de-assembly.

To summarise, the quenching established in this set of control titrations was seen to adhere to the trend of **Eu.51S$_3$** > **Eu.43S$_3$** > **Eu.41S$_3$**, with this being the exact reverse trend of that determined from the previous studies (see Section 3.9.3). Applying this knowledge to the original titrations of **56**, one can conclude that the dynamic quenching contribution of this ferrocenyl compound far outweighed the effects of static quenching. Moreover, by negating dynamic pathways through use of **53**, the ability of this novel crown ether-sliotar complex to associate with ammonium threads was verified through evidence of static quenching, thus, strengthening the argument for **56**. With respect to the UV-vis titrations with **53**, one of the more unusual features (as discussed earlier) was the formation of the band at 360 nm, a band with conceivable roots in the threading process. To trace this potentially characteristic band upon treatment with ferrocenyl **56**, additional UV-vis experiments were conducted.

3.9.5 UV-vis spectroscopic investigation into the interaction of threads 53 and 56 with the dibenzo[24]crown-8 compound 63

Employing UV-vis spectroscopy, the experiments detailed within this section were constructed to examine the potential for interaction between the thread compound **56** and a dibenzo[24]crown-8 ring, on the basis of comparison to control measurements with **53**. For these studies, the crown intermediate **63** (see Section 3.2) was used in place of ligand **51S/R** to both simplify analysis and to ensure greater focus on the macrocycle. This investigation mainly focused on identifying absorption spectral changes, with particular attention paid to the region of the spectrum where a band centred at 360 nm was seen to evolve in the UV-vis titrations of **Eu.51S/R$_3$** with **53**. Unfortunately, little could be deduced from the emergence of a comparable band at 360 nm in the titration of **Eu.51S/R$_3$** with **56** (see Section 3.9.2), owing to the absorbance of the ferrocenyl thread in this region (Figure A3.16). Therefore, the described measurements were devised with the aim of addressing this, and were performed according to the following procedure:

(i) A stock solution (3mL; 2.2×10^{-5} M) of **63** was prepared and the absorption spectrum recorded.

(ii) Defined aliquots corresponding to a molar ratio of 1 eq., 2 eq., and 3 eq. were added from a standard solution of thread **53** or **56** to the stock solution of **63** and the absorption spectrum recorded after each addition, allowing 10 min for equilibration.

(iii) Using another cell, absorption spectra were recorded for the thread in the absence of **63** at the same concentrations stated in (ii) *i.e.* 1 eq., 2 eq., and 3 eq.

(iv) Each of the spectra obtained in (iii) were added to the free spectrum of **63** to give additive calculated spectra (cal).

(v) The spectra obtained in (ii) for when **53**/**56** was actually added to **63** (exp) were subtracted from the related calculated spectra (cal) to give the difference (cal – exp).

(vi) The data was plotted.

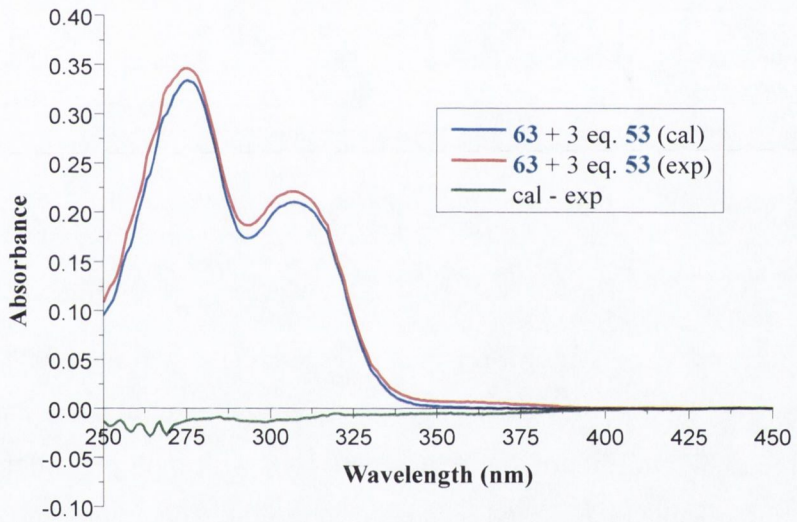

Figure 3.22: *Calculated and experimental UV-vis absorption spectra for the addition of 3 eq. of* **53** *to* **63** *(2.2 × 10^{-5} M) in $CHCl_3/CH_3CN$ (1:1; v/v) at 298 K, with the difference between the two spectra mapped by the green line.*

Figure 3.22 shows both the calculated (blue) and experimental (red) spectra for the addition of 3 eq. of dibenzylammonium **53** to compound **63**, with the difference between the two spectra illustrated by the green line (spectra for addition of 1 eq. and 2 eq. can be found in Figure A3.35 and Figure A3.36, respectively). A few noteworthy differences were clear upon comparison of the two spectra. First, absorbance across the entire range was increased for the experimental spectrum relative to the additive spectrum. Of greater significance, however, was the extension of the absorbance window in the experimental spectrum, with the band centred at *ca.* 360 nm matching that seen in the UV-vis titration. With no detectable

trace of this band in the additive spectrum, one may attribute its existence, and the other changes, to the threading of **53** through **63**, taking into consideration that the former species is a known thread for pseudorotaxane assembly with dibenzo[24]crown-8.[251,252] The results from these measurements could then be intuitively applied as a control by which to judge the changes in the analogous experiment with **56**.

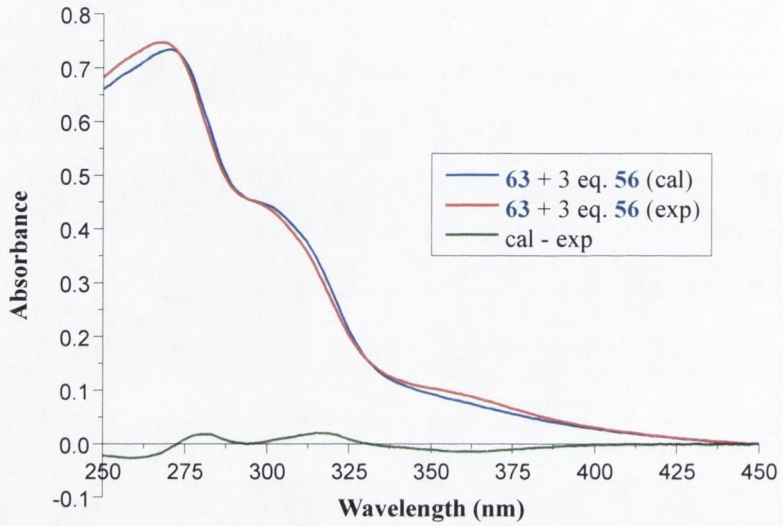

Figure 3.23: *Calculated and experimental UV-vis absorption spectra for the addition of 3 eq. of* **56** *to* **63** *(2.2 × 10^{-5} M) in $CHCl_3/CH_3CN$ (1:1; v/v) at 298 K, with the difference between the two spectra mapped by the green line.*

Figure 3.23 shows the spectra for the corresponding experiment with the ferrocenyl thread **56** following addition of 3 eq. of **56** (spectra for addition of 1 eq. and 2 eq. can be found in Figure A3.37 and Figure A3.38, respectively), with multiple differences apparent again between the calculated and experimental spectra. The most interesting deviation from the calculated spectrum was at *ca.* 360 nm, where absorbance was noted to be increased in the experimental spectrum, therefore, implying an additional contributory effect. Reconciling the enriched absorbance of this experimental band with the appearance of the new band at 360 nm in Figure 3.22 (red spectrum), it was sensible to hypothesise that **56** was interacting with the crown in an equivalent manner to **53**, which may mean pseudorotaxane formation.

Ultimately, these experiments supported the behaviour and trends seen in both the initial titrations of the crown complexes and in subsequent control studies. In doing so, these measurements have helped strengthen the case for the possible self-assembly of **Eu.51S/R_3** with the thread **56** for the generation of tris[2]pseudorotaxanes of form **Eu.[51S/R_3 · 56_3]**.

3.10 Conclusion

This chapter was devoted to probing the flexibility of the chiral sliotar ligand design towards the construction of higher-order supramolecular Ln(III) self-assemblies. To achieve this objective, the enantiomeric ligand pair **51S** (*S*,*S*) and **51R** (*R*,*R*) were synthesised for the later development of chiral tris-chelate Eu(III) complexes **Eu.51S$_3$** and **Eu.51R$_3$**. As per all sliotar analogues, ligand structure was based on the chelidamic acid scaffold, functionalised at the pyridyl 2- and 6-positions with chiral naphthyl antenna for sensitisation of the Ln(III) excited state. These sliotar derivatives were distinguished, however, by the terminal dibenzo-[24]crown-8 functionality at the *para*-position, with this motif envisaged to facilitate the threading of dialkylammonium guest molecules for the formation of tris[2]pseudorotaxanes. To fulfil this function, the histaminyl(ferrocenylmethyl)ammonium thread **56** was designed with a view to assembling interpenetrated structures of the form **Eu.[51S/R$_3$ · 56$_3$]**. Through incorporation of the electron donor ferrocenyl moiety, PET quenching of the Eu(III)-centred emission was predicted following the self-assembly of **Eu.51S/R$_3$** and **56**, thus, presenting the opportunity to photophysically evaluate the potential creation of tris[2]pseudorotaxanes.

This chapter first concentrated on the synthesis and characterisation of ligands **51S/R** and their Eu(III) complexes, along with the thread compound **56**. Prior to investigating the potential association of the components, the complexes were analysed independently of **56**, adhering to the same general work plan outlined in Chapter 2. Evidence of complexation was gained through a variety of characterisation techniques. A broadening and shifting of the resonances in the ^{1}H NMR spectra verified successful Eu(III)-binding, with participation of the ligand carbonyl groups confirmed by IR. Elemental analysis confirmed the 1:3 (M:L) stoichiometry for the complexes, this proof that the bulky crown groups did not inhibit the assembly of complexes analogous to those in Chapter 2. In each case, characteristic Eu(III) emission spectra were measured upon indirect excitation of the naphthalene chromophores at 281 nm, therefore, establishing effective population of the Eu(III) excited state.

The ability to harness the chirality of the ligands for the formation of optically pure assemblies was demonstrated utilising CD and CPL spectroscopy. CD spectra recorded for both ligands and their complexes yielded opposite sign and equal magnitude signals, thus, underlining the opposing helicity in the final complex products. The diastereoselective self-assembly of enantiopure species was further affirmed by the complex CPL spectra, which were essentially mirror images. Based on the correlation of these CPL spectra to those in Chapter 2, the metal stereochemistry was assigned as Δ for **Eu.51S$_3$** and Λ for **Eu.51R$_3$**.

Luminescence lifetime measurements conducted in both water (H_2O and D_2O) and methanol (MeOH and MeOD) permitted calculation of the complex hydration states (*q*),

which were determined to be ≈ 0 in both cases. These *q* values told of coordinative metal saturation and, as such, were indicative of the 1:3 (M:L) complex composition. To analyse the self-assembly of **51S/R** and $Eu(CF_3SO_3)_3$ *in situ*, UV-vis absorption and luminescence titrations were conducted in $CHCl_3/CH_3CN$ (1:1; *v/v*). For both enantiomers, fitting of the spectral changes with SPECFIT® confirmed formation of the desired 1:3 (M:L) complex with high stability. On comparison, the binding constants were in fact smaller than those obtained for the sliotar analogues in Chapter 2, perhaps a reflection of the placement of increased steric demands on complexation, owing to the large terminal crown.

Having confirmed the formation of the tris-chelates **Eu.51S$_3$** and **Eu.51R$_3$**, efforts turned to analysing tris[2]pseudorotaxane assembly with thread **56** in spectrophotometric titrations in $CHCl_3/CH_3CN$ (1:1; *v/v*). As envisaged, quenching of the metal ion-centred emission was observed with additions of **56**. However, quenching unexpectedly continued until titration completion, having been predicted to slow after *ca.* 3 eq. of thread, agreeing with the formation of tris[2]pseudorotaxanes. In spite of this unforeseen behaviour, it was possible to fit the phosphorescence spectral changes using SPECFIT®, with the resulting fit indicating the stepwise self-assembly of the 1:1, 1:2, and desired 1:3 (C:T) stoichiometric species. Furthermore, Stern-Volmer treatment of the phosphorescence data suggested a quenching model comprising both dynamic and static processes.

On account of the inconclusive nature of these titrations, a series of control titrations were devised. The first set of control experiments included the titrations of **56** with sliotar analogues lacking the crown ether, namely propyl-substituted **Eu.41S$_3$** and polyethoxy-substituted **Eu.43S$_3$** (used in Chapter 2). Luminescence quenching was identified for both examples, with the degree of quenching and reduction in lifetime following the trend of **Eu.41S$_3$** > **Eu.43S$_3$** > **Eu.51S/R$_3$**. With no conceivable association of **56** with **Eu.41S$_3$**, one could assume that quenching *via* electron transfer was achievable simply through collisions, and did not necessitate association. Moreover, the superior level of quenching observed for **Eu.41S$_3$** suggested that PET was more facile on a collisional basis. This would explain the reduced quenching found for **Eu.51S/R$_3$**, for which the strongest interaction with the thread was imagined.

The next set of control experiments involved titrating each **Eu.41S$_3$**, **Eu.43S$_3$**, and **Eu.51S$_3$** against the dibenzylammonium thread **53**. This salt was selected for two main reasons: (i) its well-documented threading capacity for dibenzo[24]crown-8,[251,252] and (ii) the absence of an electron donor ferrocenyl group, which would eliminate dynamic quenching. Displaying significant contrast to the earlier controls, the extent of quenching incurred in these titrations could be summarised as **Eu.51S$_3$** > **Eu.43S$_3$** > **Eu.41S$_3$**, with proof of its

purely static nature attained through lifetime measurements where little or no change was found. In fact, on this occasion, propyl **Eu.41S$_3$** did not undergo quenching of any type, producing a trend that was the exact reverse of the titrations with **56**. Considering static quenching was greatest for **Eu.51S$_3$**, it was rational to conclude that this complex, of all three, associated most strongly with **53**. Additionally, given the aptitude of **53** for pseudorotaxane synthesis, one could reasonably assert that the strength of interaction originated in the threading of this molecule through the crown cavity.

Again employing **53** as a control, the ability of ferrocenyl **56** to thread a dibenzo-[24]crown-8 ring (**63**) was inspected in a series of specially contrived UV-vis studies, the basic premise of which involved identifying the differences in the additive calculated and experimental absorption spectra following additions of the relevant thread compound. Common to the experimental spectra of both **53** and **56** was an increase in absorbance, relative to the calculated spectra, at *ca.* 360 nm. Accounting for both the known threading function of **53** and the absence of absorbance at 360 nm in the individual spectra, this band was interpreted to be a product of the threading process. Accordingly, its presence in the studies with **56** was deemed to also derive from such an interaction.

Through application of an extensive array of varied spectroscopic experiments, the work reported within this chapter presents an argument for the spontaneous formation of tris[2]pseudorotaxanes from complexes **Eu.51S/R$_3$**. It is imperative to state, however, that the evidence is not wholly definitive, thus, the need for supplementary empirical evidence. Future efforts, therefore, must be committed to unambiguously confirming this design, with X-ray crystallography and/or mass spectrometry evidence required. ^{1}H NMR spectroscopy may also be used to probe the interactions between the thread and crown to verify interpenetration of the components, as demonstrated by Loeb *et al.*[264,273-275] With this technique, possible hydrogen bonding between the thread NH^+ protons and adjacent CH protons to the oxygen atoms of the macrocycle could be ascertained by shifts in their resonances. These measurements could, however, be complicated by the paramagnetic nature of the complexed Ln(III) ion, thus, potentially limiting experiments to the ligand alone. One factor that may be used to argue against pseudorotaxane formation could be the positive charge associated with both the complexes and thread. Due to ligands **51S/R** being charge neutral, the overall metal complexes are tri-positive and, as a result, repulsive forces may be in effect between these systems and the dicationic thread **56**, thus, forbidding the threading process. To negate these repulsive forces and facilitate interpenetration, an alternative complex design using crown-substituted ligands that are anionic at the coordinating terminus and, therefore, help reduce the complex positive charge, may be considered. Irrespective of the uncertainty in tris[2]-

pseudorotaxane formation, complexes **Eu.51S$_3$** and **Eu.51R$_3$** undeniably represent another successful modification of the sliotar design developed in the Gunnlaugsson group, and serve to highlight the opportunities available to these systems through judicious choice of pyridyl *para*-functionality.

Chapter 4

Synthesis and Photophysical Analysis of Glycosylated Sliotar Derivatives

4 Introduction

Collectively, the work detailed in the previous two chapters has comprehensively communicated the tremendous viability of the pyridyl 4-substitution strategy for the development of novel chiral sliotar complexes with rich and varied function. In a continuation of the theme of Chapter 3, specifically the introduction of advanced ligand *para*-functionality, the enantiomeric glycosylated ligand pair **69S** (*S,S*) and **69R** (*R,R*) was designed, in pursuit of more structurally elaborate Ln(III) complex systems relative to the comparably more simple analogues described in Chapter 2. The inspiration for this ligand design was partly derived from literature sources, which showed how the appendage of carbohydrate substituents to known Ln(III)-coordinating motifs, such as pyridine- and cyclen-based frameworks,[276,277] could be executed with considerable success.

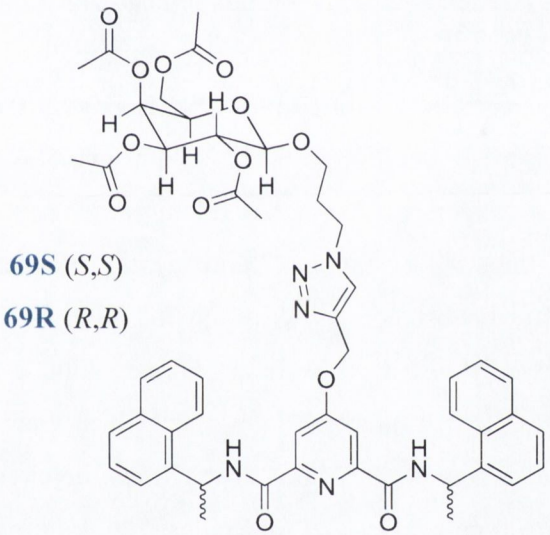

69S (*S,S*)
69R (*R,R*)

One of the principle motivating factors encouraging this particular design was a passionate desire to demonstrate the amenability of the sliotar ligand framework to further synthetic modification using *Click Chemistry* methods. Indeed, the chiral pair **69S** and **69R** was developed by adhering to such methods, employing the earlier propargyl-substituted ligands **42S** and **42R** (see Chapter 2) as precursor reagents. More precisely, the specific reaction availed of in these examples was the Cu(I)-catalysed azide-alkyne cycloaddition (CuAAC), a reaction fulfilling the necessary *Click Chemistry* criteria. Originally discovered by Sharpless *et al.*, the CuAAC reaction presents as a reliable path to bridging azide and alkyne substrates *via* the formation of 1,4-disubstituted-1,2,3-triazole linkages.[234] In recent times, this reaction has garnered immense acclaim owing to a multitude of advantageous features, namely its regioselectivity, associated high yields, and applicability to a wide

collection of substrates.[278,279] Furthermore, regarding the essential azide and alkyne reactive sites, both groups can be easily incorporated into organic compounds and are stable in the presence of common nucleophiles, electrophiles, and solvents; a rare quality in 1,3-dipolar reagents.[280] With a vast array of substrates available, the potential of this synthetic coupling approach is truly unlimited. For the purpose of this project, CuAAC delivery of an acetyl-protected monosaccharide to the sliotar binding motif was planned to help exemplify the opportunities achievable through this strategy. However, selection of a carbohydrate in this capacity was not made arbitrarily, but performed both in appreciation of the universal biological significance of this compound family, and with the desire of conferring novel function to these complex systems in the future.

In the context of biological systems, along with both nucleic acids and proteins, carbohydrates play a critical role in determining biological functions and wide-ranging physiological processes.[281] In fact, this class of biomolecules are known to be implicitly involved in processes as far ranging as cellular recognition, cell-cell communication, hormone activity, immune surveillance, inflammatory responses, and viral and bacterial infections.[282-285] Considering the integral importance of carbohydrates to biological systems, carbohydrate chemistry has experienced a massive surge in popularity recently, with particular focus directed towards elucidating fundamental biochemical processes and identifying new pharmaceutical substances.[281] With regards to application *in vivo*, however, carbohydrates alone are severely restricted by their pharmacokinetic profile, a profile that encompasses inferior permeability through the intestinal wall in view of high polarity, and rapid excretion from the body. Nevertheless, this problem can be circumvented through the design of carbohydrate-containing or -derived molecules,[286] an alternative strategy that has been effectively showcased in drug development, with notable examples being the influenza drugs Tamiflu and Relenza.[287,288]

Carbohydrate-derived systems may also enable the targeting of specific cell types through interactions with non-enzymatic cell surface proteins called lectins, with these proteins acknowledged to play an essential part in cellular functions such as trafficking, adhesion, and signalling.[289] In terms of carbohydrate recognition, some lectins display remarkable selectivity, while others are less specific and bind to more general classes of saccharide, for example, terminal mannose or galactose sugar units. Moreover, an extensive list of pathological conditions are in effect characterised by an acute over-expression of certain lectins on the cellular surface, one pertinent example being that of galectin and glucose transporters (GLUTs) in the case of tumour cells.[290,291] The rational design of sugar-derivatised molecules equipped to exploit the various lectin recognition patterns and

biological distributions, therefore, offers the chemist a privileged strategy for the targeted delivery of functional chemical systems to cell environments.

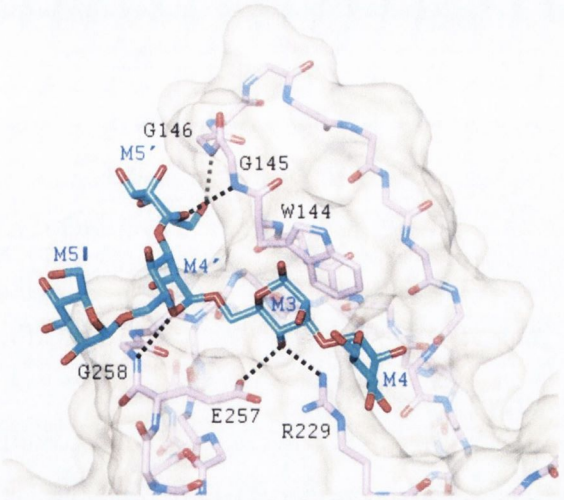

Figure 4.1: *X-ray crystal structure illustrating the binding of α3,α6-mannopentaose to the lectin myxobacterium hemagglutinin.*[292]

Serving as the main focus of this chapter, ligands **69S** and **69R** were developed to meet a number of research objectives. As previously stated, one such goal was to skilfully demonstrate the infinite potential of *Click Chemistry*, when applied to the production of sliotar ligand derivatives. More significantly, the work reported hereafter was primarily concerned with investigating the effects, positive or negative, of the terminal glyco-substituent on the self-assembly process with trivalent Eu(III). With the aim of forming monometallic tris-chelates **Eu.69S$_3$** and **Eu.69R$_3$**, this study was intended to provide an analytical platform for future biological analysis, and closely follows and supplements that reported in Chapters 2 and 3. Indeed, future efforts will be committed to exploring the bio-imaging capabilities of such complex glyco-sliotar systems, exploiting carbohydrate-lectin interactions for specific binding and localisation. This research project was conducted in collaboration with Dr. Eoin Scanlan from the School of Chemistry, Trinity College Dublin.

4.1 Design of the enantiomeric ligand pair 69S and 69R

As per the ligands described in Chapters 2 and 3, the enantiomeric pair **69S/R** were designed on the 4-hydroxypyridine-2,6-dicarboxylic acid framework and were predicted to self-assemble 1:3 (M:L) complexes.[112,116,117,128] Chiral 1-(1-naphtyl)-ethylamine groups were preferred for coupling to the 2- and 6-pyridyl carboxylic acid moieties to both sensitise the Ln(III) luminescence and confer chirality to the complexes. Attachment of the carbohydrate

functionality to the sliotar ligand scaffold was achieved through the formation of a triazole linkage, done by a CuAAC reaction between the propargyl-functionalised ligands **42S** and **42R** (see Chapter 2) and the appropriate azido-monosaccharide reagent. This approach was derived from Scanlan *et al.*, who have previously shown that triazole bridging with *Click Chemistry* is a versatile mode of linkage for tethering carbohydrates to different chemical frameworks.[291,293] The azo-reagent 2,3,4,6-tetra-*O*-acetyl-1-*O*-(3-azidopropyl)-β-D-galacto-pyranoside (synthesised by the Scanlan group) was favoured as the carbohydrate component. With a view to future bio-application, the inclusion of a propyl spacer chain to separate the sugar and triazole ring was envisaged to impart the terminal sugar group with enhanced flexibility to assist in potential lectin-binding. For this project, the decision was made to perform analysis of the ligands in their fully acetyl-protected form (**69S/R**), in expectation that the acetyl groups, compared to the free hydroxyl groups, would not interfere in Ln(III)-coordination. Eu(III) ion was selected for complexation for both better comparison with the analogues in Chapters 2 and 3 and its attractive bio-imaging visible-emitting properties.

First, an account of the synthesis and characterisation of the ligands will be provided in the next section.

4.2 Synthesis and characterisation of the enantiomeric ligand pair 69S and 69R

The synthesis of ligands **69S** and **69R** was achieved following the *Click* procedure shown in Scheme 4.1. As stated in Section 4.1, the CuAAC reaction for the formation of these glycosylated ligands used the propargyl-substituted ligands **42S** and **42R**, giving **69S** and **69R**, respectively (see Section 2.2 for a description of the synthesis of **42S/R**).

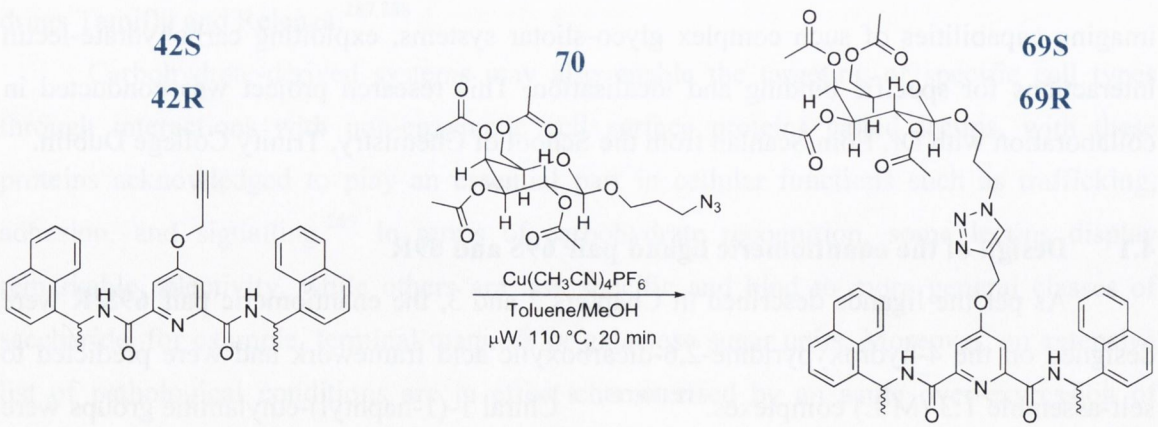

Scheme 4.1: *Synthetic pathway for **69S** and **69R**.*

This reaction entailed first heating the relevant enantiomer of dinaphthyl **42** with the azido-sugar compound 2,3,4,6-tetra-*O*-acetyl-1-*O*-(3-azidopropyl)-β-D-galactopyranoside **70** at 110 °C under microwave irradiation for 20 min in the presence of a Cu(I) catalyst using a toluene/MeOH solvent system (1:1; *v/v*). The Cu(I) catalyst selected was $Cu(CH_3CN)_4PF_6$, which is fully soluble in polar organic solvents. After heating, the solvent was evaporated under reduced pressure and the crude product purified using silica column chromatography (gradient elution 100:0 → 98:2; CH_2Cl_2/MeOH) to afford **69S** and **69R** as white solids in yields of 83% and 85%, respectively.

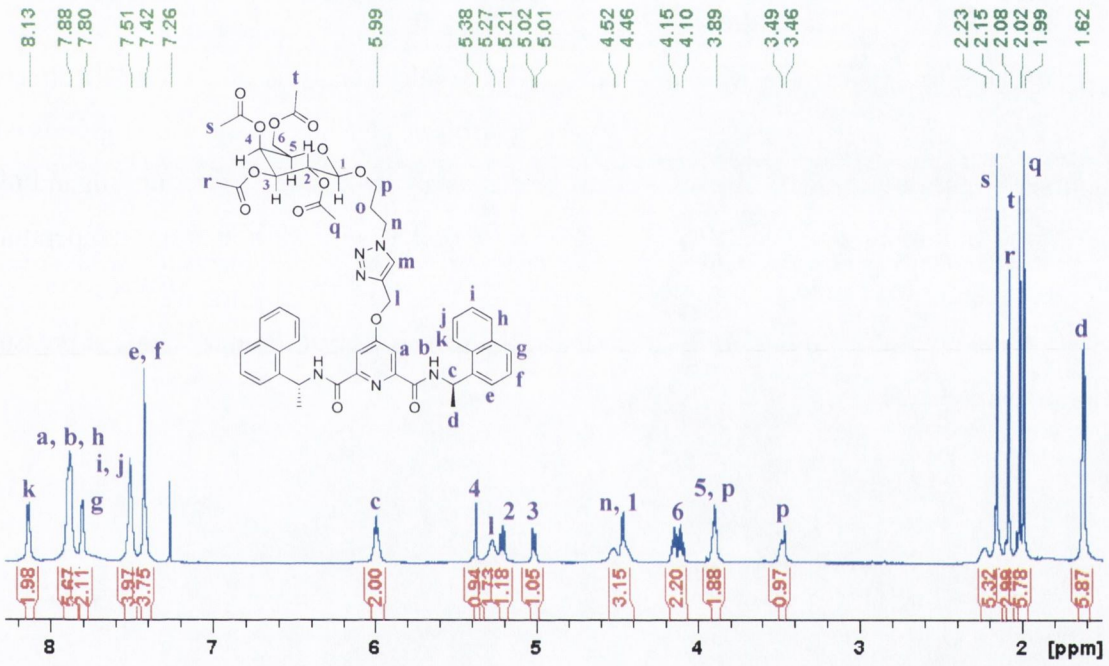

Figure 4.2: *^{1}H NMR (600 MHz, $CDCl_3$) spectrum of ligand **69R**.*

Assignment of the glyco-ligand ^{1}H NMR (600 MHz, $CDCl_3$) spectra was managed through a range of 2D NMR experiments. For both spectra (see Figure 4.2 and Figure A4.2 for **69R** and **69S**, respectively), the downfield region consisted of signals attributable to the pyridyl and naphthalene protons of the sliotar coordinating motif, therefore, confirming its incorporation in the final structure. Figure A4.1 (**69R**) focuses on the region containing the resonances representing the terminal galactopyranose functionality and the propyl chain to which it is appended. The four singlets at 2.15 ppm, 2.08 ppm, 2.02 ppm, 1.99 ppm can be assigned to the four acetyl protecting groups, with their presence in the spectra evidence of their retention in the molecule. Linkage of the sliotar and sugar units was verified by their relative proton integrations, which exhibited a 1:1 ratio. Both HRMS and elemental analysis further substantiated synthesis of ligands **69S** and **69R** (full details in Chapter 7).

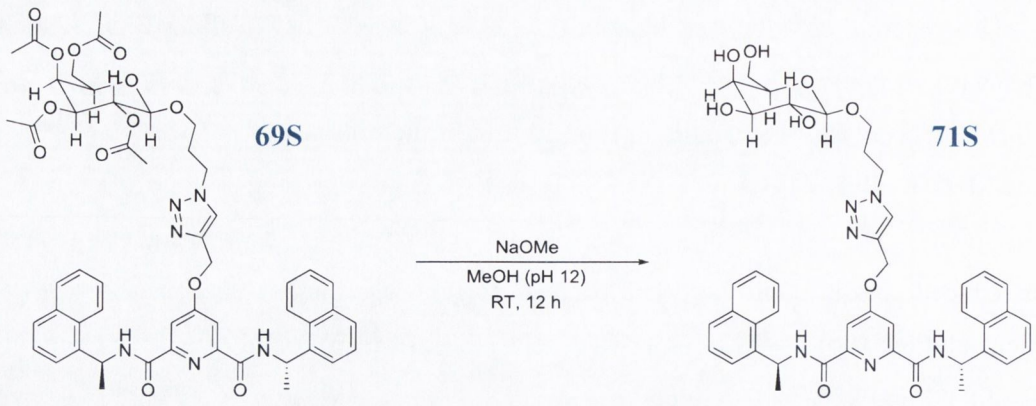

Scheme 4.2: *Synthetic pathway for* ***71S****.*

In an effort to achieve water solubility so as to allow analysis of the Ln(III)-directed self-assembly process in aqueous solution, basic hydrolytic cleavage of the acetyl groups was attempted according to the synthetic protocol in Scheme 4.2. For this procedure, ligand **69S** was stirred in a methanolic solution of NaOMe base (pH 12) for 12 h at room temperature. Following completion, the reaction solution was treated with DOWEX® 50WX8-200 ion-exchange resin until obtaining pH 7, filtered, and the solvent removed under reduced pressure to give a white solid.

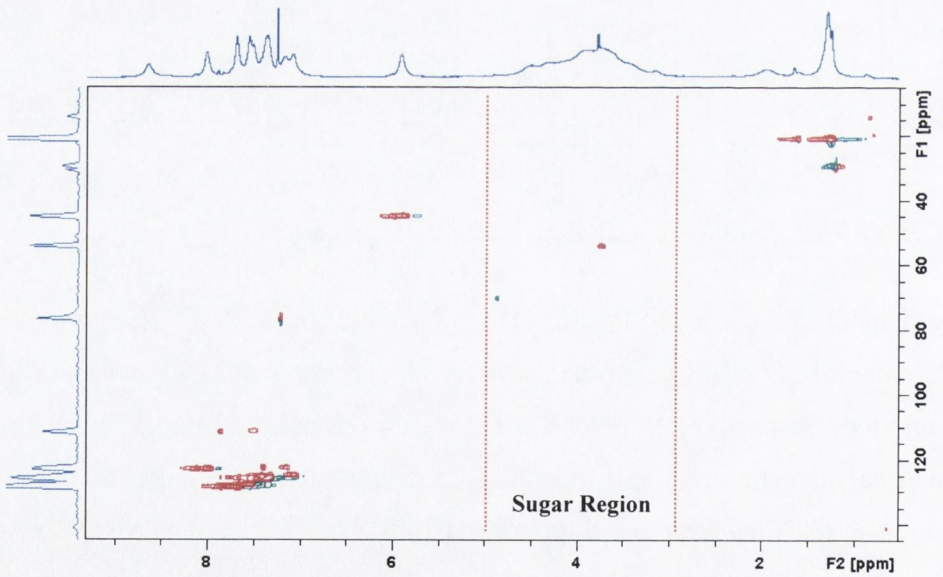

Figure 4.3: *^{1}H-^{13}C HSQC NMR (600 MHz, $CDCl_3$) spectrum of ligand "**71S**" highlighting the near absence of C-H coupling in the sugar region of the 2D spectrum.*

Proof of hydrolysis was provided by the ^{1}H NMR (600 MHz, $CDCl_3$) spectrum (see Figure A4.3), from which the acetyl signals were no longer present. However, the spectrum was noticeably broad and unresolved, particularly in the region from *ca.* 4.60 – 3.00 ppm

correlating to the carbohydrate protons. Intriguingly, the C-H coupling resonances of the sugar could not be ascertained in the HSQC (600 MHz, $CDCl_3$) spectrum (Figure 4.3), despite the C-H connectivity of the sliotar component being plain to see. This phenomenon, coupled with the broad nature of the signals in the ^{13}C NMR (150 MHz, $CDCl_3$) spectrum (Figure A4.4), was interpreted to be evidence of either (i) the formation of a high molecular weight species generated by oligomerisation occurring at the sugar after deprotection or (ii) the aggregation of deprotected monomers in solution through extensive hydrogen bonding interactions between the free monosaccharide hydroxy groups. Further evidence is, therefore, required to distinguish between the two stated possibilities. Evidence favouring option (ii) may be obtained by either performing the NMR measurements at reduced concentrations or in more competitive protic solvents (*e.g.* MeOD and D_2O) with the capability of disrupting hydrogen bonding in order to probe if spectral resolution is improved. Such measurements would be highly informative as to whether the synthesis was successful or not.

Irrespective of the uncertainty in the characterisation of **71**, the original plan was to analyse the self-assembly of protected glycosylated Eu(III) sliotar complexes first, before studying the deprotected analogues. As a result, discussion for the remainder of this chapter will deal exclusively with ligands **69S/R**.

4.3 Synthesis and characterisation of Eu(III) complexes of 69S and 69R

With the objective of synthesising 1:3 (M:L) complexes akin to the original sliotar complexes (CN = 9),[223] the glyco-ligands **69S** and **69R** were complexed with Eu(III) ion, as outlined in Scheme 4.3.

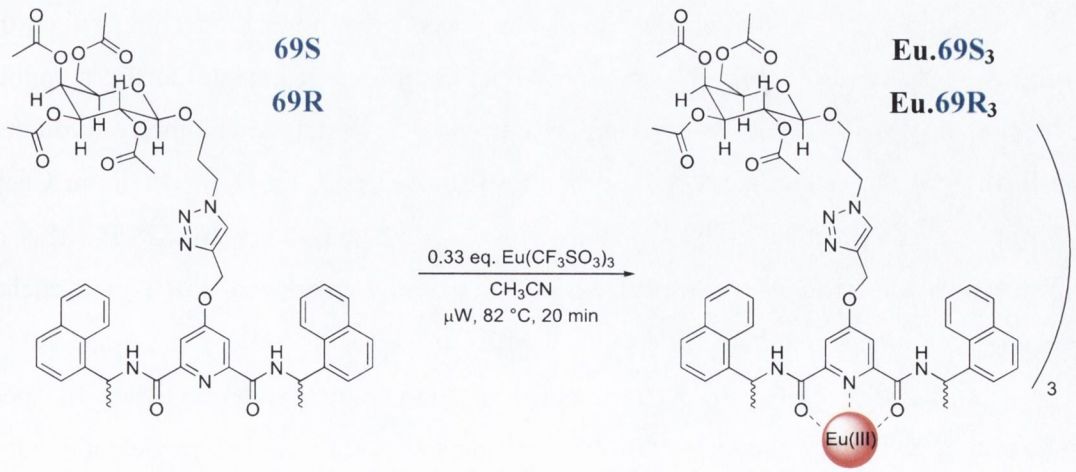

Scheme 4.3: *Synthetic pathway for* ***Eu.69S₃*** *and* ***Eu.69R₃*** *by complexation of* ***69S*** *and* ***69R*** *with* $Eu(CF_3SO_3)_3$.

In this procedure, the relevant enantiomer was refluxed with 0.33 eq. of $Eu(CF_3SO_3)_3$ for 20 min in HPLC grade CH_3CN under microwave radiation. Vapour diffusion of diethyl ether into the solutions resulted in precipitation of the complexes, which were isolated by filtration as white solids in yields of 72% and 86% for **Eu.69S$_3$** and **Eu.69R$_3$**, respectively. ^{1}H NMR and IR spectroscopy confirmed Eu(III) ion complexation, with elemental analysis establishing the 1:3 (M:L) complex composition.

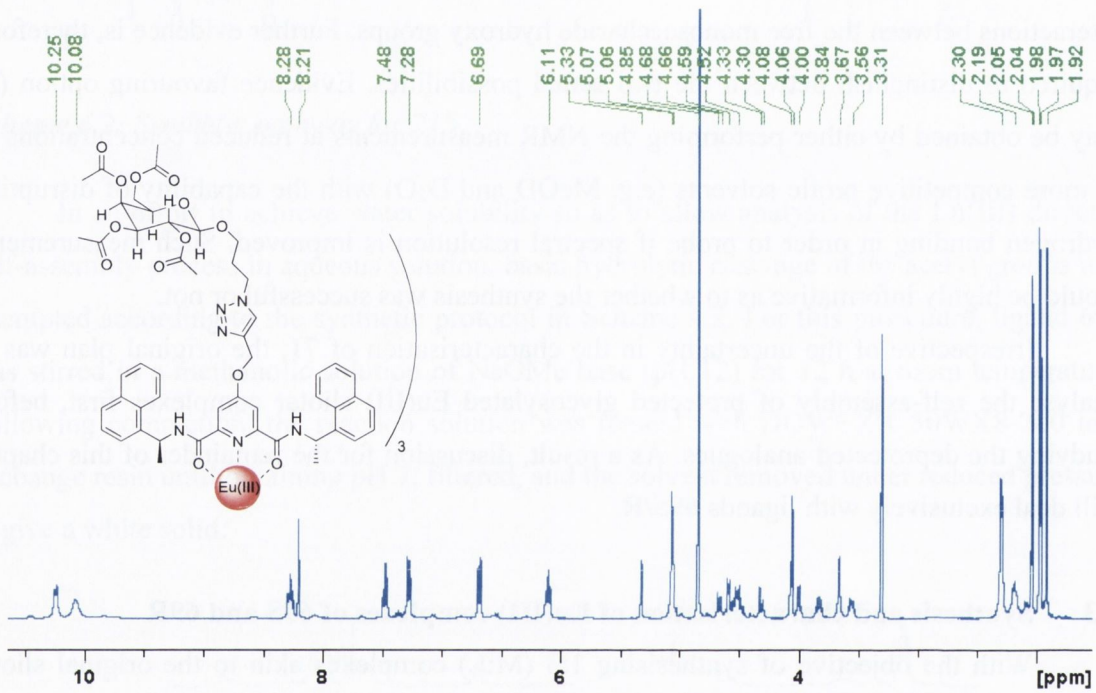

Figure 4.4: *^{1}H NMR (400 MHz, CD_3OD-d_4) spectrum of complex* ***Eu.69S$_3$****.*

Comparison of the ^{1}H NMR complex spectra (400 MHz, CD_3OD-d_4) of both **Eu.69S$_3$** and **Eu.69R$_3$** (Figure 4.4 and Figure A4.5, respectively) to that of their corresponding free ligands revealed a shift in the resonances, accompanied by a minor broadening effect, thus, corroborating successful complexation.[238] For both complexes, elemental analysis endorsed the formation of self-assemblies with the anticipated 1:3 (M:L) stoichiometry through the identification of molecular species with formula **[Eu.69S/R$_3$](CF$_3$SO$_3$)$_3$** (details in Chapter 7). Similar to the dibenzo[24]crown-8-substituted sliotar complexes **Eu.51S/R$_3$**, this data confirmed that the terminal substituent did not impede the creation of Eu(III) tris-chelates. Regrettably, no hits were obtained for the 1:3 (M:L) structures with HRMS analysis.

Much like the ^{1}H NMR spectra, contrasting the complex and free ligand IR spectra highlighted differences evidential of Eu(III) complexation. Indeed, the participation of the amide carbonyl groups in metal-binding gave rise to a shift in their associated IR stretching frequency to a lower wavenumber in the complex spectra (all pertinent data summarised in

Table 4.1). All in all, the characterisation data reported in this section proved the formation of 1:3 (M:L) complexes of **69S/R** using synthetic methods.

Table 4.1: *Summary of the IR stretching frequencies (cm^{-1}) of the amide carbonyl groups of the free ligands **69S** and **69R** and their corresponding complexes **Eu.69S$_3$** and **Eu.69R$_3$**.*

Compound	Free Ligand C=O Stretch (cm^{-1})	Complex C=O Stretch (cm^{-1})
69S	1662	1619
69R	1652	1619

4.4 Photophysical properties of Eu.69S$_3$ and Eu.69R$_3$

UV-vis absorption, phosphorescence excitation and emission spectra were recorded for the synthesised complexes **Eu.69S$_3$** and **Eu.69R$_3$** in CH_3CN. The UV-vis spectrum of each complex was characterised by two principle bands; a high energy band positioned at 220 nm and a longer wavelength one centred at 281 nm that possessed two well-defined shoulders at 271 nm and 292 nm (Figure 4.5a and Figure A4.6a for **Eu.69R$_3$** and **Eu.69S$_3$**, respectively), the lower energy band assigned to the π-π^* transitions of the naphthyl groups.

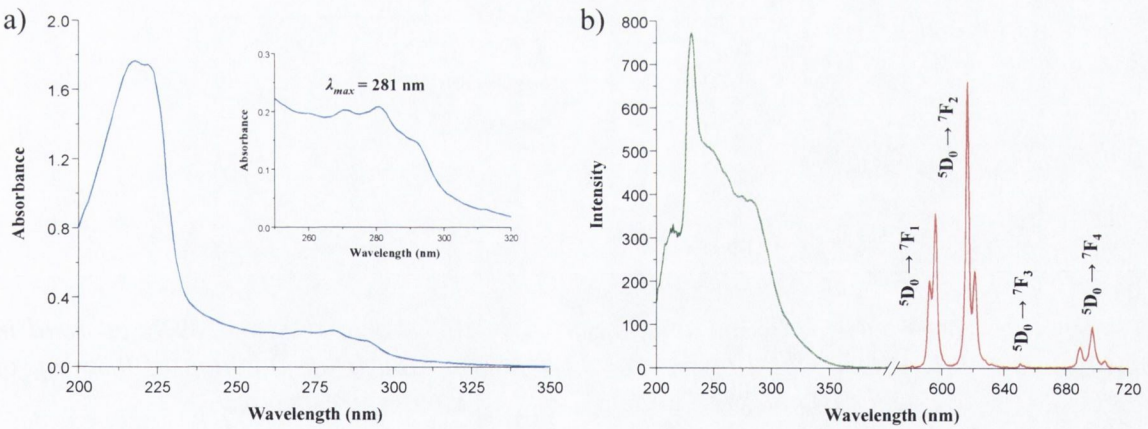

Figure 4.5: *a) UV-vis absorption and b) phosphorescence excitation (green) and emission (red) spectra (λ_{exc} = 281 nm) of **Eu.69R$_3$** (ca. 5.6 × 10^{-6} M) recorded in CH_3CN at 298 K.*

Figure 4.5b and Figure A4.6b shows the phosphorescence excitation and emission spectra obtained for **Eu.69R$_3$** and **Eu.69S$_3$**, respectively. The emission spectra were each recorded by excitation of the aromatic naphthyl groups (λ_{exc} = 281 nm), and verified energy transfer from the ligands to the Eu(III) centre. Both spectra displayed well-resolved, line-like emission bands typical of trivalent Eu(III), with these bands assignable to the $^5D_0 \rightarrow {}^7F_J$

transitions; where $J = 1 - 4$. In line with those of the sliotar analogues in Chapters 2 and 3, these spectra were typified by the absence of the $J = 0$ band, therefore, emphasising the symmetrical character of the complexes in solution.[239]

Central to complex design was the grafting of chiral antenna moieties to enable the formation of enantiomeric Eu(III) species by asymmetric induction. To assess chirality, the systems were subjected to CD and CPL spectroscopic investigation.

4.5 Circular dichroism studies of ligands 69S and 69R and their Eu(III) complexes

CD spectroscopy underscored the enantiomeric relationship between the glycosylated ligand pair **69S/R**, and the subsequent transfer of chirality to the later Eu(III) complexes. Figure 4.6 shows the overlaid spectra of both ligands and their complexes. All spectra were recorded in CH_3CN, with measurement of the complex spectra performed following *in situ* self-assembly, achieved by the addition of 0.33 eq. of $Eu(CF_3SO_3)_3$ to the ligand solutions.

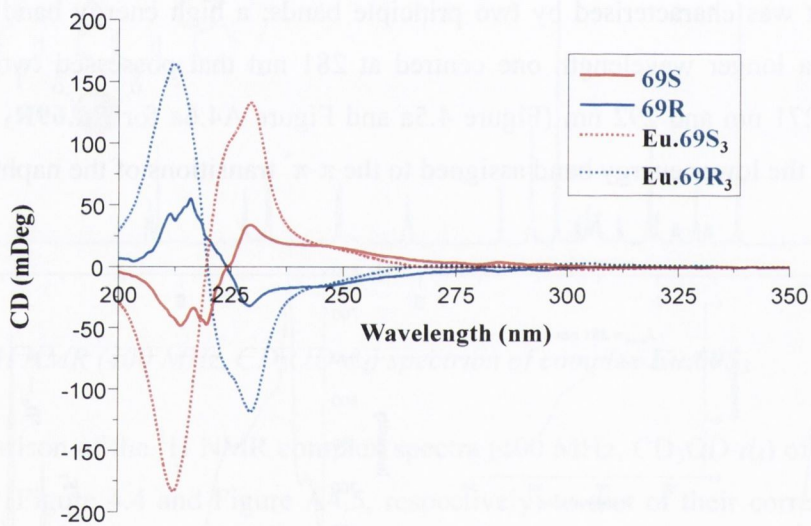

Figure 4.6: *CD spectra of ligand solutions (2.0×10^{-5} M) of **69S** and **69R** recorded in CH_3CN at 298 K before (solid lines) and after (dashed lines) the addition of 0.33 eq. of $Eu(CF_3SO_3)_3$ to give the complexes "**Eu.69S$_3$**" and "**Eu.69R$_3$**", respectively.*

The existence of ligands **69S** and **69R** as an enantiomeric pair was confirmed by the mirror image relationship between the two spectra. Ligand **69S** gave rise to a large negative dichroism band from *ca.* 200 – 225 nm, with two maxima at 214 nm and 219 nm, and a wide positive band stretching from *ca.* 225 – 300 nm, with shoulder at *ca.* 250 nm. In opposing fashion, ligand **69R** produced a positive band from *ca.* 200 – 225 nm, with a negative band from *ca.* 225 – 300 nm. Paralleling the complex CD spectra discussed in Chapter 2 (see Section 2.7), *in situ* complex formation triggered an enhancement in the CD intensity of the

bands relative to the unbound ligands. As with the previous analogues, an onset of increased topological chirality from the helical wrapping of ligands was deemed to be the cause of the observed CD intensification. As well as the changes in intensity, the lower energy dichroism bands experienced a small blue shift. Indeed, all the described changes matched those found for the complex set **Eu.(41 – 43)$_3$**. Of greatest significance, however, was that both complex spectra displayed exciton signals of opposite sign and approximately equal magnitude, thus, establishing **Eu.69S$_3$** and **Eu.69R$_3$** as an enantiomeric pair of contrasting helicity.

4.6 Circularly polarised luminescence studies of Eu.69S$_3$ and Eu.69R$_3$

With the dual purpose of supplementing the CD spectral data while simultaneously evaluating the potential for Eu(III)-centred chiral emissions, CPL spectra of the complexes **Eu.69S$_3$** and **Eu.69R$_3$** were recorded. This analysis was perfomed in collaboration with Dr. R. D. Peacock of the University of Glasgow, with the spectra measured in CH_3CN using an excitation wavelength of 281 nm. For all radiative transitions ($^5D_0 \rightarrow {}^7F_J$, where $J = 1 - 4$), the complexes gave rise to CPL signals of opposite sign and equal intensity, confirming that the transfer of chirality from the ligands occurred diastereoselectively, and resulted in the formation of enantiopure self-assemblies of opposing helicity (Figure 4.7). Referring to the sign of the CPL bands, these spectra correlated to those of the original sliotar complexes **Eu.32S/R$_3$** and the analogues in Chapters 2 and 3 *i.e.* all (*S*) spectra matched, and all (*R*) spectra matched. Therefore, the metal stereochemistry of the two complexes could then be assigned as Δ for **Eu.69S$_3$** and Λ for **Eu.69R$_3$**.

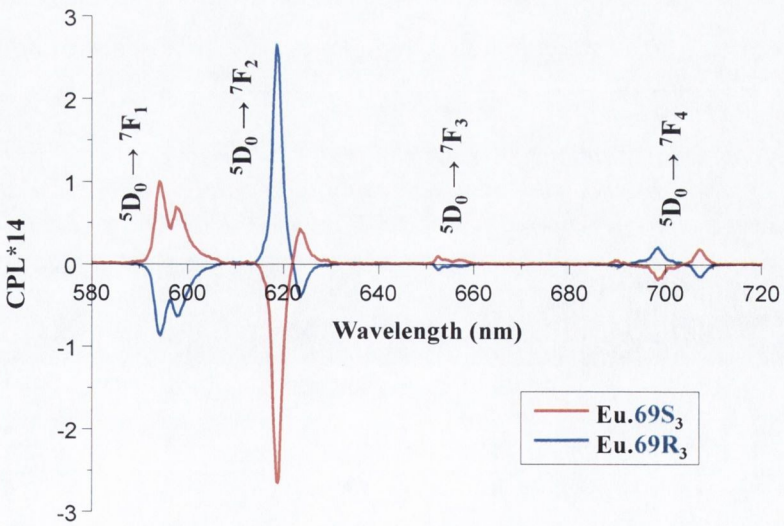

Figure 4.7: *CPL emission spectra of* ***Eu.69S$_3$*** *and* ***Eu.69R$_3$*** *recorded in CH_3CN at 298 K (λ_{exc} = 281 nm).*

Luminescence dissymmetry factors (g_{lum}) were then calculated for the J = 1 and 2 transitions using **Equation 1.4** (Section 1.5.1), with both enantiomers showing exceptional agreement (Table 4.2). Compellingly, the magnitude of these values was also found to be in close agreement to those obtained for the complex set **Eu.(41 – 43)$_3$** (Table 2.4). Based on this correspondence in the g_{lum} values, one may conclude that the terminal sugar units of **Eu.69S/R$_3$** are too far removed for their chirality to bear any influence over the bound metal ion. The CPL activity can, therefore, be prescribed to the effect of the naphthyl groups only.

Table 4.2: *Summary of the g_{lum} dissymmetry factor values calculated from the CPL spectra of* ***Eu.69S$_3$*** *and* ***Eu.69R$_3$*** *for the J = 1 and 2 transitions at 595 nm and 619 nm, respectively.*

Complex	g_{lum} value 595 nm (J = 1)	g_{lum} value 619 nm (J = 2)
Eu.69S$_3$	+ 0.27	− 0.24
Eu.69R$_3$	− 0.26	+ 0.25

Photophysical spectroscopy was used to elucidate crucial information pertaining to both complex stoichiometry and stability, with specific attention paid to the role of the monosaccharide substituent, and will be discussed in the coming sections.

4.7 Determination of metal-bound water molecules for Eu.69S$_3$ and Eu.69R$_3$

Luminescence lifetime measurements were performed for the synthesised complexes to allow calculation of their respective hydration states (q values). Considering ligands **69S** and **69R** were built upon the dpa framework, their self-assembly with trivalent Eu(III) was expected to afford 1:3 (M:L) stoichiometric complexes with an absence of bound solvent.

Table 4.3: *Lifetime measurements of* ***Eu.69S$_3$*** *and* ***Eu.69R$_3$*** *in water (H_2O and D_2O) and methanol (MeOH and MeOD) with their corresponding rate constants (k) and calculated q values. Each lifetime is an average of six measurements with different gate times.*

Complex	Solvent	$\tau_{O\text{-}H}$ (ms)	$\tau_{O\text{-}D}$ (ms)	$k_{O\text{-}H}$ (ms^{-1})	$k_{O\text{-}D}$ (ms^{-1})	q (± 0.5)
Eu.69S$_3$	Water	1.51 ± 0.02	2.12 ± 0.05	0.66	0.47	− 0.07
	Methanol	1.65 ± 0.01	3.55 ± 0.15	0.61	0.28	+ 0.16
Eu.69R$_3$	Water	1.39 ± 0.01	1.95 ± 0.03	0.72	0.51	− 0.05
	Methanol	1.48 ± 0.02	2.74 ± 0.01	0.68	0.36	+ 0.14

Measurements were conducted in both water and methanol, with all lifetimes values obtained (see Table 4.3) by fitting to a mono-exponential decay after naphthyl excitation at 281 nm. Applying the refined Horrocks equation to the lifetime data (**Equation 1.1**; where A = 1.2 ms and 2.0 ms for water and methanol, respectively),[38,66,67] q values ≈ 0 were calculated for the two complexes in both solvent media (see Table 4.3), thus, reinforcing the elemental analysis for the production of 1:3 (M:L) tris-chelates.

A series of spectrophotometric titrations were conducted to inform of the stabilities and distributions of the stepwise species formed in the self-assembly process. The results of these titrations will be subject to discussion in the following sections.

4.8 UV-vis and luminescence titration studies of 69S and 69R

The self-assembly process between ligands **69S/R** and Eu(III) was elucidated by UV-vis and luminescence titrations, with all studies performed by the so-called dilution method (see Section 2.10). Data fitting was achieved by non-linear least squares regression analysis. All spectroscopic titrations were carried out in aprotic CH_3CN, with selection of this solvent governed by a desire for a true comparison with earlier analogues.

4.8.1 Titration experimental and data fitting details

All studies were conducted in CH_3CN. In both cases, a stock solution (3 mL; 1×10^{-5} M) of the pertinent ligand (**69S** or **69R**) was prepared and titrated against known volumes of a standard solution of $Eu(CF_3SO_3)_3$. After additions, UV-vis absorption and phosphorescence spectra were recorded, allowing 5 min for equilibration. Titrations were repeated in triplicate to ensure reproducibility. Fits of the UV-vis spectral changes were attained for both systems using the non-linear least squares regression program SPECFIT® (see Section 2.10.5), with successful phosphorescence fitting also managed in the case of **69S**. All fits were achieved for the equilibria set **Equation 4.1 – 4.3**, which was used to depict the self-assembly pathway (as suggested by the evolving factor analysis, which told of two complex species).

$$Eu^{3+} + 3\ \mathbf{69S/R} \xrightleftharpoons{\beta_{1:3}} \mathbf{[Eu.69S/R_3]^{3+}} \qquad \textbf{Equation 4.1}$$

$$\mathbf{[Eu.69S/R_3]^{3+}} + Eu^{3+} \xrightleftharpoons{K_{2:3}} \mathbf{[Eu_2.69S/R_3]^{6+}} \qquad \textbf{Equation 4.2}$$

$$\beta_{2:3} = \beta_{1:3} \times K_{2:3} \qquad \textbf{Equation 4.3}$$

Within experimental error, both enantiomers demonstrated near identical behaviour. Discussion in the following section will, therefore, focus on the photophysical titrations of **69S** (spectra for the titrations of **69R** can be found in Appendix 4). Discussion will reference the two systems when addressing matters of data fitting.

4.8.2 UV-vis and luminescence titrations of 69S with $Eu(CF_3SO_3)_3$ in CH_3CN

The transformation of the ligand UV-vis absorption spectrum was firstly monitored upon titration with $Eu(CF_3SO_3)_3$. The ligand spectrum mirrored that of the ligands discussed in Chapter 2, and was comprised of a characteristic three-pronged naphthyl band centred at 281 nm (ε = 16435 M^{-1} cm^{-1}), with two small shoulders at 272 nm and 292 nm. Eu(III) addition resulted in a hypochromic shift in the naphthyl band, accompanied with a loss of spectral definition in the band (see Figure 4.8a). These changes coincided with the evolution of a new band at *ca.* 310 nm, which led to the concomitant generation of isosbestic points at 268 nm and 297 nm. The binding isotherms in Figure 4.8b best highlighted these changes, with the changes steadily progressing up until *ca.* 0.3 eq. of Eu(III) ion, before ceasing. The plateau at *ca.* 0.3 eq. was suggestive of the dominant formation of the 1:3 (M:L) complex.

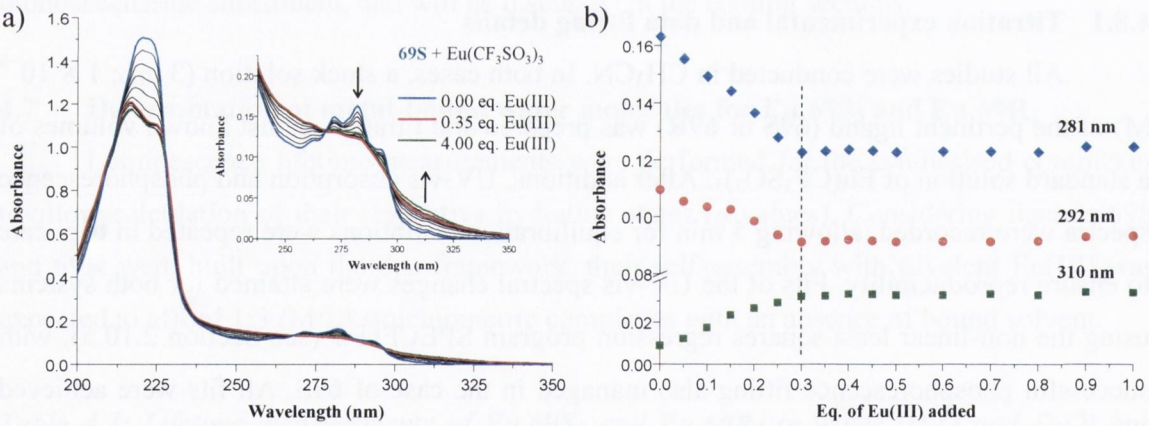

Figure 4.8: *a) Changes in the absorption spectra of* ***69S*** *(1×10^{-5} M) upon titrating with $Eu(CF_3SO_3)_3$ (0.00 → 4.00 eq.) in CH_3CN at 298 K. b) Binding isotherms for the titration measured at 281 nm, 292 nm, and 310 nm.*

With indirect excitation at 281 nm, a continual *switching on* of the Eu(III)-centred emission was observed in the phosphorescence titration (Figure 4.9a). Successive additions of metal were noticed to trigger an intensity enhancement, with all spectra evidencing the characteristic Eu(III) emission structure, including bands at 594 nm, 615 nm, 649 nm, and 695 nm (J = 1 – 4, respectively). The intensity increase, evident in the binding isotherms in Figure 4.9b, was identified to stop at *ca.* 0.3 eq. of Eu(III), yielding a defined plateau in the

titration profiles at this point. Similar to the UV-vis measurements, the trends were taken to infer the predominance in solution of the 1:3 (M:L) stoichiometry.

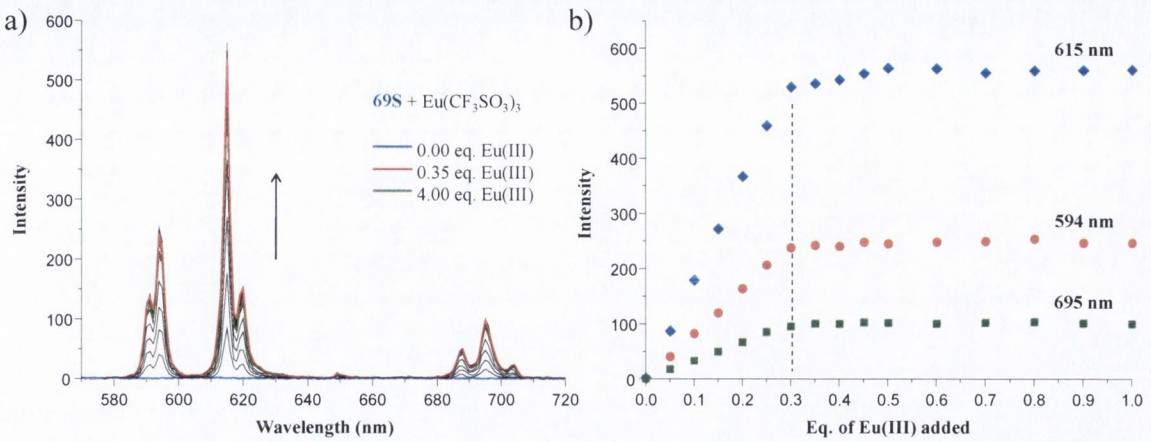

Figure 4.9: *a) Evolution of the phosphorescence emission in the titration of* ***69S*** *(1×10^{-5} M) with $Eu(CF_3SO_3)_3$ (0.00 → 4.00 eq.) in CH_3CN at 298 K (λ_{exc} = 281 nm). b) Binding isotherms for the titration measured at 594 nm, 615 nm, and 695 nm.*

Fitting of the titration data was subsequently undertaken using SPECFIT®. For both enantiomers, excellent fits of the UV-vis spectral changes were obtained, in addition to an exceptional fit for the phosphorescence titration with **69S**. Table 4.4 summarises the species detected, and their corresponding binding constants. All fits identified the presence of two complex stoichiometries in solution, one being the desired 1:3 (M:L) complex. Examination of the speciation graphs revealed the dominance of this tris-chelate species at reduced Eu(III) concentrations, with maximal formation (*ca.* 90%) achieved at *ca.* 0.33 eq of Eu(III) ion (Figure 4.10b as an example). Somewhat unexpected, however, was the 2:3 (M:L) complex, which was found to become increasingly prevalent at excess metal ion concentrations. With binding established at the ligand dpa terminus, the formation of the 2:3 (M:L) system (which was not observed in the studies reported in Chapters 2 and 3) was interpreted to imply the coordination of a second Eu(III) ion by the ligand sugar unit. In fact, Ln(III)-binding with carbohydrate-based compounds has been reported throughout the literature, and in this particular case,[294-297] was deemed to involve both the acetyl protecting groups and nearby triazole, another well-documented Ln(III)-coordinating motif.[298] Eu(III)-coordination by the terminal carbohydrate also helps to explain the notable absence of the less saturated complex species from the data fits, specifically the 1:1 and 1:2 (M:L) assemblies found for previous analogues, as de-assembly of the 1:3 (M:L) complex was no longer necessary to satisfy the coordination demands of the Eu(III) ion at excess.

Table 4.4: *Summary of the binding constants obtained through data fitting for the UV-vis and phosphorescence titrations of* ***69S*** *and* ***69R*** *(1×10^{-5} M) with $Eu(CF_3SO_3)_3$ in CH_3CN, with percentage composition of the 1:3 (M:L) species at 0.33 eq. of Eu(III). *Value fixed.*

Ligand	Mode	$\log \beta_{1:3}$	$\log \beta_{2:3}$	% of 1:3 (M:L) species at 0.33 eq. of Eu(III)
69S	**UV-vis**	20.05 ± 0.19	24.25 ± 0.00*	92
	Phosphorescence	18.94 ± 0.20	24.41 ± 0.32	83
69R	**UV-vis**	19.44 ± 0.31	24.25 ± 0.30	90
	Phosphorescence	–	–	–

Despite participation of the sugar, it is imperative to re-emphasise that the desired **Eu.69S/R$_3$** supramolecular complexes were still formed, and with enviable stability. Indeed, comparison of the log $\beta_{1:3}$ values calculated for ligands **69S/R** (Table 4.4) to those of the *para*-derivatised ligands in Chapter 2 (Table 2.6) highlighted a minor reduction relative to **39**, **41**, and **42**. One may rationalise that this stability decrease originates from either the enhanced steric bulk of the glyco-substituent, or its ability to competitively bind.

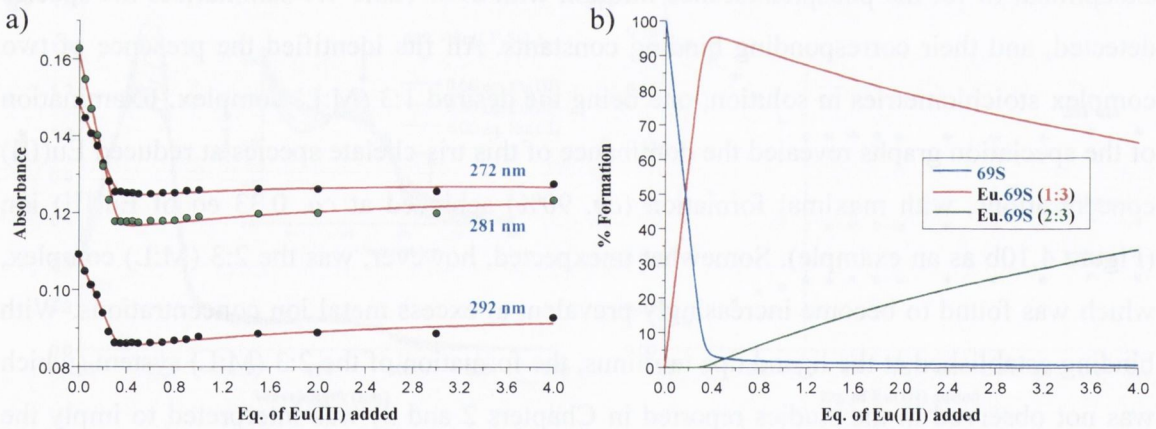

Figure 4.10: *a) Experimental binding isotherms for the UV-vis absorption titration of* ***69S*** *(1×10^{-5} M) with $Eu(CF_3SO_3)_3$ in CH_3CN at 298 K (λ_{exc} = 281 nm) and their corresponding fit by means of SPECFIT. b) Speciation-distribution diagram obtained from the fit.*

Further evidence implicating Eu(III)-sugar binding was procured by measuring the luminescent lifetimes at set points in the titrations. For complex de-assembly, one would expect a dramatic lifetime reduction, a reflection of the presence of species with reduced ligand-coordination in solution. However, sufficiently clear upon review of the lifetime values was the fact that they remained predominantly unchanged throughout (Table 4.5), therefore, proving that the coordination environment of the emissive Eu(III) ion did not

change either. Signifying full retention of the 1:3 (M:L) stoichiometry at the ligand dpa position, these lifetime studies fundamentally supported the speciation data gained through fitting. Formation of the 2:3 (M:L) component at excess Eu(III) ion evidently had no effect on the lifetimes, this explained by the carbohydrate not being a chromophore. Most likely, sensitisation of the second Eu(III) ion was very low and, thus, not observable.

Table 4.5: *Summary of lifetime measurements taken during the titrations of* ***69S*** *and* ***69S*** *(1 × 10^{-5} M) with $Eu(CF_3SO_3)_3$ (0.00 → 4.00 eq.) in CH_3CN at 298 K (λ_{exc} = 281 nm). All obtained by fitting to a mono-exponential decay, with each lifetime an average of three measurements with different gate times.*

Eq. of Eu(III)	69S	69R
	τ (ms)	
0.1	1.75 ± 0.01	1.65 ± 0.02
0.2	1.75 ± 0.02	1.66 ± 0.01
0.3	1.75 ± 0.02	1.66 ± 0.01
0.4	1.73 ± 0.01	1.66 ± 0.01
0.5	1.73 ± 0.01	1.67 ± 0.02
1.0	1.74 ± 0.01	1.67 ± 0.01
4.0	1.74 ± 0.01	1.64 ± 0.02

4.9 Kinetic studies with Eu.69S$_3$ in CH_3CN and MeOH

Proving the glyco-substituent to not impede formation or drastically affect stability, the previous titrations confirmed the spontaneous self-assembly of **Eu.69S$_3$** and **Eu.69R$_3$** in CH_3CN. The next challenge was to analyse the self-assembly process in a more competitive protic, hydrogen bonding solvent. To achieve this, $Eu(CF_3SO_3)_3$ titrations analogous to those described in the last section were performed for the ligand enantiomers **69S/R** in MeOH. However, the titrations, which were repeated numerous times, returned inconsistent results with unexplainable trends. Additionally, all attempts at data fitting were unsuccessful. Based on the problems encountered, it was theorised that a kinetic effect was potentially in effect in MeOH, with changes occurring in solution over time. In order to assess whether this was the case, a series of kinetic spectroscopic experiments were carried out, including a number of control studies. These kinetic experiments involved recording the phosphorescence spectra of a solution (3 mL, 3.33 × 10^{-6} M) of the pre-synthesised complex **Eu.69S$_3$** in either CH_3CN (control) or MeOH every 30 min for a 16 h period.

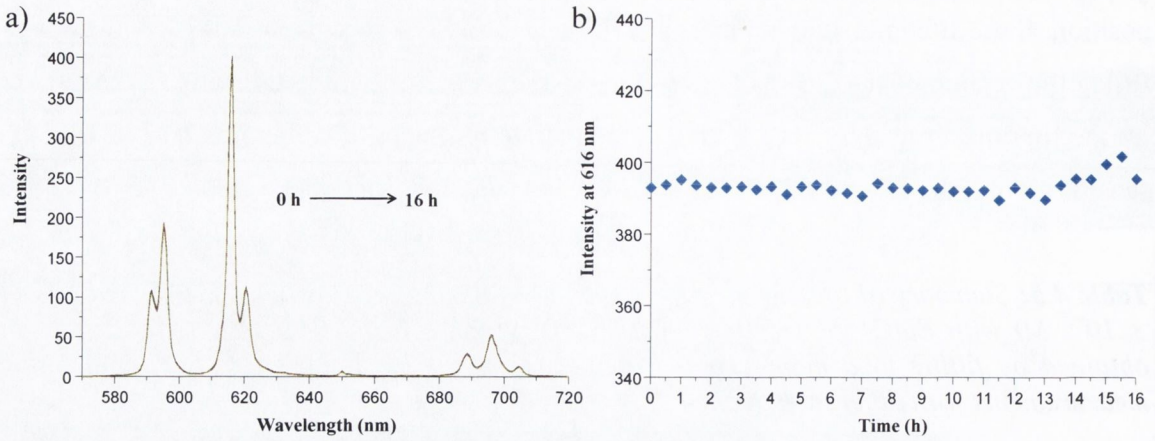

Figure 4.11: *a) Kinetic study with overlaid phosphorescence spectra recorded for* ***Eu.69S$_3$*** *(3.33×10^{-6} M) in CH_3CN at 298 K every 30 min over a 16 h time period. b) Emission profile at 616 nm.*

In the control kinetic experiment with **Eu.69S$_3$** in CH_3CN, the spectra were found to experience little or no change in terms of both emission intensity and band structure (see Figure 4.11). Indeed, the emission profile at 616 nm remained relatively constant, evidence that the integrity of the complex was maintained in this medium.

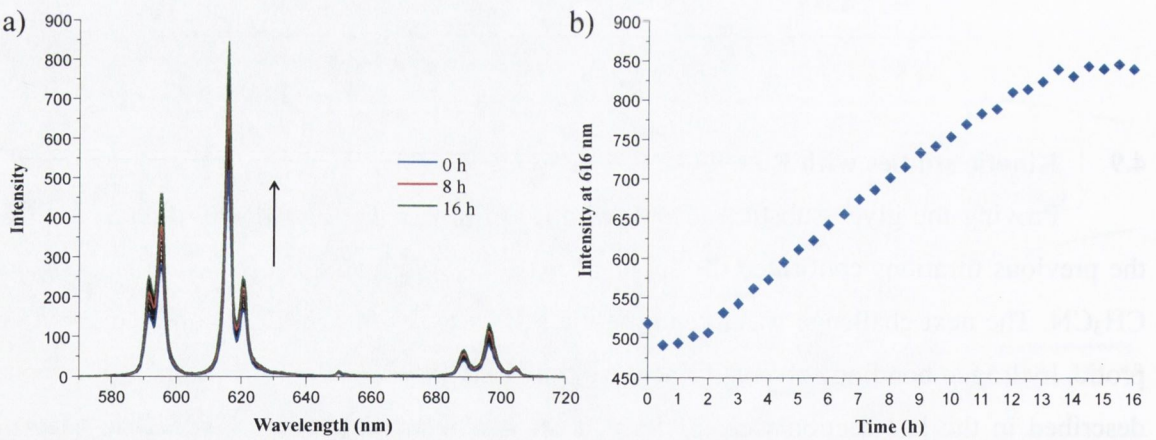

Figure 4.12: *a) Kinetic study with overlaid phosphorescence spectra recorded for* ***Eu.69S$_3$*** *(3.33×10^{-6} M) in MeOH at 298 K every 30 min over a 16 h time period. b) Emission profile at 616 nm.*

Conversely in MeOH, a significant emission enhancement was discerned when these measurements were repeated (Figure 4.12). Analysing the 616 nm profile, emission intensity was found to sharply rise after an initial decrease at 30 min, before reaching a maximum intensity at *ca.* 13.5 h. By completion, the intensity increase accounted for a *ca.* 1.6-fold enhancement over that found at Time = 0 h.

As an additional control experiment, the propargyl-substituted precursory complex **Eu.42S$_3$** (see Chapter 2) was also studied in MeOH, to probe whether or not this behaviour was representative of other sliotar analogues in this solvent. However, unlike that seen in Figure 4.12, the intensity of phosphorescence did not undergo appreciable change (Figure 4.13), with the 616 nm emission profile resembling that of the kinetic study with **Eu.69S$_3$** in CH_3CN, albeit slightly noisier.

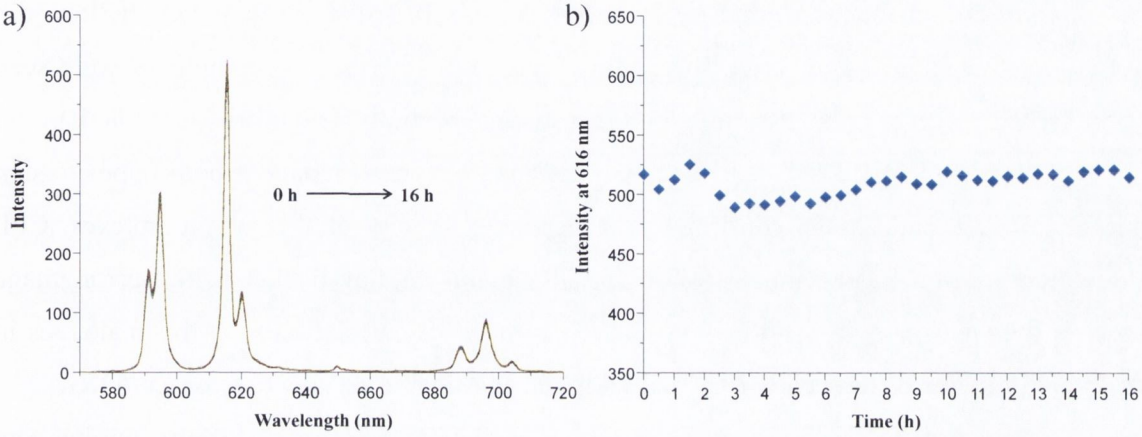

Figure 4.13: *a) Kinetic study with overlaid phosphorescence spectra recorded for* ***Eu.42S$_3$*** *(3.33×10^{-6} M) in MeOH at 298 K every 30 min over a 16 h time period. b) Emission profile at 616 nm.*

These results informed of the existence of a definite kinetic effect in MeOH, where the glycosylated Eu(III) sliotar system was subject to some form of change or interaction that slowly transpired in solution over time. From these simple experiments, nothing concrete can be concluded as to the precise origin and nature of this effect, therefore, necessitating future investigation. However, irrespective of the finer details, these measurements have helped to account for the difficulties suffered in titration analysis of the Eu(III)-mediated assembly of ligands **69S/R** in MeOH.

4.10 Conclusion

Applying *Click Chemistry* methodology, this chapter concentrated on the delivery of sugar functionality to the pyridyl 4-position of the sliotar ligand motif, with the view of creating chiral homoleptic Eu(III) complexes **Eu.69S$_3$** and **Eu.69R$_3$**. The constituent ligands **69S** (*S*,*S*) and **69R** (*R*,*R*) were developed from the propargyl-substituted dinaphthyl ligands **42S** and **42R**, respectively, where CuAAC reaction facilitated triazole linkage of a tetra-acetyl protected β-D-galactopyranoside unit. Through the photophysical analysis of these

Eu(III) glyco-sliotar analogues, this project was dedicated to both proving the design and determining the effect of the substituent, with a view to future bioapplication.

Firstly, this chapter focused on the synthesis and characterisation of ligands **69S/R** and their Eu(III) complexes. For the latter, a wide array of characterisation techniques were used to verify complexation. The resonances in the complex ^{1}H NMR spectra exhibited a broadening and shifting effect, and involvement of the amide carbonyl groups was betrayed by a shift in their IR stretch to a lower frequency. Elemental analysis established the 1:3 (M:L) composition for the synthesised complexes, indicating the terminal carbohydrate did not restrict formation. Thereafter, the emissive properties of the two complexes were seen upon naphthyl excitation at 281 nm, with the resultant spectra typical of trivalent Eu(III).

CD spectra of **Eu.69S$_3$** and **Eu.69R$_3$** contained exciton signals of both opposite sign and equal magnitude, thus, confirming the opposing helicity of the two complexes. CPL studies proved the Eu(III) ion to reside within a chiral binding pocket, with mirror image spectra obtained for both enantiomers. Based on the CPL correlation with the analogues in Chapter 2, the metal stereochemistry was assigned as Δ for **Eu.69S$_3$** and Λ for **Eu.69R$_3$**.

Calculation of the complex hydration states (q) was accomplished by luminescent lifetime measurements in both water (H_2O and D_2O) and methanol (MeOH and MeOD). In each case, q values ≈ 0 were obtained, affirming metal ion saturation by the ligands and, consequently, inferring the 1:3 (M:L) stoichiometry. UV-vis and luminescence titrations were subsequently undertaken to analyse the self-assembly process between ligands **69S/R** and $Eu(CF_3SO_3)_3$ in CH_3CN solution. Data fitting with SPECFIT® conclusively verified formation of the desired 1:3 (M:L) complex with both ligands. Unanticipated, however, was the identification of a 2:3 (M:L) species, whose contribution increased at excess Eu(III) ion concentrations. In this instance, coordination of a second Eu(III) ion by the carbohydrate substituent was hypothesised. Incidentally, this would help to explain why the regular 1:1 and 1:2 (M:L) complexes were not observed in data fitting, as complex de-assembly was not necessary to meet the coordination demands of the metal when in excess. This was further corroborated by lifetime measurements taken during the titrations, which did not change, thus, demonstrating that the coordination environment around the luminescent Eu(III) ion remained constant.

In its entirety, the work detailed in this chapter has effectively communicated the practicality of this design, whereby terminal carbohydrate functionality can be successfully appended to derivatised sliotar ligands with minimal interference in Eu(III) tris-chelate formation. Casting an eye to future *in vivo* application, research efforts will be devoted to optimising this design for the purposes of bio-imaging, profiting from carbohydrate-lectin

interactions to effect binding. When bound, the time-delayed emission of the sensitised Eu(III) ion would be envisaged to provide superior signal-to-noise ratios. In their current condition, **Eu.69S$_3$** and **Eu.69R$_3$** are unfortunately limited by a lack of aqueous solubility. Nevertheless, for referencing in future refinement and development, these self-assemblies represent excellent model systems. As a final remark, the advances made through this work have also helped to accentuate the vast future potential of *Click Chemistry* in synthesising large libraries of derivatised sliotar ligands.

Chapter 5

Design and Photophysical Evaluation of Chiral Multimetallic Lanthanide Self-Assemblies

5 Introduction

In Chapter 1, the merits of multimetallic Ln(III) self-assemblies were discussed at length, employing a wide array of structural examples from recent literature to tactfully illustrate the immense attraction that systems of this variety offer to the supramolecular chemist. With examples covering Ln(III)-containing helicates, cage compounds, and MOFs, Section 1.4.2 accounted the potential of Ln(III)-directed self-assembly methods for the construction of elaborate polynuclear architectures, where the unique structural features of the designs may be exploited for novel application. For their part, the Gunnlaugsson group have contributed immensely to multimetallic system development by manipulating self-assembly strategies for the synthesis of chiral bimetallic triple-stranded Ln(III) helicates from ligands **36S/R**, **37S/R**, and **38S** (see Section 1.6.1).[228-230] These ligands, through incorporation of two distinct Ln(III)-binding domains, can indeed be viewed as ditopic variants of the sliotar framework.

72S (*S,S,S,S*)

72R (*R,R,R,R*)

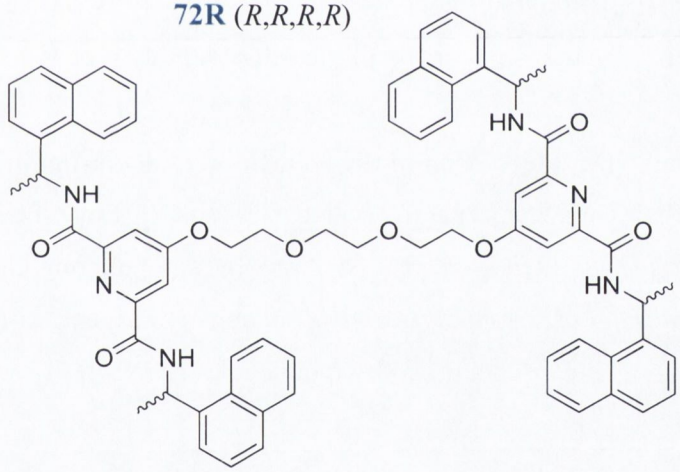

Recognising the great importance of supramolecular multimetallic assemblies, the principle objective of this particular project was to advance recent endeavours by the group within this field. To achieve this goal, the design of the ditopic sliotar ligands **72S** (*S,S,S,S*) and **72R** (*R,R,R,R*) was undertaken, with these representing a more truthful derivation of the original sliotar binding core, which was perfectly replicated in the final ligands, relative to the aforementioned helicate ligands. Availing of the directing effects of trivalent Ln(III), the ability of ligands **72S** and **72R** to spontaneously organise into chiral polymetallic complexes could then be probed, and the resulting M:L stoichiometries elucidated.

5.1 Design of the enantiomeric ligand pair 72S and 72R

Similar to the monometallic Ln(III) systems in Chapters 2 – 4, the chiral ditopic pair **72S/R** were built upon the 4-hydroxy-2,6-dicarboxylic acid framework, which was chosen for its ability to enable 1:3 (M:L) coordination at each ligand end.[112,116,117,128] Chiral 1-(1-naphthyl)-ethylamine chromophores were again elected for coupling to the carboxylic acids at the pyridyl 2- and 6-positions for the purpose of both sensitisation and chirality transfer. The pyridyl 4-hydroxy group was to facilitate the tethering of a flexible polyethoxy chain to bridge two discrete sliotar binding pockets and afford the final ligand products. Eu(III) was selected for complexation for consistency with the previous studies, which would serve as a reference point for the development of structurally advanced polynuclear systems.

On account of the additional Ln(III)-binding motif, the enantiomeric ligands **72S/R** were envisaged to form polymetallic self-assemblies. However, in contrast with the previous chapters where the ligand designs were comparably more simple, predictions as to the final structures and their M:L stoichiometries could not be made with full confidence prior to analysis. Using the knowledge gained in the monometallic studies where 1:3 (M:L) binding was observed, a 2:3 (M:L) binding mode was predicted. Analysis was required, therefore, to answer to develop a rational understanding of the self-assembly process.

5.2 Synthesis and characterisation of the enantiomeric ligand pair 72S and 72R

As regards their chemical structure, ligands **72S** and **72R** may be simply described as two sliotar units linked *via* their pyridyl 4-positions by a polyethoxy chain. To accomplish the linkage, the synthesis of a suitably reactive polyethoxy reagent, di-(iodo-ethoxy)ethane **74**, was performed for the later tethering of two molecules of **39S/R**.

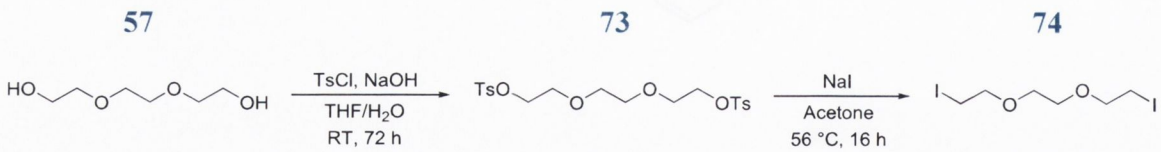

Scheme 5.1: *Synthetic pathway for 74.*

The synthesis of **74** was achieved according to Scheme 5.1,[236] where the first step involved the tosylation of the two free alcohol moieties of triethylene glycol. Triethylene glycol **57** and 4-toluenesulfonyl chloride were reacted together in the presence of NaOH in THF/H_2O solvent mixture, utilising a 2.4:1 ratio of the tosylating reagent. After stirring at room temperature for 72 h, the solvent was removed under reduced pressure, and the crude

product was dissolved in $CHCl_3$, before washing with 1M NaOH and H_2O. Finally, solvent evaporation followed by MeOH recrystallisation gave **73** as a white crystalline solid in 63% yield. Successful di-substitution was confirmed in the ^1H NMR (400 MHz, $CDCl_3$) spectrum by a singlet resonance at 2.45 ppm, and two aromatic doublets at 7.79 ppm and 7.34 ppm, with an overall integral of 14, attributable to the tosyl groups. Subsequent exchange of the tosyl functionalities for iodo leaving groups was accomplished by refluxing NaI and **73** in acetone for 16 h. Thereafter, the resultant precipitate was separated by filtration and the filtrate solvent removed under vacuo. The crude residue was dissolved in $CHCl_3$, washed with H_2O and brine, and the solvent evaporated to yield **74** as a red/brown oil with 88% yield. Verification of leaving group exchange was given by the ^1H NMR (400 MHz, $CDCl_3$) spectrum, from which the tosyl resonances were no longer observable. Electrospray mass spectrometry (ES^+) established the inclusion of iodine within the final structure.

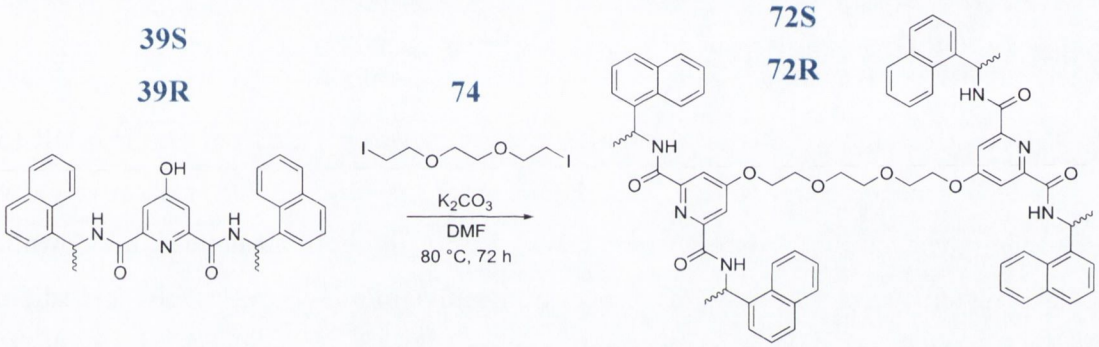

Scheme 5.2: *Synthetic pathway for 72S and 72R.*

The final stage in ligand synthesis set out to attach two molecules of either **39S** or **39R** to each end of the polyethoxy reagent **74** through nucleophilic substitution of the C-I bonds by the pyridyl *para*-hydroxy groups, to give **72S** or **72R**, respectively (Scheme 5.2 – see Section 2.2 for the synthetic details of **39S/R**).[237] These S_N2 reactions entailed initial stirring of the relevant enantiomer of **39** (*S* or *R*) with anhydrous K_2CO_3 in anhydrous DMF for 30 min at 25 °C. Subsequently, the di-iodo chain compound **74** was added (1:2.1 molar ratio of **74**:**39**) and the reaction mixture was heated for an additional 72 h at 80 °C. Upon completion, the solvent was evaporated, the residue dissolved in CH_2Cl_2, and the organic phase washed with 1% acetic acid (aqueous) and H_2O. Purification was lastly achieved by dropping a minimal volume CH_2Cl_2 solution of the crude product into MeOH, and allowing sufficient time for the product to crystallise out. This method gave **72S** and **72R** in a pure crystalline form with yields of 31% and 35%, respectively.

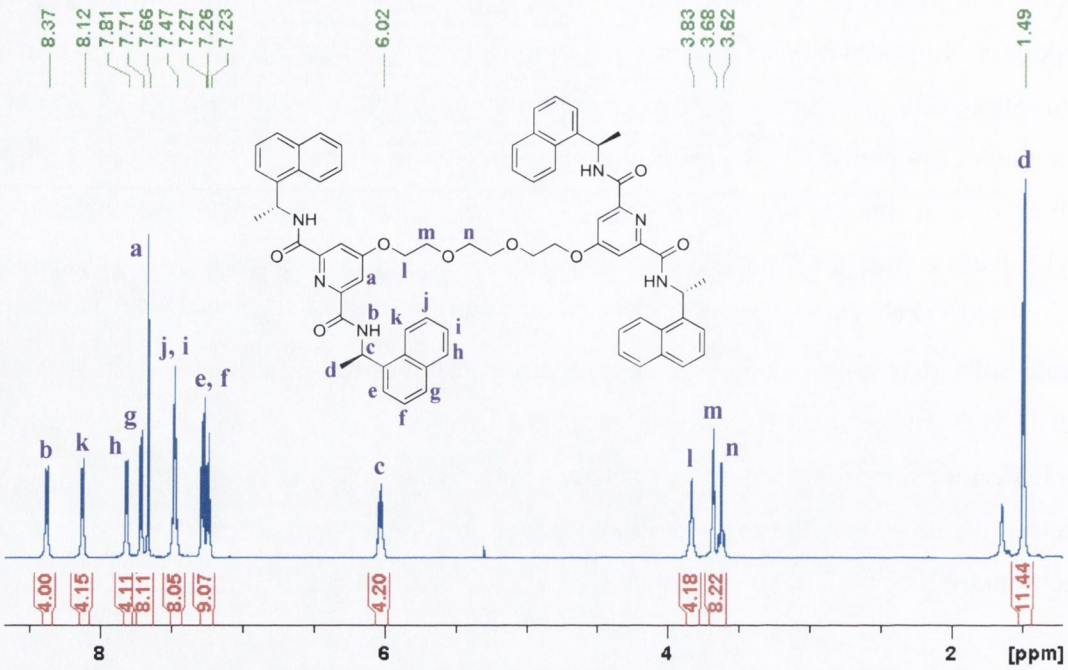

Figure 5.1: *^{1}H NMR (600 MHz, $CDCl_3$) of ligand* ***72R****.*

Definitive proof of product formation and purity was gained from the ^{1}H NMR (600 MHz, $CDCl_3$) spectra (see Figure 5.1 and Figure A5.2 for **72R** and **72S**, respectively), with assignment achieved by 2D NMR experiments. As per all sliotar analogues, the downfield aromatic region contained proton resonances designative of the central pyridyl and adjoined naphthalene rings. the signals at 3.83 ppm, 3.68 ppm, and 3.62 ppm correlated to the CH_2 protons of the bridging polyethoxy chain, and confirmed incorporation of the linker in the final structure, with the relative integration to the aromatic resonances endorsing pyridyl-substitution at the two C-I termini.

As previously mentioned, the purification technique employed for these ligands gave both compounds in a crystalline form. Indeed, the clear plate-shaped single crystals obtained were subjected to X-ray crystal structure analysis, with structural elucidation performed by Dr. J. A. Kitchen of the Gunnlaugsson group. Unfortunately, the resolved structures were not of a publishable standard (R factor = 15.23 and 14.97 for **72S** and **72R**, respectively), but they clearly showed the atom connectivity and served as further proof of successful product synthesis (see Figure 5.2). Also evident upon observation was the enantiomeric relationship between **72S** and **72R**, with both structures easily identifiable as non-superimposable mirror images of each other. Perhaps the most intriguing feature of these structures was the noted flexibility of the polyethoxy linker chain, which allowed the molecules to fold and bring the coordinating termini close together. From the perspective of Ln(III) binding, the ability of these ligands to fold could potentially have implications in the complexes they form.

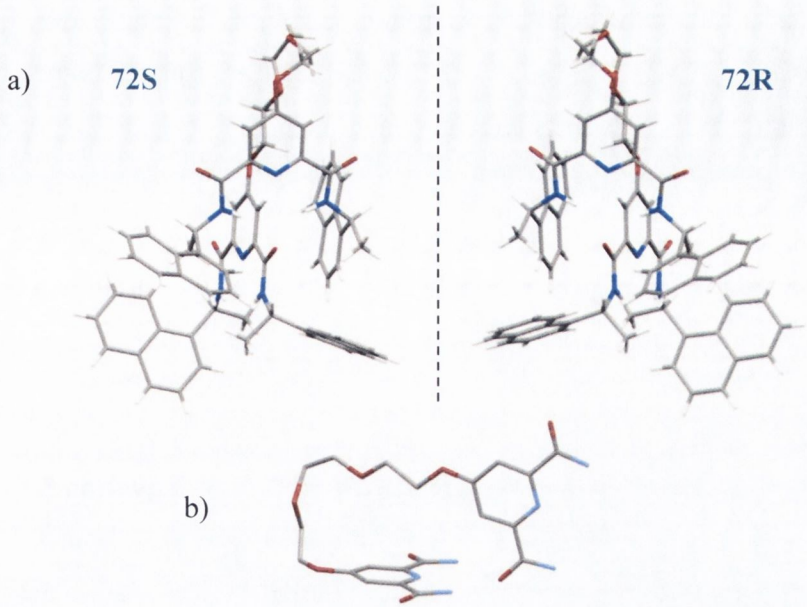

Figure 5.2: *a) X-ray crystal structures (capped stick) of ligands* ***72S*** *and* ***72R*** *highlighting the enantiomeric relationship between the two (solvent molecules omitted for clarity). b) Structure of* ***72R*** *excluding the naphthyl groups to help emphasise the folding of the chain.*

As stated in Section 5.1, by virtue of the extra derivatised-dpa terminal, ligands **72S** and **72R** were expected to form complex polynuclear structures, but with a limited idea of what structural topologies to expect (although a 2:3 (M:L) ratio was anticipated). Therefore, the Eu(III)-mediated self-assembly process was first studied *in situ* through photophysical titrations, with the information accrued applied to later complex synthesis.

5.3 UV-vis and luminescence titration studies of 72S and 72R

UV-vis and luminescence titrations were carried out to help in resolving the self-assembly process between ligands **72S/R** and Eu(III) in solution. All measurements were conducted according to the so-called dilution method (see Section 2.10), using a mixed aprotic organic solvent system, $CHCl_3/CH_3CN$ (1:1; *v/v*). Selection of this mix was solely dictated by solubility reasons. The phosphorescence data was fit through non-linear least squares regression analysis to elucidate the stoichiometric M:L species present.

5.3.1 Titration experimental and data fitting details

All measurements were conducted in $CHCl_3/CH_3CN$ (1:1; *v/v*). For both systems, a stock solution (3 mL, 1×10^{-5} M) of the pertinent ligand (**72S** or **72R**) was prepared and titrated against known volumes of a standard solution of $Eu(CF_3SO_3)_3$. Following additions, UV-vis absorption and phosphorescence spectra were recorded, after 5 min equilibration.

Titrations were performed in triplicate to ensure reproducibility. In both cases, fitting of the phosphorescence changes was achieved by the non-linear least squares regression program SPECFIT® (Section 2.10.5). Two fits were obtained for both **72S** and **72R**, one fit defined by **Equation 5.1**, and the other alternatively by **Equation 5.2**. The enantiomers showed near identical behaviour within experimental error. Therefore, discussion in the next section will focus only on the photophysical titrations of **72R** (spectra for the titrations of **72S** can be found in Appendix 5), but will discuss both with regards to data fitting.

$$2\ Eu^{3+} + 3\ \mathbf{72S/R} \overset{\beta_{2:3}}{\rightleftharpoons} [Eu_2.\mathbf{72S/R}_3]^{6+} \qquad \textbf{Equation 5.1}$$

$$4\ Eu^{3+} + 6\ \mathbf{72S/R} \overset{\beta_{4:6}}{\rightleftharpoons} [Eu_4.\mathbf{72S/R}_6]^{12+} \qquad \textbf{Equation 5.2}$$

5.3.2 UV-vis and luminescence titrations of 72R with $Eu(CF_3SO_3)_3$ in $CHCl_3/CH_3CN$

To analyse the self-assembly process, the changes in the ligand UV-vis absorption spectrum upon titration with $Eu(CF_3SO_3)_3$ were studied. Preceding metal addition, the free ligand spectrum was in fact typical of a substituted naphthalene derivative, comprising a characteristic band centred at 283 nm (ε = 40812 M^{-1} cm^{-1}) with shoulders at 273 nm and 294 nm.

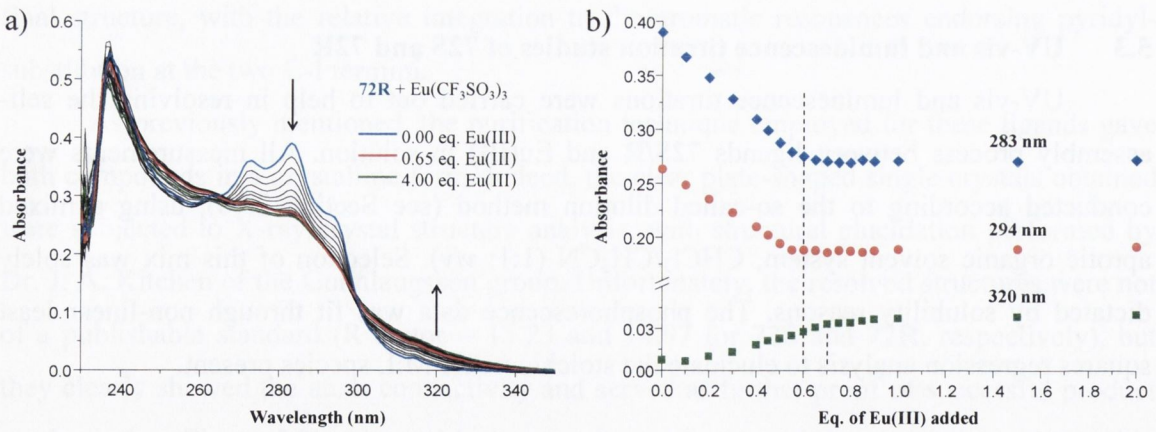

Figure 5.3: *a) Changes in the absorption spectra of 72R (1×10^{-5} M) upon titrating with $Eu(CF_3SO_3)_3$ (0.00 → 4.00 eq.) in $CHCl_3/CH_3CN$ (1:1; v/v) at 298 K. b) Binding isotherms for the titration measured at 283 nm, 294 nm, 320 nm.*

Additions of Eu(III) ion were found to induce hypochromic shifts in the naphthalene band, simultaneously accompanied by a broadening effect. Concurrently, the evolution of a

new band at *ca.* 320 nm was identified, with the combined changes causing the formation of an isosbestic point at 299 nm (see Figure 5.3a). From the binding isotherms in Figure 5.3b, the described trends were found to continue up until *ca.* 0.6 eq. of Eu(III) at 283 and 294 nm and *ca.* 0.7 eq. at 320 nm. Thereafter, these changes ceased, resulting in plateaus in the titration profiles at these positions. Tellingly, plateau formation at *ca.* 0.7 eq. of Ln(III) ion (as seen at 320 nm) was also observed in the titrations probing the assembly of bimetallic triple-stranded helicates $\mathbf{Ln_2.L_3}$ developed by Gunnlaugsson *et al.*[228-230]

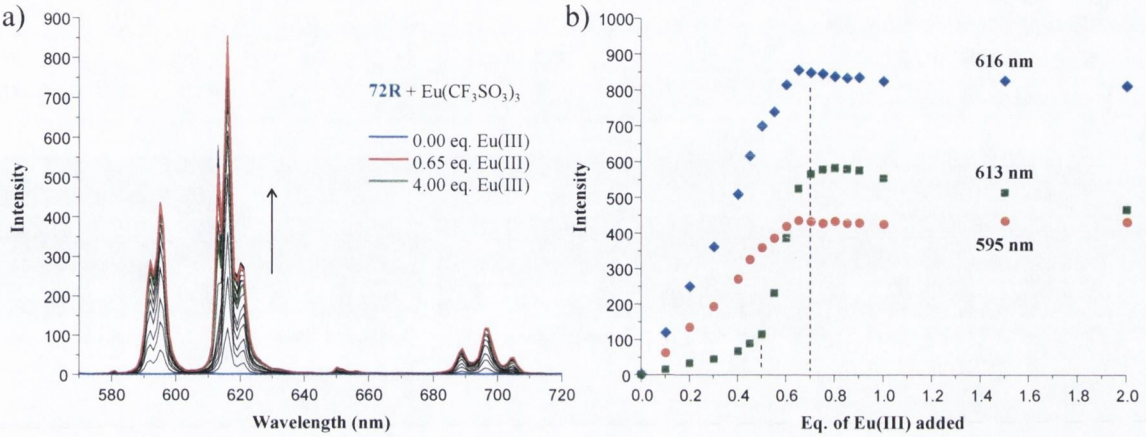

Figure 5.4: *a) Evolution of the phosphorescence emission in the titration of* **72R** *(1×10^{-5} M) with $Eu(CF_3SO_3)_3$ (0.00 → 4.00 eq.) in $CHCl_3/CH_3CN$ (1:1; v/v) at 298 K (λ_{exc} = 281 nm). b) Binding isotherms for the titration measured at 595 nm, 613 nm, and 616 nm.*

The overlaid phosphorescence spectra for the phosphorescence titration are shown in Figure 5.4a, all obtained upon indirect naphthyl excitation at 281 nm, thus, proving ligand-metal energy transfer by the *antenna effect*. All spectra exhibited the distinctive Eu(III) ion emission structure, with bands for the $J = 0 - 4$ transitions found to undergo an intensity enhancement with increasing amounts of Eu(III). These emission spectra were differentiated to those recorded in the monometallic sliotar titrations (see Chapters 2 – 4) by a number of features, one being the presence of the electronic-dipole $J = 0$ band in the titration of **72R**. Of greater interest, however, was the emergence of a band split in the hypersensitive $J = 2$ transition at 613 nm as the titration progressed. It should be noted that this split was not observed in the Eu(III) titrations of ligands **36S/R**, **37S/R**, and **38S** (see Chapter 1), used previously by Gunnlaugsson *et al.* to form bimetallic triple-stranded Ln(III) helicates.[228-230] Informed by its absence in the titrations of related ligand systems, this band was interpreted to signify a relative change in the site-symmetry about the Eu(III) ion,[239] thus, inferring the self-organisation of a novel multimetallic species. The aforementioned luminescent increase was observed in the binding isotherms in Figure 5.4b to continue till *ca.* 0.7 eq. of Eu(III)

ion, before levelling to yield a plateau at this point. It was evident from the 613 nm profile that the split at this wavelength only came to prominence after the addition of *ca.* 0.5 eq. of Eu(III), thus, implying significant structural reorganisation at this stage with a change in the metal ion site-symmetry. Based on the identified trends and spectral transformations, these measurements were taken to suggest the dominant formation of a complex system with the 2:3 (M:L) complex stoichiometry, but structurally different to the previously reported helicates.[228-230]

Table 5.1: *Summary of the binding constants obtained through data fitting for the phosphorescence titrations of* ***72S*** *and* ***72R*** *(1 × 10^{-5} M) with $Eu(CF_3SO_3)_3$ in $CHCl_3/CH_3CN$ (1:1; v/v), with percentage composition of the 2:3 (M:L) species at 0.7 eq. of Eu(III).*

Ligand	log $\beta_{1:2}$	log $\beta_{2:3}$	log $\beta_{2:1}$	% of 2:3 (M:L) species at 0.7 eq. of Eu(III)
72S	18.58 ± 0.59	34.67 ± 0.74	15.39 ± 0.40	81
72R	18.62 ± 0.53	35.15 ± 0.70	15.28 ± 0.37	91

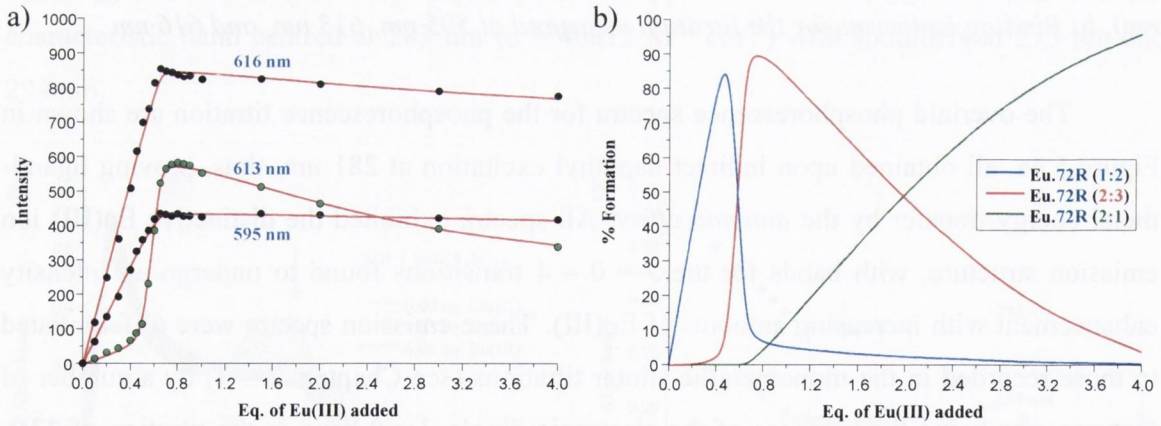

Figure 5.5: *a) Experimental binding isotherms for the phosphorescence titration of* ***72R*** *(1 × 10^{-5} M) with $Eu(CF_3SO_3)_3$ in $CHCl_3/CH_3CN$ (1:1; v/v) at 298 K (λ_{exc} = 281 nm) and their corresponding fit by means of SPECFIT, accounting for the 2:3 (M:L) species. b) Speciation-distribution diagram obtained from the fit.*

Excellent data fits were obtained for both enantiomers using SPECFIT®, with Table 5.1 summarising the species established and their binding constants. For both fits, three luminescent complexes were recognised to form in solution as instructed by the evolving factor analysis; specifically the 1:2, 2:1 and, most significantly, 2:3 (M:L) complex (Figure

5.5 and Figure A5.10 for **72R** and **72S**, respectively), which was found to form with high stability. The speciation graphs showed the 1:2 (M:L) complex to be favoured until *ca.* 0.6 eq. of Eu(III), after which the polynuclear 2:3 (M:L) assembly was preferentially formed, with maximal formation achieved at *ca.* 0.7 eq. of Eu(III) (see Figure 5.5b). In fact, the percentage formation of the 2:3 (M:L) species was comparable to that obtained with the helicate-forming ligand **38S**.[230] Upon reaching *ca.* 2 eq. of metal ion, the equilibrium was displaced in favour of de-assembly to the 2:1 (M:L) complex. Furthermore, the speciation graphs were taken to support the assignment of the $J = 2$ band split at 613 nm to the 2:3 (M:L) complex. Indeed, the evolution of emission at 613 nm was noticed to correlate with the formation of this structure in the distribution profile.

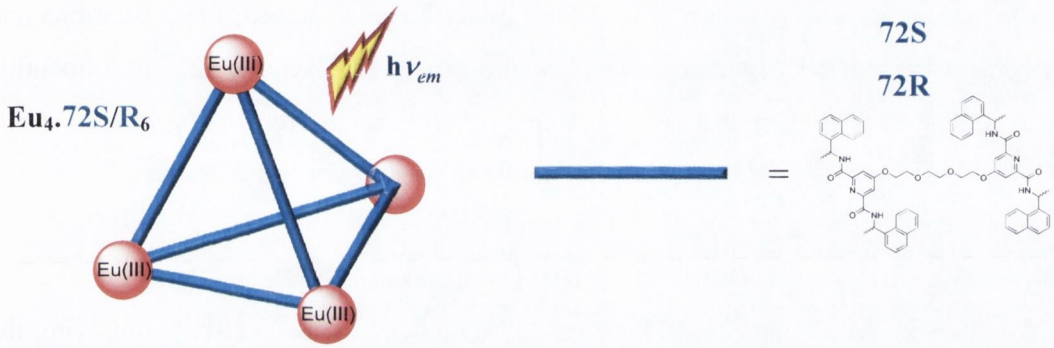

Figure 5.6: *Cartoon representation of* ***Eu$_4$.72S/R$_6$*** *with tetrahedral complex structure.*

As discussed earlier, in terms of Eu(III) sliotar and helicate systems designed in the Gunnlaugsson group, the band split at 613 nm was unique to this set of titrations, therefore, suggesting a unique complex topology. Moreover, the assembly of Eu(III)-based helicates from ligands **72S/R** would be predicted to yield severely constrained systems, therefore, making their construction difficult to imagine. One structure that can be hypothesised that still satisfies the 2:3 (M:L) fit is a structure consisting of four Eu(III) ions and six ligand molecules, where the Eu(III) ions constitute the four vertices of a tetrahedron (Figure 5.6). Such supramolecular $\mathbf{M_4L_6}$ clusters, formed through the metal-directed self-assembly of symmetrical ditopic ligands, have been extensively reported in the literature, particularly by the Kenneth Raymond research group.[299,300] Raymond *et al.* have vastly explored the many factors that preferentially control the assembly of $\mathbf{M_4L_6}$ species ahead of $\mathbf{M_2L_3}$ species, the latter normally favoured for entropic reasons.[301] They propose in order to obtain the higher order system, the ligand must either be rigidly fixed or at least conformationally restricted (potentially true of **72S** and **72R**) from forming the $\mathbf{M_2L_3}$ complex. For the $\mathbf{M_4L_6}$ tetrahedral structure described by Raymond, each metal ion is known to possess a C_3 symmetry axis,

with adjacent ligands stationed at 60° to one another. In terms of symmetry, this differs from the pseudo-D_3 symmetries observed in the X-ray crystal structures of related monometallic sliotar complexes (see Section 2.5). A change in symmetry would, however, be expected to occur with a change in the emission band profile, an effect which was indeed observed for the Eu(III) luminescence titrations of **72S/R**. It was found to be possible to alternatively fit the phosphorescence data with the 4:6 (M:L) species instead of the 2:3 (M:L) complex (fits and binding constants can be found in Appendix 5). Unfortunately, however, the SPECFIT® program only recognises M:L ratios and not the precise complex make-up, thus, meaning it cannot distinguish between the 2:3 and 4:6 complexes.

Despite a lack of conclusive evidence acquired from these studies, the formation of complexes of formula **Eu_4.72S/R_6** possessing tetrahedral structure was still considered to represent the most realistic possibility for these ditopic ligands. Indeed, these titrations and their fits demonstrated the capacity of ligands **72S/R** to self-assemble into multimetallic architectures. The next challenge was to implement the learnings from these measurements into the actual synthesis of polynuclear Eu(III) complexes with **72S** and **72R**.

5.4 Synthesis and characterisation of Eu(III) complexes of 72S and 72R

The ditopic ligands **72S** and **72R** were next complexed with Eu(III) by applying the knowledge gained in the photophysical titrations (Scheme 5.3). The complexation procedure involved refluxing the relevant ligand enantiomer with 0.67 eq. of $Eu(CF_3SO_3)_3$ in HPLC grade $CHCl_3$ under microwave irradiation for 45 min.

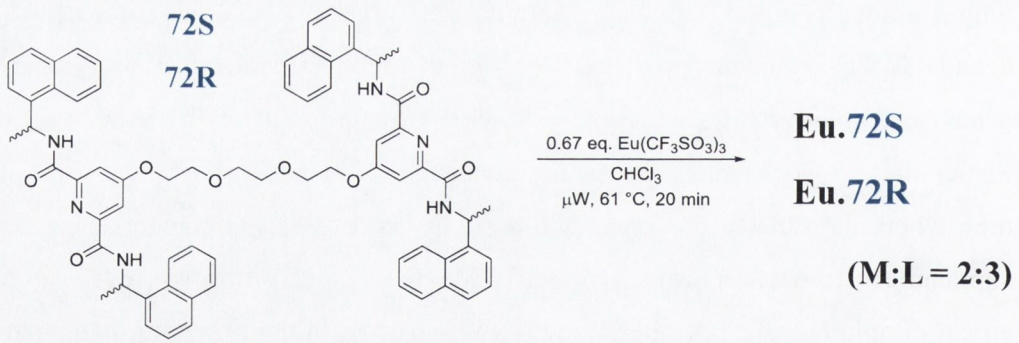

Scheme 5.3: *Synthetic pathway for* ***Eu.72S*** *and* ***Eu.72R*** ***(M:L = 2:3)*** *by complexation of* ***72S*** *and* ***72R*** *with* $Eu(CF_3SO_3)_3$.

Selection of the 2:3 (M:L) reaction ratio was made with a view to synthesising 2:3 (M:L) polymetallic complexes analogous to those formed *in situ*. After reflux, the complex products were precipitated as white solids through the addition of CH_3CN. The complexes

were deposited by centrifugation and isolated by decanting to afford **Eu.72S/R (M:L = 2:3)** in yields of 67% each. The two systems were characterised by ^{1}H NMR and IR spectroscopy to verify complexation, and elemental analysis to establish their respective compositions.

Both complex ^{1}H NMR (400 MHz, DMSO-d_6) spectra, relative to their free ligands. evidenced a detectable shift in their proton resonances, along with minor signal broadening (Figure 5.7 for **Eu.72S** and Figure A5.12 for **Eu.72R**), thus, telling of successful Ln(III)-coordination. Furthermore, the two complex spectra were identical.

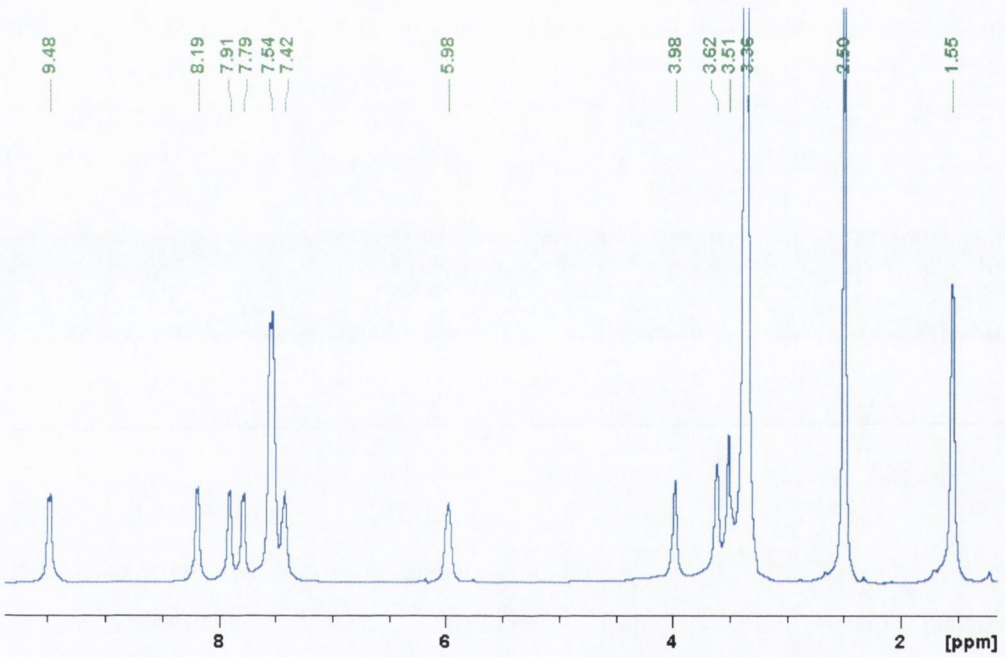

Figure 5.7: *^{1}H NMR (400 MHz, DMSO-d_6) spectrum of complex* ***Eu.72S (M:L = 2:3).***

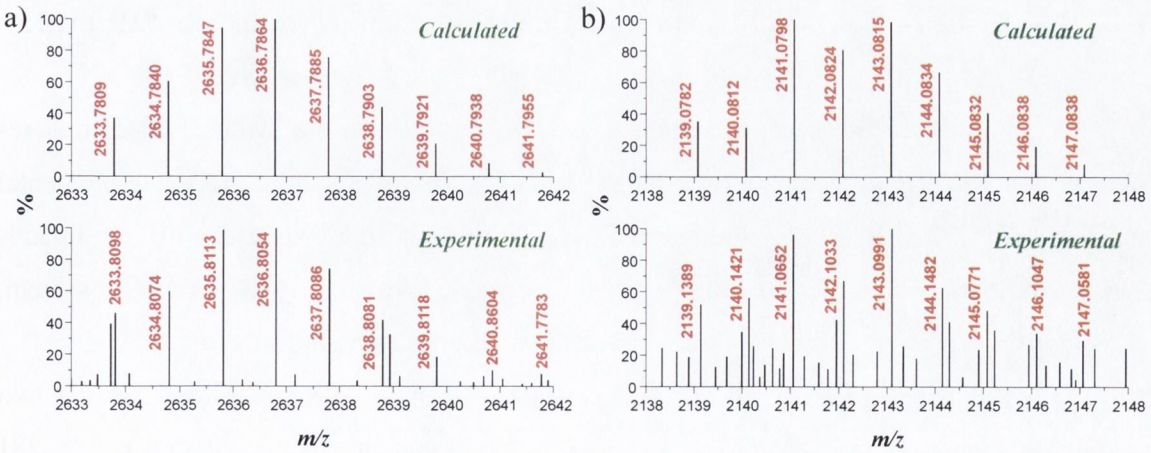

Figure 5.8: *The calculated and experimental isotopic distribution patterns (MALDI^{+}) for complex* ***Eu.72R*** *showing the a) 1:2 and b) 2:1 (M:L) stoichiometric pattern for molecular species of formula $[M - CF_3SO_3]^{+}$ (spectra are normalised – dominant peak set to 100%).*

For both synthesised complexes, the elemental analysis confirmed the predicted 2:3 (M:L) structure (see full details in Chapter 7). Having identified this stoichiometry in the photophysical studies, the elemental analysis proved the transferability of this design using synthetic methods. However, as was the case in the titration fits, the elemental analysis was incapable of differentiating between $\mathbf{M_2L_3}$ and $\mathbf{M_4L_6}$, hence, no conclusions as to the final structures could be made. Unfortunately, HRMS analysis failed to detect either polynuclear species, with only the 1:2 and 2:1 (M:L) species found (Figure 5.8), as seen from the fits. Crystal growth for X-ray analysis was also unsuccessful, having tried vapour diffusion of diethyl ether, *t*-butyl methyl ether, and MeOH into DMF and DMSO complex solutions.

Table 5.2: *Summary of the IR stretching frequencies (cm^{-1}) of the amide carbonyl groups of the free ligands* ***72S*** *and* ***72R*** *and their corresponding complexes* ***Eu.72S*** *and* ***Eu.72R*** *(**M:L = 2:3**).*

Compound	Free Ligand C=O Stretch (cm^{-1})	Complex C=O Stretch (cm^{-1})
72S	1658	1618
72R	1658	1618

Complexation was further endorsed upon comparison of the complex and ligand IR spectra, where Eu(III) ion-binding by the amide carbonyl groups was betrayed by a shift to a lower wavenumber in the associated IR stretching frequency for the former. These shifts are summarised in Table 5.2.

5.5 Determination of metal-bound water molecules for Eu.72S and Eu.72R (M:L = 2:3)

Luminescence lifetime measurements were conducted on the synthesised complexes **Eu.72S** and **Eu.72R** to calculate their hydration states (q values) and corroborate elemental analysis for the 2:3 (M:L) stoichiometry. Based on the dpa framework, the ditopic ligands **72S/R** would be anticipated to afford $q \approx 0$ if organised in a 2:3 (M:L) complex system, reflecting full Eu(III) coordinative saturation and an absence of bound solvent.

The luminescent lifetimes of the Eu(III) excited states were measured for the two complexes separately in H_2O ($\tau_{O\text{-}H}$) and D_2O ($\tau_{O\text{-}D}$) upon naphthalene excitation (λ_{exc} = 281 nm) by fitting to a mono-exponential decay (Table 5.3). Expectedly, the lifetime values in D_2O were longer, owing to the absence of high frequency O-H oscillators. Upon treating the

lifetime data with the modified Horrocks equation (**Equation 1.1**; where A = 1.2 ms for water)[38,66,67] q values ≈ 0 were calculated for both complexes (see Table 5.3), therefore, indicating the complete omission of metal-bound solvent and supplementing the elemental analysis for the formation of coordinatively saturated 2:3 (M:L) multimetallic edifices.

Table 5.3: *Lifetime measurements of* ***Eu.72S*** *and* ***Eu.72R*** ***(M:L = 2:3)*** *in water (H_2O and D_2O) with their corresponding rate constants (k) and calculated q values. Each lifetime is an average of six measurements with different gate times.*

Complex	Solvent	$\tau_{O\text{-}H}$ (ms)	$\tau_{O\text{-}D}$ (ms)	$k_{O\text{-}H}$ (ms^{-1})	$k_{O\text{-}D}$ (ms^{-1})	q (± 0.5)
Eu.72S	Water	1.40 ± 0.01	2.62 ± 0.01	0.71	0.38	+ 0.10
Eu.72R		1.42 ± 0.01	2.75 ± 0.04	0.70	0.36	+ 0.11

Similar to the derivatised sliotar ligands used to construct monometallic complexes, ligands **72S/R** also incorporated chiral naphthalene groups and, as such, were envisaged to diastereoselectively transfer their chirality for the self-assembly formation of enantiopure polymetallic structures. **Eu.72S** and **Eu.72R** **(M:L = 2:3)** were, therefore, subjected to CD and CPL analysis to assess the conferral of chirality.

5.6 Circular dichroism studies of ligands 72S and 72R and their Eu(III) complexes

CD spectra of the ligands **72S** and **72R** were recorded in $CHCl_3/CH_3CN$ (1:1; *v/v*) to acquire chiroptical evidence confirming the enantiomeric ligand relationship. The complex spectra were subsequently measured following *in situ* self-assembly, accomplished by the addition of 0.67 eq. of $Eu(CF_3SO)_3$, with the aim of probing chirality transfer to the later 2:3 (M:L) complexes. The recorded CD spectra are overlaid in Figure 5.9.

The free ligand spectra were found to be mirror images of one another, underscoring the enantiomeric relationship already established from their X-ray crystal structures (Figure 5.2). Ligand **72S** gave rise to both a large positive band stretching from *ca.* 240 – 280 nm, with a maximum at 252 nm, and a smaller positive band centred at 292 nm. Contrastingly, ligand **72R** resulted in the exact opposite spectrum, showing both a sizeable negative band from *ca.* 240 – 280 nm and an analogous smaller negative band at 292 nm. Pronounced morphological changes were seen in the spectra of the complexes after *in situ* formation. Examination of the **Eu.72S** spectrum revealed a reduction in intensity for the two positive bands, with the higher energy one disappearing, accompanied by the development of a new negative dichroism band from *ca.* 295 – 335 nm. These changes were closely replicated in

the **Eu.72R** spectrum, albeit in an opposite manner, where both negative bands experienced an intensity decrease, along with the emergence of a matching positive band from *ca.* 295 – 335 nm. Noteworthy was the fact that the emergent dichroism bands surfaced in a spectral region where no CD activity had been observed for the ligands, therefore, intimating their formation was a result of the topological chirality of the complexes, which likely originates from the helical organisation of ligands around the Eu(III) ions.

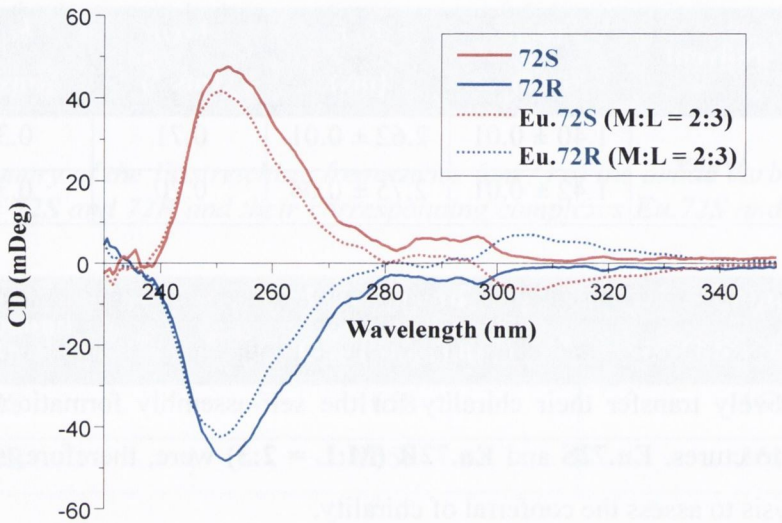

Figure 5.9: *CD spectra of ligand solutions (2.0 × 10^{-5} M) of **72S** and **72R** recorded in $CHCl_3/CH_3CN$ (1:1; v/v) at 298 K before (solid lines) and after (dashed lines) the addition of 0.67 eq. of $Eu(CF_3SO_3)_3$ to give the complexes "**Eu.72S**" and "**Eu.72R**" **(M:L = 2:3)** respectively.*

Most importantly, as was for their component ligands, the complex spectra produced exciton signals of opposite sign and approximately equal magnitude, confirming a retention of chirality in the final multimetallic assemblies **Eu.72S** and **Eu.72R (M:L = 2:3)**, which were proven to exist themselves as an enantiomeric pair.

5.7 Circularly polarised luminescence studies of Eu.72S and Eu.72R (M:L = 2:3)

In collaboration with Dr. R. D. Peacock (University of Glasgow), CPL analysis of **Eu.72S** and **Eu.72R (M:L = 2:3)** was then undertaken to assess the feasibility of Eu(III)-centred chiral emissions and to establish whether the bound metal ions were residing in a chiral pocket. The CPL spectra of the complexes were recorded in $CHCl_3/CH_3CN$ (1:1; *v/v*) using an excitation wavelength of 281 nm, and were shown, for all transitions ($^5D_0 \rightarrow {}^7F_J$, where $J = 1 - 4$) to be opposite on comparison, thus, reinforcing the earlier CD studies for the diastereoselective formation of an enantiomeric complex pair (Figure 5.10). Additionally,

the shape and sign of the emission bands for the (*S*) and (*R*) stereochemical assignments corresponded to those found for the original sliotar complexes **Eu.32S/R$_3$** and the analogues in Chapters 2 – 4 *i.e.* all (*S*) matched (*S*), and likewise for (*R*). Rooted in this correlation, the metal stereochemistry of **Eu.72S** and **Eu.72R (M:L = 2:3)** could be assigned as Δ and Λ, respectively (see Section 2.8).

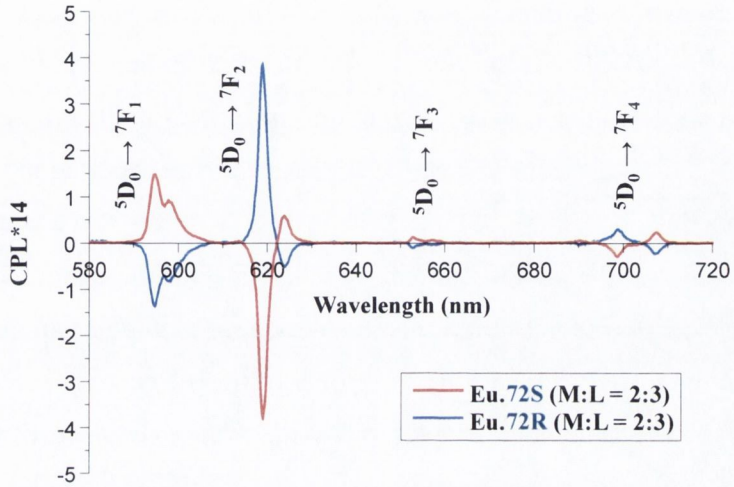

Figure 5.10 *CPL emission spectra of* ***Eu.72S*** *and* ***Eu.72R (M:L = 2:3)*** *recorded in $CHCl_3$/ CH_3CN (1:1; v/v) at 298 K (λ_{exc} = 281 nm).*

Using **Equation 1.4** (see Section 1.5.1), the luminescence dissymmetry factors (g_{lum}) were then calculated for the J = 1 and 2 transitions, with the values listed in Table 5.4. The values for both enantiomers were found to be in good agreement, with slightly larger values obtained at 595 nm due to the magnetic-dipole nature of the J = 1 emission band.[240,302] Of keen interest was the close similarity of these values to those calculated for the monometallic sliotar derivatives in Chapter 2 (see Table 2.4), therefore, proving that the degree of chirality experienced by the ions in these more advanced multimetallic complexes was comparable.

Table 5.4: *Summary of the g_{lum} dissymmetry factor values calculated from the CPL spectra of* ***Eu.72S*** *and* ***Eu.72R (M:L = 2:3)*** *for the J = 1 and 2 transitions at 595 nm and 619 nm, respectively.*

Complex	g_{lum} value 595 nm (J = 1)	g_{lum} value 619 nm (J = 2)
Eu.72S	+ 0.25	− 0.24
Eu.72R	− 0.25	+ 0.20

5.8 Conclusion

Motivated by an ambition to form structurally elegant supramolecular edifices, this chapter has concentrated on the design and development of chiral multimetallic Eu(III) self-assemblies. In order to meet this research objective, the chiral ligands **72S** (*S,S,S,S*) and **72R** (*R,R,R,R*) were synthesised, these essentially consisting of two sliotar binding units bridged together by a polyethoxy linker chain at their pyridyl 4-positions. Through incorporation of an additional coordinating terminus, these ditopic sliotar ligand variants were anticipated to facilitate the creation of polynuclear complex structures. Simultaneously, this work, which represented an extension of the sliotar design to multimetallic Ln(III) synthesis, was intended to supplement the studies of the monometallic sliotar analogues reported in Chapters 2 – 4.

At the start, this chapter was concerned with the synthesis and characterisation of the ligands **72S/R**. Based on the added complexity inherent with the extra coordinating group, one could not confidently predict in advance the structural topologies and compositions that would result from the Eu(III)-directed self-assembly of these ligands. Therefore, with a view to stoichiometric M:L elucidation, parallel UV-vis and luminescence titrations were next conducted to analyse the complexation process *in situ*, prior to complex formation using synthetic methods. The trends noticed in the titration binding isotherms were deemed to suggest the predominance of the 2:3 (M:L) complex stoichiometry, a fact later confirmed through fitting the phosphorescence spectral changes with SPECFIT®. Indeed, this system was proven to form with high stability, which in turn, yielded high percentage formation. Intriguingly, the 2:3 (M:L) complex ratio was also identified for chiral bimetallic triple-stranded helicates developed before in the Gunnlaugsson group.[228-230] However, in the titrations of **72S/R**, the phosphorescence spectra were distinguished by the emergence of a split in the $J = 2$ emission band, a split which was not observed for either the aforementioned helicates or monometallic sliotar complexes. Reaching maximal intensity at *ca.* 0.7 eq. of Eu(III), this band split was taken to imply a relative change in the site symmetry around the metal ions, thus, advancing the theory that the 2:3 (M:L) systems generated from ligands **72S/R** were structurally different to the helicates. Still satisfying the 2:3 (M:L) fit, a possible structure that can be proposed is one comprised of six ligand molecules and four Eu(III) ions, with these ions positioned at the four vertices of a tetrahedron. Regrettably, SPECFIT® only perceives M:L ratios, and cannot distinguish between different structural forms *e.g.* 2:3, 4:6, 6:9, *etc.*

Transferring the knowledge gained in the titrations to synthetic procedure, ligands **72S/R** were each complexed using 0.67 eq. of $Eu(CF_3SO_3)_3$ *i.e.* M:L = 2:3. Successful Eu(III)-coordination was manifested in the ^1H NMR complex spectra by a broadening and

shifting of the resonances. More specifically, metal-binding by the amide carbonyl groups was indicated by a determined shift in their IR frequency to a lower energy. In terms of composition, elemental analysis verified the 2:3 (M:L) stoichiometry for the synthesised complexes, therefore, establishing that this multimetallic design could be achieved both synthetically and *in situ*. To further corroborate the 2:3 (M:L) composition, the complex hydration states (q) were calculated following the performance of luminescent lifetime measurements in water (H_2O and D_2O). As expected, q values ≈ 0 were obtained for both **Eu.72S** and **Eu.72R**, informing of complete Eu(III) saturation by the ligands.

Through the employment of chiral ligands, the polymetallic assemblies **Eu.72S/R (M:L = 2:3)** were envisaged to form as an enantiopure pair themselves, as a result of asymmetric induction. Utilising both CD and CPL techniques, the spectra recorded for the two complexes were shown to be perfectly opposite in each case, thus, verifying on two fronts (absorption and emission) the opposing helicity of **Eu.72S** and **Eu.72R (M:L = 2:3)**. Owing to the spectral correlation with previous sliotar analogues, the CPL analysis further permitted the assignment of the metal stereochemistry, which was labelled Δ and Λ for **Eu.72S** and **Eu.72R (M:L = 2:3)**, respectively.

The evidence communicated throughout this chapter, notably that acquired from the spectrophotometric titration analysis, has conclusively demonstrated the self-assembly of chiral luminescent multimetallic constructs with 2:3 (M:L) stoichiometry. However, future efforts will be required to address unanswered questions pertaining to the precise structure and make-up of these systems, with X-ray crystallography and/or mass spectrometry proof essential. In spite of this drawback, these novel polynuclear edifices serve to accentuate, along with the previously developed Ln(III) helicates,[228-230] the flexibility of the chiral sliotar design to multimetallic system development.

Chapter 6

Development of Multimeric Ternary Lanthanide-Cyclen Systems for Application in Anion Sensing

6 Introduction

Expanding their expertise for metal-directed methodologies, the Gunnlaugsson group have amassed considerable experience in the self-assembly of ternary Ln(III) complexes. Originally developed from the aza-macrocyclic cyclen framework, these systems have been skilfully employed for the detection of an extensive range of analytes, from simple ions to larger biomolecules, *via* a modulation of the Ln(III)-centred luminescent output.[218,303] Indeed, luminescent Ln(III) sensors have emerged as attractive research targets in recent times, stemming from their ability to address many of the shortcomings of traditional fluorescent sensors.[20,304] As explained in Section 1.1.2, the Ln(III) ions possess long-lived excited states, in the ms range, giving rise to time-delayed emissions. On this time scale, the light scattering and short-lived autofluorescence (ns) of the biological background is dramatically reduced, which results in an enhanced signal-to-noise ratio for luminescent Ln(III) complexes relative to their fluorescent counterparts, therefore, making them invaluable for sensing in biological media.[42,47,48]

The first forays within the group towards the design of functional supramolecular ternary systems involved the use of kinetically stable coordinatively unsaturated cyclen complexes (**Ln.75**; where Ln = Eu or Tb), constructed from the heptadentate ligand **75**.[303,305-307]

Ln.75

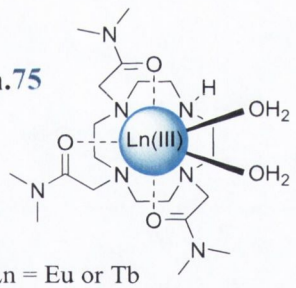

Ln = Eu or Tb

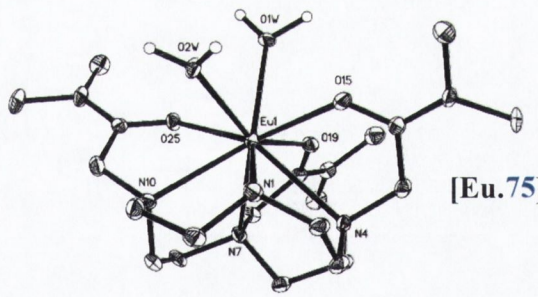

[Eu.75](H$_2$O)$_2$

76

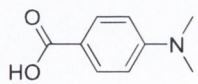

77

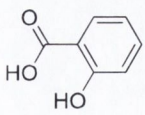

78

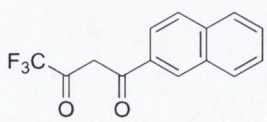

Notable from the structure of **75**, however, was the lack of a covalently attached antenna for Ln(III)-sensitisation. Nevertheless, the omission of a sensitising chromophore was an intentional design feature, with a *switching on* of the metal-centred emission envisaged upon administering a suitable non-covalently linked antenna to **Ln.75**. The foundation for this assumption was drawn from earlier work by Parker *et al.*, which showed

analogous complexes to possess two metal-bound water molecules.[308,309] With the same predicted for **Ln.75**, it was anticipated that displacement of these labile water molecules by an independent chromophoric unit would provide for a ternary complex displaying large luminescence enhancements.

Regarding **Ln.75**, both X-ray crystallographic analysis and q value determination verified the presence of two water molecules within the first coordination sphere of the Eu(III) and Tb(III) complexes. To assess the potential for ternary complex formation and subsequent sensitisation, tests with a number of aromatic carboxylates were undertaken in water. In the case of **Tb.75**, *N*,*N*-dimethylaminobenzoic acid (**76**) and salicylic acid (**77**) proved especially efficient in sensitising the Tb(III) emission, which was observed to be *switched on*, an observation not true of the Eu(III) analogue.[303,305] Upon addition of either antenna, q values were ascertained to be ≈ 0, indicative of the expulsion of metal-bound water and the self-assembly of a ternary system. Furthermore, photophysical titrations in water (buffered at pH 7.4) evidenced the predicted 1:1 stoichiometry between antenna and complex for both examples. Moving in a more functional direction, utilisation of an aromatic β-diketone antenna (**78**) was later effected to afford a ternary Eu(III) complex (**78-Eu.75**) with anion sensing capabilities.[307] Inspired by Anslyn *et al.*,[310,311] the ability of **78-Eu.75** to detect anions was capably demonstrated in a number of luminescent displacement assays, whereby appropriate anions were shown to supplant the coordinated antenna, leading to a reduction in emission intensity.

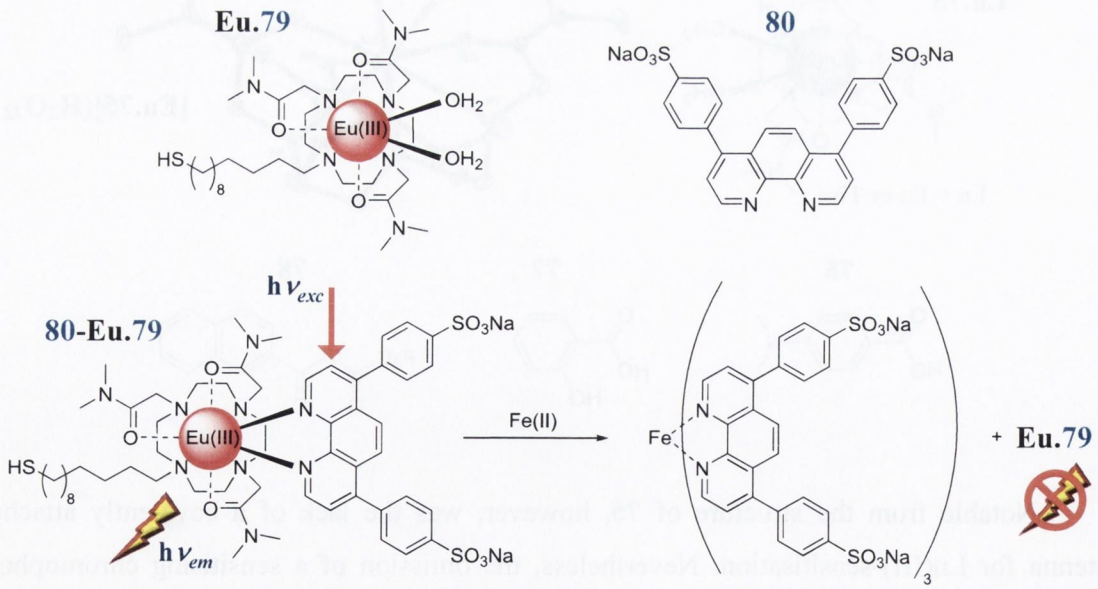

Scheme 6.1: *Schematic illustration of the emissive ternary complex* ***80-Eu.79****, a sensor for Fe(II) that operated by antenna displacement quenching the metal-centred luminescence.*[33]

Applying the same principles of antenna displacement, **80-Eu.79** was developed with a view to sensing *d*-block cations; Fe(II) in this particular instance.[33] The basis for this sensing function derives from the fact that the 4,7-diphenyl-1,10-phenanthroline-disulfonate chromophore (**80**), although an efficient chelator and sensitiser of Eu(III), exhibits preferential binding to Fe(II).[28,86] Naturally, addition of Fe(II) was found to trigger de-assembly of the ternary system and *switch off* luminescence, with this process driven by the formation of robustly stable **Fe.80$_3$**. Moreover, the selectivity of **80-Eu.79** for Fe(II) over Zn(II) was conclusively established in competitive photophysical titrations.

Enabled by the presence of a long alkyl thiol chain, **Eu.79** has since been used for adsorption onto the surface of gold nanoparticles (AuNPs). For specific projects, the resultant nanoparticulate conjugate (**Eu.79-AuNP**) was then administered an antenna in the form of the previously mentioned naphthyl β-diketone **78** to yield the ternary system **78-Eu.79-AuNP**.[218,220] Effectively marrying the advantageous properties of two chemically distinct entities, application of such luminescent surface-functionalised AuNPs in fields such as sensing, signifies an emerging discipline in modern supramolecular chemistry.[218,220,312]

81

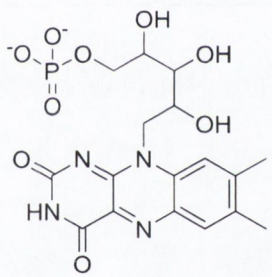

Using **78-Eu.79-AuNP**, early endeavours in this area were dedicated to the detection of biologically relevant phosphates, for example flavin monophosphate (**81**), in buffered aqueous solution (pH 7.4).[220] Analogous to the models discussed previously, sensing of the analyte manifested as a quenching of the Eu(III) emission, observed upon displacement of the bound antenna moiety (**78**) by the anion. For the mononucleotide **81**, almost complete quenching was noted, evidential of the formation of non-emissive **81-Eu.79-AuNP**.

Extending studies to larger biomolecules, **78-Eu.79-AuNP** has been employed more recently to sense bovine serum albumin (BSA), a protein that is the main plasma carrier for a wealth of endogenous and exogenous substances.[218] As before, an appreciable reduction in the luminescent output was identified following sequential addition of the analyte. Conversely, intensive and varied spectroscopic analysis confirmed that the quenching seen, on this occasion, was not a product of antenna removal. In fact, quenching was unequivocally

proven to originate from a strong interaction between the β-diketone and BSA protein, with **78-Eu.79-AuNP** remaining intact throughout.

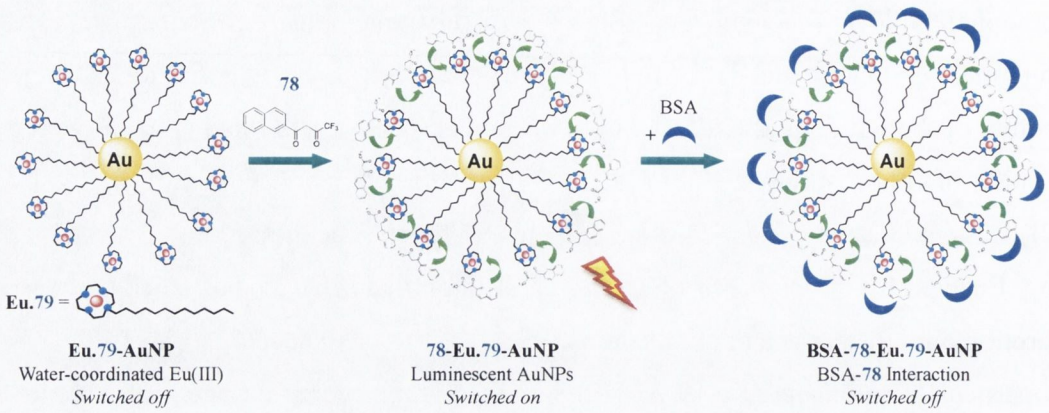

Figure 6.1: *Cartoon depiction of (left to right)* ***Eu.79-AuNP****,* ***78-Eu.79-AuNP****, and* ***BSA-78-Eu.79-AuNP****. The Eu(III)-centred emission was switched on following addition of antenna* ***78****. Switching off was subsequently triggered by the interaction of BSA with* ***78****.*[218]

In recent years, the Gunnlaugsson group have advanced the development of ternary Ln(III)-cyclen complexes through the incorporation of NIR-emitting Ln(III) ions.[207,219] The advantages of these ions *e.g.* low energy emissions with improved tissue penetration,[313,314] are numerous and are discussed in greater detail in Section 1.3.1.

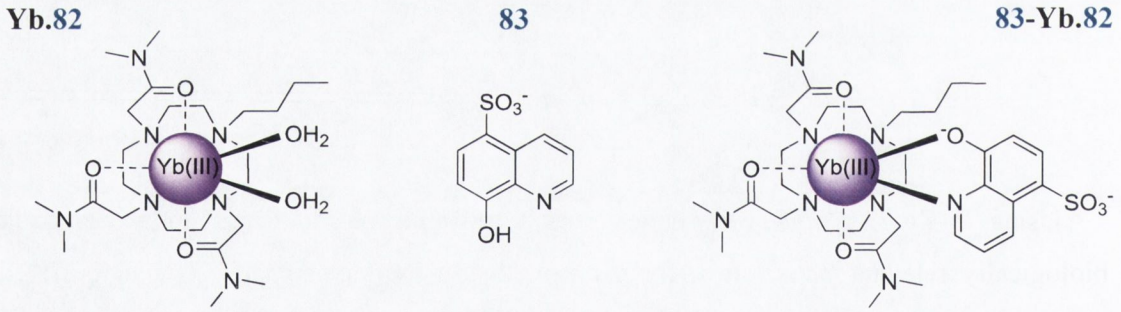

Reported in a 2012 publication, the novel Yb(III) complex **Yb.82** was shown to display emission in the NIR range upon binding of the sulfonated 8-hydroxyquinoline sensitiser (**83**) in buffered aqueous solution (pH 7.4).[207] The resulting ternary assembly (**83-Yb.82**) was further deployed as a dual emissive Zn(II) sensor, progressing by the familiar route of antenna displacement with Zn(II) addition *switching off* emission. Reference to its dual emissive properties was born from the intense ligand-centred green fluorescence exhibited by the Zn(II)-chelate of **83**, which was formed as a by-product. Consequently, two different emission channels, both visible and NIR, could be simultaneously monitored to probe the Zn(II)-binding event.

Yb.79

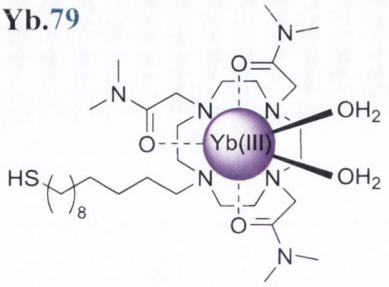

84

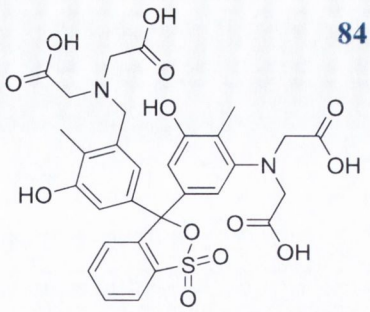

Gunnlaugsson *et al.* later managed to functionalise the surface of AuNPs with the ternary Yb(III) complex of ligand **79** (**Yb.79**), successfully achieving emission upon coordination of visible-absorbing xylenol orange (**84**).[219] These functionalised AuNPs (**84-Yb.79-AuNP**) represented the first example of NIR-emitting Ln(III)-based AuNPs, and were extremely attractive from a potential biomedical viewpoint, owing to their aqueous solubility and long wavelength excitation wavelengths (up to 600 nm).

Tb_2.85

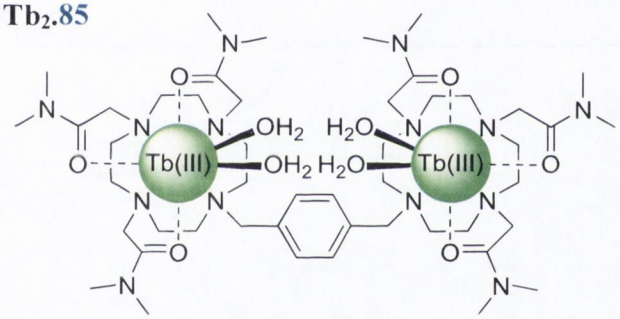

More relevant to this particular project was the development of the xylyl-containing di-lanthanide complex **Tb_2.85**, which was designed with the purpose of sensing aromatic dicarboxylates.[315] Indeed, this complex was shown to detect the presence of both mono and bisaromatic carboxylates, such as terephthalic acid, in buffered aqueous solution (pH 7.4). The mode of sensing in this example again centred around the expulsion of metal bound water by the antenna, thus, leading to significant enhancements of the Tb(III) ion emission. Contrastingly, the recognition process involving tartaric acid resulted in quenching of the emission.

This introductory section summarises some of the more recent and relevant advances in the development of ternary cyclen systems within the Gunnlaugsson group. Additionally, it serves to illustrate how such structures can be self-assembled, de-assembled, structurally altered, or their function modulated by a range of chemical inputs. The work described

herein, therefore, offers as a prelude and source of inspiration to the research described throughout the remainder of Chapter 6. More specifically, the majority of this chapter is dedicated to investigating the formation of dimeric ternary Ln(III)-cyclen self-assemblies **86-(Ln.75)$_2$** (where Ln = Eu or Tb), with the anion sensing ability of the Tb(III) analogue showcased in a number of displacement assays. To complement this work, discussion will later shift to the development of novel trimeric ternary Ln(III)-cyclen complexes **87-(Ln.75)$_3$** (where Ln = Eu or Tb), with keen emphasis placed on photophysical characterisation of the resulting system.

86-(Ln.75)$_2$

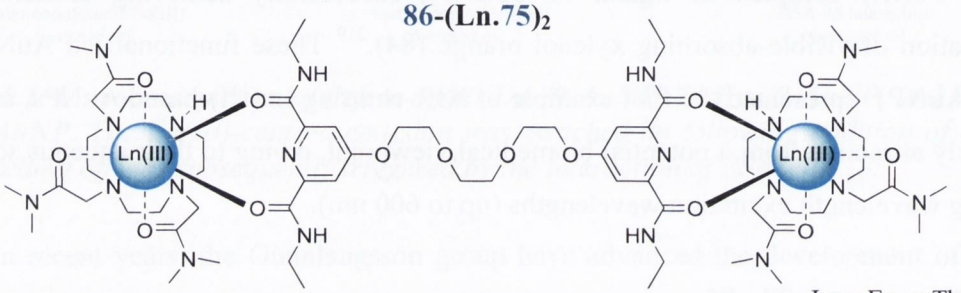

87-(Ln.75)$_3$

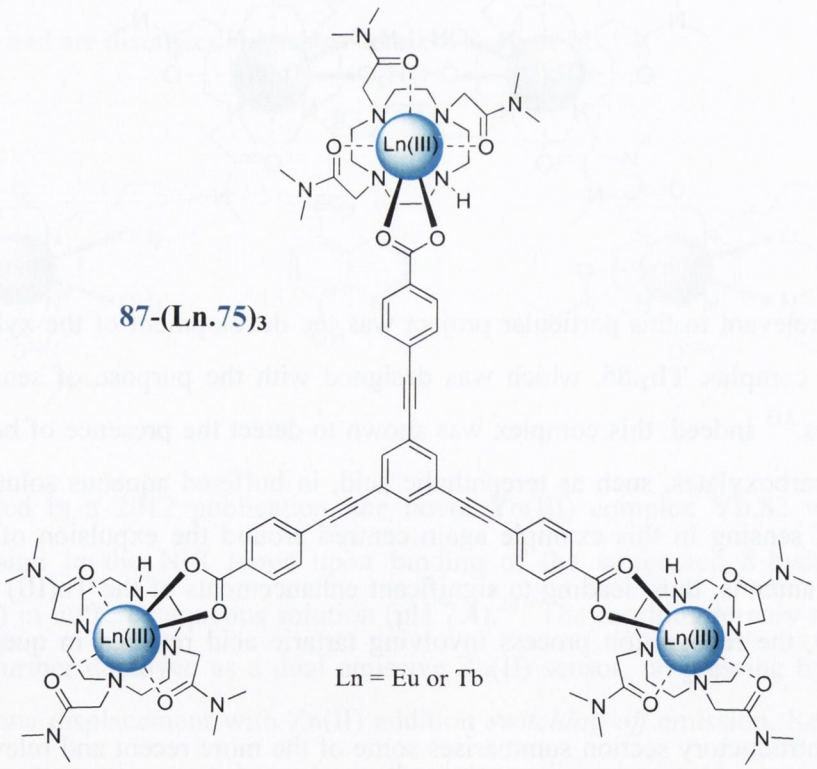

6.1 Design of the dimeric ternary cyclen complex **86**-(**Ln.75**)$_2$

Heptadentate coordinatively unsaturated complex **Ln.75**, previously designed within the group, was selected for use to develop novel dimeric ternary Ln(III)-cyclen complexes. This triacetamide-substituted cyclen derivative does not possess a chromophore covalently attached to the ligand skeleton to facilitate Ln(III)-sensitisation. As a result, the complex is non-emissive and may be described as being *photophysically silent*. In spite of this, earlier work showed that the two Ln(III)-coordinated water molecules can be readily displaced in the presence of a suitable metal-chelating antenna, thus, *switching on* luminescence. In this particular case, ditopic ligand **86**, a variant of the dpa framework comprising two discrete metal ion-binding pockets, was designed to function as the antenna and displace the water molecules. As specified in Section 1.4.1, dpa-derivatised ligands are capable of producing high stability self-assemblies with the Ln(III) ions.[128] Relevant to this work, their application has been extended to fulfilling the role as sensitiser in ternary Ln(III)-cyclen systems, as demonstrated by Ponce *et al.*[316] Furthermore, dpa is known for efficient population of the excited states of visible-emitting Eu(III) and Tb(III) and, for that reason, **Eu.75** and **Tb.75** were chosen for ternary self-assembly.[116]

The ditopic ligand **86** was predicted to bind two molecules of complex **Ln.75**, one at each end, to grant a system with 1:2 (L:C) stoichiometry (where L:C represents the ligand to complex ratio). In this design, the two Ln(III)-cyclen termini would be bridged by the ligand polyethoxy chain, whose inclusion in the structure was implemented to aid solubility in polar media. Ligand **86** is essentially the tetraethyl-amide analogue of **72S/R**, the ligand central to discussion in Chapter 5. For this specific project, the decision to opt for achiral **86** ahead of its chiral naphthyl derivative **72S/R**, was made in anticipation of the latter ligands being too bulky for optimal Ln(III)-coordination (this prediction for **72S/R** was tested and confirmed, with minimal Ln(III) emission observed and no clear trend identified in the data). Regardless of this, the similarities between the two are strong enough to propose that this research exemplifies a practical combination of the sliotar and ternary complex self-assembly work.

With regards to a potential application for this complex system, it was foreseen that the coordinating antenna, ligand **86**, would be displaced from the metal ion core by a more strongly chelating anion.[303,317] As witnessed previously,[220,307] anion-induced displacement would be reflected by a *switching off* of the emission, **Ln.75** being poorly luminescent in the absence of a chromophore. Subject to this behaviour holding true of **86**-(**Ln.75**)$_2$, the ternary species may be considered as a novel luminescent anion sensor. A schematic representation of the formation of the dimeric ternary complex and its hypothesised mode of action as an anion sensor is illustrated below in Scheme 6.2.

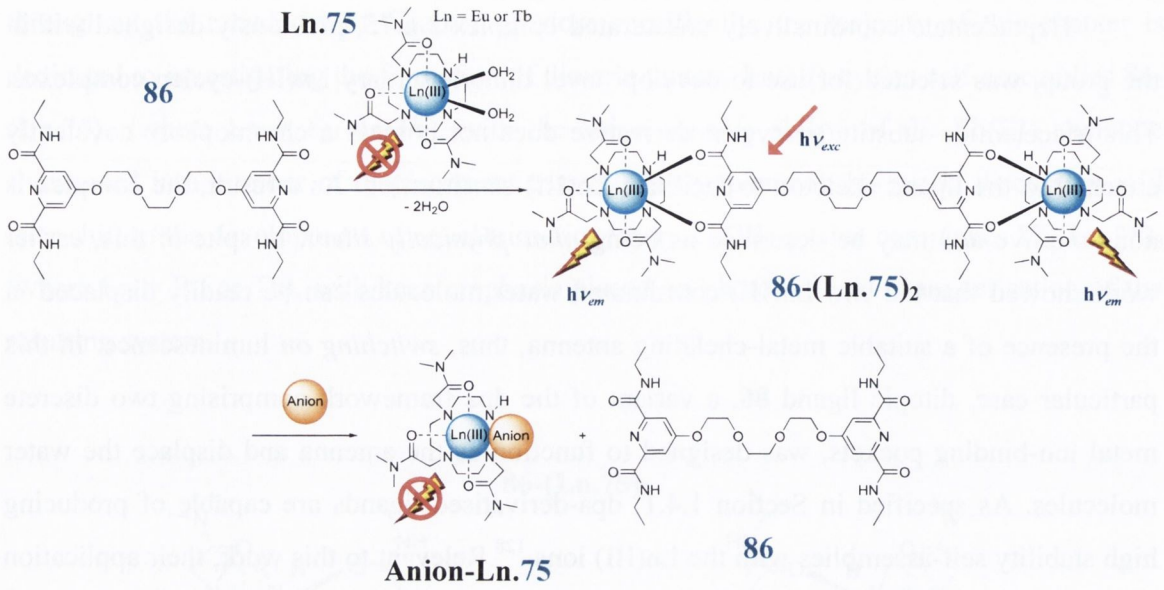

Scheme 6.2: *Schematic illustration of the formation of the ternary assembly* ***86-(Ln.75)$_2$****, accompanied by the switching on of the metal-centred luminescence. Subsequent addition of the anion was envisaged to displace ligand* ***86****, and switch off the luminescence.*

The ultimate goal of this design was to construct novel ternary Ln(III) systems, and to establish, through a series of displacement assays, applicability for anion sensing. The next section will deliver an account of the synthesis and characterisation of ligand **86**, and the complexes **Eu.75** and **Tb.75**.

6.2 Synthesis and characterisation of ligand 86 and complex Ln.75

Ligand **86** was designed with the aim of linking two molecules of complex **Ln.75**, with each dpa-derived end enacting the dual role of both Ln(III)-coordinator and -sensitiser. Accordingly, ligand development required the synthesis of a reactive chain intermediate to join two independent dpa units. To fulfil this function, the di-iodo-polyethoxy reagent **74**, used previously in the synthesis of ligands **72S/R**, was employed. This compound was made by adhering to the synthetic procedure shown in Scheme 5.1 (Section 5.2).

The first step prior to incorporation of the dpa component of ditopic **86** into the final ligand structure was the protection, *via* acid-catalysed esterification, of the two carboxylic acid groups of chelidamic acid (Scheme 6.3).[318] Esterification was achieved by refluxing chelidamic acid with sulphuric acid in EtOH for 4 h. Thereafter, the reaction solution was neutralised with a saturated aqueous solution of $NaHCO_3$ and extracted with CH_2Cl_2. Solvent evaporation afforded the di-ethyl ester product **88** as a pale yellow oil in 70% yield, an oil

which later solidified upon drying under vacuum. ^{1}H-NMR spectroscopy supplied evidence of product formation, with the presence of a quartet at 4.46 ppm and a triplet at 1.42 ppm identifiable, these signals corresponding to the ethyl CH_2 and CH_3 groups, respectively.

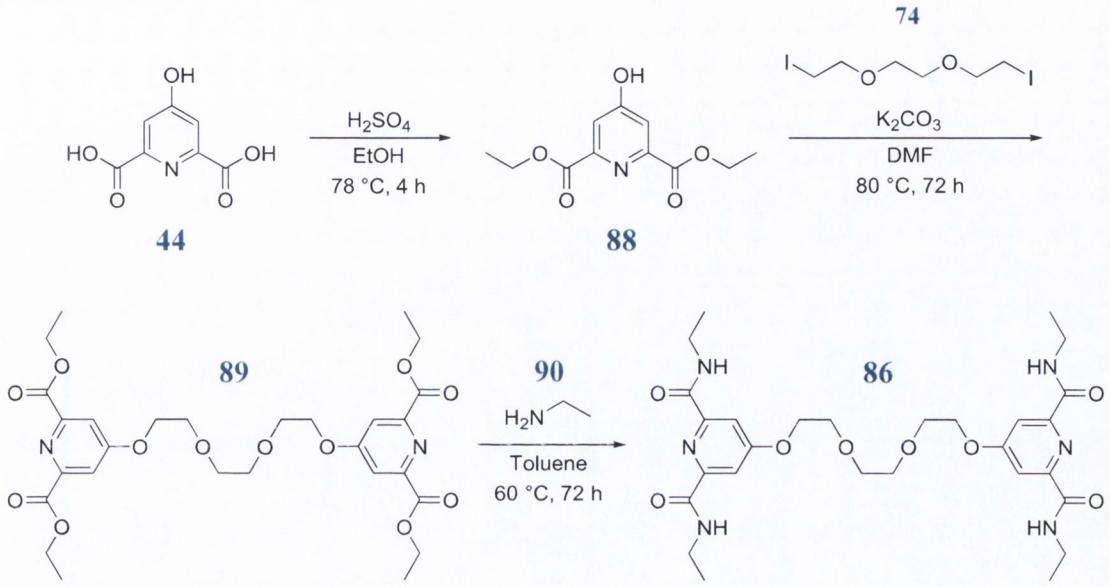

Scheme 6.3: *Synthetic pathway for* ***86****.*

Following this, the introduction of a molecule of **88** to each end of the linker reagent **74** was accomplished through nucleophilic substitution of the chain C-I bonds by the pyridyl *para*-hydroxy group (Scheme 6.3).[237] This reaction involved initial stirring of **88** with K_2CO_3 in anhydrous DMF for 30 min at 25 °C, before adding **74** and heating at 80 °C for a further 72 h. An excess of **88** relative to **74** (2.2:1.0 eq.) was used to ensure attachment at both chain termini. After completion, the solvent was removed and the residue dissolved in CH_2Cl_2. Washing with both 1% acetic acid (aqueous) and H_2O, and recrystallising from EtOH gave the desired tetra-ester **89** as a white solid in 44% yield. The ^{1}H NMR spectrum revealed a singlet at 7.80 ppm and three distinct resonances further upfield in the range of 4.30 – 3.74 ppm. These signals were assigned to the pyridine CH and linker CH_2 protons, respectively, and confirmed appendage of the chain.

The final step of the synthetic pathway was committed to converting the ester groups of **89** into the equivalent ethyl amides (Scheme 6.3). To execute this transformation, **89** and ethylamine (40% *w/v* in toluene) were stirred together at 60 °C for 72 h, with no further solvent addition. The reaction mixture was then poured over ice and the resulting brown precipitate filtered upon melting of the ice. Dissolution of the precipitate in CH_2Cl_2, H_2O washing of the organic phase, and final purification by flash silica column chromatography

(gradient elution 100:0 → 95:5; CH_2Cl_2/MeOH) gave **86** as a white solid in 32% yield. In order to verify product formation, a variety of characterisation techniques were availed of, the full details of which can be found in the experimental section of Chapter 7.

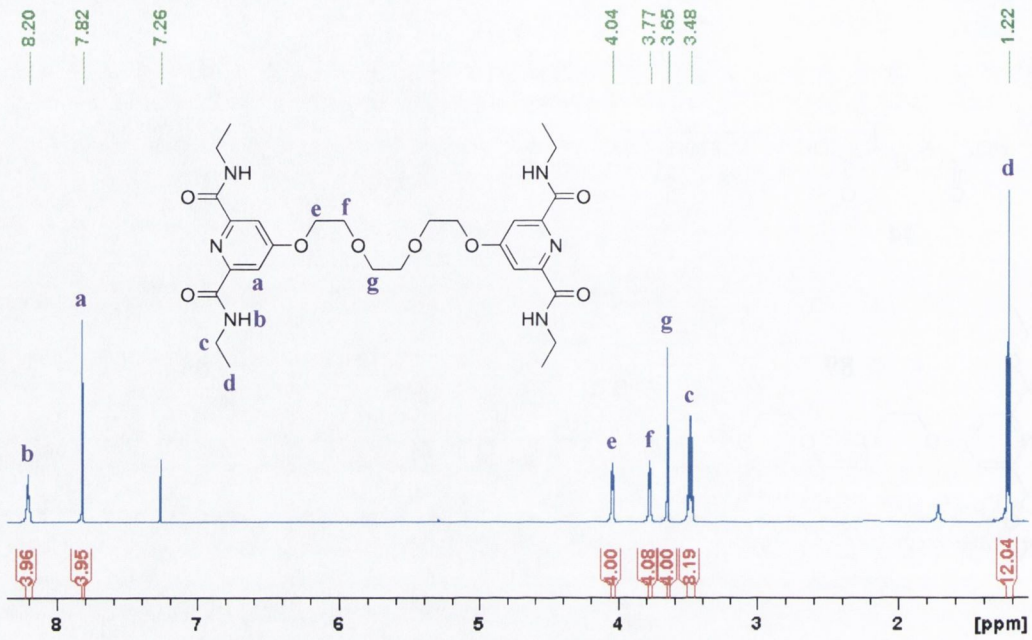

Figure 6.2: *^{1}H NMR (600 MHz, $CDCl_3$) spectrum of ligand **86**.*

In the ^{1}H NMR spectrum (see Figure 6.2), the downfield region contained a singlet at 7.82 ppm representing the pyridyl proton, and a triplet resonance at 8.20 ppm correlating to the newly constituted NH protons. This finding was supplemented by an observable upfield shift of the ethyl CH_2 and CH_3 signals at 3.48 ppm and 1.22 ppm, respectively. This shifting effect, most pronounced in the case of the adjacent CH_2 protons, can be accredited to the reduced electronegativity of nitrogen relative to oxygen. Further proof of conversion to the amide was provided by electrospray mass spectrometry (ES^+), from which a peak at m/z = 611.2805, attributed to the $[M + Na]^+$ species in solution, was detected.

Both the synthesis and characterisation of the cyclen compound **75** and its Ln(III) complexes, **Ln.75**, (where Ln = Eu or Tb) have been reported by the Gunnlaugsson group previously.[303,305,306] Therefore, in this thesis, discussion pertaining to these molecules has been kept to a minimum. All relevant experimental procedures, however, can be found in Chapter 7. For the experiments described hereafter, **75** and **Ln.75** where freshly synthesised according to the synthetic protocol shown in Scheme 6.4. The first step was the reaction of cyclen and 2-chloro-*N*,*N*-dimethylacetamide (**92**) in a 1:3 molar ratio to give ligand **75**, followed by complexation with the $Ln(CF_3SO_3)_3$ salt, Eu(III) or Tb(III), to form **Ln.75**.

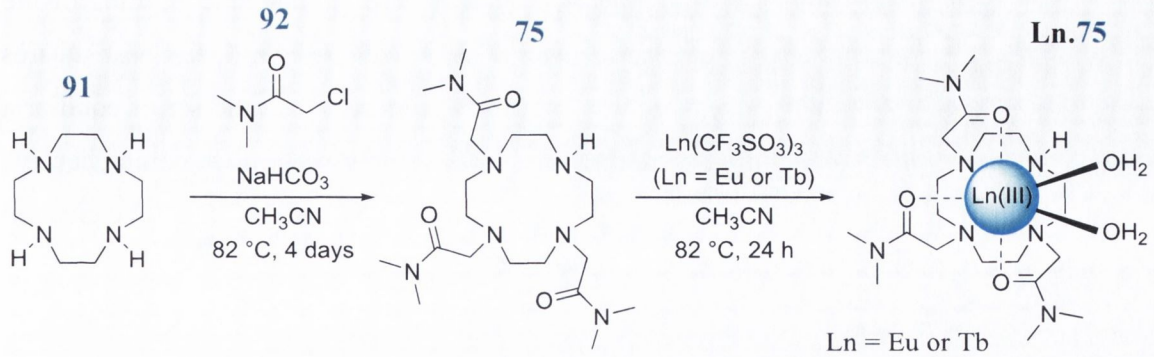

Scheme 6.4: *Synthetic pathway for ligand 75 and its Ln(III) complex* ***Ln.75*** *(where Ln = Eu or Tb).*

6.3 UV-vis and luminescence titration studies of 86 and Ln.75

Having successfully synthesised the requisite components, **86** and **Ln.75**, the next challenge was to monitor their self-assembly in solution through a series of photophysical titrations. These were devised to evaluate whether, as per Scheme 6.2, the predicted ternary complex **86**-(**Ln.75**)$_2$ could be formed, and were conducted by the so-called dilution method (see Section 2.10). Using this method, one anticipated a progressive *switching on* of the metal ion-centred emission upon addition of **Ln.75**, therefore, signalling direct coordination of **86** to the cyclen-bound Ln(III) ion. The recorded data was subsequently treated by non-linear least squares regression analysis to ascertain the stoichiometric species present, and their respective speciations and binding constants.

6.3.1 Titration experimental and data fitting details

The titration studies in the next two sections were conducted in MeOH for solubility reasons. In each case, a stock solution (3 mL; 1×10^{-5} M) of ligand **86** was prepared and titrated against known volumes of a standard solution of either complex **Eu.75** or **Tb.75**. After each addition, UV-vis absorption and phosphorescence spectra were recorded after 5 min of equilibration.

$$\mathbf{86} + \mathbf{Ln.75} \overset{K_{1:1}}{\rightleftharpoons} \mathbf{86\text{-}Ln.75} \qquad \textbf{Equation 6.1}$$

$$\mathbf{86\text{-}Ln.75} + \mathbf{Ln.75} \overset{K_{1:2}}{\rightleftharpoons} \mathbf{86\text{-}(Ln.75)_2} \qquad \textbf{Equation 6.2}$$

$$\beta_{1:2} = K_{1:1} \times K_{1:2} \qquad \textbf{Equation 6.3}$$

All titrations were repeated in triplicate to ensure full reproducibility. Fitting of the phosphorescence spectral changes was later accomplished with the non-linear least squares regression program SPECFIT® (see Section 2.10.5) by conforming to the set of equilibria equations **Equation 6.1 – 6.3** used to define this self-assembly process. A comprehensive report of the UV-vis and luminescence titrations of **86** with **Eu.75** and **Tb.75** will be given in the next two sections, beginning with the former.

6.3.2 UV-vis and luminescence titrations of 86 with Eu.75 in MeOH

The self-assembly of a ternary complex in MeOH was first probed by analysing the changes in the UV-vis absorption spectrum of **86** with additions of **Eu.75**. Prior to Eu(III) complex addition, the absorption spectrum displayed one main band assigned to the pyridyl π-π^* transitions, which was spread over a wide wavelength range (*ca.* 200 – 287 nm) and possessed a high energy maximum at 214 nm (ε = 75662 M^{-1} cm^{-1}). This ligand spectrum was found to experience hyperchromism when aliquots of **Eu.75** were added, with the most significant changes occurring between 0 and 2 eq. of complex, although no isosbestic point was observed (see Figure 6.3a). Indeed, the titration profiles (see Figure 6.3b) revealed a sharp, regular increase in absorbance up to *ca.* 2 eq. of **Eu.75**, after which the increase which became comparably less severe. Such a trend supported the formation of a 1:2 (L:C) ternary system between **86** and **Eu.75** in solution.

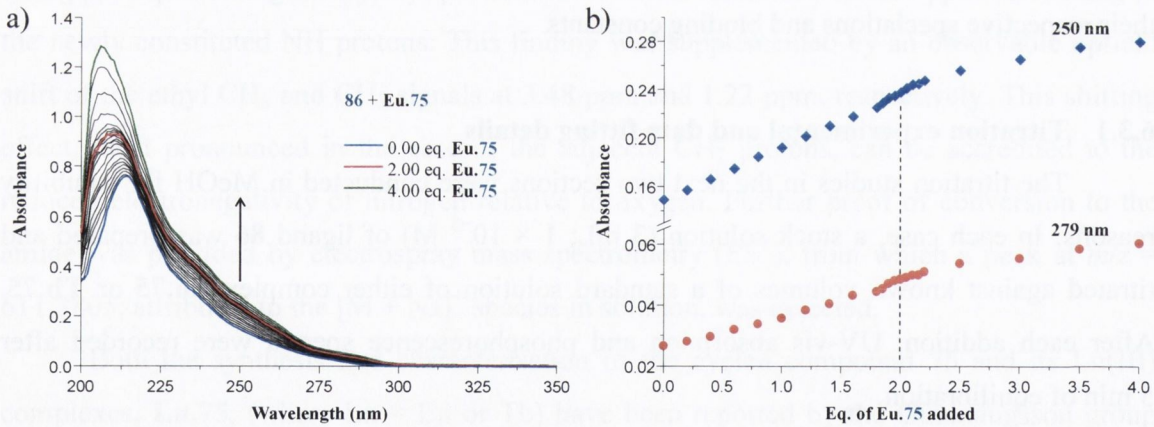

Figure 6.3: *a) Changes in the absorption spectra of **86** (1×10^{-5} M) upon titrating with complex **Eu.75** (0.00 → 4.00 eq.) in MeOH at 298 K. b) Binding isotherms for the titration measured at 250 nm and 279 nm.*

With dpa and its derivatives renowned for efficient sensitisation of visible-emitting Ln(III) ions,[116] the self-assembly process was further studied by monitoring the evolution of the phosphorescence emission by titration. As previously explained, **Ln.75** (Ln = Eu or Tb)

is non-emissive due to the absence of a chromophore within the cyclen structure. However, upon titrating **86** with **Eu.75**, the characteristic Eu(III)-centred emission was observed to be *switched on*, indicative of coordination between the dpa motif and Ln(III) ion (Figure 6.4a). The emission bands in the resultant spectra can be ascribed to the $^5D_0 \rightarrow {}^7F_J$ transitions of Eu(III); where $J = 0$ (580 nm), 1 (split; 592 and 594 nm), 2 (split; 616 and 620 nm), 3 (650 nm), and 4 (split; 689, 694, 697, and 703 nm). The presence of the $J = 0$ band throughout was suggestive of a lack of symmetry at the Ln(III) ion in the final assembly.[239] Moreover, all bands underwent an increase in intensity, albeit with no structural change, upon additions of the complex. This enhancement can be seen in the binding isotherms at 594 nm and 616 nm (Figure 6.4b), which showed luminescence to increase for up to *ca.* 2 eq. of complex before gradually levelling, this trend further implying the predominance of the **86-(Eu.75)$_2$** ternary species. Eu(III)-sensitisation was also established by recording excitation spectra at various stages of the titration (Figure A6.2). These spectra closely matched the absorption spectra and assured sensitisation of the luminescence to occur through bound ligand only.

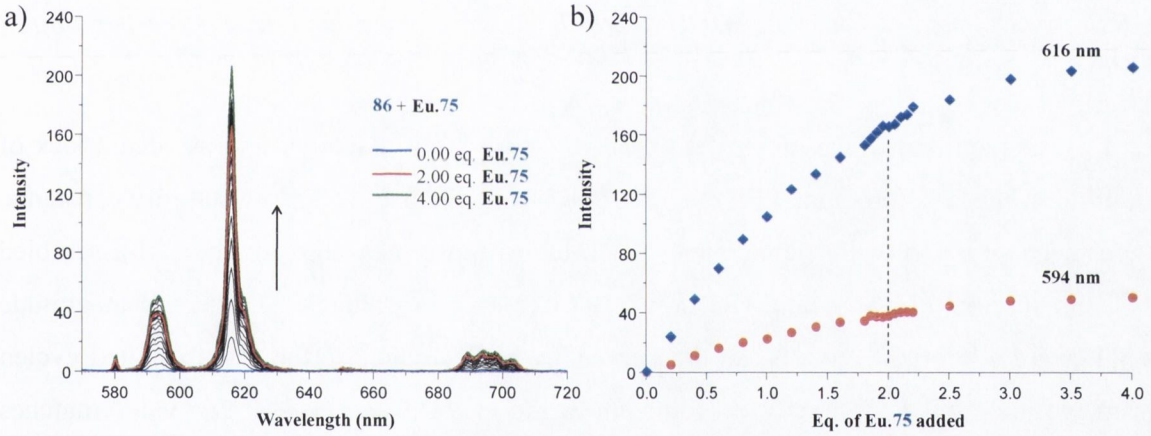

Figure 6.4: *a) Evolution of the phosphorescence emission in the titration of* **86** *(1×10^{-5} M) with complex* **Eu.75** *(0.00 → 4.00 eq.) in MeOH at 298 K (λ_{exc} = 279 nm). b) Binding isotherms for the titration measured at 594 nm and 616 nm.*

Identification of the stoichiometric species present was made possible by fitting the phosphorescence spectral changes with SPECFIT®. In the case of the **Eu.75** titration, the excellent fit obtained disclosed the formation of two luminescent ternary complexes, **86-Eu.75** and **86-(Eu.75)$_2$** (Figure 6.5), with formation of the desired dimeric product validating the design strategy used. Binding constants were calculated as $\log \beta_{1:1} = 4.93 \pm 0.22$ and $\log \beta_{1:2} = 10.42 \pm 0.09$, respectively (Table 6.1). Based on these values, the individual stepwise constants can be described as being approximately additive, meaning that one can assume that coordination of the first molecule of **Eu.75** does not impede binding of the second. In

reference to product evolution and distribution, the associated speciation graph exposed a slight preference for the 1:1 (L:C) stoichiometry up until *ca.* 1 eq. of **Eu.75**. Beyond this point, however, assembly of the 1:2 (L:C) system was found to take precedence. In fact, the percentage formation of this species continued to rise up to titration completion (4 eq. of **Eu.75**), at which point, the value stood at 81%.

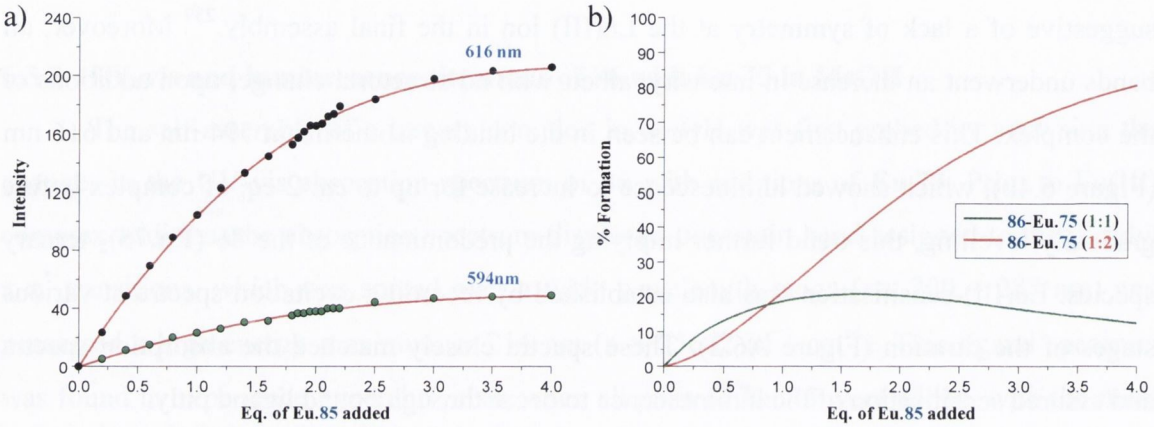

Figure 6.5: *a) Experimental binding isotherms for the phosphorescence titration of* **86** *(1×10^{-5} M) with complex* ***Eu.75*** *in MeOH at 298 K (λ_{exc} = 279 nm) and their corresponding fit by means of SPECFIT. b) Speciation-distribution diagram obtained from the fit.*

The requirement for an excess of **Eu.75** to drive self-assembly underscored a lack of stability in the final product, with this reflected in the comparatively low stability constants. Indeed, comparison of the ternary log $\beta_{1:1}$ value to those measured for the self-assembled systems described in Chapter 2 (Section 2.10.6), revealed a value *ca.* 2 orders of magnitude smaller. This inferior constant can most probably be accredited to the tri-substituted cyclen framework, which may restrict coordination to the metal. Nevertheless, this value matches that calculated for the ternary binding of **Tb.75** and *N*,*N*-dimethyl-aminobenzoic acid (**76**); log $\beta_{1:1}$ = 4.9.[303] These titrations definitively confirmed formation of the dimeric ternary cyclen complex **86-(Eu.75)$_2$**, thus, reinforcing the feasibility of the design.

Table 6.1: *Summary of the binding constants obtained through data fitting for the phosphorescence titration of* **86** *(1×10^{-5} M) with complex* ***Eu.75*** *in MeOH, with percentage composition of the 1:2 and 1:1 (L:C) species at 2 eq. of* ***Eu.75***.

Ligand	Complex	log $\beta_{1:2}$	log $\beta_{1:1}$	% of 1:2 (L:C) at 2 eq. of Eu.75	% of 1:1 (L:C) at 2 eq. of Eu.75
86	**Eu.75**	10.42 ± 0.09	4.93 ± 0.22	49	20

6.3.3 UV-vis and luminescence titrations of 86 with Tb.75 in MeOH

The ability of **86** to form an equivalent 1:2 (L:C) ternary complex with **Tb.75** was first tested by UV-vis absorption titration. Following additions of the cyclen substrate, the progression of the spectra was shown to essentially mirror the **Eu.75** titration, with complex addition resulting in an increase in absorbance across the full spectrum *i.e.* hyperchromic effect (Figure 6.6a). However, the two binding isotherms at 250 nm and 279 nm revealed subtle differences to **Eu.75**. As witnessed for **Eu.75**, absorbance increased sharply for up to *ca.* 2 eq. of **Tb.75**. However, the profiles for the **Tb.75** titration were distinguished by the existence of defined plateaus at *ca.* 2 eq. of **Tb.75** (see Figure 6.6b). Relative to **Eu.75**, the sharpness of the plateaus provided the first hint of a dimeric Tb(III) system with enhanced stability.

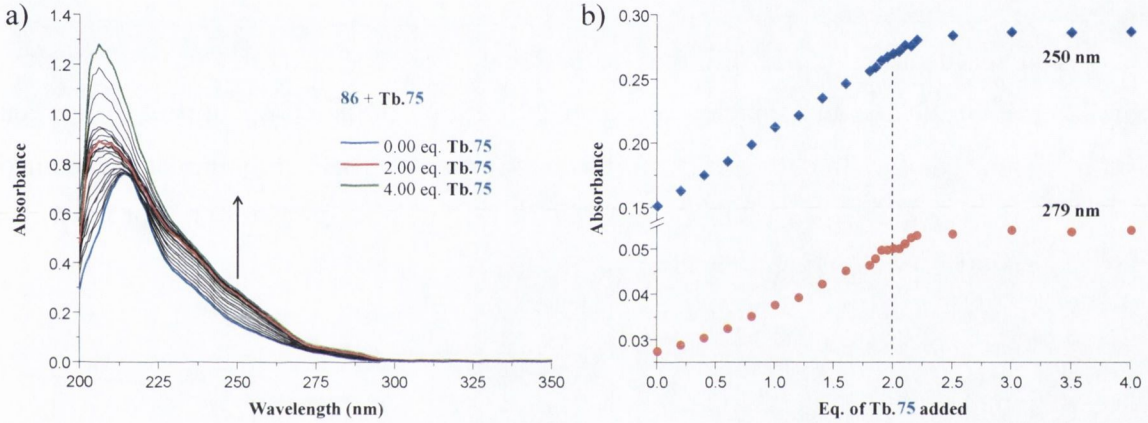

Figure 6.6: *a) Changes in the absorption spectra of* **86** *(1×10^{-5} M) upon titrating with complex* ***Tb.75*** *(0.00 → 4.00 eq.) in MeOH at 298 K. b) Binding isotherms for the titration measured at 250 nm and 279 nm.*

In the phosphorescence titration, excitation of the bridging pyridyl ligand (λ_{exc} = 279 nm) was shown to give rise to the distinctive phosphorescence of trivalent Tb(III) ion, thus, verifying population of the $^5D_4$ excited state by **86** (see Figure 6.7). Additional evidence of the sensitisation process was obtained by recording the phosphorescence excitation spectra, which correlated with absorption (Figure A6.4). Each phosphorescence spectrum displayed well-resolved, line-like emission bands characteristic of Tb(III), and assigned to the metal $^5D_4 \rightarrow {}^7F_J$ transitions; where J = 6 (487 nm), 5 (split; 542 and 545 nm), 4 (split; 583, 586, and 587 nm), 3 (621 nm), 2 (649 nm), 1 (669 nm), and 0 (680 nm) (Figure 6.7a). With no change in band structure, emission intensity was found to increase with additions of **Tb.75**. Interestingly, the binding isotherms adhered to the same trend seen in the UV-vis titration, with intensity increasing before reaching a plateau at *ca.* 2 eq of **Tb.75** (see Figure 6.7b).

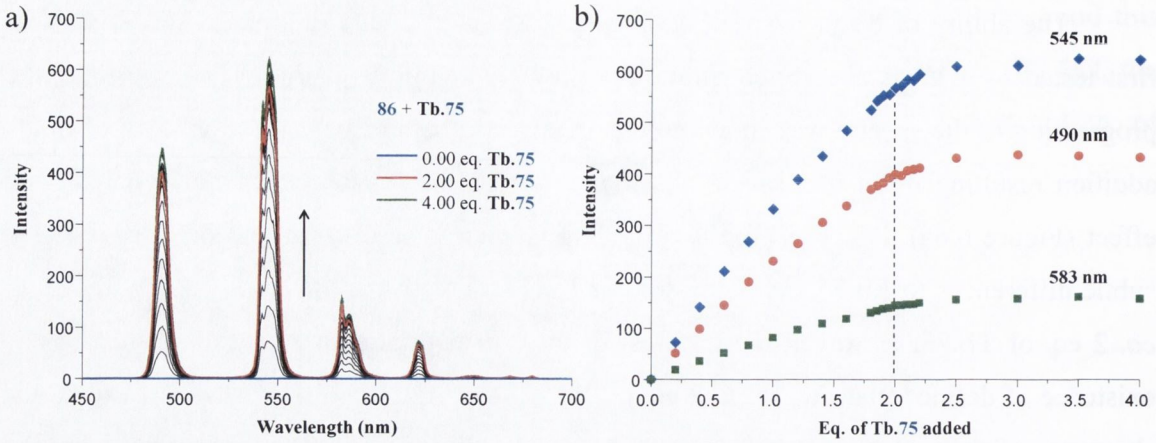

Figure 6.7: *a) Evolution of the phosphorescence emission in the titration of* **86** *(1 × 10^{-5} M) with complex* ***Tb.*****75** *(0.00 → 4.00 eq.) in MeOH at 298 K (λ_{exc} = 279 nm). b) Binding isotherms for the titration measured at 487 nm, 594 nm, and 616 nm.*

Having identified trends inferring the predominance of a 1:2 (L:C) ternary complex, definitive proof of product formation was gained by fitting of the phosphorescence titration data. As found for **Eu.75**, the excellent fit for the titration of **Tb.75** (Figure 6.8a) accounted for two luminescent systems, **86-Tb.75** and **86-(Tb.75)$_2$**, with binding constants of log $\beta_{1:1}$ = 5.23 ± 0.24 and log $\beta_{1:2}$ = 11.86 ± 0.07, respectively (Table 6.2).

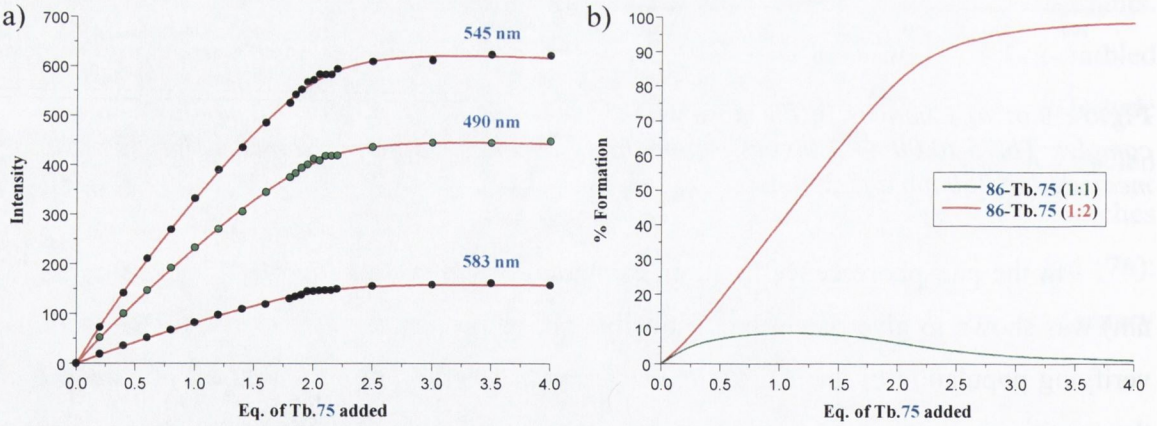

Figure 6.8: *a) Experimental binding isotherms for the phosphorescence titration of* **86** *(1 × 10^{-5} M) with complex* ***Tb.*****75** *in MeOH at 298 K (λ_{exc} = 279 nm) and their corresponding fit by means of SPECFIT. b) Speciation-distribution diagram obtained from the fit.*

In contrast to **Eu.75**, the individual formation constants were not additive. Somewhat unexpectedly, the stepwise constant for coordination of a second **Tb.75** molecule was *ca.* 2 orders of magnitude greater than the log $\beta_{1:1}$ value. Under these circumstances, this system may be proposed as a viable example of positive cooperativity, whereby binding of the first

cyclen unit promotes increased affinity for the second. One possible explanation for this could be that the ligands are folded in solution so that the pyridine rings are close together (similar to that seen from the crystal structures of the related ligands **72S/R** – Figure 5.2). If true of this system, binding of the first complex molecule may free the opposite terminus to bind. Irrespective of the origin of this effect, the overall stability of the dimeric Tb(III) self-assembly was larger than that of its Eu(III) analogue, for which $\log \beta_{1:2} = 10.42 \pm 0.09$ (see Table 6.1). Consequently, its percentage formation, with values of 82% and 98% at 2 and 4 eq. of **Tb.75**, respectively, was emphatically improved relative to **86-(Eu.75)$_2$** (Figure 6.8b).

Table 6.2: *Summary of the binding constants obtained through data fitting for the phosphorescence titration of **86** (1×10^{-5} M) with complex **Tb.75** in MeOH, with percentage composition of the 1:2 and 1:1 (L:C) species at 2 eq. of **Tb.75**.*

Ligand	Complex	$\log \beta_{1:2}$	$\log \beta_{1:1}$	% of 1:2 (L:C) at 2 eq. of Tb.75	% of 1:1 (L:C) at 2 eq. of Tb.75
86	**Tb.75**	11.86 ± 0.07	5.23 ± 0.24	82	6

To summarise, the spontaneous arrangement of 1:2 (L:C) ternary systems from ligand **86** and **Ln.75** (where Ln = Eu or Tb) was demonstrated in a series of photophysical titrations. Of the two systems, however, the Tb(III) analogue proved appreciably more stable.

6.4 Luminescent displacement assays for the detection of anions by 86-(Tb.75)$_2$

Critical to physiological function as well as various industrial processes, the role of anions as essential chemical components simply cannot be understated.[132,317] Indeed, their environmental implications accentuate both the importance and diversity of their function, with these species capable of either sustaining growth or acting as harmful pollutants.[132] Unsurprisingly, the development of luminescent and colorimetric sensors for anions has become an increasingly topical area of research in recent years.[319] Contributing to this, the Gunnlaugsson group have repeatedly demonstrated the suitability of ternary Ln(III)-cyclen complexes for anion sensing applications.[220,307]

Aiming to expand on previous efforts, the ability of the dimeric ternary complex **86-(Tb.75)$_2$** to function as a responsive luminescent probe for the detection of anions was assessed in a series of luminescent displacement assays. As discussed in Section 6.1, anion-binding of the cyclen-bound Ln(III) ion was predicted to occur at the expense of the dpa-derivatised antenna, whose expulsion would trigger a *switching off* of the luminescence. By

monitoring the luminescent output with anion additions, the validity of this hypothesis could be ascertained, with the extent of quenching acting as a measure of the sensory capabilities of the system. For the purpose of these experiments, selection of the Tb(III) analogue was made in view of its heightened stability and percentage formation relative to Eu(III).

6.4.1 Experimental and fitting details for luminescent displacement assays

These displacement assays were conducted in MeOH, the solvent in which the earlier titrations probing ternary complex formation were first performed (see Section 6.3). For each assay, the 1:2 (L:C) Tb(III) system was prepared *in situ* by adding 2 eq. of **Tb.75** to a stock solution (3mL; 1×10^{-5} M) of ligand **86**. Following self-assembly, dimeric **86-(Tb.75)$_2$** was titrated against known volumes of a standard solution of anion. The anions chosen for these studies were used as their tetrabutylammonium (TBA) salts and included; acetate ($CH_3CO_2^-$), chloride (Cl^-), nitrate (NO_3^-), phosphate ($H_2PO_4^-$), and pyrophosphate ($HP_2O_7^{2-}$). Upon each addition, UV-vis absorption and phosphorescence spectra were recorded following a 5 min equilibration time. All assays were repeated in triplicate for reproducibility. Where possible, fitting of the phosphorescence data was achieved by either linear or non-linear (SPECFIT®) regression analysis. Linear fits were made according to the Stern-Volmer equation (Equation 6.4), where [A^-] represents the anion concentration, K is the formation constant, I is the emission intensity, and I_0 is the emission intensity when [A^-] = 0.

$$I_0/I = 1 + K[\,A^-\,] \qquad \textbf{Equation 6.4}$$

Note: All references to *anion eq.* are relative to the cell concentration (1×10^{-5} M) of **86**.

6.4.2 Results of luminescent displacement assays

Beginning with the titration of phosphate, the addition of anion to **86-(Tb.75)$_2$** was shown to induce rapid quenching of the Tb(III)-centred emission (see Figure 6.9a), giving credence to the hypothesised mode of sensing *i.e.* antenna displacement. The changes in the hypersensitive $J = 5$ band as a function of added $H_2PO_4^-$ are plotted in Figure 6.9b. This graph showed that luminescence was 87% quenched upon addition of only 1 eq. of $H_2PO_4^-$, with the luminescent output being fully quenched (*ca.* 100%) before titration completion. Furthermore, the resultant plateau in the quenching profile, which signified an approximate 1:1 ratio of $H_2PO_4^-$ to dimeric ternary complex, implied the possibility that both terminal cyclen substituents were displaced by a single anion. A comparable trend was also observed

in the binding isotherm at 250 nm for the complementary UV-vis titration. In this case, anion addition resulted in spectral hypochromism in the range of *ca.* 223 – 287 nm (Figure A6.5).

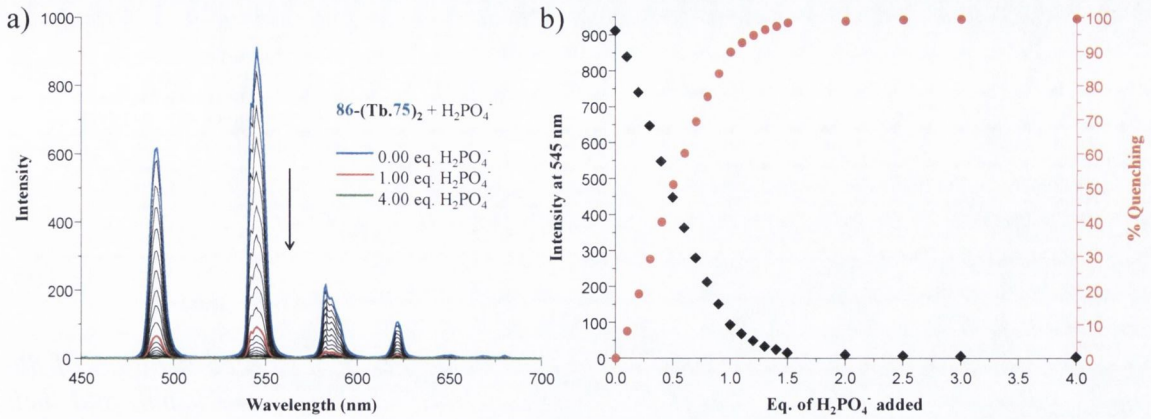

Figure 6.9: *a) Changes in the phosphorescence spectra of* ***86-(Tb.75)$_2$*** *([**86**] = 1 × 10^{-5} M) upon titrating with $H_2PO_4^-$ (0.00 → 4.00 eq.) in MeOH at 298 K (λ_{exc} = 279 nm). b) Changes in the emission intensity at 545 nm (black diamonds) and the percentage quenching (red circles).*

The changes in the recorded phosphorescence spectra were subsequently fit using the non-linear regression analysis program SPECFIT® in pursuit of more conclusive evidence. In order to deliver a quality fit, the original 1:2 and 1:1 (L:C) ternary Tb(III) systems, along with their affiliated binding constants, were uploaded to the fitting program. This measure was principally taken to account for their *in situ* self-assembly and percentage distribution prior to anion addition. As a consequence of this, their respective profiles were observable in the final speciation graph (red and green lines in Figure 6.10b), with the initial percentage formation of each species correlating to the fit in Figure 6.8. Applying the stated measures, an excellent fit was achieved proving the formation of chelates between $H_2PO_4^-$ and **Tb.75** in both 1:1 and 1:2 (A:C) stoichiometries; binding constants of log $\beta_{1:1}$ = 6.59 ± 0.10 and log $\beta_{1:2}$ = 13.82 ± 0.04, respectively (Table 6.3).

Table 6.3: *Summary of the binding constants obtained through data fitting for the phosphorescence titration of* ***86-(Tb.75)$_2$*** *([**86**] = 1 × 10^{-5} M) with $H_2PO_4^-$ in MeOH, with percentage composition of the 1:2 and 1:1 (A:C) species at 1 eq. of $H_2PO_4^-$.*

Anion	Complex	log $\beta_{1:2}$	log $\beta_{1:1}$	% of 1:2 (A:C) at 1 eq. of $H_2PO_4^-$	% of 1:1 (A:C) at 1 eq. of $H_2PO_4^-$
$H_2PO_4^-$	**86-(Tb.75)$_2$**	13.82 ± 0.04	6.59 ± 0.10	80	6

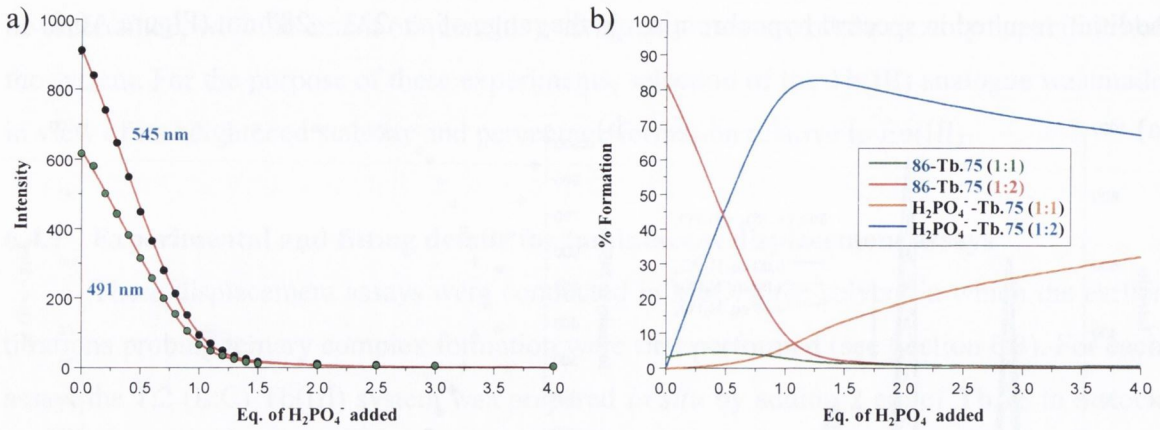

Figure 6.10: *a) Experimental binding isotherms for the phosphorescence titration of* ***86-(Tb.75)$_2$*** *([**86**] = 1 × 10^{-5} M) with $H_2PO_4^-$ in MeOH at 298 K (λ_{exc} = 279 nm) and their corresponding fit by means of SPECFIT. b) Speciation-distribution diagram obtained from the fit.*

Comparison of the calculated constants to those in Table 6.2, helped to emphasise the stability of the newly-formed anion adducts relative to the original ternary assemblies. With a log $\beta_{1:1}$ value *ca.* 1.4 orders of magnitude greater for the **anion-Tb.75** chelate, it was clear that $H_2PO_4^-$ held a natural preference for **Tb.75** over ligand **86**. This preference manifested in the speciation graph, from which the formation of the anionic chelates was shown to drive concomitant ternary complex dissociation (Figure 6.10b). With regards to both anionic conjugates, the 1:2 (A:C) stoichiometric species was favoured, reaching 80% formation at 1 eq. of $H_2PO_4^-$.

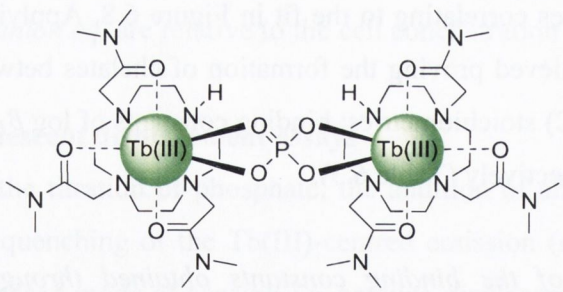

Figure 6.11: *Schematic illustration of the proposed binding model for the 1:2 (A:C) species.*

The identification of this particular chelate suggested an unusual binding model, in which $H_2PO_4^-$, much like ligand **86**, bridged two complex molecules of **Tb.75** (Figure 6.11). One literature example of a similar binding mode is the linkage of two independent Eu(III)-cyclen complexes by an individual F^- anion, previously reported by Lima and co-workers

(**1.Eu-F-Eu.1**, Figure 1.5).[70] Within the Gunnlaugsson group, the capacity of $H_2PO_4^-$ to bind multiple molecules was shown for a diaryl-urea receptor compound, where anion chelates were proven to form with 1:1, 2:1, and, most significantly, 1:2 (A:L) stoichiometries.[320]

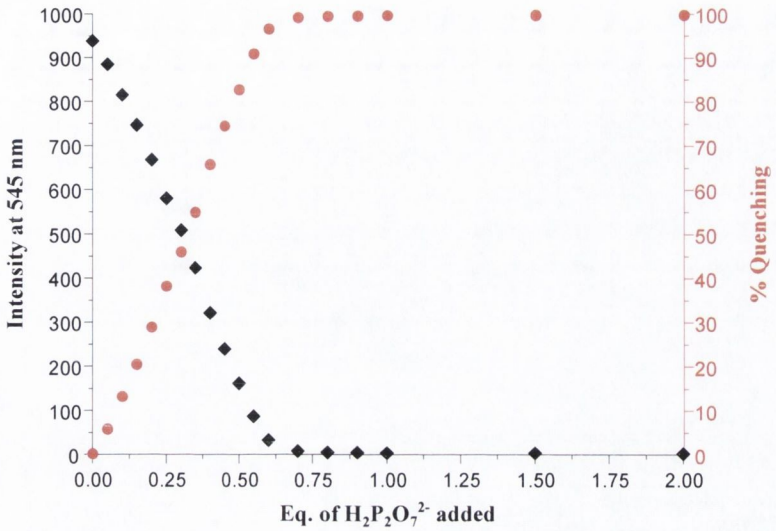

Figure 6.12: *Changes in the emission intensity at 545 nm (black diamonds) and the percentage quenching (red circles) for the phosphorescence titration of* ***86-(Tb.75)$_2$*** *([**86**] = 1×10^{-5} M) with $H_2P_2O_7^{2-}$ (0.00 → 2.00 eq.) in MeOH at 298 K (λ_{exc} = 279 nm).*

For the pyrophosphate displacement assay, Figure 6.12 follows the quenching profile at 545 nm for **86-(Tb.75)$_2$** upon titration with $H_2P_2O_7^{2-}$. As per its monomer, $H_2PO_4^-$, the addition of $H_2P_2O_7^{2-}$ elicited a quenching of the Tb(III) luminescence, indicative again of anion-binding displacing the ligand (Figure A6.7). In fact, the quenching experienced was shown to be significantly enhanced compared to that with $H_2PO_4^-$. Indeed, the emission of the $J = 5$ band was 83% quenched at 0.5 eq. of $H_2P_2O_7^{2-}$, and near fully quenched after only 0.7 eq. of anion. Based on both the extent and relative rates of quenching, one may assume stronger binding to **Tb.75** in the case of $H_2P_2O_7^{2-}$ anion. Unfortunately, attempts at fitting the data using linear and non-linear methods proved unsuccessful. Such difficulties may arise from the potential of $H_2P_2O_7^{2-}$ to form multiple binding interactions, thus, making accurate quantification troublesome.

Relative to $H_2PO_4^-$ and $H_2P_2O_7^{2-}$, the quenching profile of the nitrate titration was symptomatic of a weakened interaction between anion and **Tb.75** (see Figure 6.13a). The reduced affinity for NO_3^- was effectively underscored by the percentage quenching values, with only 60% quenching observed after 3 eq. of anion. Even at the point of completion (25 eq.), the emission was only 89% quenched and not fully *switched off*. Determination of the binding constant for the **anion-Tb.75** chelate was later achieved through linear fitting of the

phosphorescence data (Figure 6.13b). This yielded a log $\beta_{1:1}$ value of 4.70 ± 0.01, a smaller constant to that calculated for the binding of **86** to **Tb.75** (Table 6.2), therefore, accentuating the need for a large excess of NO_3^- to force ligand displacement (as evidenced from Figure 6.13a). Though comparatively reduced, the NO_3^- sensing capacity of **86-(Tb.75)$_2$** cannot be denied. For both acetate and chloride anion, however, only minor levels of quenching were incurred; 5% and 8% at 4 eq. of anion, respectively (see Figure A6.10 and A6.11).

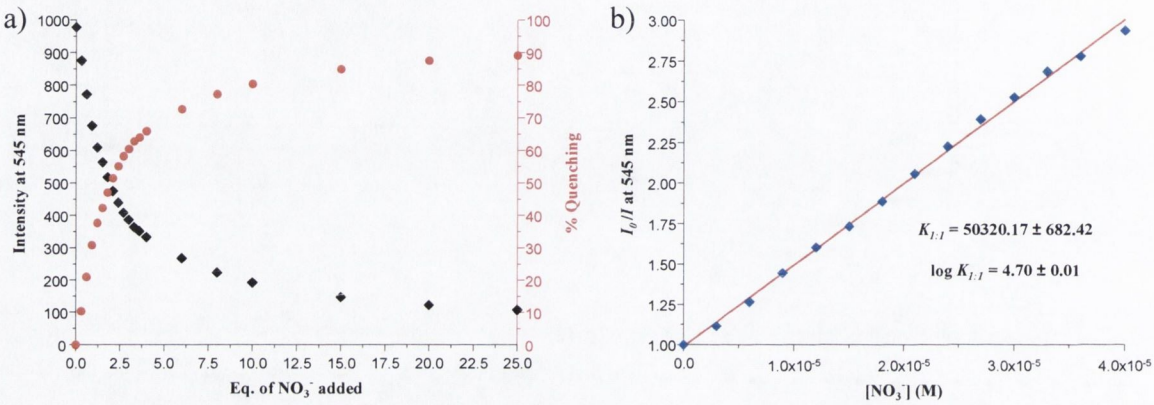

Figure 6.13: *a) Changes in the emission intensity at 545 nm (black diamonds) and the percentage quenching (red circles) for the phosphorescence titration of* ***86-(Tb.75)$_2$*** *([**86**] = 1 × 10^{-5} M) with NO_3^- (0.00 → 25.00 eq.) in MeOH at 298 K (λ_{exc} = 279 nm). b) Stern-Volmer linear fit of the changes in the emission intensity at 545 nm.*

The luminescent displacement assays conducted have showcased the anion sensing proficiency of the dimeric ternary complex **86-(Tb.75)$_2$**. Upon review of the assay results, the sensing capabilities of this novel assembly, in terms of sensitivity, may be summarised as follows; $H_2P_2O_7^{2-}$ > $H_2PO_4^-$ > NO_3^- > Cl^- > $CH_3CO_2^-$. Such differential sensing bodes well for the potential of this system to selectively operate in competitive anionic media. All in all, **86-(Tb.75)$_2$** represents an excellent example of how, through careful and measured design, structure can be manipulated to confer function.

6.5 Design of the trimeric ternary cyclen complex 87-(Ln.75)$_3$

Research targeting the formation of luminescent ternary Ln(III) self-assemblies was not only confined to the dimeric system **86-(Ln.75)$_2$**. In collaboration with Prof. Wolfgang Schmitt at the School of Chemistry, Trinity College Dublin, the formation of novel trimeric ternary Ln(III)-cyclen complexes was also investigated. *Photophysically silent* tri-armed **Ln.75** (where Ln = Eu or Tb) was again chosen as the cyclen component of these trimeric ternary systems, having been used to great effect in the development of **86-(Ln.75)$_2$**. This time, however, the tritopic ligand **87** was selected to fulfil the dual role of both linker and

Ln(III)-sensitiser. Ligand **87** (known more formally as 1,3,5-benzene-trisethynylbenzoate) was supplied by the Schmitt research group and was prepared in accordance with literature procedures.[321] This highly conjugated, planar aromatic compound has a triangular topology, and is comprised of three benzoate moieties adjoined to a central benzene ring by alkynyl linkers. In recent years, this trifunctional ligand (in its carboxylic acid form) has been employed for the synthesis of *d*-metal-containing framework materials, one such example being the construction of porous Zn(II)-based MOFs by Schmitt *et al.*[322] In relation to the self-assembly of the trimeric ternary systems herein, the three benzoate groups were each anticipated to bind a molecule of complex **Ln.75**, affording a ternary product displaying the desired 1:3 (L:C) stoichiometry. Moreover, these coordinating functionalities are further endowed with the ability to sensitise the Ln(III) excited state, thus, facilitating a *switching on* of the metal ion-centred luminescence. A schematic representation for the formation of these luminescent trimeric complexes is shown below in (see Scheme 6.5).

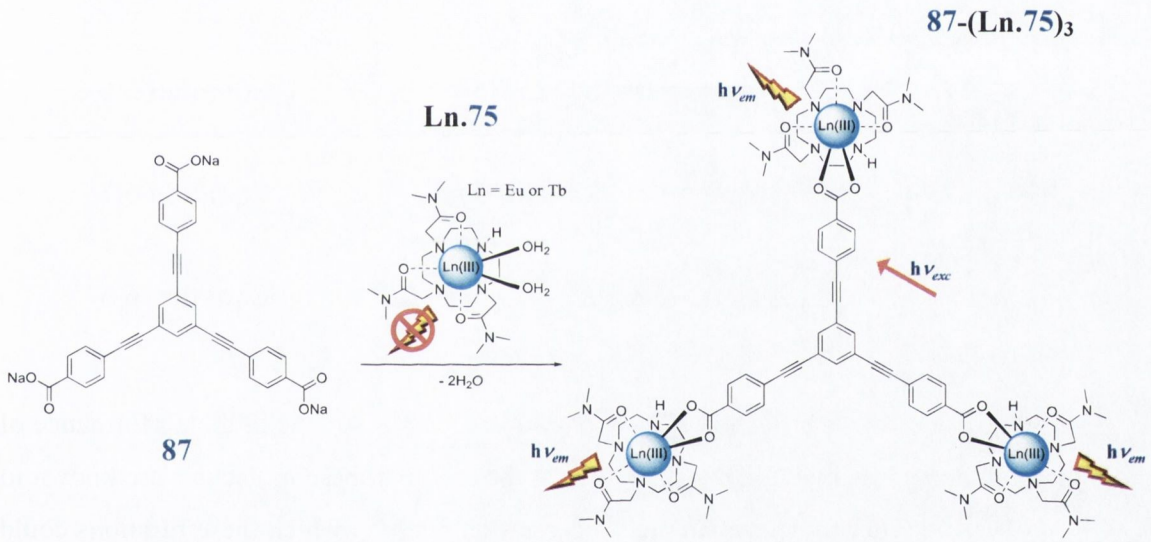

Scheme 6.5: *Schematic illustration of the formation of the trimeric ternary assembly* ***87-(Ln.75)3****, accompanied by the switching on of the metal-centred luminescence.*

The inspiration for the development of **87-(Ln.75)3** was a desire to introduce an added layer of structural complexity to ternary complex design. Additionally, these structures were foreseen to be water soluble, therefore, negating the principle drawback of **86-(Ln.75)2**. To probe the self-assembly of ligand **87** and complex **Ln.75** (where Ln = Eu or Tb), a series of photophysical titrations were conducted, the results of which will be discussed in subsequent sections.

6.6 UV-vis and luminescence titration studies of 87 and Ln.75: titration experimental and data fitting details

The titration studies of ligand **87** were performed in 0.1 M Tris aqueous buffer (pH 7.4). A stock solution (3mL; 2.5×10^{-6} M) of **87**, used in its sodium carboxylate form, was prepared and titrated against known volumes of a standard solution of either complex **Eu.75** or **Tb.75**. After each addition, UV-vis absorption and phosphorescence spectra were recorded following an equilibration time of 5 min. All titrations were repeated in triplicate to ensure reproducibility. The changes in the UV-vis spectra were then fit using the non-linear least squares regression program SPECFIT® (see Section 2.10.5). Excellent fits were acquired by fitting to the set of equilibria equations shown below, which were used to define this self-assembly process (**Equation 6.5 – 6.8**).

$$\mathbf{87} + \mathbf{Ln.75} \overset{K_{1:1}}{\rightleftharpoons} \mathbf{87\text{-}Ln.75} \qquad \textbf{Equation 6.5}$$

$$\mathbf{87\text{-}Ln.75} + \mathbf{Ln.75} \overset{K_{1:2}}{\rightleftharpoons} \mathbf{87\text{-}(Ln.75)_2} \qquad \textbf{Equation 6.6}$$

$$\mathbf{87\text{-}(Ln.75)_2} + \mathbf{Ln.75} \overset{K_{1:3}}{\rightleftharpoons} \mathbf{87\text{-}(Ln.75)_3} \qquad \textbf{Equation 6.7}$$

$$\beta_{1:3} = K_{1:1} \times K_{1:2} \times K_{1:3} \qquad \textbf{Equation 6.8}$$

The decision to use a ligand cell concentration of 2.5×10^{-6} M in the performance of these measurements was made in consideration of the fact that these molecules are known to readily stack.[323] In order to determine the concentration range in which these titrations could be conducted without the detrimental influence of the inner-filter effect (where the molecules no longer behave as independent entities), both UV-vis absorption and fluorescence spectra of ligand **87** were recorded at different concentrations to establish a range of linearity (Figure A6.12 and A6.13, respectively). Based on this concentration study, the ligand concentration of 2.5×10^{-6} M was selected for these studies.

6.6.1 UV-vis and luminescence titrations of 87 and Eu.75 in 0.1 M Tris buffer (pH 7.4)

The formation of a ternary complex between ligand **87** and **Eu.75** was first observed in solution by UV-vis absorption titration. Preceding addition of the cyclen substrate, the spectrum of the free ligand was characterised by two main bands; a high energy one centred at *ca.* 207 nm, and a two-pronged band with maxima at 296 nm and 314 nm, corresponding

to the π-π^* transitions of the phenyl rings (see Figure 6.14a). Additions of **Eu.75** were later found to induce a hypochromic shift in the latter band, with the concomitant formation of a new band at *ca.* 350 nm resulting in an isosbestic point at 322 nm. Evolution of the band at *ca.* 350 nm was deemed in line with the assembly of a new species in solution. Interestingly, the hypochromism experienced at both 296 nm and 314 nm, and the hyperchromism at 350 nm were seen in the binding isotherms to continue steadily till *ca.* 3 eq. of **Eu.75**, with these effects becoming less pronounced thereafter (Figure 6.14b). Such trends could potentially be interpreted to imply the predominance of a 1:3 (L:C) stoichiometric species.

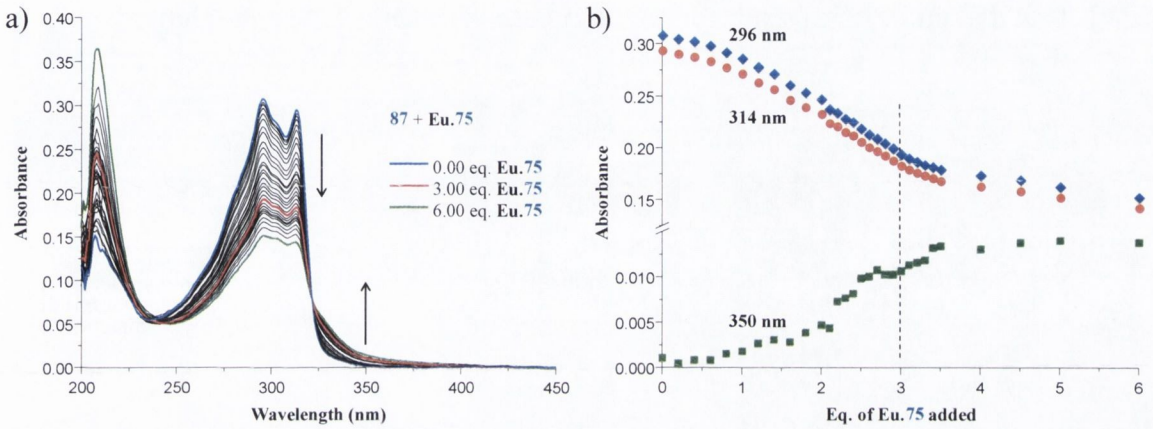

Figure 6.14: *a) Changes in the absorption spectra of* **87** *(2.5×10^{-6} M) upon titrating with complex* **Eu.75** *(0.00 → 6.00 eq.) in 0.1 M Tris aqueous buffer (pH 7.4) at 298 K. b) Binding isotherms for the titration measured at 296 nm, 314 nm, and 350 nm.*

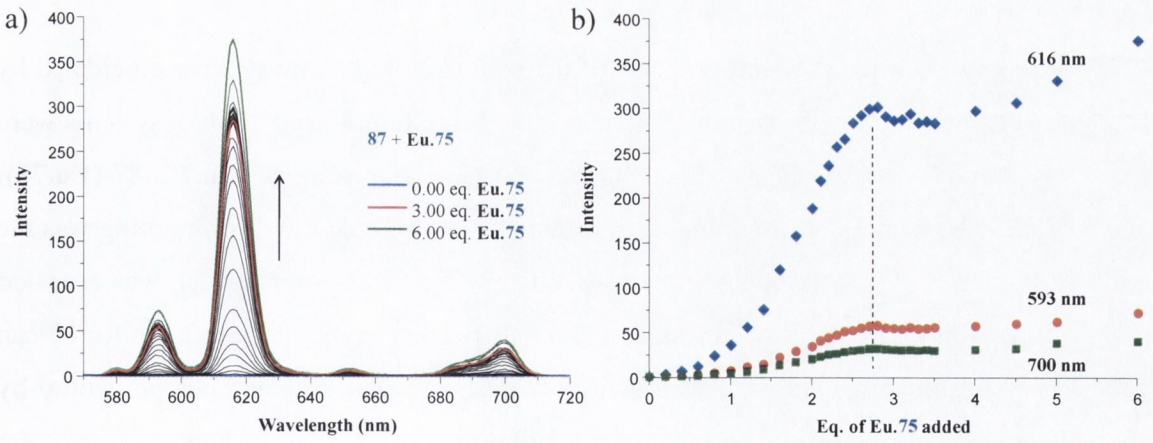

Figure 6.15: *a) Evolution of the phosphorescence emission in the titration of* **87** *(2.5×10^{-6} M) with complex* **Eu.75** *(0.00 → 6.00 eq.) in 0.1 M Tris aqueous buffer (pH 7.4) at 298 K (λ_{exc} = 296 nm). b) Binding isotherms for the titration measured at 593 nm, 616 nm, and 700 nm.*

Coordination of the ligand benzoate groups was evidenced upon excitation of **87** at 296 nm. Indeed, ligand excitation was found to yield phosphorescence spectra exhibiting the characteristic Eu(III)-centred emission structure, with bands centred at 580 nm, 593 nm, 616 nm, 652 nm, and 695 nm attributed to the $J = 0 - 4$ transitions, respectively (Figure 6.15a). All bands were seen to undergo an intensity increase with successive additions of complex **Eu.75**, with no observable change in band fine-structure. This pattern of intensification was highlighted by the binding isotherms shown in Figure 6.15b, where emission intensity was found to rapidly rise before levelling off at *ca.* 2.75 eq. of **Eu.75**. Despite implicating the presence of other L:C stoichiometries (1:1 and 1:2), the plateau at this position (close to 3 eq.) helped to reinforce the prominence of the predicted trimeric system in solution.

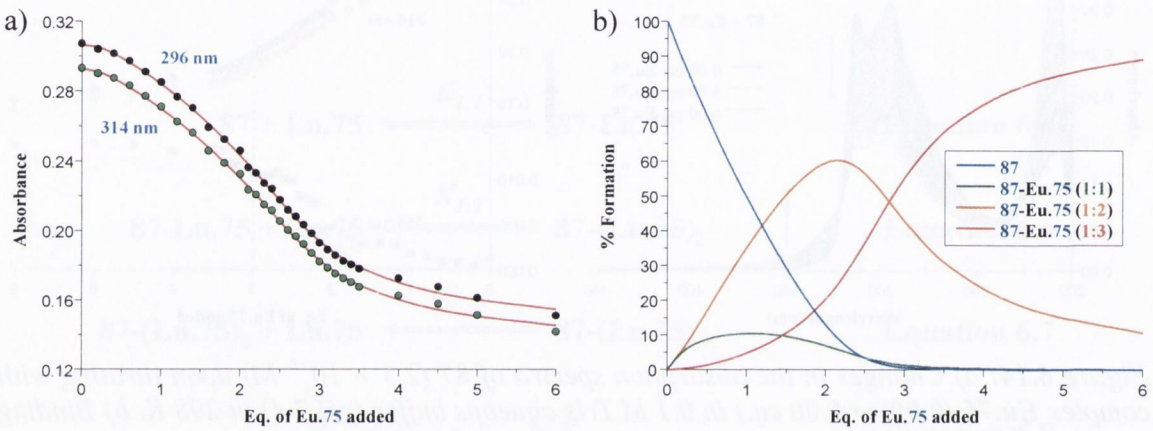

Figure 6.16: *a) Experimental binding isotherms for the UV-vis titration of* **87** *(2.5×10^{-6} M) with complex* ***Eu.75*** *in 0.1 M Tris aqueous buffer (pH 7.4) at 298 K and their corresponding fit by means of SPECFIT. b) Speciation-distribution diagram obtained from the fit.*

The key intermediates and products of the self-assembly pathway were elucidated by fitting the changes in the UV-vis absorption spectra. Three luminescent ternary systems were positively identified from the excellent fit obtained (Figure 6.16a); **87-Eu.75**, **87-(Eu.75)$_2$** and **87-(Eu.75)$_3$**, with associated binding constants listed in Table 6.4. Worth noting was the increase in stability at the binding sites relative to the dimeric system, which was revealed upon comparison to the stability constants in Table 6.1. The stability enhancement for **87** can be accredited to the negatively charged benzoate groups, ligand **86** being charge neutral by comparison. Furthermore, the constants representing the individual coordination steps were approximately additive, indicative of independent binding at the three chelating sites with an absence of cooperativity. In terms of product distribution, the 1:2 (L:C) species dominated from 0 → 3 eq. of **Eu.75**, with both 1:1 and 1:3 (L:C) stoichiometries comparatively minor components. However, formation of the desired trimeric complex became favoured at 3 eq.

of **Eu.75**, its self-assembly becoming increasingly preferred at excess (89% formation at 6 eq.). Such an excess was required to drive formation because the titrations, relative to those with ditopic **86**, were conducted at a lower ligand concentration (2.5×10^{-6} M). The natural preference for trimeric **87**-**(Eu.75)$_3$** at excess cyclen was most definitely the cause of the increase in intensity observed in the phosphorescence titrations from *ca.* 4 – 6 eq. of **Eu.75**, after the initial plateau at *ca.* 2.75 eq. (Figure 6.15b).

Table 6.4: *Summary of the binding constants obtained through data fitting for the UV-vis titration of **87** (2.5×10^{-6} M) with complex **Eu.75** in 0.1 M Tris aqueous buffer (pH 7.4), with percentage composition of the 1:3 (L:C) species at 3 eq. of Eu(III).*

Ligand	Complex	log $\beta_{1:3}$	log $\beta_{1:2}$	log $\beta_{1:1}$	% of 1:3 (L:C) at 3 eq. of Eu.75
87	**Eu.75**	19.74 ± 0.18	13.69 ± 0.19	6.24 ± 0.39	55

6.6.2 UV-vis and luminescence titrations of 87 and Tb.75 in 0.1 M Tris buffer (pH 7.4)

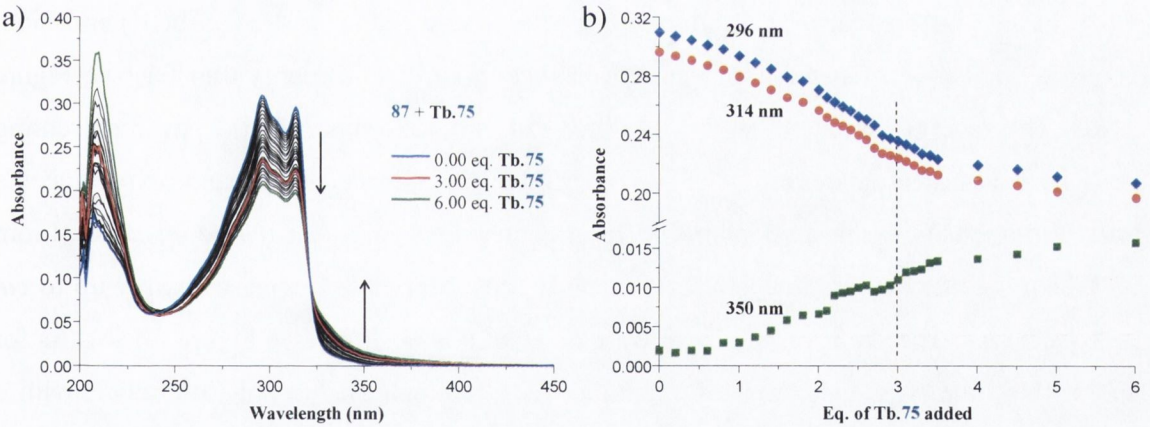

Figure 6.17: *a) Changes in the absorption spectra of **87** (2.5×10^{-6} M) upon titrating with complex **Tb.75** (0.00 → 6.00 eq.) in 0.1 M Tris aqueous buffer (pH 7.4) at 298 K. b) Binding isotherms for the titration measured at 296 nm, 314 nm, and 350 nm.*

Similar in almost every way, the UV-vis absorption titration between **87** and **Tb.75** was found to correlate to the **Eu.75** titration As witnessed previously, the distinctive two-pronged band (*ca.* 305 nm) characteristic of the free ligand underwent a hypochromic shift with each **Tb.75** addition, and was accompanied by the evolution of a new band at *ca.* 350 nm and the formation of an isosbestic point at *ca.* 322 nm (Figure 6.17a). The resemblance also extended to the titration binding isotherms, where the degree of hypochromism at 296

nm and 314 nm, and hyperchromism at 350 nm, was observed again to be most pronounced up to 3 eq. of **Tb.75** (see Figure 6.17b). Reconciling these similarities with the fitting results in Section 6.6.1, one may predict a comparable species profile to that determined for **Eu.75** in which the 1:3 (L:C) system predominates.

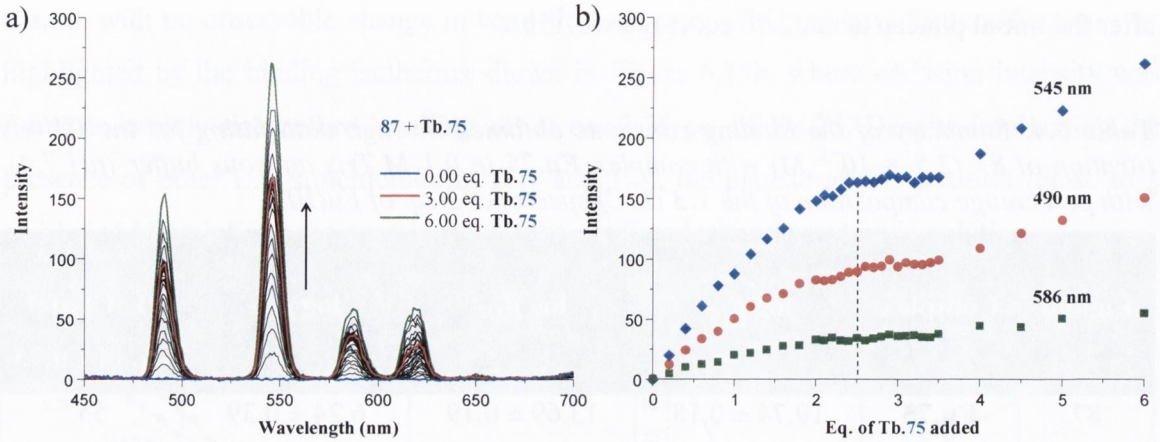

Figure 6.18: *a) Evolution of the phosphorescence emission in the titration of* **87** *(2.5×10^{-6} M) with complex* ***Tb.75*** *(0.00 → 6.00 eq.) in 0.1 M Tris aqueous buffer (pH 7.4) at 298 K (λ_{exc} = 296 nm). b) Binding isotherms for the titration measured at 487 nm, 545 nm, and 586 nm.*

In the phosphorescence titration, the spectra where characteristic of Tb(III) emission, therefore, indicative of successful ligand-coordination and facile energy transfer (see Figure 6.18a). The spectra contained bands at 487 nm, 545 nm, 586 nm, and 618 nm, representing the $^5D_4 \rightarrow {}^7F_J$ transitions where $J = 6 - 3$, respectively. As expected, all bands experienced a growth in intensity with additions of **Tb.75** aliquots, signifying a *switching on* effect. From the binding isotherms, the intensity of the bands was observed to increase sharply up to *ca.* 2.5 eq. of **Tb.75**, before levelling to give a plateau at this position (see Figure 6.18b). As for **Eu.75**, this trend was evidential of a mixture of stoichiometries in solution, albeit with a preference for **87-(Tb.75)$_3$**.

The stoichiometric species formed in solution were lastly determined by fitting the UV-vis titration data. The excellent fit achieved was in essence identical to the fit obtained for **Eu.75** (see Section 6.6.1), and again verified the self-assembly of the 1:1, 1:2, and 1:3 (L:C) ternary systems. Intriguingly, the calculated binding constants in Table 6.5 were each *ca.* 1 order of magnitude greater than their equivalent Eu(III) value (see Table 6.4), perhaps a result of the greater charge density of the Tb(III) ion. Nevertheless, the stepwise stability constants were again approximately additive. However, there existed a few subtle differences between the fits and their speciation graphs (Figure 6.19b). For the **Tb.75** titration, the 1:1

(L:C) complex made a far greater contribution, its formation being favoured from *ca.* 0 → 1.3 eq. of cyclen. After this point, the 1:2 (L:C) self-assembly took precedence before the trimeric complex finally became favoured at *ca.* 2.7 eq. of **Tb.75**. Similar to complex **Eu.75**, the percentage formation of **87-(Tb.75)$_3$** was found to increase up to titration completion, reaching 92% after 6 eq. added.

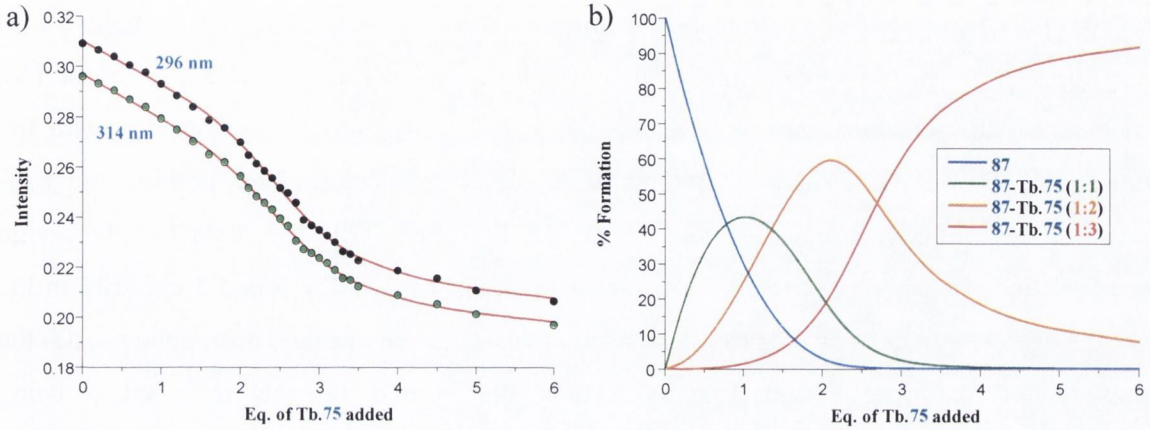

Figure 6.19: *a) Experimental binding isotherms for the UV-vis titration of* **87** *(2.5×10^{-6} M) with complex* ***Tb.75*** *in 0.1 M Tris aqueous buffer (pH 7.4) at 298 K and their corresponding fit by means of SPECFIT. b) Speciation-distribution diagram obtained from the fit.*

By adhering to the design plan outlined in Section 6.5, the self-assembly of novel trimeric ternary Ln(III)-cyclen complexes was predicted. The photophysical measurements discussed in the last two sections unequivocally confirmed the formation of these triangular 1:3 (L:C) self-assemblies for both **Eu.75** and **Tb.75**, the latter species being the more stable of the two.

Table 6.5: *Summary of the binding constants obtained through data fitting for the UV-vis titration of* **87** *(2.5×10^{-6} M) with complex* ***Tb.75*** *in 0.1 M Tris aqueous buffer (pH 7.4), with percentage composition of the 1:3 (L:C) species at 3 eq. of Tb(III). *Value fixed.*

Ligand	Complex	log $\beta_{1:3}$	log $\beta_{1:2}$	log $\beta_{1:1}$	% of 1:3 (L:C) at 3 eq. of Tb.75
87	**Tb.75**	20.98 ± 0.18	14.78 ± 0.22	7.60 ± 0.00*	60

Preliminary studies have been performed examining the possibility of threading the benzoate arms of tritopic **87** through the cavity of β-cyclodextrin, before finally stoppering with **Ln.75** to form novel rotaxane structures. As of yet, this design has not been achieved, with UV-vis monitoring of the ligand spectrum upon additions of β-cyclodextrin showing no

change in the spectrum both before and after addition of the cyclen substrate (and also with heating). Efforts to form this higher-order structure will not be abandoned, with future work dedicated to exploring alternative strategies.

6.7 Conclusion

With major importance attached to photophysical analysis, this chapter has focused on the design and formation of luminescent multimeric ternary Ln(III)-cyclen complexes, all developed from the triacetamide-substituted cyclen derivative **Ln.75** (where Ln = Eu or Tb). In essence, this chapter may be considered a story of two halves, dealing first with the development of dimeric ternary systems from ligand **86**, before later probing the self-assembly of trimeric complexes from ligand **87**. Fundamentally, the basis for the design strategy finds its roots in the very structure of complex **Ln.75**, developed previously in the Gunnlaugsson group. Through both the omission of a sensitising chromophore and the presence of two metal-bound water molecules, this system may be described as being *photophysically silent*. Consequently, one may anticipate that coordination of either ligand, at the expense of bound solvent, would *switch on* the metal-centred emission, therefore, providing a platform to photophysically track self-assembly *in situ*.

Concerning the dimeric self-assemblies, discussion began with the synthesis and characterisation of **86**, a modified dpa ligand consisting of two ethyl-amide-functionalised chelidamic acid units linked to either end of a polyethoxy chain. Possessing two coordinating motifs, this ligand was envisaged to bridge two complex molecules of **Ln.75**, thus, affording novel ternary complexes of formula **86-(Ln.75)$_2$** (where Ln = Eu or Tb).

Thereafter, a series of UV-vis and luminescence titrations were conducted between **86** and **Eu.75**/**Tb.75** in MeOH, devised so as to evaluate whether the hypothesised dimeric species was indeed formed. In both cases, a progressive *switching on* of the luminescence was observed, indicial of ligand-binding and Ln(III)-sensitisation. Fitting of the phosphorescence spectral changes by SPECFIT®, for both examples, elucidated two stoichiometric species; the 1:1 and desired 1:2 (L:C) ternary complex. Manifesting in a vastly improved percentage formation of **86-(Tb.75)$_2$**, comparison of the log $\beta_{1:2}$ values revealed a considerable stability enhancement for **Tb.75** relative to **Eu.75**.

With regards to application, the anion sensing faculty of dimeric **86-(Tb.75)$_2$** was remarkably demonstrated in a series of luminescent displacement assays. To varying extents, the anions tested in these experiments were all shown to *switch off* emission, the quenching observed suggestive of a mode of action whereby the anion supplants the ligand (*i.e.* antenna) from the metal. The sensitivity of the ternary complex to the various anions may be described

in terms of the degree of quenching experienced, to be summarised as follows; $H_2P_2O_7^{2-}$ > $H_2PO_4^-$ > NO_3^- > Cl^- > $CH_3CO_2^-$. In the case of $H_2PO_4^-$, an excellent fit of the phosphorescence data was obtained with SPECFIT®, which implicated the anion in the simultaneous binding of two molecules of **Tb.75**.

In collaboration with Prof. Wolfgang Schmitt (TCD), trimeric ternary systems were constructed *via* the self-assembly of trifunctional ligand **87** and **Ln.75** (where **Ln.75** = Eu or Tb). On account of its three benzoate moieties, ligand **87** was foreseen to independently bind three molecules of the cyclen complex. In an attempt to resolve the stepwise assembly pathway, UV-vis and luminescence titrations were later performed between **87** and **Eu.75**/**Tb.75** in 0.1 M Tris aqueous buffer (pH 7.4), with fitting of the UV-vis data proving crucial. For both substrates, the fits each identified three luminescent species; 1:1, 1:2, and 1:3 (L:C). Specifically, formation of the desired trimeric complex was shown, from the resultant speciation graphs, to become increasing favoured with excess amounts of **Ln.75**. Regarding ternary stability, the trimeric systems **87**-(**Ln.75**)$_3$ were determined to be comparably more stable than their dimeric counterparts **86**-(**Ln.75**)$_2$ at the site of coordination, perhaps attributable to the charge of the carboxylate groups. Furthermore, the Tb(III) analogue was again the more stable of the two.

Incorporating extensive evidence corroborating the formation of both dimeric and trimeric ternary assemblies, the work reported throughout this chapter has served to validate the synthetic self-assembly strategy employed. In the dimeric case, the pivotal role of structure in determining function was expertly communicated through anion displacement studies, with **86**-(**Tb.75**)$_2$ acting as a wonderful example of the sort of stimuli responsive behaviour achievable with such systems. Informed by this research, one can conclude that luminescent ternary Ln(III) complexes are equally desirable in both initial assembly and subsequent de-assembly, the latter process giving way to novel application.

Chapter 7

Experimental

7 General experimental details

All chemicals were purchased from Sigma-Aldrich Ireland Ltd., Acros Organics, and TCI Ltd., and were used without further purification, unless otherwise stated. Deuterated solvents for NMR analysis were all obtained from Apollo Scientific. Dry solvents were prepared in accordance with standard procedures described by Vogel, with distillation prior to each use.[324] Chromatographic columns were performed manually using either silica gel 60 (230-240 mesh ASTM) or aluminium oxide (activated, neutral, Brockman I STD grade, 150 mesh). Chromatographic columns were also run on a Teldyne Isco Combiflash Companion automatic machine using pre-packed silica or alumina columns. Thin-layer chromatography (TLC) was conducted using both Merck Kiesegel 60 F_{254} silica plates and Polygram Alox N/UV_{254} aluminium oxide plates, and observed by UV light or developed in an iodine chamber. Melting Points were determined using an Electrothermal IA900 digital melting point apparatus.

NMR spectra were recorded using either a Bruker Spectrospin DPX-400 instrument, operating at 400.1 MHz for ^{1}H NMR and 100.6 MHz for ^{13}C NMR, or a Bruker AV-600 instrument, operating at 600.1 MHz for ^{1}H NMR and 150.2 MHz for ^{13}C NMR. All NMR spectra were measured at 293 K. Chemical shifts are expressed in parts per million (ppm or δ) relative to the non-deuterated solvent peak and, for ^{1}H NMR spectra, are reported alongside the number of protons, splitting pattern, coupling constant where applicable, and proton assignment (in that order). Multiplicities are abbreviated as follows; singlet (s), doublet (d), triplet (t), quartet (q), multiplet (m), and broad (br).

Electro mass spectra were recorded using a Mass Lynx NT V 3.4 on a Waters 600 controller connected to a 996 photodiode array detector, with HPLC grade carried solvents. Accurate molecular weights were determined by a peak-matching method, using leucine enkephaline (H-Tyr-Gly-Gly-Phe-Leu-OH) as the standard reference (m/z = 556.2771); all accurate mass were reported within ± 5 ppm of the expected mass. Infrared spectra were recorded on a Perkin Elmer Spectrum One FT-IR spectrometer fitted with a universal ATR sampling accessory. Elemental analysis was carried out at the Microanalysis Laboratory, School of Chemistry and Chemical Biology, University College Dublin.

7.1 UV-vis absorption and luminescence spectroscopy

Using a 1.0 cm path length quartz cell, UV-vis absorption and luminescence spectra were recorded using a Varian CARY 50 and a Varian Cary Eclipse spectrophotometer, respectively. The solvents utilised were of either HPLC or spectrophotometric grade. The concentrations of the ligands and complexes analysed were the same for both UV-vis and luminescence titrations. All measurements were performed at 298 K, with this maintained using a thermostated unit block. Baseline correction measurements were employed for all UV-vis spectra, where the blank was a sample of the solvent system in which the titration was performed. The parameters used for the UV-vis absorption and luminescence titration studies reported in Chapters 2 – 6 are listed below in Table 7.1 – 7.4. Voltage was adjusted as necessary to prevent signal saturation.

Table 7.1: *UV-vis absorption settings for all titrations in Chapters 2 – 6.*

Scan: 200 – 450 nm
Exc. Slit: 1 nm
Em. Slit: 1 nm
Scan Rate: 600 nm min^{-1}

Table 7.2: *Phosphorescence settings for all titrations in Chapters 2 – 5.*

Mode: Phosphorescence	**Excitation:** 281 nm	**Scan:** 570 – 720 nm
Exc. Slit: 20 nm	**Em. Slit:** 1.5 nm	**Voltage:** Variable
Flash Count: 1	**Gate Time:** 5 ms	**Delay Time:** 0.1 ms
Averaging Time: 0.1 s	**Total Decay Time:** 0.02 s	**Data Interval:** 1 nm

Table 7.3: *Phosphorescence settings for titrations involving* ***85*** *and* ***Eu.75/Tb.75*** *in Chapter 6 (including anion displacement assays).*

Mode: Phosphorescence	**Excitation:** 279 nm	**Scan:** 570 – 720 nm (Eu) 450 – 700 nm (Tb)
Exc. Slit: 20 nm	**Em. Slit:** 1.5 nm	**Voltage:** Variable
Flash Count: 1	**Gate Time:** 5 ms	**Delay Time:** 0.1 ms
Averaging Time: 0.1 s	**Total Decay Time:** 0.02 s	**Data Interval:** 1 nm

Table 7.4: *Phosphorescence settings for titrations involving* ***90*** *and* ***Eu.75/Tb.75*** *in Chapter 6.*

Mode: Phosphorescence	**Excitation:** 296 nm	**Scan:** 570 – 720 nm (Eu) 450 – 700 nm (Tb)
Exc. Slit: 20 nm	**Em. Slit:** 5 nm	**Voltage:** 650 V (Eu) 850 V (Tb)
Flash Count: 1	**Gate Time:** 5 ms	**Delay Time:** 0.1 ms
Averaging Time: 0.1 s	**Total Decay Time:** 0.02 s	**Data Interval:** 1 nm

7.2 Luminescence lifetime measurements

The luminescence lifetime measurements for the synthesised Eu(III) complexes in Chapters 2 – 5 were conducted using a Varian Carey Eclipse Fluorimeter in time-resolved mode at 298 K. All lifetime values were obtained from an average of six independent measurements, each recorded with a different gate time in the range 0.020 – 0.045 ms. The fluorimeter settings for the lifetime measurements are shown in Table 7.5.

Table 7.5: *Luminescence settings for the lifetime measurements of the Eu(III) complexes in Chapters 2 – 5.*

Excitation: 281 nm	**Emission:** 616 nm	**Delay Time:** 0.01 ms
Exc. Slit: 20 nm	**Em. Slit:** 20 nm	**Gate Time:** Variable
Flash Count: 1	**Total Decay Time:** 20 ms	**Delay Time:** 0.1 ms

7.3 Circular dichroism and circularly polarised luminescence measurements

CD spectra were recorded on a Jasco J-810-150S spectropolarimeter. Each CD trace represents an average of three scans. CPL spectra were recorded by Dr. R. D. Peacock at the University of Glasgow. Calibration of the emission monochromator was managed by passing scattered light from a low power HeNe laser through the detection system. This optical detection system consisted of a photoelastic modulator (PEM, Hinds Int.) operating at 50 kHz and a linear polariser, which together combine to act as a circular analyser, followed by a long pass filter, focusing lens, and a 0.22 m double monochromator. The emitted light was detected by a cooled EMI-9558QB photomultiplier tube operating in photon counting mode. The 50 kHz reference signal from the photoelastic modulator was used to direct the incoming

pulses into two separated counters. An up counter, which counts every photon pulse and, therefore, is a measure of the total luminescence signal ($I = I_L + I_R$), and an up-down counter, which adds pulses when the analyser is transmitting left-handed circularly polarised light, and subtracts pulses when the analyser is transmitting right-handed circularly polarised light. The second counter then provides a measure of the differential emission intensity ($\Delta I = I_L - I_R$).

7.4 X-ray crystallographic characterisation

X-ray data was collected on either a Rigaku Saturn 724 CCD Diffractometer using graphite-monochromated MoK_α radiation (α = 0.71073 Å) or a Bruker APEX II CCD Diffractometer using graphite-monochromated MoK_α radiation (α = 0.71073 Å) or CuK_α radiation (α = 1.54178 Å). Depending on the instrument used, the datasets were collected using either CrystalClear (Rigaku) or APEX2 (Bruker) software; with data integration, reduction, and correction for absorption and polarisation effects, as well as space group determinations, all performed using this software. The structures were solved by direct methods (SHELXS-97) and refined against all F2 data (SHELXS-97).[325] With the exception of OH and NH protons, all H atoms were positioned geometrically and refined using riding model with d(CH) = 0.95 Å, Uiso = 1.2 Ueq (C). OH and NH protons were found from the difference map and fixed to the attached atoms with UH = 1.2 UX.

7.5 General experimental procedures

Procedure 1: Nucleophile substitution reactions of 39S and 39R[237]

Nucleophilic substitution at the 4-hydroxy group of **39S/R** was accomplished by first stirring **39S/R** with anhydrous K_2CO_3 in anhydrous DMF for 30 min at 25 °C. The relevant organic halide was then added, along with a catalytic amount of KI, and the solution heated at 80 °C for 72 h. After reaction completion, the solvent was removed under reduced pressure and CH_2Cl_2 was added to the residue. The organic layer was subsequently washed twice with 1% aqueous acetic acid and H_2O, before drying over $MgSO_4$. In each case, removal of the solvent under reduced pressure yielded a crude oil requiring further purification.

Procedure 2: Synthesis of monometallic Eu(III) sliotar complexes using $Eu(CF_3SO_3)_3$

All monometallic Eu(III) self-assemblies found within were prepared by refluxing, under microwave irradiation, the pertinent ligand with 0.33 eq. of $Eu(CF_3SO_3)_3$ in HPLC grade solvent (MeOH or CH_3CN) for 20 min. The resulting clear solution was subjected to slow vapour diffusion of diethyl ether, precipitating the desired complex solid. The product was then isolated by filtration and dried under vacuum. Owing to the paramagnetic nature of the Eu(III) ion, ^{1}H NMR spectra of the complexes consisted of broad signals and, therefore, were not fully characterised. These paramagnetic properties also prevent ^{13}C NMR spectra from being recorded.

7.6 Experimental details for Chapter 2

2-(2-Methoxy-ethoxy)ethyl 4-tosylate (47)[236]

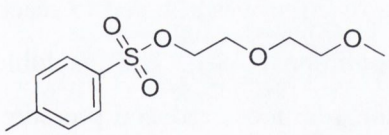

Diethylene glycol monomethyl ether (10.00 g, 9.09 mL, 83.22 mmol, 1.00 eq.) in THF (30 mL) was added to a solution of NaOH (4.90 g, 122.53 mmol, 1.50 eq.) in H_2O (50 mL) at 0 °C. 4-toluenesulfonyl chloride (17.40 g, 91.27 mmol, 1.10 eq.) was added to the solution and the mixture was allowed to warm to room temperature. The reaction was then left stirring for 72 h. The THF was removed under reduced pressure and the aqueous solution was extracted with $CHCl_3$ and dried over $MgSO_4$. The solvent was removed under reduced pressure to give **47** as a colourless oil (13.72 g, 50.01 mmol, 60% yield). HRMS (*m/z*) (ES^+) Calculated for $C_{12}H_{19}O_5S$ *m/z* = 275.0953 $[M + H]^+$. Found *m/z* = 275.0941; ^{1}H NMR (400 MHz, $CDCl_3$) δ_H: 7.79 (2H, d, *J* = 7.8 Hz, ar-H), 7.33 (2H, d, *J* = 7.8 Hz, ar-H), 4.16 (2H, t, *J* = 4.5 Hz, CH_2), 3.71 (2H, t, *J* = 4.5 Hz, CH_2), 3.57 (2H, m, CH_2), 3.47 (2H, m, CH_2), 3.35

(3H, s, OC<u>H</u>$_3$), 2.44 (3H, s, C<u>H</u>$_3$); ^{13}C NMR (100 MHz, $CDCl_3$) δ_C: 144.4, 132.4, 129.4, 127.6, 71.3, 70.2, 68.8, 68.3, 58.6, 21.2; IR υ_{max} (cm^{-1}): 2880, 1739, 1598, 1452, 1353, 1174, 1096, 1010, 916, 815, 773, 662.

1-Iodo-2-(2-methoxy-ethoxy)ethane (48)[236]

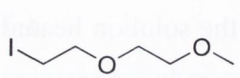

Compound **47** (13.72 g, 50.01 mmol, 1.00 eq.) and NaI (10.50 g, 70.05 mmol, 1.40 eq.) were refluxed in acetone (100 mL) for 16 h. The white precipitate which formed was removed by suction filtration and the solvent was removed under reduced pressure. The residue was then dissolved in $CHCl_3$ and washed twice with H_2O, brine, and dried over $MgSO_4$. The solvent was removed under reduced pressure to give **48** as a red/brown oil (8.51 g, 36.99 mmol, 74% yield). HRMS (*m/z*) (ES$^+$) Calculated for $C_5H_{11}O_2INa$ *m/z* = 252.9702 [M + Na]$^+$. Found *m/z* = 252.9693; ^{1}H NMR (400 MHz, $CDCl_3$) δ_H: 3.74 (2H, t, *J* = 6.9 Hz, C<u>H</u>$_2$CH$_2$I), 3.63 (2H, m, C<u>H</u>$_2$), 3.54 (2H, m, C<u>H</u>$_2$OCH$_3$), 3.37 (3H, s, OC<u>H</u>$_3$), 3.25 (2H, t, *J* = 6.8 Hz, C<u>H</u>$_2$I); ^{13}C NMR (100 MHz, $CDCl_3$) δ_C: 71.6, 71.4, 69.6, 58.7, 2.3; IR υ_{max} (cm^{-1}): 2875, 1738, 1453, 1354, 1263, 1198, 1170, 1092, 1032, 978, 880, 850, 750.

4-Hydroxy-*N*,*N*'-bis((*S*)-1-(naphthalen-1-yl)ethyl)pyridine-2,6-dicarboxamide (39S)[231]

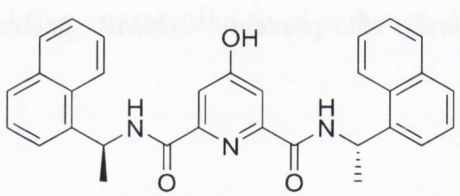

To a stirred solution of (*S*)-(-)-1-(1-naphthyl)-ethylamine (1.96 g, 1.84 mL, 11.47 mmol, 2.10 eq.) in anhydrous THF (35 mL), HOBt (1.48 g, 10.92 mmol, 2.00 eq.) and chelidamic acid (1.00 g, 5.46 mmol, 1.00 eq.) were added. The solution was stirred for 30 min at 0 °C before addition of EDCI.HCl (2.15 g, 11.19 mmol, 2.05 eq.) and triethylamine (1.10 g, 1.52 mL, 10.92 mmol, 2.00 eq.), with stirring for a further 30 min under argon. The reaction was allowed to reach room temperature and the mixture was left stirring for an additional 48 h. The insoluble residue was removed by suction filtration and the solvent removed under reduced pressure. CH_2Cl_2 was added to the crude oil before washing twice with 1 M HCl, a saturated solution of $NaHCO_3$, and H_2O. The organic layer was then dried over $MgSO_4$, filtered, and the solvent removed under reduced pressure. Purification was achieved by flash silica column chromatography (gradient elution 100:0 → 95:5; CH_2Cl_2/MeOH) followed by precipitation, done by dissolution in a minimum volume of MeOH, and dropping into H_2O. The product was isolated by filtration and dried over P_2O_5, affording **39S** as a cream coloured solid (1.68 g, 3.43 mmol, 63% yield). m.p. 159 – 161 °C; HRMS (*m/z*) (ES$^+$) Calculated for $C_{31}H_{27}N_3O_3Na$ *m/z* = 512.1950 [M + Na]$^+$. Found *m/z* = 512.1964; ^{1}H NMR (600 MHz,

CD_3CN-d_3) δ_H: 8.55 (1H, d, J = 1.3 Hz, NH), 8.25 (2H, d, J = 1.4 Hz, naph-H), 7.97 (2H, d, J = 1.6 Hz, naph-H), 7.87 (2H, d, J = 1.4 Hz, naph-H), 7.70 (2H, d, J = 0.7 Hz, py-H), 7.68 (2H, d, J = 1.2 Hz, naph-H), 7.58 (2H, m, naph-H), 7.55 (2H, m, naph-H), 7.54 (2H, m, naph-H), 6.07 (2H, m, CH), 1.73 (6H, d, J = 1.1 Hz, CH_3); ^{13}C NMR (150 MHz, CD_3CN-d_3) δ_C: 167.1, 163.7, 152.2, 140.2, 134.8, 131.9, 129.7, 128.8, 127.3, 126.7, 126.4, 124.1, 123.9, 113.1, 46.1, 21.4; IR υ_{max} (cm^{-1}): 3283, 1653, 1600, 1521, 1449, 1355, 1238, 1178, 1136, 997, 889, 857, 799, 775, 691.

4-Hydroxy-*N*,*N*'-bis((*R*)-1-(naphthalen-1-yl)ethyl)pyridine-2,6-dicarboxamide (39R)[231]

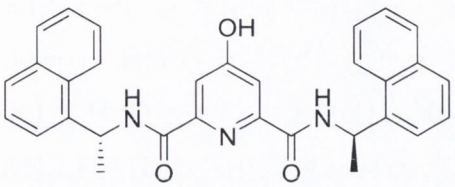

To a stirred solution of (*R*)-(+)-1-(1-naphthyl)-ethylamine (1.96 g, 1.84 mL, 11.47 mmol, 2.10 eq.) in anhydrous THF (35 mL), HOBt (1.48 g, 10.92 mmol, 2.00 eq.) and chelidamic acid (1.00 g, 5.46 mmol, 1.00 eq.) were added. The solution was stirred for 30 min at 0 °C before addition of EDCI.HCl (2.15 g, 11.19 mmol, 2.05 eq.) and triethylamine (1.10 g, 1.52 mL, 10.92 mmol, 2.00 eq.), with stirring for a further 30 min under argon. The reaction was allowed to reach room temperature and the mixture was left stirring for an additional 48 h. The insoluble residue was removed by suction filtration and the solvent removed under reduced pressure. CH_2Cl_2 was added to the crude oil before washing twice with 1 M HCl, a saturated solution of $NaHCO_3$, and H_2O. The organic layer was then dried over $MgSO_4$, filtered, and the solvent removed under reduced pressure. Purification was achieved by flash silica column chromatography (gradient elution 100:0 → 95:5; CH_2Cl_2/MeOH) followed by precipitation, done by dissolution in a minimum volume of MeOH, and dropping into H_2O. The product was isolated by filtration and dried over P_2O_5, affording **39R** as a cream coloured solid (1.50 g, 3.06 mmol, 56% yield). m.p. 159 – 161 °C; HRMS (*m/z*) (ES^-) Calculated for $C_{31}H_{26}N_3O_3$ *m/z* = 488.1974 $[M - H]^-$. Found *m/z* = 488.1978; ^{1}H NMR (600 MHz, CD_3CN-d_3) δ_H: 8.55 (1H, d, J = 1.3 Hz, NH), 8.25 (2H, d, J = 1.4 Hz, naph-H), 7.97 (2H, d, J = 1.6 Hz, naph-H), 7.87 (2H, d, J = 1.4 Hz, naph-H), 7.70 (2H, d, J = 0.7 Hz, py-H), 7.68 (2H, d, J = 1.2 Hz, naph-H), 7.58 (2H, m, naph-H), 7.55 (2H, m, naph-H), 7.54 (2H, m, naph-H), 6.07 (2H, m, CH), 1.73 (6H, d, J = 1.1 Hz, CH_3); ^{13}C NMR (150 MHz, CD_3CN-d_3) δ_C: 167.1, 163.7, 152.2, 140.2, 134.8, 131.9, 129.8, 128.8, 127.3, 126.7, 126.4, 124.2, 123.9, 113.1, 46.2, 21.4; IR υ_{max} (cm^{-1}): 3283, 1653, 1600, 1521, 1449, 1355, 1238, 1178, 1136, 997, 889, 857, 799, 775, 691.

4-Propoxy-*N*,*N*'-bis((*S*)-1-(naphthalen-1-yl)ethyl)pyridine-2,6-dicarboxamide (41S)[237]

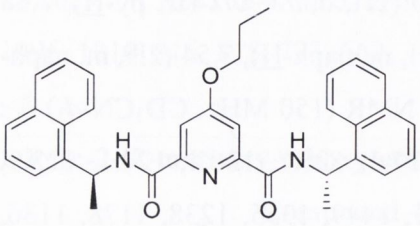

Compound **41S** was synthesised according to **Procedure 1** using 1-bromopropane as the alkylating agent. The quantities of the respective reagents and solvent were as follows; **39S** (0.20 g, 0.41 mmol, 1.00 eq.), K_2CO_3 (0.11 g, 0.82 mmol, 2.00 eq.), 1-bromopropane (0.15 g, 0.11 mL, 1.23 mmol, 3.00 eq.), DMF (5 mL). The crude product was recrystallised from EtOH to give **41S** as a white crystalline solid (0.07 g, 0.13 mmol, 32% yield). m.p. 197 – 199 °C; HRMS (*m/z*) (ES^+) Calculated for $C_{34}H_{34}N_3O_3$ *m/z* = 532.2600 $[M + H]^+$. Found *m/z* = 532.2603; ^1H NMR (600 MHz, $CDCl_3$) δ_H: 8.15 (2H, m, naph-H), 7.92 (2H, d, *J* = 8.4 Hz, NH), 7.88 (2H, m, naph-H), 7.84 – 7.78 (4H, m, py-H + naph-H), 7.54 – 7.47 (4H, m, naph-H), 7.45 – 7.40 (4H, m, naph-H), 6.01 (2H, m, CH), 4.04 (2H, t, *J* = 6.5 Hz, OCH_2), 1.83 (2H, m, OCH_2CH_2), 1.63 (6H, d, *J* = 6.9 Hz, CH_3), 1.02 (3H, t, *J* = 7.3 Hz, $OCH_2CH_2CH_3$); ^{13}C NMR (150 MHz, $CDCl_3$) δ_C: 168.1, 162.5, 150.6, 138.4, 134.1, 131.1, 129.1, 128.6, 126.8, 126.1, 125.4, 123.4, 122.9, 111.6, 70.6, 45.5, 22.3, 21.2, 10.4; IR υ_{max} (cm^{-1}): 3285, 3050, 2968, 2877, 1659, 1638, 1597, 1509, 1474, 1453, 1354, 1305, 1262, 1236, 1210, 1172, 1120, 1094, 1081, 1033, 996, 949, 910, 882, 855, 813, 800, 776, 753, 733, 697, 620, 604, 587, 565.

4-Propoxy-*N*,*N*'-bis((*R*)-1-(naphthalen-1-yl)ethyl)pyridine-2,6-dicarboxamide (41R)[237]

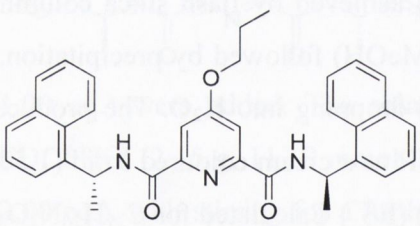

Compound **41R** was synthesised according to **Procedure 1** using 1-bromopropane as the alkylating agent. The quantities of the respective reagents and solvent were as follows; **39R** (0.20 g, 0.41 mmol, 1.00 eq.), K_2CO_3 (0.11 g, 0.82 mmol, 2.00 eq.), 1-bromopropane (0.15 g, 0.11 mL, 1.23 mmol, 3.00 eq.), DMF (5 mL). The crude product was recrystallised from EtOH to give **41R** as a white crystalline solid (0.08 g, 0.15 mmol, 37% yield). m.p. 197 – 199 °C; HRMS (*m/z*) (ES^+) Calculated for $C_{34}H_{34}N_3O_3$ *m/z* = 532.2600 $[M + H]^+$. Found *m/z* = 532.2582; ^1H NMR (400 MHz, $CDCl_3$) δ_H: 8.15 (2H, m, naph-H), 7.95 (2H, d, *J* = 8.4 Hz, NH), 7.88 (2H, m, naph-H), 7.84 – 7.78 (4H, m, py-H + naph-H), 7.54 – 7.47 (4H, m, naph-H), 7.45 – 7.39 (4H, m, naph-H), 6.01 (2H, m, CH), 4.04 (2H, t, *J* = 6.5 Hz, OCH_2), 1.83 (2H, m, OCH_2CH_2), 1.63 (6H, d, *J* = 6.9 Hz, CH_3), 1.02 (3H, t, *J* = 7.3 Hz, $OCH_2CH_2CH_3$); ^{13}C NMR (150 MHz, $CDCl_3$) δ_C: 168.1, 162.4, 150.5, 138.4, 134.1, 131.1, 129.1, 128.5, 126.7, 126.0, 125.4, 123.4, 122.9, 111.7, 70.6, 45.5, 22.2, 21.1, 10.4; IR υ_{max} (cm^{-1}): 3282, 3050, 2963, 2877, 1658, 1636, 1597, 1509, 1474, 1453, 1354, 1304, 1261, 1237, 1210, 1173,

1119, 1095, 1081, 1033, 996, 949, 911, 882, 855, 813, 799, 775, 754, 733, 691, 620, 604, 587, 564.

4-(Prop-2-ynyloxy)-*N*,*N*'-bis((*S*)-1-(naphthalen-1-yl)ethyl)pyridine-2,6-dicarboxamide (42S)[237]

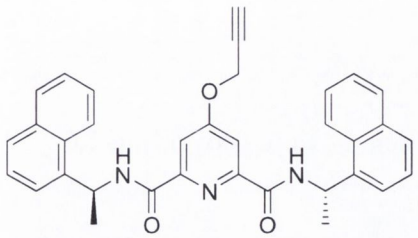

Compound **42S** was synthesised according to **Procedure 1** using propargyl bromide as the alkylating agent. The quantities of the respective reagents and solvent were as follows; **39S** (0.50 g, 1.02 mmol, 1.00 eq.), K_2CO_3 (0.28 g, 2.04 mmol, 2.00 eq.), propargyl bromide solution (80% *w*/*v* in toluene) (0.75 g, 0.56 mL, 5.10 mmol, 5.00 eq.), DMF (20 mL). The crude product was recrystallised from EtOH to give **42S** as a white fibrous solid (0.31 g, 0.59 mmol, 58% yield). m.p. 130 – 133 °C; Calculated for $C_{36}H_{37}N_3O_5$ + $0.5H_2O$: C, 76.57; H, 5.57; N, 7.79. Found C, 76.73; H, 5.18; N, 7.70; HRMS (*m*/*z*) (ES^+) Calculated for $C_{34}H_{29}N_3O_3Na$ *m*/*z* = 550.2107 $[M + Na]^+$. Found *m*/*z* = 550.2116; ^1H NMR (600 MHz, $CDCl_3$) δ_H: 8.15 (2H, m, naph-H), 7.91 – 7.84 (6H, m, NH + py-H + naph-H), 7.81 (2H, m, naph-H), 7.53 – 7.48 (4H, m, naph-H), 7.44 – 7.40 (4H, m, naph-H), 6.00 (2H, m, NHCH), 4.80 (2H, t, *J* = 3.2 Hz, CH_2), 2.58 (1H, t, *J* = 2.3 Hz, alkyne-CH), 1.63 (6H, d, *J* = 6.7 Hz, CH_3); ^{13}C NMR (150 MHz, $CDCl_3$) δ_C: 166.4, 162.2, 150.8, 138.2, 134.0, 130.9, 129.0, 128.5, 126.6, 125.9, 125.3, 123.3, 122.7, 111.7, 56.3, 45.4, 21.0; IR υ_{max} (cm^{-1}): 3273, 2971, 1643, 1597, 1510, 1445, 1372, 1343, 1305, 1261, 1236, 1172, 1132, 1032, 997, 950, 914, 881, 800, 776, 695, 636, 587, 574.

4-(Prop-2-ynyloxy)-*N*,*N*'-bis((*R*)-1-(naphthalen-1-yl)ethyl)pyridine-2,6-dicarboxamide (42R)[237]

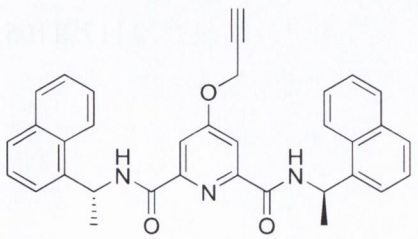

Compound **42R** was synthesised according to **Procedure 1** using propargyl bromide as the alkylating agent. The quantities of the respective reagents and solvent were as follows; **39R** (0.50 g, 1.02 mmol, 1.00 eq.), K_2CO_3 (0.28 g, 2.04 mmol, 2.00 eq.), propargyl bromide solution (80% *w*/*v* in toluene) (0.75 g, 0.56 mL, 5.10 mmol, 5.00 eq.), DMF (20 mL). The crude product was recrystallised from EtOH to give **42R** as a white fibrous solid (0.36 g, 0.68 mmol, 67% yield). m.p. 130 – 133 °C; Calculated for $C_{34}H_{29}N_3O_3$ + $0.2CHCl_3$: C, 74.48; H, 5.34; N, 7.62. Found C, 74.32; H, 5.02; N, 7.38; HRMS (*m*/*z*) (ES^+) Calculated for $C_{34}H_{30}N_3O_3$ *m*/*z* = 528.2287 $[M + H]^+$. Found *m*/*z* = 528.2283; ^1H NMR

(600 MHz, $CDCl_3$) δ_H: 8.15 (2H, m, naph-H), 7.92 – 7.86 (6H, m, NH + py-H + naph-H), 7.82 (2H, m, naph-H), 7.53 – 7.48 (4H, m, naph-H), 7.44 – 7.41 (4H, m, naph-H), 6.01 (2H, m, NHCH), 4.80 (2H, t, J = 3.2 Hz, CH_2), 2.58 (1H, t, J = 2.3 Hz, alkyne-CH), 1.63 (6H, d, J = 6.7 Hz, CH_3); ^{13}C NMR (150 MHz, $CDCl_3$) δ_C: 166.6, 162.3, 150.9, 138.3, 134.1, 131.1, 129.1, 128.6, 126.8, 126.1, 125.4, 123.4, 122.9, 111.9, 56.5, 45.5, 21.2; IR υ_{max} (cm^{-1}): 3281, 2979, 1645, 1598, 1511, 1446, 1373, 1343, 1305, 1261, 1236, 1173, 1132, 1041, 997, 949, 914, 882, 801, 776, 696, 639, 587, 575.

4-(2-(2-Methoxy-ethoxy)ethoxy)-*N*,*N*'-bis((*S*)-1-(naphthalen-1-yl)ethyl)pyridine-2,6-dicarboxamide (43S)[237]

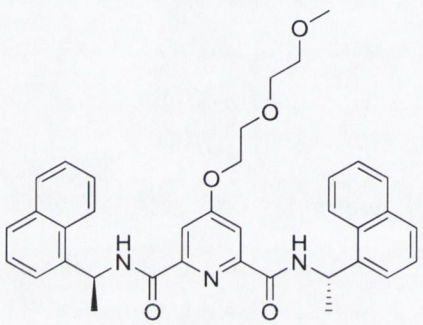

Compound **43S** was synthesised according to **Procedure 1** using **48** as the alkylating agent. The quantities of the respective reagents and solvent were as follows; **39S** (0.50 g, 1.02 mmol, 1.00 eq.), K_2CO_3 (0.28 g, 2.04 mmol, 2.00 eq.), **48** (0.35 g, 1.53 mmol, 1.50 eq.), DMF (20 mL). The crude product was recrystallised from EtOH to give **43S** as a white crystalline solid (0.31 g, 0.52 mmol, 51% yield). m.p. 155 – 157 °C; Calculated for $C_{36}H_{37}N_3O_5$ + $0.25H_2O$: C, 72.52; H, 6.34; N, 7.05. Found C, 72.50; H, 6.06; N, 6.89; HRMS (*m/z*) (ES^+) Calculated for $C_{36}H_{37}N_3O_5Na$ *m/z* = 614.2631 $[M + Na]^+$. Found *m/z* = 614.2631; ^1H NMR (600 MHz, $CDCl_3$) δ_H: 8.15 (2H, m, naph-H), 7.89 (2H, m, naph-H), 7.85 – 7.79 (6H, m, NH + py-H + naph-H), 7.53 – 7.49 (4H, m, naph-H), 7.45 – 7.41 (4H, m, naph-H), 6.00 (2H, m, CH), 4.27 (2H, m, CH_2), 3.88 (2H, m, CH_2), 3.71 (2H, m, CH_2), 3.57 (2H, m, CH_2), 3.38 (3H, s, OCH_3), 1.64 (6H, d, J = 6.7 Hz, CH_3); ^{13}C NMR (150 MHz, $CDCl_3$) δ_C: 167.5, 162.3, 150.6, 138.2, 133.9, 130.9, 128.9, 128.4, 126.6, 125.9, 125.2, 123.2, 122.7, 111.4, 71.9, 70.8, 69.1, 68.3, 59.1, 45.2, 20.9; IR υ_{max} (cm^{-1}): 3287, 3049, 2973, 2928, 2872, 1655, 1636, 1598, 1568, 1512, 1443, 1398, 1371, 1349, 1335, 1307, 1279, 1236, 1209, 1172, 1128, 1117, 1105, 1081, 1061, 1028, 996, 963, 950, 889, 862, 853, 803, 775, 753, 736, 725, 696, 687.

4-(2-(2-Methoxy-ethoxy)ethoxy)-*N*,*N*'-bis((*R*)-1-(naphthalen-1-yl)ethyl)pyridine-2,6-dicarboxamide (43R)[237]

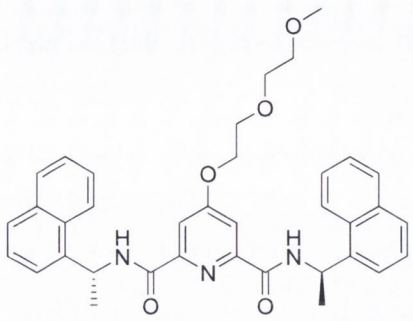

Compound **43R** was synthesised according to **Procedure 1** using **48** as the alkylating agent. The quantities of the respective reagents and solvent were as follows; **39R** (0.50 g, 1.02 mmol, 1.00 eq.), K_2CO_3 (0.28 g, 2.04 mmol, 2.00 eq.), **48** (0.35 g, 1.53 mmol, 1.50 eq.), DMF (20 mL). The crude product was recrystallised from EtOH to give **43R** as a white crystalline solid (0.29 g, 0.49 mmol, 48% yield). m.p. 155 – 157 °C; Calculated for $C_{36}H_{37}N_3O_5 + 0.25H_2O$: C, 72.52; H, 6.34; N, 7.05. Found C, 72.52; H, 6.10; N, 6.94; HRMS (*m/z*) (ES^+) Calculated for $C_{36}H_{38}N_3O_5$ *m/z* = 592.2811 $[M + H]^+$. Found *m/z* = 592.2828; ^1H NMR (600 MHz, $CDCl_3$) δ_H: 8.15 (2H, m, naph-H), 7.89 (2H, m, naph-H), 7.86 – 7.79 (6H, m, NH + py-H + naph-H), 7.53 – 7.49 (4H, m, naph-H), 7.45 – 7.41 (4H, m, naph-H), 6.01 (2H, m, CH), 4.27 (2H, m, CH_2), 3.88 (2H, m, CH_2), 3.71 (2H, m, CH_2), 3.57 (2H, m, CH_2), 3.39 (3H, s, OCH_3), 1.64 (6H, d, J = 6.7 Hz, CH_3); ^{13}C NMR (150 MHz, $CDCl_3$) δ_C: 167.6, 162.2, 150.5, 138.2, 134.0, 130.9, 128.9, 128.4, 126.6, 125.9, 125.3, 123.2, 122.7, 111.5, 71.9, 70.9, 69.1, 68.3, 59.1, 45.3, 21.0; IR υ_{max} (cm^{-1}): 3287, 2972, 2927, 2872, 1655, 1636, 1599, 1568, 1513, 1444, 1397, 1371, 1349, 1307, 1236, 1172, 1118, 1105, 1081, 1061, 1028, 996, 889, 862, 803, 775, 753, 725, 688.

Complex Eu.41S$_3$

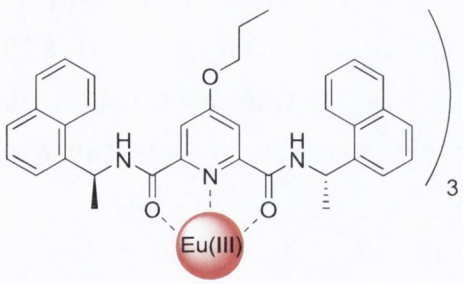

Complex **Eu.41S$_3$** was synthesised according to **Procedure 2** using ligand **41S** (0.018 g, 0.033 mmol, 1.00 eq.) and $Eu(CF_3SO_3)_3$ (0.007 g, 0.011 mmol, 0.33 eq.) in MeOH (5 mL). A white crystalline solid was obtained (0.019 g, 0.009 mmol, 82% yield). m.p. decomposed above 230 °C; Calculated for $C_{102}H_{99}N_9O_9Eu + 3CF_3SO_3 + 0.75CHCl_3$: C, 55.62; H, 4.40; N, 5.52. Found C, 55.69; H, 3.93; N, 5.10; HRMS (*m/z*) ($MALDI^+$) Calculated for $C_{102}H_{97}N_9O_9Eu$ *m/z* = 1744.6640 $[M - 3CF_3SO_3 - 2H]^+$. Found *m/z* = 1744.6824; ^1H NMR (400 MHz, CD_3OD-d_4) δ_H: 10.27, 10.18, 8.27, 7.42, 7.13, 6.58, 6.05, 3.03, 2.33, 1.66, 1.00; IR υ_{max} (cm^{-1}): 3277, 3098, 2972, 1618, 1596, 1555, 1448, 1361, 1291, 1237, 1164, 1032, 964, 913, 856, 796, 774, 731, 636, 573.

Complex Eu.41R$_3$

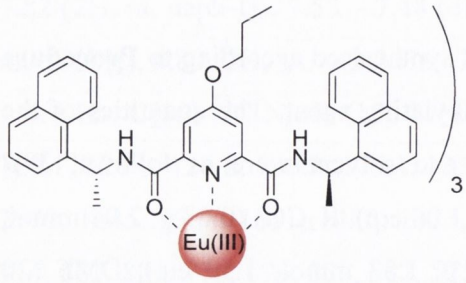

Complex **Eu.41R$_3$** was synthesised according to **Procedure 2** using ligand **41R** (0.018 g, 0.033 mmol, 1.00 eq.) and Eu(CF_3SO_3)$_3$ (0.007 g, 0.011 mmol, 0.33 eq.) in MeOH (5 mL). A white crystalline solid was obtained (0.015 g, 0.007 mmol, 64% yield). m.p. decomposed above 220 °C; Calculated for $C_{102}H_{99}N_9O_9Eu$ + $3CF_3SO_3$: C, 57.48; H, 4.55; N, 5.75. Found C, 57.23; H, 4.34; N, 5.48; HRMS (*m/z*) (MALDI$^+$) Calculated for $C_{102}H_{97}N_9O_9Eu$ *m/z* = 1744.6640 [M – $3CF_3SO_3$ – 2H]$^+$. Found *m/z* = 1744.6713; ^{1}H NMR (400 MHz, CD_3OD-d_4) δ_H: 10.38, 8.31, 7.42, 7.11, 6.54, 6.00, 2.98, 2.35, 1.64, 0.99; IR υ_{max} (cm^{-1}): 3280, 3103, 2976, 1618, 1596, 1556, 1449, 1361, 1291, 1237, 1164, 1032, 964, 918, 856, 796, 774, 731, 636, 573.

Complex Eu.42S$_3$

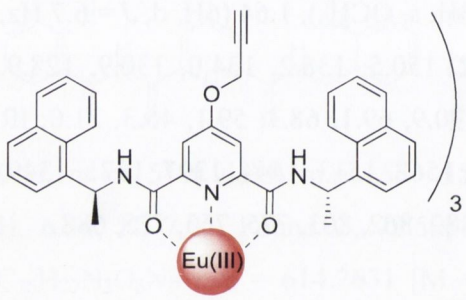

Complex **Eu.42S$_3$** was synthesised according to **Procedure 2** using ligand **42S** (0.030 g, 0.057 mmol, 1.00 eq.) and Eu(CF_3SO_3)$_3$ (0.011 g, 0.019 mmol, 0.33 eq.) in MeOH (5 mL). A white crystalline solid was obtained (0.031 g, 0.014 mmol, 74% yield). m.p. decomposed above 220 °C; Calculated for $C_{102}H_{87}N_9O_9Eu$ + $3CF_3SO_3$ + $1.5CH_2Cl_2$: C, 55.39; H, 3.93; N, 5.46. Found C, 55.68; H, 3.66; N, 5.24; HRMS (*m/z*) (MALDI$^+$) Calculated for $C_{102}H_{85}N_9O_9Eu$ *m/z* = 1732.5701 [M – $3CF_3SO_3$ – 2H]$^+$. Found *m/z* = 1732.5735; ^{1}H NMR (400 MHz, CD_3OD-d_4) δ_H: 10.31, 8.29, 7.45, 7.22, 6.62, 6.04, 4.15, 3.80, 3.50, 2.35; IR υ_{max} (cm^{-1}): 3273, 3100, 2978, 1747, 1618, 1597, 1556, 1447, 1369, 1274, 1234, 1152, 1047, 1030, 946, 921, 877, 798, 776, 749, 636, 574.

Complex Eu.42R$_3$

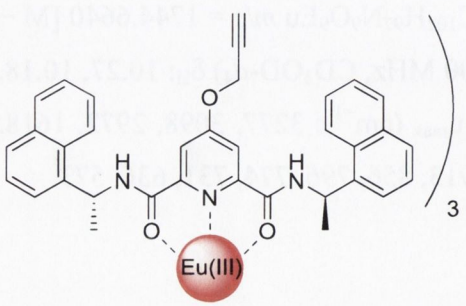

Complex **Eu.42R$_3$** was synthesised according to **Procedure 2** using ligand **42R** (0.030 g, 0.057 mmol, 1.00 eq.) and Eu(CF_3SO_3)$_3$ (0.011 g, 0.019 mmol, 0.33 eq.) in MeOH (5 mL). A white crystalline solid was obtained (0.028 g, 0.013 mmol, 68% yield). m.p. decomposed above 230 °C; Calculated for $C_{102}H_{87}N_9O_9Eu$ + $3CF_3SO_3$ + $1.5CH_2Cl_2$: C, 55.39; H, 3.93; N, 5.46. Found C, 55.37; H,

3.63; N, 5.19; HRMS (*m/z*) (MALDI$^+$) Calculated for $C_{102}H_{85}N_9O_9Eu$ *m/z* = 1732.5701 [M – $3CF_3SO_3$ – 2H]$^+$. Found *m/z* = 1732.5709; ^{1}H NMR (400 MHz, CD_3OD-d_4) δ_H: 10.29, 8.29, 7.47, 7.24, 6.65, 6.08, 4.16, 3.82, 3.53, 2.34; IR υ_{max} (cm^{-1}): 3272, 3098, 2979, 1746, 1619, 1597, 1556, 1447, 1368, 1272, 1234, 1152, 1046, 1030, 946, 920, 876, 801, 777, 749, 637, 574.

Complex Eu.43S$_3$

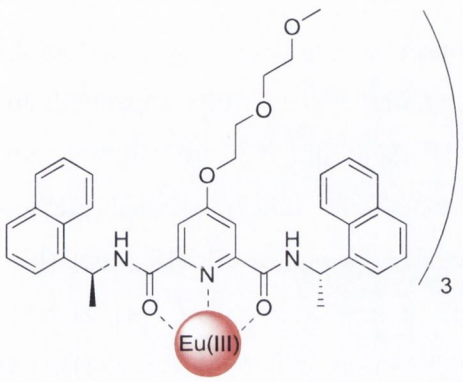

Complex **Eu.43S$_3$** was synthesised according to **Procedure 2** using ligand **43S** (0.028 g, 0.047 mmol, 1.00 eq.) and Eu(CF_3SO_3)$_3$ (0.010 g, 0.016 mmol, 0.33 eq.) in MeOH (5 mL). A white crystalline solid was obtained (0.026 g, 0.011 mmol, 69% yield). m.p. decomposed above 240 °C; Calculated for $C_{108}H_{111}N_9O_{15}Eu$ + $3CF_3SO_3$ + $5H_2O$: C, 54.10; H, 4.95; N, 5.12. Found C, 53.89; H, 4.33; N, 4.69; HRMS (*m/z*) (MALDI$^+$) Calculated for $C_{108}H_{109}N_9O_{15}Eu$ *m/z* = 1924.7277 [M – $3CF_3SO_3$ – 2H]$^+$. Found *m/z* = 1924.7225; ^{1}H NMR (400 MHz, CD_3OD-d_4) δ_H: 10.26, 10.11, 8.26, 7.41, 7.27, 6.59, 5.99, 3.58, 3.51, 3.41, 3.24, 2.25; IR υ_{max} (cm^{-1}): 3284, 2971, 2935, 1739, 1619, 1597, 1557, 1448, 1354, 1287, 1237, 1136, 1060, 1032, 1004, 963, 923, 881, 857, 797, 775, 759, 749, 716.

Complex Eu.43R$_3$

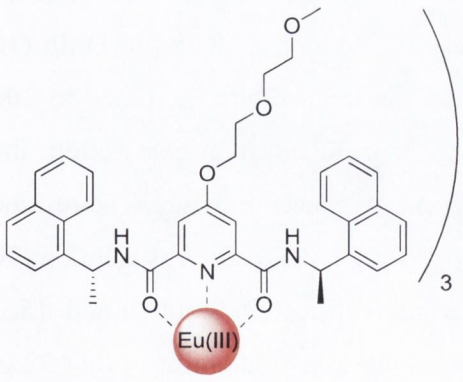

Complex **Eu.43R$_3$** was synthesised according to **Procedure 2** using ligand **43R** (0.028 g, 0.047 mmol, 1.00 eq.) and Eu(CF_3SO_3)$_3$ (0.010 g, 0.016 mmol, 0.33 eq.) in MeOH (5 mL). A white crystalline solid was obtained (0.028 g, 0.012 mmol, 75% yield). m.p. decomposed above 240 °C; Calculated for $C_{108}H_{111}N_9O_{15}Eu$ + $3CF_3SO_3$ + $3H_2O$: C, 54.90; H, 5.19; N, 5.12. Found C, 54.86; H, 4.45; N, 4.98; HRMS (*m/z*) (MALDI$^+$) Calculated for $C_{108}H_{109}N_9O_{15}Eu$ *m/z* = 1924.7277 [M – $3CF_3SO_3$ – 2H]$^+$. Found *m/z* = 1924.7211; ^{1}H NMR (400 MHz, CD_3OD-d_4) δ_H: 10.29, 10.13, 8.28, 7.43, 7.29, 6.61, 6.00, 3.60, 3.53, 3.42, 3.26, 2.27; IR υ_{max} (cm^{-1}): 3283, 2971, 2936, 1739, 1619, 1597, 1556, 1447, 1353, 1288, 1237, 1135, 1059, 1032, 1004, 962, 923, 882, 857, 797, 775, 759, 749, 716.

7.7 Experimental details for Chapter 3

Triethylene glycol monotosylate (58)[265]

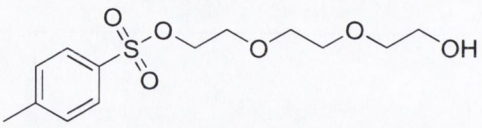

A solution of NaOH (1.64 g, 41.01 mmol, 1.56 eq.) in H_2O (10 mL) was added to a mixture of triethylene glycol (39.39 g, 35.04 mL, 262.30 mmol, 10.00 eq.) and THF (10mL). After cooling the mixture to 5 °C, a solution of 4-toluenesulfonyl chloride (5.00 g, 26.23 mmol, 1.00 eq.) in THF (30 mL) was added over 1 h using a pressure-equalised dropping funnel. The reaction mixture was stirred for a further 2 h at 5 °C before pouring onto ice water (150 mL). The organic layer was then separated, and the aqueous layer extracted with CH_2Cl_2. The resultant organic phases were combined and washed twice with H_2O. Drying over $MgSO_4$ and evaporation under reduced pressure afforded **58** as a clear yellow oil (4.16 g, 13.66 mmol, 52% yield). HRMS (*m/z*) (ES^+) Calculated for $C_{13}H_{20}O_6SNa$ *m/z* = 327.0878 $[M + Na]^+$. Found *m/z* = 327.0874; ^1H NMR (400 MHz, $CDCl_3$) δ_H: 7.79 (2H, d, *J* = 8.1 Hz, ar-H), 7.34 (2H, d, *J* = 8.1 Hz, ar-H), 4.16 (2H, t, *J* = 4.5 Hz, CH_2), 3.70 (4H, m, CH_2), 3.60 (4H, s, CH_2), 3.57 (2H, t, *J* = 4.5 Hz, CH_2), 2.44 (3H, s, CH_3); ^{13}C NMR (100 MHz, $CDCl_3$) δ_C: 145.0, 132.8, 129.9, 128.0, 72.3, 70.7, 69.3, 68.7, 67.0, 61.6, 21.6.

3,4-Bis[2-(2-[2-(4-toluenesulfonyloxy)ethoxy]ethoxy)ethoxy]benzaldehyde (61)[265,266]

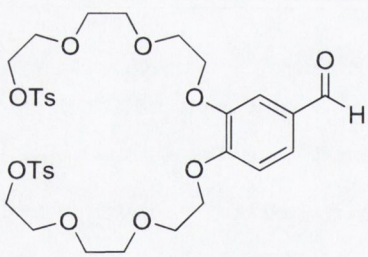

3,4-Dihydroxybenzaldehyde (0.83 g, 6.01 mmol, 1.00 eq.) and anhydrous K_2CO_3 (2.08 g, 15.03 mmol, 2.50 eq.) were stirred in anhydrous DMF (25 mL) for 30 min at room temperature. **58** (4.02 g, 13.22 mmol, 2.20 eq.) in DMF (10 mL) was then added and the temperature increased to 100 °C, with stirring for a further 72 h. Upon completion, the reaction mixture was filtered and the solvent evaporated under reduced pressure. The residue obtained was partitioned between CH_2Cl_2 (70 mL) and 10% *w/v* K_2CO_3 aqueous solution (70 mL). After separation, the organic layer was washed twice with K_2CO_3 solution and dried over $MgSO_4$. Solvent removal under reduced pressure gave **60** as a crude brown oil (1.72 g, 4.27 mmol, 71% crude yield). Without purification, the crude product **60** (1.72 g, 4.27 mmol, 1.00 eq.), triethylamine (4.32 g, 5.95 mL, 42.70 mmol, 10.00 eq.), and a catalytic amount of 4-(dimethylamino)pyridine were dissolved in dry CH_2Cl_2, and the solution cooled to 0 – 5 °C. A solution of 4-toluenesulfonyl chloride (4.07 g, 21.35 mmol, 5.00 eq.) in CH_2Cl_2 (15 mL) was then added over 1 h using a pressure-equalised dropping funnel, maintaining a

temperature below 5 °C. Following addition, the reaction mixture was allowed to warm to room temperature and left to stir overnight. Subsequently, the mixture was acidified with 5 M HCl and the organic layer was separated. The organic phase was washed once with 2 M HCl and twice with brine, before drying over $MgSO_4$, followed by solvent evaporation under reduced pressure. Final purification of the crude product was achieved by flash silica column chromatography (gradient elution 80:20 → 20:80; Hex/EtOAc) to yield **61** as a pale yellow oil (1.68 g, 2.36 mmol, 39% overall yield). HRMS (*m/z*) (ES^+) Calculated for $C_{33}H_{42}O_{13}S_2Na$ *m/z* = 733.1965 $[M + Na]^+$. Found *m/z* = 733.1985; ^1H NMR (400 MHz, $CDCl_3$) δ_H: 9.82 (1H, s, aldehyde-H), 7.77 (4H, d, *J* = 8.2 Hz, Ts-H), 7.45 – 7.39 (2H, m, ar-H), 7.32 (4H, d, *J* = 8.2 Hz, Ts-H), 6.99 (1H, d, *J* = 8.3 Hz, ar-H), 4.24 – 4.07 (8H, m, CH_2), 3.89 – 3.82 (4H, m, CH_2), 3.70 – 3.64 (8H, m, CH_2), 3.62 – 3.57 (4H, m, CH_2), 2.42 (6H, s, CH_3); ^{13}C NMR (100 MHz, $CDCl_3$) δ_C: 191.0, 154.4, 149.2, 144.9, 144.9, 133.0, 130.4, 130.0, 128.0, 126.9, 112.6, 111.9, 70.9, 70.9, 70.9, 69.7, 69.5, 69.4, 69.4, 68.8, 68.7, 21.7.

(2-Formyl)dibenzo[24]crown-8 (63)[266,267]

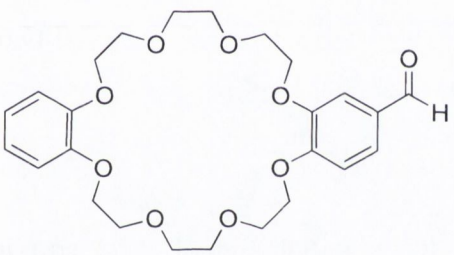

Cs_2CO_3 (3.62 g, 11.1 mmol, 5.00 eq.) was placed in a 250 mL RBF fitted with condenser and pressure-equalised dropping funnel. The system was flushed with argon, and anhydrous DMF (50 mL) was added to the flask. **61** (1.58 g, 2.22 mmol, 1.00 eq.) and 1,2-dihydroxybenzene (0.24 g, 2.22 mmol, 1.00 eq.) were then dissolved in anhydrous DMF (50 mL) and added to the dropping funnel. The suspension in the flask was heated to 100 °C with stirring, and the ditosylate/catechol solution was added dropwise over 5 h. The mixture was stirred at 100 °C for 7 days. After completion, the solvent was removed under reduced pressure, and the residue partitioned between toluene (60 mL) and 10% *w/v* K_2CO_3 aqueous solution (60 mL). The aqueous layer was extracted a further three times with toluene, and the combined organic layers then washed with 10% *w/v* K_2CO_3 solution. This organic phase was then dried over $MgSO_4$, and the solvent evaporated under reduced pressure to give a crude yellow oil. Final purification of the crude product was accomplished by flash silica column chromatography (gradient elution 100:0 → 95:5; EtOAc/MeOH) to yield **63** as a pale yellow oil (0.45 g, 0.94 mmol, 42% yield). HRMS (*m/z*) (ES^+) Calculated for $C_{25}H_{32}O_9Na$ *m/z* = 499.1944 $[M + Na]^+$. Found *m/z* = 499.1941; ^1H NMR (400 MHz, $CDCl_3$) δ_H: 9.80 (1H, s, aldehyde-H), 7.41 (1H, dd, *J* = 1.8 Hz + 8.1 Hz, ar-H), 7.36 (1H, d, *J* = 1.8 Hz, ar-H), 6.92 (1H, d, *J* = 8.1 Hz, ar-H), 6.90 – 6.82 (4H, m, ar-H), 4.20 (4H, m, CH_2), 4.13 (4H, t, *J* = 4.3 Hz, CH_2), 3.96 – 3.89 (8H, m, CH_2), 3.84 – 3.81 (8H,

m C$\underline{H}_2$); ^{13}C NMR (100 MHz, $CDCl_3$) δ_C: 190.8, 154.3, 149.1, 148.8, 148.8, 130.1, 126.8, 121.4, 121.3, 113.9, 111.8, 111.0, 71.5, 71.3, 71.2, 69.9, 69.6, 69.4, 69.4, 69.3, 69.2.

(2-Benzyl-hydroxy)dibenzo[24]crown-8 (64)[264]

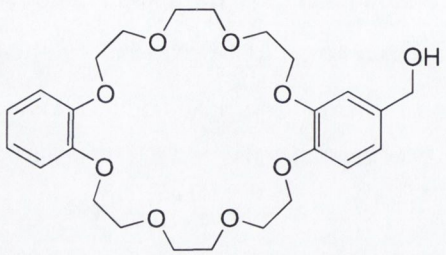

$NaBH_4$ (0.10 g, 2.52 mmol, 3.00 eq.) was slowly added to a solution of **63** (0.40 g, 0.84 mmol, 1.00 eq.) in EtOH (10 mL) and CH_2Cl_2 (10 mL) cooled to 0 °C. After addition, the solution was allowed to reach room temperature and stirred overnight. The reaction solution was then acidified with 1 M HCl before extracting three times with CH_2Cl_2. The combined organic phases were subsequently washed three times with 1 M $NaHCO_3$ and twice with H_2O, and dried over $MgSO_4$. Solvent evaporation under reduced pressure afforded **64** as a white solid (0.39 g, 0.81 mmol, 96% yield). m.p. 93 – 95 °C (Lit. m.p.[264] 95 – 96 °C); HRMS (*m/z*) (ES^+) Calculated for $C_{25}H_{34}O_9Na$ *m/z* = 501.2101 $[M + Na]^+$. Found *m/z* = 501.2098; ^{1}H NMR (400 MHz, $CDCl_3$) δ_H: 6.90 – 6.79 (7H, m, ar-$\underline{H}$), 4.56 (2H, s, benzyl-C$\underline{H}_2$), 4.13 (8H, t, *J* = 4.0 Hz, C$\underline{H}_2$), 3.89 (8H, t, *J* = 4.0 Hz, C$\underline{H}_2$), 3.81 (8H, s, C$\underline{H}_2$); ^{13}C NMR (100 MHz, $CDCl_3$) δ_C: 149.1, 149.0, 148.4, 134.4, 121.5, 120.0, 114.2, 114.0, 113.0, 71.3, 70.0, 69.6, 69.4, 65.1.

(2-Benzyl-chloride)dibenzo[24]crown-8 (65)[264]

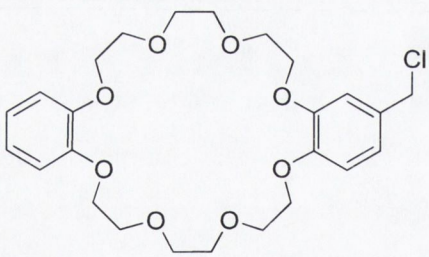

A solution of **64** (0.39 g, 0.81 mmol, 1.00 eq.) in CH_2Cl_2 (4 mL) was added to a solution of pyridine (0.31 g, 0.32 mL, 3.97 mmol, 4.90 eq.) and thionyl chloride (0.44 g, 0.27 mL, 3.73 mmol, 4.60 eq.) in CH_2Cl_2 (4 mL), and stirred at room temperature for 1 h. After this time, $CHCl_3$ (10 mL) was added before pouring the reaction solution onto ice water (20 mL). The aqueous layer was extracted twice with CH_2Cl_2. The combined organic layers were then washed twice with H_2O, 1 M $NaHCO_3$, and brine. The organic phase was subsequently dried over $MgSO_4$, and the solvent removed under reduced pressure. The crude product obtained was dissolved in a minimum volume of CH_2Cl_2. Hexane was finally added to this concentrated solution to precipitate **65** as a white solid (0.36 g, 0.73 mmol, 90% yield). m.p. 90 – 93 °C (Lit. m.p.[264] 90 – 91 °C); HRMS (*m/z*) (ES^+) Calculated for $C_{25}H_{33}O_8ClNa$ *m/z* = 519.1762 $[M + Na]^+$. Found *m/z* = 519.1737; ^{1}H NMR (400 MHz, $CDCl_3$) δ_H: 6.91 – 6.84 (6H, m, ar-$\underline{H}$), 6.80 (1H, m, ar-$\underline{H}$), 4.52 (2H, s, benzyl-C$\underline{H}_2$), 4.14 (8H, m, C$\underline{H}_2$), 3.91 (8H, m, C$\underline{H}_2$), 3.83 (8H, s, C$\underline{H}_2$); ^{13}C NMR (100 MHz,

$CDCl_3$) δ_C: 149.2, 149.1, 149.0, 130.6, 121.8, 121.5, 114.4, 114.2, 113.7, 71.4, 71.4, 70.0, 69.9, 69.9, 69.6, 69.5, 69.5, 46.7.

4-[(Dibenzo[24]crown-8)methoxy]-*N,N'*-bis((*S*)-1-(naphthalen-1-yl)ethyl)pyridine-2,6-dicarboxamide (51S)[237]

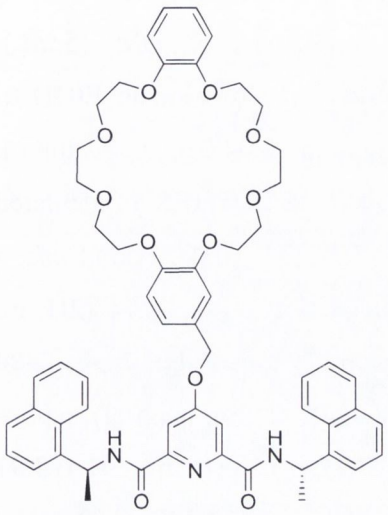

Compound **51S** was synthesised according to **Procedure 1** using **65** as the alkylating agent. The quantities of the respective reagents and solvent were as follows; **39S** (0.054 g, 0.110 mmol, 1.00 eq.), K_2CO_3 (0.030 g, 0.220 mmol, 2.00 eq.), **65** (0.060 g, 0.121 mmol, 1.10 eq.), DMF (5 mL). The crude product was purified by trituration in EtOH to give **51S** as a yellow waxy solid (0.042 g, 0.044 mmol, 40% yield). m.p. 64 – 66 °C; HRMS (*m/z*) (ES^+) Calculated for $C_{56}H_{59}N_3O_{11}Na$ *m/z* = 972.4047 $[M + Na]^+$. Found *m/z* = 972.4009; ^1H NMR (600 MHz, $CDCl_3$) δ_H: 8.15 (2H, m, naph-H), 7.91 – 7.87 (4H, m, py-H + naph-H), 7.83 (2H, m, naph-H), 7.80 (2H, d, *J* = 8.4 Hz, NH), 7.53 – 7.49 (4H, m, naph-H), 7.45 – 7.41 (4H, m, naph-H), 6.95 – 6.84 (7H, m, ar-H), 6.01 (2H, m, CH), 5.09 (2H, s, benzyl-CH_2), 4.15 (8H, m, CH_2), 3.91 (8H, m, CH_2), 3.83 (8H, m, CH_2), 1.64 (6H, d, *J* = 6.9 Hz, CH_3); ^{13}C NMR (150 MHz, $CDCl_3$) δ_C: 167.6, 162.5, 150.9, 149.3, 149.3, 149.1, 138.4, 134.2, 131.1, 129.1, 128.6, 128.0, 126.8, 126.1, 125.4, 123.4, 122.8, 121.6, 121.2, 114.3, 113.9, 113.6, 111.8, 71.5, 71.4, 70.7, 70.1, 70.0, 69.6, 69.6, 45.5, 21.2; IR υ_{max} (cm^{-1}): 3290, 3059, 2923, 2871, 1720, 1657, 1597, 1506, 1451, 1395, 1351, 1330, 1257, 1174, 1122, 1025, 997, 931, 885, 857, 801, 778, 744, 690, 655, 588.

4-[(Dibenzo[24]crown-8)methoxy]-*N*,*N*'-bis((*R*)-1-(naphthalen-1-yl)ethyl)pyridine-2,6-dicarboxamide (51R)[237]

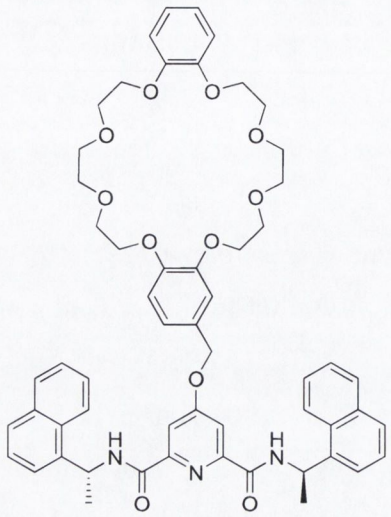

Compound **51R** was synthesised according to **Procedure 1** using **65** as the alkylating agent. The quantities of the respective reagents and solvent were as follows; **39R** (0.054 g, 0.110 mmol, 1.00 eq.), K_2CO_3 (0.030 g, 0.220 mmol, 2.00 eq.), **65** (0.060 g, 0.121 mmol, 1.10 eq.), DMF (5 mL). The crude product was purified by trituration in EtOH to give **51R** as a yellow waxy solid (0.047 g, 0.049 mmol, 45% yield). m.p. 64 – 65 °C; HRMS (*m/z*) (ES^-) Calculated for $C_{56}H_{58}N_3O_{11}$ *m/z* = 948.4071 $[M - H]^-$. Found *m/z* = 948.4109; ^1H NMR (600 MHz, $CDCl_3$) δ_H: 8.14 (2H, m, naph-H), 7.90 – 7.86 (4H, m, py-H + naph-H), 7.84 – 7.80 (4H, m, naph-H + NH), 7.53 – 7.48 (4H, m, naph-H), 7.45 – 7.40 (4H, m, naph-H), 6.95 – 6.83 (7H, m, ar-H), 6.00 (2H, m, CH), 5.07 (2H, s, benzyl-CH_2), 4.15 (8H, m, CH_2), 3.91 (8H, m, CH_2), 3.83 (8H, m, CH_2), 1.63 (6H, d, *J* = 6.9 Hz, CH_3); ^{13}C NMR (150 MHz, $CDCl_3$) δ_C: 167.5, 162.5, 150.8, 149.3, 149.2, 149.1, 138.3, 134.1, 131.1, 129.0, 128.6, 128.0, 126.7, 126.0, 125.4, 123.4, 122.8, 121.6, 121.1, 114.3, 113.9, 113.6, 111.8, 71.4, 70.7, 70.1, 70.0, 69.6, 69.5, 45.4, 21.2; IR υ_{max} (cm^{-1}): 3291, 3061, 2924, 2870, 1717, 1656, 1596, 1507, 1451, 1397, 1351, 1330, 1257, 1174, 1121, 1024, 998, 944, 882, 858, 801, 778, 743, 690, 659, 587.

Complex Eu.51S$_3$

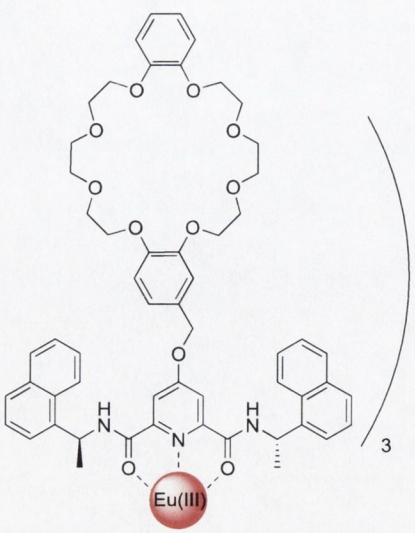

Complex **Eu.51S$_3$** was synthesised according to **Procedure 2** using ligand **51S** (0.030 g, 0.032 mmol, 1.00 eq.) and $Eu(CF_3SO_3)_3$ (0.007 g, 0.011 mmol, 0.33 eq.) in CH_3CN (5 mL). A yellow solid was obtained (0.024 g, 0.007 mmol, 65% yield). m.p. decomposed above 110 °C; Calculated for $C_{168}H_{177}N_9O_{33}Eu$ + $3CF_3SO_3$ + $0.5CH_3CN$: C, 59.54; H, 5.19; N, 3.83. Found C, 59.62; H, 5.47; N, 3.59; ^1H NMR (400 MHz, CD_3CN-d_3) δ_H: 9.85, 9.72, 8.13, 7.40, 7.09, 6.97 – 6.82, 6.67, 6.15, 5.34, 4.45, 4.20, 4.09, 3.76, 3.65, 3.51, 2.45, 2.16; IR υ_{max} (cm^{-1}): 3291, 3094, 2933, 2875, 1619, 1596, 1556, 1507, 1451, 1395, 1357, 1334, 1243, 1135, 1031, 944, 925, 800, 776, 749, 636, 573.

Complex Eu.51R$_3$

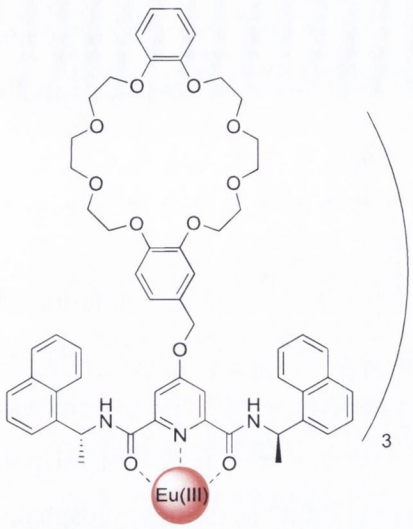

Complex **Eu.51R$_3$** was synthesised according to **Procedure 2** using ligand **51R** (0.030 g, 0.032 mmol, 1.00 eq.) and Eu(CF_3SO_3)$_3$ (0.007 g, 0.011 mmol, 0.33 eq.) in CH_3CN (5 mL). A yellow solid was obtained (0.021 g, 0.006 mmol, 56% yield). m.p. decomposed above 110 °C; Calculated for $C_{168}H_{177}N_9O_{33}Eu$ + $3CF_3SO_3$ + $0.3CH_3CN$: C, 59.54; H, 5.18; N, 3.76. Found C, 59.41; H, 5.10; N, 3.28; ^{1}H NMR (400 MHz, CD_3CN-d_3) δ_H: 9.84, 9.72, 8.13, 7.40, 7.08, 6.96 – 6.82, 6.67, 6.16, 5.35, 4.45, 4.21, 4.10, 3.77, 3.65, 3.51, 2.44, 2.15; IR υ_{max} (cm^{-1}): 3281, 3094, 2933, 2872, 1619, 1596, 1556, 1507, 1451, 1391, 1357, 1330, 1243, 1133, 1030, 946, 923, 800, 777, 749, 636, 573.

***N*-Histaminyl-*N*-(ferrocenylmethyl)ammonium hexafluorophosphate (56)[326,327]**

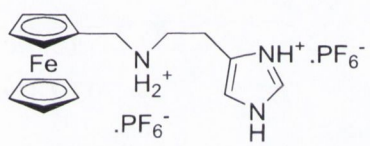

Ferrocenecarboxaldehyde (0.29 g, 1.35 mmol, 1.01 eq.) and anhydrous K_2CO_3 (0.01 g, 0.07 mmol, 0.05 eq.) were dissolved in dry MeOH (20 mL), and kept under argon at room temperature. Histamine dihydrochloride (0.25 g, 1.34 mmol, 1.00 eq.) in dry MeOH (20 mL) was added over 30 min using a pressure-equalised dropping funnel. The solution was then refluxed for 7 h in darkness. After this time, the reaction mixture was cooled to 0 °C before adding $NaBH_4$ (0.05 g, 1.35 mmol, 1.01 eq.) and leaving to stir overnight at room temperature. The solution was hydrolysed with ice water (1 mL) and the solvent removed under reduced pressure. The crude residue was then dissolved in CH_2Cl_2 and washed twice with H_2O. The organic phase was dried over $MgSO_4$ and the solvent evaporated under reduced pressure to yield an orange oil. Purification was achieved by flash silica column chromatography (gradient elution 100:0 → 80:20; CH_2Cl_2/MeOH) to give the intermediate **68** as a green solid. A concentrated aqueous solution of HCl was subsequently added to a solution of **68** in MeOH (20 mL) until pH 2, and the mixture was stirred for 1 h. The solvent was then removed under reduced pressure and the residue suspended in acetone (20 mL). Upon dropwise addition of a concentrated aqueous solution of ammonium hexafluorophosphate, the product went into solution. The organic solvent was then evaporated, and the precipitated product filtered off, washed with H_2O, and air dried to give **56** as a dark green solid (0.02 g, 0.03 mmol, 2% overall yield). m.p. 72 – 74 °C; HRMS (*m/z*) (ES$^+$) Calculated for $C_{16}H_{20}N_3Fe$ *m/z* = 310.1007 [M − H]$^+$. Found *m/z* = 310.0996; ^{1}H

NMR (400 MHz, CD_3CN-d_3) δ_H: 8.46 (1H, s, im-H), 7.24 (1H, s, im-H), 4.35 (2H, s, Cp-H), 4.25 (2H, s, Cp-H), 4.18 (5H, s, Cp-H), 4.03 (2H, t, J = 5.7 Hz, CH_2), 3.22 (2H, m, CH_2), 3.03 (2H, t, J = 7.1 Hz, CH_2); ^{13}C NMR (100 MHz, CD_3CN-d_3) δ_C: 135.6, 129.8, 72.0 – 69.6, 49.2, 46.5, 22.0; ^{19}F NMR (376 MHz, CD_3CN-d_3) δ_F: − 72.4 (d, $J_{F,P}$ = 706.9 Hz, PF_6); IR υ_{max} (cm^{-1}): 3091, 1578, 1476, 1409, 1299, 1257, 1106, 1053, 1001, 805, 563.

Dibenzylammonium hexafluorophosphate (53)[327]

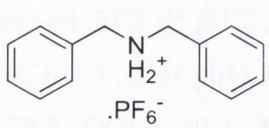

A concentrated aqueous solution of HCl was added to a solution of dibenzylamine (0.60 g, 0.58 mL, 3.04 mmol, 1.00 eq.) in MeOH (50 mL) until pH 2, and the mixture was stirred for 1 h. The solvent was then evaporated under reduced pressure and the residue suspended in acetone (20 mL). Upon dropwise addition of a concentrated aqueous solution of ammonium hexafluorophosphate, the product went into solution. The organic solvent was then evaporated, and the precipitated product filtered off, washed with H_2O, and air dried to give **53** as a white solid (0.89 g, 2.59 mmol, 85% yield). m.p. 202 – 203 °C (Lit. m.p.[251] 205 – 208 °C); HRMS (*m/z*) (ES^+) Calculated for $C_{14}H_{16}N$ *m/z* = 198.1283 $[M]^+$. Found *m/z* = 198.1275; ^1H NMR (400 MHz, CD_3CN-d_3) δ_H: 7.47 (10H, s, ar-H), 4.24 (4H, s, CH_2); ^{13}C NMR (100 MHz, CD_3CN-d_3) δ_C: 131.2, 130.8, 130.1, 52.5; ^{19}F NMR (376 MHz, CD_3CN-d_3) δ_F: − 72.7 (d, $J_{F,P}$ = 707.2 Hz, PF_6).

7.8 Experimental details for Chapter 4

4-[(2,3,4,6-Tetra-*O*-acetyl-β-D-galactopyranoside)oxypropyl-5'-H-1',2',3'-triazol-1'-yl-methoxy]-*N*,*N*'-bis((*S*)-1-(naphthalen-1-yl)ethyl)pyridine-2,6-dicarboxamide (69S)[328]

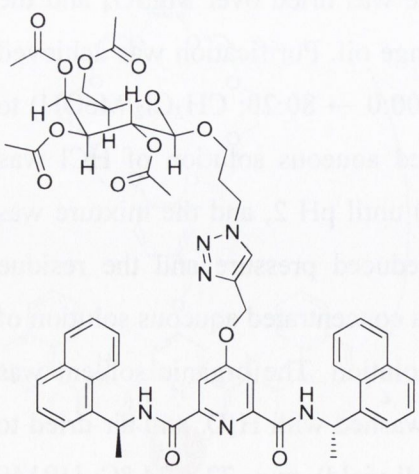

Compound **42S** (0.021 g, 0.040 mmol, 1.00 eq.), $Cu(CH_3CN)_4PF_6$ (1.4×10^{-3} g, 0.004 mmol, 0.10 eq.), and 2,3,4,6-tetra-*O*-acetyl-1-*O*-(3-azidopropyl)-β-D-galactopyranoside (0.017 g, 0.040 mmol, 1.00 eq.) were added to a 10 mL microwave vial and dissolved in toluene/MeOH (2mL − 1:1; *v/v*). The mixture was then heated to 110 °C under microwave irradiation for 20 min. After completion, the solvent was removed under reduced pressure, and the crude product purified by flash silica column chromatography (gradient elution 100:0 → 98:2; CH_2Cl_2/MeOH) to give **69S** as a white solid (0.032 g, 0.033 mmol, 83% yield). m.p.

134 – 137 °C; Calculated for $C_{51}H_{54}N_6O_{13}$ + CH_2Cl_2 + 0.6C_7H_8: C, 61.41; H, 5.58; N, 7.65. Found C, 61.69; H, 5.29; N, 7.80; HRMS (*m/z*) (MALDI$^+$) Calculated for $C_{51}H_{55}N_6O_{13}$ *m/z* = 959.3827 $[M + H]^+$. Found *m/z* = 959.3864; ^{1}H NMR (600 MHz, $CDCl_3$) δ_H: 8.12 (2H, m, naph-H), 7.95 – 7.85 (6H, m, py-H + NH + naph-H), 7.81 (2H, m, naph-H), 7.55 – 7.47 (4H, m, naph-H), 7.47 – 7.39 (4H, m, naph-H), 5.99 (2H, m, NHCH), 5.38 (1H, d, *J* = 3.1 Hz, carbo-H4), 5.30 (2H, br s, triazole-CH_2O), 5.21 (1H, m, carbo-H2), 5.05 – 4.98 (1H, m, carbo-H3), 4.57 – 4.39 (3H, m, $CH_2CH_2CH_2O$ + carbo-H1), 4.19 – 4.06 (2H, m, carbo-H6), 3.89 (2H, m, carbo-H5 + $CH_2CH_2CH_2O$), 3.49 (1H, br s, $CH_2CH_2CH_2O$), 2.29 – 2.13 (5H, m, $CH_2CH_2CH_2O$ + acetyl-CH_3), 2.08 (3H, s, acetyl-CH_3), 2.02 (3H, s, acetyl-CH_3), 1.99 (3H, s, acetyl-CH_3), 1.63 (6H, d, *J* = 6.6 Hz, CH_3); ^{13}C NMR (150 MHz, $CDCl_3$) δ_C: 170.5, 170.3, 170.2, 169.7, 167.2, 162.4, 151.0, 138.3, 134.1, 131.1, 129.1, 128.6, 126.8, 126.1, 125.4, 123.4, 122.8, 111.6, 101.4, 70.9, 69.0, 67.2, 65.9, 62.5, 61.4, 47.2, 45.5, 30.3, 21.2, 21.0, 20.8, 20.7; IR υ_{max} (cm^{-1}): 2933, 1747, 1662, 1599, 1517, 1437, 1367, 1218, 1175, 1136, 1036, 903, 802, 778, 738.

4-[(2,3,4,6-Tetra-*O*-acetyl-β-D-galactopyranoside)oxypropyl-5'-H-1',2',3'-triazol-1'-yl-methoxy]-*N*,*N*'-bis((*R*)-1-(naphthalen-1-yl)ethyl)pyridine-2,6-dicarboxamide (69R)[328]

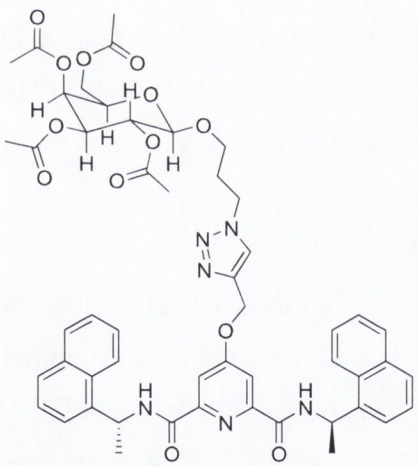

Compound **42R** (0.021 g, 0.040 mmol, 1.00 eq.), $Cu(CH_3CN)_4PF_6$ (1.4×10^{-3} g, 0.004 mmol, 0.10 eq.), and 2,3,4,6-tetra-*O*-acetyl-1-*O*-(3-azidopropyl)-β-D-galactopyranoside (0.017 g, 0.040 mmol, 1.00 eq.) were added to a 10 mL microwave vial and dissolved in toluene/MeOH (2mL – 1:1; *v/v*). The mixture was then heated to 110 °C under microwave irradiation for 20 min. After completion, the solvent was removed under reduced pressure, and the crude product purified by flash silica column chromatography (gradient elution 100:0 → 98:2; CH_2Cl_2/MeOH) to give **69R** as a white solid (0.033 g, 0.034 mmol, 85% yield). m.p. 134 – 136 °C; Calculated for $C_{51}H_{54}N_6O_{13}$ + 0.6CH_2Cl_2: C, 61.36; H, 5.51; N, 8.32. Found C, 61.64; H, 5.53; N, 8.03; HRMS (*m/z*) (ES$^+$) Calculated for $C_{51}H_{54}N_6O_{13}Na$ *m/z* = 981.3647 $[M + Na]^+$. Found *m/z* = 981.3686; ^{1}H NMR (600 MHz, $CDCl_3$) δ_H: 8.13 (2H, d, *J* = 7.9 Hz, naph-H), 7.92 – 7.85 (6H, m, py-H + NH + naph-H), 7.80 (2H, m, naph-H), 7.54 – 7.48 (4H, m, naph-H), 7.44 – 7.39 (4H, m, naph-H), 5.99 (2H, m, NHCH), 5.38 (1H, d, *J* = 3.1 Hz, carbo-H4), 5.27 (2H, br s, triazole-CH_2O), 5.21 (1H, m, carbo-H2), 5.04 – 4.99 (1H, m, carbo-H3), 4.56 – 4.40 (3H, m, $CH_2CH_2CH_2O$ + carbo-H1), 4.18 – 4.07 (2H, m, carbo-H6),

3.89 (2H, m, carbo-H5 + $CH_2CH_2CH_2O$), 3.49 (1H, br s, $CH_2CH_2CH_2O$), 2.26 – 2.13 (5H, m, $CH_2CH_2CH_2O$ + acetyl-CH_3), 2.08 (3H, s, acetyl-CH_3), 2.02 (3H, s, acetyl-CH_3), 1.99 (3H, s, acetyl-CH_3), 1.62 (6H, d, J = 6.6 Hz, CH_3); ^{13}C NMR (150 MHz, $CDCl_3$) δ_C: 170.5, 170.3, 170.2, 169.7, 167.2, 162.4, 151.0, 138.3, 134.1, 131.1, 129.1, 128.6, 126.8, 126.1, 125.4, 123.4, 122.8, 111.6, 101.4, 70.9, 70.9, 68.9, 67.1, 65.9, 62.5, 61.4, 47.1, 45.5, 30.3, 21.2, 21.0, 20.8, 20.8, 20.7; IR υ_{max} (cm^{-1}): 2923, 1747, 1652, 1597, 1513, 1448, 1368, 1218, 1175, 1140, 1040, 902, 801, 778, 738.

Complex Eu.69S$_3$

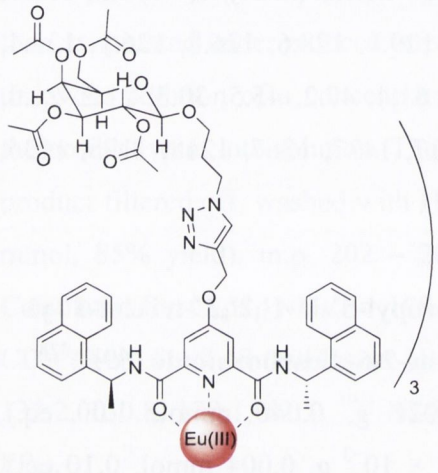

Complex **Eu.69S$_3$** was synthesised according to **Procedure 2** using ligand **69S** (0.023 g, 0.024 mmol, 1.00 eq.) and $Eu(CF_3SO_3)_3$ (0.005 g, 0.008 mmol, 0.33 eq.) in CH_3CN (5 mL). A white solid was obtained (0.021 g, 0.006 mmol, 72% yield). m.p. decomposed above 250 °C; Calculated for $C_{153}H_{162}N_{18}O_{39}Eu$ + $3CF_3SO_3$ + CH_2Cl_2: C, 52.95; H, 4.64; N, 7.08. Found C, 52.75; H, 4.29; N, 6.87; ^1H NMR (400 MHz, CD_3OD-d_4) δ_H: 10.25, 10.08, 8.28, 8.21, 7.48, 7.28, 6.69, 6.11, 5.33, 5.07, 4.68, 4.66, 4.63 – 4.46, 4.32, 4.07, 4.00, 3.84, 3.67, 3.56, 2.30, 2.19, 2.05, 1.98; IR υ_{max} (cm^{-1}): 3269, 3096, 2981, 1746, 1619, 1597, 1555, 1448, 1368, 1222, 1153, 1029, 954, 917, 802, 780, 636, 573.

Complex Eu.69R$_3$

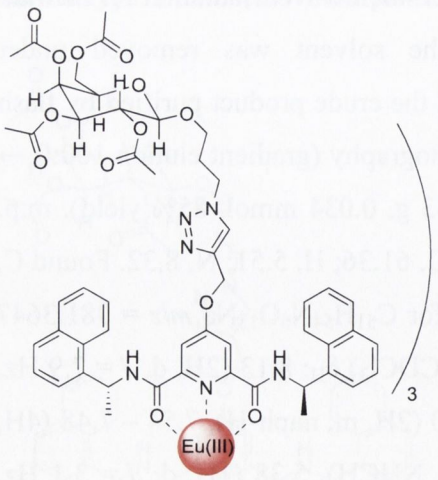

Complex **Eu.69R$_3$** was synthesised according to **Procedure 2** using ligand **69R** (0.020 g, 0.021 mmol, 1.00 eq.) and $Eu(CF_3SO_3)_3$ (0.004 g, 0.007 mmol, 0.33 eq.) in CH_3CN (5 mL). A white solid was obtained (0.021 g, 0.006 mmol, 86% yield). m.p. decomposed above 250 °C; Calculated for $C_{153}H_{162}N_{18}O_{39}Eu$ + $3CF_3SO_3$ + CH_2Cl_2: C, 52.95; H, 4.64; N, 7.08. Found C, 52.67; H, 4.16; N, 6.92; ^1H NMR (400 MHz, CD_3OD-d_4) δ_H: 10.34, 10.22, 8.31, 8.22, 7.48, 7.27, 6.67, 6.08, 5,33, 5.04, 4.68 – 4.44, 4.29, 4.13 – 3.97, 3.85, 3.59, 2.32, 2.17, 2.04, 1.97, 1.92; IR υ_{max} (cm^{-1}): 3268, 3094, 2936, 1745, 1619, 1598, 1556, 1448, 1369, 1222, 1155, 1030, 956, 907, 802, 779, 637, 574.

7.9 Experimental details for Chapter 5

Di-(tosyl-ethoxy)ethane (73)[236]

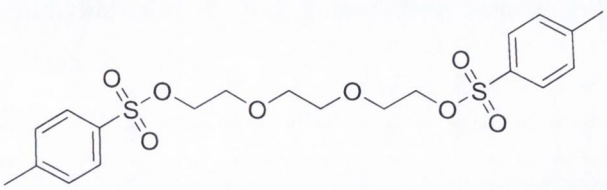

Triethylene glycol (4.84 g, 4.31 mL, 32.23 mmol, 1.00 eq.) in THF (50 mL) was added to a solution of NaOH (4.12 g, 103.03 mmol, 3.20 eq.) in H_2O (30 mL) at 0 °C. 4-toluenesulfonyl chloride (14.75 g, 77.37 mmol, 2.40 eq.) was added to the solution, and the mixture was allowed to warm to room temperature. The reaction was then left stirring for 72 h, after which time, the THF was removed under reduced pressure to give a white solid. This was dissolved in $CHCl_3$ before washing twice with 1M NaOH and once with H_2O. The organic phase was dried over $MgSO_4$ and the solvent evaporated. Recrystallisation of the crude product from MeOH gave **73** as a white crystalline solid (9.31 g, 20.30 mmol, 63% yield). m.p. 82 – 84 °C (Lit. m.p.[329] 80 – 81 °C); HRMS (*m/z*) (ES^+) Calculated for $C_{20}H_{26}O_8S_2Na$ *m/z* = 481.0967 $[M + Na]^+$. Found *m/z* = 481.0962; ^1H NMR (400 MHz, $CDCl_3$) δ_H: 7.79 (4H, d, *J* = 8.1 Hz, ar-H), 7.34 (4H, d, *J* = 8.1 Hz, ar-H), 4.14 (4H, t, *J* = 4.8 Hz, CH_2), 3.65 (4H, t, *J* = 4.8 Hz, CH_2), 3.53 (4H, s, CH_2), 2.45 (6H, s, CH_3); ^{13}C NMR (100 MHz, $CDCl_3$) δ_C: 145.0, 133.2, 130.0, 128.1, 70.9, 69.3, 68.9, 21.8; IR υ_{max} (cm^{-1}): 2897, 1596, 1457, 1352, 1261, 1175, 1132, 1071, 982, 911, 850, 815, 779, 664, 584, 553.

Di-(iodo-ethoxy)ethane (74)[236]

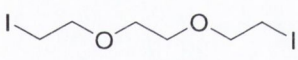

Compound **73** (5.02 g, 10.95 mmol, 1.00 eq.) and NaI (4.92 g, 32.82 mmol, 3.00 eq.) were refluxed in acetone (50 mL) for 16 h. The white precipitate which formed was removed by suction filtration, and the solvent was removed under reduced pressure. The residue was then dissolved in $CHCl_3$ and washed twice with H_2O, brine, and dried over $MgSO_4$. The solvent was removed under reduced pressure to give **74** as a red/brown oil (3.56 g, 9.62 mmol, 88% yield); HRMS (*m/z*) (ES^+) Calculated for $C_6H_{12}O_2I_2Na$ *m/z* = 392.8825 $[M + Na]^+$. Found *m/z* = 392.8822; ^1H NMR (400 MHz, $CDCl_3$) δ_H: 3.76 (4H, t, *J* = 7.0 Hz, CH_2), 3.66 (4H, s, CH_2), 3.26 (4H, t, *J* = 7.0 Hz, CH_2); ^{13}C NMR (100 MHz, $CDCl_3$) δ_C: 72.1, 70.3, 3.1; IR υ_{max} (cm^{-1}): 2864, 1722, 1460, 1412, 1350, 1262, 1188, 1168, 1089.

4,4'-(2,2'-(Ethane-1,2-diylbis(oxy))bis(ethane-2,1-diyl))bis(oxy)bis(*N*,*N*'-bis((*S*)-1-(naphthalen-1-yl)ethyl)pyridine-2,6-dicarboxamide) (72S)[237]

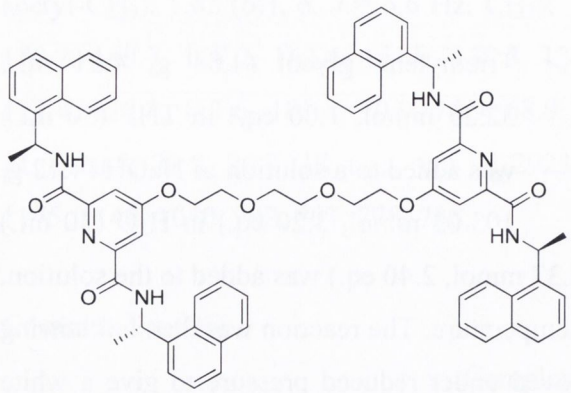

Compound **72S** was synthesised according to **Procedure 1** using **74** as the alkylating agent. The quantities of the respective reagents and solvent were as follows; **39S** (0.20 g, 0.41 mmol, 2.10 eq.), K_2CO_3 (0.08 g, 0.60 mmol, 3.00 eq.), **74** (0.07 g, 0.20 mmol, 1.00 eq.), DMF (10 mL). The crude product was purified by dissolution in a minimum volume of CH_2Cl_2 and dropping into MeOH, with slow crystallisation affording **72S** as a crystalline solid isolated by decanting (0.07 g, 0.06 mmol, 31% yield). m.p. 147 – 150 °C; HRMS (*m/z*) (ES^+) Calculated for $C_{68}H_{64}N_6O_8Na$ *m/z* = 1115.4683 $[M + Na]^+$. Found *m/z* = 1115.4681; ^1H NMR (400 MHz, $CDCl_3$) δ_H: 8.38 (4H, d, *J* = 8.7 Hz, NH), 8.11 (4H, d, *J* = 8.1 Hz, naph-H), 7.81 (4H, m, naph-H), 7.72 (4H, d, *J* = 8.1 Hz, naph-H), 7.65 (4H, s, py-H), 7.50 – 7.43 (8H, m, naph-H), 7.29 – 7.20 (8H, m, naph-H), 6.02 (4H, m, CH), 3.81 (4H, m, CH_2), 3.68 (4H, t, *J* = 4.6 Hz, CH_2), 3.62 (4H, m, CH_2), 1.49 (12H, d, *J* = 6.9 Hz, CH_3); ^{13}C NMR (100 MHz, $CDCl_3$) δ_C: 167.4, 162.8, 150.4, 138.6, 133.9, 131.1, 129.1, 128.4, 126.7, 126.0, 125.3, 123.4, 123.0, 111.8, 71.1, 69.2, 67.5, 45.2, 21.3; IR υ_{max} (cm^{-1}): 3288, 3252, 3047, 2963, 2931, 1737, 1658, 1637, 1597, 1508, 1445, 1398, 1371, 1346, 1323, 1307, 1236, 1174, 1128, 1108, 1083, 1060, 1043, 1016, 996, 967, 953, 908, 892, 878, 861, 853, 832, 812, 796, 775, 753, 731, 687.

4,4'-(2,2'-(Ethane-1,2-diylbis(oxy))bis(ethane-2,1-diyl))bis(oxy)bis(*N*,*N*'-bis((*R*)-1-(naphthalen-1-yl)ethyl)pyridine-2,6-dicarboxamide) (72R)[237]

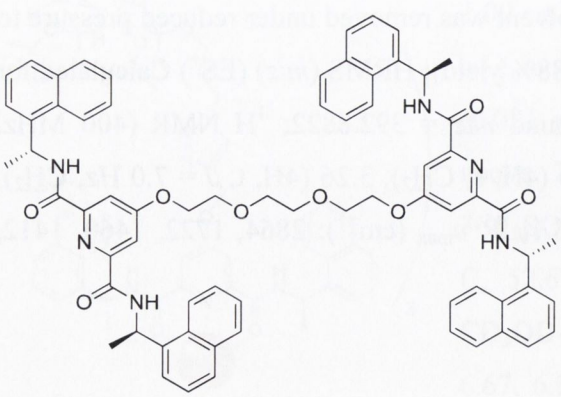

Compound **72R** was synthesised according to **Procedure 1** using **74** as the alkylating agent. The quantities of the respective reagents and solvent were as follows; **39R** (0.20 g, 0.41 mmol, 2.10 eq.), K_2CO_3 (0.08 g, 0.60 mmol, 3.00 eq.), **74** (0.07 g, 0.20 mmol, 1.00 eq.), DMF (10 mL). The crude product was purified by dissolution in a minimum volume of CH_2Cl_2 and dropping into MeOH, with slow crystallisation affording **72R** as a crystalline solid isolated by decanting (0.08 g, 0.07 mmol, 35% yield). m.p. 147 – 151 °C; HRMS (*m/z*)

(MALDI$^+$) Calculated for $C_{68}H_{65}N_6O_8$ m/z = 1093.4864 $[M + H]^+$. Found m/z = 1093.4893; ^{1}H NMR (600 MHz, $CDCl_3$) δ_H: 8.37 (4H, d, J = 8.7 Hz, NH), 8.12 (4H, d, J = 8.1 Hz, naph-H), 7.81 (4H, m, naph-H), 7.71 (4H, d, J = 8.1 Hz, naph-H), 7.66 (4H, s, py-H), 7.50 – 7.44 (8H, m, naph-H), 7.29 – 7.21 (8H, m, naph-H), 6.02 (4H, m, CH), 3.83 (4H, m, CH_2), 3.68 (4H, t, J = 4.6 Hz, CH_2), 3.62 (4H, m, CH_2), 1.49 (12H, d, J = 6.9 Hz, CH_3); ^{13}C NMR (150 MHz, $CDCl_3$) δ_C: 167.4, 162.8, 150.4, 138.6, 134.0, 131.1, 129.1, 128.4, 126.6, 126.0, 125.3, 123.4, 123.0, 111.8, 71.1, 69.2, 67.5, 45.2, 21.3; IR υ_{max} (cm^{-1}): 3289, 3254, 3047, 2964, 2931, 1737, 1658, 1637, 1597, 1509, 1446, 1398, 1371, 1346, 1323, 1307, 1236, 1174, 1129, 1109, 1083, 1060, 1043, 1015, 996, 967, 953, 907, 892, 879, 861, 853, 833, 811, 797, 775, 753, 731, 687.

Complex Eu.72S (M:L = 2:3)

Ligand **72S** (0.021 g, 0.019 mmol, 1.00 eq.) and $Eu(CF_3SO_3)_3$ (0.008 g, 0.013 mmol, 0.67 eq.) were added to a 10 mL microwave vial and dissolved in $CHCl_3$ (5 mL). The mixture was then refluxed under microwave irradiation for 45 min. Following completion, CH_3CN (1 mL) was added to the solution, resulting in precipitation of a white fluffy solid. The solid was deposited by centrifugation and isolated by decanting to give **Eu.72S (M:L = 2:3)** as a white solid. (0.016 g, "0.004 mmol", 67% yield). m.p. decomposed above 270 °C; Calculated for $C_{204}H_{192}N_{18}O_{24}Eu_2 + 6CF_3SO_3 + 2.5CHCl_3$: C, 53.43; H, 4.10; N, 5.28. Found C, 53.81; H, 4.27; N, 5.45; ^{1}H NMR (400 MHz, DMSO-d_6) δ_H: 9.48, 8.19, 7.91, 7.79, 7.54, 7.42, 5.98, 3.98, 3.62, 3.51, 1.55; IR υ_{max} (cm^{-1}): 3429, 3284, 3096, 1618, 1596, 1554, 1447, 1355, 1239, 1163, 1055, 1028, 960, 880, 801, 778.

Complex Eu.72R (M:L = 2:3)

Ligand **72R** (0.021 g, 0.019 mmol, 1.00 eq.) and $Eu(CF_3SO_3)_3$ (0.008 g, 0.013 mmol, 0.67 eq.) were added to a 10 mL microwave vial and dissolved in $CHCl_3$ (5 mL). The mixture was then refluxed under microwave irradiation for 45 min. Following completion, CH_3CN (1 mL) was added to the solution, resulting in precipitation of a white fluffy solid. The solid was deposited by centrifugation and isolated by decanting to give **Eu.72R (M:L = 2:3)** as a white solid (0.018 g, "0.004 mmol", 67% yield). m.p. decomposed above 270 °C; Calculated for $C_{204}H_{192}N_{18}O_{24}Eu_2 + 6CF_3SO_3 + 3CHCl_3$: C, 52.90; H, 4.06; N, 5.21. Found C, 52.81; H, 3.96; N, 5.37; ^{1}H NMR (400 MHz, DMSO-d_6) δ_H: 9.48, 8.19, 7.91, 7.79, 7.54, 7.42, 5.98, 3.99, 3.62, 3.52, 1.55; IR υ_{max} (cm^{-1}): 3428, 3281, 3095, 1618, 1596, 1554, 1446, 1354, 1240, 1157, 1055, 1028, 960, 880, 800, 778.

7.10 Experimental details for Chapter 6

Diethyl 4-hydroxypyridine-2,6-dicarboxylate (88)[318]

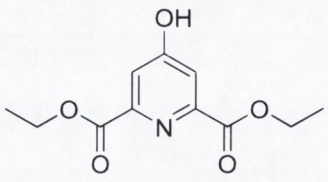

4-Hydroxypyridine-2,6-dicarboxylic acid (1.50 g, 8.19 mmol, 1.00 eq.) and H_2SO_4 (5.62 g, 3.05 mL, 57.30 mmol, 7.00 eq.) were refluxed together in EtOH (100 mL) for 4 h. The EtOH was removed under reduced pressure and the residue neutralised using a saturated aqueous solution of $NaHCO_3$. The aqueous solution was then extracted with CH_2Cl_2 before drying over $MgSO_4$. The solvent was removed under vacuum to give a pale yellow oil **88**, which solidified upon drying under vacuum (1.37 g, 5.73 mmol, 70% yield). m.p. 119 – 121 °C (Lit. m.p.[330] 120 – 122 °C); HRMS (*m/z*) (ES^+) Calculated for $C_{11}H_{13}NO_5Na$ *m/z* = 262.0691 $[M + Na]^+$. Found *m/z* = 262.0696; ^1H NMR (400 MHz, $CDCl_3$) δ_H: 7.34 (2H, s, py-H), 4.46 (4H, q, *J* = 7.3 Hz, CH_2), 1.42 (6H, t, *J* = 7.3 Hz, CH_3); ^{13}C NMR (100 MHz, $CDCl_3$) δ_C: 161.7, 150.1, 138.9, 119.7, 63.4, 14.0; IR υ_{max} (cm^{-1}): 3425, 2974, 2676, 1728, 1600, 1569, 1444, 1366, 1236, 1160, 1103, 1018, 995, 888, 865, 788, 703.

4,4'-((Ethoxy)ethoxy)ethyl)-bis(diethylester-2,6-pyridine) (89)[237]

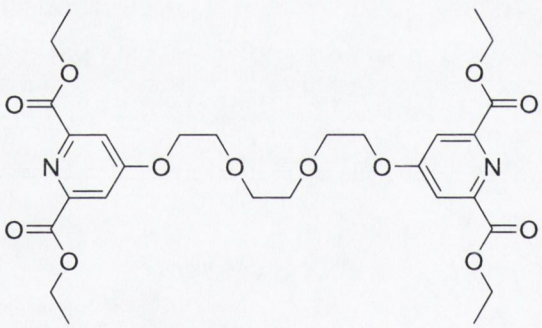

Compound **88** (0.85 g, 3.55 mmol, 2.20 eq.) and anhydrous K_2CO_3 (0.67 g, 4.85 mmol, 3.00 eq.) were stirred in anhydrous DMF (30 mL) at 25 °C for 30 min. **74** (0.60 g, 1.62 mmol, 1.00 eq.) was added and the solution was heated at 80 °C for 72 h. The solvent was then removed under reduced pressure and CH_2Cl_2 was added to the residue. The organic layer was washed twice with 1% aqueous acetic acid and H_2O before drying over $MgSO_4$. Solvent evaporation under reduced pressure afforded a crude yellow oil, which was subsequently recrystallised from EtOH to give **89** as a white solid (0.42 g, 0.71 mmol, 44% yield); m.p. 77 – 79 °C; HRMS (*m/z*) (ES^+) Calculated for $C_{28}H_{36}N_2O_{12}Na$ *m/z* = 615.2166 $[M + Na]^+$. Found *m/z* = 615.2156; ^1H NMR (400 MHz, $CDCl_3$) δ_H: 7.80 (4H, s, py-H), 4.45 (8H, q, *J* = 7.2 Hz, CH_2CH_3), 4.30 (4H, t, *J* = 4.5 Hz, CH_2), 3.90 (4H, t, *J* = 4.5 Hz, CH_2), 3.74 (4H, s, CH_2), 1.43 (12H, t, *J* = 7.2 Hz, CH_2CH_3); ^{13}C NMR (100 MHz, $CDCl_3$) δ_C: 166.8, 164.7, 150.2, 114.4, 71.0, 69.3, 68.3, 62.5, 14.2; IR υ_{max} (cm^{-1}): 3076, 2983, 2933, 2905, 1742, 1706, 1594, 1567, 1478, 1435, 1371, 1369, 1342, 1328, 1244, 1230, 1158, 1134, 1102, 1067, 1023, 994, 938, 887, 866, 817, 786, 732, 701.

4,4'-((Ethoxy)ethoxy)ethyl)-bis(diethylamide-2,6-pyridine) (86)

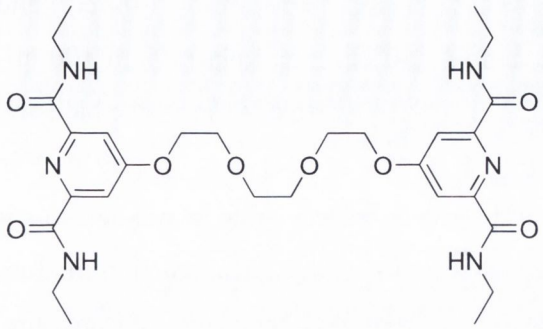

Compound **89** (0.15 g, 0.25 mmol, 1.00 eq.) and ethylamine (40 % *w/v* in toluene; 50 mL) were heated together at 60 °C for 72 h. The reaction mixture was then poured onto ice, resulting in the precipitation of a brown solid. Upon melting of the ice, the solid was isolated by filtration and dissolved in CH_2Cl_2. The organic phase was washed twice with H_2O before drying over $MgSO_4$. The solvent was then removed under reduced pressure to give a crude brown solid. Purification by flash silica column chromatography (gradient elution 100:0 → 95:5; CH_2Cl_2/MeOH) yielded **86** as a white solid (0.05g, 0.08 mmol, 32% yield). m.p. 222 – 224 °C; HRMS (*m/z*) (ES^+) Calculated for $C_{28}H_{40}N_6O_8Na$ *m/z* = 611.2805 $[M + Na]^+$. Found *m/z* = 611.2808; ^1H NMR (600 MHz, $CDCl_3$) δ_H: 8.20 (4H, t, *J* = 5.9 Hz, NH), 7.82 (4H, s, py-H), 4.04 (4H, t, *J* = 4.5 Hz, CH_2), 3.77 (4H, t, *J* = 4.5 Hz, CH_2), 3.65 (4H, s, CH_2), 3.48 (8H, m, CH_2CH_3), 1.22 (12H, t, *J* = 7.3 Hz, CH_2CH_3); ^{13}C NMR (150 MHz, $CDCl_3$) δ_C: 167.9, 163.6, 151.1, 111.5, 71.1, 69.3, 68.0, 34.6, 15.0; IR υ_{max} (cm^{-1}): 3310, 3080, 2972, 2934, 2876, 1737, 1647, 1601, 1523, 1445, 1366, 1281, 1241, 1144, 1129, 1056, 1044, 997, 885, 875, 817, 752, 695.

2-Chloro-*N,N*-dimethylacetamide (92)[331]

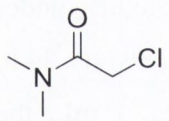

Dimethylamine (6.31 g, 9.28 mL, 139.97 mmol, 1.00 eq.) and NaOH (5.59 g, 139.79 mmol, 1.00 eq.) were added to CH_2Cl_2 (25 mL), and the solution was cooled to −15 °C using an acetone/ice bath. Chloroacetyl chloride (15.81 g, 11.14 mL, 139.97 mmol, 1.00 eq.) was dissolved in CH_2Cl_2 (20 mL) and added over 1 h using a pressure-equalised dropping funnel. The reaction mixture was left stirring at room temperature overnight. Upon completion, the resulting organic solution was washed three times with 0.1 M HCl and once with H_2O before drying over anhydrous K_2CO_3. Removal of the solvent under reduced pressure yielded **92** as a yellow oil (5.10 g, 41.95 mmol, 30% yield). HRMS (*m/z*) (ES^+) Calculated for $C_4H_8NOClNa$ *m/z* = 144.0192 $[M + Na]^+$. Found *m/z* = 144.0185; ^1H NMR (400 MHz, $CDCl_3$) δ_H: 4.05 (2H, s, CH_2), 3.06 (3H, s, CH_3), 2.94 (3H, S, CH_3); ^{13}C NMR (100 MHz, $CDCl_3$) δ_C: 166.5, 41.2, 37.6, 35.9. IR υ_{max} (cm^{-1}): 3490, 2942, 1729, 1658, 1500, 1444, 1402, 1257, 1021, 1120, 1060, 979, 929, 794, 748, 657.

2,2',2''-(1,4,7,10-Tetraazacyclododecane-1,4,7-triyl)tris(*N*,*N*-dimethylacetamide) (75)[305]

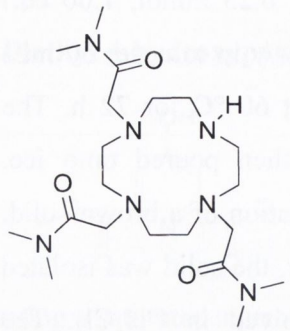

1,4,7,10-tetraazacyclododecane (2.34 g, 13.58 mmol, 1.00 eq.) and $NaHCO_3$ (3.42 g, 40.74 mmol, 3.00 eq.) were placed in a 100 mL RBF with CH_3CN (40 mL). The RBF was placed in an ice bath and allowed to cool to 0 °C. **92** (4.95 g, 40.74 mmol, 3.00 eq.) in CH_3CN (10 mL) was swiftly added and the solution was left to stir at 0 °C for 5 min before refluxing for 4 days. The reaction mixture was then filtered and the solvent removed under reduced pressure. The residue was suspended in CH_2Cl_2, filtered and purified by neutral alumina column chromatography (gradient elution 100:0 → 80:20; CH_2Cl_2/MeOH) to give **75** as a white solid (1.27 g, 2.97 mmol, 22% yield). HRMS (*m/z*) (ES^+) Calculated for $C_{20}H_{42}N_7O_3$ *m/z* = 428.3344 $[M + H]^+$. Found *m/z* = 428.3333; ^1H NMR (400 MHz, $CDCl_3$) δ_H: 10.00 (1H, br s, NH), 3.59 (2H, s, CH_2CO), 3.56 (4H, s, CH_2CO), 3.08 (8H, s, cyclen-CH_2), 3.03 (3H, s, CH_3), 2.95 (6H, s, CH_3), 2.89 (9H, s, CH_3), 2.83 (8H, s, cyclen-CH_2); ^{13}C NMR (100 MHz, $CDCl_3$) δ_C: 170.4, 170.3, 55.7, 53.6, 51.7, 50.3, 49.8, 46.2, 36.8, 36.4, 35.3; IR υ_{max} (cm^{-1}): 3434, 2927, 2852, 1637, 1508, 1475, 1402, 1338, 1261, 1103, 1064, 1022, 881, 806, 769, 667, 649, 574, 484.

Complex Eu.75[305]

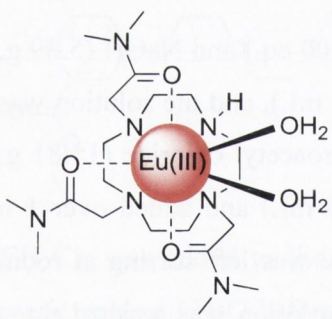

Ligand **75** (0.028 g, 0.065 mmol, 1.00 eq.) and $Eu(CF_3SO_3)_3$ (0.039 g, 0.065 mmol, 1.00 eq.) were refluxed together, under an inert atmosphere, in freshly distilled CH_3CN (6 mL) for 24 h. Following reduction of the solvent volume to *ca.* 1 mL, the product was precipitated from swirling dry diethyl ether. Isolation by decanting afforded the complex **Eu.75** as a yellow/brown solid (0.055 g, 0.054 mmol, 83% yield). m.p. decomposed above 180 °C; HRMS (*m/z*) ($MALDI^+$) Calculated for $C_{21}H_{40}N_7O_6SF_3Eu$ *m/z* = 728.1925 $[M - 2CF_3SO_3 - H]^+$. Found *m/z* = 728.1909; ^1H NMR (400 MHz, CD_3CN-d_3) δ_H: 27.76, 18.39, 15.55, 11.47, 5.49, 3.37, 2.74, −1.49, −3.54, −6.25, −10.19, −12.30, −13.94; IR υ_{max} (cm^{-1}): 3434, 2982, 2927, 2884, 1625, 1508, 1459, 1438, 1413, 1280, 1258, 1173, 1084, 1031, 960, 824, 762, 641, 573, 518.

Complex Tb.75[305]

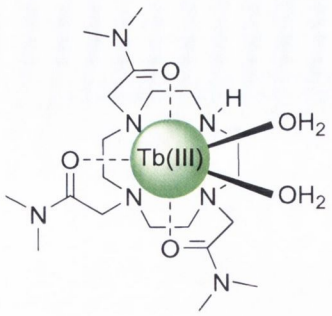

Ligand **75** (0.029 g, 0.068 mmol, 1.00 eq.) and $Tb(CF_3SO_3)_3$ (0.041 g, 0.068 mmol, 1.00 eq.) were refluxed together, under an inert atmosphere, in freshly distilled CH_3CN (6 mL) for 24 h. Following reduction of the solvent volume to *ca.* 1 mL, the product was precipitated from swirling dry diethyl ether. Isolation by decanting afforded the complex **Tb.75** as a yellow/brown solid (0.056 g, 0.054 mmol, 79% yield). m.p. decomposed above 190 °C; HRMS (*m/z*) (MALDI$^+$) Calculated for $C_{21}H_{40}N_7O_6SF_3Tb$ *m/z* = 734.1966 $[M - 2CF_3SO_3 - H]^+$. Found *m/z* = 734.1940; ^1H NMR (400 MHz, CD_3CN-d_3) δ_H: 183.78, 142.59, 117.67, 93.7, 75.9, 42.97, 25.3, 17.96, 17.38, 15.44, 14.98, 13.10, 12.39, 11.29, 8.76, 7.25, −36.6, −58.37, −70.86, −105.92, −141.03; IR υ_{max} (cm^{-1}): 3434, 2957, 2927, 2856, 1625, 1508, 1465, 1438, 1412, 1279, 1256, 1171, 1084, 1030, 960, 824, 761, 640, 574, 518.

References

References

(1) Steed, J. W.; Atwood, J. L. *Supramolecular Chemistry*; Wiley: Chichester, **2000**.
(2) Dodzuick, H. *Introduction to Supramolecular Chemistry*; Springer, **2002**.
(3) de Bettencourt-Dias, A. *Dalton Trans.* **2007**, 2229.
(4) Piepenbrock, M.-O. M.; Lloyd, G. O.; Clarke, N.; Steed, J. W. *Chem. Rev.* **2009**, *110*, 1960.
(5) Molander, G. A.; Romero, J. A. C. *Chem. Rev.* **2002**, *102*, 2161.
(6) Löhnwitz, K.; Molski, M. J.; Lühl, A.; Roesky, P. W.; Dochnahl, M.; Blechert, S. *Eur. J. Inorg. Chem.* **2009**, *2009*, 1369.
(7) Elmes, R. B. P.; Erby, M.; Bright, S. A.; Williams, D. C.; Gunnlaugsson, T. *Chem. Commun.* **2012**, *48*, 2588.
(8) Elmes, R. B. P.; Orange, K. N.; Cloonan, S. M.; Williams, D. C.; Gunnlaugsson, T. *J. Am. Chem. Soc.* **2011**, *133*, 15862.
(9) Pedersen, C. J. *J. Am. Chem. Soc.* **1967**, *89*, 2495.
(10) Kyba, E. P.; Helgeson, R. C.; Madan, K.; Gokel, G. W.; Tarnowski, T. L.; Moore, S. S.; Cram, D. J. *J. Am. Chem. Soc.* **1977**, *99*, 2564.
(11) Lehn, J.-M. *Science* **1985**, *227*, 849.
(12) Lehn, J.-M. *Angew. Chem. Int. Ed.* **1988**, *27*, 89.
(13) Li, M.; Selvin, P. R. *J. Am. Chem. Soc.* **1995**, *117*, 8132.
(14) Fatin-Rouge, N.; Tóth, É.; Perret, D.; Backer, R. H.; Merbach, A. E.; Bünzli, J.-C. G. *J. Am. Chem. Soc.* **2000**, *122*, 10810.
(15) Roznyatovskiy, V. V.; Lee, C.-H.; Sessler, J. L. *Chem. Soc. Rev.* **2013**, *42*, 1921.
(16) Beer, P. D.; Szemes, F.; Passaniti, P.; Maestri, M. *Inorg. Chem.* **2004**, *43*, 3965.
(17) Lehn, J.-M. *Supramolecular Chemistry: Concepts and Perspectives*; Wiley-VCH, **1995**.
(18) Eliseeva, S. V.; Bünzli, J.-C. G. *Chem. Soc. Rev.* **2010**, *39*, 189.
(19) Bünzli, J.-C. G. *Acc. Chem. Res.* **2006**, *39*, 53.
(20) dos Santos, C. M. G.; Harte, A. J.; Quinn, S. J.; Gunnlaugsson, T. *Coord. Chem. Rev.* **2008**, *252*, 2512.
(21) Zheng, X.-L.; Liu, Y.; Pan, M.; Lü, X.-Q.; Zhang, J.-Y.; Zhao, C.-Y.; Tong, Y.-X.; Su, C.-Y. *Angew. Chem. Int. Ed.* **2007**, *46*, 7399.
(22) Gunnlaugsson, T.; Leonard, J. P.; Sénéchal, K.; Harte, A. J. *J. Am. Chem. Soc.* **2003**, *125*, 12062.
(23) McCoy, C. P.; Stomeo, F.; Plush, S. E.; Gunnlaugsson, T. *Chem. Mater.* **2006**, *18*, 4336.
(24) Bonnet, C. S.; Gunnlaugsson, T. *New J. Chem.* **2009**, *33*, 1025.
(25) Hanaoka, K.; Kikuchi, K.; Kobayashi, S.; Nagano, T. *J. Am. Chem. Soc.* **2007**, *129*, 13502.
(26) Montgomery, C. P.; Murray, B. S.; New, E. J.; Pal, R.; Parker, D. *Acc. Chem. Res.* **2009**, *42*, 925.
(27) Deiters, E.; Song, B.; Chauvin, A.-S.; Vandevyver, C. D. B.; Gumy, F.; Bünzli, J.-C. G. *Chem. - Eur. J.* **2009**, *15*, 885.
(28) Bünzli, J.-C. G.; Piguet, C. *Chem. Soc. Rev.* **2005**, *34*, 1048.
(29) Cotton, S. *Lanthanides and Actinides*; McMillan Education: London, **1991**.
(30) Binnemans, K. *Chem. Rev.* **2009**, *109*, 4283.
(31) Gunnlaugsson, T.; Stomeo, F. *Org. Biomol. Chem.* **2007**, *5*, 1999.
(32) Faulkner, S.; Pope, S. J. A.; Burton-Pye, B. P. *Appl. Spectrosc. Rev.* **2005**, *40*, 1.
(33) Kotova, O.; Comby, S.; Gunnlaugsson, T. *Chem. Commun.* **2011**, *47*, 6810.
(34) Bonnet, C. S.; Devocelle, M.; Gunnlaugsson, T. *Org. Biomol. Chem.* **2012**, *10*, 126.

(35) Bünzli, J.-C. G.; Comby, S.; Chauvin, A.-S.; Vandevyver, C. D. B. *J. Rare Earth* **2007**, *25*, 257.
(36) Moore, E. G.; Samuel, A. P. S.; Raymond, K. N. *Acc. Chem. Res.* **2009**, *42*, 542.
(37) Melhuish, W. H. *Pure Appl. Chem.* **1984**, *56*, 231.
(38) Beeby, A.; Clarkson, I. M.; Dickins, R. S.; Faulkner, S.; Parker, D.; Royle, L.; de Sousa, A. S.; Gareth Williams, J. A.; Woods, M. *J. Chem. Soc., Perk. Trans. 2* **1999**, 493.
(39) Supkowski, R. M.; Horrocks, W. D. *Inorg. Chim. Acta* **2002**, *340*, 44.
(40) Cheng, Z.; Ma, P.; Hou, Z.; Wang, W.; Dai, Y.; Zhai, X.; Lin, J. *Dalton Trans.* **2012**, *41*, 1481.
(41) Tremblay, M. S.; Halim, M.; Sames, D. *J. Am. Chem. Soc.* **2007**, *129*, 7570.
(42) Parker, D. *Coord. Chem. Rev.* **2000**, *205*, 109.
(43) Parkesh, R.; Veale, E. B.; Gunnlaugsson, T. *Fluorescent Detection Principles and Strategies*; John Wiley and Sons Ltd., **2010**.
(44) Nieβner, R. *Angew. Chem. Int. Ed.* **1994**, *33*, 1673.
(45) Bünzli, J.-C. G.; Eliseeva, S. V. *Chem. Sci.* **2013**.
(46) Weissleder, R.; Ntziachristos, V. *Nat. Med.* **2003**, *9*, 123.
(47) Bünzli, J.-C. G. *Chem. Rev.* **2010**, *110*, 2729.
(48) Gunnlaugsson, T.; Leonard, J. P. *Chem. Commun.* **2005**, 3114.
(49) Bünzli, J.-C. G.; Piguet, C. *Encyclopedia of Materials: Science and Technology*; Elsevier Science Ltd.: Oxford, **2001**.
(50) Leonard, J. P.; Nolan, C. B.; Stomeo, F.; Gunnlaugsson, T. *Photochemistry and Photophysics of Coordination Compounds: Lanthanides*; Springer, **2007**; Vol. 281.
(51) Wolbers, M. P. O.; van Veggel, F. C. J. M.; Snellink-Ruel, B. H. M.; Hofstraat, J. W.; Geurts, F. A. J.; Reinhoudt, D. N. *J. Chem. Soc., Perk. Trans. 2* **1998**, 2141.
(52) Heller, A.; Barkleit, A.; Bernhard, G.; Ackermann, J.-U. *Inorg. Chim. Acta* **2009**, *362*, 1215.
(53) McMahon, B. K. PhD Thesis, Trinity College Dublin, **2011**.
(54) Beeby, A.; Parker, D.; Williams, J. A. G. *J. Chem. Soc., Perk. Trans. 2* **1996**, 1565.
(55) Puntus, L. N.; Chauvin, A.-S.; Varbanov, S.; Bünzli, J.-C. G. *Eur. J. Inorg. Chem.* **2007**, *2007*, 2315.
(56) Atkins, P. W. *Physical Chemistry*; 6th ed.; W. H. Freeman & Co., **1998**.
(57) Eliseeva, S. V.; Pleshkov, D. N.; Lyssenko, K. A.; Lepnev, L. S.; Bünzli, J.-C. G.; Kuzmina, N. P. *Inorg. Chem.* **2011**, *50*, 5137.
(58) de Silva, A. P.; Gunaratne, H. Q. N.; Rice, T. E. *Angew. Chem. Int. Ed.* **1996**, *35*, 2116.
(59) Dickins, R. S.; Howard, J. A. K.; Maupin, C. L.; Moloney, J. M.; Parker, D.; Riehl, J. P.; Siligardi, G.; Williams, J. A. G. *Chem. - Eur. J.* **1999**, *5*, 1095.
(60) Wu, J.; Li, H.-Y.; Xu, Q.-L.; Zhu, Y.-C.; Tao, Y.-M.; Li, H.-R.; Zheng, Y.-X.; Zuo, J.-L.; You, X.-Z. *Inorg. Chim. Acta* **2010**, *363*, 2394.
(61) Bünzli, J.-C. G. *Spectroscopic Properties of Rare Earths in Optical Materials*; Springer Verlag: Berlin, **2005**.
(62) Dexter, D. *J. Phys. Chem.* **1953**, *21*, 836.
(63) Förster, T. *Ann. Phys.* **1948**, *2*, 55.
(64) Shinoda, S.; Miyake, H.; Tsukube, H. *Handbook of the Physics and Chemistry of Rare Earths*; Elsevier: North Holland, **2005**; Vol. 35.
(65) Parker, D.; Williams, J. A. G. *Metal Ions in Biological Systems*; Marcel Dekker Inc.: New York, **2003**; Vol. 40.
(66) Horrocks, W. D.; Sudnick, J. D. S. *J. Am. Chem. Soc.* **1979**, *101*, 334.
(67) Horrocks, W. D.; Sudnick, J. D. S. *Acc. Chem. Res.* **1981**, *14*, 384.
(68) Sabbatini, N.; Guardigli, M.; Lehn, J.-M. *Coord. Chem. Rev.* **1993**, *123*, 201.

(69) Aime, S.; Botta, M.; Parker, D.; Williams, J. A. G. *J. Chem. Soc., Dalton Trans.* **1996**, 17.
(70) Lima, L. M. P.; Lecointre, A.; Morfin, J.-F.; de Blas, A.; Visvikis, D.; Charbonnière, L. J.; Platas-Iglesias, C.; Tripier, R. *Inorg. Chem.* **2011**, *50*, 12508.
(71) Law, G.-L.; Pham, T. A.; Xu, J.; Raymond, K. N. *Angew. Chem. Int. Ed.* **2012**, *51*, 2371.
(72) Beeby, A.; Burton-Pye, B. P.; Faulkner, S.; Motson, G. R.; Jeffery, J. C.; McCleverty, J. A.; Ward, M. D. *J. Chem. Soc., Dalton Trans.* **2002**, 1923.
(73) Davies, G. M.; Aarons, R. J.; Motson, G. R.; Jeffery, J. C.; Adams, H.; Faulkner, S.; Ward, M. D. *Dalton Trans.* **2004**, 1136.
(74) Davies, G. M.; Adams, H.; Pope, S. J. A.; Faulkner, S.; Ward, M. D. *Photochem. Photobiol. Sci.* **2005**, *4*, 829.
(75) Albrecht, M.; Osetska, O.; Fröhlich, R.; Bünzli, J.-C. G.; Aebischer, A.; Gumy, F.; Hamacek, J. *J. Am. Chem. Soc.* **2007**, *129*, 14178.
(76) Jones, C.; Junk, P. C.; Smith, M. K.; Thomas, R. C. *Z. Anorg. Allg. Chem.* **2000**, *626*, 2491.
(77) Starynowicz, P.; Bukietyńska, K.; Gołąb, S.; Ryba-Romanowski, W.; Sokolnicki, J. *Eur. J. Inorg. Chem.* **2002**, *2002*, 2344.
(78) Bünzli, J.-C. G.; André, N.; Elhabiri, M.; Muller, G.; Piguet, C. *J. Alloys Compd.* **2000**, *303–304*, 66.
(79) Cotton, F. A.; Wilkinson, G. *Advanced Inorganic Chemistry*; 5th ed.; Wiley Interscience, **1988**.
(80) McMahon, B. K.; Gunnlaugsson, T. *J. Am. Chem. Soc.* **2012**, *134*, 10725.
(81) Molloy, J. K.; Kotova, O.; Peacock, R. D.; Gunnlaugsson, T. *Org. Biomol. Chem.* **2012**, *10*, 314.
(82) Fairbairn, R. E.; McLellan, R.; McIntosh, R. D.; Taylor, S. M.; Brechin, E. K.; Dalgarno, S. J. *Chem. Commun.* **2012**, *48*, 8493.
(83) Bonnet, C.; Gadelle, A.; Pécaut, J.; Fries, P. H.; Delangle, P. *Chem. Commun.* **2005**, 625.
(84) Caravan, P.; Ellison, J. J.; McMurry, T. J.; Lauffer, R. B. *Chem. Rev.* **1999**, *99*, 2293.
(85) Kitchen, J. A.; Parkesh, R.; Veale, E. B.; Gunnlaugsson, T. *Luminescent Sensing*; John Wiley & Sons Ltd., **2012**.
(86) Thibon, A.; Pierre, V. C. *Anal. Bioanal. Chem.* **2009**, *394*, 107.
(87) Bretonniere, Y.; Cann, M. J.; Parker, D.; Slater, R. *Org. Biomol. Chem.* **2004**, *2*, 1624.
(88) New, E. J.; Parker, D.; Peacock, R. D. *Dalton Trans.* **2009**, 672.
(89) Smith, D. G.; Pal, R.; Parker, D. *Chem. - Eur. J.* **2012**, *18*, 11604.
(90) Law, G.-L.; Man, C.; Parker, D.; Walton, J. W. *Chem. Commun.* **2010**, *46*, 2391.
(91) Walton, J. W.; Bourdolle, A.; Butler, S. J.; Soulie, M.; Delbianco, M.; McMahon, B. K.; Pal, R.; Puschmann, H.; Zwier, J. M.; Lamarque, L.; Maury, O.; Andraud, C.; Parker, D. *Chem. Commun.* **2013**, *49*, 1600.
(92) D'Aléo, A.; Bourdolle, A.; Brustlein, S.; Fauquier, T.; Grichine, A.; Duperray, A.; Baldeck, P. L.; Andraud, C.; Brasselet, S.; Maury, O. *Angew. Chem. Int. Ed.* **2012**, *51*, 6622.
(93) Døssing, A. *Eur. J. Inorg. Chem.* **2005**, *2005*, 1425.
(94) Faulkner, S.; Pope, S. J. A.; Burton-Pye, B. P. *Appl. Spectrosc. Rev.* **2005**, *40*, 1.
(95) Becker, A.; Hessenius, C.; Licha, K.; Ebert, B.; Sukowski, U.; Semmler, W.; Wiedenmann, B.; Grötzinger, C. *Nat. Biotechnol.* **2001**, *19*, 327.
(96) Kim, S.; Lim, Y. T.; Soltesz, E. G.; De Grand, A. M.; Lee, J.; Nakayama, A.; Parker, J. A.; Mihaljevic, T.; Laurence, R. G.; Dor, D. M.; Cohn, L. H.; Bawendi, M. G.; Frangioni, J. V. *Nat. Biotechnol.* **2004**, *22*, 93.
(97) Müller, M. G.; Georgakoudi, I.; Zhang, Q.; Wu, J.; Feld, M. S. *Appl. Opt.* **2001**, *40*, 4633.

(98) Weissleder, R. *Nat. Biotechnol.* **2001**, *19*, 316.
(99) Faulkner, S.; Pope, S. J. A. *J. Am. Chem. Soc.* **2003**, *125*, 10526.
(100) Andrews, M.; Jones, J. E.; Harding, L. P.; Pope, S. J. A. *Chem. Commun.* **2011**, *47*, 206.
(101) Merbach, A. E.; Tóth, É. *The Chemistry of Contrast Agents in Medical Magnetic Resonance Imaging*; John Wiley & Sons Ltd., **2001**.
(102) Boros, E.; Polasek, M.; Zhang, Z.; Caravan, P. *J. Am. Chem. Soc.* **2012**, *134*, 19858.
(103) Kitchen, J. A.; Gunnlaugsson, T. *Supramolecular Chemistry: From Sensors and Imaging Agents to Functional Mononuclear and Polynuclear Self-Assembly Lanthanide Complexes*; John Wiley & Sons Ltd., **2012**.
(104) Kruger, P. E.; Gunnlaugsson, T. *Dalton Trans.* **2011**, *40*, 12003.
(105) Steed, J. W.; Atwood, J. L. *Supramolecular Chemistry*; 2nd ed.; John Wiley & Sons Ltd., **2009**.
(106) Lehn, J.-M. *Pure Appl. Chem.* **1994**, *66*.
(107) Thomas, J. A. *Dalton Trans.* **2011**, *40*, 12005.
(108) Comby, S.; Scopelliti, R.; Imbert, D.; Charbonnière, L.; Ziessel, R.; Bünzli, J.-C. G. *Inorg. Chem.* **2006**, *45*, 3158.
(109) Zebret, S.; Dupont, N.; Besnard, C.; Bernardinelli, G.; Hamacek, J. *Dalton Trans.* **2012**, *41*, 4817.
(110) Floquet, S.; Ouali, N.; Bocquet, B.; Bernardinelli, G.; Imbert, D.; Bünzli, J.-C. G.; Hopfgartner, G.; Piguet, C. *Chem. - Eur. J.* **2003**, *9*, 1860.
(111) Senegas, J.-M.; Koeller, S.; Bernardinelli, G.; Piguet, C. *Chem. Commun.* **2005**, 2235.
(112) Piguet, C.; Borkovec, M.; Hamacek, J.; Zeckert, K. *Coord. Chem. Rev.* **2005**, *249*, 705.
(113) Lincheneau, C.; Stomeo, F.; Comby, S.; Gunnlaugsson, T. *Aust. J. Chem.* **2011**, *64*, 1315.
(114) Bünzli, J.-C. G.; Comby, S.; Chauvin, A.-S.; Vandevyver, C. D. B. *J. Rare Earth* **2007**, *25*, 257.
(115) Piguet, C.; Bünzli, J.-C. G. *Chem. Soc. Rev.* **1999**, *28*, 347.
(116) Chauvin, A.-S.; Gumy, F.; Imbert, D.; Bünzli, J.-C. G. *Spectrosc. Lett.* **2004**, *37*, 517.
(117) Aebischer, A.; Gumy, F.; Bünzli, J.-C. G. *Phys. Chem. Chem. Phys.* **2009**, *11*, 1346.
(118) Reinhard, C.; Güdel, H. U. *Inorg. Chem.* **2002**, *41*, 1048.
(119) Platas-Iglesias, C.; Piguet, C.; Andre, N.; Bünzli, J.-C. G. *J. Chem. Soc., Dalton Trans.* **2001**, 3084.
(120) Pompidor, G.; D'Aléo, A.; Vicat, J.; Toupet, L.; Giraud, N.; Kahn, R.; Maury, O. *Angew. Chem. Int. Ed.* **2008**, *47*, 3388.
(121) Picot, A.; D'Aléo, A.; Baldeck, P. L.; Grichine, A.; Duperray, A.; Andraud, C.; Maury, O. *J. Am. Chem. Soc.* **2008**, *130*, 1532.
(122) Kervern, G.; D'Aléo, A.; Toupet, L.; Maury, O.; Emsley, L.; Pintacuda, G. *Angew. Chem. Int. Ed.* **2009**, *48*, 3082.
(123) Shavaleev, N. M.; Eliseeva, S. V.; Scopelliti, R.; Bünzli, J.-C. G. *Inorg. Chem.* **2010**, *49*, 3927.
(124) Jia, W. L.; McCormick, T.; Tao, Y.; Lu, J.-P.; Wang, S. *Inorg. Chem.* **2005**, *44*, 5706.
(125) He, L.; Qiao, J.; Duan, L.; Dong, G.; Zhang, D.; Wang, L.; Qiu, Y. *Adv. Funct. Mater.* **2009**, *19*, 2950.
(126) Shavaleev, N. M.; Eliseeva, S. V.; Scopelliti, R.; Bünzli, J.-C. G. *Chem. - Eur. J.* **2009**, *15*, 10790.
(127) Escande, A.; Guénée, L.; Buchwalder, K.-L.; Piguet, C. *Inorg. Chem.* **2009**, *48*, 1132.
(128) Andreiadis, E. S.; Imbert, D.; Pécaut, J.; Demadrille, R.; Mazzanti, M. *Dalton Trans.* **2012**, *41*, 1268.
(129) de Bettencourt-Dias, A.; Barber, P. S.; Viswanathan, S.; de Lill, D. T.; Rollett, A.; Ling, G.; Altun, S. *Inorg. Chem.* **2010**, *49*, 8848.

(130) de Bettencourt-Dias, A.; Viswanathan, S.; Rollett, A. *J. Am. Chem. Soc.* **2007**, *129*, 15436.
(131) Moore, E. G.; Xu, J.; Jocher, C. J.; Werner, E. J.; Raymond, K. N. *J. Am. Chem. Soc.* **2006**, *128*, 10648.
(132) Duke, R. M.; Veale, E. B.; Pfeffer, F. M.; Kruger, P. E.; Gunnlaugsson, T. *Chem. Soc. Rev.* **2010**, *39*, 3936.
(133) Lindström, U. M. *Chem. Rev.* **2002**, *102*, 2751.
(134) Kobayashi, S.; Manabe, K. *Acc. Chem. Res.* **2002**, *35*, 209.
(135) de Bettencourt-Dias, A.; Barber, P. S.; Bauer, S. *J. Am. Chem. Soc.* **2012**, *134*, 6987.
(136) Gassner, A.-L.; Duhot, C. l.; Bünzli, J.-C. G.; Chauvin, A.-S. *Inorg. Chem.* **2008**, *47*, 7802.
(137) Bünzli, J.-C. G.; Piguet, C. *Chem. Rev.* **2002**, *102*, 1897.
(138) Terazzi, E.; Guénée, L.; Varin, J.; Bocquet, B.; Lemonnier, J.-F.; Emery, D.; Mareda, J.; Piguet, C. *Chem. - Eur. J.* **2011**, *17*, 184.
(139) Lessmann, J. J.; Horrocks, W. D. *Inorg. Chem.* **2000**, *39*, 3114.
(140) Kawano, M.; Kobayashi, Y.; Ozeki, T.; Fujita, M. *J. Am. Chem. Soc.* **2006**, *128*, 6558.
(141) Yu, K.; Wan, B.; Yu, Y.; Wang, L.; Su, Z.-h.; Wang, C.-m.; Wang, C.-x.; Zhou, B.-B. *Inorg. Chem.* **2013**, *52*, 485.
(142) Cook, T. R.; Zheng, Y.-R.; Stang, P. J. *Chem. Rev.* **2012**, *113*, 734.
(143) Cui, Y.; Xu, H.; Yue, Y.; Guo, Z.; Yu, J.; Chen, Z.; Gao, J.; Yang, Y.; Qian, G.; Chen, B. *J. Am. Chem. Soc.* **2012**, *134*, 3979.
(144) Piguet, C.; Bernardinelli, G.; Hopfgartner, G. *Chem. Rev.* **1997**, *97*, 2005.
(145) Albrecht, M. *Chem. Rev.* **2001**, *101*, 3457.
(146) Lehn, J.-M.; Rigault, A.; Siegel, J.; J., H.; B., C.; Moras, D. *Proc. Natl. Acad. Sci. USA* **1987**, *84*.
(147) Albrecht, M.; Witt, K.; Rottele, H.; Fröhlich, R. *Chem. Commun.* **2001**, 1330.
(148) Riis-Johannessen, T.; Bernardinelli, G.; Filinchuk, Y.; Clifford, S.; Favera, N. D.; Piguet, C. *Inorg. Chem.* **2009**, *48*, 5512.
(149) Elhabiri, M.; Scopelliti, R.; Bünzli, J.-C. G.; Piguet, C. *J. Am. Chem. Soc.* **1999**, *121*, 10747.
(150) Aboshyan-Sorgho, L.; Nozary, H.; Aebischer, A.; Bünzli, J.-C. G.; Morgantini, P.-Y.; Kittilstved, K. R.; Hauser, A.; Eliseeva, S. V.; Petoud, S.; Piguet, C. *J. Am. Chem. Soc.* **2012**, *134*, 12675.
(151) Cantuel, M.; Bernardinelli, G.; Imbert, D.; Bünzli, J.-C. G.; Hopfgartner, G.; Piguet, C. *J. Chem. Soc., Dalton Trans.* **2002**, 1929.
(152) Telfer, S. G.; Tajima, N.; Kuroda, R.; Cantuel, M.; Piguet, C. *Inorg. Chem.* **2004**, *43*, 5302.
(153) Cantuel, M.; Bernardinelli, G.; Muller, G.; Riehl, J. P.; Piguet, C. *Inorg. Chem.* **2004**, *43*, 1840.
(154) Wang, B.; Zang, Z.; Wang, H.; Dou, W.; Tang, X.; Liu, W.; Shao, Y.; Ma, J.; Li, Y.; Zhou, J. *Angew. Chem. Int. Ed.* **2013**, *52*, 3756.
(155) Bain, L.; Bullock, S.; Harding, L.; Riis-Johannessen, T.; Midgley, G.; Rice, C. R.; Whitehead, M. *Chem. Commun.* **2010**, *46*, 3496.
(156) Ayme, J.-F.; Beves, J. E.; Leigh, D. A.; McBurney, R. T.; Rissanen, K.; Schultz, D. *Nat. Chem.* **2012**, *4*, 15.
(157) Beer, P. D.; Hayes, E. J. *Coord. Chem. Rev.* **2003**, *240*, 167.
(158) Umemoto, K.; Yamaguchi, K.; Fujita, M. *J. Am. Chem. Soc.* **2000**, *122*, 7150.
(159) Mal, P.; Breiner, B.; Rissanen, K.; Nitschke, J. R. *Science* **2009**, *324*, 1697.
(160) Pluth, M. D.; Raymond, K. N. *Chem. Soc. Rev.* **2007**, *36*, 161.
(161) El Aroussi, B.; Guénée, L.; Pal, P.; Hamacek, J. *Inorg. Chem.* **2011**, *50*, 8588.
(162) Hamacek, J.; Bernardinelli, G.; Filinchuk, Y. *Eur. J. Inorg. Chem.* **2008**, *2008*, 3419.

(163) Hamacek, J.; Poggiali, D.; Zebret, S.; Aroussi, B. E.; Schneider, M. W.; Mastalerz, M. *Chem. Commun.* **2012**, *48*, 1281.
(164) Yaghi, O. M.; O'Keeffe, M.; Ockwig, N. W.; Chae, H. K.; Eddaoudi, M.; Kim, J. *Nature* **2003**, *423*, 705.
(165) Eddaoudi, M.; Moler, D. B.; Li, H.; Chen, B.; Reineke, T. M.; O'Keeffe, M.; Yaghi, O. M. *Acc. Chem. Res.* **2001**, *34*, 319.
(166) Zhou, H.-C.; Long, J. R.; Yaghi, O. M. *Chem. Rev.* **2012**, *112*, 673.
(167) Rosi, N. L.; Eckert, J.; Eddaoudi, M.; Vodak, D. T.; Kirn, J.; O'Keeffe, M.; Yaghi, O. M. *Science* **2003**, *300*, 1127.
(168) Horcajada, P.; Gref, R.; Baati, T.; Allan, P. K.; Maurin, G.; Couvreur, P.; Férey, G.; Morris, R. E.; Serre, C. *Chem. Rev.* **2011**, *112*, 1232.
(169) Wang, Z.; Chen, G.; Ding, K. *Chem. Rev.* **2008**, *109*, 322.
(170) Tang, Q.; Liu, S.; Liu, Y.; Miao, J.; Li, S.; Zhang, L.; Shi, Z.; Zheng, Z. *Inorg. Chem.* **2013**, *52*, 2799.
(171) Rocha, J.; Carlos, L. D.; Paz, F. A. A.; Ananias, D. *Chem. Soc. Rev.* **2011**, *40*, 926.
(172) White, K. A.; Chengelis, D. A.; Gogick, K. A.; Stehman, J.; Rosi, N. L.; Petoud, S. *J. Am. Chem. Soc.* **2009**, *131*, 18069.
(173) Eliel, E. L.; Wilen, S. H. *Stereochemistry of Organic Compounds*; Wiley & Sons: New York, **1994**.
(174) Crassous, J. *Chem. Soc. Rev.* **2009**, *38*, 830.
(175) Zehnacker, A.; Suhm, M. A. *Angew. Chem. Int. Ed.* **2008**, *47*, 6970.
(176) Ali, I.; Gupta, V. K.; Aboul-Enein, H. Y.; Singh, P.; Sharma, B. *Chirality* **2007**, *19*, 453.
(177) Ali, H. D. P.; Kruger, P. E.; Gunnlaugsson, T. *New J. Chem.* **2008**, *32*, 1153.
(178) Berthod, A. *Chirality* **2009**, *21*, 167.
(179) Arjmand, F.; Parveen, S. *RSC Adv.* **2012**, *2*, 6354.
(180) Montgomery, C. P.; New, E. J.; Parker, D.; Peacock, R. D. *Chem. Commun.* **2008**, 4261.
(181) Muller, G. *Dalton Trans.* **2009**, 9692.
(182) Rodgers, A.; Norden, B. *Circular Dichroism and Linear Dichroism*; Oxford Chemistry Press: New York, Tokyo, **1997**.
(183) Riehl, J. P.; Richardson, F. S. *Chem. Rev.* **1986**, *86*, 1.
(184) Carr, R.; Evans, N. H.; Parker, D. *Chem. Soc. Rev.* **2012**, *41*, 7673.
(185) Field, J. E.; Muller, G.; Riehl, J. P.; Venkataraman, D. *J. Am. Chem. Soc.* **2003**, *125*, 11808.
(186) Tsumatori, H.; Nakashima, T.; Kawai, T. *Org. Lett.* **2010**, *12*, 2362.
(187) Coughlin, F. J.; Westrol, M. S.; Oyler, K. D.; Byrne, N.; Kraml, C.; Zysman-Colman, E.; Lowry, M. S.; Bernhard, S. *Inorg. Chem.* **2008**, *47*, 2039.
(188) Lunkley, J. L.; Shirotani, D.; Yamanari, K.; Kaizaki, S.; Muller, G. *J. Am. Chem. Soc.* **2008**, *130*, 13814.
(189) Riehl, J. P.; Muller, G. *Handbook on the Physics and Chemistry of Rare Earths*; North-Holland Publishing Company: Amsterdam, **2005**; Vol. 34.
(190) Carr, R.; Di Bari, L.; Lo Piano, S.; Parker, D.; Peacock, R. D.; Sanderson, J. M. *Dalton Trans.* **2012**, *41*, 13154.
(191) Bruce, J. I.; Dickins, R. S.; Govenlock, L. J.; Gunnlaugsson, T.; Lopinski, S.; Lowe, M. P.; Parker, D.; Peacock, R. D.; Perry, J. J. B.; Aime, S.; Botta, M. *J. Am. Chem. Soc.* **2000**, *122*, 9674.
(192) Moussa, A.; Pham, C.; Bommireddy, S.; Muller, G. *Chirality* **2009**, *21*, 497.
(193) Parker, D.; Dickins, R. S.; Puschmann, H.; Crossland, C.; Howard, J. A. K. *Chem. Rev.* **2002**, *102*, 1977.
(194) Cahn, R. S.; Ingold, C.; Prelog, V. *Angew. Chem. Int. Ed.* **1966**, *5*, 385.

(195) Jacques, J.; Collet, A.; Wilen, S. H. *Enantiomers, Racemates and Resolutions*; John Wiley & Sons Ltd.: New York, **1981**.
(196) Grinberg, N.; Burakowski, T.; Stalcup, A. M. *HPLC for Pharmaceutical Scientists*; Wiley and Sons: New Jersey, **2007**.
(197) Knof, U.; von Zelewsky, A. *Angew. Chem. Int. Ed.* **1999**, *38*, 302.
(198) Mamula, O.; von Zelewsky, A. *Coord. Chem. Rev.* **2003**, *242*, 87.
(199) Faulkner, S.; Matthews, J. L. *Comprehensive Coordination Chemistry II*; Elsevier: Oxford, **2004**; Vol. 9.
(200) Seitz, M.; Moore, E. G.; Ingram, A. J.; Muller, G.; Raymond, K. N. *J. Am. Chem. Soc.* **2007**, *129*, 15468.
(201) Tsukube, H.; Shinoda, S. *Chem. Rev.* **2002**, *102*, 2389.
(202) Gregoliński, J.; Starynowicz, P.; Hua, K. T.; Lunkley, J. L.; Muller, G.; Lisowski, J. *J. Am. Chem. Soc.* **2008**, *130*, 17761.
(203) Walton, J. W.; Bari, L. D.; Parker, D.; Pescitelli, G.; Puschmann, H.; Yufit, D. S. *Chem. Commun.* **2011**, *47*, 12289.
(204) Hua, K. T.; Xu, J.; Quiroz, E. E.; Lopez, S.; Ingram, A. J.; Johnson, V. A.; Tisch, A. R.; de Bettencourt-Dias, A.; Straus, D. A.; Muller, G. *Inorg. Chem.* **2011**, *51*, 647.
(205) Bozoklu, G.; Marchal, C.; Gateau, C.; Pécaut, J.; Imbert, D.; Mazzanti, M. *Chem. - Eur. J.* **2010**, *16*, 6159.
(206) Bozoklu, G.; Gateau, C.; Imbert, D.; Pécaut, J.; Robeyns, K.; Filinchuk, Y.; Memon, F.; Muller, G.; Mazzanti, M. *J. Am. Chem. Soc.* **2012**, *134*, 8372.
(207) Comby, S.; Tuck, S. A.; Truman, L. K.; Kotova, O.; Gunnlaugsson, T. *Inorg. Chem.* **2012**, *51*, 10158.
(208) Veale, E. B.; Kitchen, J. A.; Gunnlaugsson, T. *Supramol. Chem.* **2013**, *25*, 101.
(209) Duke, R. M.; McCabe, T.; Schmitt, W.; Gunnlaugsson, T. *J. Org. Chem.* **2012**, *77*, 3115.
(210) Duke, R. M.; Gunnlaugsson, T. *Tetrahedron Lett.* **2011**, *52*, 1503.
(211) Elmes, R. B. P.; Kitchen, J. A.; Williams, D. C.; Gunnlaugsson, T. *Dalton Trans.* **2012**, *41*, 6607.
(212) Kitchen, J. A.; Boyle, E. M.; Gunnlaugsson, T. *Inorg. Chim. Acta* **2012**, *381*, 236.
(213) Elmes, R. B. P.; Gunnlaugsson, T. *Tetrahedron Lett.* **2010**, *51*, 4082.
(214) Banerjee, S.; Veale, E. B.; Phelan, C. M.; Murphy, S. A.; Tocci, G. M.; Gillespie, L. J.; Frimannsson, D. O.; Kelly, J. M.; Gunnlaugsson, T. *Chem. Soc. Rev.* **2013**, *42*, 1601.
(215) Banerjee, S.; Kitchen, J. A.; Gunnlaugsson, T.; Kelly, J. M. *Org. Biomol. Chem.* **2012**, *10*, 3033.
(216) Veale, E. B.; Gunnlaugsson, T. *J. Org. Chem.* **2010**, *75*, 5513.
(217) Veale, E. B.; Frimannsson, D. O.; Lawler, M.; Gunnlaugsson, T. *Org. Lett.* **2009**, *11*, 4040.
(218) Comby, S.; Gunnlaugsson, T. *ACS Nano* **2011**, *5*, 7184.
(219) Truman, L. K.; Comby, S.; Gunnlaugsson, T. *Angew. Chem. Int. Ed.* **2012**, *51*, 9624.
(220) Massue, J.; Quinn, S. J.; Gunnlaugsson, T. *J. Am. Chem. Soc.* **2008**, *130*, 6900.
(221) Kotova, O.; Daly, R.; dos Santos, C. M. G.; Boese, M.; Kruger, P. E.; Boland, J. J.; Gunnlaugsson, T. *Angew. Chem. Int. Ed.* **2012**, *51*, 7208.
(222) Aspinall, H. C. *Chem. Rev.* **2002**, *102*, 1807.
(223) Leonard, J. P.; Jensen, P.; McCabe, T.; O'Brien, J. E.; Peacock, R. D.; Kruger, P. E.; Gunnlaugsson, T. *J. Am. Chem. Soc.* **2007**, *129*, 10986.
(224) Lincheneau, C. PhD Thesis, Trinity College Dublin, **2010**.
(225) Lincheneau, C.; Leonard, J. P.; McCabe, T.; Gunnlaugsson, T. *Chem. Commun.* **2011**, *47*, 7119.
(226) Lincheneau, C.; Destribats, C.; Barry, D. E.; Kitchen, J. A.; Peacock, R. D.; Gunnlaugsson, T. *Dalton Trans.* **2011**, *40*, 12056.

(227) Kitchen, J. A.; Barry, D. E.; Mercs, L.; Albrecht, M.; Peacock, R. D.; Gunnlaugsson, T. *Angew. Chem. Int. Ed.* **2012**, *51*, 704.
(228) Stomeo, F.; Lincheneau, C.; Leonard, J. P.; O'Brien, J. E.; Peacock, R. D.; McCoy, C. P.; Gunnlaugsson, T. *J. Am. Chem. Soc.* **2009**, *131*, 9636.
(229) Lincheneau, C.; Peacock, R. D.; Gunnlaugsson, T. *Chem. - Asian J.* **2010**, *5*, 500.
(230) Comby, S.; Stomeo, F.; McCoy, C. P.; Gunnlaugsson, T. *Helv. Chim. Acta* **2009**, *92*, 2461.
(231) Murray, N. S. PhD Thesis, Trinity College Dublin, **2008**.
(232) Cantuel, M.; Lincheneau, C.; Buffeteau, T.; Jonusauskaite, L.; Gunnlaugsson, T.; Jonusauskas, G.; McClenaghan, N. D. *Chem. Commun.* **2010**, *46*, 2486.
(233) Dickens, R. S.; Howard, J. A. K.; Maupin, C. L.; Moloney, J. M.; Parker, D.; Peacock, R. D.; Riehl, J. P.; Siligardi, G. *New J. Chem.* **1998**, *22*, 891.
(234) Kolb, H. C.; Finn, M. G.; Sharpless, K. B. *Angew. Chem. Int. Ed.* **2001**, *40*, 2004.
(235) Chauvin, A.-S.; Comby, S.; Song, B.; Vandevyver, C. D. B.; Thomas, F.; Bünzli, J.-C. G. *Chem. - Eur. J.* **2007**, *13*, 9515.
(236) Arnaud, A.; Belleney, J.; Boué, F.; Bouteiller, L.; Carrot, G.; Wintgens, V. *Angew. Chem. Int. Ed.* **2004**, *43*, 1718.
(237) Duke, R. M. PhD Thesis, Trinity College Dublin, **2009**.
(238) Akitt, J. W. *NMR and Chemistry: An Introduction to Modern NMR Spectroscopy*; 4th ed.; Stanley Thornes, **2000**.
(239) Bünzli, J.-C. G.; Choppin, G. R. *Lanthanide Probes in Life, Chemical and Earth Sciences*; Elsevier: Amsterdam, Oxford, New York, Tokyo, **1987**.
(240) Seitz, M.; Do, K.; Ingram, A. J.; Moore, E. G.; Muller, G.; Raymond, K. N. *Inorg. Chem.* **2009**, *48*, 8469.
(241) Kotova, O.; Kitchen, J. A.; Lincheneau, C.; Peacock, R. D.; Gunnlaugsson, T. *Chem. - Eur. J.* **2013**, *Accepted Manuscript*.
(242) Berlman, I. B. *Handbook of Fluorescence Spectra of Aromatic Compounds*; Academic Press: London, **1965**.
(243) Murov, S. L.; Carmichael, I.; Hug, G. L. *Handbook of Photochemistry*; 2nd ed.; Mercel Dekker Inc.: New York, **1993**.
(244) Castellano, B. M.; Eggers, D. K. *J. Phys. Chem. B* **2013**, *117*, 8180.
(245) Maeder, M.; Zuberbühler, A. D. *Anal. Chem.* **1990**, *62*, 2220.
(246) Gampp, H.; Maeder, M.; Meyer, C. J.; Zuberbühler, A. D. *Talanta* **1985**, *32*, 95.
(247) Ruruck, K. *Fluorescence Quantum Yields: Methods of Determination and Standards*; Springer, **2008**; Vol. 5.
(248) Chauvin, A.-S.; Gumy, F.; Imbert, D.; Bünzli, J.-C. G. *Spectrosc. Lett.* **2007**, *40*, 193.
(249) Werts, M. H. V.; Jukes, R. T. F.; Verhoeven, J. W. *Phys. Chem. Chem. Phys.* **2002**, *4*, 1542.
(250) Wu, D.; O'Shea, D. F. *Org. Lett.* **2013**, *15*, 3392.
(251) Ashton, P. R.; Campbell, P. J.; Glink, P. T.; Philp, D.; Spencer, N.; Stoddart, J. F.; Chrystal, E. J. T.; Menzer, S.; Williams, D. J.; Tasker, P. A. *Angew. Chem. Int. Ed.* **1995**, *34*, 1865.
(252) Ashton, P. R.; Chrystal, E. J. T.; Glink, P. T.; Menzer, S.; Schiavo, C.; Spencer, N.; Stoddart, J. F.; Tasker, P. A.; White, A. J. P.; Williams, D. J. *Chem. - Eur. J.* **1996**, *2*, 709.
(253) Raymo, F. M.; Stoddart, J. F. *Chem. Rev.* **1999**, *99*, 1643.
(254) Balzani, V.; Credi, A.; Raymo, F. M.; Stoddart, J. F. *Angew. Chem. Int. Ed.* **2000**, *39*, 3348.
(255) Yamaguchi, N.; Hamilton, L. M.; Gibson, H. W. *Angew. Chem. Int. Ed.* **1998**, *37*, 3275.
(256) Zong, Q.-S.; Zhang, C.; Chen, C.-F. *Org. Lett.* **2006**, *8*, 1859.
(257) Yamaguchi, N.; Gibson, H. W. *Angew. Chem. Int. Ed.* **1999**, *38*, 143.

(258) Han, M.; Zhang, H.-Y.; Yang, L.-X.; Jiang, Q.; Liu, Y. *Org. Lett.* **2008**, *10*, 5557.
(259) Christensen, K. M.; Bakac, A.; Espenson, J. H. *Chem. Phys.* **1993**, *176*, 359.
(260) Tropiano, M.; Kilah, N. L.; Morten, M.; Rahman, H.; Davis, J. J.; Beer, P. D.; Faulkner, S. *J. Am. Chem. Soc.* **2011**, *133*, 11847.
(261) Kihara, N.; Hashimoto, M.; Takata, T. *Org. Lett.* **2004**, *6*, 1693.
(262) Horie, M.; Suzaki, Y.; Osakada, K. *Inorg. Chem.* **2005**, *44*, 5844.
(263) Horie, M.; Suzaki, Y.; Osakada, K. *J. Am. Chem. Soc.* **2004**, *126*, 3684.
(264) Loeb, S. J.; Tramontozzi, D. A. *Org. Biomol. Chem.* **2005**, *3*, 1393.
(265) Ashton, P. R.; Huff, J.; Menzer, S.; Parsons, I. W.; Preece, J. A.; Stoddart, J. F.; Tolley, M. S.; White, A. J. P.; Williams, D. J. *Chem. - Eur. J.* **1996**, *2*, 31.
(266) Cantrill, S. J.; Youn, G. J.; Stoddart, J. F.; Williams, D. J. *J. Org. Chem.* **2001**, *66*, 6857.
(267) Ashton, P. R.; Baxter, I.; Cantrill, S. J.; Fyfe, M. C. T.; Glink, P. T.; Stoddart, J. F.; White, A. J. P.; Williams, D. J. *Angew. Chem. Int. Ed.* **1998**, *37*, 1294.
(268) Paiva, T. B.; Tominaga, M.; Paiva, A. C. M. *J. Med. Chem.* **1970**, *13*, 689.
(269) Di Bernardo, P.; Melchior, A.; Tolazzi, M.; Zanonato, P. L. *Coord. Chem. Rev.* **2012**, *256*, 328.
(270) Terai, T.; Kikuchi, K.; Iwasawa, S.-y.; Kawabe, T.; Hirata, Y.; Urano, Y.; Nagano, T. *J. Am. Chem. Soc.* **2006**, *128*, 6938.
(271) Lakowicz, J. R. *Principles of Fluorescence Spectroscopy*; 3rd ed.; Springer: New York, **2006**.
(272) Valeur, B. *Molecular Fluorescence: Principles and Applications*; Wiley: Weinheim, **2002**.
(273) Loeb, S. J.; Wisner, J. A. *Angew. Chem. Int. Ed.* **1998**, *37*, 2838.
(274) Mercer, D. J.; Vella, S. J.; Guertin, L.; Suhan, N. D.; Tuburcio, J.; Vukotic, V. N.; Wisner, J. A.; Loeb, S. J. *Eur. J. Org. Chem.* **2011**, 1763.
(275) Loeb, S. J.; Wisner, J. A. *Chem. Commun.* **2000**, 845.
(276) Gouin, S. G.; Roger, M.; Leygue, N.; Deniaud, D.; Julienne, K.; Benoist, E.; Picard, C.; Kovensky, J.; Galaup, C. *Bioorg. Med. Chem. Lett.* **2012**, *22*, 2684.
(277) Milne, M.; Chicas, K.; Li, A.; Bartha, R.; Hudson, R. H. E. *Org. Biomol. Chem.* **2012**, *10*, 287.
(278) Crowley, J. D.; Bandeen, P. H. *Dalton Trans.* **2010**, *39*, 612.
(279) Meudtner, R. M.; Ostermeier, M.; Goddard, R.; Limberg, C.; Hecht, S. *Chem. - Eur. J.* **2007**, *13*, 9834.
(280) Finn, M. G.; Fokin, V. V. *Chem. Soc. Rev.* **2010**, *39*, 1231.
(281) Jelinek, R.; Kolusheva, S. *Chem. Rev.* **2004**, *104*, 5987.
(282) Di Stasio, B.; Frochot, C.; Dumas, D.; Even, P.; Zwier, J.; Müller, A.; Didelon, J.; Guillemin, F.; Viriot, M.-L.; Barberi-Heyob, M. *Eur. J. Med. Chem.* **2005**, *40*, 1111.
(283) Varki, A. *Glycobiology* **1993**, *3*, 97.
(284) Gamblin, D. P.; Scanlan, E. M.; Davis, B. G. *Chem. Rev.* **2008**, *109*, 131.
(285) Dwek, R. A. *Chem. Rev.* **1996**, *96*, 683.
(286) Ernst, B.; Magnani, J. L. *Nat. Rev. Drug Discov.* **2009**, *8*, 661.
(287) Kim, C. U.; Lew, W.; Williams, M. A.; Liu, H.; Zhang, L.; Swaminathan, S.; Bischofberger, N.; Chen, M. S.; Mendel, D. B.; Tai, C. Y.; Laver, W. G.; Stevens, R. C. *J. Am. Chem. Soc.* **1997**, *119*, 681.
(288) von Itzstein, M.; Wu, W.-Y.; Kok, G. B.; Pegg, M. S.; Dyason, J. C.; Jin, B.; Phan, T. V.; Smythe, M. L.; White, H. F.; Oliver, S. W.; Colman, P. M.; Varghese, J. N.; Ryan, D. M.; Woods, J. M.; Bethell, R. C.; Hotham, V. J.; Cameron, J. M.; Penn, C. R. *Nature* **1993**, *363*, 418.
(289) Yamazaki, N.; Kojima, S.; Bovin, N. V.; André, S.; Gabius, S.; Gabius, H. J. *Adv. Drug Deliver. Rev.* **2000**, *43*, 225.
(290) Birnbaum, M.; Haspel, H.; Rosen, O. *Science* **1987**, *235*, 1495.

(291) Locos, O. B.; Heindl, C. C.; Corral, A.; Senge, M. O.; Scanlan, E. M. *Eur. J. Org. Chem.* **2010**, *2010*, 1026.
(292) Koharudin, L. M. I.; Kollipara, S.; Aiken, C.; Gronenborn, A. M. *J. Biol. Chem.* **2012**, *287*, 33796.
(293) Daly, R.; Vaz, G.; Davies, A. M.; Senge, M. O.; Scanlan, E. M. *Chem. - Eur. J.* **2012**, *18*, 14671.
(294) Israëli, Y.; Lhermet, C.; Morel, J.-P.; Morel-Desrosiers, N. *Carbohydr. Res.* **1996**, *289*, 1.
(295) Yang, L.; Su, Y.; Xu, Y.; Wang, Z.; Guo, Z.; Weng, S.; Yan, C.; Zhang, S.; Wu, J. *Inorg. Chem.* **2003**, *42*, 5844.
(296) Su, Y.; Yang, L.; Xu, Y.; Wang, Z.; Weng, S.; Yan, C.; Wang, D.; Wu, J. *Inorg. Chem.* **2007**, *46*, 5508.
(297) Yang, L.; Hua, X.; Xue, J.; Pan, Q.; Yu, L.; Li, W.; Xu, Y.; Zhao, G.; Liu, L.; Liu, K.; Chen, J.; Wu, J. *Inorg. Chem.* **2011**, *51*, 499.
(298) Rybak, J. C.; Meyer, L. V.; Wagenhöfer, J.; Sextl, G.; Müller-Buschbaum, K. *Inorg. Chem.* **2012**, *51*, 13204.
(299) Caulder, D. L.; Powers, R. E.; Parac, T. N.; Raymond, K. N. *Angew. Chem. Int. Ed.* **1998**, *37*, 1840.
(300) Hastings, C. J.; Pluth, M. D.; Bergman, R. G.; Raymond, K. N. *J. Am. Chem. Soc.* **2010**, *132*, 6938.
(301) Caulder, D. L.; Brückner, C.; Powers, R. E.; König, S.; Parac, T. N.; Leary, J. A.; Raymond, K. N. *J. Am. Chem. Soc.* **2001**, *123*, 8923.
(302) Luk, C. K.; Richardson, F. S. *J. Am. Chem. Soc.* **1975**, *97*, 6666.
(303) Gunnlaugsson, T.; Harte, A. J.; Leonard, J. P.; Nieuwenhuyzen, M. *Supramol. Chem.* **2003**, *15*, 505.
(304) Butler, S. J.; Parker, D. *Chem. Soc. Rev.* **2013**, *42*, 1652.
(305) Gunnlaugsson, T.; Harte, A. J.; Leonard, J. P.; Nieuwenhuyzen, M. *Chem. Commun.* **2002**, 2134.
(306) Gunnlaugsson, T.; Leonard, J. P.; Mulready, S.; Nieuwenhuyzen, M. *Tetrahedron* **2004**, *60*, 105.
(307) Leonard, J. P.; dos Santos, C. M. G.; Plush, S. E.; McCabe, T.; Gunnlaugsson, T. *Chem. Commun.* **2007**, 129.
(308) S. Dickins, R.; Gunnlaugsson, T.; Parker, D.; D. Peacock, R. *Chem. Commun.* **1998**, 1643.
(309) Dickins, R. S.; Aime, S.; Batsanov, A. S.; Beeby, A.; Botta, M.; Bruce, J. I.; Howard, J. A. K.; Love, C. S.; Parker, D.; Peacock, R. D.; Puschmann, H. *J. Am. Chem. Soc.* **2002**, *124*, 12697.
(310) Wright, A. T.; Anslyn, E. V. *Chem. Soc. Rev.* **2006**, *35*, 14.
(311) Wiskur, S. L.; Ait-Haddou, H.; Lavigne, J. J.; Anslyn, E. V. *Acc. Chem. Res.* **2001**, *34*, 963.
(312) Labande, A.; Ruiz, J.; Astruc, D. *J. Am. Chem. Soc.* **2002**, *124*, 1782.
(313) Imbert, D.; Comby, S.; Chauvin, A.-S.; Bünzli, J.-C. G. *Chem. Commun.* **2005**, 1432.
(314) Nonat, A. M.; Allain, C.; Faulkner, S.; Gunnlaugsson, T. *Inorg. Chem.* **2010**, *49*, 8449.
(315) Harte, A. J.; Jensen, P.; Plush, S. E.; Kruger, P. E.; Gunnlaugsson, T. *Inorg. Chem.* **2006**, *45*, 9465.
(316) Cable, M. L.; Kirby, J. P.; Sorasaenee, K.; Gray, H. B.; Ponce, A. *J. Am. Chem. Soc.* **2007**, *129*, 1474.
(317) Gale, P. A. *Acc. Chem. Res.* **2006**, *39*, 465.
(318) Vandevyver, C. D. B.; Chauvin, A.-S.; Comby, S.; Bünzli, J.-C. G. *Chem. Commun.* **2007**, 1716.

(319) dos Santos, C. M. G.; Fernandez, P. B.; Plush, S. E.; Leonard, J. P.; Gunnlaugsson, T. *Chem. Commun.* **2007**, 3389.
(320) dos Santos, C. M. G.; McCabe, T.; Watson, G. W.; Kruger, P. E.; Gunnlaugsson, T. *J. Org. Chem.* **2008**, *73*, 9235.
(321) Castellano, R. K.; Rebek, J. *J. Am. Chem. Soc.* **1998**, *120*, 3657.
(322) Zhu, N.; Tobin, G.; Schmitt, W. *Chem. Commun.* **2012**, *48*, 3638.
(323) Garcia, F.; Korevaar, P. A.; Verlee, A.; Meijer, E. W.; Palmans, A. R. A.; Sanchez, L. *Chem. Commun.* **2013**, *49*, 8674.
(324) Vogel, A. I.; Tatchell, A. R.; Furnis, B. S.; Hannaford, A. J.; Smith, P. W. G. *Vogel's Textbook of Practical Organic Chemistry*; 5th ed.; Prentice Hall: New York, **1996**.
(325) Sheldrick, G. *Acta Crystallogr., Sect. A* **2008**, *64*, 112.
(326) Zhang, H.; Xin, F.; An, W.; Hao, A.; Wang, X.; Zhao, X.; Liu, Z.; Sun, L. *Colloids Surf., A* **2010**, *363*, 78.
(327) Johnsen, C.; Stein, P. C.; Nielsen, K. A.; Bond, A. D.; Jeppesen, J. O. *Eur. J. Org. Chem.* **2011**, *2011*, 759.
(328) Moylan, C. PhD Transfer Report, Trinity College Dublin, **2012**.
(329) Ouchi, M.; Inoue, Y.; Liu, Y.; Nogamune, S.; Wada, K.; Hakushi, T. *Bull. Chem. Soc. Jpn.* **1990**, *63*, 1260.
(330) Froidevaux, P.; Harrowfield, J. M.; Sobolev, A. N. *Inorg. Chem.* **2000**, *39*, 4678.
(331) Parker, D.; Williams, J. A. G. *J. Chem. Soc., Perk. Trans. 2* **1995**, 1305.
(332) Gampp, H.; Maeder, M.; Meyer, C. J.; Zuberbühler, A. D. *Talanta* **1986**, *33*, 943.
(333) Meloun, M.; Bordovská, S.; Syrový, T.; Vrána, A. *Anal. Chim. Acta* **2006**, *580*, 107.

Appendices

Appendix 2 – 6

Spectrophotometric titration data fitting with SPECFIT®

All UV-vis and phosphorescence titration data reported in this thesis were fit using the non-linear least squares regression program SPECFIT®. SPECFIT® is a commercial program, based on an algorithm developed by Gampp *et. al*,[246,332] for the determination of speciation and stability constants from spectrophotometric titration data for equilibrium processes. This program works by analysing multi-wavelength data and, therefore, presents numerous advantages compared to single wavelength analysis. Such advantages include: (i) significantly more robust data analysis, (ii) determination of the pure spectra for all species and intermediates of an equilibrium mixture and (iii) application of a range of model-free analyses (from simple factor analysis to ascertain the number of species to more advanced evolving factor analysis).[333]

The so-called "model-free" method employed does not make any guesses as to the unique chemistry of the system, other than the number of species present *i.e.* SPECFIT® does not automatically solve the problem of finding both the correct chemical model and obtaining initial guesses as to the underlying parameters.[333] However, the program is capable of delivering optimal parameters for any reasonable chemical model and any set of sensible starting values, and has proven to be reliable and robust in doing so.[245] More specifically, this program operates by the user uploading an initial proposal of the stoichiometric species that define the chemical equilibrium model.[333] Therefore, selection of the correct model must be informed by an underlying knowledge of the principles governing the equilibrium so as to afford acceptable convergence. In regards to complexation reactions, based on the ability of the theoretical data to fit the empirical data in the form of the sum of the squared deviation, this program allows the user to test the legitimacy of different M:L stoichiometries for the complexation process under investigation. When the presence of a particular stoichiometric species is established, corresponding binding constants ($\log \beta_{M:L}$) can be obtained, along with speciation graphs that present the percentage formation of the various components of the mixture. SPECFIT® is slightly restricted, however, by an inability to accurately fit data when $K \geq 10^7$ dm^3 mol^{-1}, a situation whereby the concentration ratio of the metal complex to its precursors is large, thus, magnifying the error. In addition, the evolving factor analysis can be used to specify the precise number of absorbing/luminescent species present. For all fits in this thesis, the number of species used to provide good convergence corresponded to that told by the evolving factor analysis.

SPECFIT® uses multi-wavelength and multi-variate data to enable global analysis for equilibrium systems through both singular value decomposition and non-linear least squares

regression modelling (Levenberg-Marquardt method),[333] with its suitability demonstrated in various research publications. The least squares fit aids in providing statistical information such as standard deviations in the calculated parameters.[245] In the field of supramolecular Ln(III)-directed self-assembly, this program has been widely used by researchers such as Prof. Thorfinnur Gunnlaugsson,[230] Prof. Jean-Claude G. Bünzli,[136] Prof. Claude Piguet,[153] and others for determining the M:L stoichiometries present in self-assembly complexation equilibria, along with their relative speciation and binding constants.

Quantum yield and sensitisation efficiency determination

Q_L^{Ln} is the quantum yield of the metal-centred luminescence upon ligand excitation and is the product of two contributions, η_{sens} and Q_{Ln}^{Ln} (**Equation A1**); η_{sens} represents the overall efficiency of the ligand-to-metal energy transfer, whereas Q_{Ln}^{Ln} signifies the intrinsic quantum yield of the Ln(III) ion upon direct excitation.[116,117,248] The latter contribution is inherent to the Ln(III) ion and can be further simplified as $Q_{Ln}^{Ln} = \tau_{obs}/\tau_{rad}$, where τ_{obs} is the observed lifetime and τ_{rad} is the radiative lifetime *i.e.* the lifetime in the absence of non-radiative deactivation processes.

$$Q_L^{Ln} = \eta_{sens} \times Q_{Ln}^{Ln} = \eta_{sens} \times (\tau_{obs}/\tau_{rad}) \qquad \textbf{Equation A1}$$

$$1/\tau_{rad} = A_{MD,0} \times n^3 \times (I_{tot}/I_{MD}) \qquad \textbf{Equation A2}$$

Exclusive to the case of Eu(III), the radiative lifetime can be calculated according to **Equation A2**, an equation founded on the assumption that the intensity of the pure magnetic-dipole $J = 1$ transition is unperturbed by the external chemical environment.[249] In this formula, $A_{MD,0}$ is the spontaneous emission probability of the $J = 1$ transition *in vacuo* and has a value of 14.65 s^{-1}, n is the solvent refractive index, and I_{tot}/I_{MD} is the ratio of the total integrated emission to the integrated emission of the $J = 1$ transition.

$$Q_x = Q_{std} \times \left(\frac{A_{std}(\lambda_{std})}{A_x(\lambda_x)}\right) \times \left(\frac{I_{std}(\lambda_{std})}{I_x(\lambda_x)}\right) \times \left(\frac{n_x^2}{n_{std}^2}\right) \times \left(\frac{E_x}{E_{std}}\right) \qquad \textbf{Equation A3}$$

For the work described in this thesis, quantum yield determination was achieved by adhering to the *relative method*, whereby the synthesised complexes were compared to a

standard for which the absolute quantum yield is known. In this case, $Cs_3[Eu.(dpa)_3]\cdot 9H_2O$ complex in 0.1 M Tris buffer (pH = 7.45) (Q_L^{Ln} = 24.0 ± 2.5%) was selected as the standard to which the absorbance and emission intensity of the samples were compared.[116,248] The quantum yield was then calculated by means of **Equation A3**, where the subscript *x* stands for the sample and *std* for the standard; *A* is the absorbance at the excitation wavelength λ (279 nm); *I* is the intensity of the excitation light at the same wavelength; *n* is the solvent refractive index and *E* is the integrated emission.

Appendix 2

Table A2.1: *Crystal data and structure refinement for ligand* ***43R****.*

Empirical formula	$C_{74}H_{72}N_4O_{14}$	
Formula weight	1241.36	
Temperature	293(2) K	
Wavelength	0.71073 Å	
Crystal system	Orthorhombic	
Space group	$P2_12_12_1$	
Unit cell dimensions	a = 14.906(5) Å	α = 90°
	b = 19.311(5) Å	β = 90°
	c = 23.190(5) Å	γ = 90°
Volume	6675(3) $Å^3$	
Z	4	
Density (calculated)	1.235 mg m^{-3}	
Absorption coefficient	0.086 mm^{-1}	
F(000)	2624	
Crystal size	0.68 × 0.26 × 0.24 mm	
Theta range for data collection	1.37 – 27.86°	
Index ranges	$-19 \leq h \leq 19$, $-25 \leq k \leq 25$, $-29 \leq l \leq 30$	
Reflections collected	73958	
Independent reflections	15588 [R(int) = 0.0223]	
Completeness to theta = 27.86°	98.3%	
Absorption correction	None	
Refinement method	Full-matrix least-squares on F^2	
Data / restraints / parameters	15588 / 0 / 847	
Goodness-of-fit on F^2	1.059	
Final R indices [I>2sigma(I)]	R1 = 0.0688, wR2 = 0.1980	
R indices (all data)	R1 = 0.0810, wR2 = 0.2139	
Largest diff. peak and hole	1.168 and −0.748 e.$Å^{-3}$	

Table A2.2: *Crystal data and structure refinement for complex* ***Eu.39R3.***

Empirical formula	$C_{100}H_{100}Cl_3EuF_9N_9O_{12}$	
Formula weight	2049.20	
Temperature	101(2) K	
Wavelength	0.71073 Å	
Crystal system	Monoclinic	
Space group	$P6_322$	
Unit cell dimensions	a = 22.777(8) Å	α = 90°
	b = 22.777(8) Å	β = 90°
	c = 12.964(5) Å	γ = 120°
Volume	5825(4) $Å^3$	
Z	2	
Density (calculated)	1.168 mg m^{-3}	
Absorption coefficient	0.676 mm^{-1}	
F(000)	2108	
Crystal size	0.21 × 0.15 × 0.11 mm	
Theta range for data collection	1.79 – 26.39°	
Index ranges	$-28 \leq h \leq 28, -28 \leq k \leq 28, -16 \leq l \leq 16$	
Reflections collected	58773	
Independent reflections	4000 [R(int) = 0.0336]	
Completeness to theta = 26.39°	100.0%	
Absorption correction	None	
Refinement method	Full-matrix least-squares on F^2	
Data / restraints / parameters	4000 / 7 / 163	
Goodness-of-fit on F^2	2.386	
Final R indices [I>2sigma(I)]	R1 = 0.0832, wR2 = 0.2545	
R indices (all data)	R1 = 0.0882, wR2 = 0.2589	
Largest diff. peak and hole	1.714 and −1.224 e.$Å^{-3}$	

Table A2.3: *Crystal data and structure refinement for complex* ***Eu.41S3****.*

Empirical formula	$C_{100}H_{100}Cl_3EuF_9N_9O_{15}$	
Formula weight	2097.20	
Temperature	100(2) K	
Wavelength	1.54178 Å	
Crystal system	Monoclinic	
Space group	$P6_322$	
Unit cell dimensions	a = 22.880(6) Å	α = 90°
	b = 22.880(6) Å	β = 90°
	c = 12.981(4) Å	γ = 120°
Volume	5885(3) $Å^3$	
Z	2	
Density (calculated)	1.184 mg m^{-3}	
Absorption coefficient	5.043 mm^{-1}	
F(000)	2156	
Crystal size	0.36 × 0.07 × 0.04 mm	
Theta range for data collection	3.86 – 64.45°	
Index ranges	$-25 \leq h \leq 24, -23 \leq k \leq 20, -14 \leq l \leq 15$	
Reflections collected	14291	
Independent reflections	3255 [R(int) = 0.0464]	
Completeness to theta = 64.45°	98.9%	
Absorption correction	None	
Refinement method	Full-matrix least-squares on F^2	
Data / restraints / parameters	3255 / 4 / 169	
Goodness-of-fit on F^2	1.048	
Final R indices [I>2sigma(I)]	R1 = 0.0820, wR2 = 0.2283	
R indices (all data)	R1 = 0.0900, wR2 = 0.2384	
Largest diff. peak and hole	0.711 and −0.607 e.$Å^{-3}$	

Table A2.4: *Crystal data and structure refinement for complex* ***Eu.43S$_3$.***

Empirical formula	$C_{111}H_{111}EuF_9N_9O_{24}S_3$	
Formula weight	2374.23	
Temperature	105(2) K	
Wavelength	0.71073 Å	
Crystal system	Monoclinic	
Space group	$P6_3$	
Unit cell dimensions	a = 22.727(11) Å	α = 90°
	b = 22.727(11) Å	β = 90°
	c = 13.025(6) Å	γ = 120°
Volume	5826(5) Å^3	
Z	2	
Density (calculated)	1.353 mg m^{-3}	
Absorption coefficient	0.678 mm^{-1}	
F(000)	2448	
Crystal size	0.49 × 0.11 × 0.10 mm	
Theta range for data collection	1.03 – 26.37°	
Index ranges	$-28 \leq h \leq 28$, $-28 \leq k \leq 28$, $-16 \leq l \leq 16$	
Reflections collected	42836	
Independent reflections	7884 [R(int) = 0.0274]	
Completeness to theta = 26.37°	99.9%	
Absorption correction	None	
Refinement method	Full-matrix least-squares on F^2	
Data / restraints / parameters	7884 / 25 / 472	
Goodness-of-fit on F^2	1.090	
Final R indices [I>2sigma(I)]	R1 = 0.0536, wR2 = 0.1412	
R indices (all data)	R1 = 0.0604, wR2 = 0.1463	
Largest diff. peak and hole	1.417 and −0.787 e.Å^{-3}	

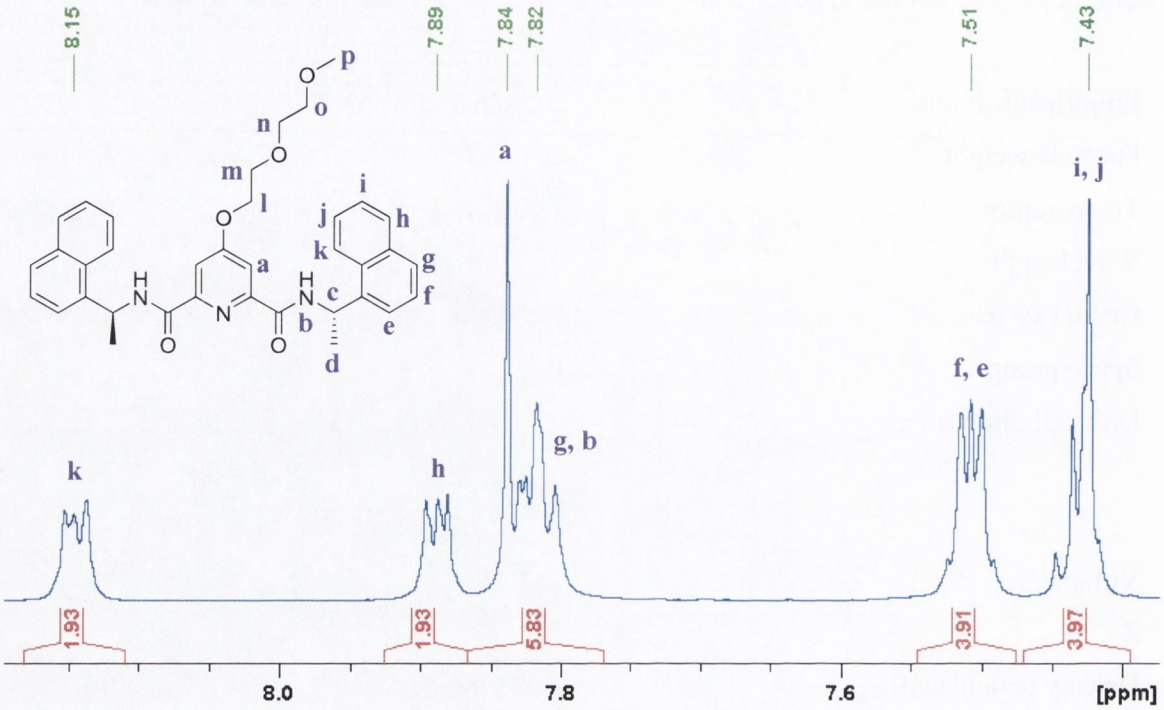

Figure A2.1: *^{1}H NMR (600 MHz, $CDCl_3$) spectrum of ligand **43S** focusing on the aromatic signals.*

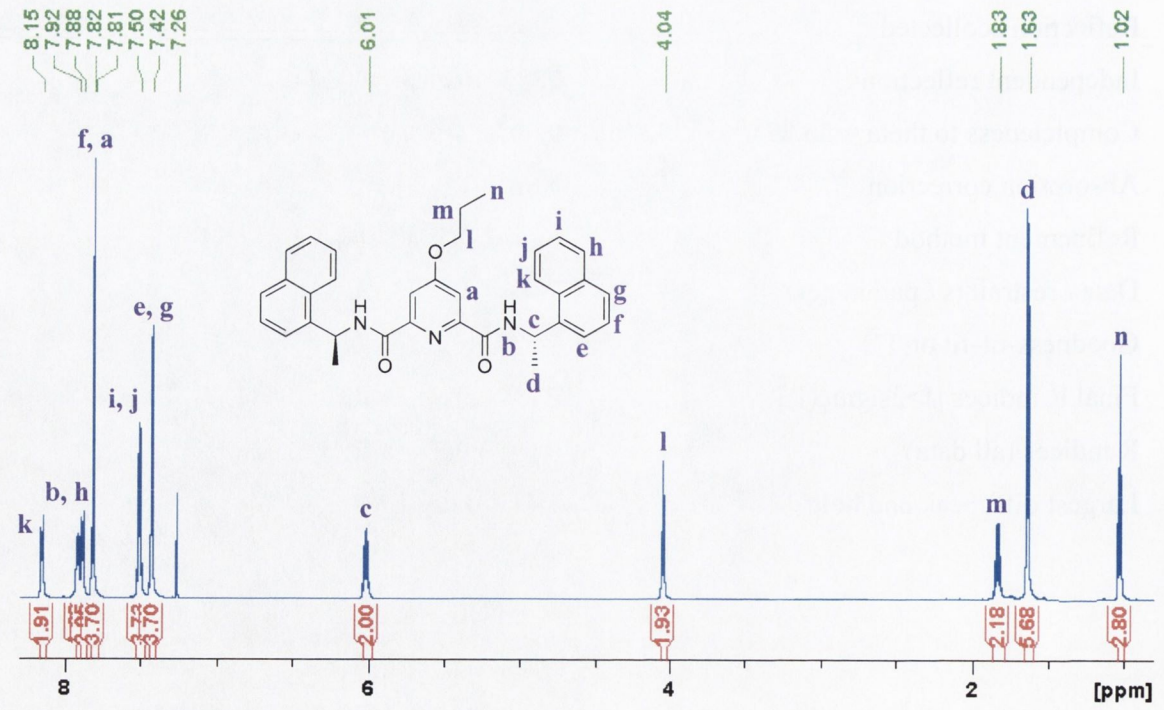

Figure A2.2: *^{1}H NMR (600 MHz, $CDCl_3$) spectrum of ligand **41S**.*

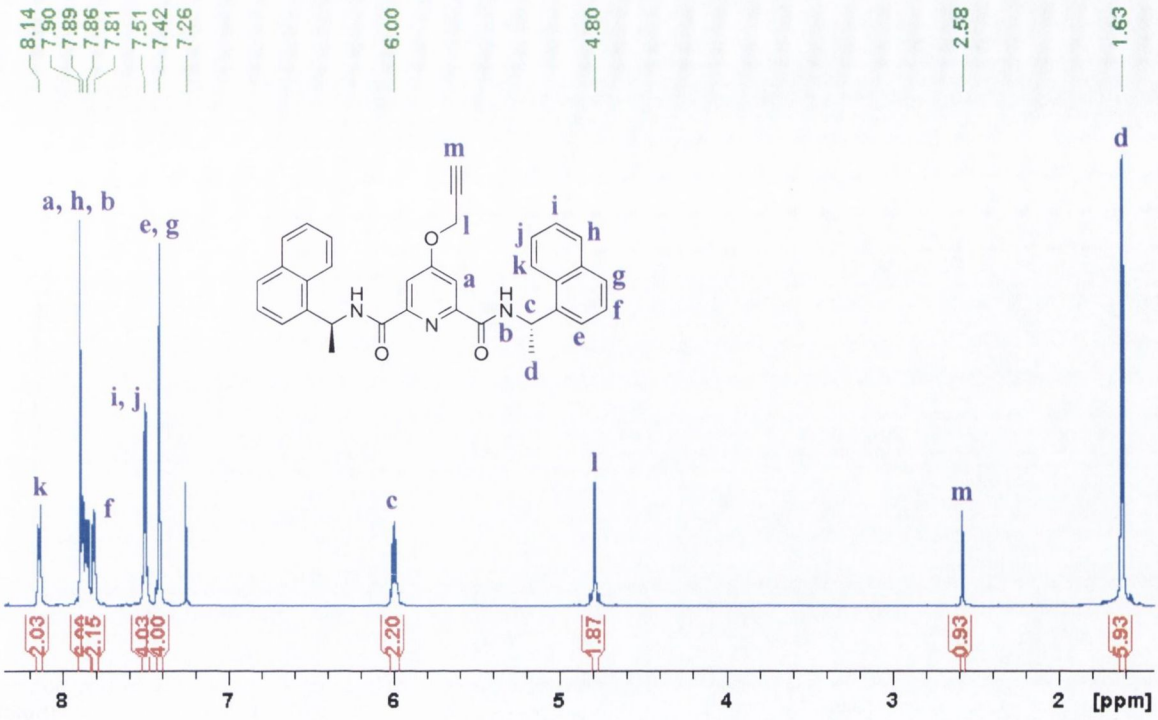

Figure A2.3: *^{1}H NMR (600 MHz, $CDCl_3$) spectrum of ligand* ***42S****.*

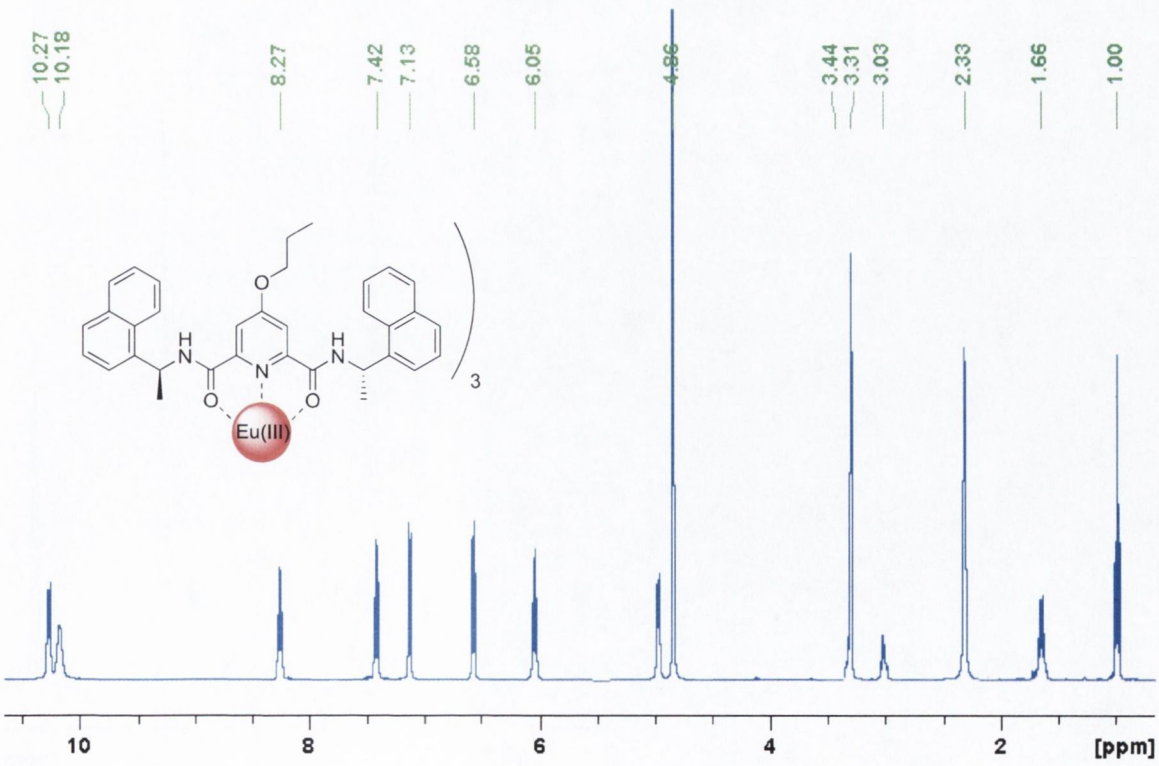

Figure A2.4: *^{1}H NMR (400 MHz, CD_3OD-d_4) spectrum of complex* ***Eu.41S$_3$****.*

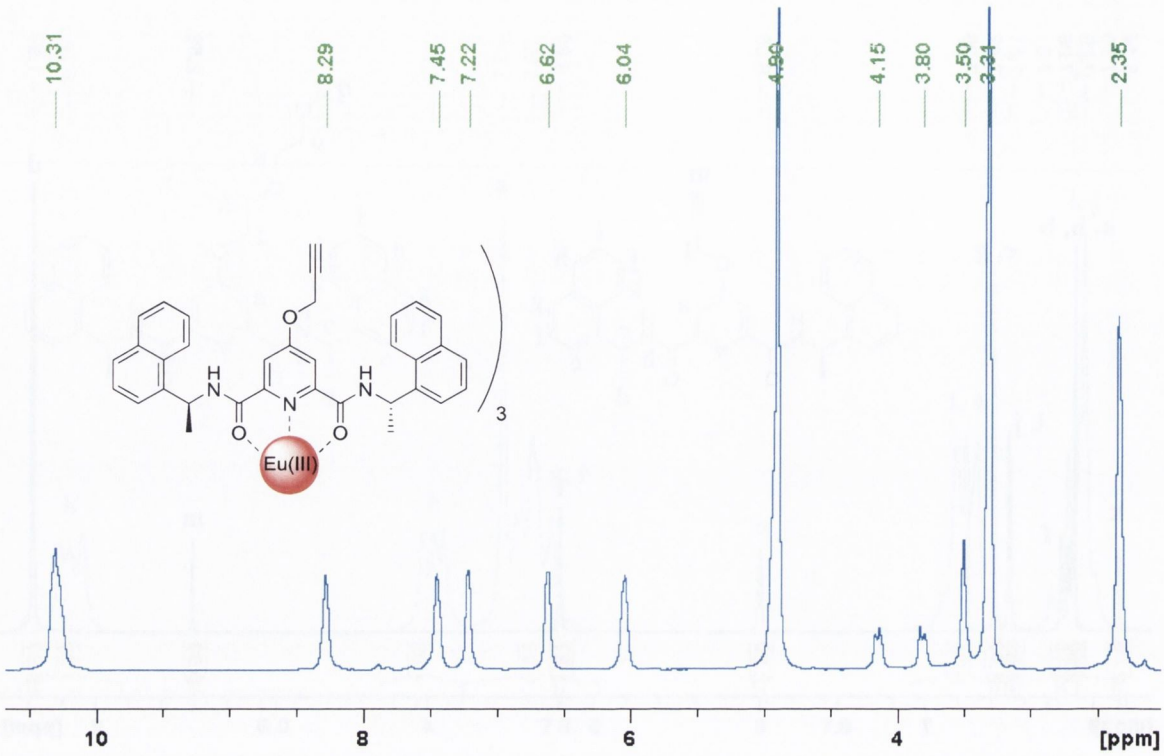

Figure A2.5: *^{1}H NMR (400 MHz, CD_3OD-d_4) spectrum of complex* ***Eu.42S$_3$****.*

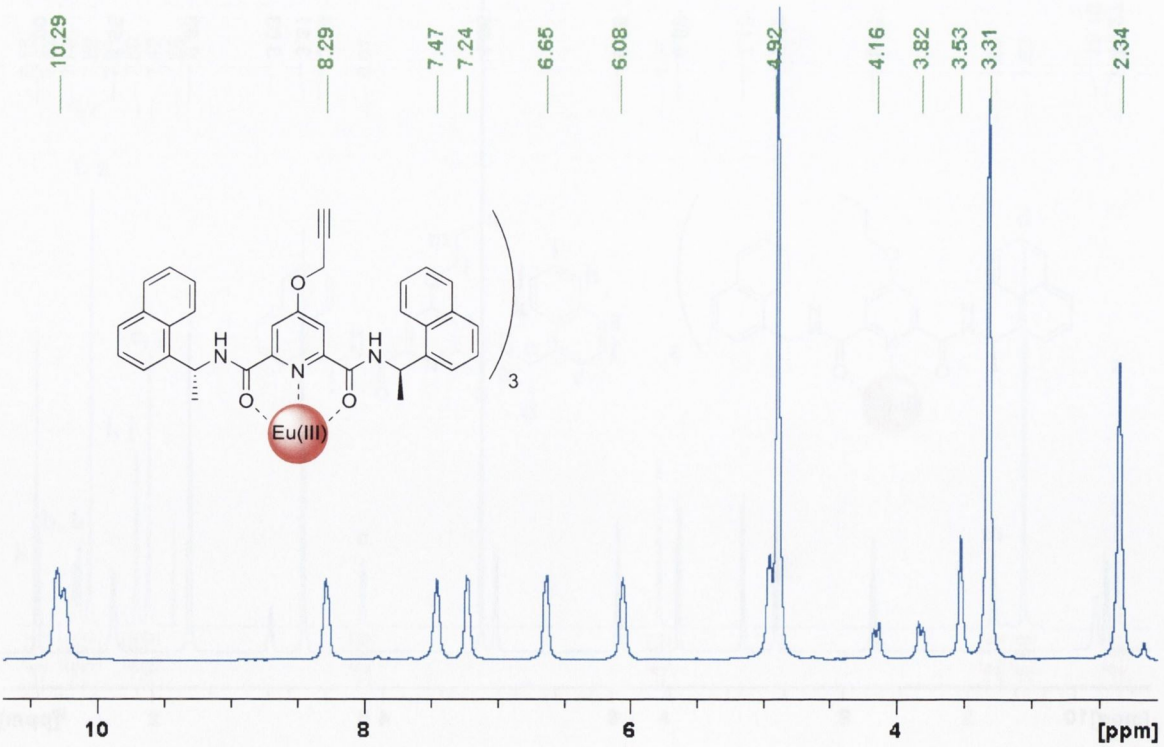

Figure A2.6: *^{1}H NMR (400 MHz, CD_3OD-d_4) spectrum of complex* ***Eu.42R$_3$****.*

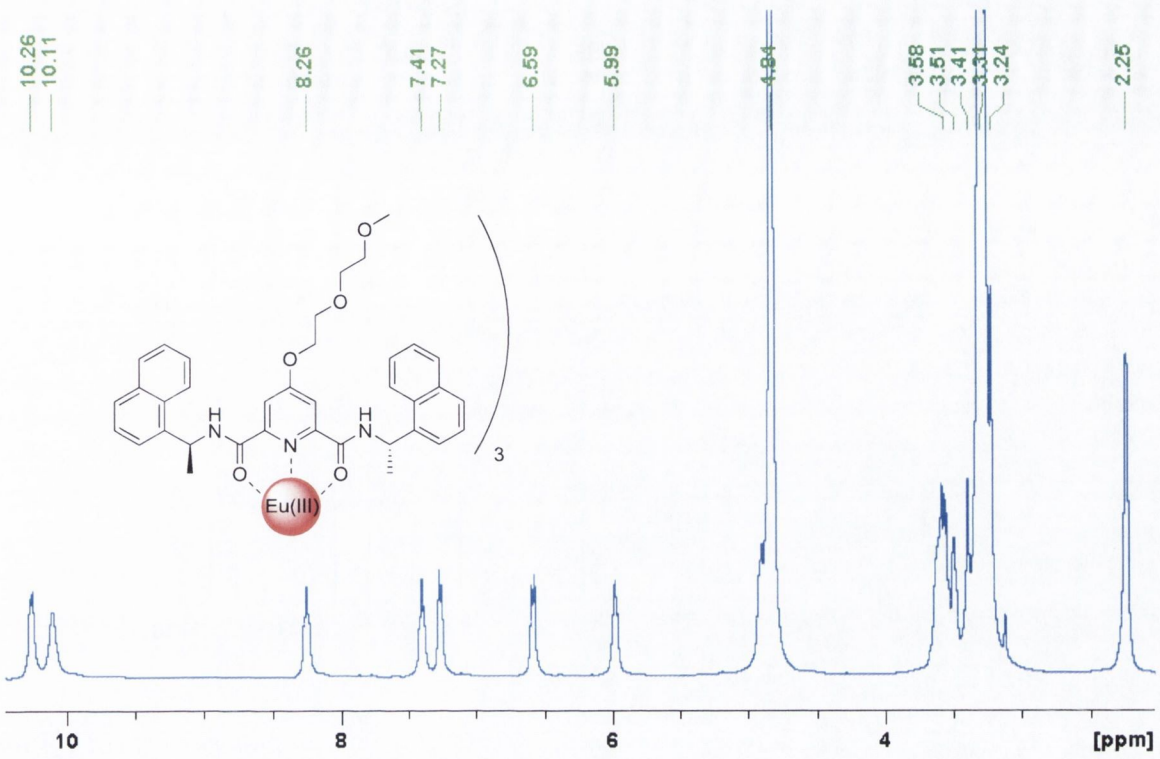

Figure A2.7: *^{1}H NMR (400 MHz, CD_3OD-d_4) spectrum of complex* ***Eu.43S$_3$.***

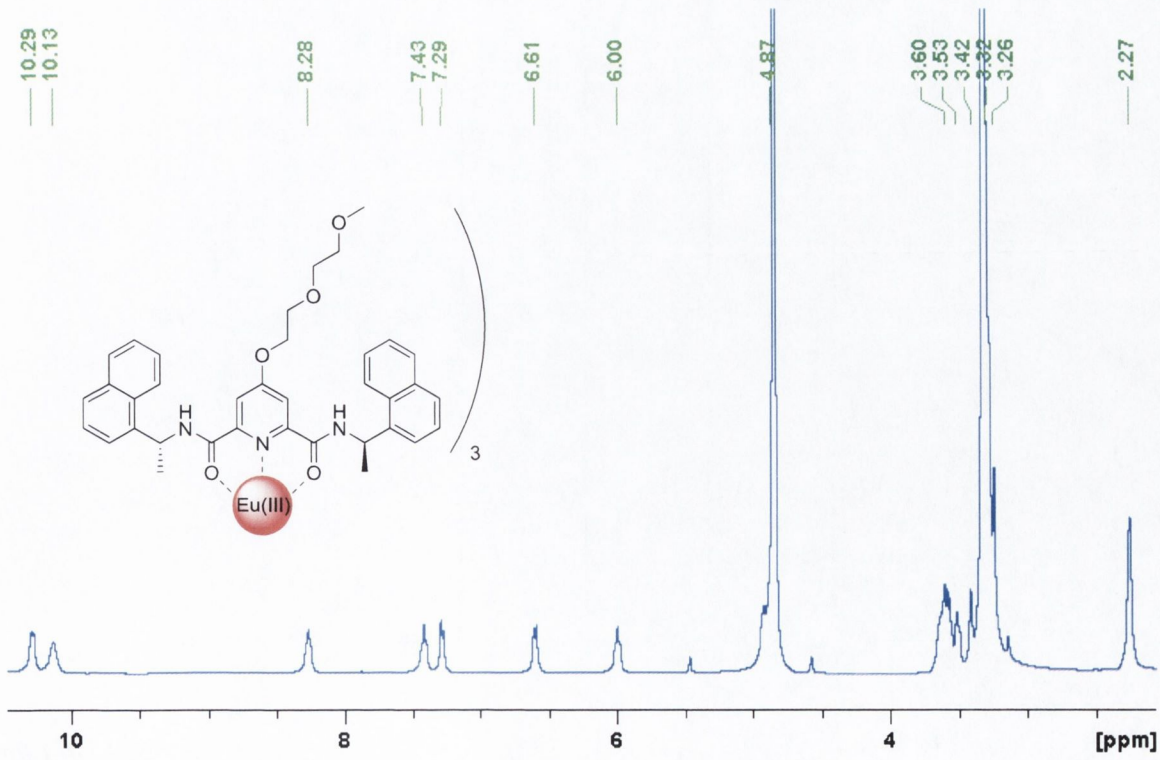

Figure A2.8: *^{1}H NMR (400 MHz, CD_3OD-d_4) spectrum of complex* ***Eu.43R$_3$.***

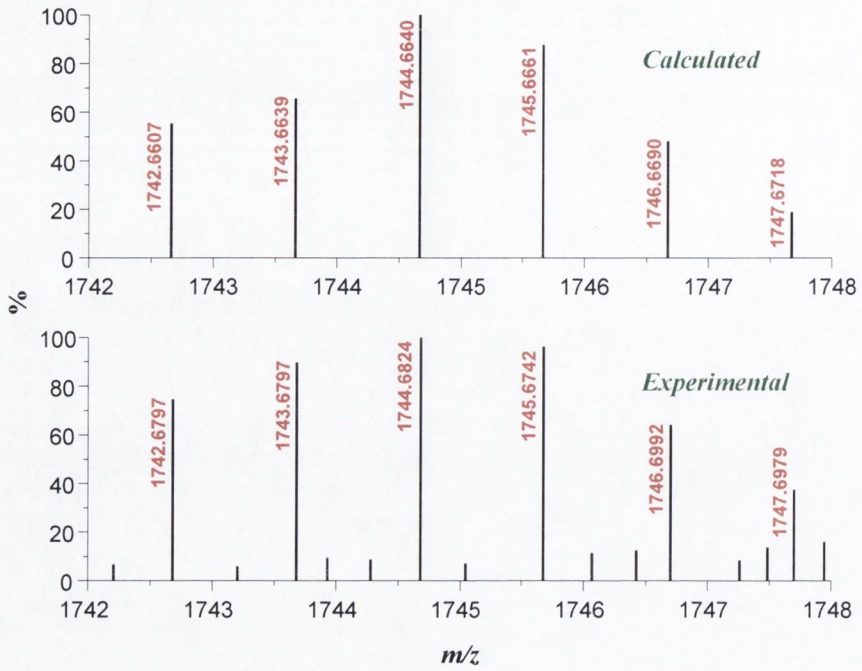

Figure A2.9: *The calculated and experimental isotopic distribution patterns (MALDI$^+$) for complex* ***Eu.41S$_3$*** *showing the 1:3 (M:L) stoichiometric pattern for a molecular species of formula [M – 3CF$_3$SO$_3$ – 2H]$^+$ (spectra are normalised – dominant peak set to 100%).*

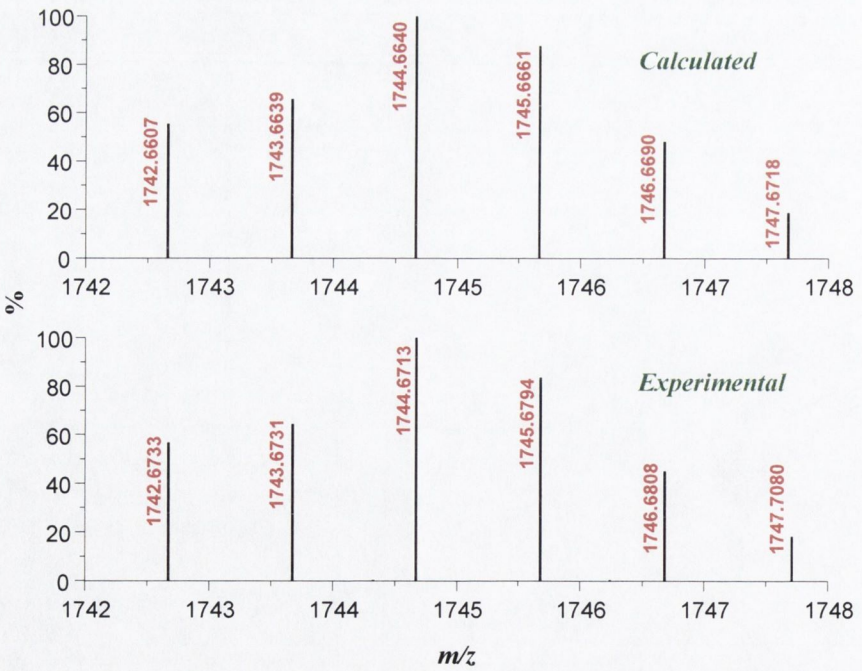

Figure A2.10: *The calculated and experimental isotopic distribution patterns (MALDI$^+$) for complex* ***Eu.41R$_3$*** *showing the 1:3 (M:L) stoichiometric pattern for a molecular species of formula [M – 3CF$_3$SO$_3$ – 2H]$^+$ (spectra are normalised – dominant peak set to 100%).*

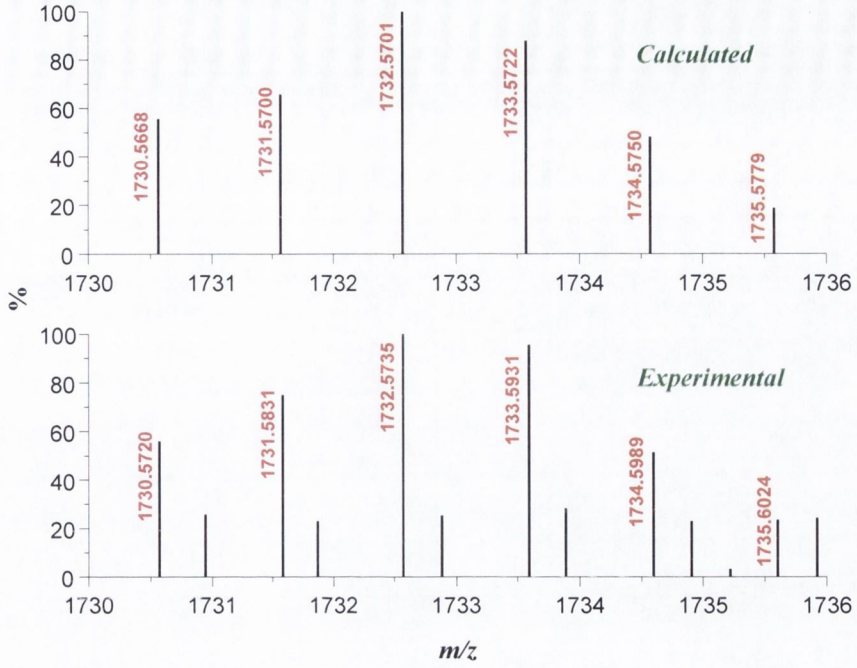

Figure A2.11: *The calculated and experimental isotopic distribution patterns (MALDI$^+$) for complex* ***Eu.42S$_3$*** *showing the 1:3 (M:L) stoichiometric pattern for a molecular species of formula [M – 3CF$_3$SO$_3$ – 2H]$^+$ (spectra are normalised – dominant peak set to 100%).*

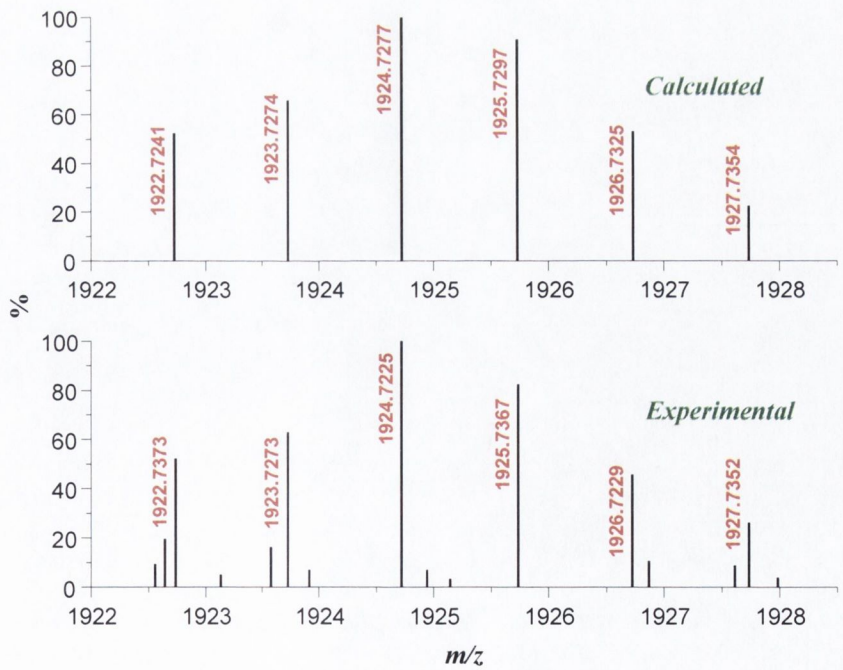

Figure A2.12: *The calculated and experimental isotopic distribution patterns (MALDI$^+$) for complex* ***Eu.43S$_3$*** *showing the 1:3 (M:L) stoichiometric pattern for a molecular species of formula [M – 3CF$_3$SO$_3$ – 2H]$^+$ (spectra are normalised – dominant peak set to 100%).*

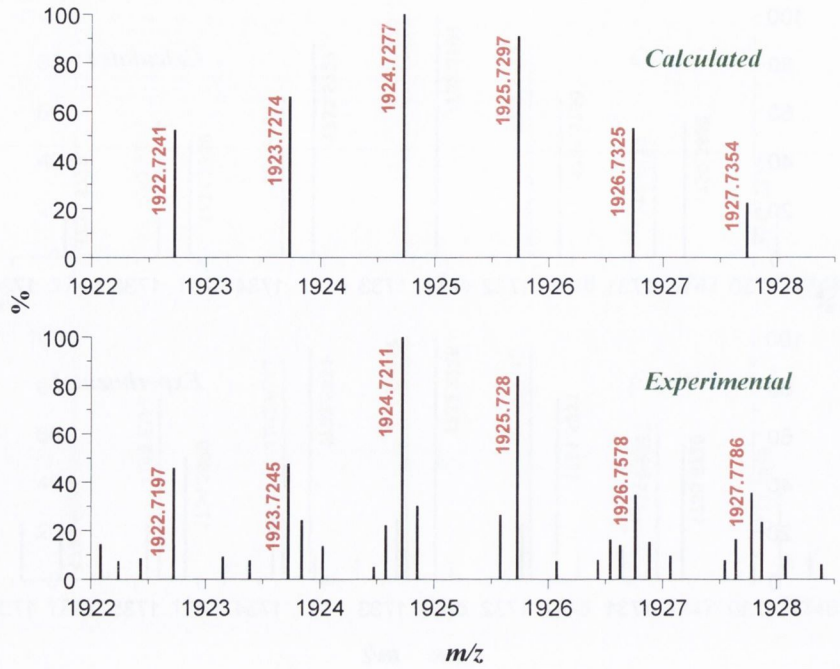

Figure A2.13: *The calculated and experimental isotopic distribution patterns (MALDI$^+$) for complex* ***Eu.43R$_3$*** *showing the 1:3 (M:L) stoichiometric pattern for a molecular species of formula [M – 3CF$_3$SO$_3$ – 2H]$^+$ (spectra are normalised – dominant peak set to 100%).*

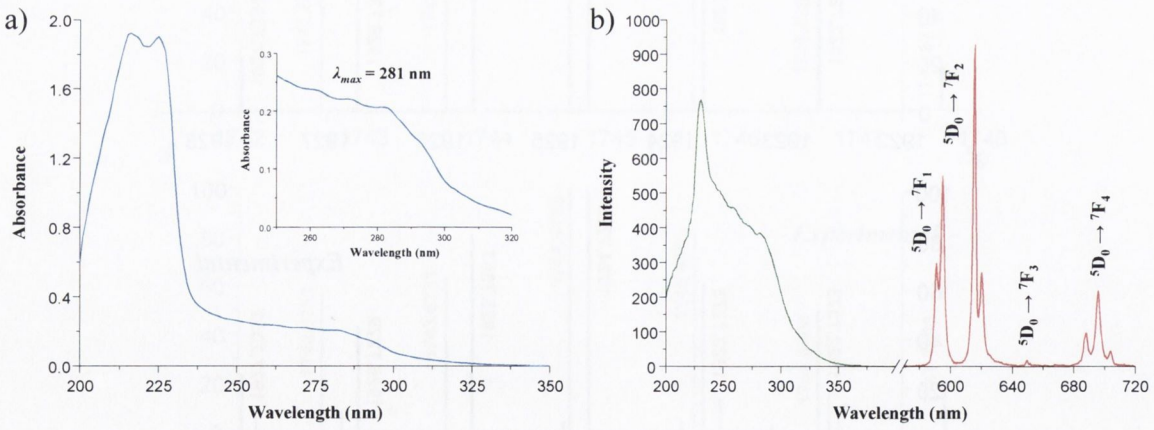

Figure A2.14: *a) UV-vis absorption and b) phosphorescence excitation (green) and emission (red) spectra (λ_{exc} = 281 nm) of* ***Eu.41S$_3$*** *(ca. 5.3 × 10^{-6} M) recorded in MeOH at 298 K.*

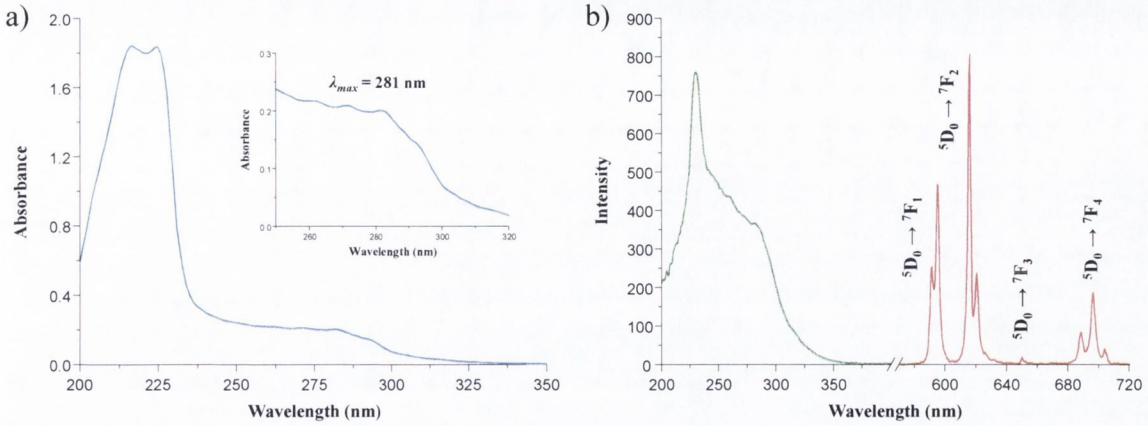

Figure A2.15: *a) UV-vis absorption and b) phosphorescence excitation (green) and emission (red) spectra (λ_{exc} = 281 nm) of* ***Eu.41R3*** *(ca. 5.1 × 10^{-6} M) recorded in MeOH at 298 K.*

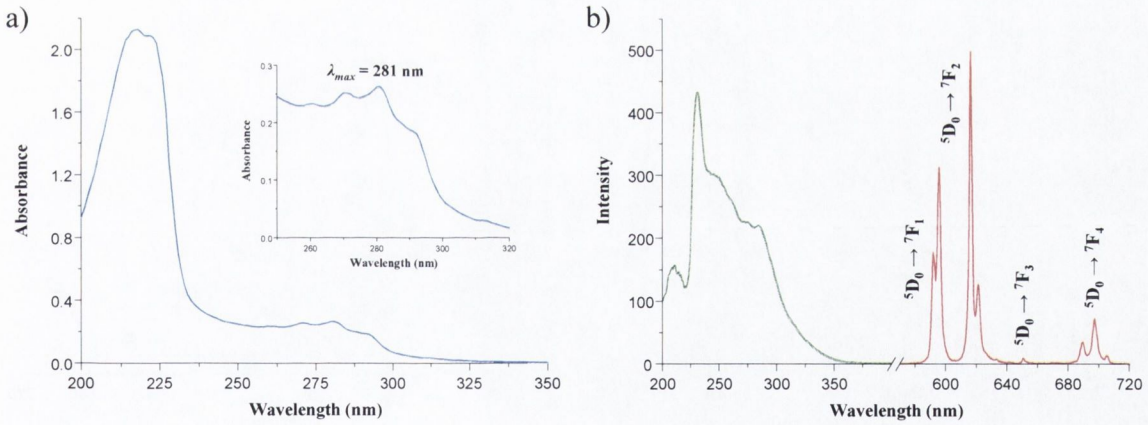

Figure A2.16: *a) UV-vis absorption and b) phosphorescence excitation (green) and emission (red) spectra (λ_{exc} = 281 nm) of* ***Eu.42S3*** *(ca. 6.4 × 10^{-6} M) recorded in MeOH at 298 K.*

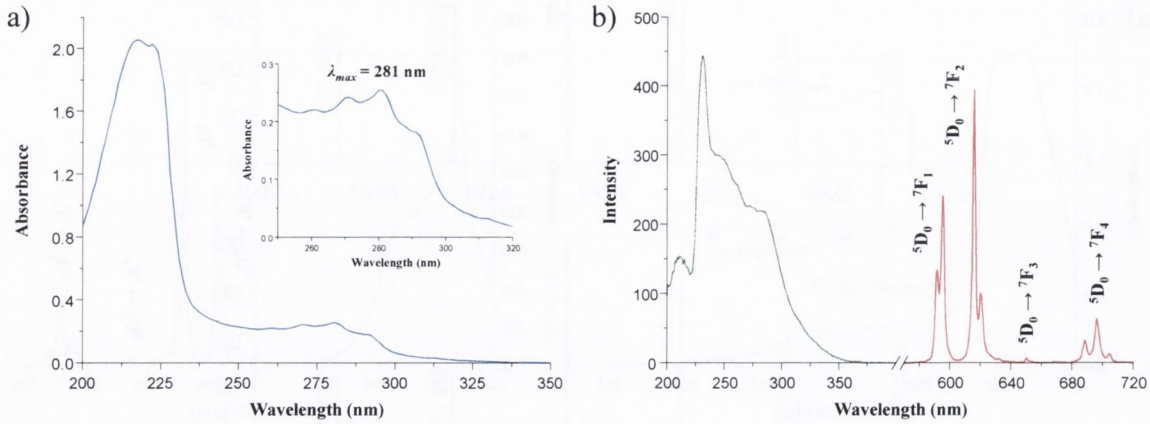

Figure A2.17: *a) UV-vis absorption and b) phosphorescence excitation (green) and emission (red) spectra (λ_{exc} = 281 nm) of* ***Eu.42R$_3$*** *(ca. 6.3 × 10^{-6} M) recorded in MeOH at 298 K.*

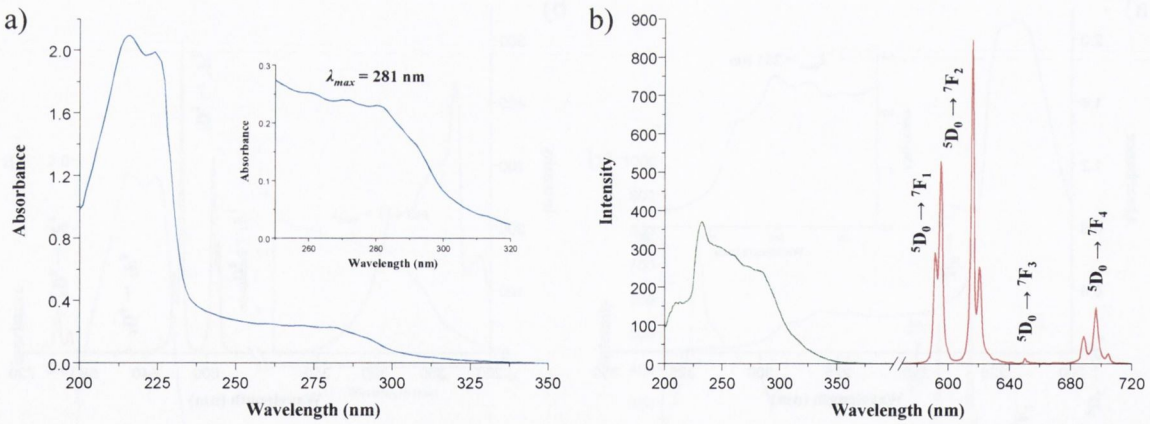

Figure A2.18: *a) UV-vis absorption and b) phosphorescence excitation (green) and emission (red) spectra (λ_{exc} = 281 nm) of* ***Eu.43R$_3$*** *(ca. 8.4 × 10^{-6} M) recorded in MeOH at 298 K.*

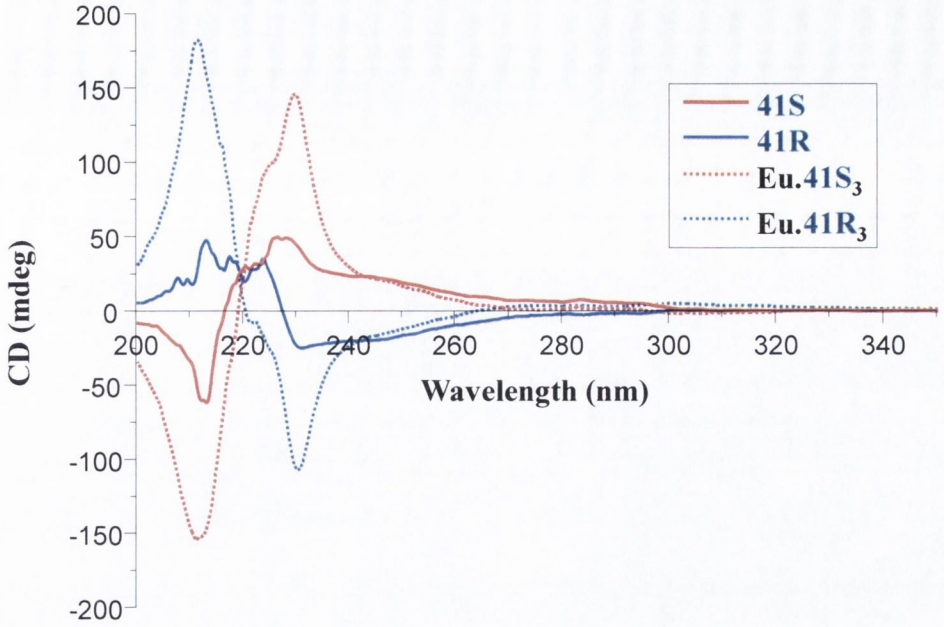

Figure A2.19: *CD spectra of ligand solutions (2.0 × 10^{-5} M) of **41S** and **41R** recorded in CH_3CN at 298 K before (solid lines) and after (dashed lines) the addition of 0.33 eq. of $Eu(CF_3SO_3)_3$ to give the complexes "**Eu.41S$_3$**" and "**Eu.41R$_3$**", respectively.*

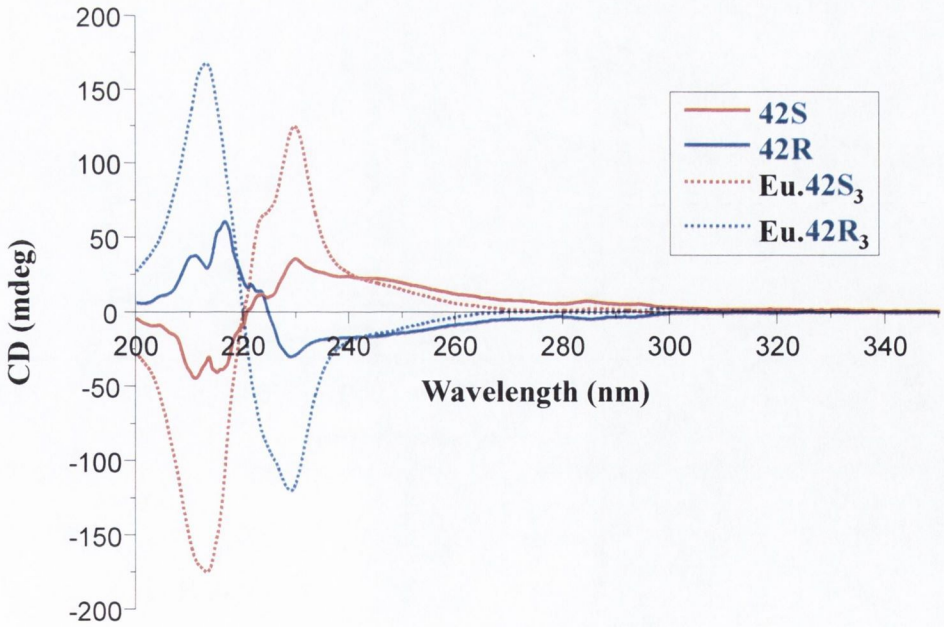

Figure A2.20: *CD spectra of ligand solutions (2.0 × 10^{-5} M) of **42S** and **42R** recorded in CH_3CN at 298 K before (solid lines) and after (dashed lines) the addition of 0.33 eq. of $Eu(CF_3SO_3)_3$ to give the complexes "**Eu.42S$_3$**" and "**Eu.42R$_3$**", respectively.*

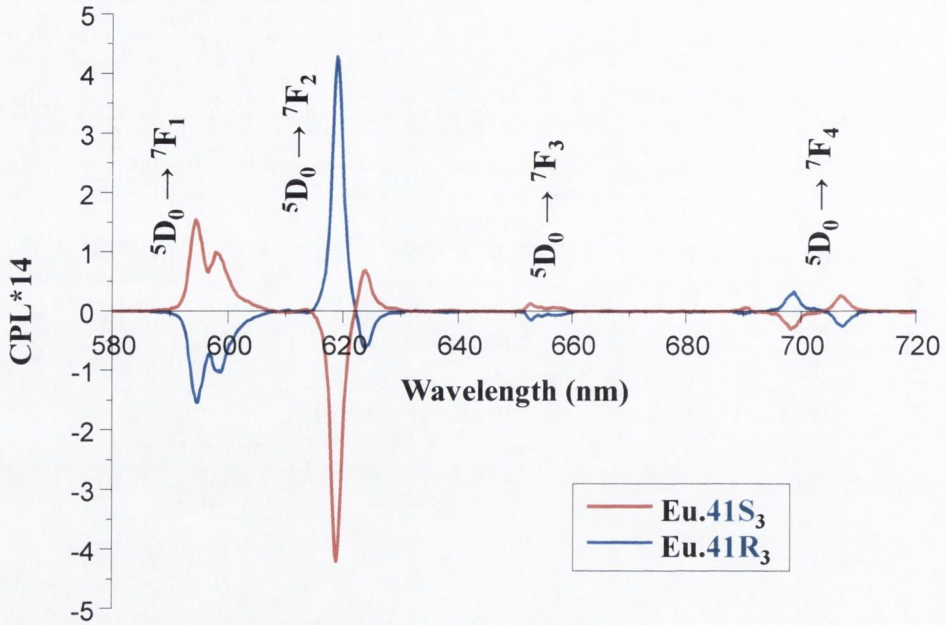

Figure A2.21: *CPL emission spectra of* ***Eu.41S$_3$*** *and* ***Eu.41R$_3$*** *recorded in CH_3CN at 298 K (λ_{exc} = 281 nm).*

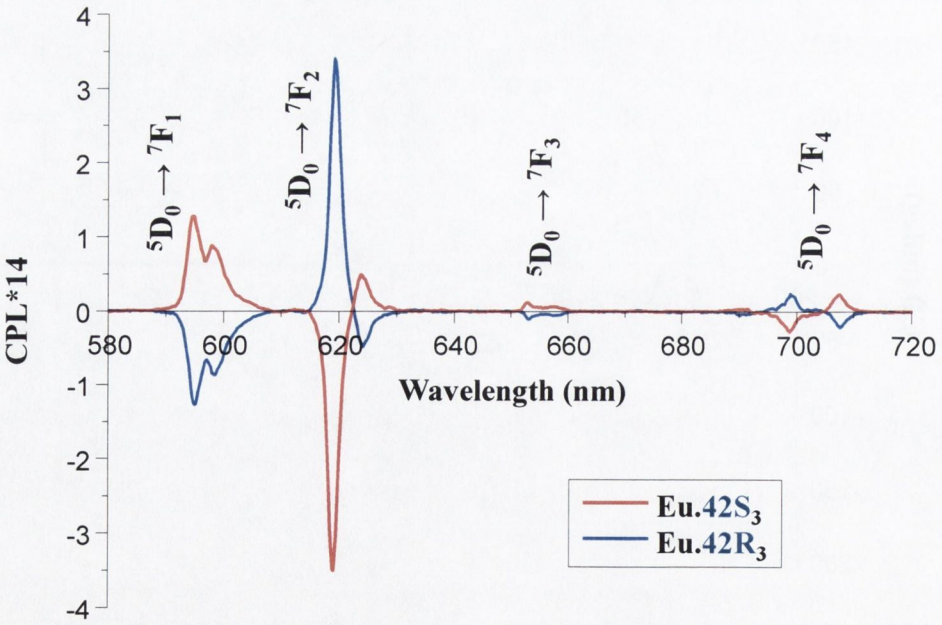

Figure A2.22: *CPL emission spectra of* ***Eu.42S$_3$*** *and* ***Eu.42R$_3$*** *recorded in CH_3CN at 298 K (λ_{exc} = 281 nm).*

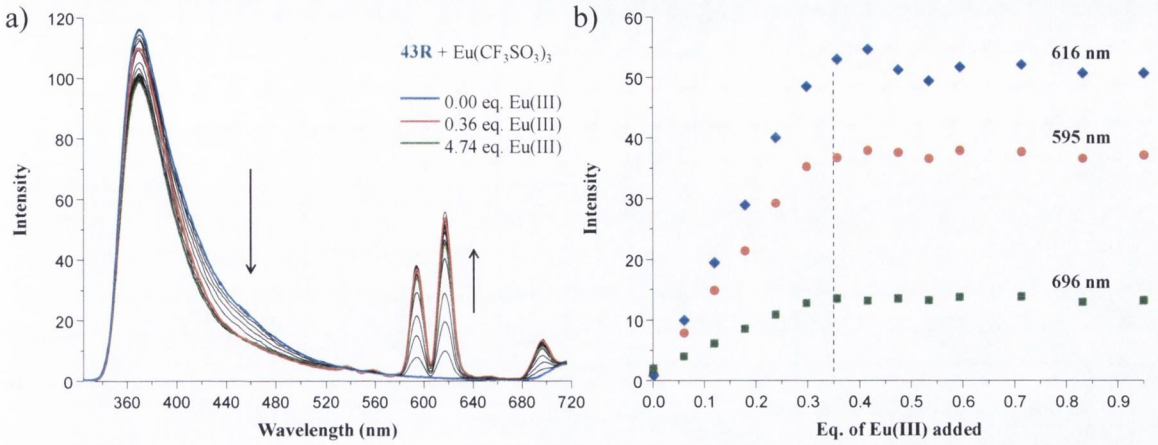

Figure A2.23: *a) Changes in the fluorescence spectra of* ***43R*** *(1×10^{-5} M) upon titrating with $Eu(CF_3SO_3)_3$ (0.00 → 4.74 eq.) in CH_3CN at 298 K. b) Binding isotherms for the titration measured at 595 nm, 616 nm, and 696 nm.*

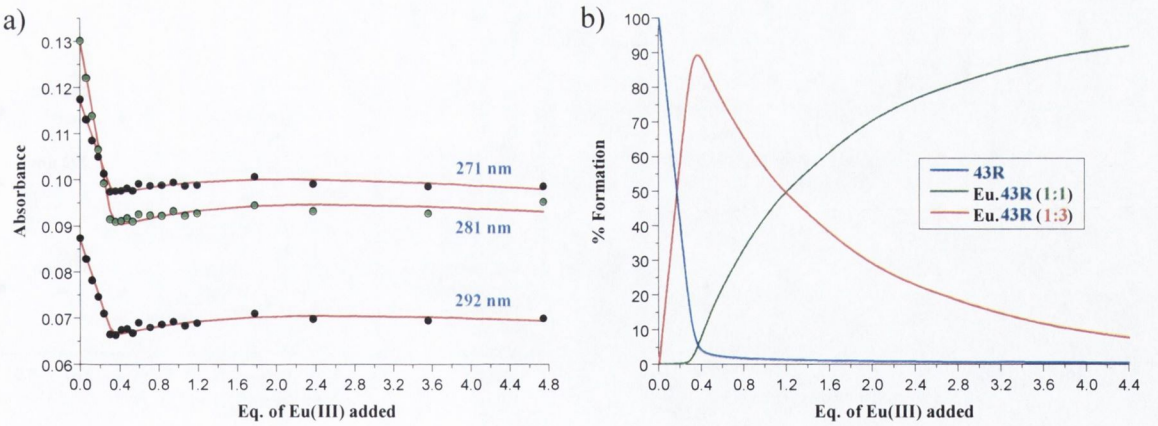

Figure A2.24: *a) Experimental binding isotherms for the UV-vis absorption titration of* ***43R*** *(1×10^{-5} M) with $Eu(CF_3SO_3)_3$ in CH_3CN at 298 K and their corresponding fit by means of SPECFIT. b) Speciation-distribution diagram obtained from the fit.*

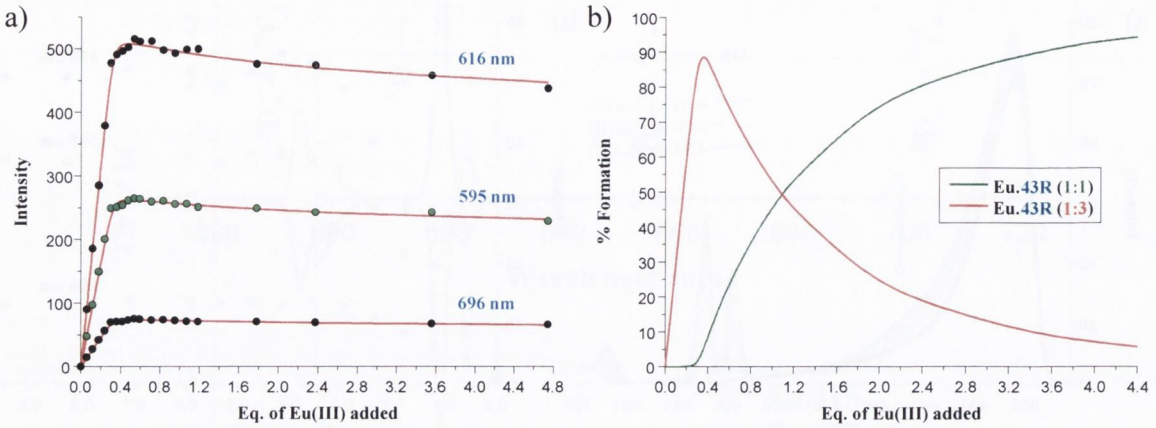

Figure A2.25: *a) Experimental binding isotherms for the phosphorescence titration of* ***43R*** *(1×10^{-5} M) with $Eu(CF_3SO_3)_3$ in CH_3CN at 298 K (λ_{exc} = 281 nm) and their corresponding fit by means of SPECFIT. b) Speciation-distribution diagram obtained from the fit.*

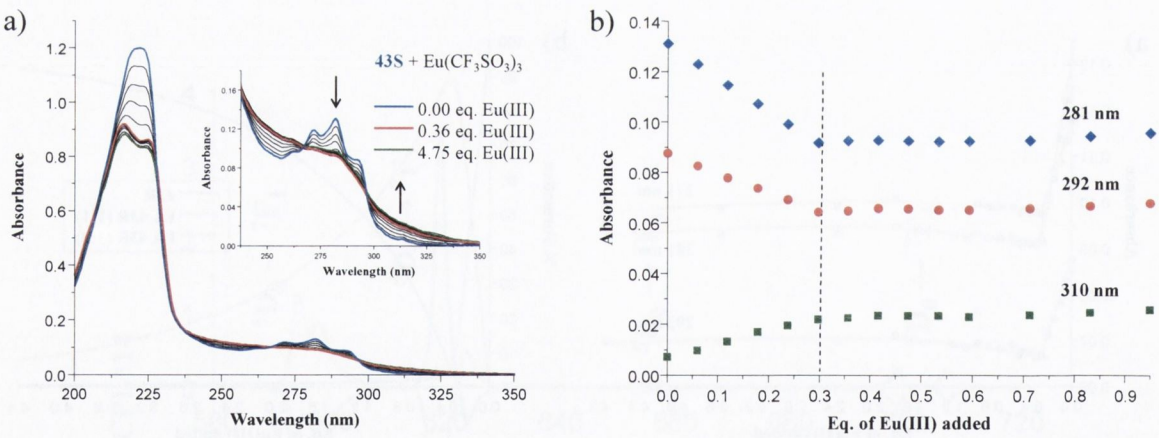

Figure A2.26: *a) Changes in the absorption spectra of* ***43S*** *(1×10^{-5} M) upon titrating with $Eu(CF_3SO_3)_3$ (0.00 → 4.75 eq.) in CH_3CN at 298 K. b) Binding isotherm for the titration measured at 281 nm, 292 nm, and 310 nm.*

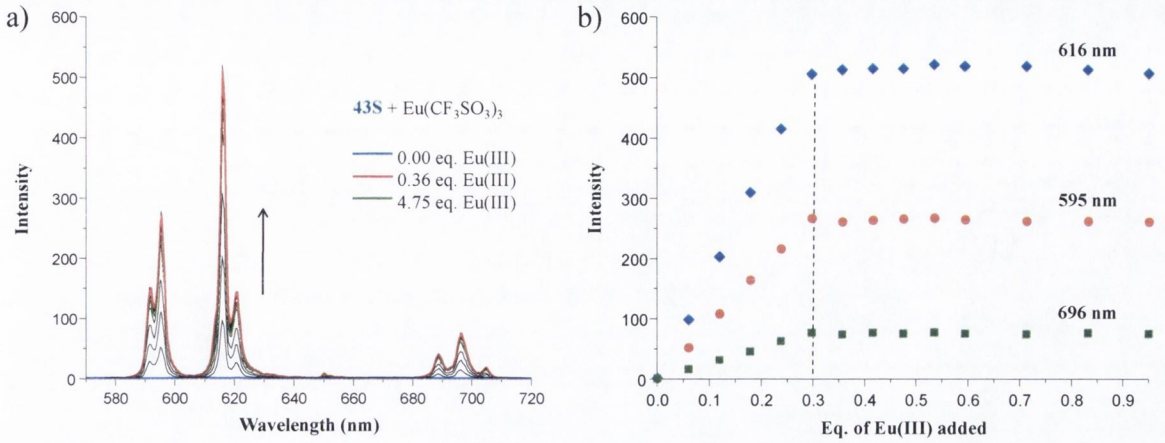

***Figure A2.27**: a) Evolution of the phosphorescence emission in the titration of **43S** (1×10^{-5} M) with $Eu(CF_3SO_3)_3$ (0.00 → 4.75 eq.) in CH_3CN at 298 K (λ_{exc} = 281 nm). b) Binding isotherm for the titration measured at 595 nm, 616 nm, and 696 nm.*

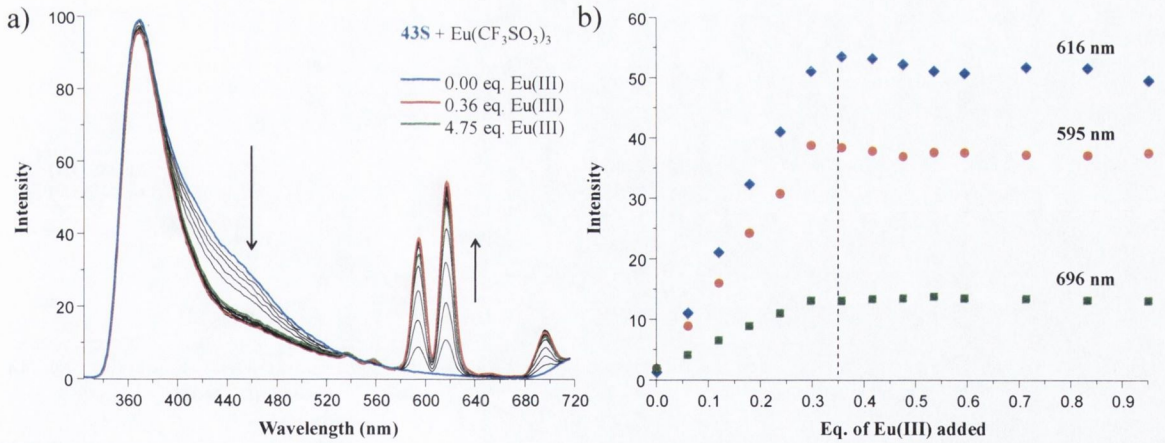

***Figure A2.28:** a) Changes in the fluorescence spectra of **43S** (1×10^{-5} M) upon titrating with $Eu(CF_3SO_3)_3$ (0.00 → 4.75 eq.) in CH_3CN at 298 K. b) Binding isotherms for the titration measured at 595 nm, 616 nm, and 696 nm.*

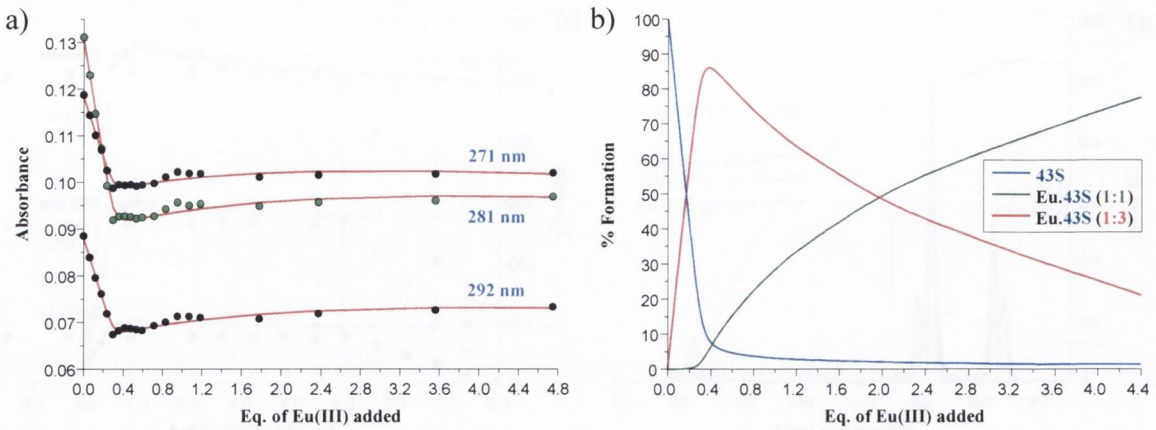

Figure A2.29: *a) Experimental binding isotherms for the UV-vis absorption titration of* ***43S*** *(1 × 10^{-5} M) with $Eu(CF_3SO_3)_3$ in CH_3CN at 298 K and their corresponding fit by means of SPECFIT. b) Speciation-distribution diagram obtained from the fit.*

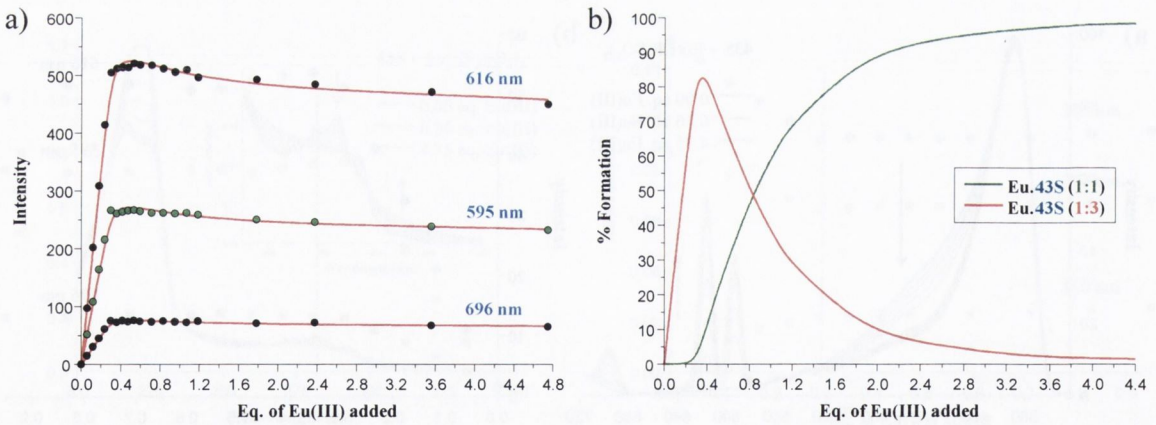

Figure A2.30: *a) Experimental binding isotherms for the phosphorescence titration of* ***43S*** *(1 × 10^{-5} M) with $Eu(CF_3SO_3)_3$ in CH_3CN at 298 K (λ_{exc} = 281 nm) and their corresponding fit by means of SPECFIT. b) Speciation-distribution diagram obtained from the fit.*

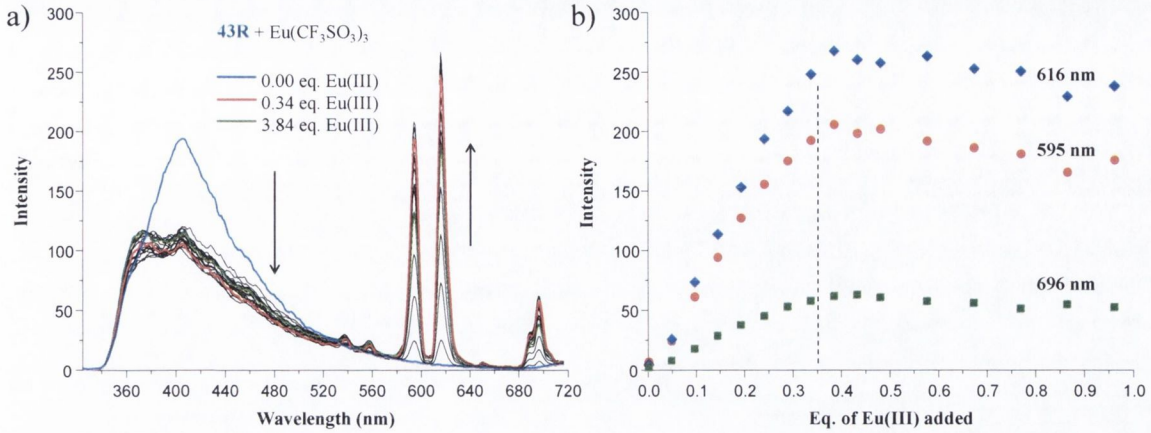

Figure A2.31: *a) Changes in the fluorescence spectra of* ***43R*** *(1×10^{-5} M) upon titrating with $Eu(CF_3SO_3)_3$ (0.00 → 3.84 eq.) in MeOH at 298 K. b) Binding isotherms for the titration measured at 595 nm, 616 nm, and 696 nm.*

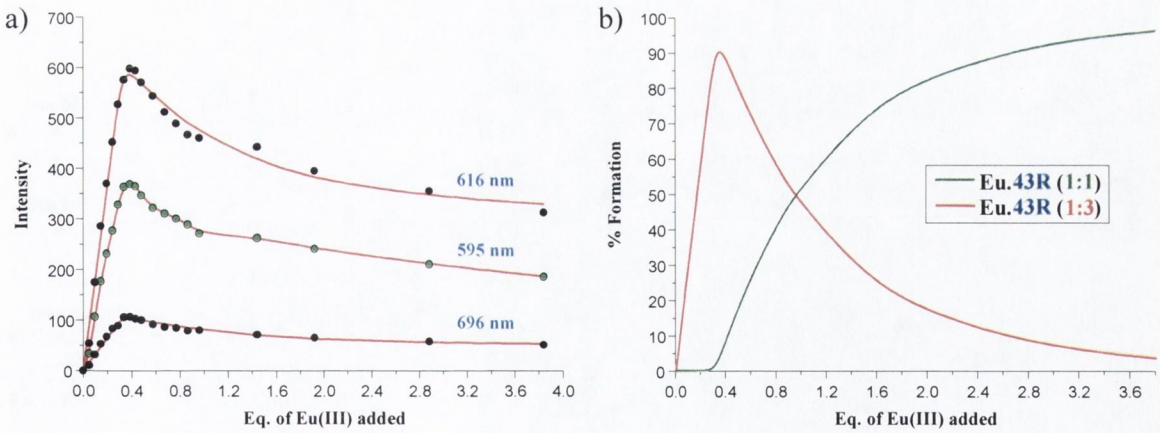

Figure A2.32: *a) Experimental binding isotherms for the phosphorescence titration of* ***43R*** *(1×10^{-5} M) with $Eu(CF_3SO_3)_3$ in MeOH at 298 K (λ_{exc} = 281 nm) and their corresponding fit by means of SPECFIT. b) Speciation-distribution diagram obtained from the fit.*

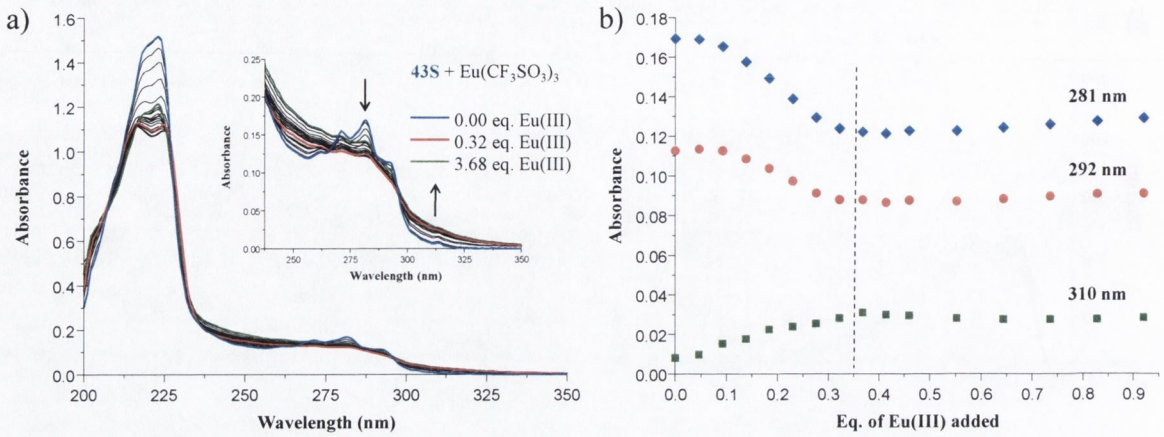

Figure A2.33: *a) Changes in the absorption spectra of* ***43S*** *(1×10^{-5} M) upon titrating with $Eu(CF_3SO_3)_3$ (0.00 → 3.68 eq.) in MeOH at 298 K. b) Binding isotherm for the titration measured at 281 nm, 292 nm, and 310 nm.*

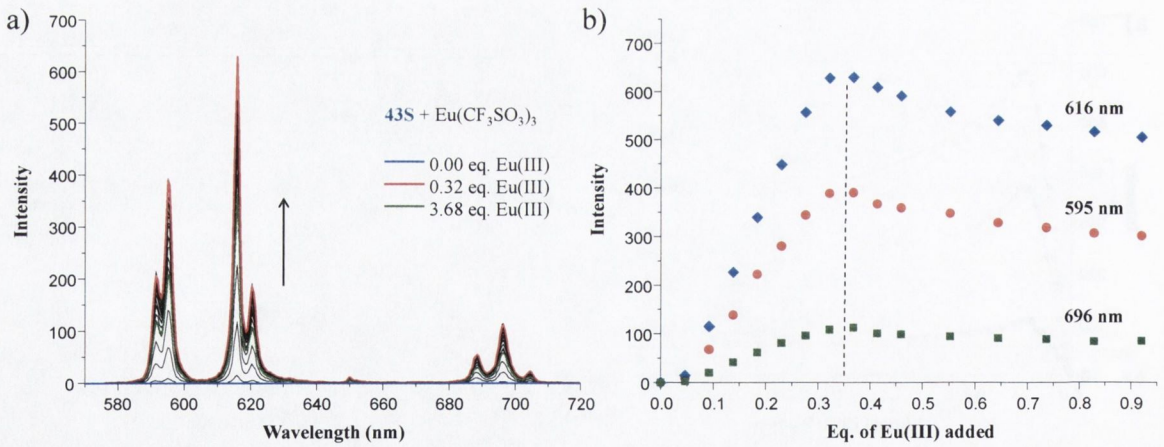

Figure A2.34: *a) Evolution of the phosphorescence emission in the titration of* ***43S*** *(1×10^{-5} M) with $Eu(CF_3SO_3)_3$ (0.00 → 3.68 eq.) in MeOH at 298 K (λ_{exc} = 281 nm). b) Binding isotherm for the titration measured at 595 nm, 616 nm, and 696 nm.*

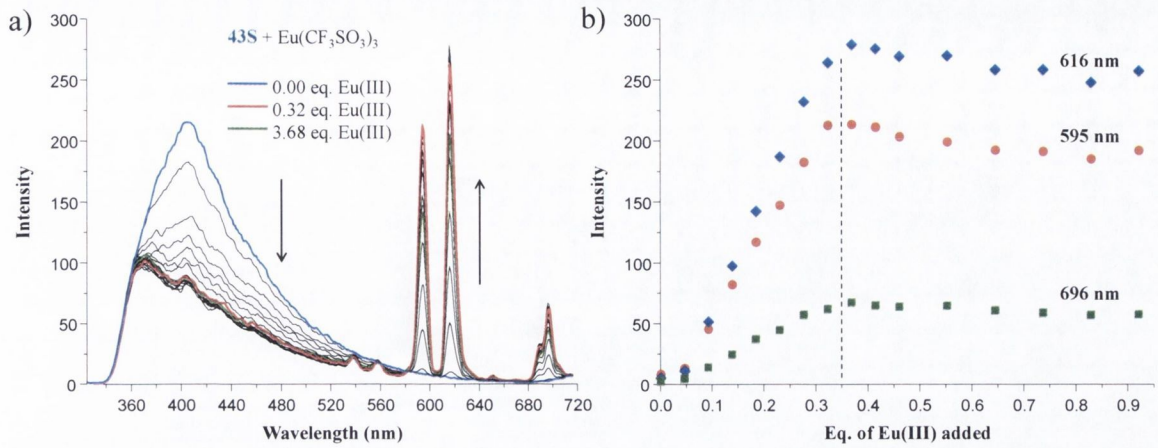

Figure A2.35: *a) Changes in the fluorescence spectra of* ***43S*** *(1×10^{-5} M) upon titrating with $Eu(CF_3SO_3)_3$ (0.00 → 3.68 eq.) in MeOH at 298 K. b) Binding isotherms for the titration measured at 595 nm, 616 nm, and 696 nm.*

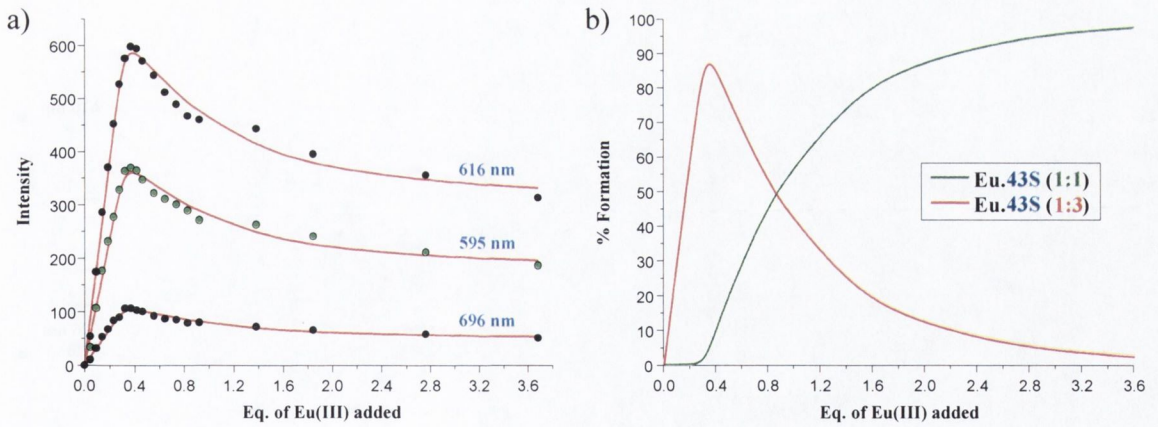

Figure A2.36: *a) Experimental binding isotherms for the phosphorescence titration of* ***43S*** *(1×10^{-5} M) with $Eu(CF_3SO_3)_3$ in MeOH at 298 K (λ_{exc} = 281 nm) and their corresponding fit by means of SPECFIT. b) Speciation-distribution diagram obtained from the fit.*

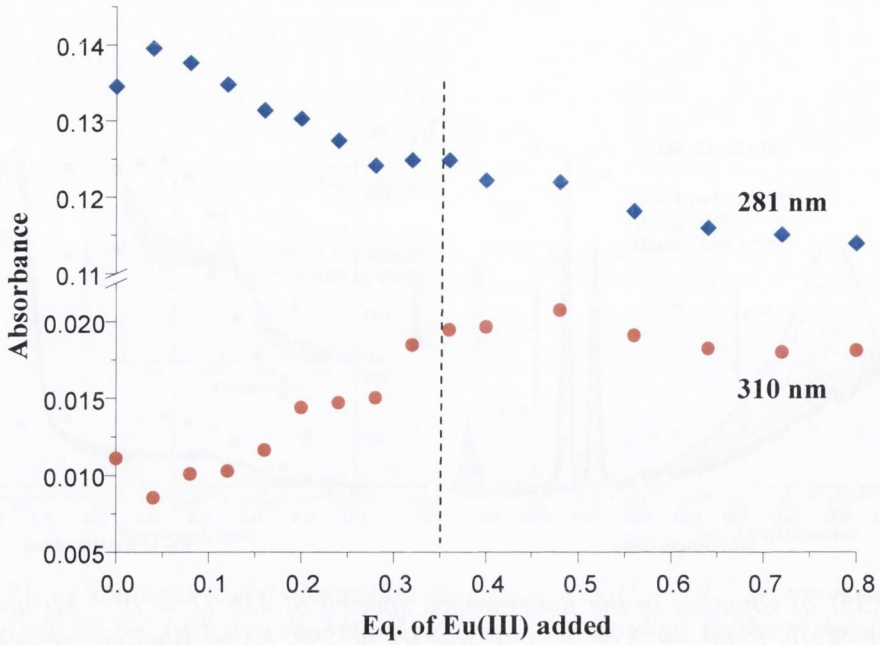

Figure A2.37: *Binding isotherms measured at 281 nm and 310 nm for the titration of* ***43R*** *(1 × 10^{-5} M) with $Eu(CF_3SO_3)_3$ (0.00 → 3.20 eq.) in H_2O/MeOH (1:1; v/v) at 298 K.*

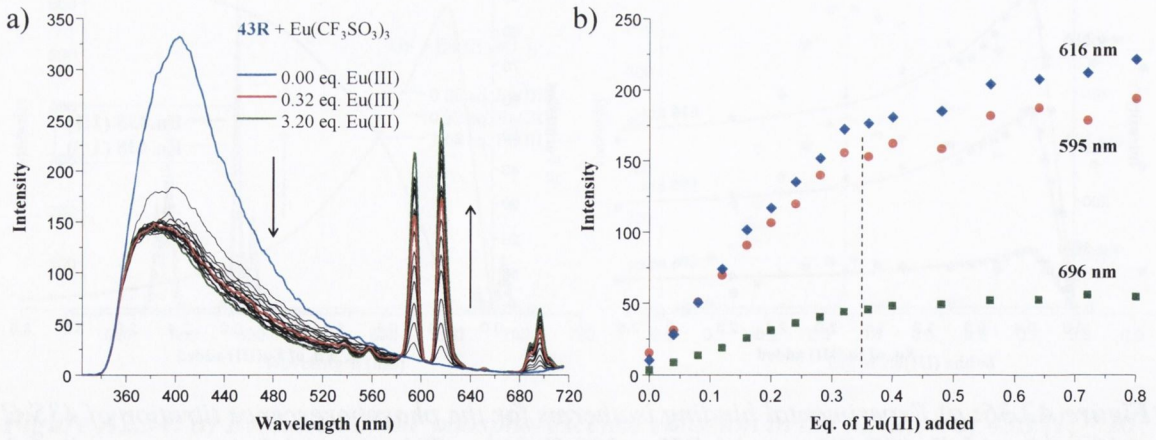

Figure A2.38: *a) Changes in the fluorescence spectra of* ***43R*** *(1 × 10^{-5} M) upon titrating with $Eu(CF_3SO_3)_3$ (0.00 → 3.20 eq.) in H_2O/MeOH (1:1; v/v) at 298 K. b) Binding isotherms for the titration measured at 595 nm, 616 nm, and 696 nm.*

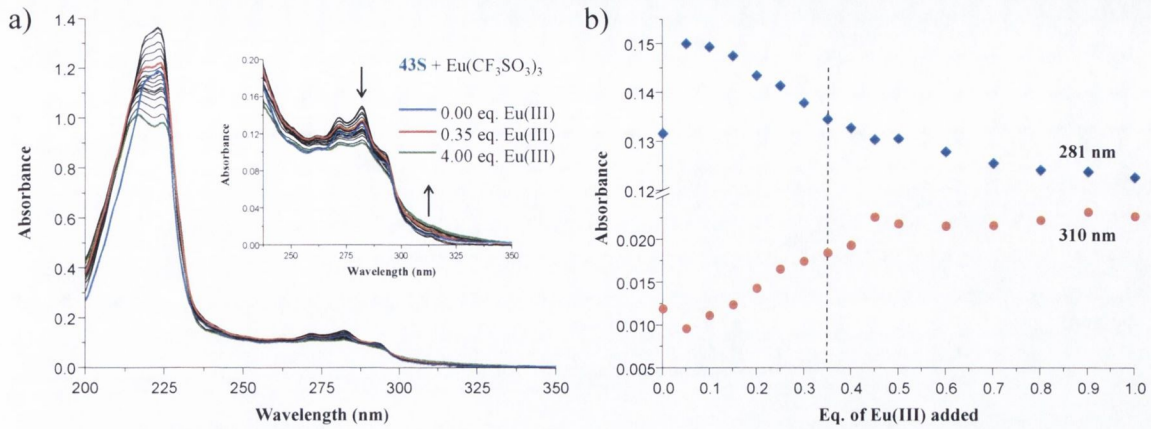

Figure A2.39: *a) Changes in the absorption spectra of* ***43S*** *(1×10^{-5} M) upon titrating with $Eu(CF_3SO_3)_3$ (0.00 → 4.00 eq.) in H_2O/MeOH (1:1; v/v) at 298 K. b) Binding isotherm for the titration measured at 281 nm, 292 nm, and 310 nm.*

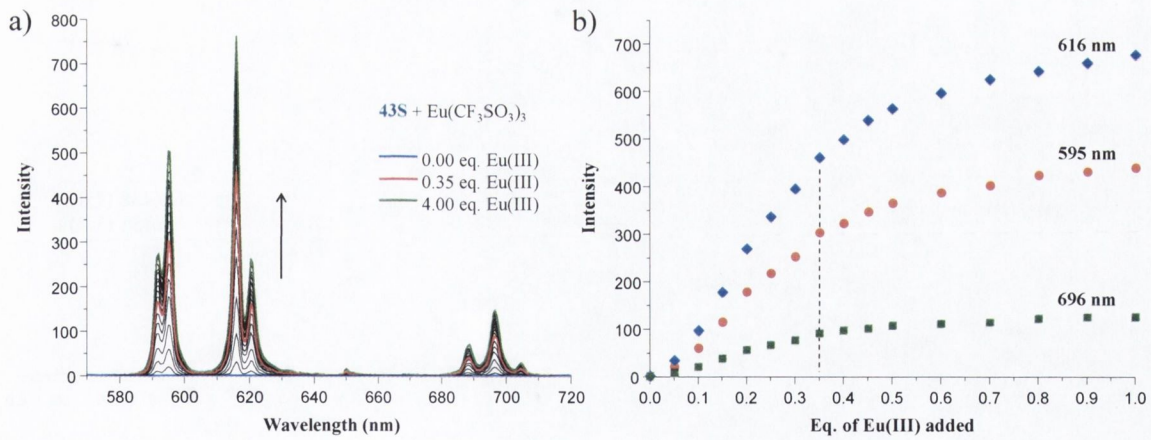

Figure A2.40: *a) Evolution of the phosphorescence emission in the titration of* ***43S*** *(1×10^{-5} M) with $Eu(CF_3SO_3)_3$ (0.00 → 4.00 eq.) in H_2O/MeOH (1:1; v/v) at 298 K (λ_{exc} = 281 nm). b) Binding isotherm for the titration measured at 595 nm, 616 nm, and 696 nm.*

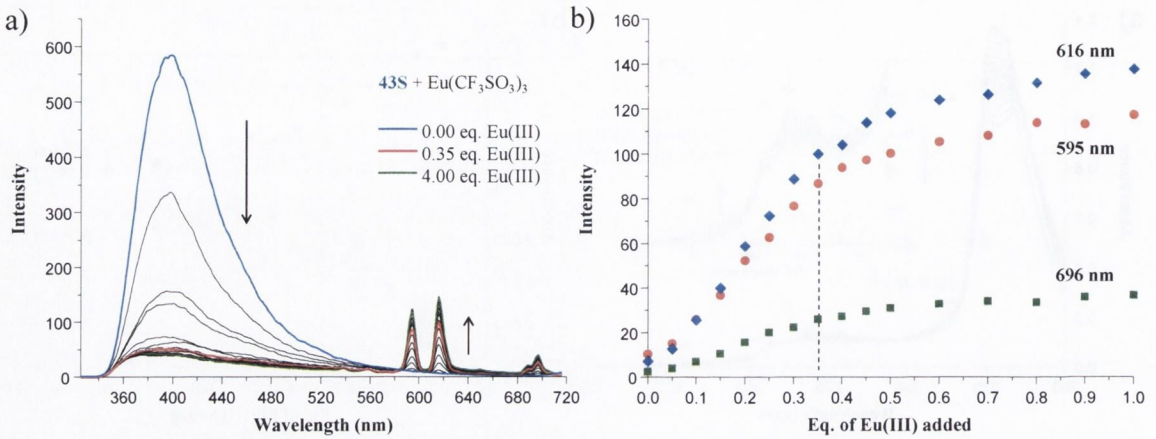

Figure A2.41: *a) Changes in the fluorescence spectra of* ***43S*** *(1 × 10^{-5} M) upon titrating with $Eu(CF_3SO_3)_3$ (0.00 → 4.00 eq.) in H_2O/MeOH (1:1; v/v) at 298 K. b) Binding isotherms for the titration measured at 595 nm, 616 nm, and 696 nm..*

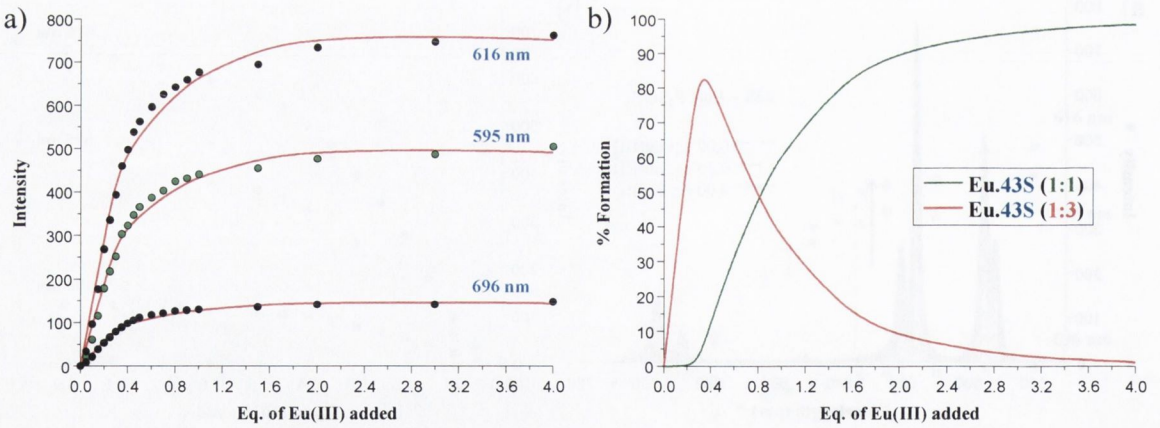

Figure A2.42: *a) Experimental binding isotherms for the phosphorescence titration of* ***43S*** *(1 × 10^{-5} M) with $Eu(CF_3SO_3)_3$ in H_2O/MeOH (1:1; v/v) at 298 K (λ_{exc} = 281 nm) and their corresponding fit by means of SPECFIT. b) Speciation-distribution diagram obtained from the fit.*

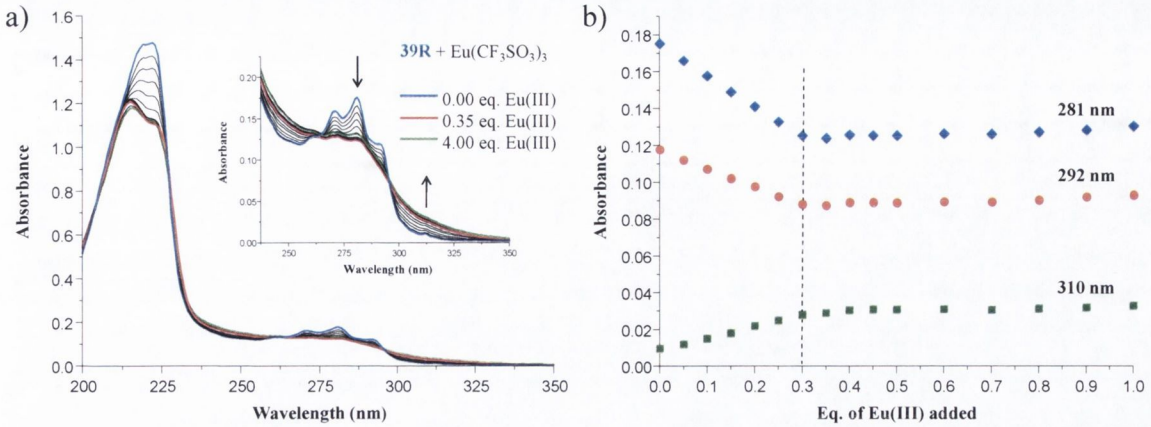

Figure A2.43: *a) Changes in the absorption spectra of* ***39R*** *(1 × 10^{-5} M) upon titrating with $Eu(CF_3SO_3)_3$ (0.00 → 4.00 eq.) in CH_3CN at 298 K. b) Binding isotherm for the titration measured at 281 nm, 292 nm, and 310 nm.*

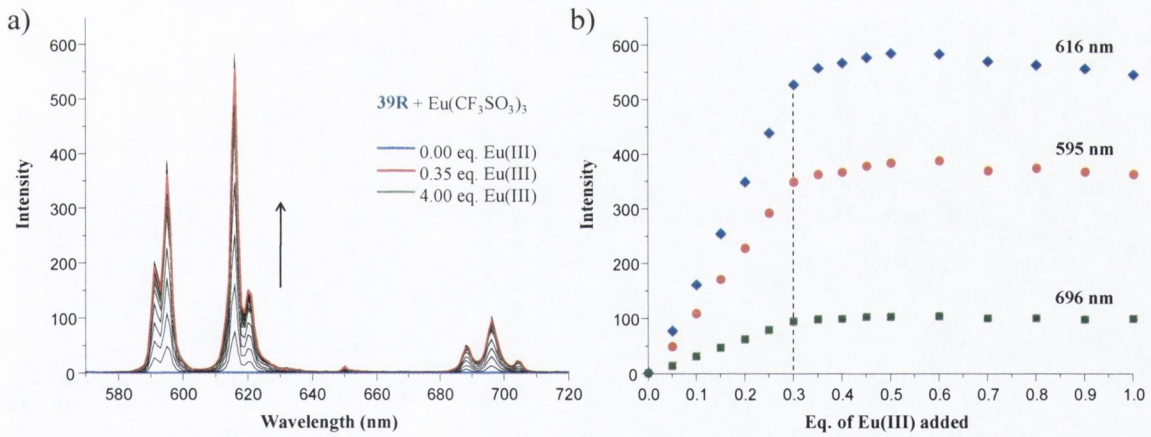

Figure A2.44: *a) Evolution of the phosphorescence emission in the titration of* ***39R*** *(1 × 10^{-5} M) with $Eu(CF_3SO_3)_3$ (0.00 → 4.00 eq.) in CH_3CN at 298 K (λ_{exc} = 281 nm). b) Binding isotherm for the titration measured at 595 nm, 616 nm, and 696 nm.*

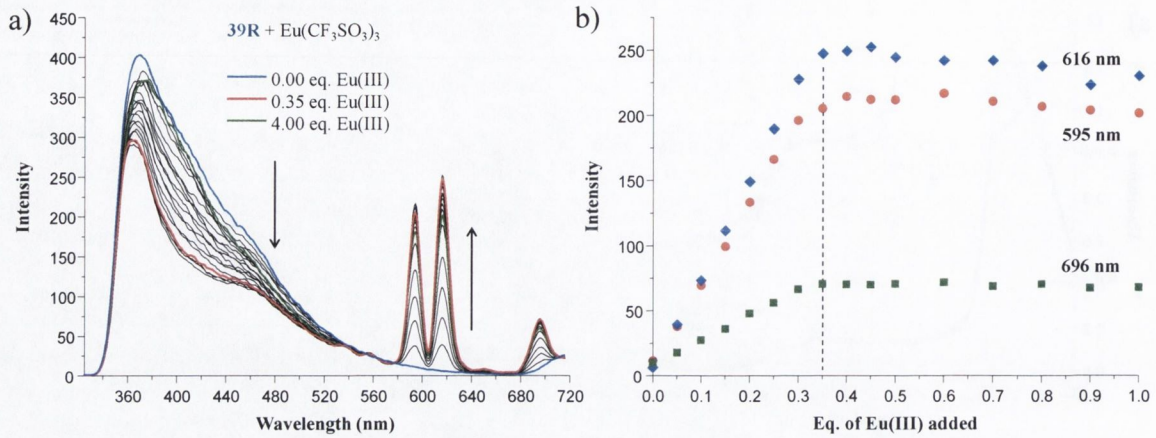

Figure A2.45: *a) Changes in the fluorescence spectra of* ***39R*** *(1×10^{-5} M) upon titrating with $Eu(CF_3SO_3)_3$ (0.00 → 4.00 eq.) in CH_3CN at 298 K. b) Binding isotherms for the titration measured at 595 nm, 616 nm, and 696 nm.*

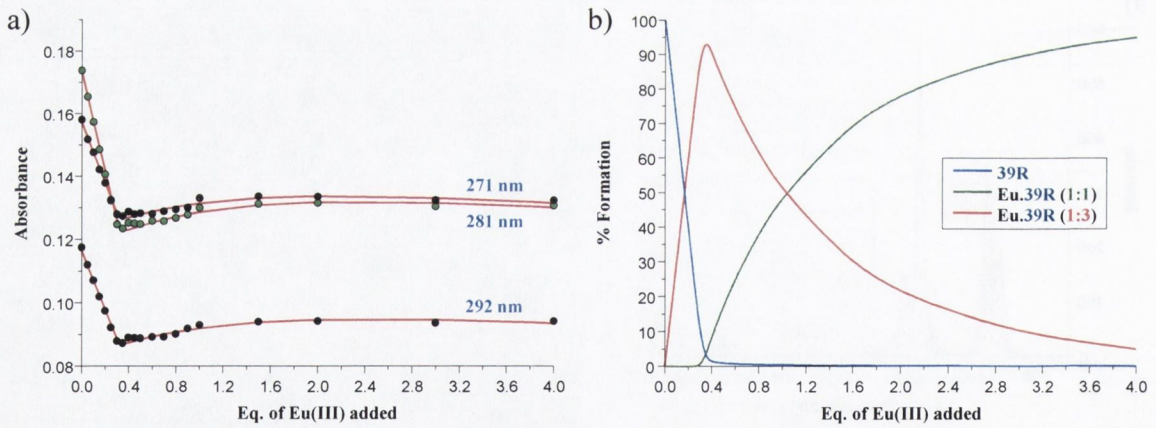

Figure A2.46: *a) Experimental binding isotherms for the UV-vis absorption titration of* ***39R*** *(1×10^{-5} M) with $Eu(CF_3SO_3)_3$ in CH_3CN at 298 K and their corresponding fit by means of SPECFIT. b) Speciation-distribution diagram obtained from the fit.*

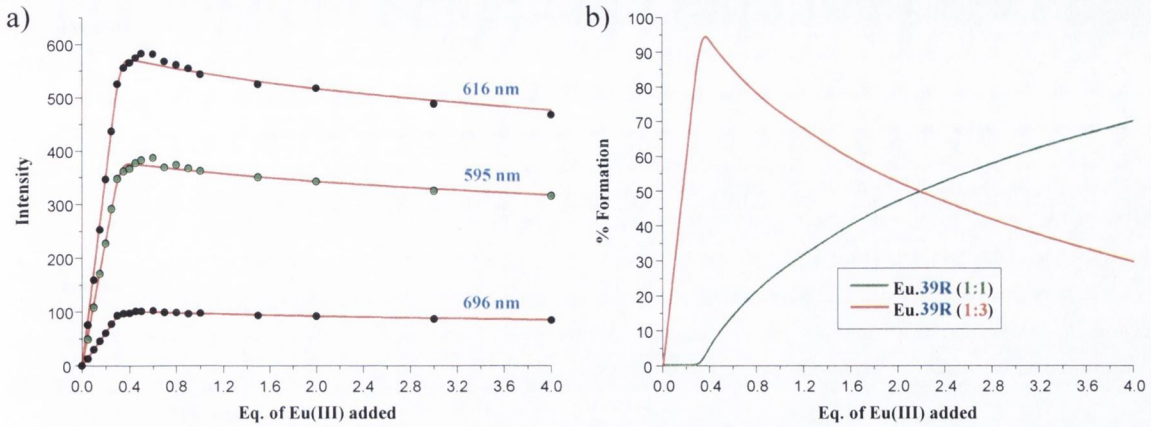

Figure A2.47: *a) Experimental binding isotherms for the phosphorescence titration of* ***39R*** *(1×10^{-5} M) with $Eu(CF_3SO_3)_3$ in CH_3CN at 298 K (λ_{exc} = 281 nm) and their corresponding fit by means of SPECFIT. b) Speciation-distribution diagram obtained from the fit.*

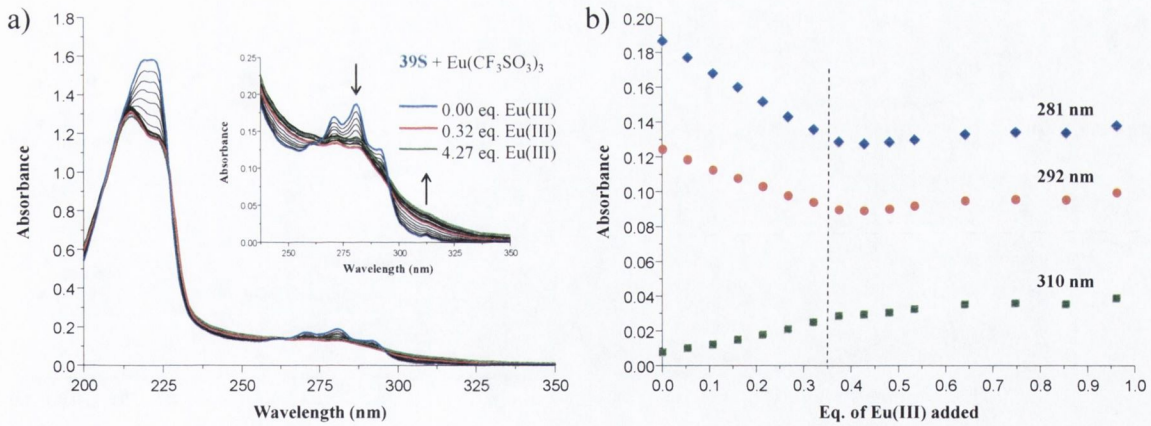

Figure A2.48: *a) Changes in the absorption spectra of* ***39S*** *(1×10^{-5} M) upon titrating with $Eu(CF_3SO_3)_3$ (0.00 → 4.27 eq.) in CH_3CN at 298 K. b) Binding isotherm for the titration measured at 281 nm, 292 nm, and 310 nm.*

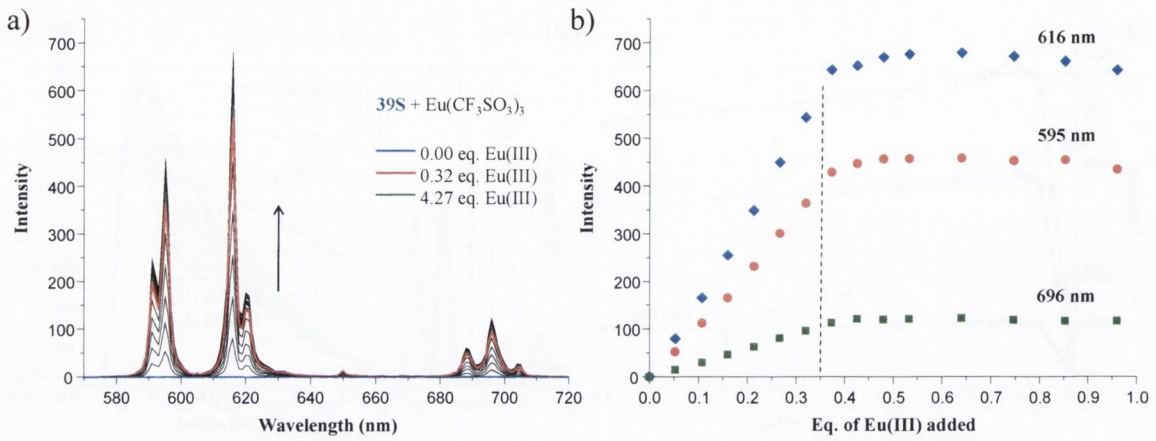

Figure A2.49: *a) Evolution of the phosphorescence emission in the titration of* ***39S*** *(1×10^{-5} M) with $Eu(CF_3SO_3)_3$ (0.00 → 4.27 eq.) in CH_3CN at 298 K (λ_{exc} = 281 nm). b) Binding isotherm for the titration measured at 595 nm, 616 nm, and 696 nm.*

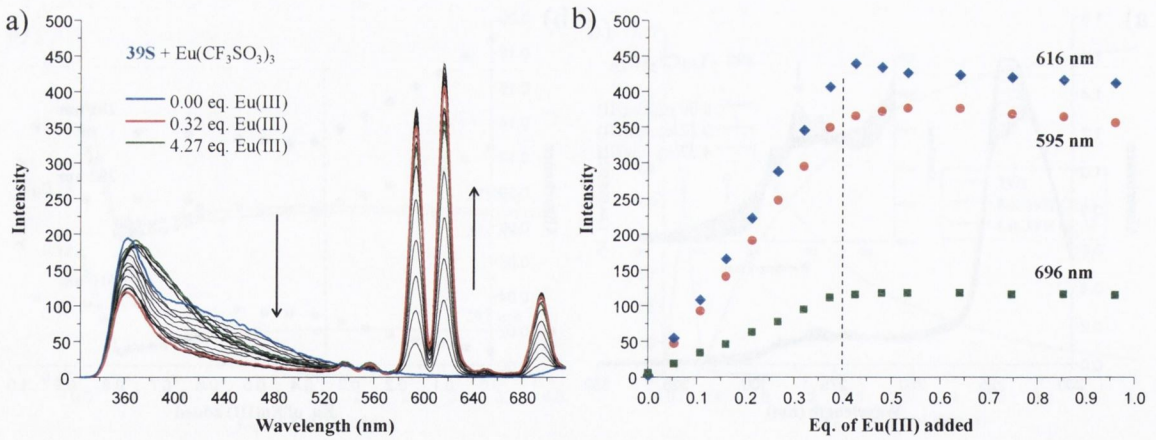

Figure A2.50: *a) Changes in the fluorescence spectra of* ***39S*** *(1×10^{-5} M) upon titrating with $Eu(CF_3SO_3)_3$ (0.00 → 4.27 eq.) in CH_3CN at 298 K. b) Binding isotherms for the titration measured at 595 nm, 616 nm, and 696 nm.*

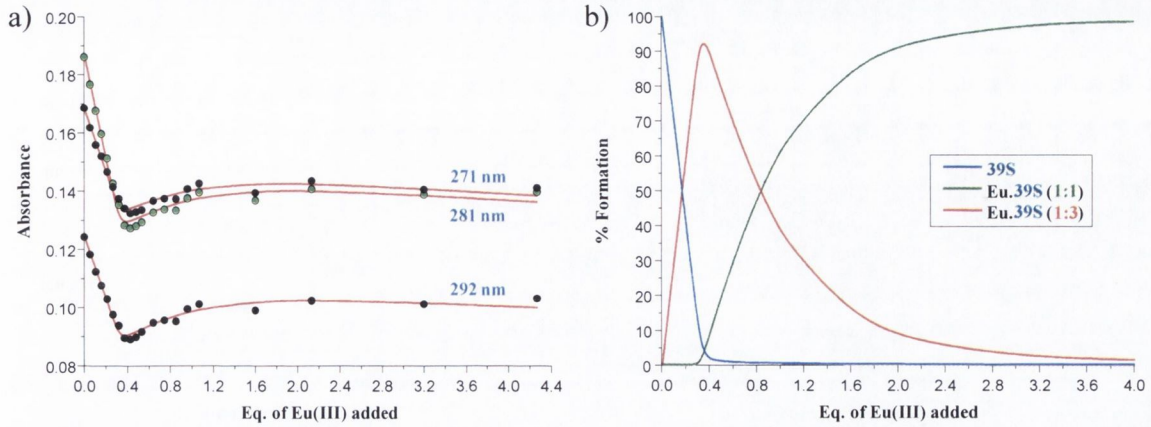

Figure A2.51: *a) Experimental binding isotherms for the UV-vis absorption titration of* ***39S*** *(1×10^{-5} M) with $Eu(CF_3SO_3)_3$ in CH_3CN at 298 K and their corresponding fit by means of SPECFIT. b) Speciation-distribution diagram obtained from the fit.*

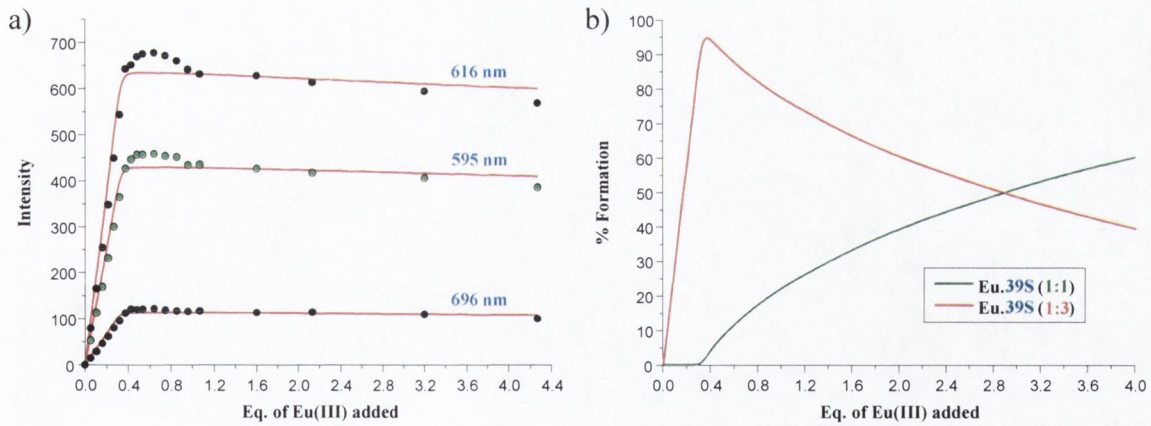

Figure A2.52: *a) Experimental binding isotherms for the phosphorescence titration of* ***39S*** *(1×10^{-5} M) with $Eu(CF_3SO_3)_3$ in CH_3CN at 298 K (λ_{exc} = 281 nm) and their corresponding fit by means of SPECFIT. b) Speciation-distribution diagram obtained from the fit.*

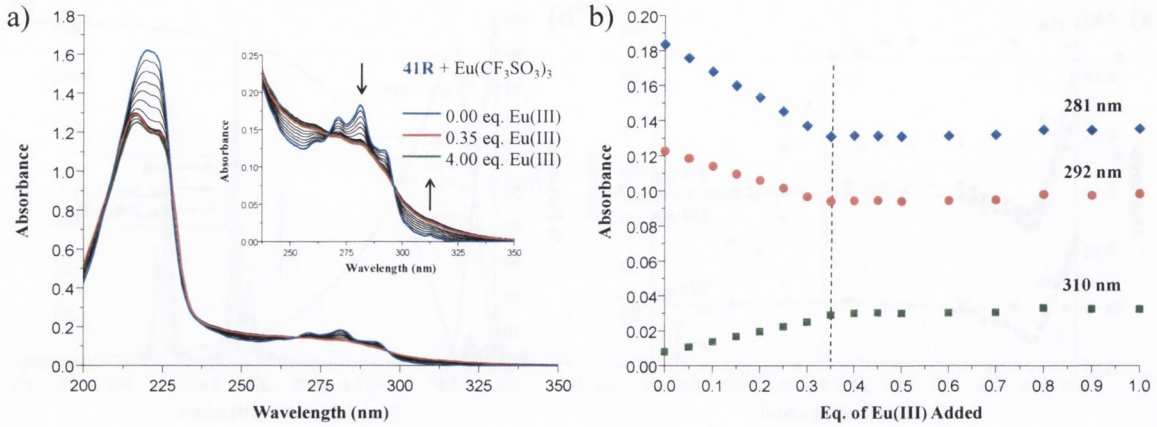

Figure A2.53: *a) Changes in the absorption spectra of* ***41R*** *(1×10^{-5} M) upon titrating with $Eu(CF_3SO_3)_3$ (0.00 → 4.00 eq.) in CH_3CN at 298 K. b) Binding isotherm for the titration measured at 281 nm, 292 nm, and 310 nm.*

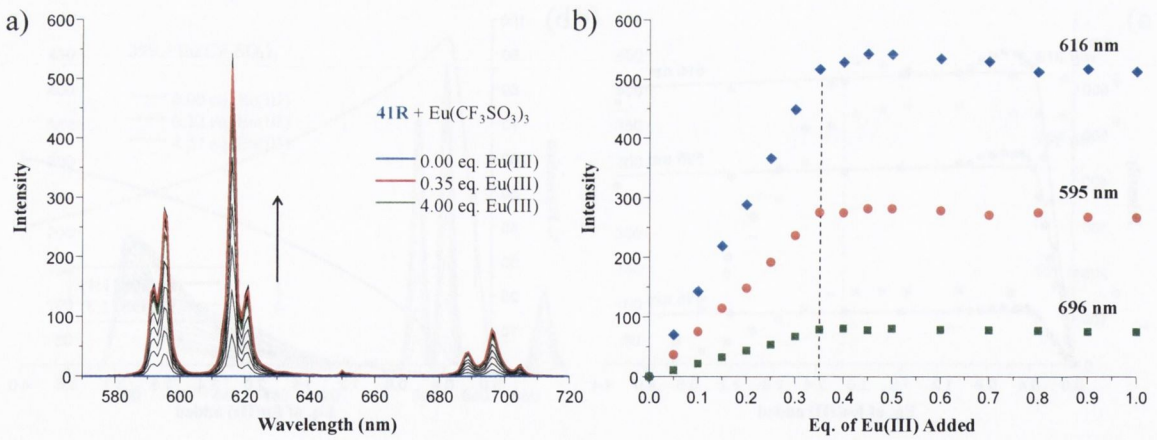

Figure A2.54: *a) Evolution of the phosphorescence emission in the titration of* ***41R*** *(1×10^{-5} M) with $Eu(CF_3SO_3)_3$ (0.00 → 4.00 eq.) in CH_3CN at 298 K (λ_{exc} = 281 nm). b) Binding isotherm for the titration measured at 595 nm, 616 nm, and 696 nm.*

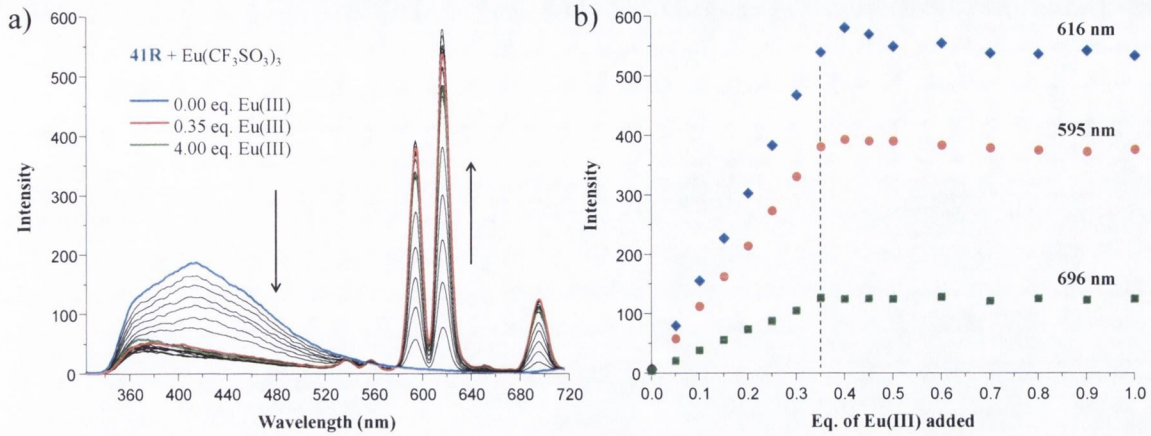

Figure A2.55: *a) Changes in the fluorescence spectra of* ***41R*** *(1×10^{-5} M) upon titrating with $Eu(CF_3SO_3)_3$ (0.00 → 4.00 eq.) in CH_3CN at 298 K. b) Binding isotherms for the titration measured at 595 nm, 616 nm, and 696 nm.*

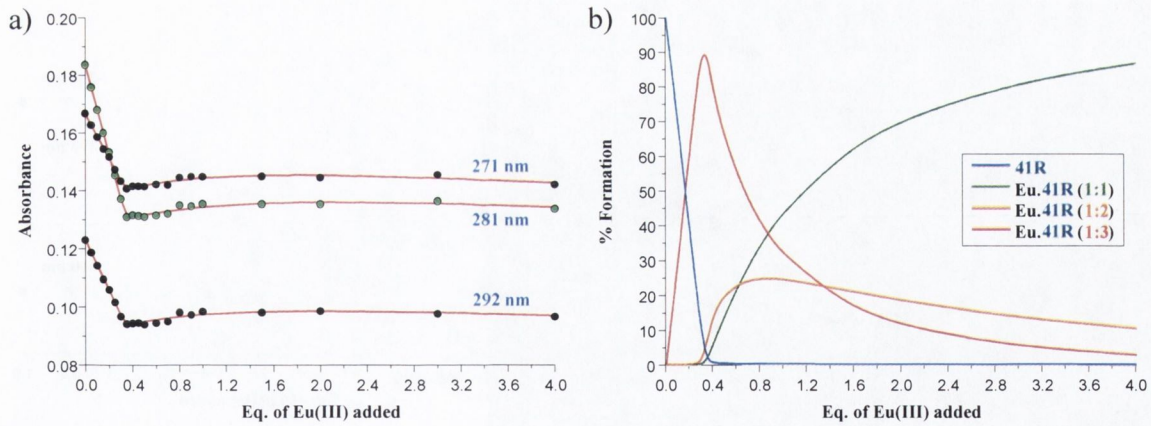

Figure A2.56: *a) Experimental binding isotherms for the UV-vis absorption titration of* ***41R*** *(1×10^{-5} M) with $Eu(CF_3SO_3)_3$ in CH_3CN at 298 K and their corresponding fit by means of SPECFIT. b) Speciation-distribution diagram obtained from the fit.*

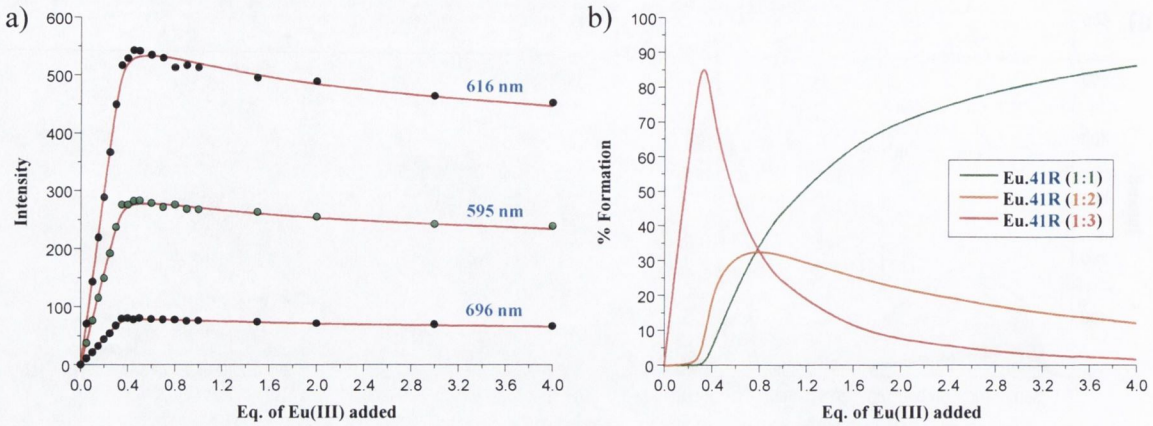

Figure A2.57: *a) Experimental binding isotherms for the phosphorescence titration of* ***41R*** *(1×10^{-5} M) with $Eu(CF_3SO_3)_3$ in CH_3CN at 298 K (λ_{exc} = 281 nm) and their corresponding fit by means of SPECFIT. b) Speciation-distribution diagram obtained from the fit.*

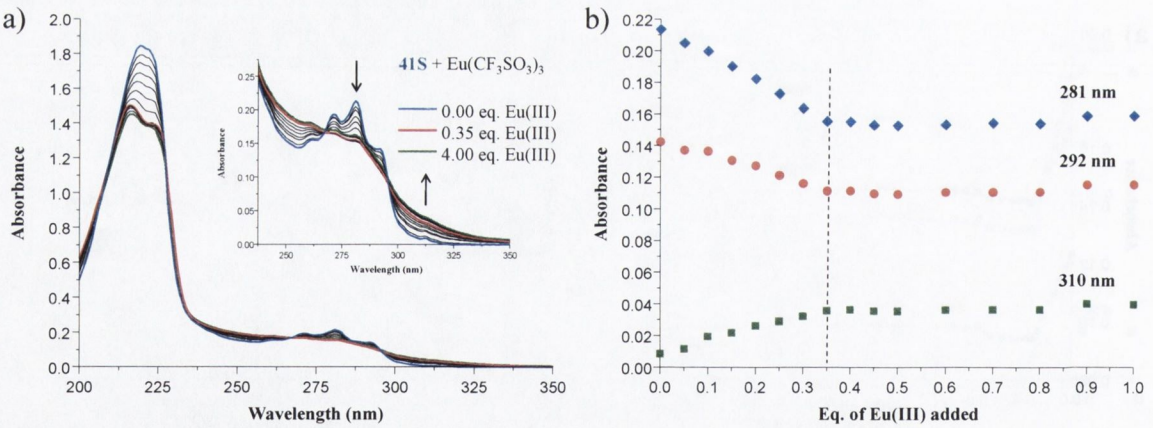

Figure A2.58: *a) Changes in the absorption spectra of* ***41S*** *(1×10^{-5} M) upon titrating with $Eu(CF_3SO_3)_3$ (0.00 → 4.00 eq.) in CH_3CN at 298 K. b) Binding isotherm for the titration measured at 281 nm, 292 nm, and 310 nm.*

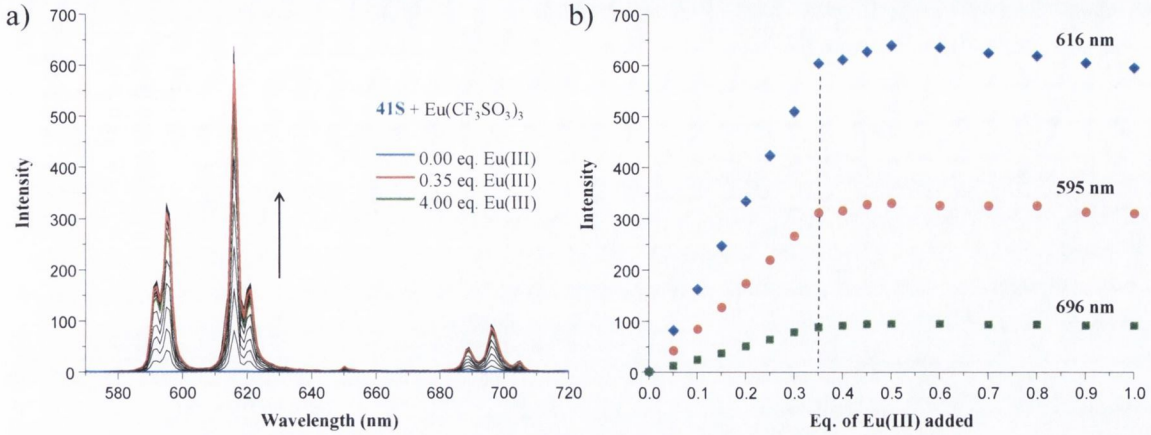

Figure A2.59: *a) Evolution of the phosphorescence emission in the titration of* ***41S*** *(1×10^{-5} M) with $Eu(CF_3SO_3)_3$ (0.00 → 4.00 eq.) in CH_3CN at 298 K (λ_{exc} = 281 nm). b) Binding isotherm for the titration measured at 595 nm, 616 nm, and 696 nm.*

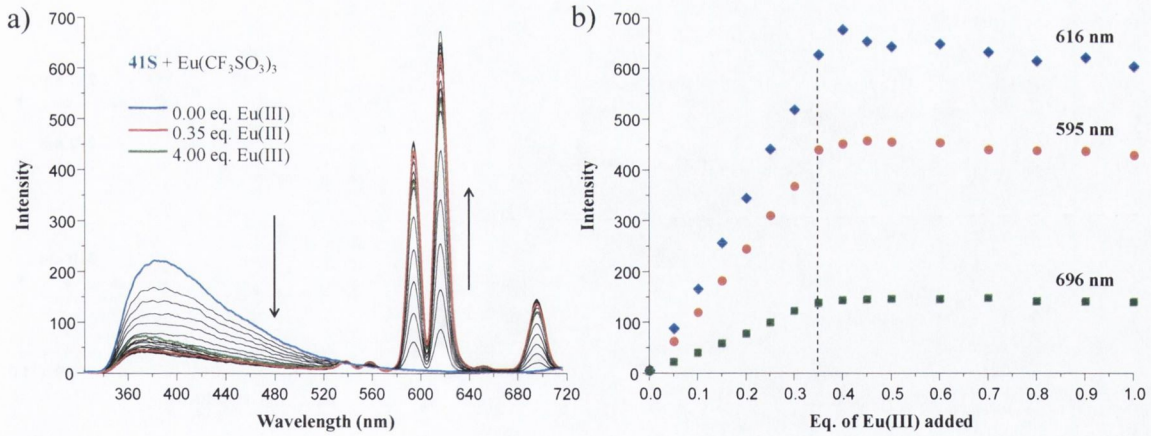

Figure A2.60: *a) Changes in the fluorescence spectra of* ***41S*** *(1×10^{-5} M) upon titrating with $Eu(CF_3SO_3)_3$ (0.00 → 4.00 eq.) in CH_3CN at 298 K. b) Binding isotherms for the titration measured at 595 nm, 616 nm, and 696 nm.*

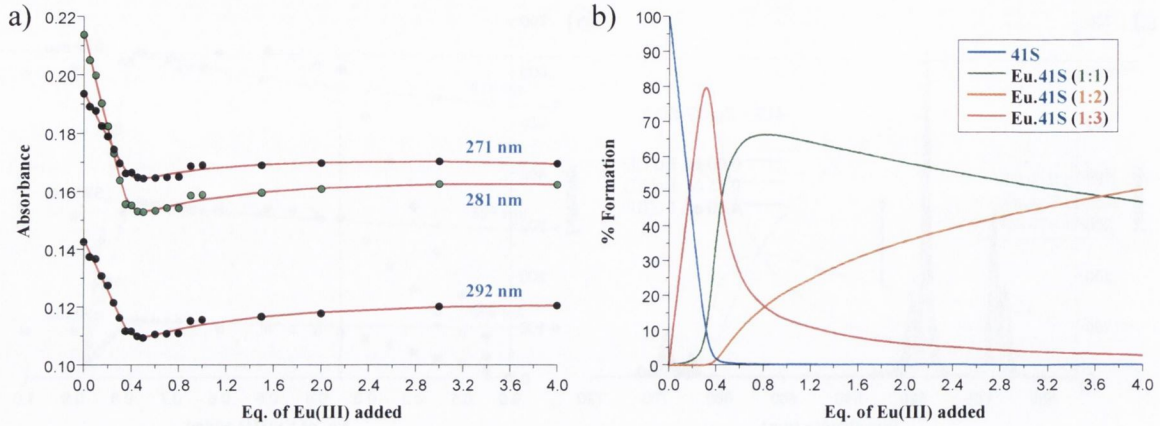

Figure A2.61: *a) Experimental binding isotherms for the UV-vis absorption titration of* ***41S*** *(1×10^{-5} M) with $Eu(CF_3SO_3)_3$ in CH_3CN at 298 K and their corresponding fit by means of SPECFIT. b) Speciation-distribution diagram obtained from the fit.*

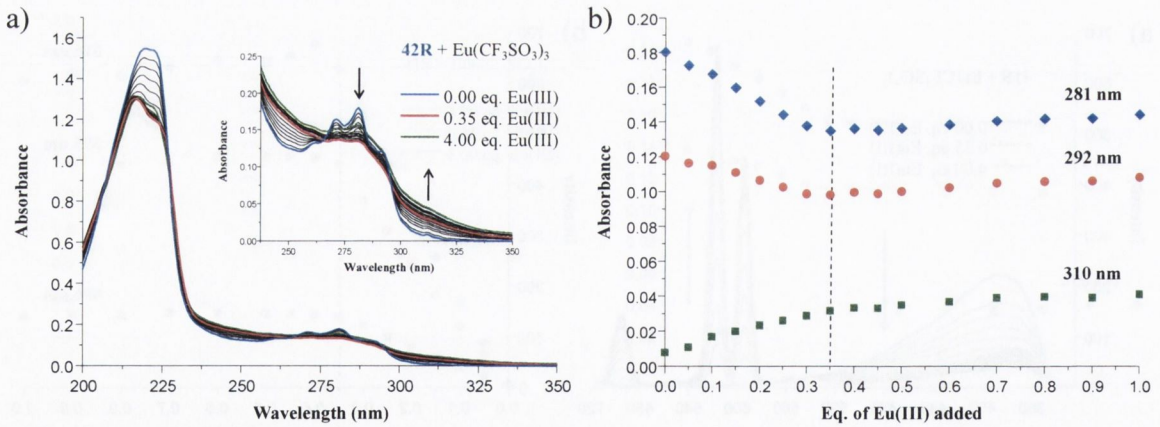

Figure A2.62: *a) Changes in the absorption spectra of* ***42R*** *(1×10^{-5} M) upon titrating with $Eu(CF_3SO_3)_3$ (0.00 → 4.00 eq.) in CH_3CN at 298 K. b) Binding isotherm for the titration measured at 281 nm, 292 nm, and 310 nm.*

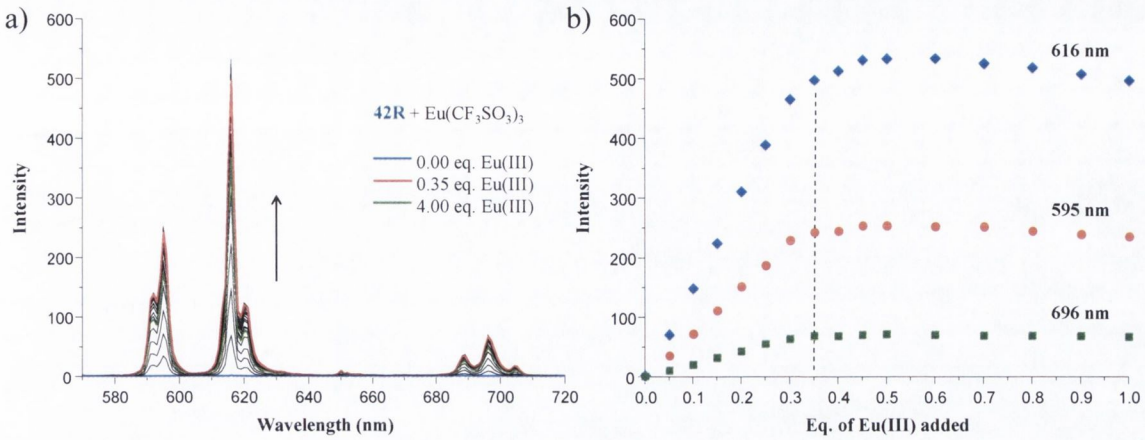

Figure A2.63: *a) Evolution of the phosphorescence emission in the titration of* ***42R*** *(1×10^{-5} M) with $Eu(CF_3SO_3)_3$ (0.00 → 4.00 eq.) in CH_3CN at 298 K (λ_{exc} = 281 nm). b) Binding isotherm for the titration measured at 595 nm, 616 nm, and 696 nm.*

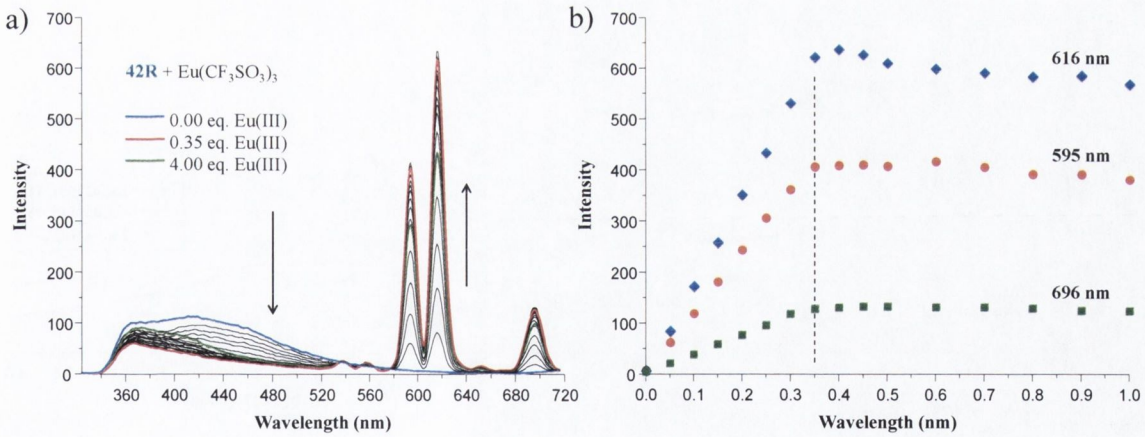

Figure A2.64: *a) Changes in the fluorescence spectra of* ***42R*** *(1×10^{-5} M) upon titrating with $Eu(CF_3SO_3)_3$ (0.00 → 4.00 eq.) in CH_3CN at 298 K. b) Binding isotherms for the titration measured at 595 nm, 616 nm, and 696 nm.*

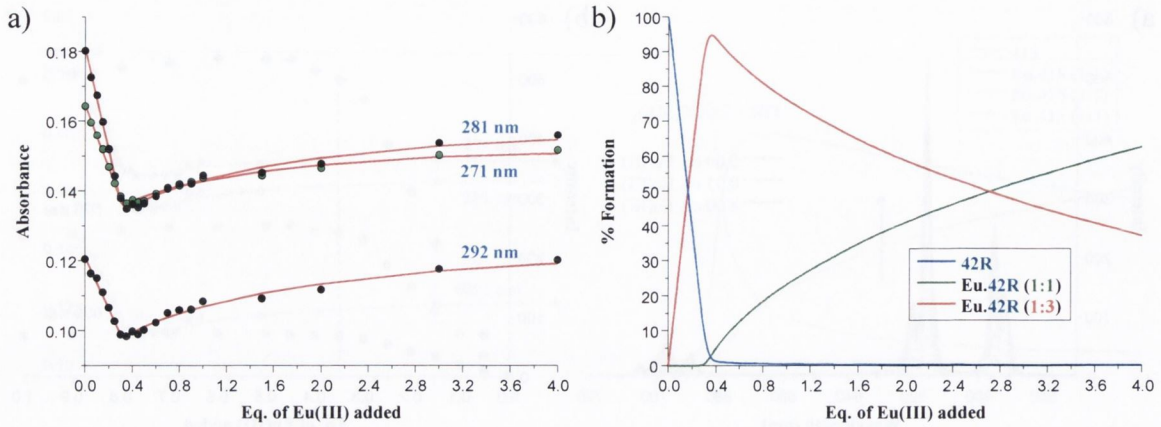

Figure A2.65: *a) Experimental binding isotherms for the UV-vis absorption titration of* ***42R*** *(1×10^{-5} M) with $Eu(CF_3SO_3)_3$ in CH_3CN at 298 K and their corresponding fit by means of SPECFIT. b) Speciation-distribution diagram obtained from the fit.*

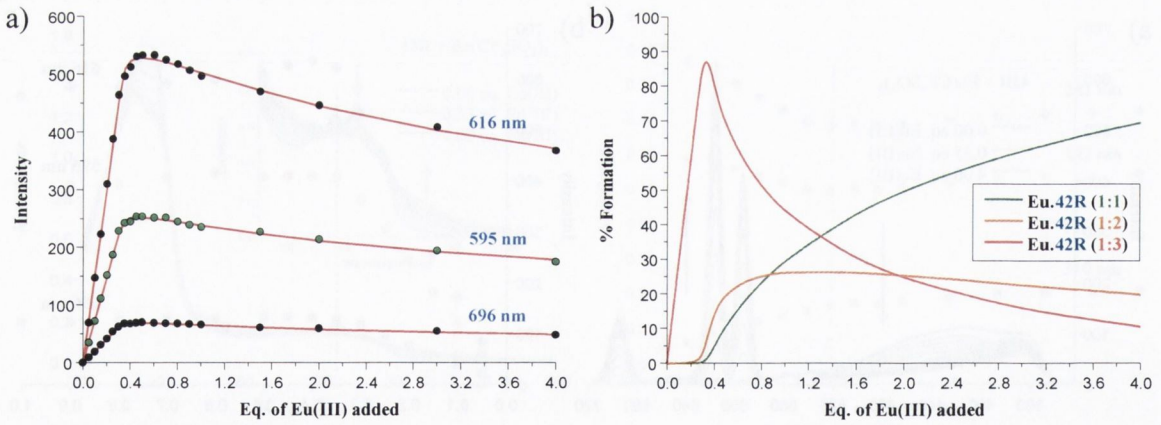

Figure A2.66: *a) Experimental binding isotherms for the phosphorescence titration of* ***42R*** *(1×10^{-5} M) with $Eu(CF_3SO_3)_3$ in CH_3CN at 298 K (λ_{exc} = 281 nm) and their corresponding fit by means of SPECFIT. b) Speciation-distribution diagram obtained from the fit.*

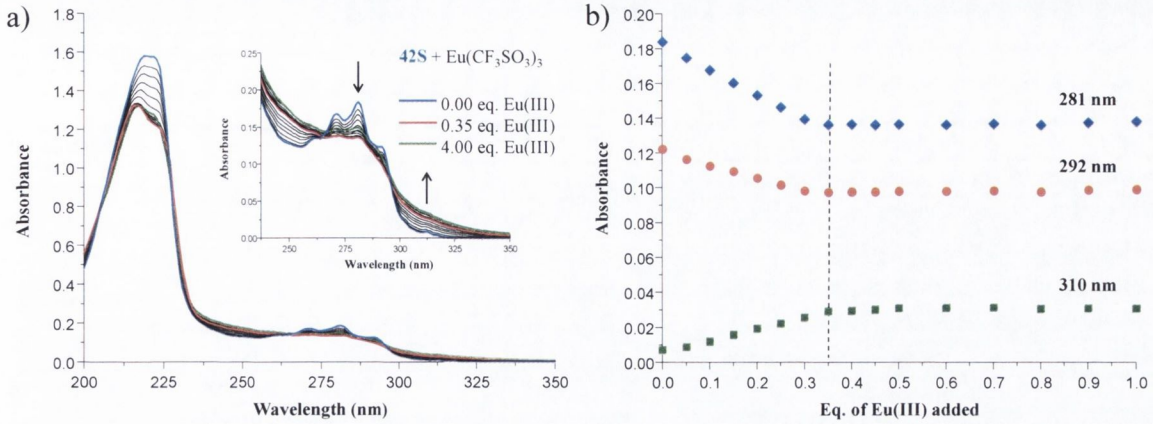

Figure A2.67: *a) Changes in the absorption spectra of* ***42S*** *(1×10^{-5} M) upon titrating with $Eu(CF_3SO_3)_3$ (0.00 → 4.00 eq.) in CH_3CN at 298 K. b) Binding isotherm for the titration measured at 281 nm, 292 nm, and 310 nm.*

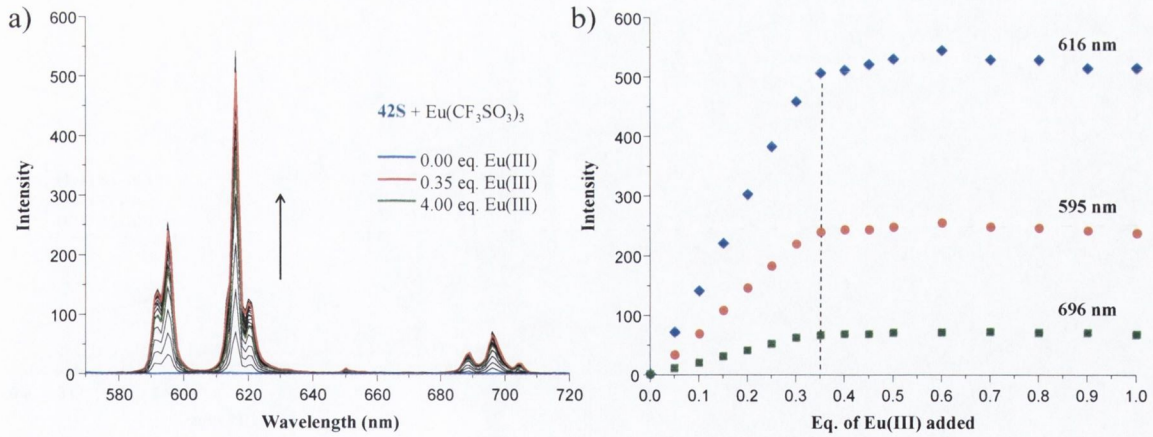

Figure A2.68: *a) Evolution of the phosphorescence emission in the titration of* ***42S*** *(1×10^{-5} M) with $Eu(CF_3SO_3)_3$ (0.00 → 4.00 eq.) in CH_3CN at 298 K (λ_{exc} = 281 nm). b) Binding isotherm for the titration measured at 595 nm, 616 nm, and 696 nm.*

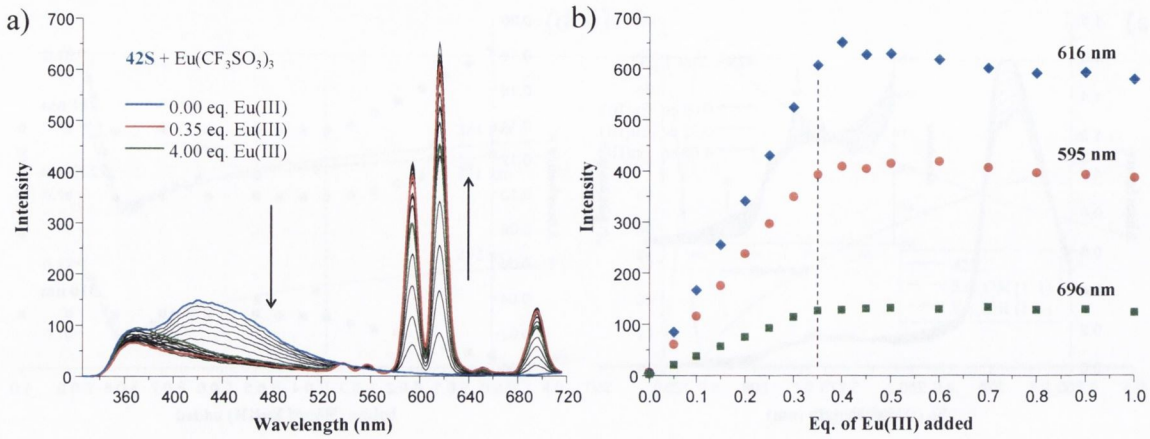

Figure A2.69: *a) Changes in the fluorescence spectra of* ***42S*** *(1 × 10^{-5} M) upon titrating with $Eu(CF_3SO_3)_3$ (0.00 → 4.00 eq.) in CH_3CN at 298 K. b) Binding isotherms for the titration measured at 595 nm, 616 nm, and 696 nm.*

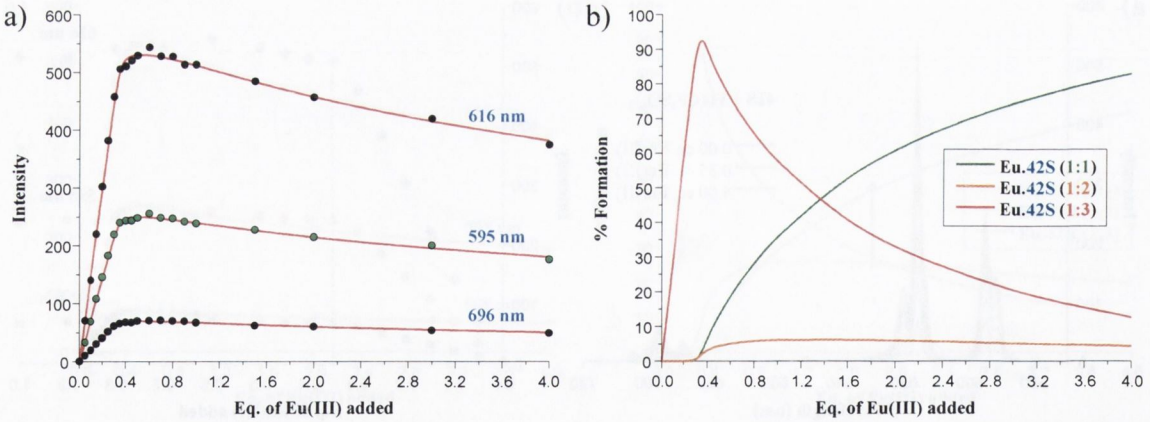

Figure A2.70: *a) Experimental binding isotherms for the phosphorescence titration of* ***42R*** *(1 × 10^{-5} M) with $Eu(CF_3SO_3)_3$ in CH_3CN at 298 K (λ_{exc} = 281 nm) and their corresponding fit by means of SPECFIT. b) Speciation-distribution diagram obtained from the fit.*

Appendix 3

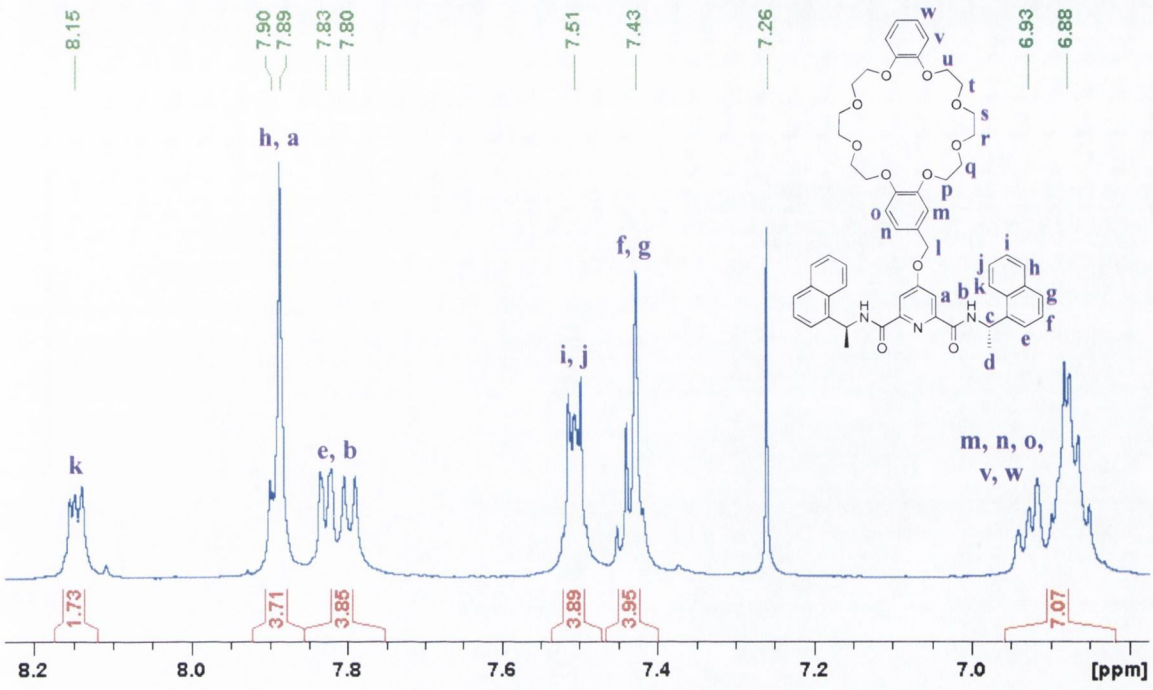

Figure A3.1: *^{1}H NMR (600 MHz, $CDCl_3$) spectrum of ligand **51S** focusing on the aromatic signals.*

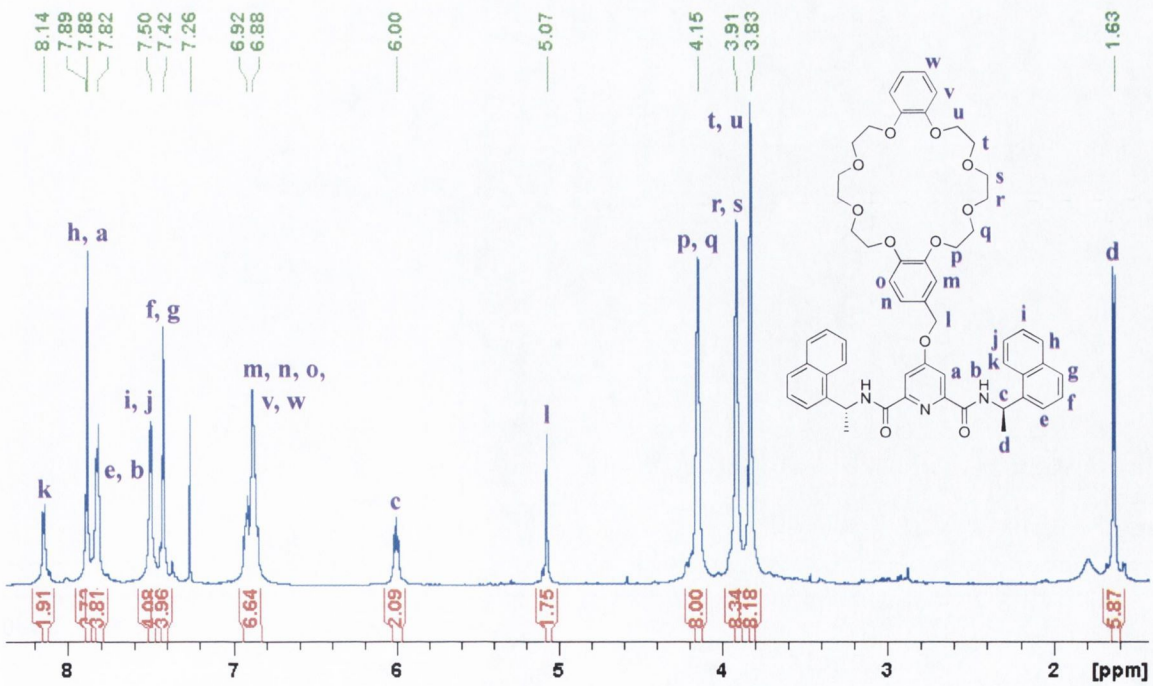

Figure A3.2: *^{1}H NMR (600 MHz, $CDCl_3$) spectrum of ligand **51R**.*

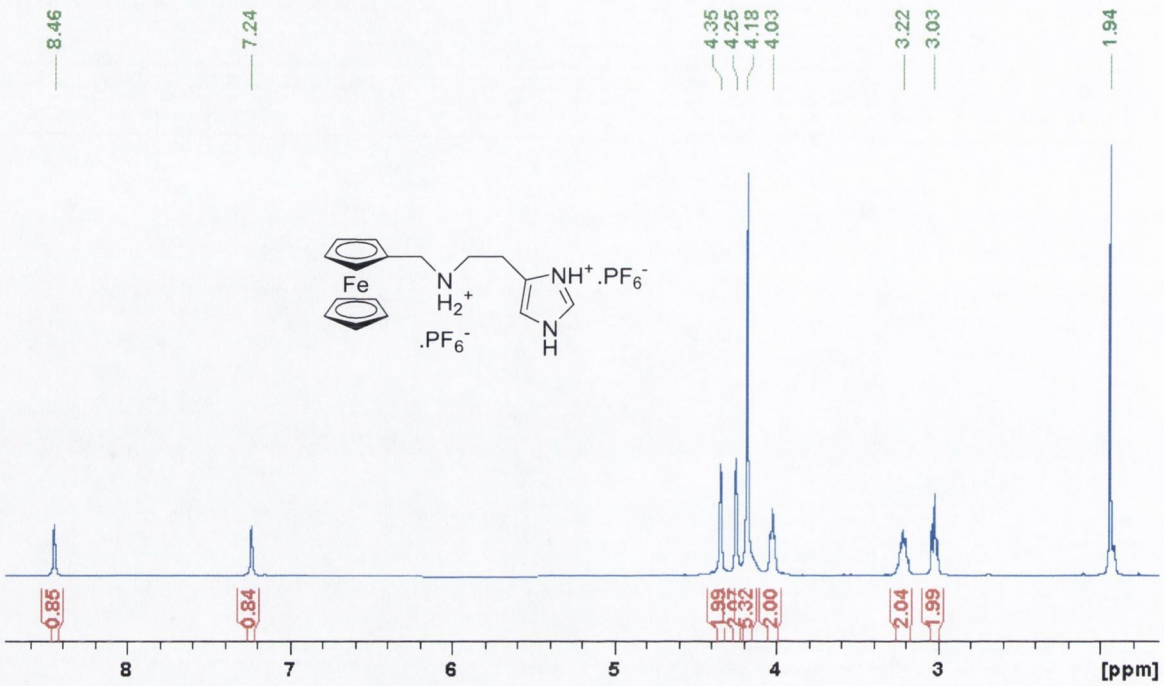

Figure A3.3: *^{1}H NMR (400 MHz, CD_3CN-d_3) spectrum of ligand* **56**.

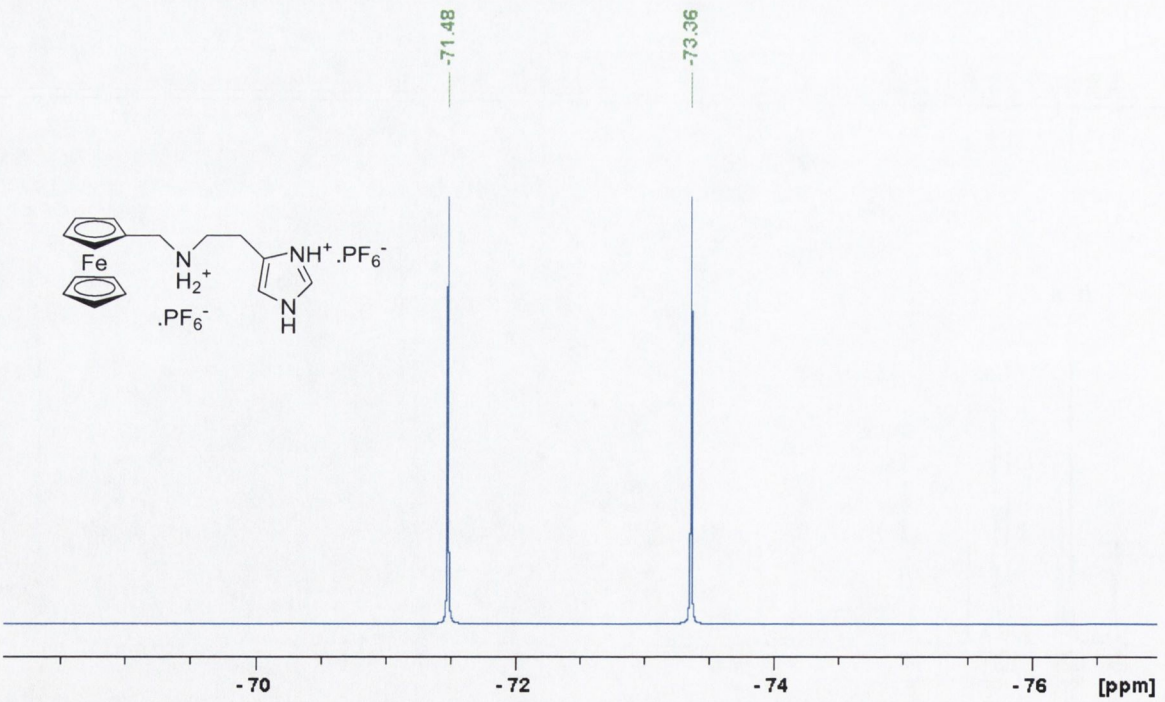

Figure A3.4: *^{19}F NMR (376 MHz, CD_3CN-d_3) spectrum of ligand* **56**.

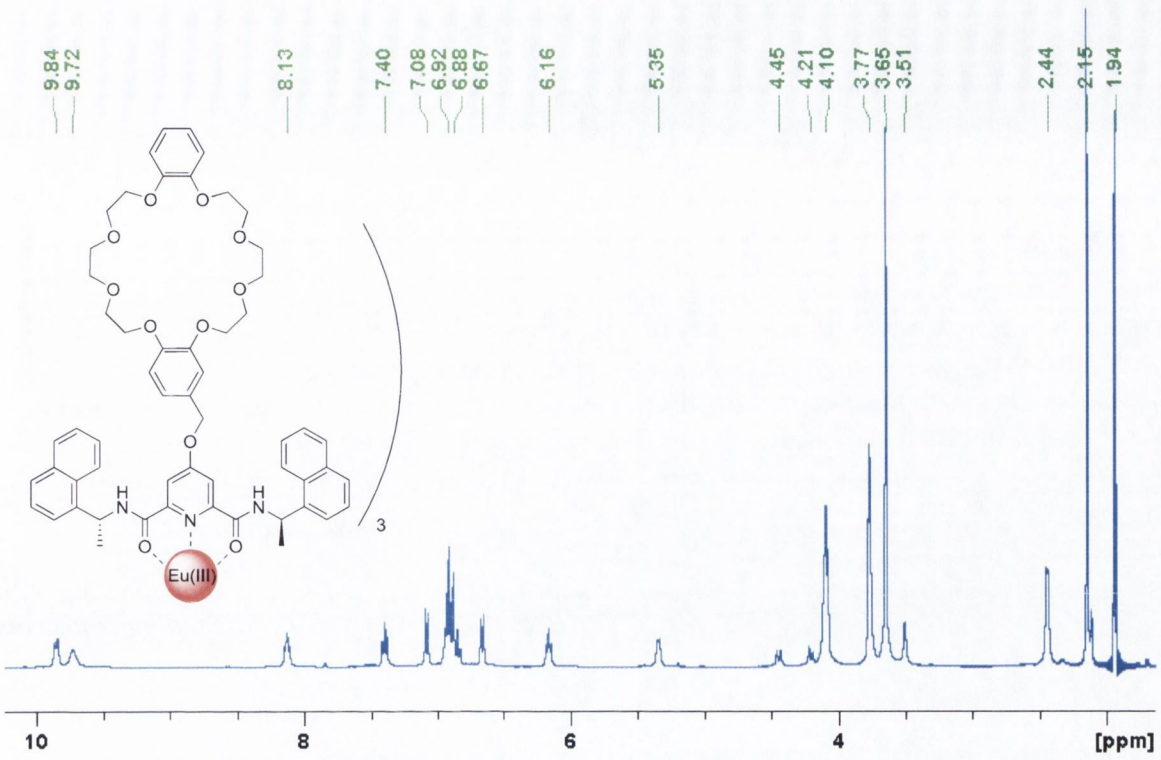

Figure A3.5: *^{1}H NMR (400 MHz, CD_3CN-d_3) spectrum of complex* ***Eu.51R$_3$****.*

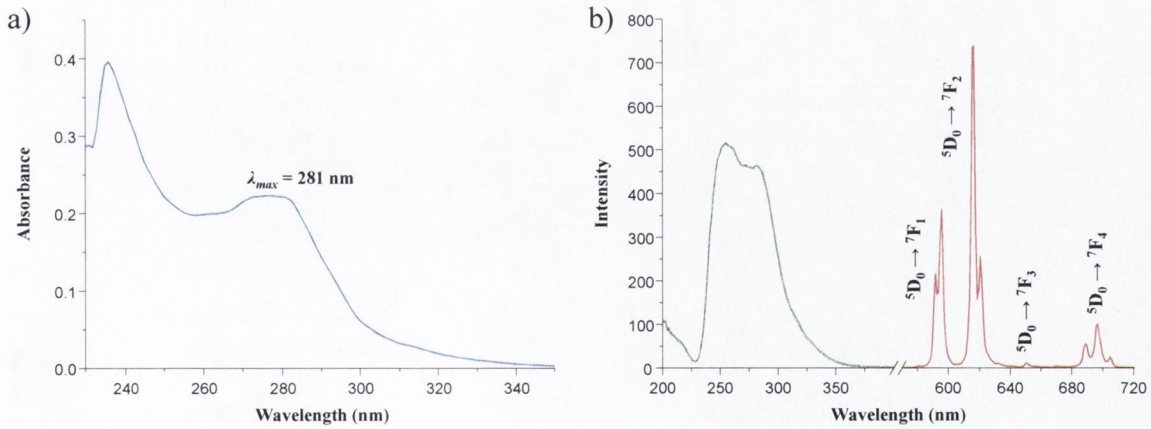

Figure A3.6: *a) UV-vis absorption and b) phosphorescence excitation (green) and emission (red) spectrum (λ_{exc} = 281 nm) of* ***Eu.51S$_3$*** *(ca. 3.33 × 10^{-6} M) recorded in $CHCl_3$/CH_3CN (1:1; v/v) at 298 K.*

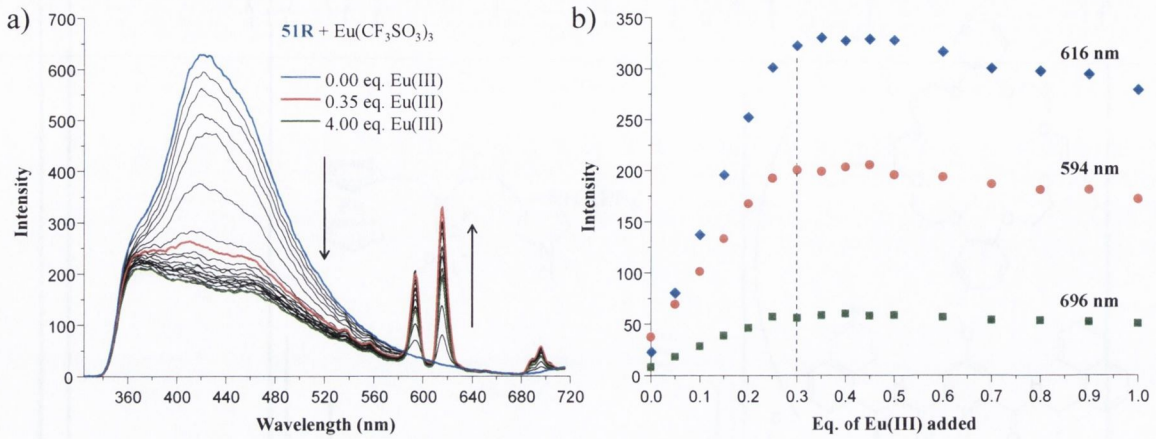

Figure A3.7: *a) Changes in the fluorescence spectra of* ***51R*** *(1×10^{-5} M) upon titrating with $Eu(CF_3SO_3)_3$ (0.00 → 4.00 eq.) in $CHCl_3/CH_3CN$ (1:1; v/v) at 298 K. b) Binding isotherms for the titration measured at 594 nm, 616 nm, and 696 nm.*

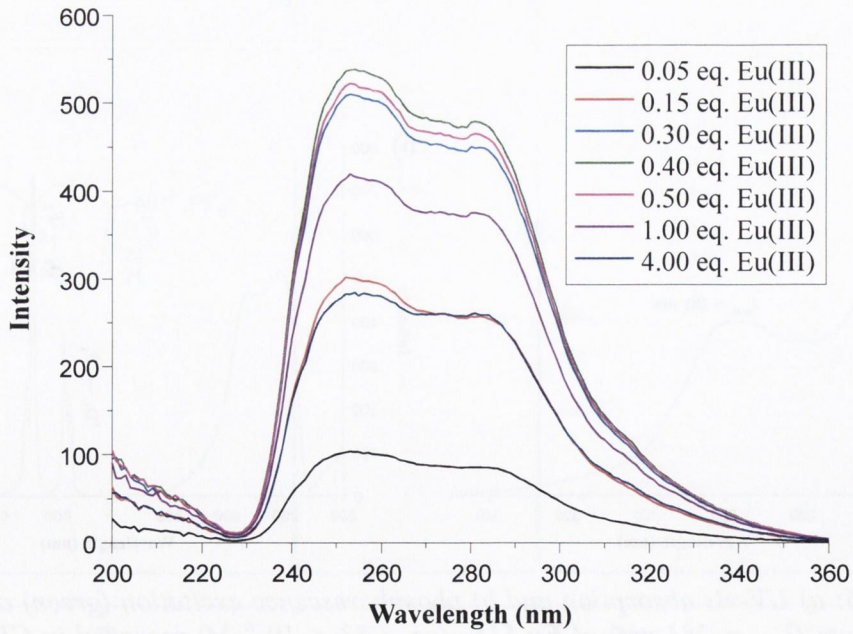

Figure A3.8: *Phosphorescence excitation spectra measured at 616 nm for the titration of* ***51R*** *(1×10^{-5} M) with $Eu(CF_3SO_3)_3$ (0.00 → 4.00 eq.) in $CHCl_3/CH_3CN$ (1:1; v/v) at 298 K.*

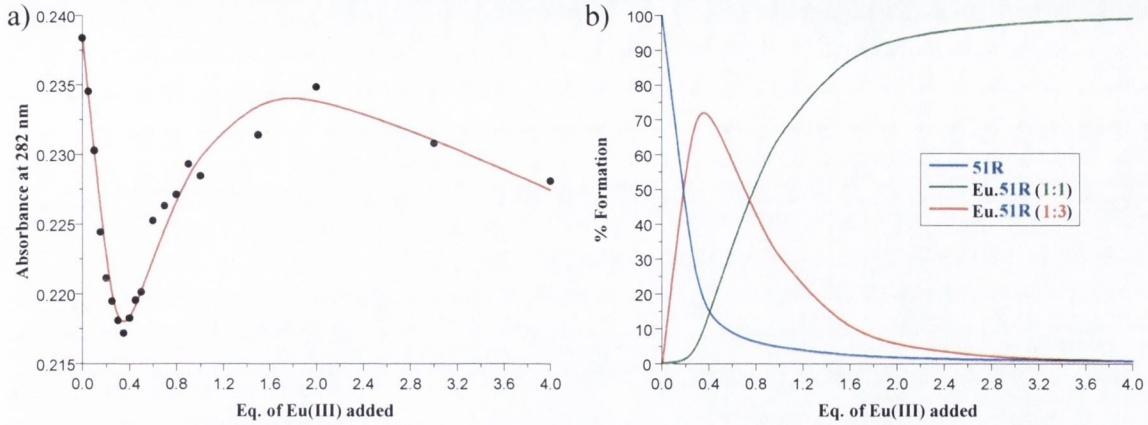

Figure A3.9: *a) Experimental binding isotherms for the UV-vis absorption titration of* ***51R*** *(1×10^{-5} M) with $Eu(CF_3SO_3)_3$ in $CHCl_3/CH_3CN$ (1:1; v/v) at 298 K and their corresponding fit by means of SPECFIT. b) Speciation-distribution diagram obtained from the fit.*

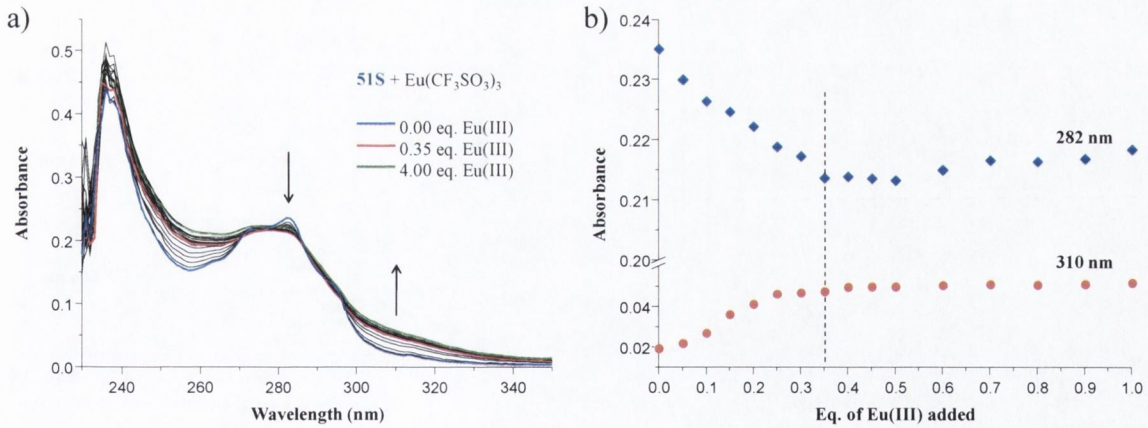

Figure A3.10: *a) Changes in the absorption spectra of* ***51S*** *(1×10^{-5} M) upon titrating with $Eu(CF_3SO_3)_3$ (0.00 → 4.00 eq.) in $CHCl_3/CH_3CN$ (1:1; v/v) at 298 K. b) Binding isotherms for the titration measured at 282 nm and 310 nm.*

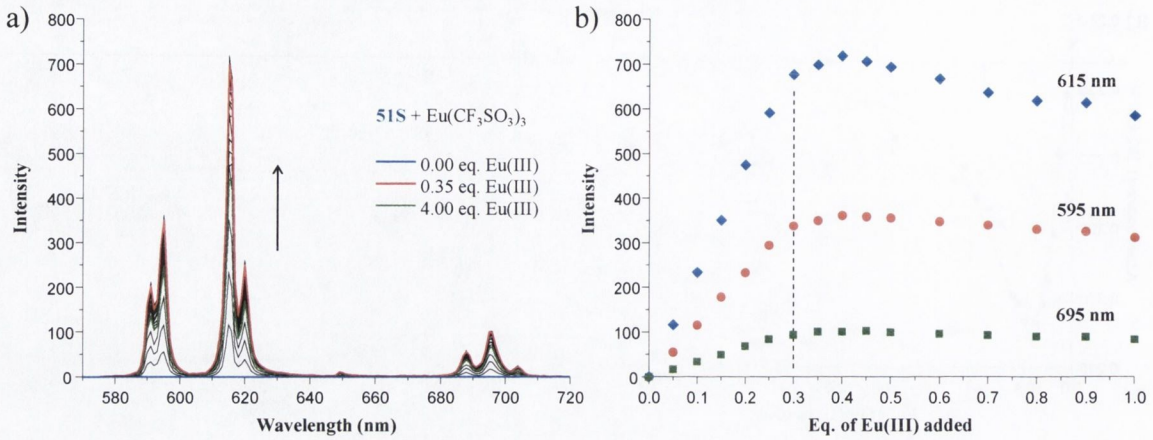

Figure A3.11: *a) Evolution of the phosphorescence emission in the titration of* ***51S*** *(1×10^{-5} M) with $Eu(CF_3SO_3)_3$ (0.00 → 4.00 eq.) in $CHCl_3/CH_3CN$ (1:1; v/v) at 298 K (λ_{exc} = 281 nm). b) Binding isotherms for the titration measured at 595 nm, 616 nm, and 696 nm.*

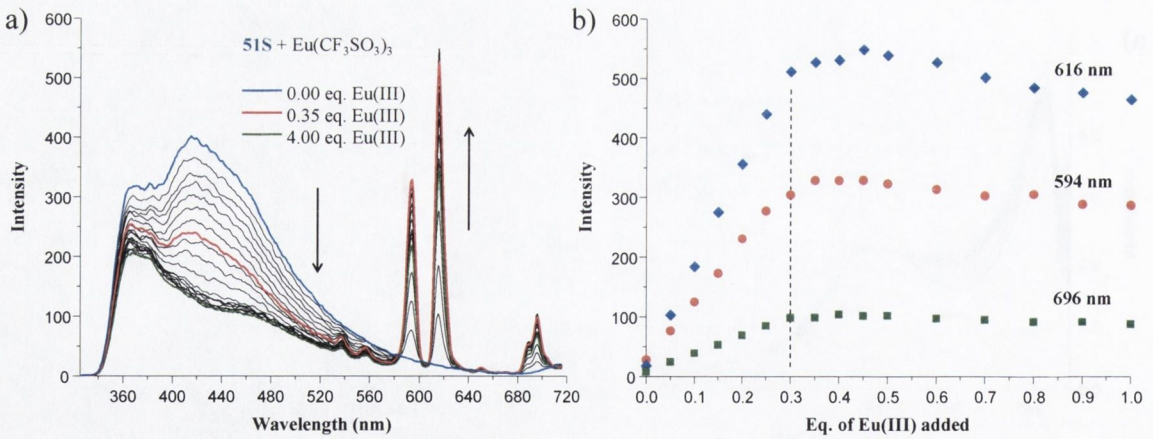

Figure A3.12: *a) Changes in the fluorescence spectra of* ***51S*** *(1×10^{-5} M) upon titrating with $Eu(CF_3SO_3)_3$ (0.00 → 4.00 eq.) in $CHCl_3/CH_3CN$ (1:1; v/v) at 298 K. b) Binding isotherms for the titration measured at 594 nm, 616 nm, and 696 nm.*

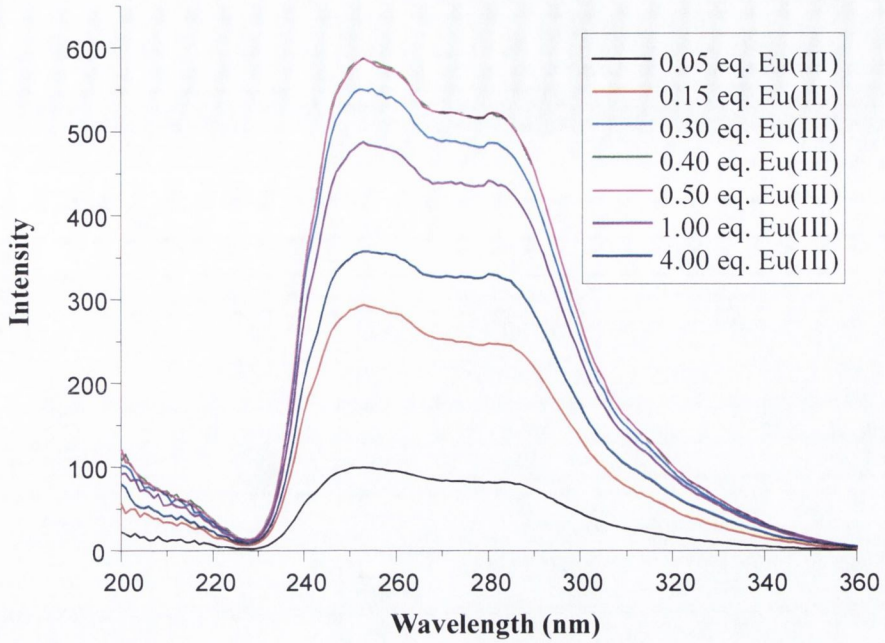

Figure A3.13: *Phosphorescence excitation spectra measured at 616 nm for the titration of* ***51S*** *(1×10^{-5} M) with $Eu(CF_3SO_3)_3$ (0.00 → 4.00 eq.) in $CHCl_3/CH_3CN$ (1:1; v/v) at 298 K.*

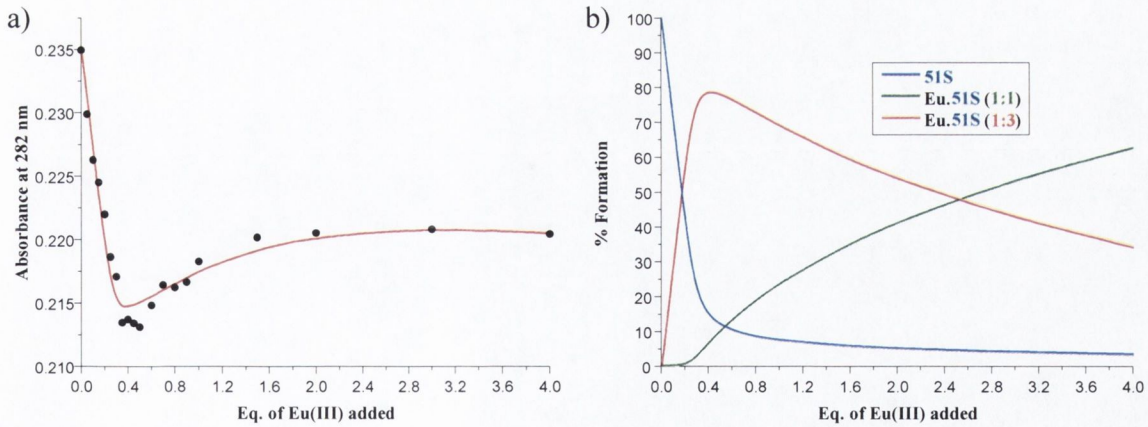

Figure A3.14: *a) Experimental binding isotherms for the UV-vis absorption titration of* ***51S*** *(1×10^{-5} M) with $Eu(CF_3SO_3)_3$ in $CHCl_3/CH_3CN$ (1:1; v/v) at 298 K and their corresponding fit by means of SPECFIT. b) Speciation-distribution diagram obtained from the fit.*

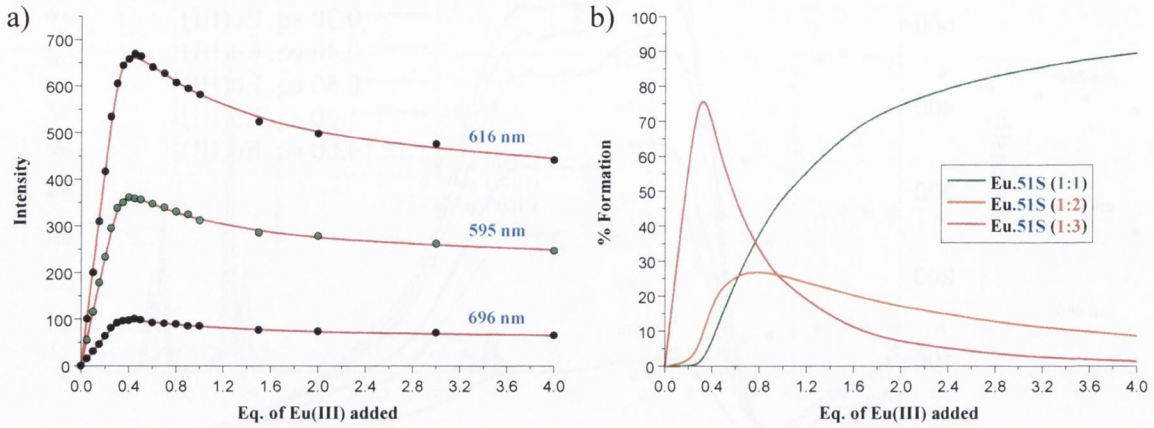

Figure A3.15: *a) Experimental binding isotherms for the phosphorescence titration of* ***51S*** *(1 × 10^{-5} M) with $Eu(CF_3SO_3)_3$ in $CHCl_3/CH_3CN$ (1:1; v/v) at 298 K (λ_{exc} = 281 nm) and their corresponding fit by means of SPECFIT. b) Speciation-distribution diagram obtained from the fit.*

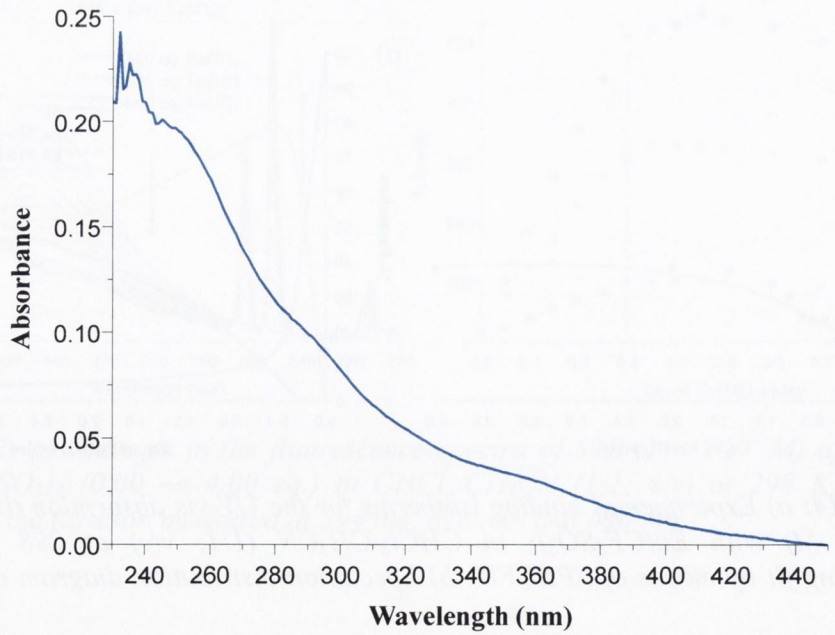

Figure A3.16: *UV-vis absorption spectrum of thread* ***56*** *(2.2 × 10^{-5} M) in $CHCl_3/CH_3CN$ (1:1; v/v).*

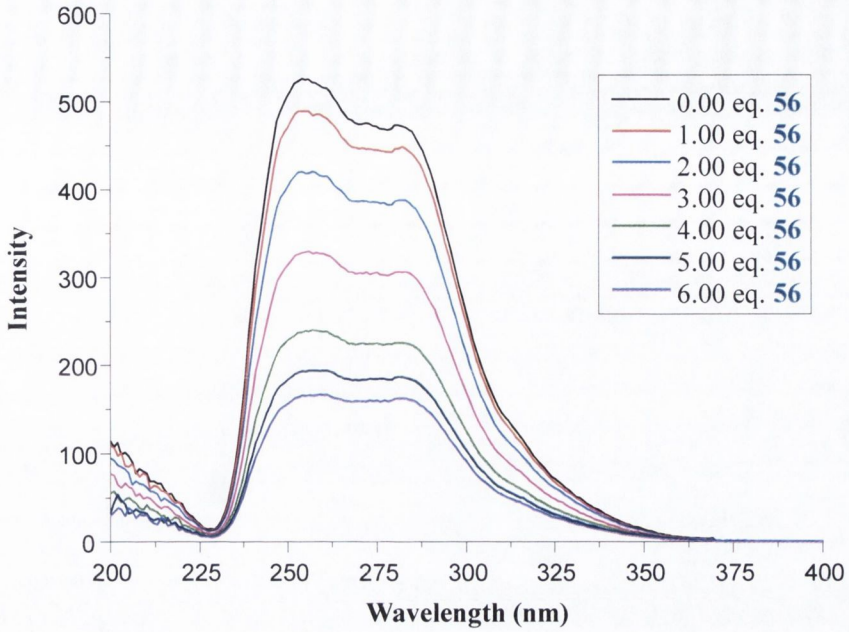

Figure A3.17: *Phosphorescence excitation spectra measured at 616 nm for the titration of* ***Eu.51S$_3$*** *(3.33 × 10^{-6} M) with* ***56*** *(0.00 → 6.00 eq.) in $CHCl_3/CH_3CN$ (1:1; v/v) at 298 K.*

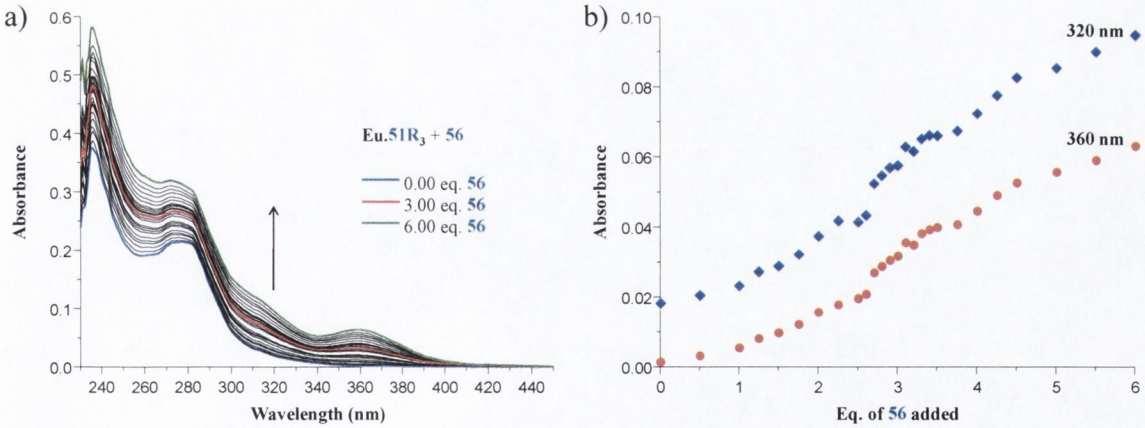

Figure A3.18: *a) Changes in the absorption spectra of* ***Eu.51R$_3$*** *(3.33 × 10^{-6} M) upon titrating with* ***56*** *(0.00 → 6.00 eq.) in $CHCl_3/CH_3CN$ (1:1; v/v) at 298 K. b) Binding isotherms for the titration measured at 320 nm and 360 nm.*

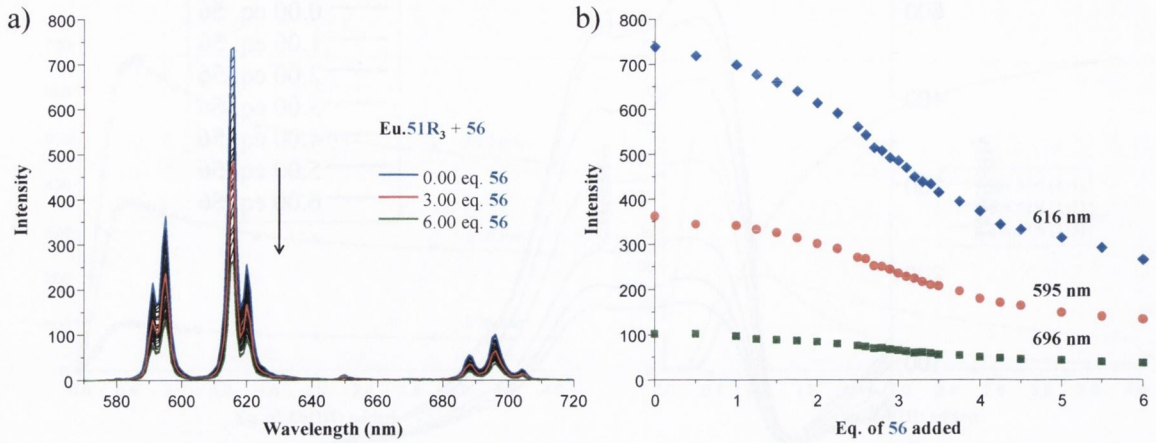

Figure A3.19: *a) Evolution of the phosphorescence emission in the titration of* ***Eu.51R$_3$*** *(3.33×10^{-6} M) upon titrating with* ***56*** *(0.00 → 6.00 eq.) in $CHCl_3/CH_3CN$ (1:1; v/v) at 298 K (λ_{exc} = 281 nm). b) Binding isotherms for the titration measured at 595 nm, 616 nm, and 696 nm.*

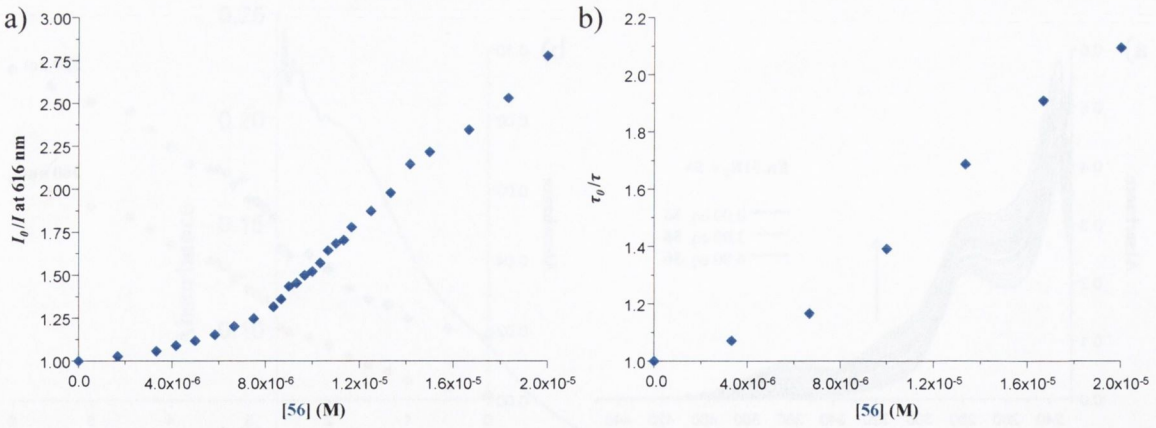

Figure A3.20: *Plots of a) I_0/I at 616 nm Vs. [56] (M) and b) τ_0/τ Vs. [56] for the titration of* ***Eu.51R$_3$*** *(3.33×10^{-6} M) with* ***56*** *(0.00 → 6.00 eq.) in $CHCl_3/CH_3CN$ (1:1; v/v) at 298 K (λ_{exc} = 281 nm).*

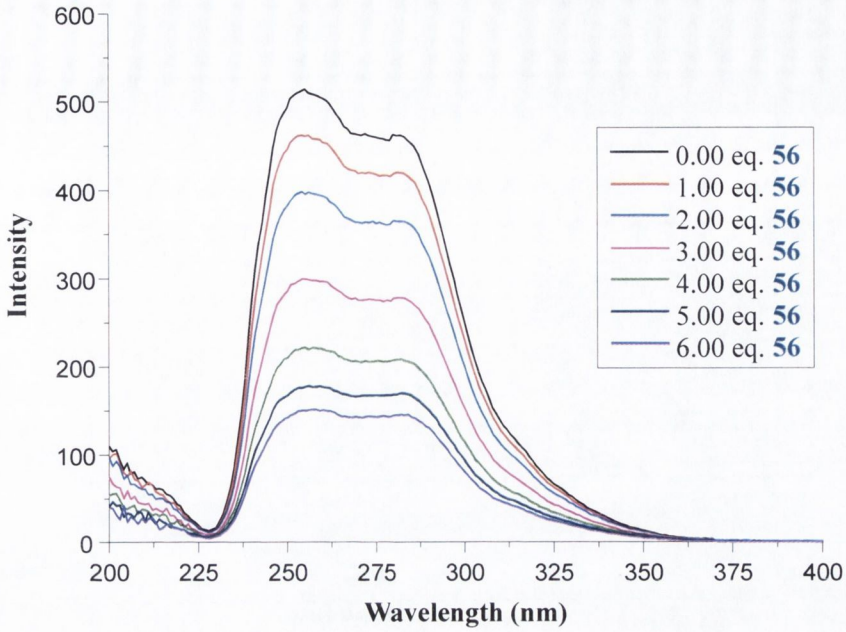

Figure A3.21: *Phosphorescence excitation spectra measured at 616 nm for the titration of* ***Eu.51R$_3$*** *(3.33 × 10^{-6} M) with* ***56*** *(0.00 → 6.00 eq.) in $CHCl_3/CH_3CN$ (1:1; v/v) at 298 K.*

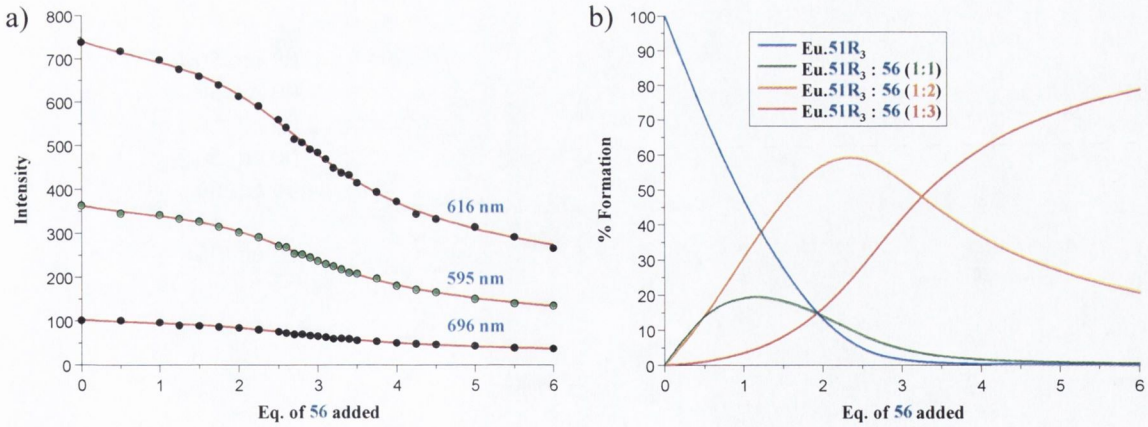

Figure A3.22: *a) Experimental binding isotherms for the phosphorescence titration of* ***Eu.51R$_3$*** *(3.33 × 10^{-6} M) with* ***56*** *in $CHCl_3/CH_3CN$ (1:1; v/v) at 298 K (λ_{exc} = 281 nm) and their corresponding fit by means of SPECFIT. b) Speciation-distribution diagram obtained from the fit.*

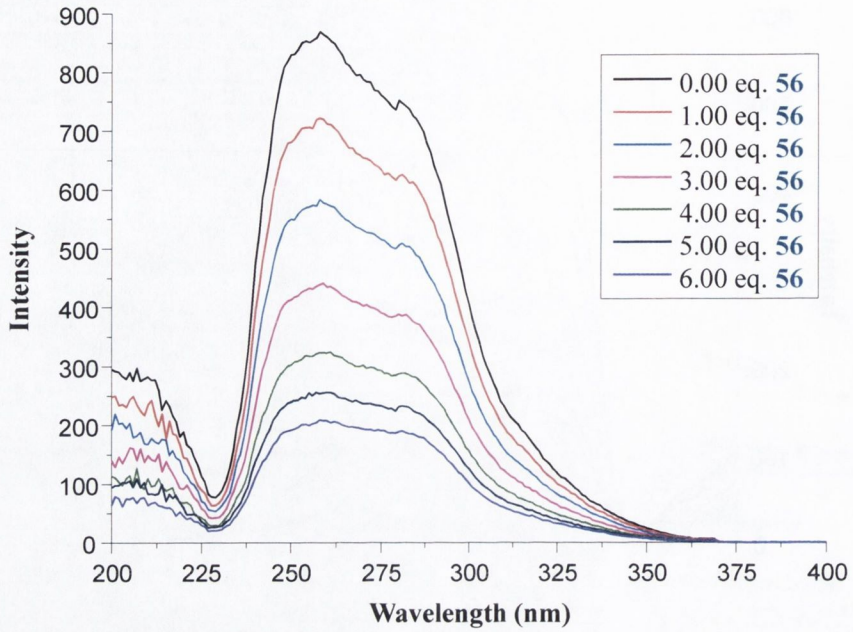

Figure A3.23: *Phosphorescence excitation spectra measured at 616 nm for the titration of* ***Eu.43S$_3$*** *(3.33×10^{-6} M) with* ***56*** *(0.00 → 6.00 eq.) in $CHCl_3/CH_3CN$ (1:1; v/v) at 298 K.*

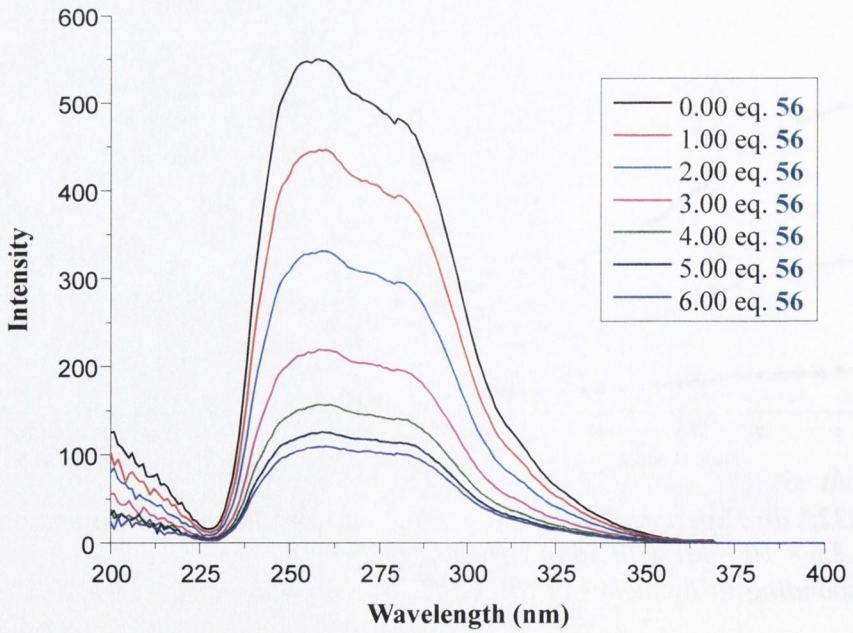

Figure A3.24: *Phosphorescence excitation spectra measured at 616 nm for the titration of* ***Eu.41S$_3$*** *(3.33×10^{-6} M) with* ***56*** *(0.00 → 6.00 eq.) in $CHCl_3/CH_3CN$ (1:1; v/v) at 298 K.*

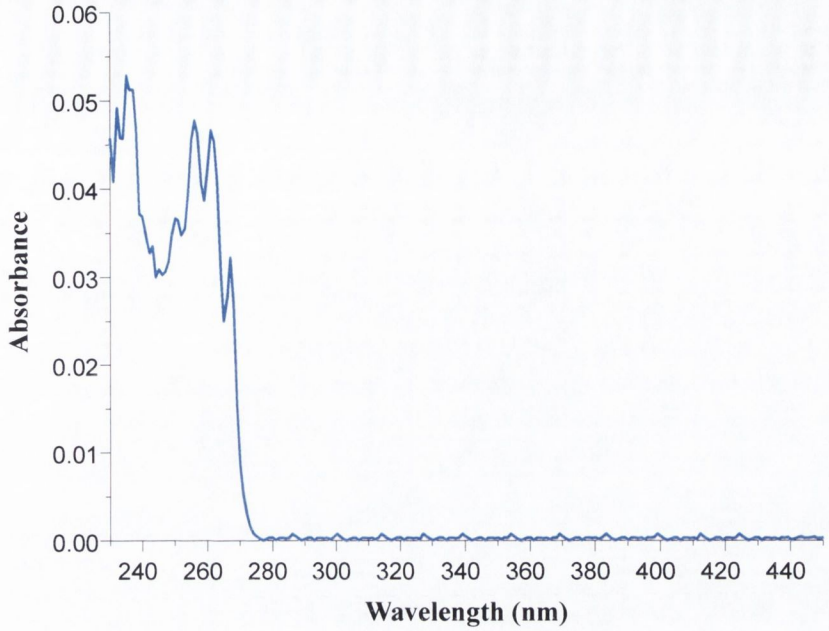

Figure A3.25: *UV-vis absorption spectrum of thread* ***53*** *(8.8 × 10^{-5} M) in $CHCl_3/CH_3CN$ (1:1; v/v).*

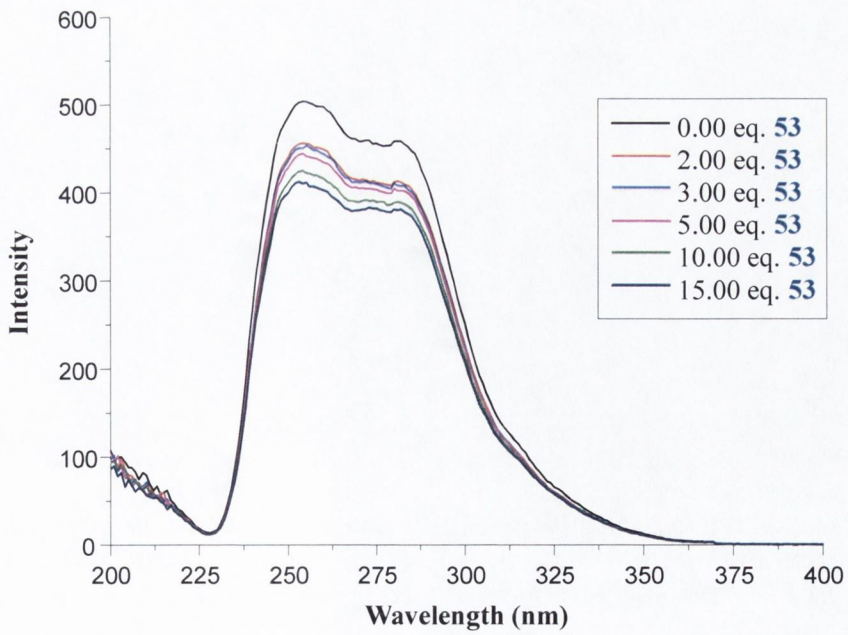

Figure A3.26: *Phosphorescence excitation spectra measured at 616 nm for the titration of* ***Eu.51S$_3$*** *(3.33 × 10^{-6} M) with* ***53*** *(0.00 → 15.00 eq.) in $CHCl_3/CH_3CN$ (1:1; v/v) at 298 K.*

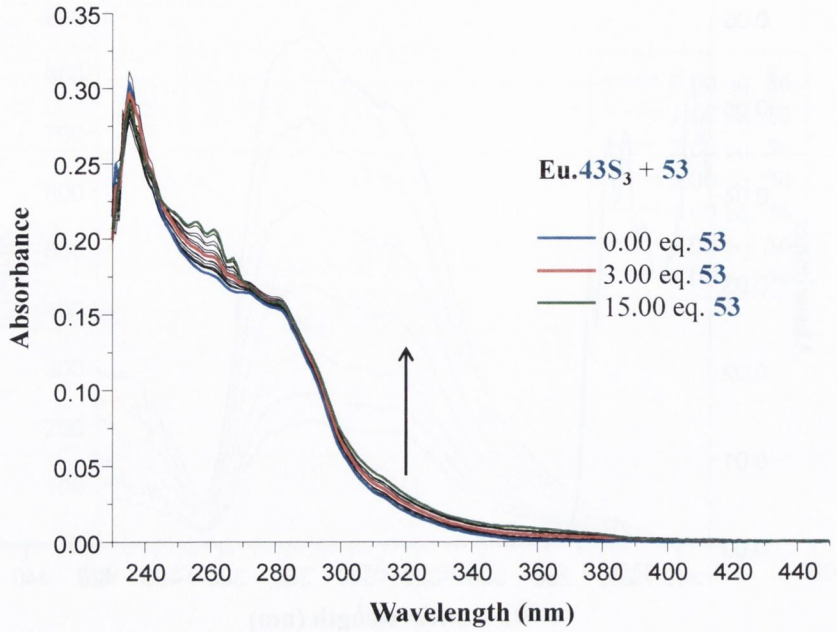

Figure A3.27: *Changes in the absorption spectra of* ***Eu.43S$_3$*** *(3.33 × 10^{-6} M) upon titrating with* ***53*** *(0.00 → 15.00 eq.) in $CHCl_3/CH_3CN$ (1:1; v/v) at 298 K.*

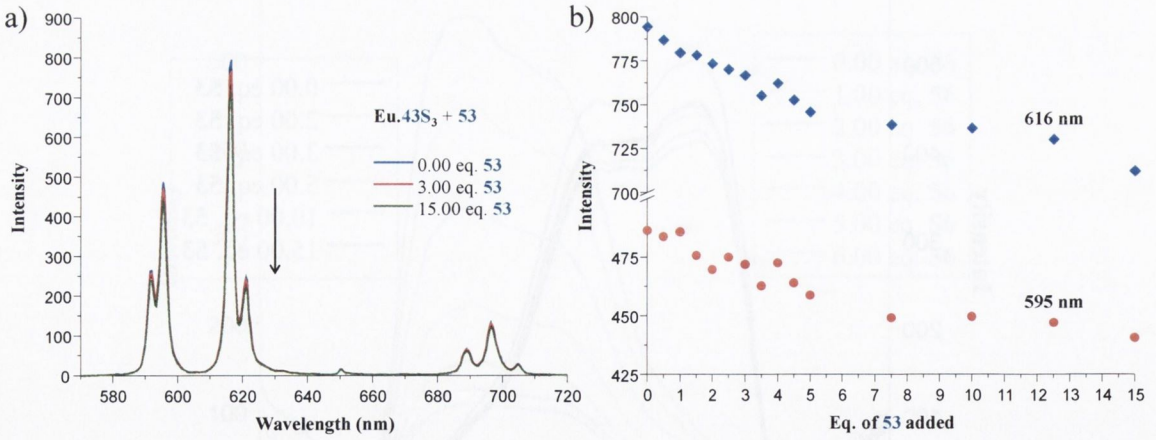

Figure A3.28: *a) Evolution of the phosphorescence emission in the titration of* ***Eu.43S$_3$*** *(3.33 × 10^{-6} M) upon titrating with* ***53*** *(0.00 → 15.00 eq.) in $CHCl_3/CH_3CN$ (1:1; v/v) at 298 K (λ_{exc} = 281 nm). b) Binding isotherms for the titration measured at 595 nm and 616 nm.*

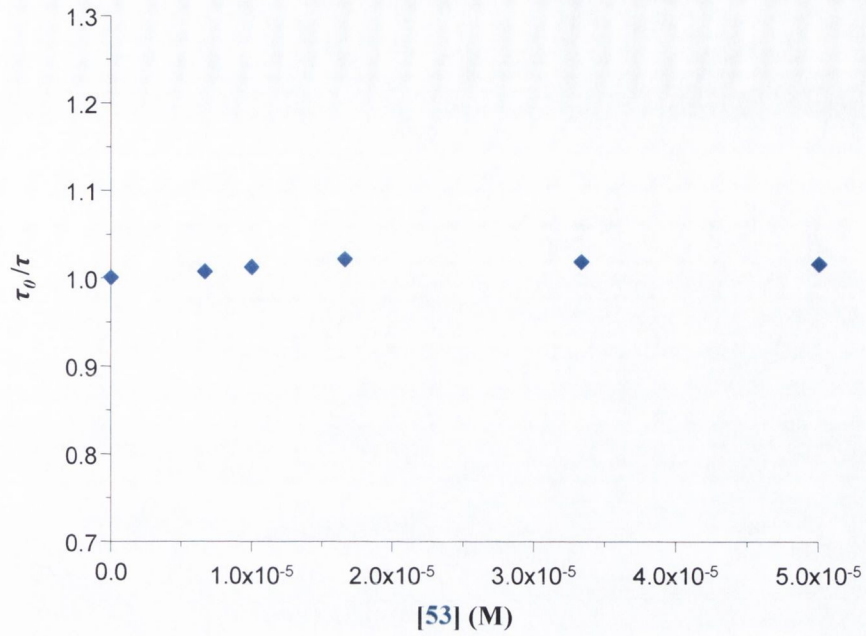

Figure A3.29: *Plots of τ_0/τ Vs. [53] for the titration of* ***Eu.43S$_3$*** *(3.33 × 10^{-6} M) with* ***53*** *(0.00 → 15.00 eq.) in $CHCl_3/CH_3CN$ (1:1; v/v) at 298 K (λ_{exc} = 281 nm).*

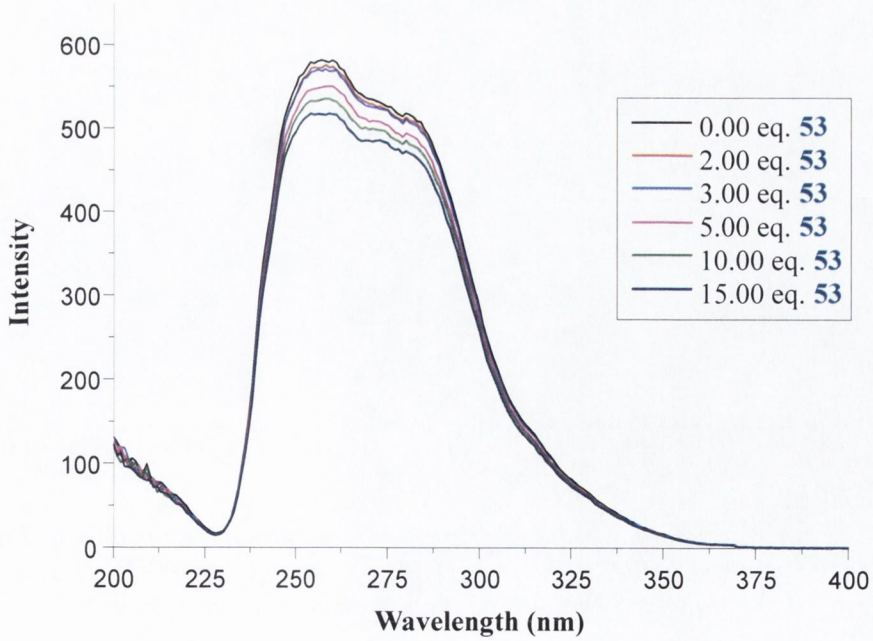

Figure A3.30: *Phosphorescence excitation spectra measured at 616 nm for the titration of* ***Eu.43S$_3$*** *(3.33 × 10^{-6} M) with* ***53*** *(0.00 → 15.00 eq.) in $CHCl_3/CH_3CN$ (1:1; v/v) at 298 K.*

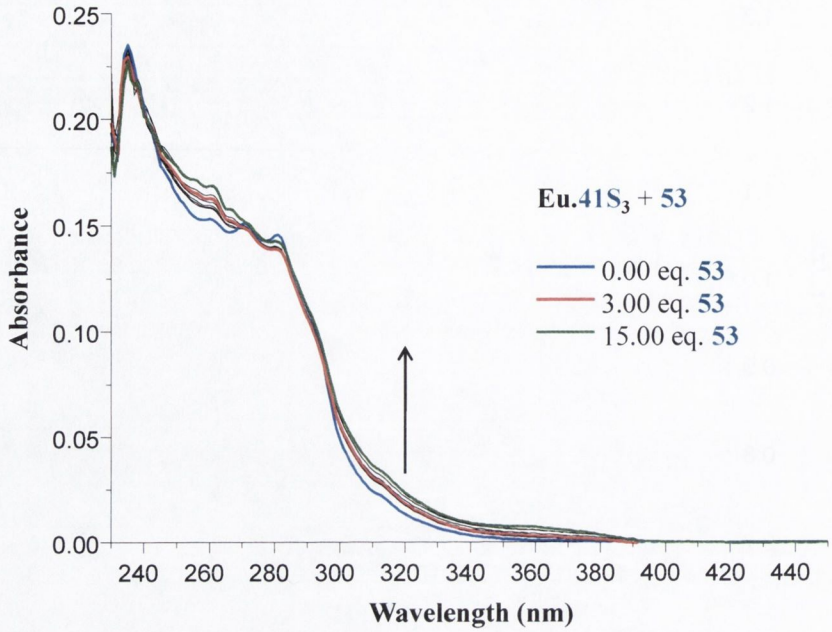

Figure A3.31: *Changes in the absorption spectra of* ***Eu.41S$_3$*** *(3.33 × 10^{-6} M) upon titrating with* ***53*** *(0.00 → 15.00 eq.) in $CHCl_3/CH_3CN$ (1:1; v/v) at 298 K.*

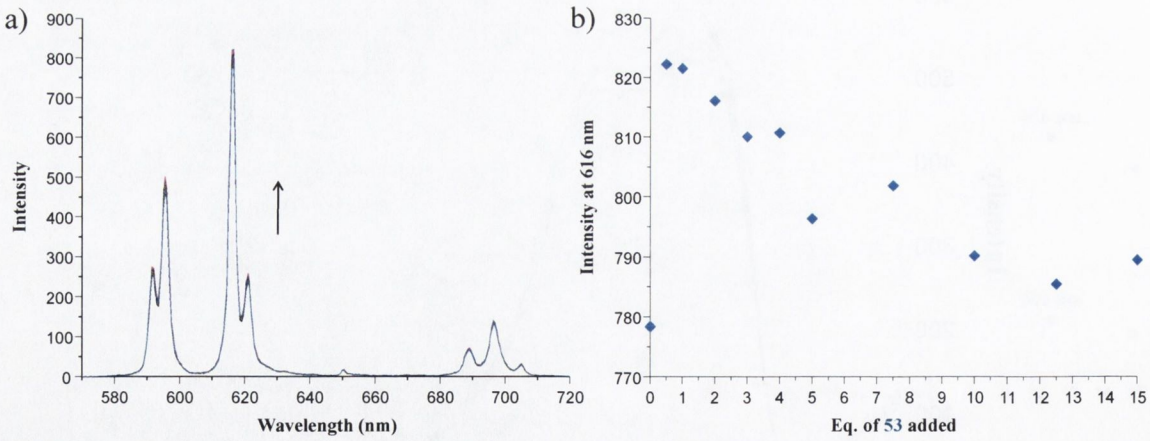

Figure A3.32: *a) Evolution of the phosphorescence emission in the titration of* ***Eu.41S$_3$*** *(3.33 × 10^{-6} M) upon titrating with* ***53*** *(0.00 → 15.00 eq.) in $CHCl_3/CH_3CN$ (1:1; v/v) at 298 K (λ_{exc} = 281 nm). b) Binding isotherm for the titration measured at 616 nm.*

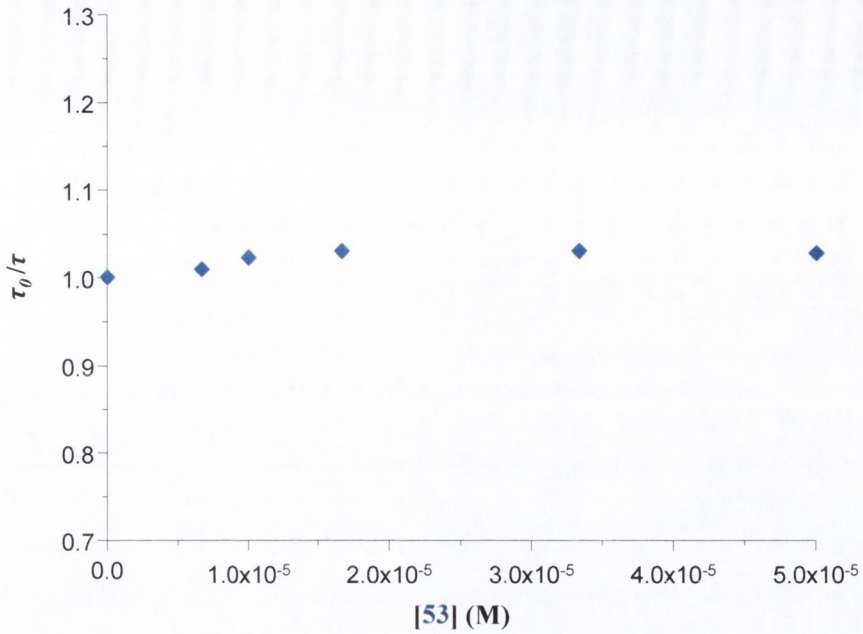

Figure A3.33: *Plots of τ_0/τ Vs. [53] for the titration of* ***Eu.41S$_3$*** *(3.33×10^{-6} M) with* ***53*** *(0.00 → 15.00 eq.) in $CHCl_3/CH_3CN$ (1:1; v/v) at 298 K (λ_{exc} = 281 nm).*

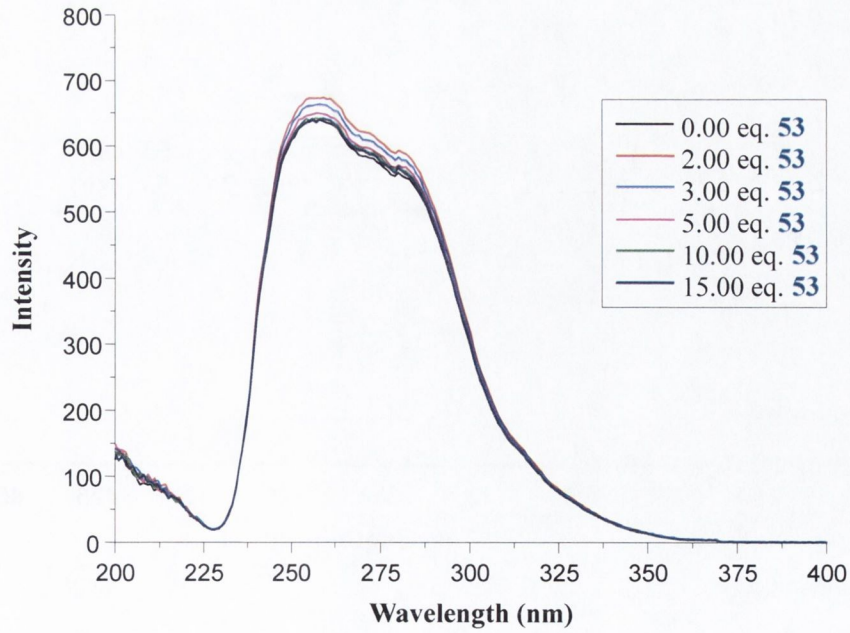

Figure A3.34: *Phosphorescence excitation spectra measured at 616 nm for the titration of* ***Eu.41S$_3$*** *(3.33×10^{-6} M) with* ***53*** *(0.00 → 15.00 eq.) in $CHCl_3/CH_3CN$ (1:1; v/v) at 298 K.*

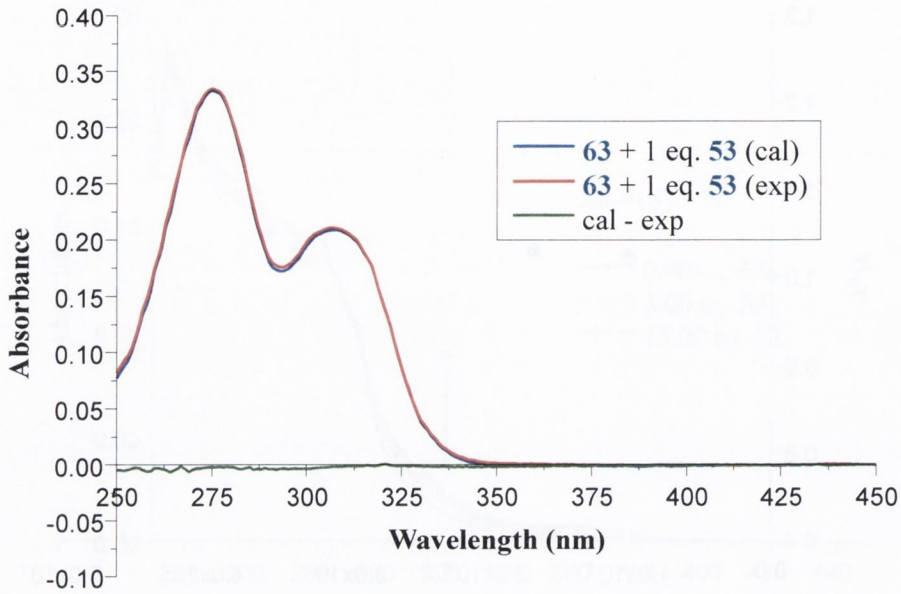

Figure A3.35: *Calculated and experimental UV-vis absorption spectra for the addition of 1 eq. of* ***53*** *to* ***63*** *(2.2×10^{-5} M) in $CHCl_3/CH_3CN$ (1:1; v/v) at 298 K, with the difference between the two spectra mapped by the green line.*

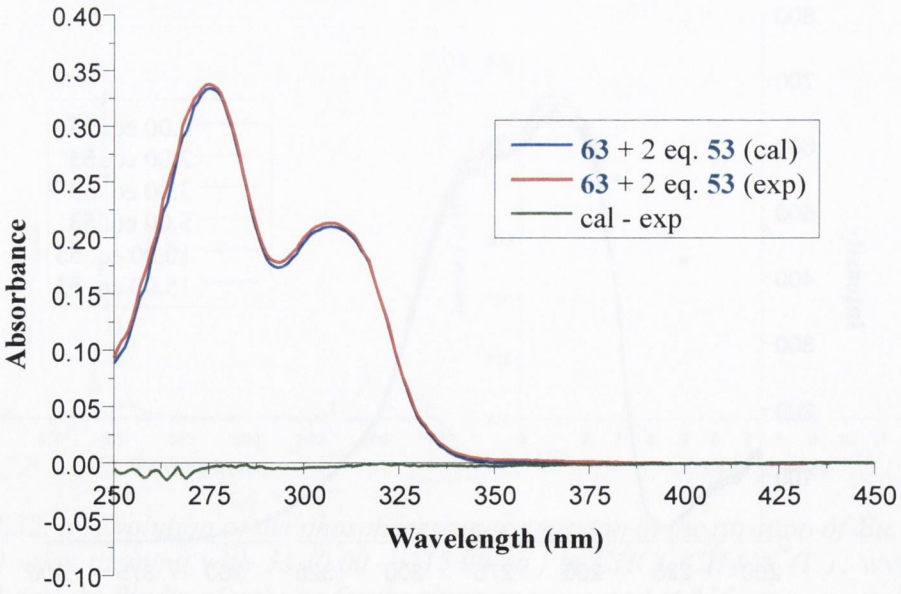

Figure A3.36: *Calculated and experimental UV-vis absorption spectra for the addition of 2 eq. of* ***53*** *to* ***63*** *(2.2×10^{-5} M) in $CHCl_3/CH_3CN$ (1:1; v/v) at 298 K, with the difference between the two spectra mapped by the green line.*

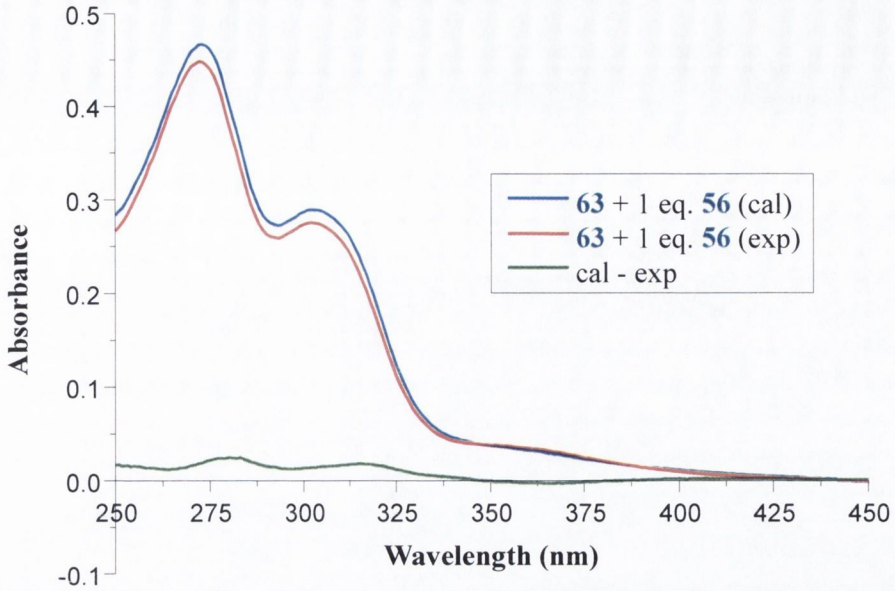

Figure A3.37: *Calculated and experimental UV-vis absorption spectra for the addition of 1 eq. of* ***56*** *to* ***63*** *(2.2 × 10^{-5} M) in $CHCl_3/CH_3CN$ (1:1; v/v) at 298 K, with the difference between the two spectra mapped by the green line.*

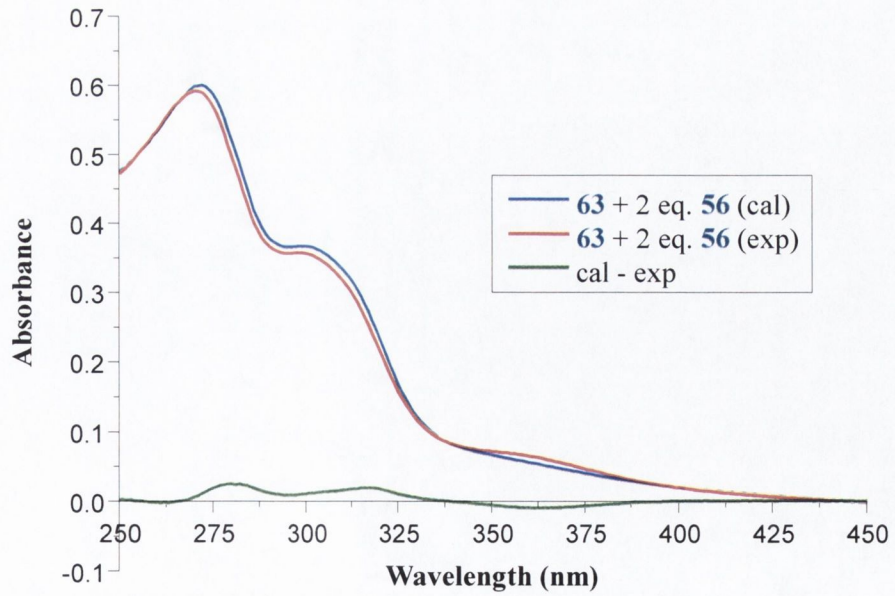

Figure A3.38: *Calculated and experimental UV-vis absorption spectra for the addition of 2 eq. of* ***56*** *to* ***63*** *(2.2 × 10^{-5} M) in $CHCl_3/CH_3CN$ (1:1; v/v) at 298 K, with the difference between the two spectra mapped by the green line.*

Appendix 4

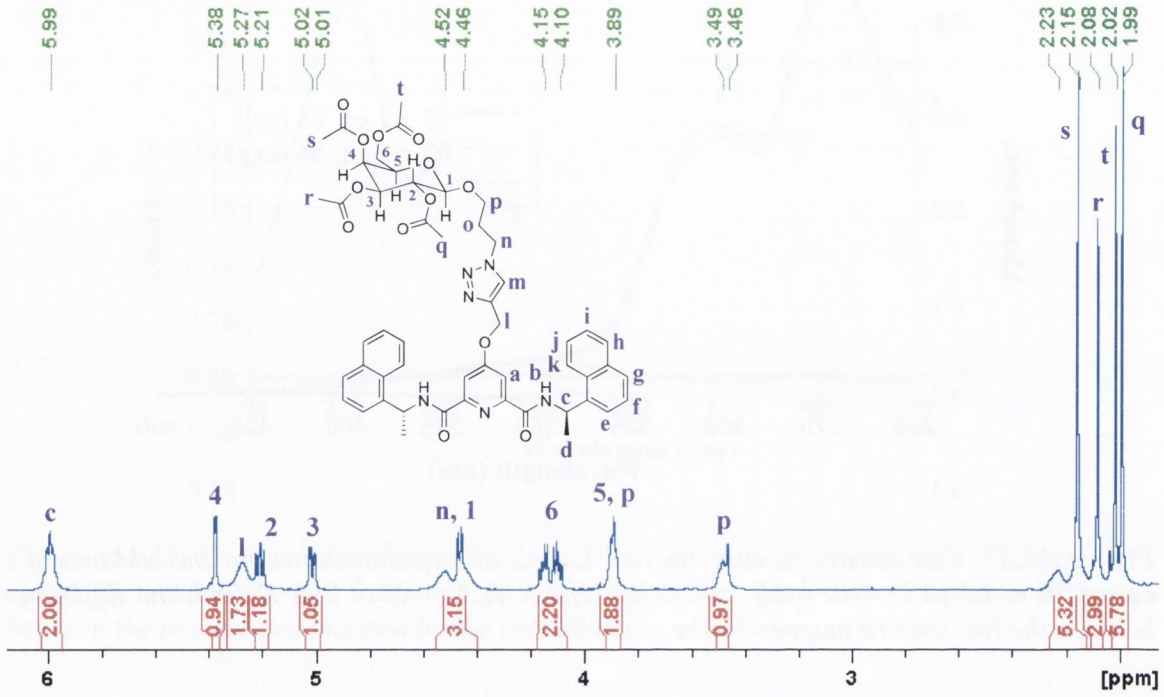

Figure A4.1: *^{1}H NMR (600 MHz, $CDCl_3$) spectrum of ligand **69R** focusing on the sugar signals.*

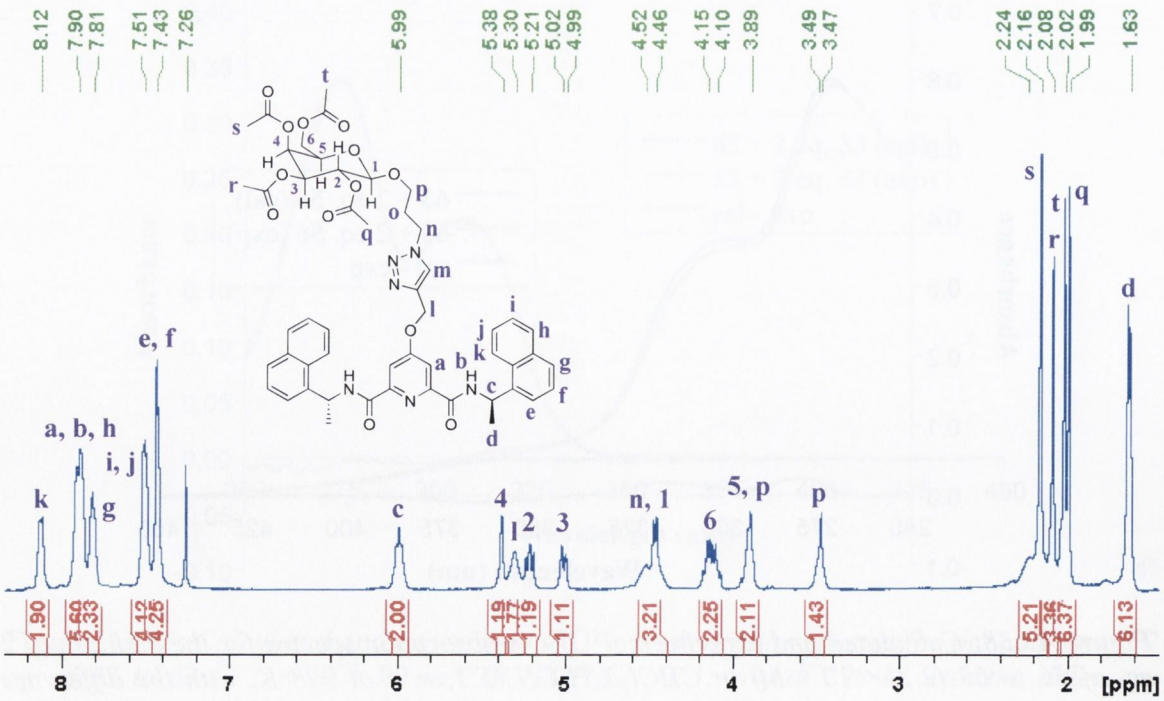

Figure A4.2: *^{1}H NMR (600 MHz, $CDCl_3$) spectrum of ligand **69S**.*

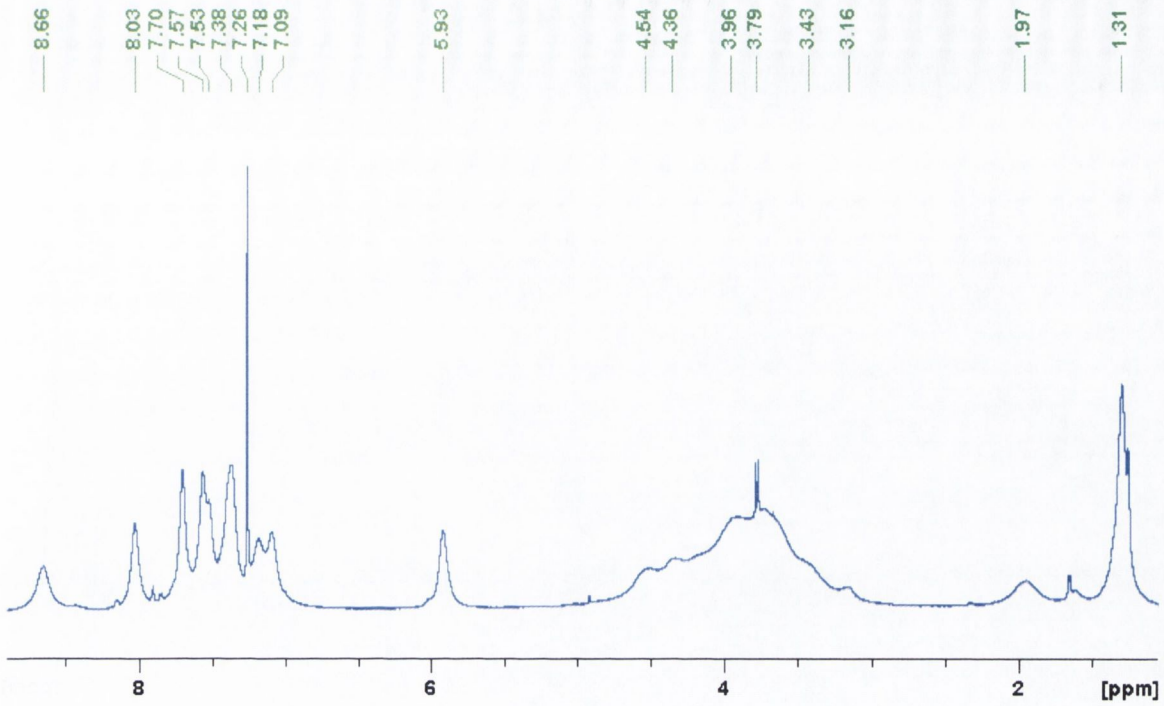

Figure A4.3: *^{1}H NMR (600 MHz, $CDCl_3$) spectrum of ligand "**71S**".*

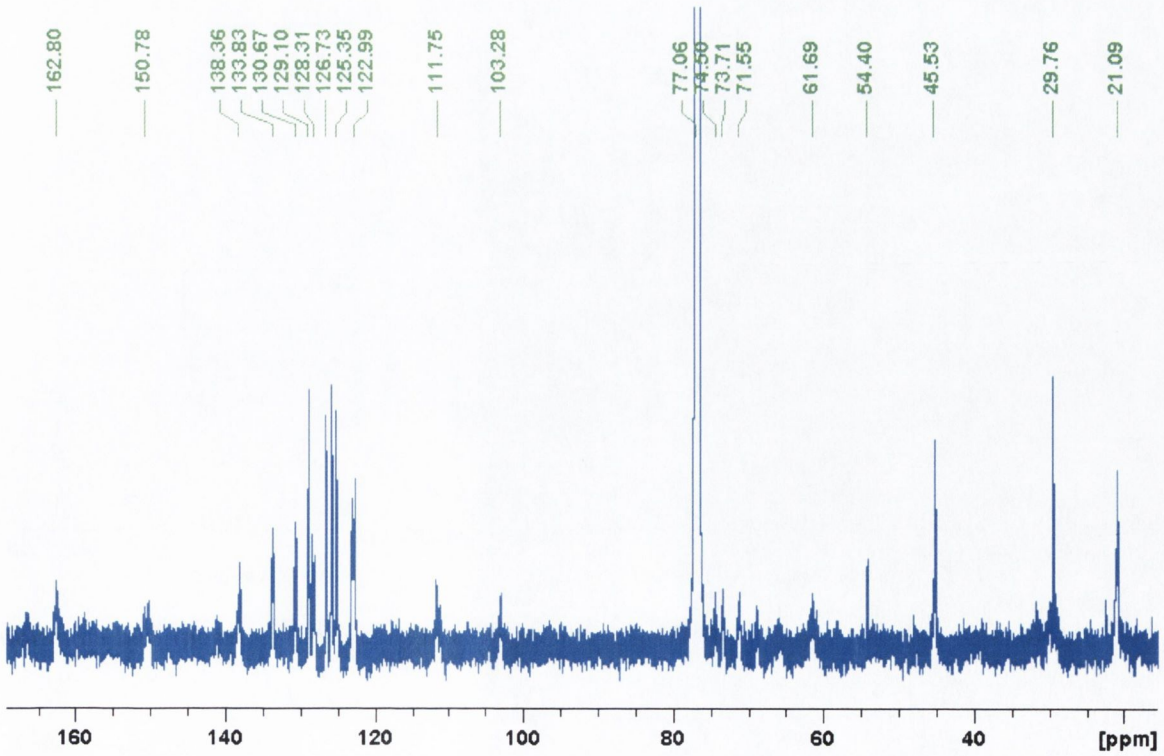

Figure A4.4: *^{13}C NMR (150 MHz, $CDCl_3$) spectrum of ligand "**71S**".*

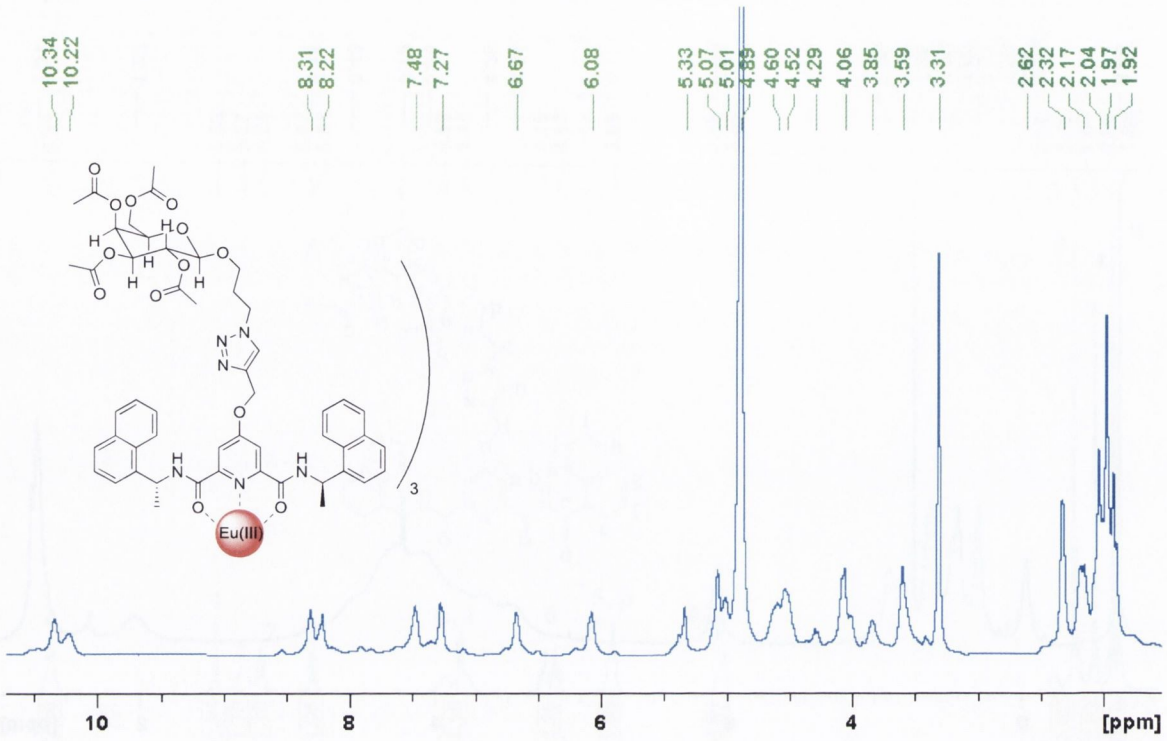

Figure A4.5: *^{1}H NMR (400 MHz, CD_3OD-d_4) of complex* ***Eu.69R$_3$****.*

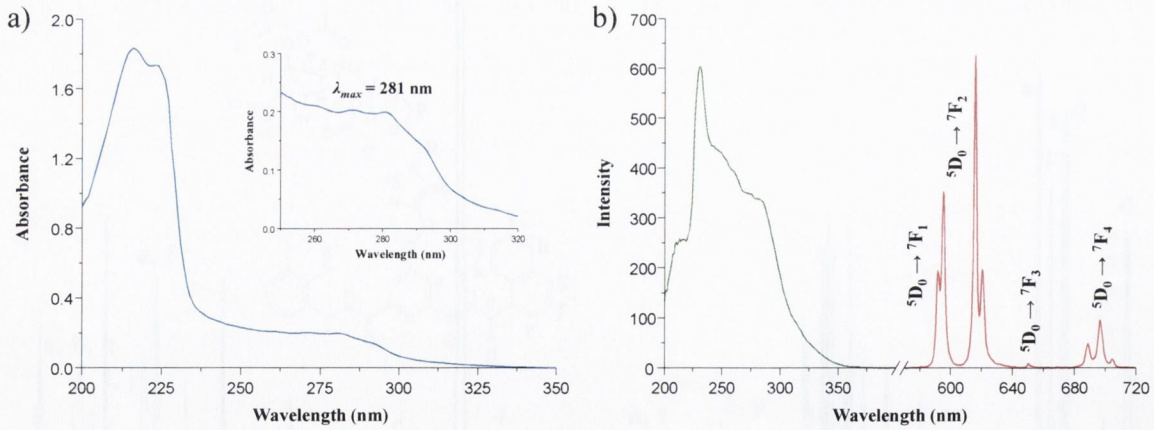

Figure A4.6: *a) UV-vis absorption and b) phosphorescence excitation (green) and emission (red) spectra (λ_{exc} = 281 nm) of* ***Eu.69S$_3$*** *(ca. 5.4 × 10^{-6} M) recorded in CH_3CN at 298 K.*

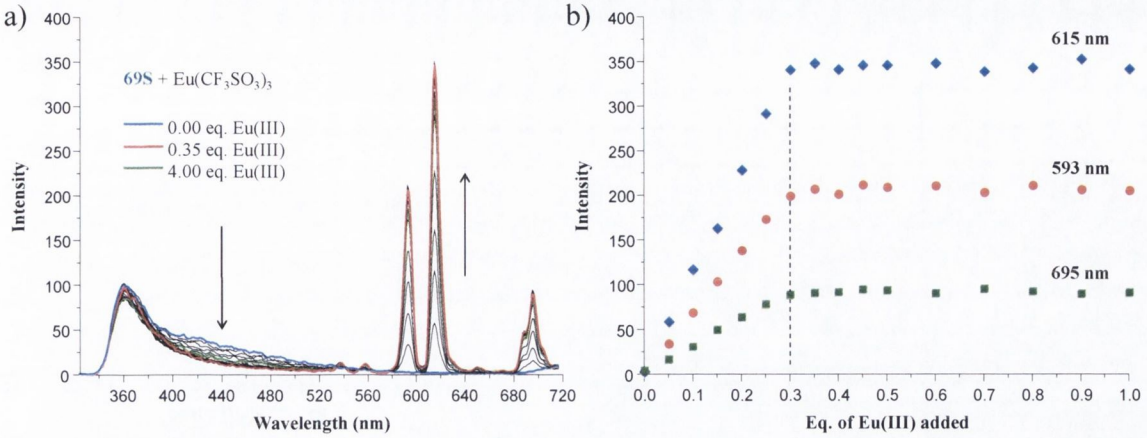

Figure A4.7: *a) Changes in the fluorescence spectra of* ***69S*** *(1×10^{-5} M) upon titrating with $Eu(CF_3SO_3)_3$ (0.00 → 4.00 eq.) in CH_3CN at 298 K. b) Binding isotherms for the titration measured at 593 nm, 615 nm, and 695 nm.*

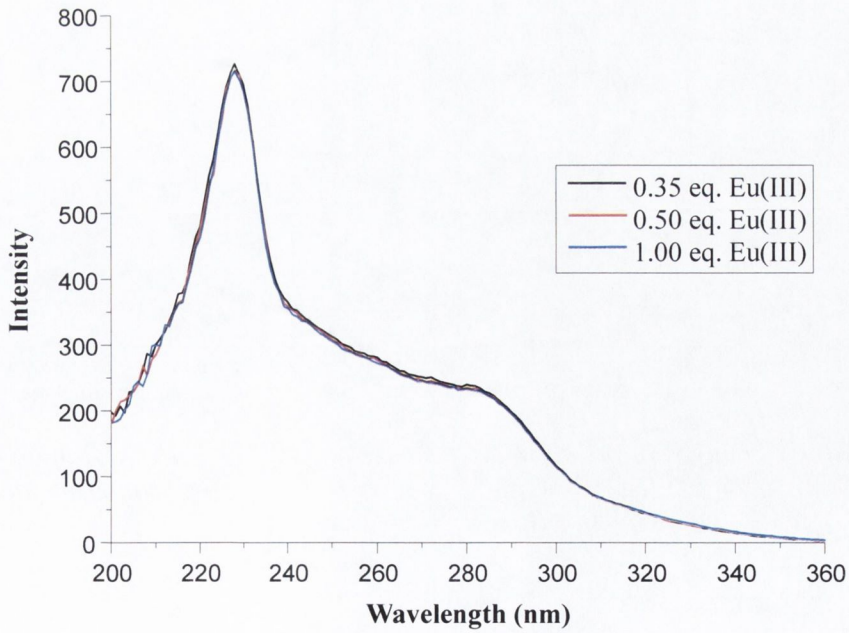

Figure A4.8: *Phosphorescence excitation spectra measured at 616 nm for the titration of* ***69S*** *(1×10^{-5} M) with $Eu(CF_3SO_3)_3$ (0.00 → 4.00 eq.) in CH_3CN at 298 K.*

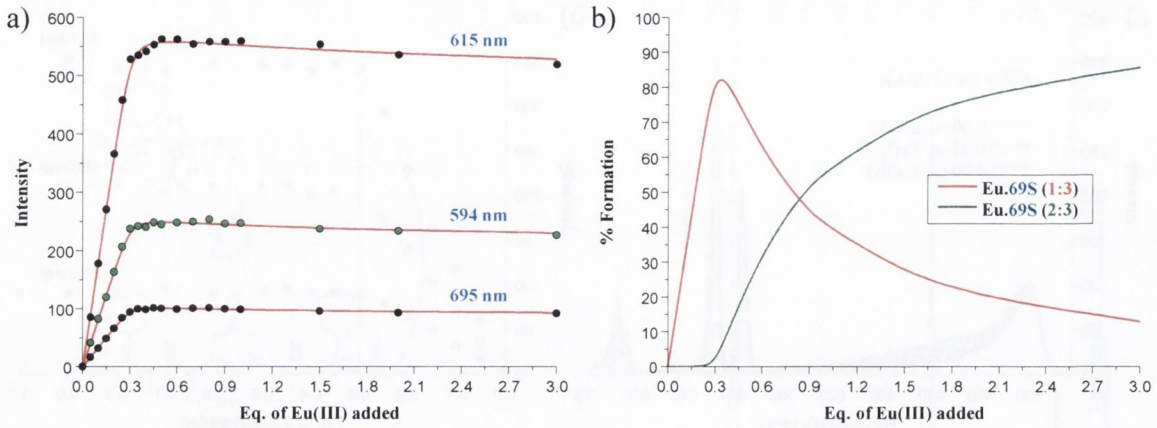

Figure A4.9: *a) Experimental binding isotherms for the phosphorescence titration of* ***69S*** *(1 × 10^{-5} M) with $Eu(CF_3SO_3)_3$ in CH_3CN at 298 K (λ_{exc} = 281 nm) and their corresponding fit by means of SPECFIT. b) Speciation-distribution diagram obtained from the fit.*

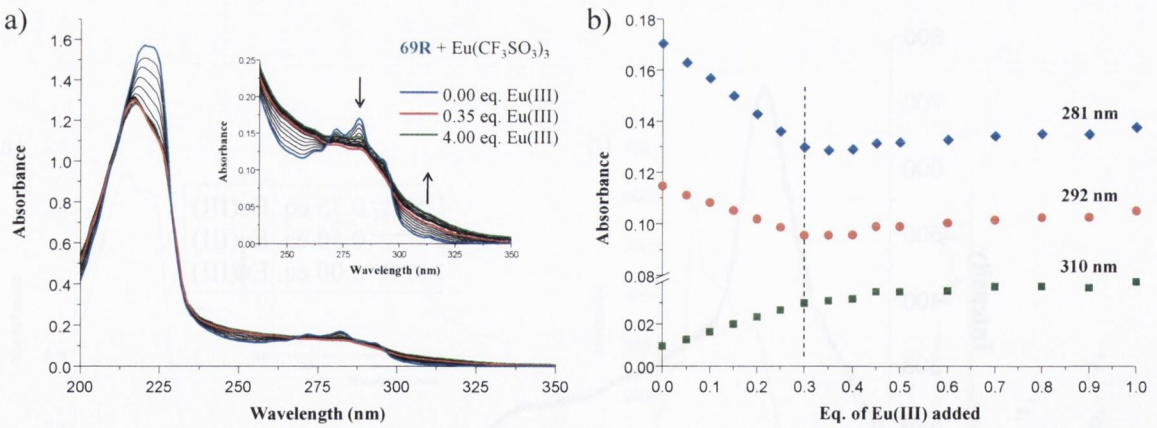

Figure A4.10: *a) Changes in the absorption spectra of* ***69R*** *(1 × 10^{-5} M) upon titrating with $Eu(CF_3SO_3)_3$ (0.00 → 4.00 eq.) in CH_3CN at 298 K. b) Binding isotherms for the titration measured at 281 nm, 292 nm, and 310 nm.*

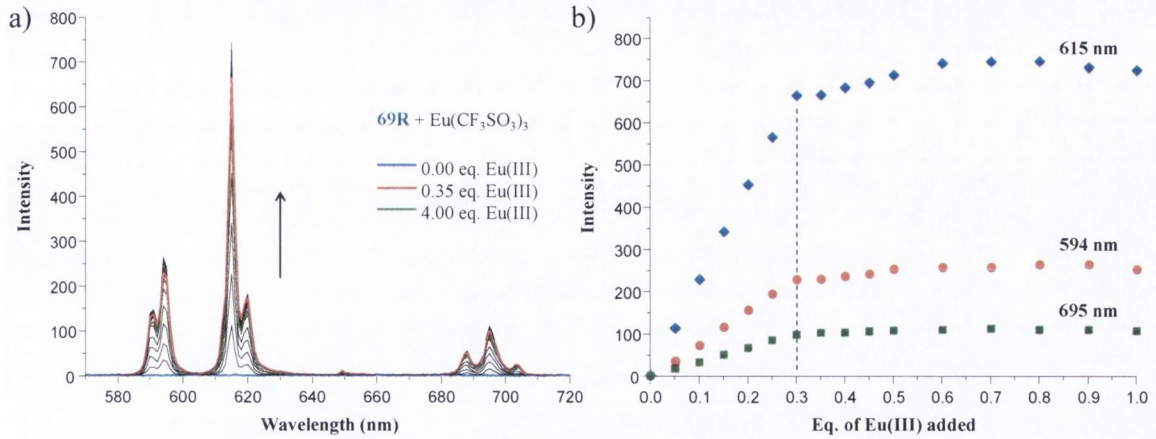

Figure A4.11: *a) Evolution of the phosphorescence emission in the titration of* ***69R*** *(1×10^{-5} M) with $Eu(CF_3SO_3)_3$ (0.00 → 4.00 eq.) in CH_3CN at 298 K (λ_{exc} = 281 nm). b) Binding isotherms for the titration measured at 594 nm, 615 nm, and 695 nm.*

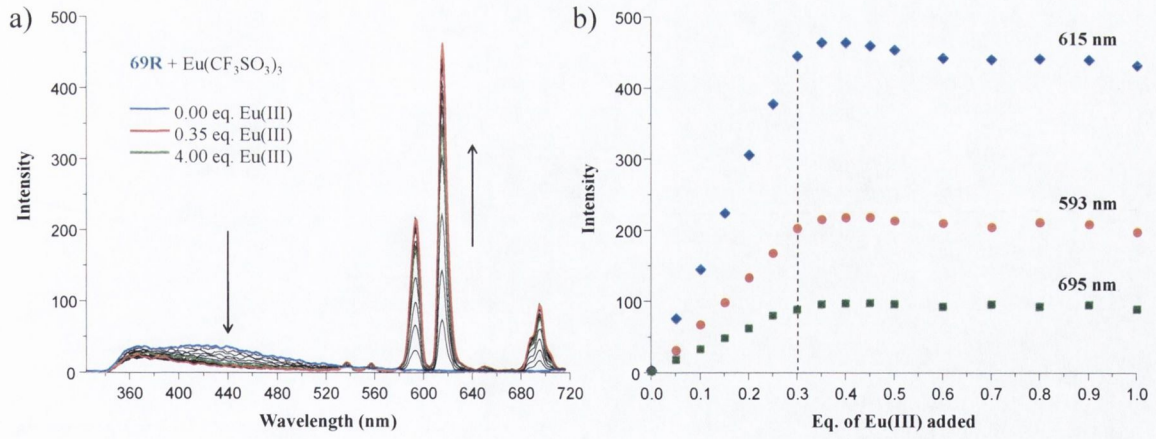

Figure A4.12: *a) Changes in the fluorescence spectra of* ***69R*** *(1×10^{-5} M) upon titrating with $Eu(CF_3SO_3)_3$ (0.00 → 4.00 eq.) in CH_3CN at 298 K. b) Binding isotherms for the titration measured at 593 nm, 615 nm, and 695 nm.*

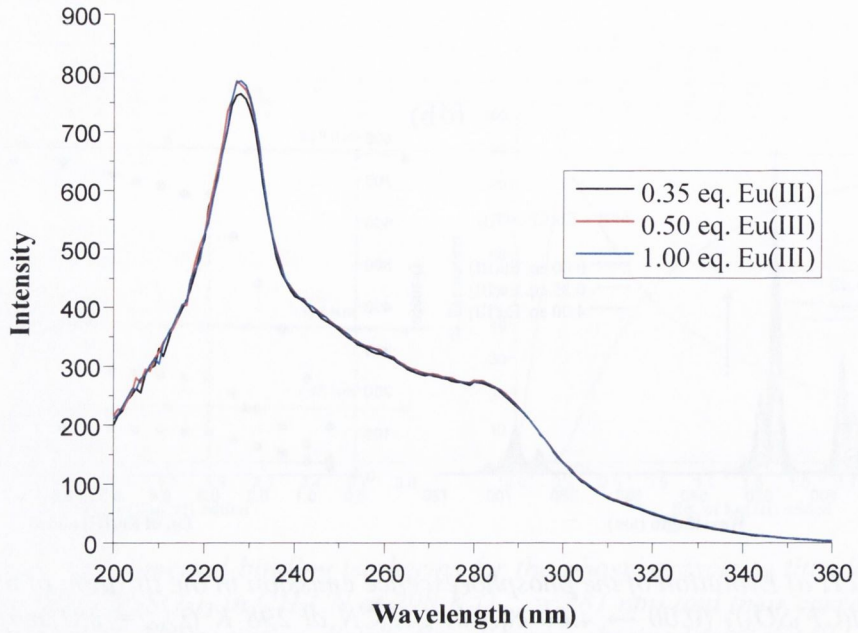

Figure A4.13: *Phosphorescence excitation spectra measured at 616 nm for the titration of* ***69R*** *(1×10^{-5} M) with $Eu(CF_3SO_3)_3$ (0.00 → 4.00 eq.) in CH_3CN at 298 K.*

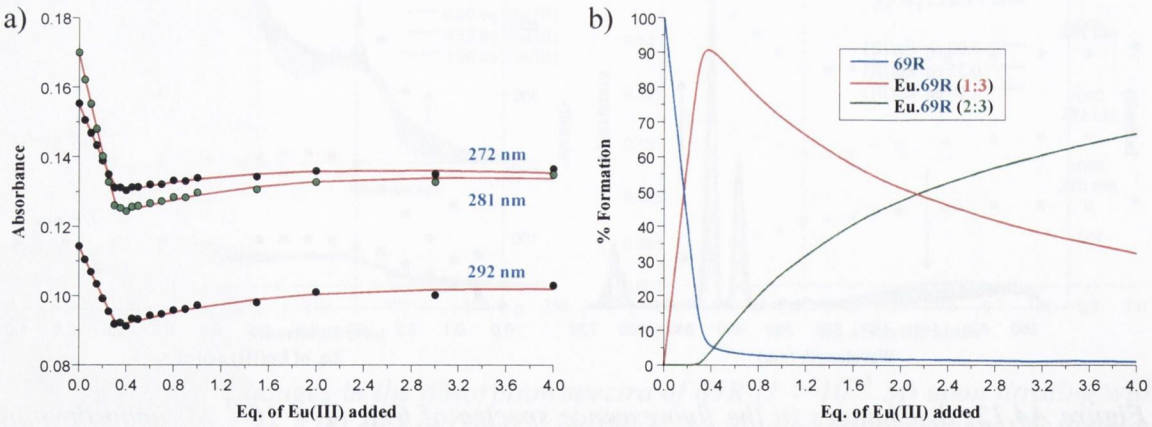

Figure A4.14: *a) Experimental binding isotherms for the UV-vis absorption titration of* ***69R*** *(1×10^{-5} M) with $Eu(CF_3SO_3)_3$ in CH_3CN at 298 K (λ_{exc} = 281 nm) and their corresponding fit by means of SPECFIT. b) Speciation-distribution diagram obtained from the fit.*

Appendix 5

Table A5.1: *Summary of the binding constants obtained through data fitting for the phosphorescence titrations of* ***72S*** *and* ***72R*** *(1 × 10^{-5} M) with $Eu(CF_3SO_3)_3$ in $CHCl_3/CH_3CN$ (1:1; v/v), with percentage composition of the 4:6 (M:L) species at 0.7 eq. of Eu(III).*

Ligand	log $\beta_{1:2}$	log $\beta_{2:3}$	log $\beta_{2:1}$	% of 4:6 (M:L) species at 0.7 eq. of Eu(III)
72S	17.92 ± 0.52	72.71 ± 0.93	15.09 ± 0.36	81
72R	18.90 ± 0.56	76.72 ± 1.01	15.37 ± 0.40	91

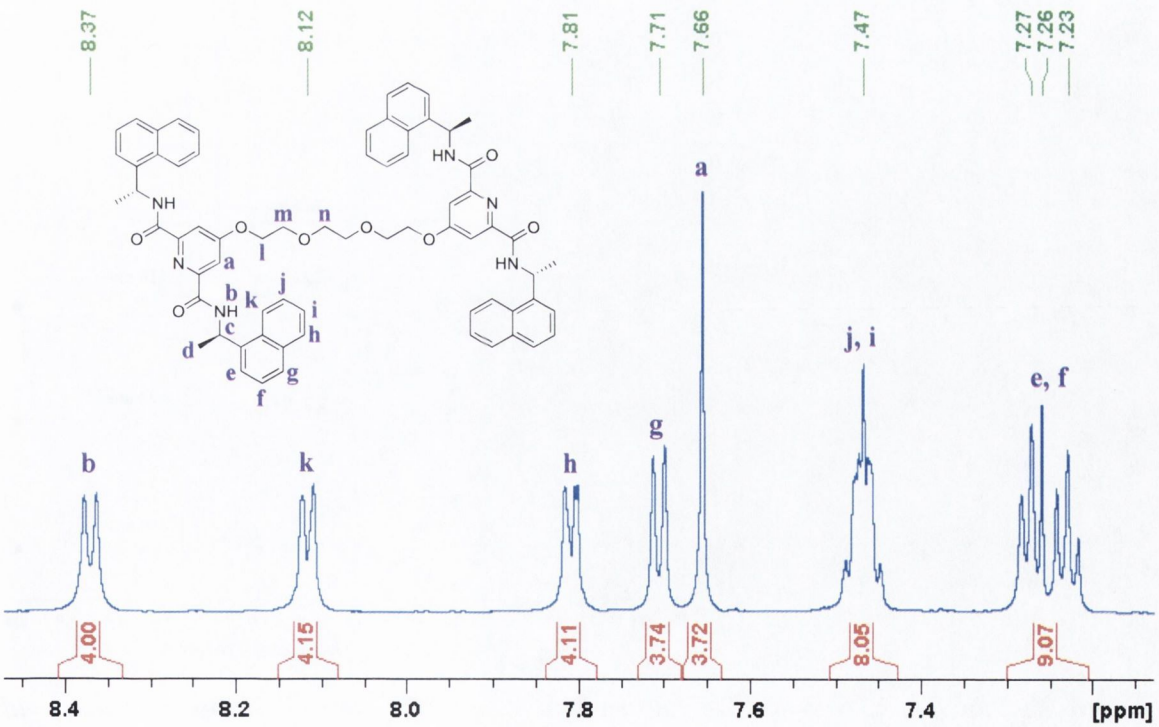

Figure A5.1: *^1H NMR (600 MHz, $CDCl_3$) spectrum of ligand* ***72R*** *focusing on the aromatic signals.*

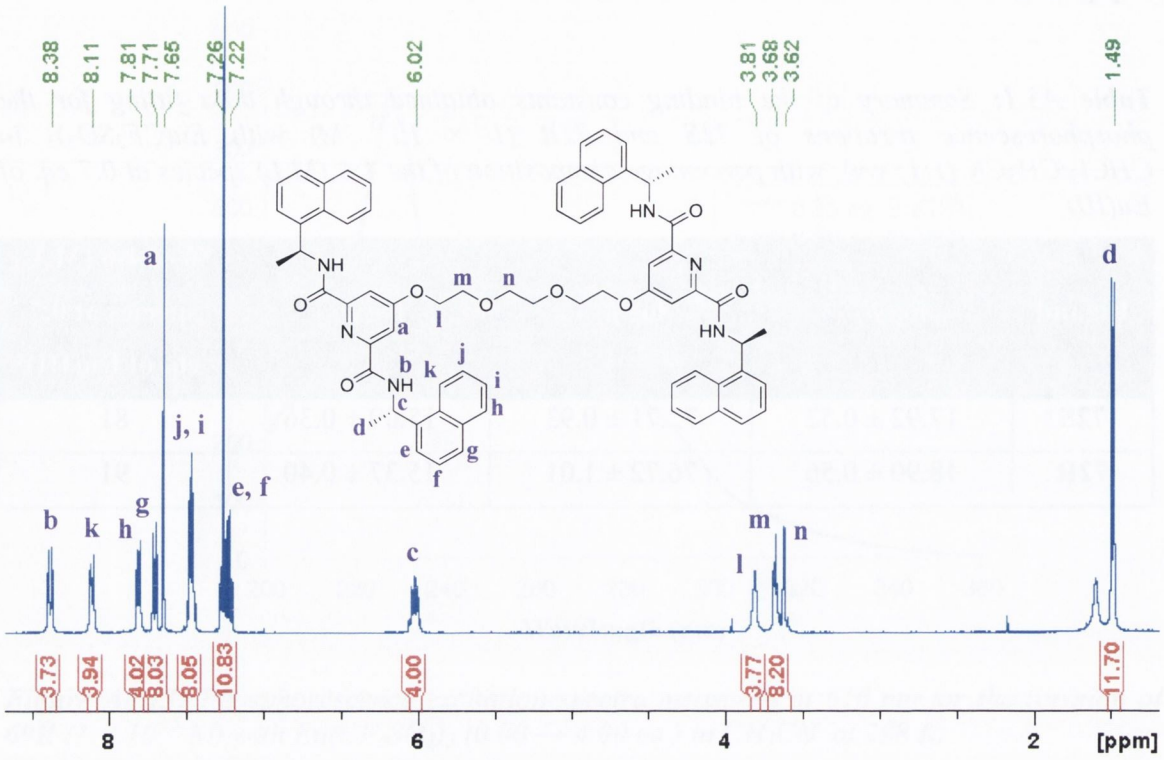

Figure A5.2: *^{1}H NMR (400 MHz, $CDCl_3$) spectrum of ligand* ***72S****.*

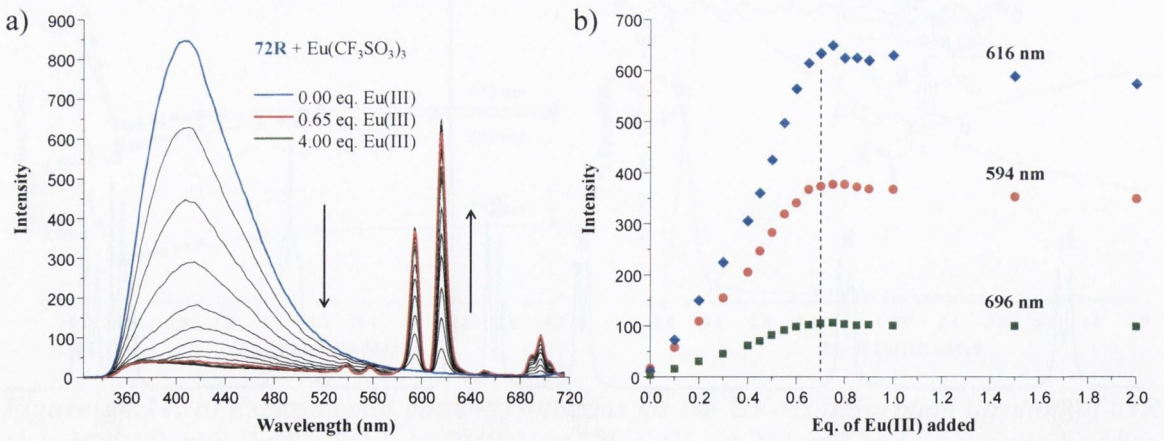

Figure A5.3: *a) Changes in the fluorescence spectra of* ***72R*** *(1×10^{-5} M) upon titrating with $Eu(CF_3SO_3)_3$ (0.00 → 4.00 eq.) in $CHCl_3/CH_3CN$ (1:1; v/v) at 298 K. b) Binding isotherms for the titration measured at 594 nm, 616 nm, 696 nm.*

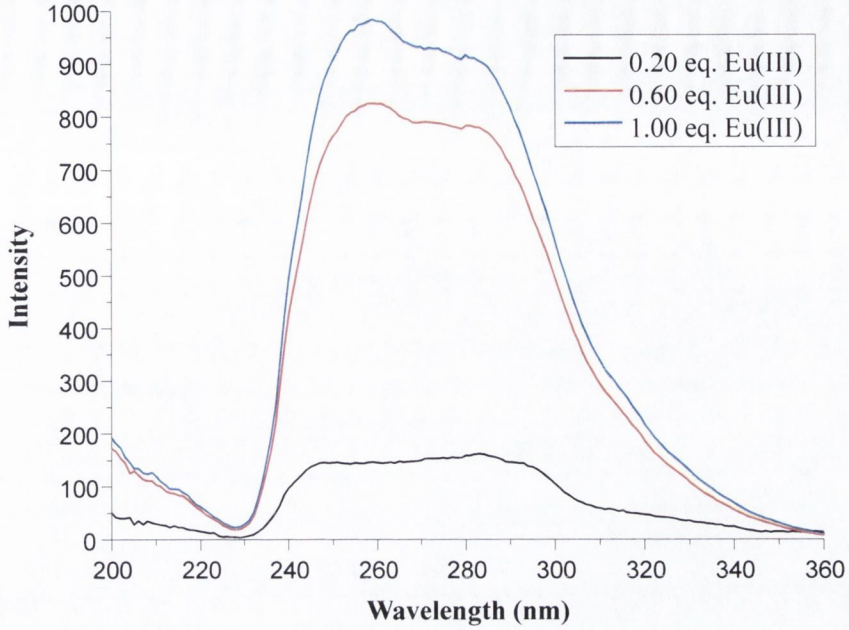

Figure A5.4: *Phosphorescence excitation spectra measured at 616 nm for the titration of* ***72R*** *(1×10^{-5} M) with $Eu(CF_3SO_3)_3$ (0.00 → 4.00 eq.) in $CHCl_3/CH_3CN$ (1:1; v/v) at 298 K.*

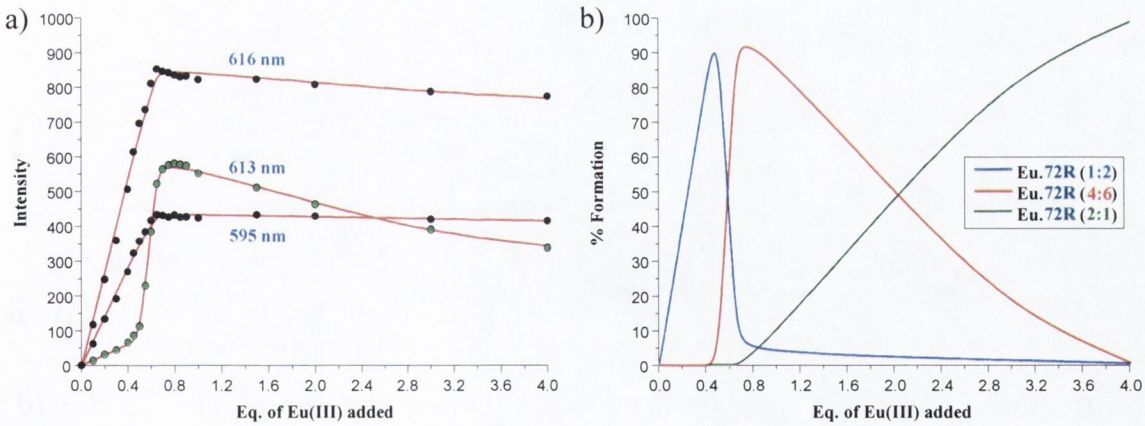

Figure A5.5: *a) Experimental binding isotherms for the phosphorescence titration of* ***72R*** *(1×10^{-5} M) with $Eu(CF_3SO_3)_3$ in $CHCl_3/CH_3CN$ (1:1; v/v) at 298 K (λ_{exc} = 281 nm) and their corresponding fit by means of SPECFIT, accounting for the 4:6 (M:L) species. b) Speciation-distribution diagram obtained from the fit.*

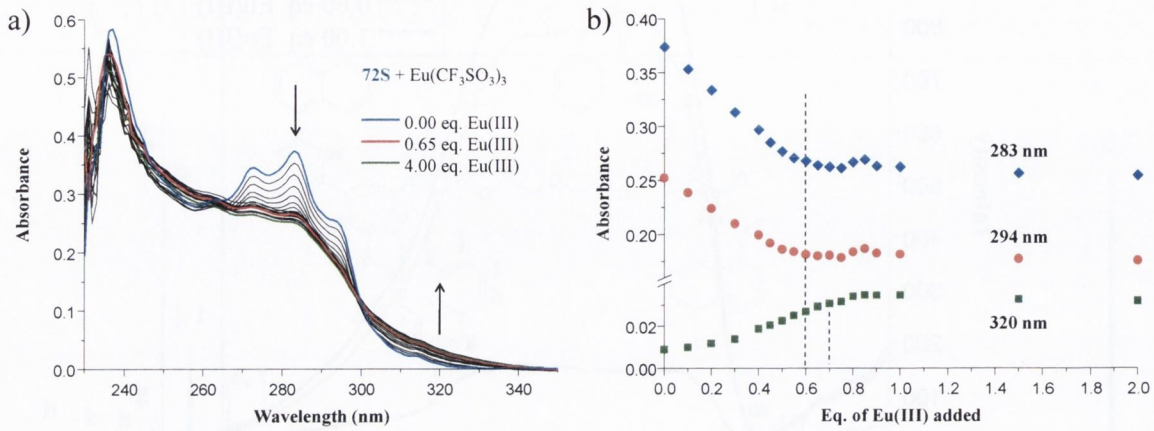

Figure A5.6: *a) Changes in the absorption spectra of* ***72S*** *(1 × 10^{-5} M) upon titrating with $Eu(CF_3SO_3)_3$ (0.00 → 4.00 eq.) in $CHCl_3/CH_3CN$ (1:1; v/v) at 298 K. b) Binding isotherm for the titration measured at 283 nm, 294 nm, 320 nm.*

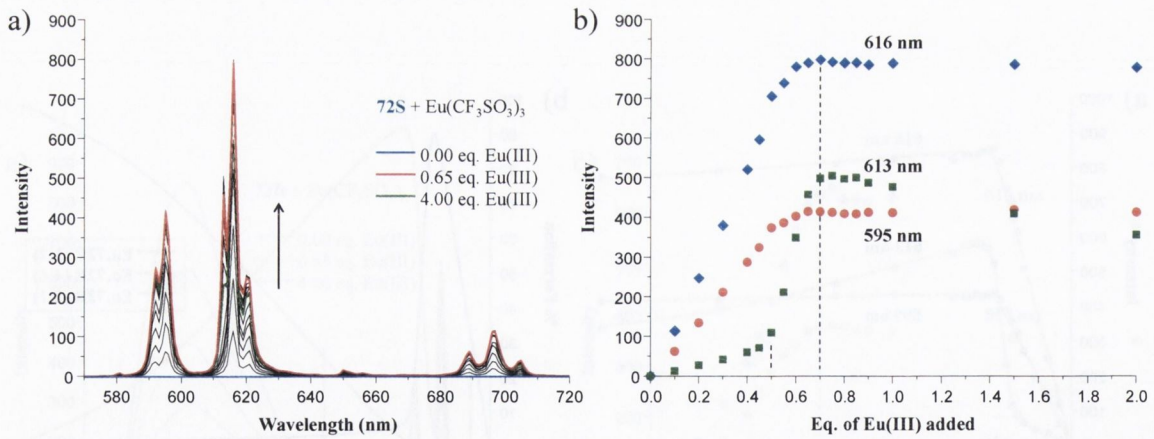

Figure A5.7: *a) Evolution of the phosphorescence emission in the titration of* ***72S*** *(1 × 10^{-5} M) with $Eu(CF_3SO_3)_3$ (0.00 → 4.00 eq.) in $CHCl_3/CH_3CN$ (1:1; v/v) at 298 K (λ_{exc} = 281 nm). b) Binding isotherms for the titration measured at 595 nm, 613 nm, and 616 nm.*

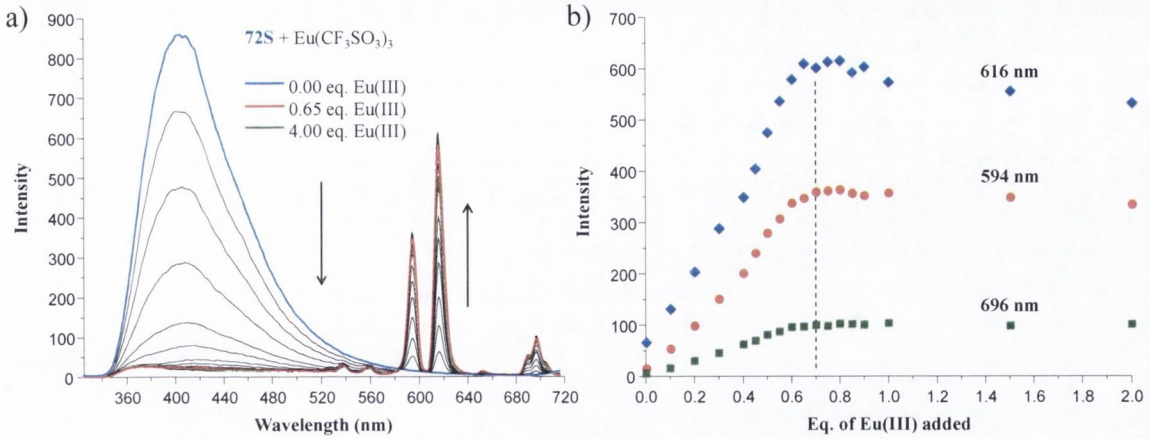

Figure A5.8: *a) Changes in the fluorescence spectra of* ***72S*** *(1×10^{-5} M) upon titrating with $Eu(CF_3SO_3)_3$ (0.00 → 4.00 eq.) in $CHCl_3/CH_3CN$ (1:1; v/v) at 298 K. b) Binding isotherms for the titration measured at 594 nm, 616 nm, 696 nm.*

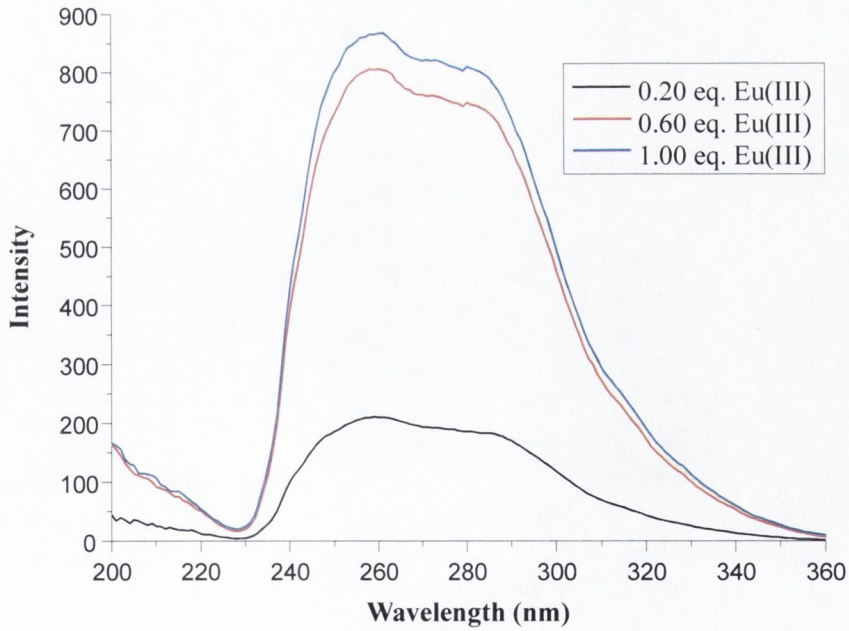

Figure A5.9: *Phosphorescence excitation spectra measured at 616 nm for the titration of* ***72S*** *(1×10^{-5} M) with $Eu(CF_3SO_3)_3$ (0.00 → 4.00 eq.) in $CHCl_3/CH_3CN$ (1:1; v/v) at 298 K.*

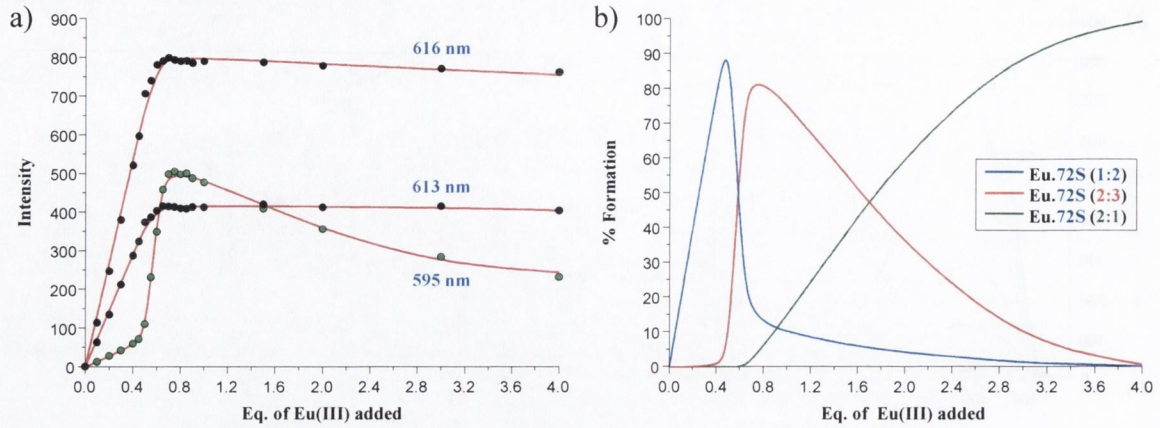

Figure A5.10: *a) Experimental binding isotherms for the phosphorescence titration of* ***72S*** *(1 × 10^{-5} M) with $Eu(CF_3SO_3)_3$ in $CHCl_3/CH_3CN$ (1:1; v/v) at 298 K (λ_{exc} = 281 nm) and their corresponding fit by means of SPECFIT, accounting for the 2:3 (M:L) species. b) Speciation-distribution diagram obtained from the fit.*

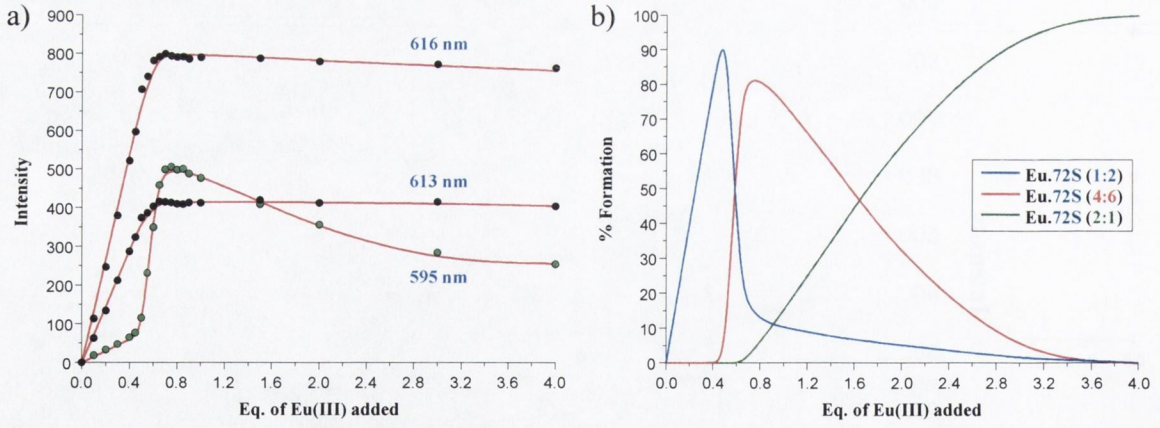

Figure A5.11: *a) Experimental binding isotherms for the phosphorescence titration of* ***72S*** *(1 × 10^{-5} M) with $Eu(CF_3SO_3)_3$ in $CHCl_3/CH_3CN$ (1:1; v/v) at 298 K (λ_{exc} = 281 nm) and their corresponding fit by means of SPECFIT, accounting for the 4:6 (M:L) species. b) Speciation-distribution diagram obtained from the fit.*

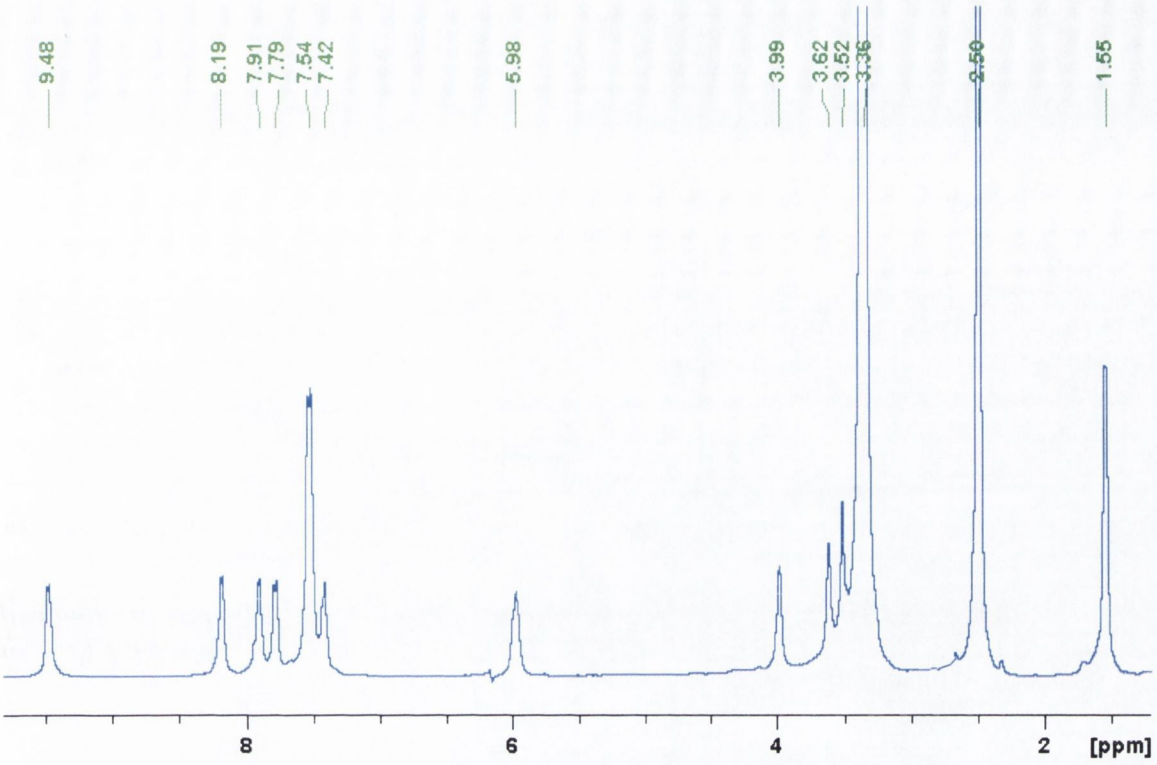

Figure A5.12: *^{1}H NMR (400 MHz, DMSO-d_6) spectrum of complex* ***Eu.72R (M:L = 2:3)****.*

Appendix 6

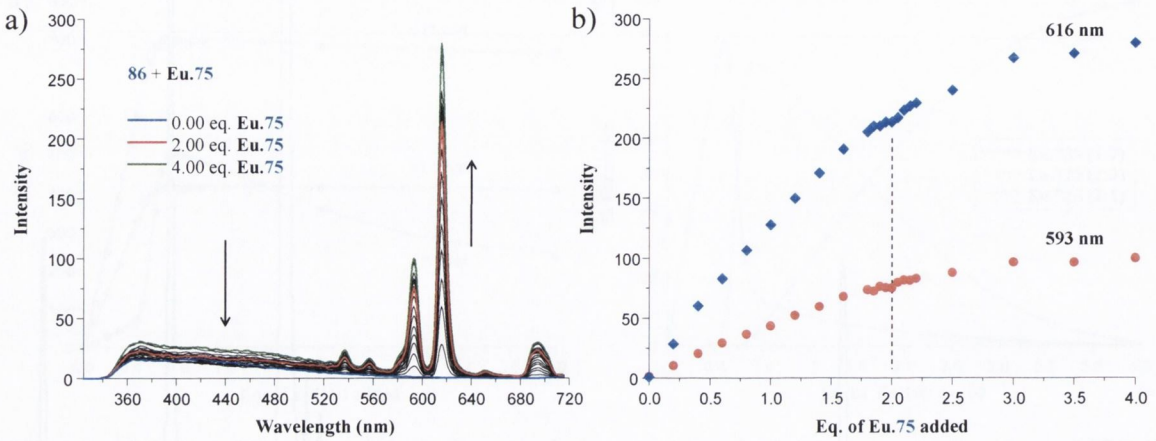

Figure A6.1: *a) Changes in the fluorescence spectra of* ***86*** *(1×10^{-5} M) upon titrating with complex* ***Eu.75*** *(0.00 → 4.00 eq.) in MeOH at 298 K. b) Binding isotherms for the titration measured at 593 nm and 616 nm.*

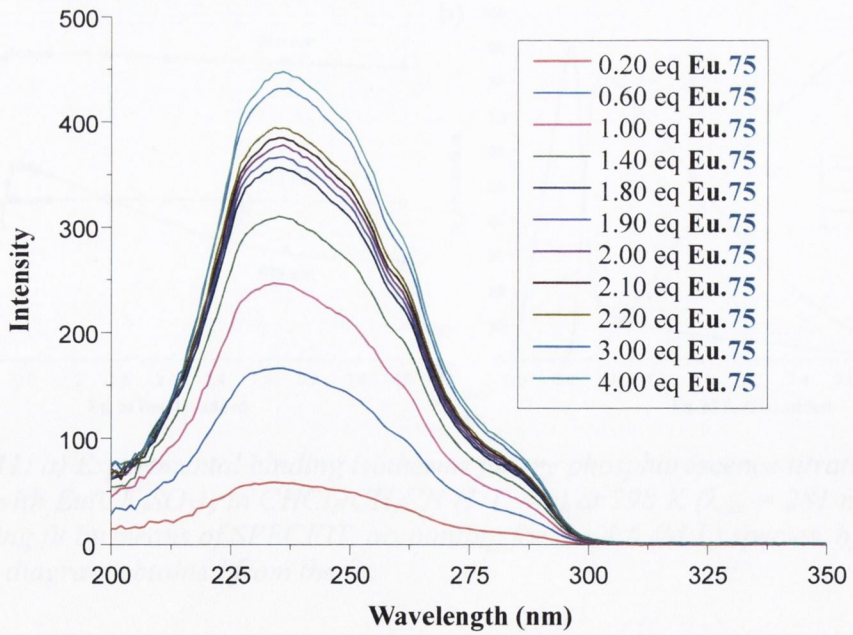

Figure A6.2: *Phosphorescence excitation spectra measured at 616 nm for the titration of* ***86*** *(1×10^{-5} M) with complex* ***Eu.75*** *(0.00 → 4.00 eq.) in MeOH at 298 K.*

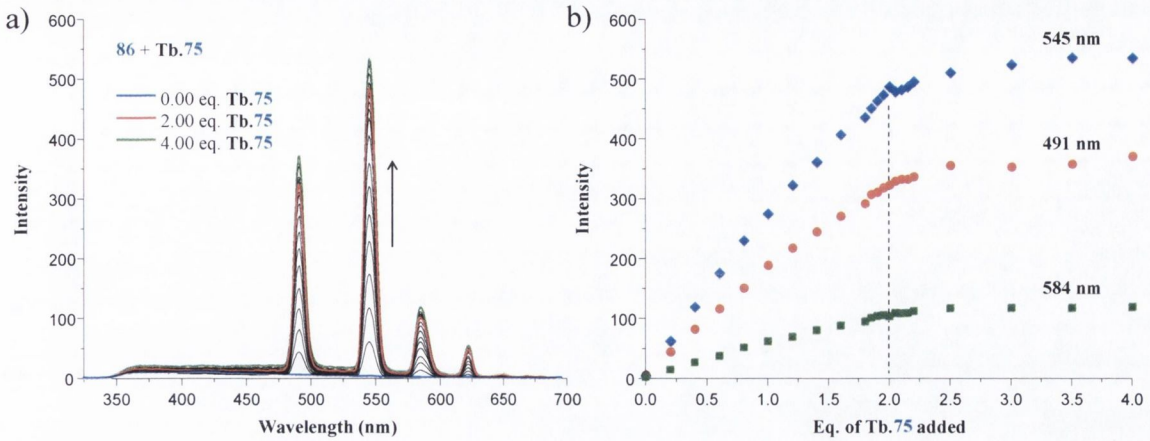

Figure A6.3: *a) Changes in the fluorescence spectra of* ***86*** *(1 × 10^{-5} M) upon titrating with complex* ***Tb.75*** *(0.00 → 4.00 eq.) in MeOH at 298 K. b) Binding isotherms for the titration measured at 491 nm, 545 nm, and 584 nm.*

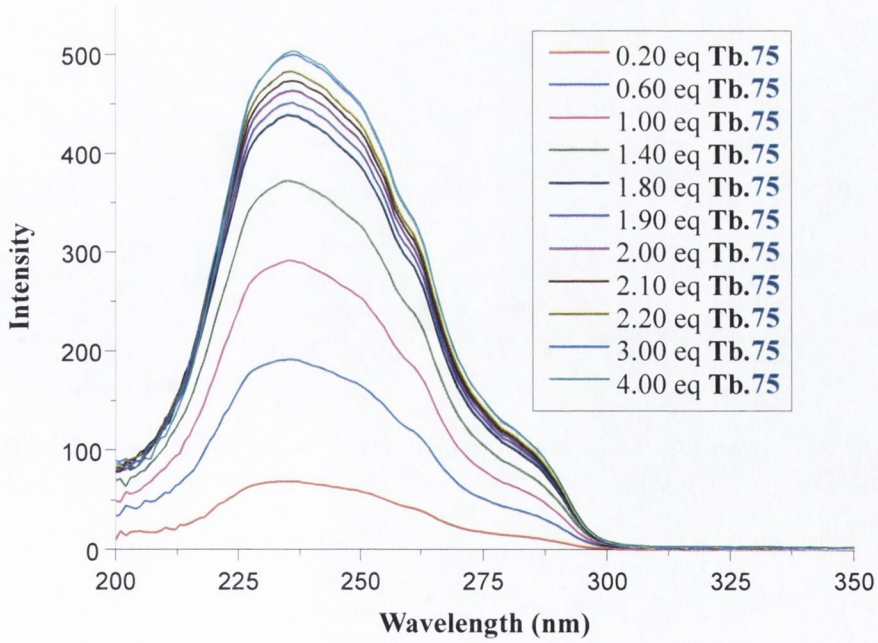

Figure A6.4: *Phosphorescence excitation spectra measured at 545 nm for the titration of* ***86*** *(1 × 10^{-5} M) with complex* ***Tb.75*** *(0.00 → 4.00 eq.) in MeOH at 298 K.*

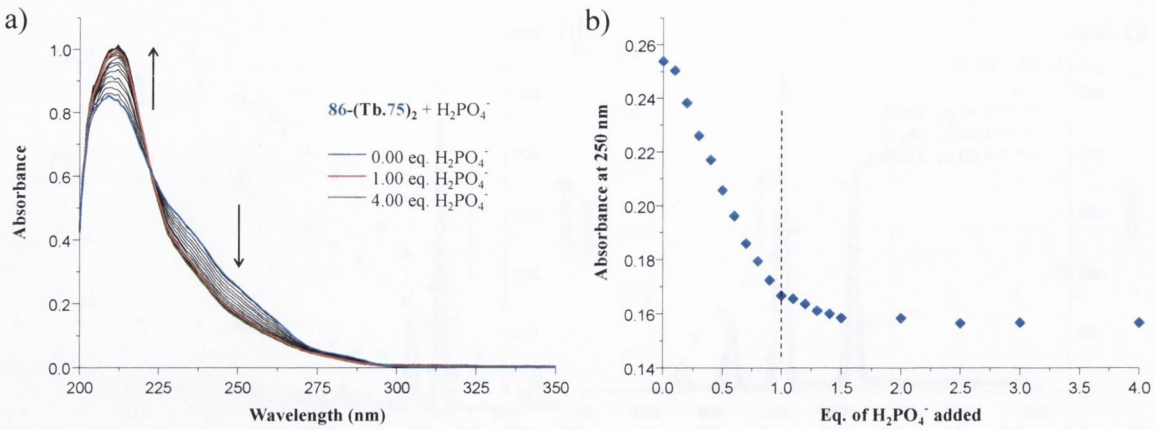

Figure A6.5: *a) Changes in the absorption spectra of* ***86-(Tb.75)$_2$*** *([**86**] = 1 × 10^{-5} M) upon titrating with $H_2PO_4^-$ (0.00 → 4.00 eq.) in MeOH at 298 K. b) Binding isotherm for the titration measured at 250 nm.*

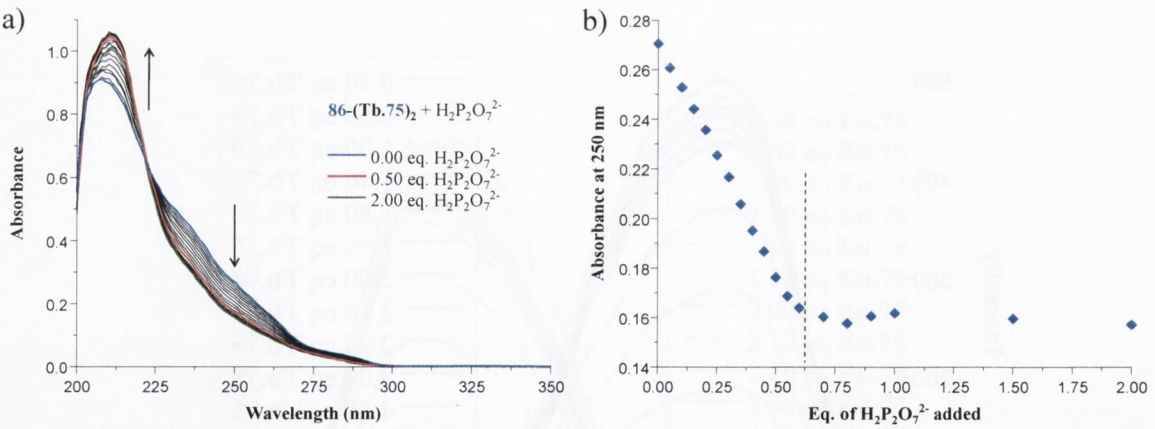

Figure A6.6: *a) Changes in the absorption spectra of* ***86-(Tb.75)$_2$*** *([**86**] = 1 × 10^{-5} M) upon titrating with $H_2P_2O_7^{2-}$ (0.00 → 2.00 eq.) in MeOH at 298 K. b) Binding isotherm for the titration measured at 250 nm.*

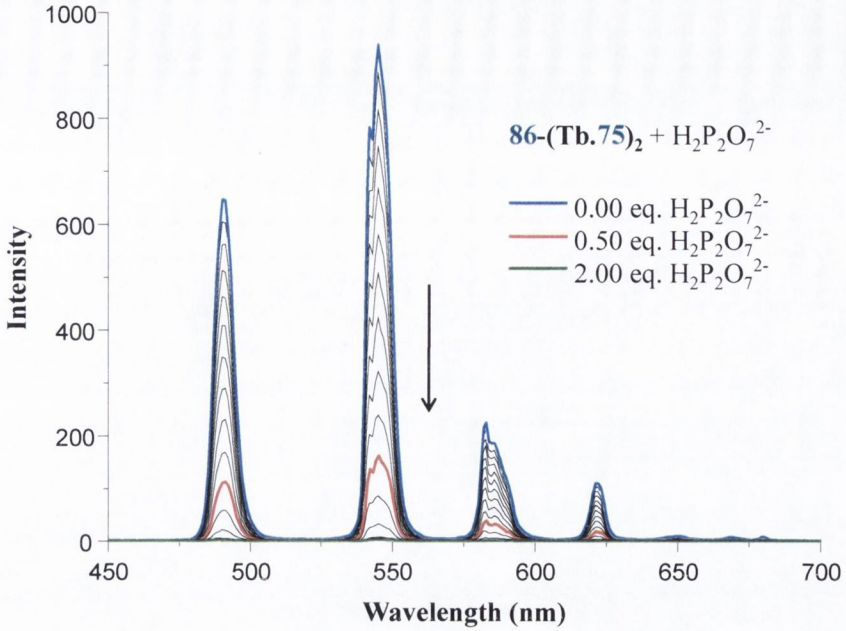

Figure A6.7: *Changes in the phosphorescence spectra of* ***86-(Tb.75)$_2$*** *([**86**] = 1 × 10^{-5} M) upon titrating with $H_2P_2O_7^{2-}$ (0.00 → 2.00 eq.) in MeOH at 298 K (λ_{exc} = 279 nm).*

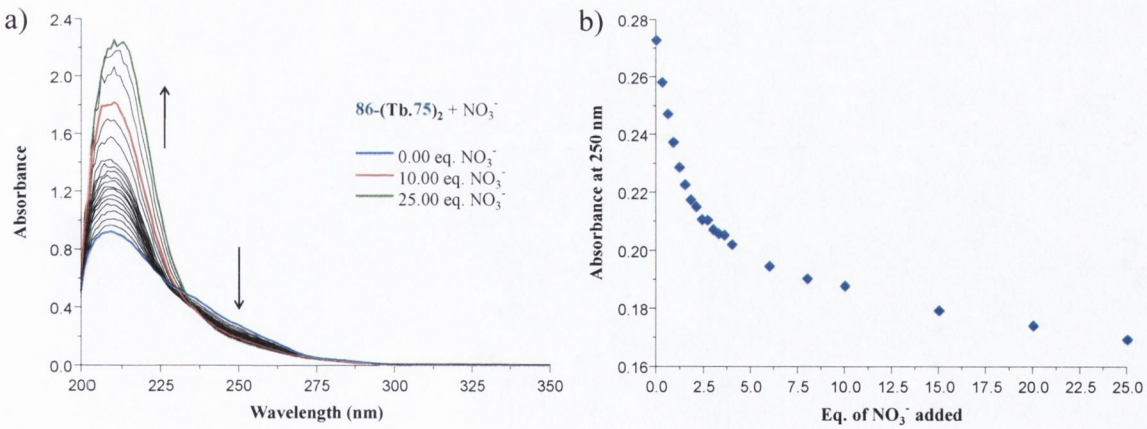

Figure A6.8: *a) Changes in the absorption spectra of* ***86-(Tb.75)$_2$*** *([**86**] = 1 × 10^{-5} M) upon titrating with NO_3^- (0.00 → 25.00 eq.) in MeOH at 298 K. b) Binding isotherm for the titration measured at 250 nm.*

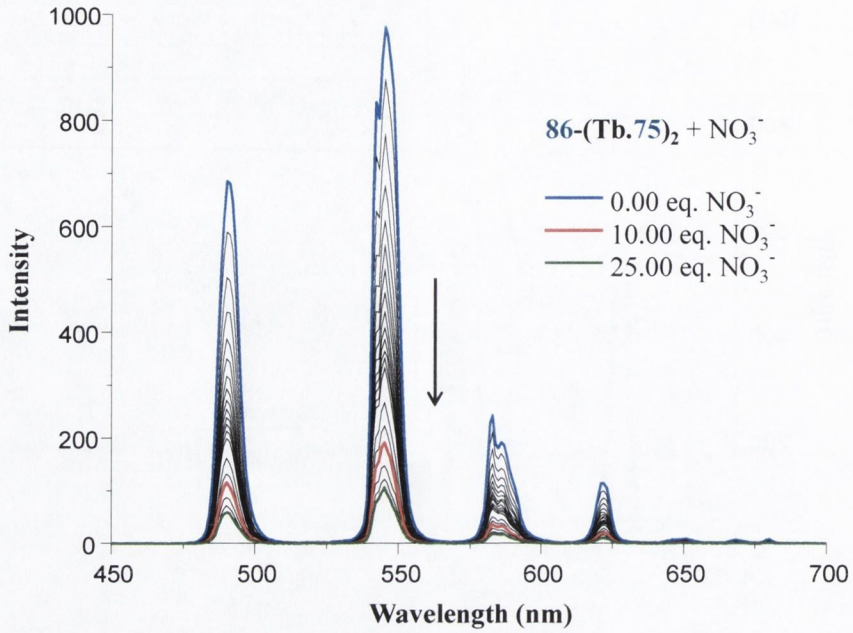

Figure A6.9: *Changes in the phosphorescence spectra of* ***86-(Tb.75)$_2$*** *([86] = 1 × 10^{-5} M) upon titrating with NO_3^- (0.00 → 25.00 eq.) in MeOH at 298 K (λ_{exc} = 279 nm).*

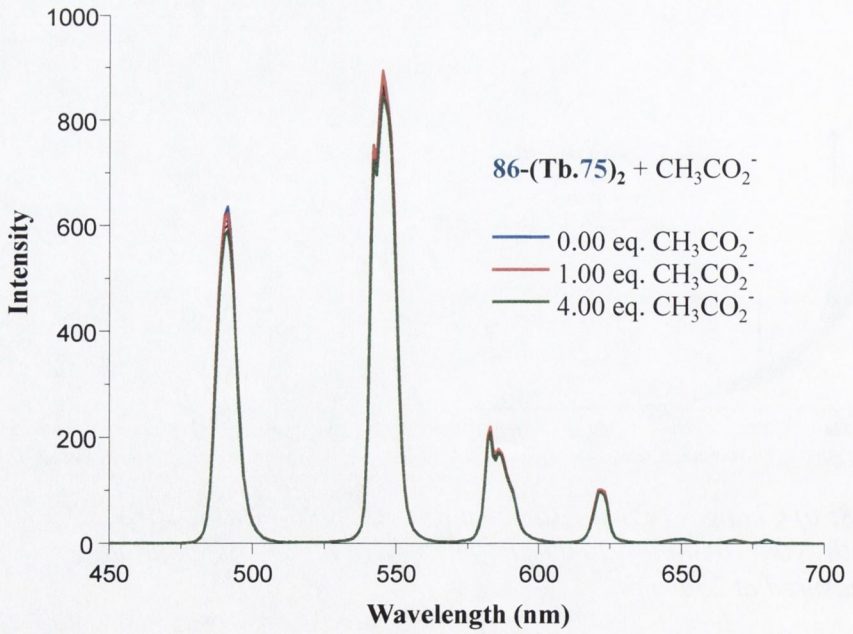

Figure A6.10: *Changes in the phosphorescence spectra of* ***86-(Tb.75)$_2$*** *([86] = 1 × 10^{-5} M) upon titrating with $CH_3CO_2^-$ (0.00 → 4.00 eq.) in MeOH at 298 K (λ_{exc} = 279 nm).*

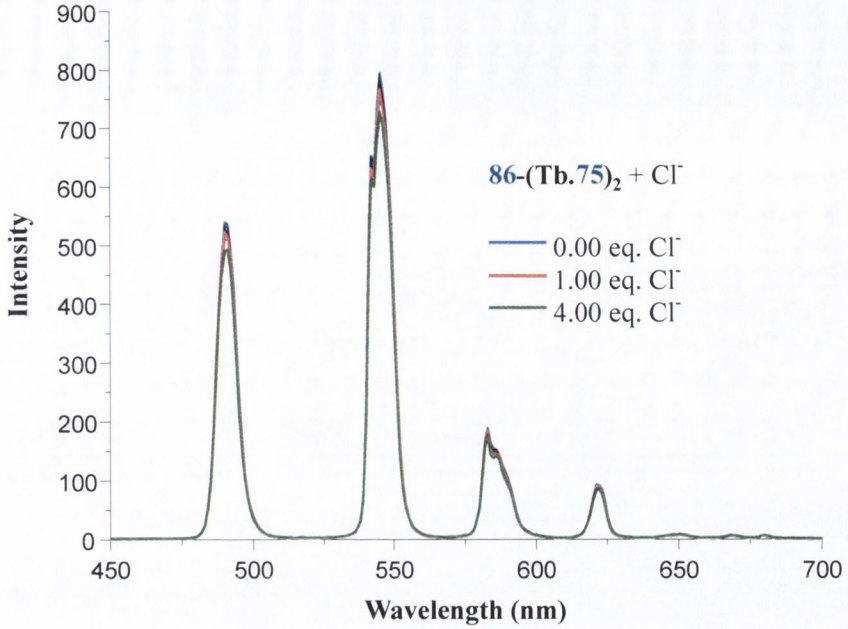

Figure A6.11: *Changes in the phosphorescence spectra of* ***86-(Tb.75)$_2$*** *([**86**] = 1 × 10^{-5} M) upon titrating with Cl^- (0.00 → 4.00 eq.) in MeOH at 298 K (λ_{exc} = 279 nm).*

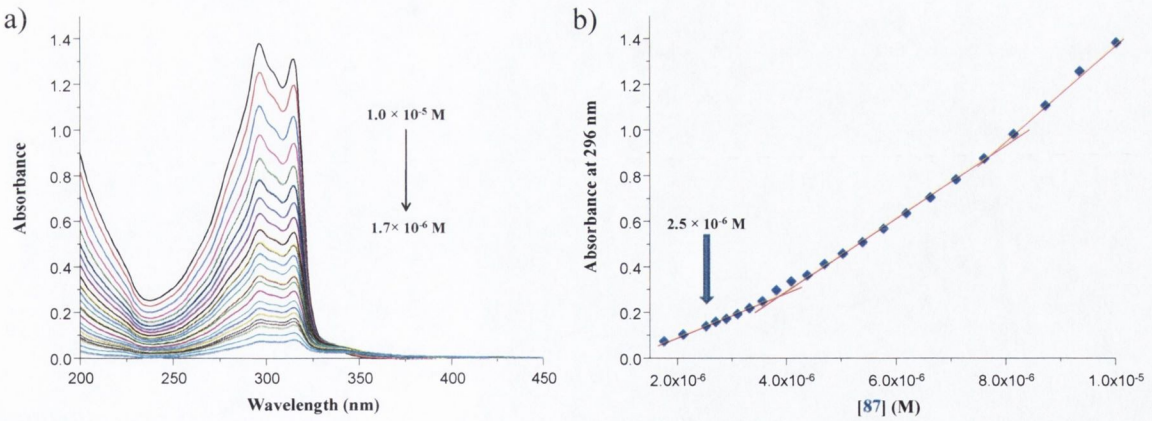

Figure A6.12: *Concentration linearity test for* ***87*** *showing a) the changes in the absorption spectra upon systematic dilution from 1.0 × 10^{-5} M → 1.7 × 10^{-6} M, with b) a plot of absorbance at 296 nm Vs. [**87**] (M).*

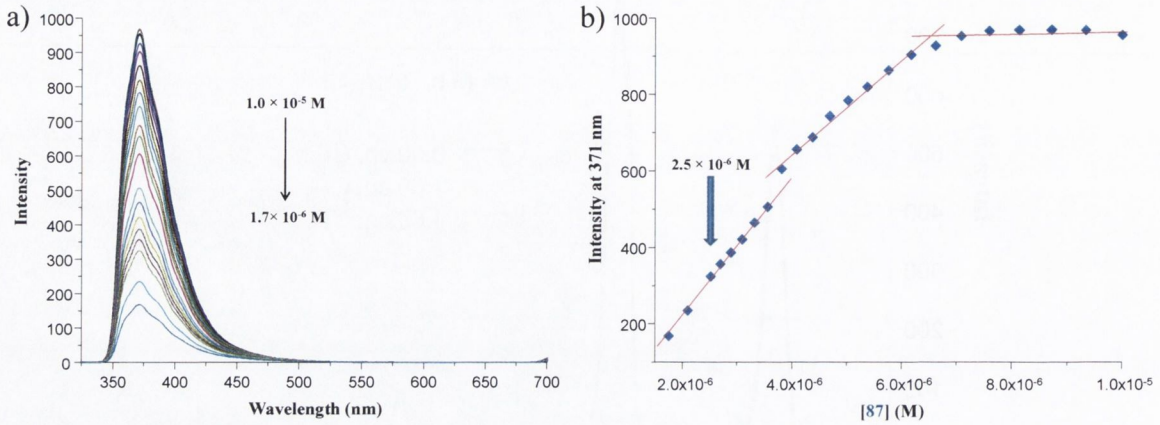

Figure A6.13: *Concentration linearity test for* ***87*** *showing a) the changes in the fluorescence spectra upon systematic dilution from 1.0 × 10^{-5} M → 1.7 × 10^{-6} M, with b) a plot of emission intensity at 371 nm Vs. [****87****] (M).*

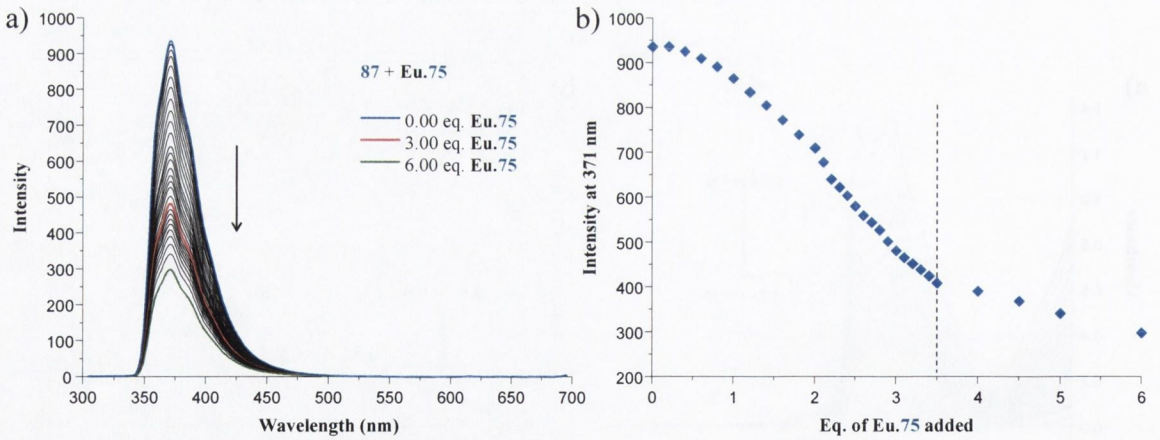

Figure A6.14: *a) Changes in the fluorescence spectra of* ***87*** *(2.5 × 10^{-6} M) upon titrating with complex* ***Eu.75*** *(0.00 → 6.00 eq.) in 0.1 M Tris aqueous buffer (pH 7.4) at 298 K. b) Binding isotherm for the titration measured at 371 nm.*

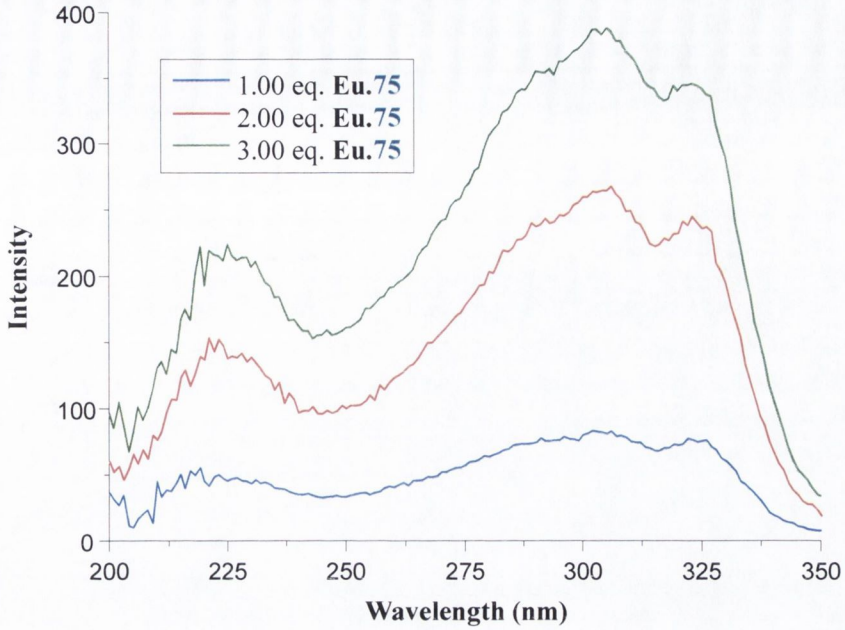

Figure A6.15: *a) Phosphorescence excitation spectra measured at 616 nm for the titration of* ***87*** *(2.5 × 10^{-6} M) with complex* ***Eu.75*** *(0.00 → 6.00 eq.) in 0.1 M Tris aqueous buffer (pH 7.4) at 298 K.*

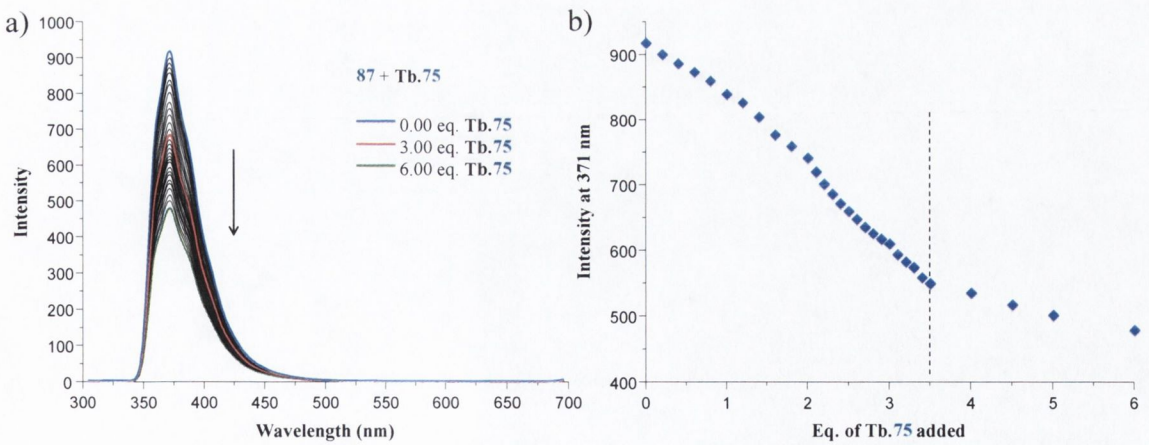

Figure A6.16: *a) Changes in the fluorescence spectra of* ***87*** *(2.5 × 10^{-6} M) upon titrating with complex* ***Tb.75*** *(0.00 → 6.00 eq.) in 0.1 M Tris aqueous buffer (pH 7.4) at 298 K. b) Binding isotherm for the titration measured at 371 nm.*

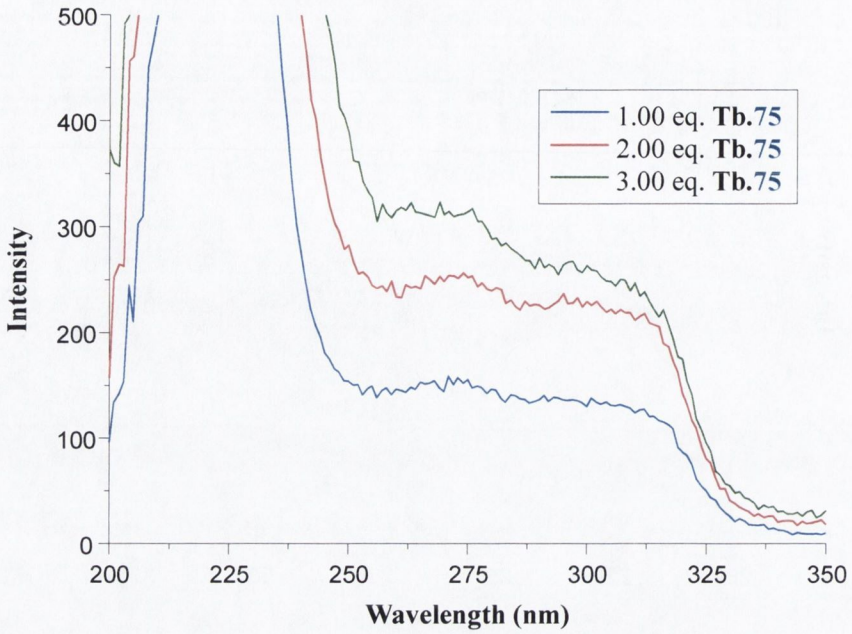

Figure A6.17: *a) Phosphorescence excitation spectra measured at 545 nm for the titration of* ***87*** *(2.5 × 10^{-6} M) with complex* ***Tb.75*** *(0.00 → 6.00 eq.) in 0.1 M Tris aqueous buffer (pH 7.4) at 298 K.*